Titre: Title:	Seismic Design and Qualification of All-Steel Buckling-Restrained Braced Frames for Canadian Applications
Auteur: Author:	Morteza Dehghani
Date:	2016
Type:	Mémoire ou thèse / Dissertation or Thesis
Référence: Citation:	Dehghani, M. (2016). Seismic Design and Qualification of All-Steel Buckling-Restrained Braced Frames for Canadian Applications [Ph.D. thesis, École Polytechnique de Montréal]. PolyPublie. https://publications.polymtl.ca/2438/

UNIVERSITÉ DE MONTRÉAL

SEISMIC DESIGN AND QUALIFICATION OF ALL-STEEL BUCKLING-RESTRAINED BRACED FRAMES FOR CANADIAN APPLICATIONS

MORTEZA DEHGHANI

DÉPARTEMENT DES GÉNIES CIVIL, GÉOLOGIQUE, ET DES MINES

ÉCOLE POLYTECHNIQUE DE MONTRÉAL

THÈSE PRÉSENTÉE EN VUE DE L'OBTENTION

DU DIPLÔME DE PHILOSOPIAE DOCTOR

(GÉNIE CIVIL)

DÉCEMBRE 2016

UNIVERSITÉ DE MONTRÉAL

ÉCOLE POLYTECHNIQUE DE MONTRÉAL

Cette thèse intitulée :

SEISMIC DESIGN AND QUALIFICATION OF ALL-STEEL BUCKLING-RESTRAINED BRACED FRAMES FOR CANADIAN APPLICATIONS

présentée par : DEHGHANI Morteza

en vue de l'obtention du diplôme de : Philosophiae Doctor

a été dûment acceptée par le jury d'examen constitué de :

M. LÉGER Pierre, Ph. D., président

M. TREMBLAY Robert, Ph. D., membre et directeur de recherche

M. BOUAANANI Najib, Ph. D., membre

M. DUSICKA Peter, Ph. D., membre

DEDICATION

To Maryam and Hanna

ACKNOWLEDGEMENTS

I would like to take this opportunity to express my deepest gratitude toward Professor Robert Tremblay whose continuous support and advice has made this work possible. I would also like to thank my evaluation committee members Professors Peter Dusicka, Pierre Léger, and Najib Bouaanani for accepting to review this dissertation. In course of these years I have been benefited from help and support of many individuals. Special thanks are given to the staff of Structural Engineering Laboratory of Polytechnique Montréal for their kind assistance during nearly four years that I spent in the lab. In particular, I am very grateful to Martin Leclerc, Patrice Bélanger, Romain Siguier and Xavier Willem for their direct involvement in this research project. I am also very thankful to my officemates Dr. Poulad Daneshvar, Dr. Fabien Eddy Lagier, Ilona Bartosh, Thierry Béland, and Armin Sadeghian for their support and friendship. Adam Korzekwa graciously shared his Master's thesis work and ideas which is appreciated. Assistance received from Abdelfettah Abouhammada and Xavier Lachapelle-Touillard in conducting BRB and material tests is acknowledged. The scholarship awarded by Structural Steel Education Foundation (SSEF) is also acknowledged and appreciated. Steel plates used to fabricate specimens for material testing and BRB cores were donated by Canam-Bridges Company. Fabrication of BRB specimens, and debonding materials were donated by Lainco Inc. Stainless steel sheets were offered by Goodco Z-Tech Company. Contributions and collaborations from the mentioned companies are greatly appreciated. GRS department secretaries Mrs. Manon Latour, Mrs. Anne-Marie Goulet, and Mrs. Julie Dallaire are saluted for their help and kindness.

This endeavor would have not been absolutely possible without unconditional love and support of my beloved wife Maryam Nowrouzi. She deserves an everlasting credit for her endless patience and great kindness. Halfway through this PhD program, our beautiful daughter Hanna was born whose fourth birthday we will be celebrating just after my defence session. Her cute smile was so powerful that I could survived all these hard years.

RÉSUMÉ

Les contreventements à diagonales ductiles confinées (DDC) sont devenus le système de contreventement standard pour les bâtiments et pont pour résister aux charges sismiques. Ce système intègre un concept spécifique de diagonales, appelé, DDC, qui ne flambent pas en compression fournissant ainsi un mécanisme de dissipation d'énergie stable. La capacité de dissipation de l'énergie sismique des DDC est fortement reliée à la performance du mécanisme de retenue du flambement qui prévient le noyau ductile interne de subir une déformation latérale excessive. La force transmise au système de confinement dépend de plusieurs facteurs qui doivent évalués avec précision et intégré lors de la conception.

Dans cette étude, un système DDC robuste aux séismes a été développé et testé expérimentalement pour les conditions de chargement sismique extrêmes qui sont attendues au Canada. Le système de confinement de la diagonale est constitué uniquement d'éléments en acier, ce qui constitue un avantage important pour les fabricants en éliminant le besoin de couler du béton ou mortier. Cette étude combine des recherches expérimentales et analytiques afin de définir les données essentielles pour la conception de ce type de contreventement.

Les contreventements à diagonales ductiles confinées ont récemment été introduits dans les normes canadiennes de conception de bâtiments (NBCC 2010 et S16-09) en tant que système ductile résistant aux forces sismiques latérales. Afin d'estimer la demande en déformation pour la conception de DDC, une étude numérique a été menée sur des bâtiments de plusieurs étages contreventés avec ce système dans l'est et sud-ouest du Canada. Pour ces analyses, on a développé une méthode statistiquement robuste pour la sélection et la mise à l'échelle des données sismiques au sol. Dans cette méthode, les enregistrements sont sélectionnés en fonction des caractéristiques attendues du mouvement du sol en termes d'amplitude, de fréquence et de durée. Contrairement aux méthodes classiques, l'approche proposée est indépendante de la période fondamentale du bâtiment et, par conséquent, un ensemble d'enregistrements échelonnés peut être utilisé pour l'analyse de bâtiments présentant différentes caractéristiques dynamiques. L'étude numérique des DDC a indiqué qu'en général, la performance sismique sous les séismes de conception était satisfaisante. Néanmoins, ces analyses prédisent un déplacement latéral résiduel permanent important qui peut entraver la fonctionnalité du bâtiment immédiatement après le séisme et entraîner un coût de réparation considérable. La demande sismique pour le DDC dans l'est du

Canada est considérablement inférieure à celle de la côte ouest. Cette étude a montré que les charges sismiques de conception du CNBC pour les diaphragmes s'est révélée insuffisante, particulièrement aux étages inférieurs.

Afin d'obtenir des données fiables sur le comportement des matériaux de base, un programme expérimental de caractérisation du matériau utilisé a été réalisé. Les caractéristiques mécaniques de l'acier CSA G40-21 350WT ont été étudiées en réalisant des essais à l'échelle locale à température ambiante et à des températures sous le point de congélation. En particulier, le comportement écrouissant sous chargement cyclique et résistance à la fatigue de cet acier ont été évalués et des modèles prédictifs ont été développés et calibrés pour être utilisés pour la conception du système de retenue. Le modèle étalonné a été mis en œuvre avec succès pour prédire la rupture par fatigue sous plusieurs protocoles de déplacements. Les résultats des essais montrent que ni la contrainte de rupture en traction, ni la fatigue à faible cycle de l'acier 350WT ne sont affectées par les conditions de température sous le point de congélation. Cependant, la combinaison d'une température en dessous de zéro et une vitesse de chargement rapide a conduit à une augmentation considérable de la limite élastique de l'acier.

Une méthode analytique a été développée pour la conception du système de confinement. Cette méthode considère diverses caractéristiques importantes du mécanisme des DDC, telles que l'écrouissage isotrope et cinématique sous sollicitation cyclique de l'acier du noyau, les forces de frottement, l'historique de friction, la rigidité du système de confinement et l'effet de Poisson. En général, les résultats obtenus de la méthode correspondent bien avec les résultats d'études expérimentales et d'analyses par éléments finis.

Dans la dernière phase de ce projet de recherche, le concept proposé pour la DDC a été validé au moyen de douze essais à grande échelle. Différents paramètres ont été étudiés, tel que l'espace libre autour du noyau, les conditions d'interface et la rigidité globale et locale du système de confinement. Trois nouvelles combinaisons de matériaux ont été étudiés pour l'interface noyau-système de confinement. Parmi celles-ci, la combinaison comprenant une tôle d'acier inoxydable et une feuille de UHMW-PE[1] a été jugée la condition d'interface la plus efficace. Une rotule

[1] Polyéthylène de masse molaire très élevée

plastique flexible a été introduite dans l'assemblage entre le DDC et le gousset pour obtenir un comportement stable tout ne minimisant les moments de flexion. Les résultats des essais ont démontré que le détail de rotule était efficace pour contrôler les moments de flexion imposés à la DDC. En plus des protocoles de chargement conventionnel, la performance du système proposé a été vérifiée sous diverses sollicitations sismiques induites par des séismes se produisant en surface de la croûte terrestre et à la jonction entre plaques tectoniques (séismes de subduction). Les observations expérimentales de ce projet ont permis de démontrer que le système DDC développé peut supporter de grandes déformations inélastiques cycliques sans perte de rigidité et de résistance et tout en offrant une ductilité résiduelle post-sismique significative.

ABSTRACT

Buckling-Restrained Braced Frames (BRBF) have become one of the standard ductile lateral systems for building structures and bridges to resist the earthquake loads. This system incorporates special diagonal elements, called BRB, that do not buckle in compression hence providing a stable and nearly symmetrical hysteretic response in tension and compression with high seismic energy dissipation capacity. The energy dissipation capability of BRBs is strongly linked to the performance of buckling restraining mechanism that constrains the internal ductile core from undergoing excessive lateral deformation. The force demand on the restraining system depends on several factors that should be precisely estimated and implemented in design.

In this study a seismically enduring patent-free BRB system was conceptually developed and experimentally qualified for extreme seismic loading conditions that are expected in Canada. The restraining system of the developed BRB is entirely built from steel that would be advantageous for steel fabricators as the need for concrete or mortar casting and curing are eliminated. In the course of this study and in order to acquire the essential data for proper design of the restraining system, a combination of analytical and experimental research is conducted.

BRBF has recently been introduced in the Canadian building design standards (NBCC 2010 and S16-09) as a ductile seismic lateral force resisting system. Aimed at estimation of design deformation demand on BRB elements, a numerical study was conducted on multi-storey code-conforming BRBFs in eastern and southwestern Canada. For time history analysis, a statistically robust method for ground motion record selection and scaling was developed. In this method records are selected based on the expected ground motion characteristics in terms of amplitude, frequency content and duration. Unlike conventional methods, the proposed approach is independent of the building fundamental period and accordingly one set of scaled records can be used for analysis of buildings with different dynamic characteristics. Numerical studies indicated that, in general, the seismic performance of BRBFs under design earthquakes is satisfactory. Nevertheless, these analyses predicted significant residual displacements which may impose considerable repair cost. The seismic demand on BRBFs in eastern Canada was found to be considerably lower than that of the west coast. This study also showed that the current NBCC design load for floor diaphragms could be significantly exceeded, especially at lower storeys.

In order to obtain reliable data on core material behaviour an experimental material characterization program was carried out. In this phase, important features of CSA G40-21 350WT steel were investigated by testing small-scale material specimens at room and subfreezing temperatures. In particular, the cyclic hardening behaviour and the low cycle fatigue life of this material were evaluated and the predictive models were developed and calibrated to be used in the design of the restrainer system. The calibrated model was successfully implemented to predict the failure life under several variable-amplitude loading patterns. For the conditions examined in this test program, the results show that neither the tensile fracture strain nor the low cycle fatigue of 350WT steel is affected by subfreezing temperature conditions. However, the combination of cold temperature and fast loading rates resulted in considerable increase in the yield strength of this type of steel.

An analytical method was developed to design the restrainer system. This method accounts for various important features of the BRB mechanism such as the cyclic strain hardening of the core, friction path, the constraining stiffness of the restrainer, and the Poisson's effect. In general, predictions from the method agree well with results from past experimental data and finite element analysis simulations.

In the final phase, the developed BRB concept was evaluated through twelve full-scale tests. Various parameters such as gap, core-restrainer interfacial condition, and global and local stiffness of restrainer were investigated. Three new debonding material were proposed and qualified experimentally. Of the three tested cases, the combination of stainless steel sheets and UHMW-PE[2] was found to be the most efficient option. A simple hinge connection for BRB-to-gusset plate joint was developed and implemented in the test specimens. Experimental observations indicated that the proposed hinge was effective to mitigate the damaging flexural demand on the BRB system. In addition to the standard loading, the performance of the developed system under repeated seismic loading was also considered and the loading histories from crustal and subduction earthquakes were included in the testing program. Experimental observations confirmed that the

[2] Ultra-high-molecular-weight polyethylene

developed BRB system can sustain repeated large inelastic deformations without stiffness and strength degradation, while offering significant post-earthquake ductility capacity.

TABLE OF CONTENTS

LIST OF TABLES

LIST OF FIGURES

LIST OF SYMBOLS AND ABBREVIATIONS

Symbols

A_c	Cross-sectional area of core
A_r	Cross-sectional area of restrainer
C	Back stress hardening modulus
C_f	Axial force demand on column
C_p	Specific heat
C_r	Factored axial force resistance of column
D	Fatigue damage
D_{5-95}	Significant duration (a duration intensity measure)
$D_{\mathrm{Brk.}}$	Bracketed duration (a duration intensity measure)
$D_{\mathrm{Uni.}}$	Uniform duration (a duration intensity measure)
D_{LCF}	Low cycle fatigue damage
E	Young modulus
EL	Elongation at fracture
E_{eff}	Effective hardening modulus
E_t	Tangent modulus at the end of compressive excursion
F_u	Ultimate tensile stress
$F_{y,0.2\%}$	Lower yield stress measured by 0.2% offset method
$F_{y,Upper}$	Upper yield stress
F_{yr}	Nominal yield stress of the restrainer
I_c	Core minor-axis moment of inertia
I_r	Section moment of inertia of BRB restrainer
K	Coefficient of thermal conductivity
K'	Cyclic strength coefficient
K^*	Coefficient of master curve (for non-Masing materials)
$K_{e,\min}$	Minimum constraining stiffness
K_e	Total available constraining stiffness against gap opening
$\boldsymbol{K}_e$	Elastic stiffness matrix of structure
L	BRB effective length (distance between knife-plate hinges)

L_{br}	BRB work-point length
L_e	Length of elastic non-yielding segment
L_s	Slip length along core yielding segment
L_{sc}	Length of core yielding segment
L_t	Moment transfer length
$L_{y,f}$	Deformed length of core yielding segment
L_y	Length of core yielding segment
L_y	Length of core yielding segment
$\mathbf{M}$	Mass matrix of structure
$\mathbf{M}$	Moment magnitude
M_f	Bending demand on column
M_k	Bending demand on knife-plate joint
$M_{p,k}$	Plastic moment capacity of knife-plate joint
M_r	Bending moment demand on restrainer due to second-order effects
M_r	Column factored bending resistance
N	Normal thrust
N_f	Number of cycles to failure
N_f	Number of significant inelastic excursions
P	Axial force acting on core
P	Axial load
P50	Fiftieth percentile
P84	Eighty-forth percentile
P96	Ninety-sixth percentile
P_{avg}	Average of maximum axial compressive and tensile force
$P_{\max}$	Maximum compressive design force
$P_{cr,e}$	Elastic critical buckling load
P_e	Euler buckling load of BRB
P_f	Total accumulated frictional force
P_n	Maximum compressive axial load carried by core
$P_{y,k}$	Axial yield resistance of knife-plate joint

P_y	Actual yield strength of BRB
P_{yc}	Axial yield strength of BRB core
Q_∞	Maximum change in yield size
R	Generic distance from earthquake source to site
R	Ratio of minimum to maximum strain in a half-cycle
RA	Area reduction at fracture
R_a	Average surface roughness
R_d	Ductility related response modification factor
R_o	Overstrength related response modification factor
R_y	Ratio of actual to nominal yield stress
$R_y F_y$	Actual yield stress of core
S_a	Spectral acceleration
$S_a(T)$	Spectral acceleration at a period T
$S_a^{\mathrm{Record}}(T)$	Spectral acceleration of as-recorded ground motion at period T
$S_a^{\mathrm{Target}}(T)$	Target spectral acceleration for scaling at period T
S_r	Section modulus of restrainer
S_x	Restrainer longitudinal bolt spacing
T	Period of vibration
T_1	Fundamental period of structure (translational or torsional mode)
T_{first}	First center of averaging window
T_{last}	Last center of averaging window
$T_{\max}$	Maximum period included in the LMA process
$T_{\min}$	Minimum period included in the LMA process
T_{LMA}	Period at which LMA scaling method is performed
T_b	Bolt tension
T_f	Bolt pretension
T_i	i^{th} period within the selected period points for LMA method
T_m	Mean period of ground motion acceleration
T_{pSa}	Period corresponding to maximum spectral acceleration
T_{pSv}	Period corresponding to maximum spectral velocity

T_r	Bolt nominal resistance
T_u	Bolt ultimate tensile strength
U	Elastic strain energy stored in the system
U_1	Moment amplification factor for compressive members
V	Shear force at base of structure
V	Work due to external loading
V_{NBCC}	Strength-design base shear as per NBCC
$V_{f,b}$	Shear force on bolts
V_{s30}	Shear wave velocity in the top 30 meters of the site soil deposit
W	Weight per unit length of restrainer
W_a	Amplitude of energy density term
W_p	Total plastic work in a single loading pass
W_{pn}	Normalized plastic work in the yielding segment
$SR_{0.2/2.0}$	Ratio of spectral accelerations at 0.2 and 2.0 seconds
X, Y	Random variables
a_1, a_2, a_3	Coefficients for cyclic hardening model
a_h	Ratio of hinge-to-hinge length to the work-point length of BRB
$a_{\max}$	Maximum absolute of floor acceleration
a_f	History of floor acceleration
b	Fatigue strength exponent
b	Saturation rat of isotropic hardening
b_c	Core width
c	Fatigue ductility exponent
e_c	Eccentricity of axial load on column
dL	Shortening of a given half-wave
dR	Resolution of distance parameter in seismic hazard deaggregation data
$\mathrm{d}\mathbf{M}$	Resolution of magnitude in seismic hazard deaggregation data
d_r	Distance between end of restrainer and gusset plate
g_y	Through-width gap between core and restrainer
g_z	Through-thickness gap

h	Hardening modulus
h_c	Convective heat transfer coefficient
$k_{e,l}$	Longitudinal stiffness of restrainer segment
$k_{e,t}$	Transversal stiffness of restrainer segment
k_e	Constraining stiffness provided by restrainer segment
k_r	Locally mobilized constraining stiffness against gap opening
ℓ	Length of buckling half-wave
n	Target number of records for selection
n	Number of buckling waves
n'	Cyclic hardening exponent
n^*	Exponent of master curve (for non-Masing materials)
n^i_{RF}	Counted cycles by Rainflow method
n_b	Number of bolts along core yielding segment
n_c	Number of loading cycle for a given strain amplitude
n_i	Number of cycles of damaging events for a given intensity
t_c	Core thickness
r	Aspect ratio of knife-plate hinge
v	Core deflection
v	Interstorey relative velocity
x	Distance from knife-plate hinge at the fixed end of brace
x_i	Ranked (sorted) random variable
Δ_0	Initial gap between core and restrainer
Δ_{roof}	Roof lateral displacement with respect to the ground
$\Delta\Lambda^i_{RF}$	Cycle counted ranges of parameter Λ
Δ_{bm}	Storey design displacement drift
Δ_f	Storey drift obtained by elastic analysis under design base shear
$\Delta\theta^i_p$	Plastic drift angle ranges obtained by cycle counting method
$\Delta\xi^i_{RF}$	Rainflow cycle counted ranges of parameter ξ
$\Delta\epsilon_{\max}$	Largest strain range in the strain signal
Δ	Storey drift (net lateral displacement between two consecutive floors)

Δ	Total gap between core and restrainer
$\Delta T_{\max}$	Maximum temperature changes in one single pass of seismic-loading
ΔW_0^t	Strain energy corresponding to the fatigue limit
ΔW^{e+}	Elastic strain energy of tensile stress in one cycle
ΔW^p	Plastic strain energy density in one cycle
ΔW^t	Total strain energy density in one cycle
$\Delta \mu_p^i$	Cycle counted ranges of core plastic ductility
$\Delta \epsilon_c$	Strain range in core yielding segment
$\Delta \epsilon_e$	Elastic strain range
$\Delta \epsilon_p$	Plastic strain range
Δ / h	Storey drift ratio
ΔT	Length of averaging window
ΔT	Total temperature changes during test
$\Delta \sigma$	Stress range
$\Delta \epsilon$	Strain range
Λ	Amplification of design storey drift
Ω^2	Matrix of eigenvalues
Ω_d	Dynamic overstrength at the base of structure
Π	Total potential energy
$\sum \mu_p$	Accumulated plastic ductility in the core yielding segment
$\sum \mu_p$	Sum of inelastic displacement an SDOF divided by its yield displacement
$\Sigma(\mathrm{d}\epsilon_p)$	Sum of plastic strain increments (absolute values)
Φ	Matrix of eigenvectors
α	Exponent of energy-life fatigue models
α	Factor defines the beginning of averaging window
β	Compressive strength adjustment factor
β	Factor defines the end of averaging window
$\beta_{2\%}$	Compressive strength adjustment factor at 2% storey drift ratio
γ	Back stress saturation rate of hardening modulus
γ	Buckling shape factor
γ	Density

γ	Ratio of core yielding segment length to work-point length of brace
δ	BRB axial deformation
δ	Gap opening due to normal thrust
δ	Total BRB global bending deflection under design axial load
δ_0	Amplitude of initial geometric imperfection
δ_c	Axial deformation in the core yielding segment
δ_e	Elastic deformation in the non-yielding segment of BRB
δ_t	Geometric imperfection at point of moment transfer
δ_{yc}	Yield deformation of the core yielding segment
ϵ	Core local axial strain
$\epsilon(T)$	Normalized residual from average spectral acceleration predicted by a given GMPE at period T
$\epsilon_{\max}$	Maximum strain amplitude
$\epsilon^{-}_{c,\max}$	Maximum compressive strain amplitude in the core yielding segment
$\epsilon^{+}_{c,\max}$	Maximum tensile strain amplitude in the core yielding segment
ϵ_c	Average longitudinal strain in the core yielding segment
ϵ_c	Peak local axial strain at the end of compressive excursion
ϵ_f	True stress at fracture
ϵ'_f	Fatigue ductility exponent
$\epsilon_{i,avg}$	Average of normalized deviations
ϵ_i	Normalized deviation from central tendency of an intensity measure
ϵ_k	Axial longitudinal strain in the extreme fiber of knife-plate hinge
ϵ_m	Average of strain signal
ϵ_p	Plastic strain
ϵ_{pD}	Elongation at maximum force
ϵ_{rms}	Root mean-square of the strain signal
ϵ_t	Peak local axial strain at the end of tensile excursion
ϵ_y	Yield strain of core
ϵ^{*}_{yc}	Yield strain of core after modification for isotropic hardening
$\bar{\epsilon}$	Average axial strain in the core yielding segment

η	Ratio of core area to the knife-plate joint area
η	Ratio of the core cross-sections in the yielding and the non-yielding segment
θ	Rotation in knife-plate hinge
θ	Storey drift ratio
$\theta_{\max}$	Maximum absolute of storey drift ratio history
θ_{roof}	Roof drift ratio
θ_i	Drift ratio at the i^{th} storey
θ_p	Plastic drift ratio
$\theta_{y,k}$	Yield rotation of knife-plate joint
κ	Coefficient of energy-life fatigue models
κ	Factor to account for column bending moment profile in S16-09
λ	Slip length ratio
μ	Coefficient of friction
μ	Ductility at core yielding segment
$\mu_{\ln X}$	Average of natural logarithm of random variable X
$\mu_{\max}$	Maximum absolute displacement of an SDOF divided by its yield displacement
$\mu_{\max}$	Maximum core ductility
$\dot{\mu}_p^i$	Rate of the i^{th} plastic excursion in the core yielding segment
ξ	Amplification of brace design displacement
ξ	Buckling length factor
ξ	Ratio of moment transfer length to BRB length between knife-plate hinges
ρ	Spearman's correlation coefficient
σ	Average axial stress in core
$\sigma_{\ln X}$	Standard deviation of natural logarithm of random variable X
σ_0	Initial yield size
$\sigma_{\max}$	Maximum amplitude of tensile stress in one cycle
$\sigma_{\max}$	Maximum combined stress due to global and local demand on restrainer
σ_{FL}	Fatigue limit stress (endurance stress)
σ_{NT}	Longitudinal stress on the restrainer due to normal thrust
σ_f'	Fatigue strength coefficient
$\sigma_{m,i}$	Average of stresses at the beginning and end of the i^{th} counted half-cycle

σ_m	Average stress signal
σ_{rms}	Root mean-square of the stress signal
σ_{yc}	Cyclic yield strength
χ	Ratio of elastic non-yielding segment length to work-point length of brace
ψ	Angle of brace with respect to floor
ω	Tensile strength adjustment factor
ϕ	Column net chord rotation between two consecutive storeys
ϕ	Resistance factor
ϕ_y	Yield curvature of the knife-plate joint
$\omega_{2\%}$	Tensile strength adjustment factor at 2% storey drift ratio

Abbreviations

2D	Two-dimensional
3D	Three-dimensional
ASCE	American Society of Civil Engineers
ASR	Average Spectral Ratio
BRB	Buckling-restrained brace
BRBF	Buckling-restrained braced frame
BS	Bare steel
CDC	Column demand/capacity ratio
CDF	Cumulative Distribution Function
CID	Cumulative Inelastic Ductility
CMS	Conditional Mean Spectrum
COV	Coefficient of Variation
CoV	Coefficient of Variation
CPD	Cumulative Plastic Ductility
CSA	Canadian Standard Association
CVN	Charpy V-Notch
DCF	Drift Concentration Factor
ELCF	Extremely Low Cycle Fatigue
ESI	Equal Spectral Intensity
ESFP	Equivalent Static Force Procedure
FE	Finite element
FF	Far-field
FP	Fixed point (no relative slip between core and restrainer)
GCIM	Generalized Conditional Intensity Measure
GMPE	Ground Motion Prediction Equation
IM	Intensity Measure
KPH	Knife Plate Hinge
LCF	Low Cycle Fatigue
LH	Low-High (a loading sequence)
LHC	Low-High-Constant (a loading sequence)

LMA	Least Moving Average
LVDT	Linear Variable Differential Transformer
MFP	Matching at Fundamental Period
MSE	Mean Squared Error
MSE	Minimum Squared Error
NBCC	National Building Code of Canada
NGA	Next Generation Attenuation
NTHA	Nonlinear Time History Analysis
OR	Ordinary (a type of seismic loading history)
PEER	Pacific Earthquake Engineering Research
PDF	Probability Density Function
PGA	Peak Ground Acceleration
PGD	Peak Ground Displacement
PGV	Peak Ground Velocity
PL	Pulse-Like (a type of seismic loading history)
PTFE	Polytetrafluoroethylene
RSA	Response Spectrum Analysis
S.F.	Safety factor
SDOF	Single Degree-of-Freedom
SF	Scale Factor
SI	Subduction Interface (a type of seismic loading history)
SLR	Slip length ratio
SMV	Sustained Maximum Velocity
SP	Point of maximum slip between core and restrainer
SR	Spectral ratio
SS	Stainless steel
SSE	Sum of Squared Error
STD	Standard deviation
TSC	Three stage cyclic loading
UHMW-PE	Ultra-high-molecular-weight polyethylene
UHS	Uniform Hazard Spectrum

ULCF	Ultra Low Cycle Fatigue
UTS	Ultimate Tensile Stress
YS	Yielding Segment

CHAPTER 1 INTRODUCTION

1.1 Background

Buckling-Restrained Braced Frame (BRBF) is an effective seismic lateral force resisting system that has shown promising ductility and energy dissipation capability. This concentrically steel braced frame system absorbs and dissipates the earthquake-induced energy through stable inelastic actions in the diagonal bracing members called buckling-restrained brace (BRB). Typically, a BRB member is composed of an internal core that carries the entire brace axial load and a stiff external encasing that restrains the global buckling of the core member. Since buckling is prohibited, the brace can be compressed beyond its yield resistance without stiffness or strength degradation thus providing substantial source of energy dissipation. Since its introduction in North America in early 2000's, interest in BRBFs has constantly grown. Canadian steel fabricators have expressed their interest in developing a fully steel BRB system as an engineering product that satisfies the seismic qualification requirements, and would be free from the fabrication issues associated with the conventional systems. In order to achieve a proper and reliable inelastic response from BRBs, the restraining mechanism has to be analyzed and designed carefully. Proper design of restrainer involves estimation of normal thrust which is generated upon the inelastic buckling of the core. This phenomenon itself depends on complex interactions between several factors. Past experimental studies have shown that lack of restraining capacity against the core's normal thrust can result in poor BRB performance and complete failure in some cases. As shown in Figure 1.1, restrainer failure typically expresses itself in the form of concentrated and excessive gap opening. To understand and investigate the behaviour of fully-steel BRBs, an experimental research program started in Polytechnique Montréal in 2002 (Bolduc *et al.*, 2003). Several design and performance issues were observed and the need for further in-depth studies was expressed. In particular, concerns raised over the effects of severe friction at the core-restrainer interface which can result in early fracture and large unwanted compressive resistance (see Figure 1.2).

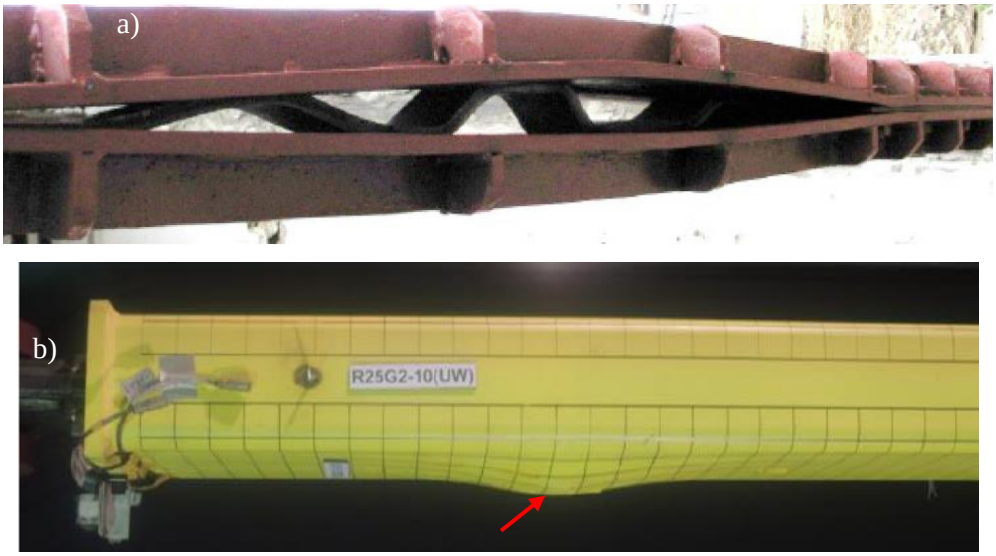

Figure 1.1: Typical failure mode of restrainer: a) all-steel restrainer (D'Aniello *et al.*, 2014); b) bulging of steel tube in conventional mortar-filled BRB (Lin *et al.*, 2016).

In the next phase of this project and to address the raised issues, an extensive analytical study was conducted by Korzekwa (2009). However, the results of this analytical study were not experimentally validated. In addition, several essential design inputs required for the normal thrust analysis were not available.

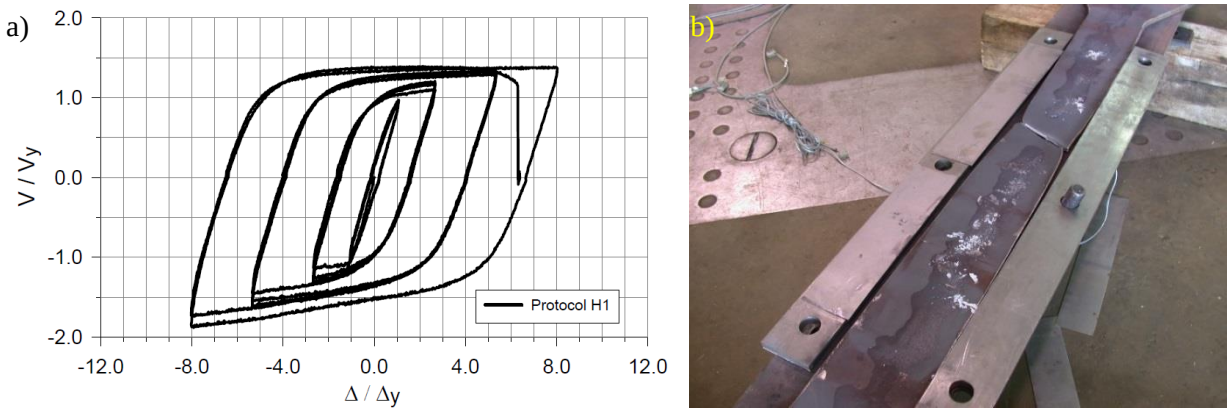

Figure 1.2: Hysteresis behaviour and fracture of an all-steel BRB with rough interfacial condition (steel versus steel) (Bolduc, *et al.*, 2003). Note: failure occurred before finishing the second cycle of −/+1.4% drift ratio.

The magnitude of the normal thrust depends on several factors such as the anticipated displacement demand, gap size, core slenderness, restrainer stiffness and strength, core material's strain hardening behaviour, and the frictional behaviour at the core-restrainer interface. In order to obtain a satisfactory performance, the effect each individual parameter and the interaction between them should be carefully studied.

Displacement demand, as a basic design parameter, is heavily dependent on the characteristics of the expected ground motions and the presumed response modification factors in the design. Earthquakes in eastern and western Canada are caused by quite different source mechanisms. On the west coast of Canada, megathrust earthquakes at the interface of Cascadia subduction zone contribute significantly to the seismic hazard. These earthquakes generate extremely long duration ground shaking which could increase the likelihood of low cycle fatigue fracture in structural system including BRBFs. The loading protocol proposed by the current Canadian standard for testing BRBs was derived from an analytical case study in Los Angeles, California (Sabelli *et al.*, 2003). This area is not facing megathrust earthquakes and, naturally, this type of earthquake was not included in the analysis. In addition, the response modification factors and global stability requirements for BRBFs in the U.S. and Canada are different (Tremblay *et al.*, 2016). Differences in seismicity source and design practice can directly affect the displacement demand. On the other hand, earthquakes expected in eastern Canada are supposed to be markedly different from those in the west coast. In particular, the high-frequency short-duration earthquakes expected in the east of Canada is believed to impose less displacement demand on building structures compared to the western events of the same size. In the current qualification procedure, site location is not explicitly accounted for and BRBs are tested under the same loading regardless of the location of the structure. Because displacement demand is a key factor in the design of restrainers, to have more economical BRBs, possible effects of seismicity source on the displacement demand should be carefully investigated.

The core's inelastic buckling response and its normal thrust is directly related to the cyclic strain hardening behaviour of the core material (Bregoli *et al.*, 2016). Strain hardening of steel is a complex phenomenon and controlled by the interaction between several loading conditions such as strain intensity, loading cycles, rate, and temperature. Reasonably precise estimation of the core normal thrust is not possible without characterizing the cyclic hardening behaviour at the expected loading condition.

Past analytical studies have shown the substantial benefits of employing BRBs in the seismic design of multi-tiered steel braced frames (Imanpour *et al.*, 2016b) and steel truss arch bridges (Usami *et al.*, 2005). BRB members of such structures can be exposed to various weather and environmental conditions (see Figure 1.3). Canadian long and cold winters poses a seismic design challenge for such exposed structures as the ductility of structural steel could be reduced at low temperatures. Combination of cold temperature and fast seismic deformation rates can also increase the force demand on the framing components. To estimate the effect of cold temperature and fast earthquake loading rates on the performance of BRBFs, the first crucial step is to acquire reliable experimental data at material level. This requires a comprehensive experimental material characterization program to be designed and executed.

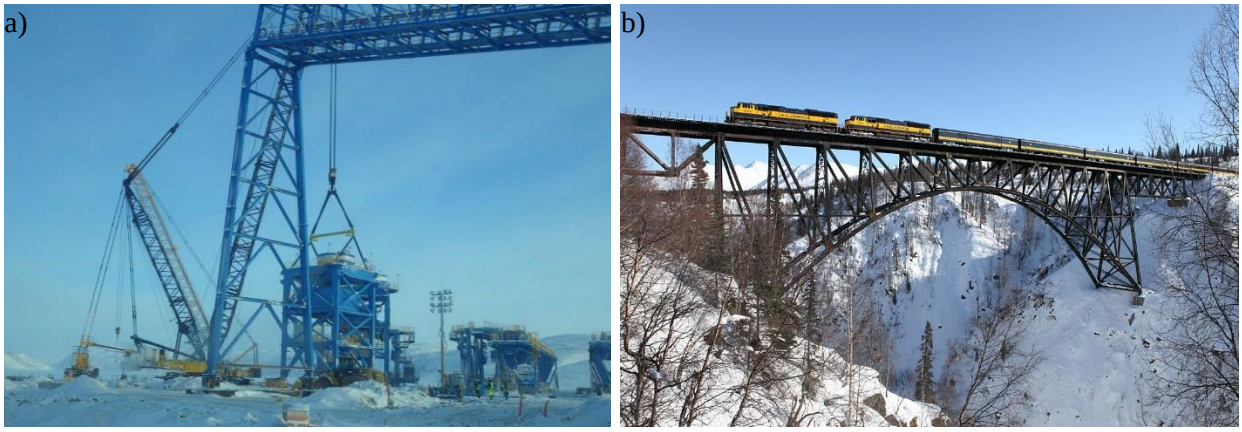

Figure 1.3: Examples of exposed steel braced structures in extremely cold environment and seismically-active region: a) multi-tiered steel braced frame as the vertical support in the material handling system of an iron ore mine in Baffin Island, Canadian territory of Nunavut with 2% in 50 years PGA of 0.125g (photo from: www.baffinland.com); b) steel arch railway bridge in Hurricane Gulch, Alaska with 2% in 50 years PGA of 0.5g) (photo by Ted Smith-Peterson obtained from www.railpictures.net).

1.2 Research objectives

The main objective of this PhD work is to develop, design, and qualify a seismically enduring all-steel buckling-restrained brace (BRB) system. This system should be simple enough to be manufactured by an ordinary steel structure fabricator. In this thesis, *endurance* refers to the ability of a structure to withstand without failure a very severe earthquake ground motion and be capable

of resisting subsequent aftershocks or smaller earthquakes occurring shortly after the main event. Available BRBs in the North American market are proprietary, thus very limited information on design of this system is publicly available. This implies a need for an in-depth study to understand and predict the core's inelastic buckling and its normal thrust as an important factor in achieving satisfactory response from BRBs.

In line with the main objective, the following secondary goals were considered:

- Estimating seismic displacement demand on the Canadian code-conforming BRBFs;
- Developing rational loading histories for testing BRBs that reflect the Canadian seismicity and design practices, while also consider anticipated loading rates;
- Understanding the possible performance difficulties, such as excessive storey drift or floor acceleration, of the BRBFs designed with the current Canadian practice, and proposing solutions to improve the behaviour;
- Developing a robust and practical method of ground motion record selection and scaling that results in a reasonable uncertainty in the estimated seismic demand;
- Characterizing the steel core's material properties that are important in the design of BRB systems;
- Investigating the core's inelastic buckling response and the resulting normal thrust to develop a rational design method for the BRB's restraining mechanism;
- Devising an effective debonding option at the core-restrainer interface to mitigate the adverse effects of friction;
- Developing a practical simple hinge connection for the BRB to gusset plate connection;
- Qualifying the performance of the developed all-steel BRB under extreme seismic loading conditions that are expected in Canada;

1.3 Research methodology

To fulfill the abovementioned objectives, a combination of analytical and experimental research is conducted in this doctoral research. The following steps were taken:

1) Past studies were reviewed, and existing design and qualification procedures are critically analyzed. Available experimental data were also collected.

2) A number of Canadian code-conforming BRBFs were designed, numerically modeled, and subjected to different types of seismic analysis. The response of these systems were subjected to statistical data treatment. The analysis results were used to build a comprehensive database of the seismic demand indices that would be important in design and evaluation of BRBFs.

3) A comprehensive material testing program were designed and executed. The tests were conducted at the Structural Engineering Laboratory of Polytechnique Montréal. A complementary testing program was also conducted at the Structural Engineering Laboratory of Laval University in Québec City.

4) A practical method for estimation of the core's normal thrust was developed and validated by experimental data and computer simulations.

5) An experimental campaign was designed and launched to qualify the seismic performance of the developed all-steel BRB. These tests were conducted in a vertical planer loading frame at the Structural Engineering Laboratory of Polytechnique Montréal.

1.4 Organization

This PhD dissertation is presented in 10 chapters. It is mainly composed of the journal articles that have been written based on the results of the outlined research. In Chapter 1 background information on the research subject together with the research objectives and activities are presented. The conducted literature review on design and qualification of steel buckling-restrained braces is presented in Chapter 2. The research methodology and the scope of work is detailed in Chapter 3. In Chapters 4, 6, 7 and 8, the following four articles that have been published or submitted for publication in a scientific journal are presented:

1) Robust Period-Independent Ground Motion Selection and Scaling for Effective Seismic Design and Assessment, Morteza Dehghani, Robert Tremblay, published in *Journal of Earthquake Engineering*, Volume 20, Issue 2, Pages 185-218

2) Fatigue Failure of 350WT Steel under Large-strain Seismic Loading at Room and Subfreezing Temperatures; by Morteza Dehghani, Robert Tremblay, and Martin Leclerc; submitted to *Construction and Building Materials* on August 2, 2016.

3) An Analytical Model for Estimating Restrainer Design Forces in Bolted Buckling-Restrained Braces; by Morteza Dehghani and Robert Tremblay; submitted to *Journal of Constructional Steel Research* on November 22, 2016.

4) Design and Full-Scale Experimental Evaluation of a Seismically Resilient Steel Buckling Restrained Brace System; by Morteza Dehghani, and Robert Tremblay; submitted to *Earthquake Engineering and Structural Dynamics* on November 14, 2016.

In Chapter 5, seismic performance of Canadian code-conforming BRBFs is discussed. In Chapter 9, a general discussion regarding the research process and results is presented. Complementary research results not included in the articles are also presented and discussed in Chapter 9. Conclusions and recommendations for future research are discussed in Chapter 10.

CHAPTER 2 LITERATURE REVIEW

2.1 General

During strong earthquakes, considerable amount of ground motion energy can be transferred to building structures. This energy has to be absorbed and dissipated in a stable manner to avoid structural collapse, human casualties, and properties loss. Dissipation of energy through ductile inelastic actions is a fundamental approach in the modern earthquake engineering practice. In this approach, certain structural elements are designed, with special considerations, to absorb the earthquake-induced energy by undergoing inelastic unrecoverable deformations in a ductile manner. In general, to provide lateral stiffness and strength against earthquakes loads, concentrically steel braced frame has been a practical choice owing to its relatively simple analysis and design, high lateral stiffness, and ease of construction and inspection (Uriz, 2005). In the conventional form of this system, seismic energy is primarily dissipated by axial yielding and inelastic flexural buckling of diagonal steel brace members (Bolduc, *et al.*, 2003). Inelastic brace buckling offers limited energy dissipation and causes several performance difficulties such as cyclic stiffness and strength degradation, premature brace fracture, and large unbalanced forces due to the difference between tensile and compressive strengths (Higginbotham *et al.*, 1976; Black *et al.*, 1980; Zayas *et al.*, 1980; Tang *et al.*, 1987; Khatib *et al.*, 1988). As a superior alternative, the idea of Buckling-Restrained Braced Frames (BRBFs) has emerged and evolved in the last four decades to resolve the performance issues associated with the brace inelastic buckling (Uang *et al.*, 2004; Xie, 2005). As the name conveys, BRBFs incorporate a special diagonal brace element, i.e. BRB, which does not globally buckle and, as a result, can offer a stable inelastic response both in tension and compression. Because of this stable inelastic response, the dissipated energy by the BRBF brace is higher than the equivalent buckling brace. Storey can also sustain larger shear deformation and more number of loading cycles, without instability, as the low cycle fatigue fracture of brace members is no longer a key issue. All these features can be translated into having a better margin of safety against structural collapse. BRBFs were introduced to north America in late 1990's and soon after it became an standard seismic lateral resisting system (SLRS) both in the U.S. and Canadian building codes. Historical development of BRBF concept is reviewed in (Uang, *et al.*, 2004) and (Xie, 2005). The first use of BRBF system in Canada was in seismic retrofit of a four-storey building in Québec City (Tremblay *et al.*, 1999).

2.1.1 Buckling-restrained brace

The idea of buckling-restrained brace (BRB) is rather simple: a slender metallic element, typically called “core”, is surrounded by a stiff encasing to restrain the core member from global buckling. Core is supposed to carry the entire brace axial force and restrainer should only play the role of lateral stabilizer with no contribution in the axial stiffness and strength of the brace member. Core typically has a dog-bone shape and is composed of a yielding segment at the middle, and non-yielding segments at the extremities. Core ends are usually enlarged and stiffened just before connection to the framing system to prevent yielding and subsequent localized instabilities. Due to its reduced section, all the inelastic actions should be concentrated in the yielding segment and the non-yielding segments are supposed to remain essentially elastic. Core can have rectangular (Isoda *et al.*, 2002), circular (Palazzo *et al.*, 2009), cruciform (Narihara *et al.*, 2000) , tube (Shimizu *et al.*, 2001), wide flange (Ju *et al.*, 2009), or other possible cross-sections. The restrainer covers a majority of the core length but it has to be interrupted at the ends to avoid mobilization of its axial stiffness that can generate large undesirable forces. When the core wants to buckle under compression, the restraining system–which can be imagined as a lateral support– prevents this unstable response and enforces the core to undergo a higher mode of buckling. If sufficient restraining is provided, core can be compressed far beyond it yield resistance without strength degradation. To disengage the axial stiffness of core and restrainer, typically the core-restrainer interface is covered by a low-friction material called debonding or unbonding layer. When compressed, core cross-section expands due to Poisson’s effect and this has to be accommodate by proving a sufficient space between core and restrainer. This is necessary as constraining of the core lateral expansion can generate a large internal pressure that is imposed upon the restrainer. Traditionally, this space is provided by flexibility of the debonding material or just by providing an air gap or clearance. Typical configuration and behaviour of BRB element is depicted in Figure 2.1. Different variations of BRB has been developed in the past.

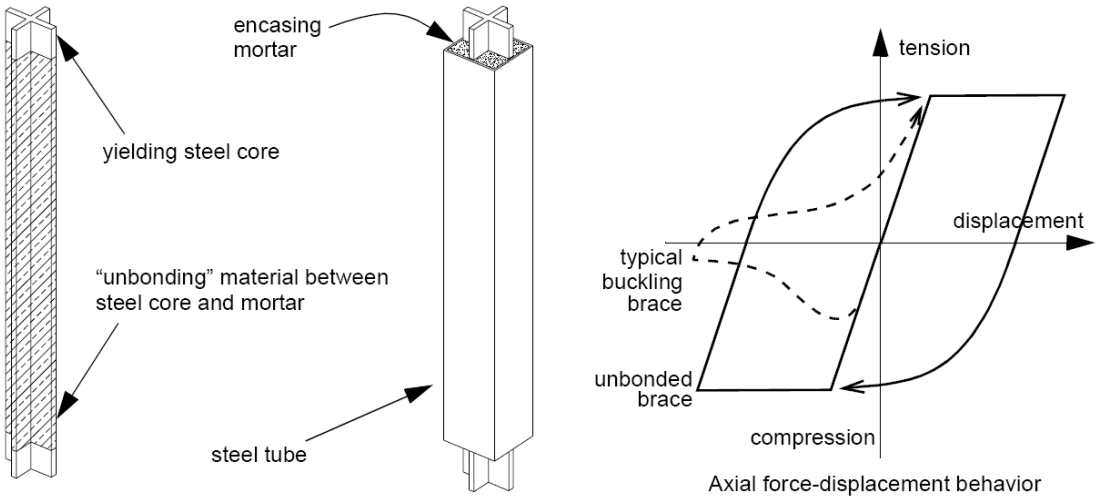

Figure 2.1: Typical configuration and behaviour of Buckling-Restrained Brace element (Black et al., 2002).

2.1.2 All-steel BRBs

Traditionally, the restraining system is a concrete- or mortar-filled steel tube. Difficulties of casting concrete or mortar in the tube, uncertainty over quality of the casted material, the time required for curing process, and the heavy brace weight are the main drawbacks of the traditional restraining system. Alternatively, restrainer can be fully made of steel sections that are jointed together using bolts (Tremblay *et al.*, 2006), welds (Eryaşar *et al.*, 2010), or by other means. An example of all-steel BRB is shown in Figure 2.2. Variety of sections can be imagined for restraining mechanism of all-steel BRB (see Figure 2.3). Bolted all-steel restrainers can also be opened for post-earthquake damage inspections. However, providing a uniformly stiff restraining such as the one offered by the conventional restrainer, can be challenging in some all-steel BRB configurations. In addition to the global stability requirements, restrainer has to be designed for an internal pressure that is generated upon core buckling. This internal pressure can impose a significant normal thrust on the restrainer and therefore must be estimated properly and considered in design of the restraining system.

Figure 2.2: Preparation of an “all-steel BRB” for test at Structural Engineering laboratory of Polytechnique Montréal in 2002 (photos by Robert Tremblay).

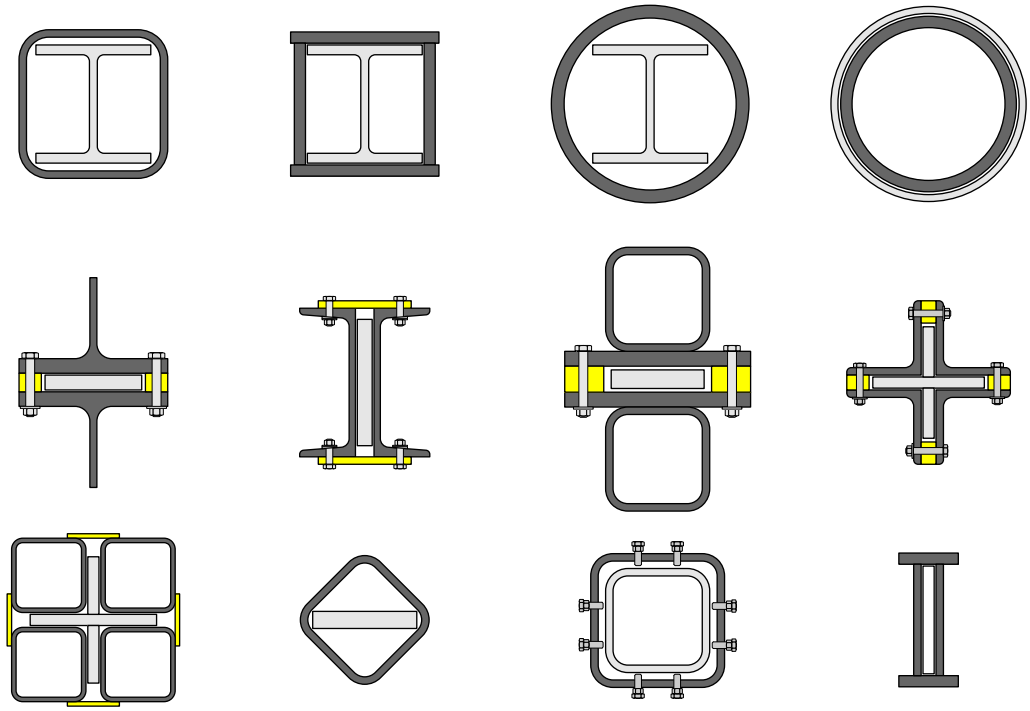

Figure 2.3: Some possible configurations of “all-steel BRBs” (Note: dark color is *restrainer* and lighter color is *core*).

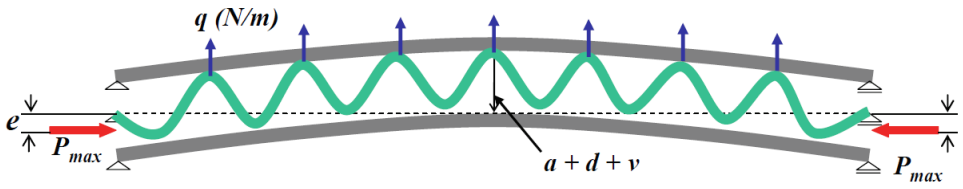

Figure 2.4: Schematic of core normal thrust on the restrainer after high-mode buckling, (Usami *et al.*, 2008).

First generation of "all-steel BRBs" was born and developed in early of 1990's in Japan as an alternative to the conventional concrete-filled BRBs (Imai *et al.*, 1997). Since then, several configurations of "all-steel BRBs" have been conceived, tested and converted to commercially-available earthquake resistant structural elements (Tada *et al.*, 1993; Suzuki *et al.*, 1994; Manabe *et al.*, 1996; Morino *et al.*, 1996; Kaneko *et al.*, 2000; Narihara, *et al.*, 2000; Isoda *et al.*, 2001; Kawamura *et al.*, 2004; Usami *et al.*, 2009b). Lighter weight, faster fabrication, and possibility of post-earthquake inspection are the key advantages of this system over its competitors. This element has been successfully used as a supplemental damping device in moment frames, and the main lateral force resisting of newly designed and rehabilitated building structures (Tremblay, *et al.*, 1999), industrial frames, and bridges (Usami *et al.*, 2009a). First analytical and experimental studies of all-steel BRB were carried out on compressive ductility capacity of double tube configuration. It was found that slenderness of the core, flexural stiffness of the restrainer, the gap between core and restrainer, core initial imperfection and loading eccentricity play key rule in compressive ductility of any all-steel BRB (Kuwahara *et al.*, 1993; Manabe, *et al.*, 1996; Shimizu *et al.*, 1997). Several frame tests also revealed that flexural rigidity of the beam-brace-column has an adverse effect on the system capacity due to generation of frame action bending moment (Imai, *et al.*, 1997; Narihara, *et al.*, 2000). Low cycle fatigue (LCF) life of core member was another vast field of study in BRBs. In these studies, core fracture life under repetitive high amplitude loading has been investigated (Yasui *et al.*, 1996; Narihara *et al.*, 2002). It was concluded that weakly-restrained local buckling is the main cause of the premature fatigue fracture. De-attachable brace, a new configuration for all-steel BRBs, was introduced (Tsai *et al.*, 2004). This system can be disassembled after an earthquake to investigate the degree of damage of the core. Recently in Japan, extensive experimental and analytical works have been conducted on development of high-performance all-steel BRBs for bridge applications (Usami, *et al.*, 2009a; Usami, *et al.*, 2009b). It

was shown that double T-sections configuration performed very well and the proposed model is about 40% lighter than equivalent mortar-filled BRB. For the first time in North America experimental studies on a simple all-steel BRB were performed and the results were reported in (Tremblay, *et al.*, 2006). This research and the accompanied one (Korzekwa, 2009) showed that the seismic performance of an all-steel BRB is highly dependent on restraining stiffness, core slenderness, and frictional actions at the core-restrainer interface. Tsai *et al.* (2009) investigated the seismic behaviour of an innovative all-steel BRB with variable core cross section using cyclic and shaking table tests. Other than Japan, Taiwan and Canada, number of experimental studies also have been conducted in Italy (D'Aniello *et al.*, 2009), China (Zhao *et al.*, 2010), Korea (Ju, *et al.*, 2009) and Turkey (Eryaşar, *et al.*, 2010). In spite of all these efforts, there is no uniform and generally accepted approach in design of restraining mechanism. For this reason, according to AISC seismic specifications (AISC, 2005) and the Canadian steel design standard (CSA, 2009), performance of this system must be confirmed by full-scale cyclic tests. In the next sections, the most important issues related to design and seismic performance of BRBs and BRBFs will be reviewed in more details.

2.2 Seismic design and demand on BRBFs

2.2.1 BRBF design

Buckling-restrained braced frames are now recognized as a standard lateral seismic force resisting system in U.S. and Canada. Canadian National Building Code (NBCC) has started to regulate BRBFs in its 2010 version by specifying the basic design parameters such as ductility-, and overstrength-related response modification factors (R_d and R_o, respectively). In NBCC 2010 (NRCC, 2010), BRBF is classified as a ductile lateral system (type D system), and $R_d = 4.0$ and $R_o = 1.2$ are prescribed for this system. NBCC recommends the same R_d factor for BRBFs and Eccentrically Brace Frames (EBFs), however the overstrength factor of EBF is higher. NBCC also prescribes an empirical expression for the braced frames' fundamental lateral period of vibration: $T_a = 0.025 h_N$, where h_N is the total frame height. According to NBCC, fundamental period can be obtained from dynamic analysis but it must not be taken greater than two times the empirical expression. Possible effects of local seismic hazard intensity and lower flexibility of BRBF compared to other braced frames are not considered in the empirical expression. In Canada, seismic

design specifications of BRBFs was first introduced in the 2009 edition of the Canadian steel design code (S16-09) (CSA, 2009). According to S16, seismic force resisting systems including BRBFs must be designed in accordance with the capacity design rules to resist the maximum expected seismic loads. For BRBFs, the seismic force demand on the framing components, namely beams, columns and connections, must be obtained from a capacity analysis assuming that the BRB members deliver their axial capacities to the system. Framing components must then be designed to remain elastic under the BRB capacities or probable strengths. The probable strength of capacity can be directly obtained from testing BRB under cyclic loading. BRB member capacity is obtained by adjusting the expected yield resistance of core element for the effects of cyclic strain hardening and frictional actions at the core-restrainer interface. The probable tensile and compressive resistances, T_{ysc} and C_{ysc}, that is delivered to the system by an individual BRB is:

$$T_{\mathrm{ysc}} = \omega R_y F_{ysc} A_{sc} \tag{2.1}$$

$$C_{\mathrm{ysc}} = \beta \omega R_y F_{ysc} A_{sc} \tag{2.2}$$

where ω and β are the tensile and compressive strength adjustment factors, R_y is the ratio of expected to nominal yield resistance, F_{ysc} is the specified minimum strength or actual yield strength of the steel core, and A_{sc} is the core cross-sectional area at the yielding segment. Both ω and β parameters are strongly correlated to the axial displacement demand on the brace yielding segment, steel grade, and frictional actions at the core-restrainer interface. BRB manufacturers typically use the results of cyclic tests under code prescribed step-wise loading protocol to construct so-called BRB backbone curve. Backbone curve is obtained by connecting the tips of hysteresis loops at different applied displacement. For given brace design displacement, the maximum strength is then obtained from this backbone. Example of this backbone is shown in Figure 2.5. According to S16, storey force corresponding to capacity of BRBs does not need to be more than storey seismic loads corresponding to $R_o R_d$ = 1.3. Except in low-seismicity areas, the BRBF frame height must not exceed 40 m unless an advanced inelastic analysis confirms a stable response. Columns in the brace bent of multi-storey BRBFs must be continuous and constant over a minimum of two storeys and must be selected from seismically-compact sections (Class 1 or 2 section in S16). Columns in the braced bay must be also designed for an additional bending moment equal to 20% of their plastic moment. Since there is no unified and well-documented approach for design,

detailing, and fabrication of BRBF brace members, satisfactory performance has to be confirmed by conducting standard cyclic tests on full-scale individual brace or brace subassembly (brace + framing system). Currently, S16 code outlines a qualification procedure for BRB members. They should be tested under a standard cyclic loading protocol and must show stable hysteresis response with no stiffness and strength degradation. For the testing procedures and acceptance criteria, S16 refers to AISC Seismic Provisions for Structural Steel Buildings (AISC, 2010). At least two successful qualifying cyclic tests must be conducted. One of these test must include the rotational demand on the brace connection that is generated due to frame action.

Force-based seismic design of BRBFs is rather simple. Typically, the entire lateral seismic load is supposed to be carried by the braced spans and the possible contribution from other sources of lateral stiffness and strength is assumed insignificant. Braced span is also considered to act as a vertical truss although the columns are continuous and the brace-beam-column joints may offer some level of rotation restraint. Seismic base shear is computed according code design spectrum and distributed along the building height. BRBs' core yielding segments are then sized for the lateral storey shear that was amplified for the *P*–Δ effects. The interstorey drift under the lateral seismic loads are then evaluated and kept below the allowable prescribed values, i.e. typically between 2 to 2.5% of the storey height. If the drift requirement cannot be met, a shorter yielding segment or larger core section can be employed. Iteration may be required until the design assumption and output converge. A BRBF design example according to the U.S. practice can be found in (López *et al.*, 2004). Comparison between BRBF design practices in Canada, U.S., Chile, New Zealand is discussed in (Tremblay, *et al.*, 2016). BRBF systems are in process of being incorporated into building codes of Europe, Chile, New Zealand, and perhaps other countries. Bosco *et al.* (2013) outlined a seismic design procedure for BRBFs and proposed the behavior factor q that should be adopted in accordance with the Euro Code 8 (CEN, 1998). According to this Euro Code, structural systems should be designed for lateral forces obtained from an elastic response spectrum that is reduced by q factor. Time history analysis of large number of designed BRBFs showed that the q factor would primarily depend on the adopted design storey drift ratio. Continuity of the braced bent column was found beneficial and resulted in an increased q factor. Including *P*–Δ effects in the design also allowed to increase the q factor. As a part of the proposed procedure, capacity design rules, similar to the Canadian approach in S16, was proposed for evaluation of the design actions in the framing components (see Figure 2.6). Other than

conventional force-based design approach, other design methodologies have been proposed for BRBFs. Kim *et al.* (2004b) proposed a direct displacement-based design method for low-rise BRBFs that deform primary in shear. Inelastic nonlinear time history analysis of 3- and 5-storey BRBF using two design spectrum-matched artificial ground motion records were used to evaluate the proposed design method. It was shown that the design objectives and the performance criteria are met when the proposed design method is implemented. (Sahoo *et al.*, 2010) proposed another direct displacement-based method, based on energy-work balance, pre-selected target drift, and yield mechanism.

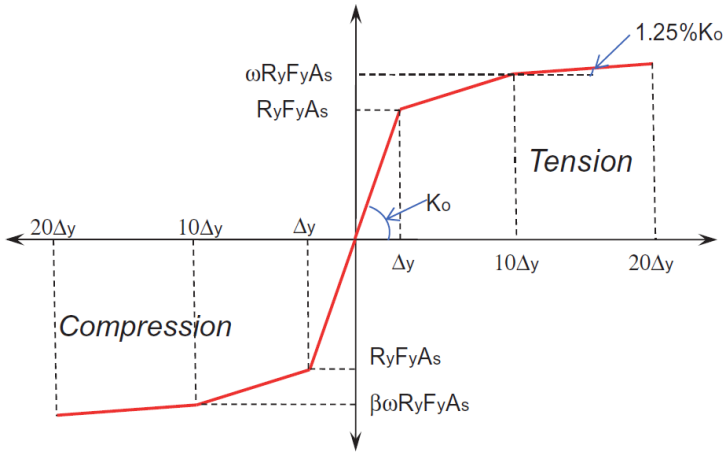

Figure 2.5: Typical BRB backbone curve for estimation of strength adjustment factors, (Dutta *et al.*, 2010).

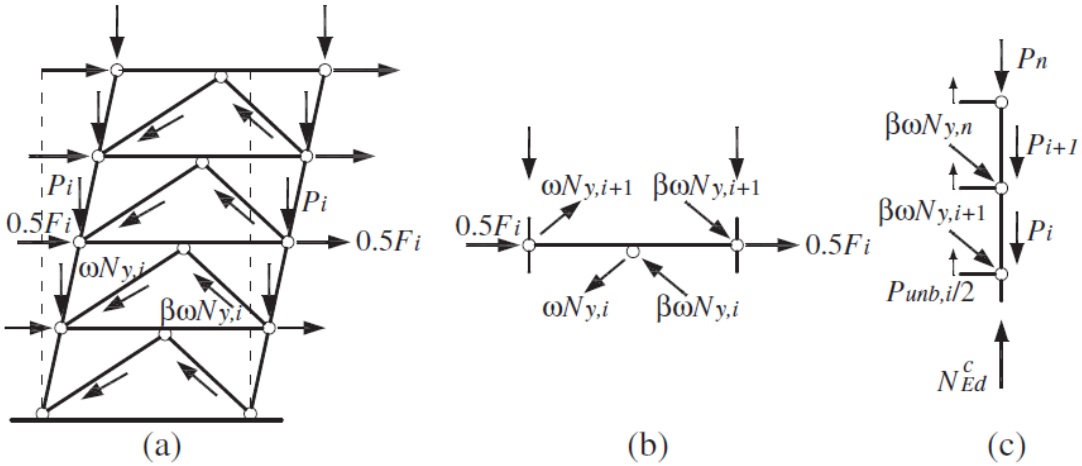

Figure 2.6: Evaluation of design forces in beam and columns of BRBF, Bosco, *et al.* (2013).

2.2.2 Inelastic models for BRBs

Inelastic numerical BRBF models are widely used in advanced nonlinear analyses to evaluate performance of this system under earthquake loading conditions. Accuracy of these numerical models heavily depends on the inelastic model used for the brace members. Since brace buckling is precluded, the inelastic response of BRB members can be modelled using elastoplastic truss element with non-deteriorating cyclic hardening behaviour. Cyclic hardening response of BRBs can be divided into two components: 1) isotropic; and 2) kinematic. The isotropic hardening is the change in the initial yield size due to cyclic loading, and the kinematic hardening is characterized by the post-yield stiffness. As a common practice, response of BRBs is modeled using simple bilinear elastoplastic models. (Sabelli, *et al.*, 2003; Kim, *et al.*, 2004b; Kiggins *et al.*, 2006) employed the simplest possible model: elastic-perfectly plastic, which literally means no isotropic hardening and zero post-yield stiffness. (Kim *et al.*, 2004a; Asgarian *et al.*, 2009; Bosco, *et al.*, 2013) assumed bilinear elastoplastic behaviour with linear kinematic hardening. In these studies, post-yield stiffness between 2% to 5% of the elastic stiffness of BRB member was assumed. Fahnestock (2006) formulated an elastoplastic truss element with combined isotropic and kinematic hardening and implemented this model into Drain-2DX computer program (Prakash *et al.*, 1988). To capture the nonlinear kinematic hardening, it was proposed to model the BRB member with several parallel bilinear truss elements having different stiffness properties. Comparison with experimental pseudo-dynamic test results showed that although the maximum storey displacement was predicted accurately, the numerically computed residual displacement was considerably far from the laboratory measurements (see Figure 2.7). Black *et al.* (2004) employed Bouc-Wen hysteresis model (Wen, 1976) to simulate inelastic dynamic response of single degree-of-freedom systems and develop displacement spectra for BRBFs. Bouc-Wen (BW) is a kinematic hardening law with smooth transition from elastic to plastic region. To approximately include the isotropic hardening effect, Black, *et al.* (2004) suggested to increase the yield strength of BRB element by a factor that depends on the maximum expected ductility and the assumed post-yield stiffness. Comparison with full-scale test under earthquake loading pattern showed that the proposed simple modification to the BW model is very effective in capturing the overall hysteresis response under complex seismic loading (see Figure 2.8). BW has been known as a versatile hysteresis model that with limited number of parameters can reproduce wide range of hysteresis shapes. However, when subjected to short unloading-reloading paths, BW model may show

nonphysical response (see Figure 2.9) as it suffers from issues such as displacement drift, force relaxation, and non-closure of hysteretic loops (Charalampakis *et al.*, 2009). Karavasilis *et al.* (2012) added the isotropic component to the classic BW model and showed that this modified model can reproduce experimentally-measured hysteresis behaviour of various stable energy dissipating devices including BRBs. Tremblay *et al.* (2008) modelled BRB members using a single truss element with a symmetrical Pyke-based Ramberg-Osgood hysteresis model available in RUAUMOKO computer program (Carr, 2008). This model includes both isotropic and kinematic hardening, and can capture the smooth transition from elastic to inelastic response (see Figure 2.10). Zona *et al.* (2012) formulated a combined uniaxial isotropic and kinematic hardening model or BRBs. This model can consider asymmetric strength, elastic and hardening stiffness in tension and compression. Rossi (2015) implemented this model in OpenSees software framework (McKenna *et al.*, 2006) and conducted a comparative study to investigate the possible improvement obtained by including isotropic hardening in the BRB model. It was concluded that the conventional kinematic-only models can be conservative. Although (Zona, *et al.*, 2012) model simulates the BRB response under symmetrical loading cycles with good precision, simulated inelastic response under dynamic asymmetric loading shows that it suffers from the same "displacement drift" problem as BW model does. Zsarnóczay (2013) developed a versatile uniaxial model that can simulate various features of BRB behaviour. This is a modified version of an existing isotropic/kinematic hardening model known as Giuffré-Menegotto-Pinto (Filippou *et al.*, 1983). The original model, which has been implemented in OpenSees under *steel02* uniaxial material model, has symmetric linear kinematic hardening but its isotropic hardening behaviour in tension and compression can be different. "*steel02*" suffers from yield overshooting problem when subjected to small amplitude unloading-reloading displacement paths (see Figure 2.12). Zsarnóczay (2013) improved the *steel02* model by correcting the yield overshooting problem, and by adding several important features including ability to simulate yield plateau, asymmetric and nonlinear hardening. This model has been implemented in OpenSees framework and available under *steel4* uniaxial material model. This would be the most advanced uniaxial elastoplastic hysteresis law for modeling BRBs. However, to accurately capture BRB response two issues should be considered: 1) rate-dependent viscoelastic hardening; and 2) abrupt increase in axial brace post-yield stiffness due to binding between restrainer and core at large compressive deformations. The former can be modelled by putting a nonlinear damper in parallel with the BRB

truss element. Latter can also be incorporated by employing a gap element in parallel with BRB element. The axial stiffness of this gap element should be activated when overclosure reaches a given limit. This limit would depend on the maximum core shortening that could be accommodated by the restrainer.

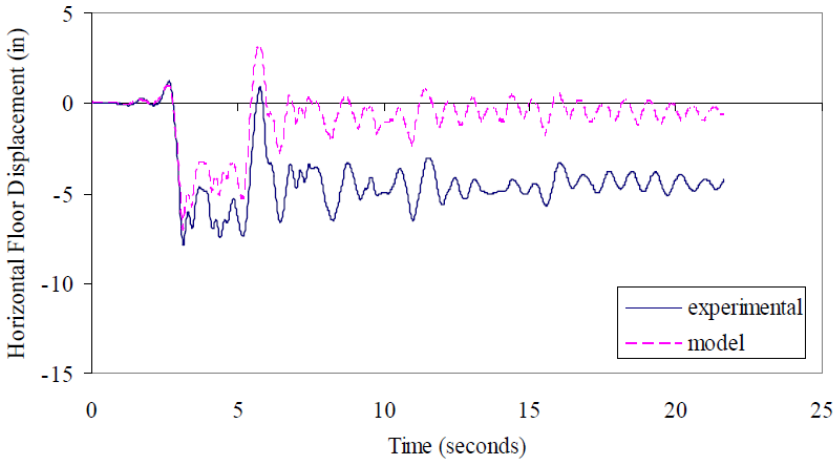

Figure 2.7: Comparison between experimentally measured and numerically predicted storey displacement, (Fahnestock, 2006).

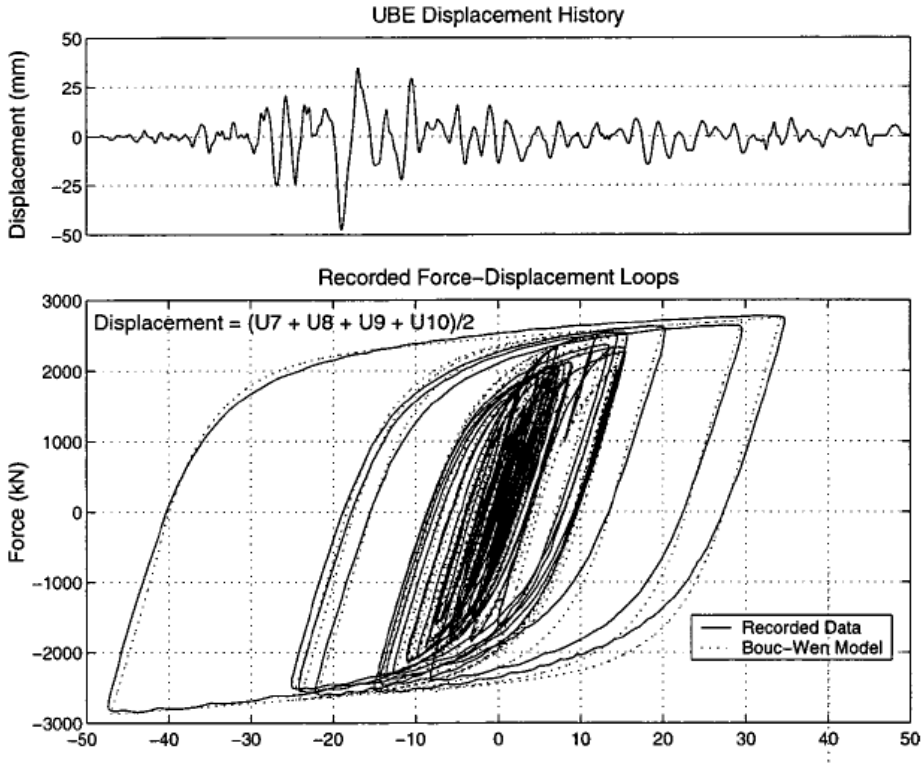

Figure 2.8: Comparison between experimental BRB response under earthquake loading history and simulated response using Bouc-Wen model, (Black, *et al.*, 2004). Note: Experiment was done under displacement-controlled loading.

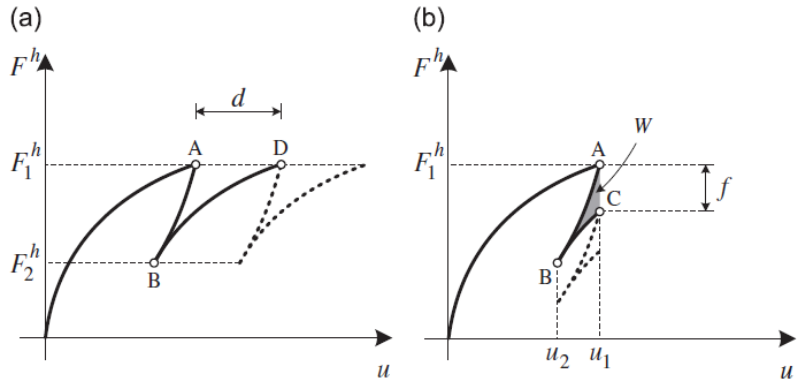

Figure 2.9: Illustration of Bouc-Wen nonphysical behaviours under small amplitude load reversal: a) displacement drift; b) force relaxation, (Charalampakis, *et al.*, 2009).

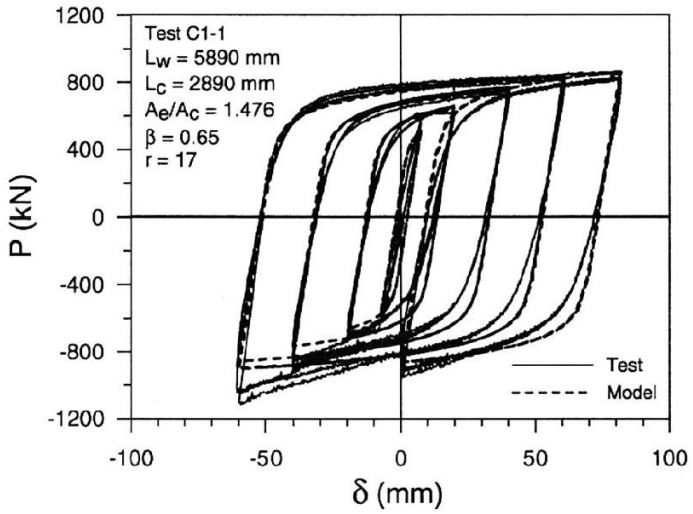

Figure 2.10: Comparison between experimental results and simulated BRB response using RUAUMOKO software, (Tremblay, *et al.*, 2008).

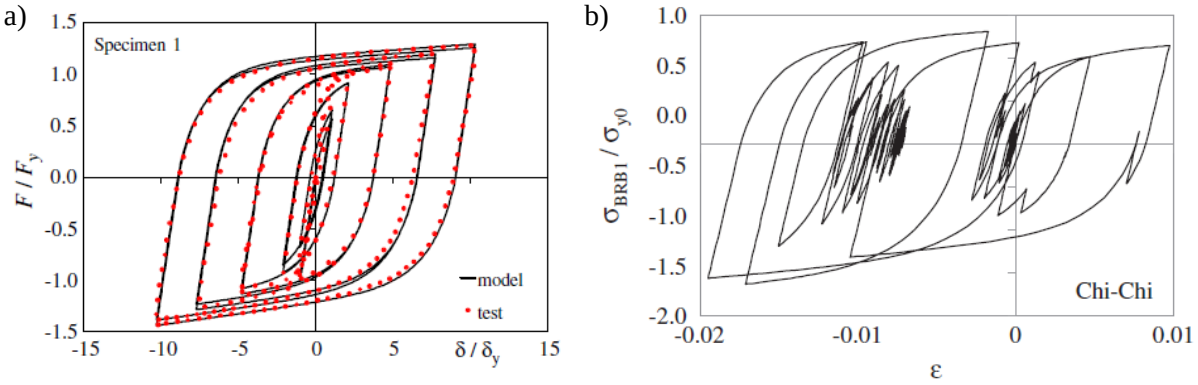

Figure 2.11: a) Comparison between experimental results and the proposed BRB model in (Zona, *et al.*, 2012). Note: loading is symmetric and displacement-controlled; b) BRB response using Zona model obtained from time history analysis, (Gu *et al.*, 2014). Note the early yielding upon reloading after partial unloading.

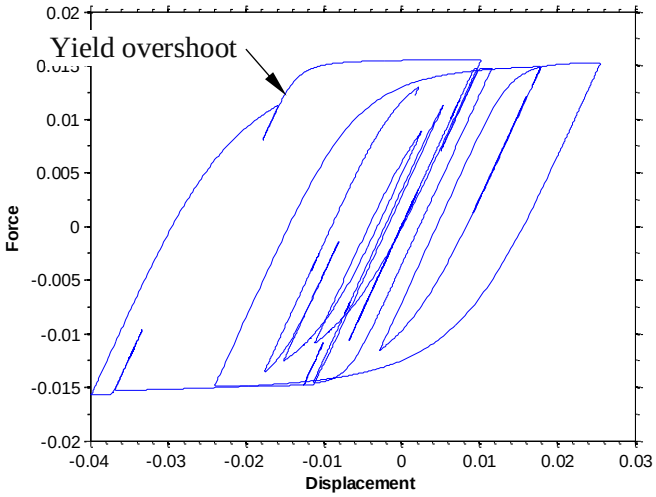

Figure 2.12: Yield overshooting phenomenon in steel02 model.

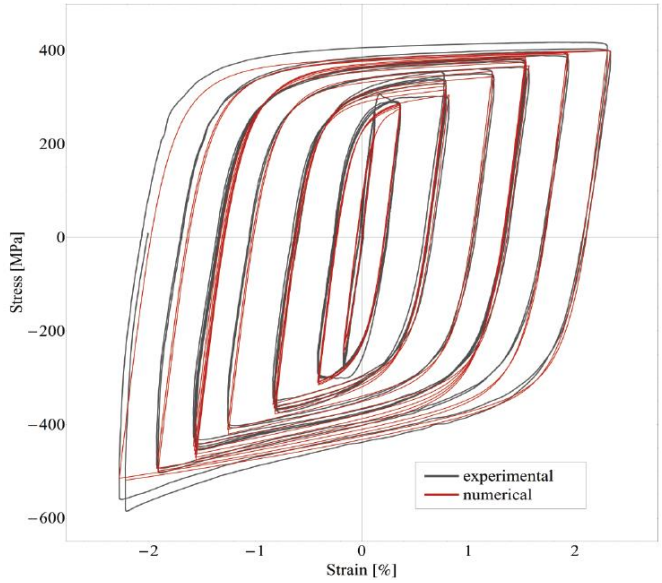

Figure 2.13: Simulated cyclic test result by the BRB model developed in (Zsarnóczay, 2013).

2.2.3 Seismic demand and performance

Seismic performance of BRBFs has been subject of many numerical studies (Tremblay *et al.*, 2002; Sabelli, *et al.*, 2003; Kim, *et al.*, 2004a; Kim, *et al.*, 2004b; Mayes *et al.*, 2004; Tremblay *et al.*, 2004; Kiggins, *et al.*, 2006; Fahnestock *et al.*, 2007b; Tremblay, *et al.*, 2008; Asgarian, *et al.*, 2009; Dutta, *et al.*, 2010; Sahoo, *et al.*, 2010; Ariyaratana *et al.*, 2011; Erochko *et al.*, 2011; Bosco, *et al.*, 2013; Zsarnóczay, 2013; Gray *et al.*, 2014; Hoveidae *et al.*, 2015). Majority of these studies were

focused on performance evaluation of U.S. code-conforming buildings designed for Los Angles, California by conducting nonlinear time history analysis on 2D models (Sabelli, *et al.*, 2003; Fahnestock, *et al.*, 2007b; Erochko, *et al.*, 2011; Hoveidae, *et al.*, 2015). In a pioneering study, (Sabelli, *et al.*, 2003) studied seismic response of 3- and 6-storey BRBF by nonlinear time history analysis. Building prototypes were designed with response modification factor of $R = 6$ and 8, and then subjected to three suites of scaled ground motion records corresponding to 50%, 10%, and 2% in 50 years probability of exceedance of seismic hazard in downtown Los Angeles, California. It was shown that BRBF can offer significantly improved response in comparison with the conventional concentrically brace frames. It was concluded that the computed demand was not sensitive to the selected R factor. Relatively, large residual drift was observed specifically at the maximum considerable earthquake (MCE) intensity level, i.e. 2% in 50 years probability of exceedance of seismic hazard. (Fahnestock, *et al.*, 2007b) studied response of 4-storey BRBF that was designed for downtown Los Angeles, California assuming $R = 8$, $\Omega_0 = 2.5$ and $C_d = 5$ where Ω_0 and C_d are the system overstrength and displacement amplification factors, respectively. Two sets of ground motion records were selected and scaled to match the DBE (design basis earthquake) and MCE seismic hazard levels. Several seismic demand indices and acceptance criteria were defined both at frame and BRB level for life safety and near collapse performance levels. It was concluded that the designed BRBF exhibited satisfactory response and met the performance objectives. Limited yielding in beam and column was observed but residual displacement was found to be large. It was suggested that the code-specified C_d factor is too small to predict the average displacement demand under DBE level. Using $C_d = R$ was suggested. The mean DBE-level BRB ductility demand was found to be significantly larger that the predicted value by the AISC Seismic Provisions (AISC, 2005) for qualification testing of BRBs. Most past numerical studies showed that a relatively large permanent residual displacement should be expected for structures with BRBF. This phenomenon was also witnessed experimentally in the large-scale hybrid pseudo-dynamic tests (Fahnestock, *et al.*, 2007b). In this study, residual drifts as large as 1.3% and 2.7% of the storey height were observed under DBE- and MCE-level ground accelerations, respectively. These residual drifts would be easily noticeable to the building occupants and are way beyond the 0.5% permissible residual deformation that was suggested by (McCormick *et al.*, 2008). In other words, buildings with BRBF may not be in *immediately operational* condition after a design-level strong earthquake and may require expensive repairs or

even demolition may be warranted. In concentrically braced frame systems including BRBFs, storey displacement response under intense seismic excitations is not symmetrical as frame laterally ratchets toward the direction that is dictated by the largest inelastic excursion. This phenomenon is attributed to the *P*–Δ effect that is strongly activated at large inter-storey displacements and reduces the lateral storey shear resistance (Tremblay, 2003). Low post-yield stiffness of BRBs and response softening caused by the *P*–Δ effect may also result in concentration of inelastic demand in one or few storeys and promoting dynamic instability and collapse (Tremblay, *et al.*, 2004). In a comparative study, Erochko, *et al.* (2011) investigated the trend of residual displacement in 2- to 12-storey BRBFs and special moment resisting frames (SMRFs) designed with ASCE 7-05 and AISC 341-05. Numerical simulations with nonlinear static and dynamic analyses showed that both systems can suffer from significant permanent residual drift. It was concluded that buildings with bare BRBF and SRMF would be total economic loss if the average peak interstorey drift ratio, under design-basis earthquake, exceeds 1.0% and 1.5%, respectively. To resolve the residual drift issue of BRBFs, several solutions have been suggested: 1) reducing the response modification factor; 2) using dual systems; and 3) adding self-centring capability. Comparison between Canadian and U.S. building codes regarding the response modification factor of BRBFs showed that the first strategy was employed in the Canada. According to U.S. code (ASCE, 2010) seismic base shear obtained from design response spectrum is divided by $R = 8$ while in Canada $R_d R_o = 4.0 \times 1.2 = 4.8$ is prescribed for reducing the elastic base shear (NRCC, 2010). Several studies investigated the possible improvement that could be gained by using moment resisting frames (MRFs) as the back-up system in dual BRBFs (Kiggins, *et al.*, 2006; Dutta, *et al.*, 2010; Deylami *et al.*, 2016; Mehdipanah *et al.*, 2016) or by using moment resisting beam-to-column connections in the braced bay (Ariyaratana, *et al.*, 2011). In particular, (Kiggins, *et al.*, 2006) compared, by numerical analysis, performance of BRBF and BRBF+MRF dual system in 3- and 6-storey building prototypes under DBE hazard level. In the dual configuration, back-up MRF was designed to resist 25% of the design base shear. This study suggested the dual BRBF configuration incur ~50% less residual drift compared to the stand-alone BRBF. To improve the seismic stability of braced frames, a dual system concept shown in Figure 2.17 using stiff elastic truss as the back-up system was proposed in (Tremblay, 2003; Tremblay *et al.*, 2007). This stiff truss was meant to enforce a uniform shear-racking displacement pattern along the building height that reduces the likelihood of drift concentration and large

permanent storey displacement. Efficiency of this system was evaluated in (Tremblay, *et al.*, 2004) by conducting incremental dynamic analysis on conventional steel concentrically brace frames, BRBF and dual BRBF. Through numerical study of 8- to 24-storey building models, Merzouq *et al.* (2006) showed that multi-storey BRBFs located at the west coast of Canada may be vulnerable to large storey drifts and dynamic instabilities. It was observed that the stand-alone BRBF system does not have enough capacity to redistribute the inelastic demand along the building height. The dual BRBF system with elastic back-up truss was found to offer superior performance with nearly uniform inelastic demand distribution along the building height under intense ground motions induced by subduction zone's megathrust and deep inslab earthquakes (see Figure 2.18). A BRB system with self-centring capability was developed and tested by (Miller *et al.*, 2012). Performance of this system at frame level was numerically studied in (Eatherton *et al.*, 2014).

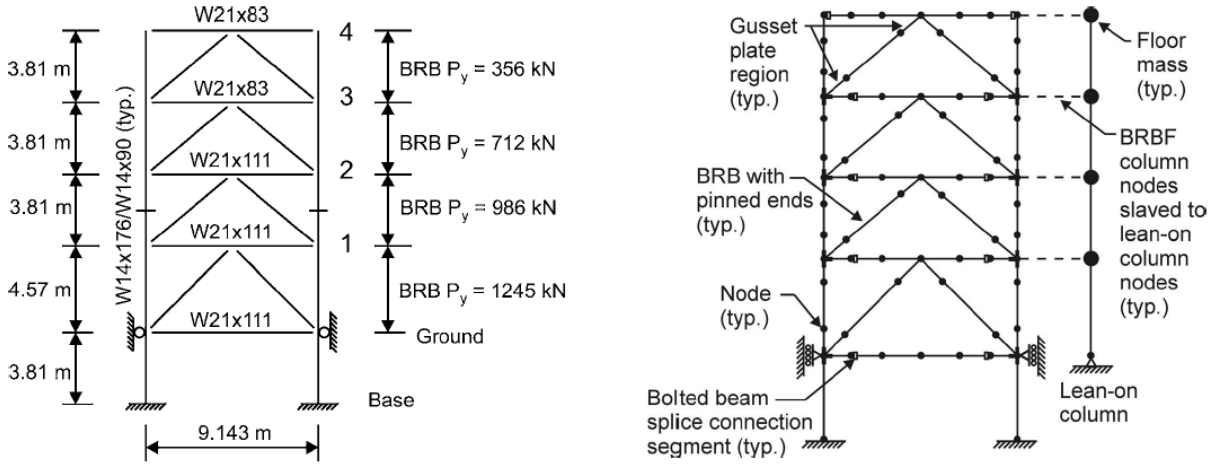

Figure 2.14: Designed frame and building prototype model studied in (Fahnestock, *et al.*, 2007b).

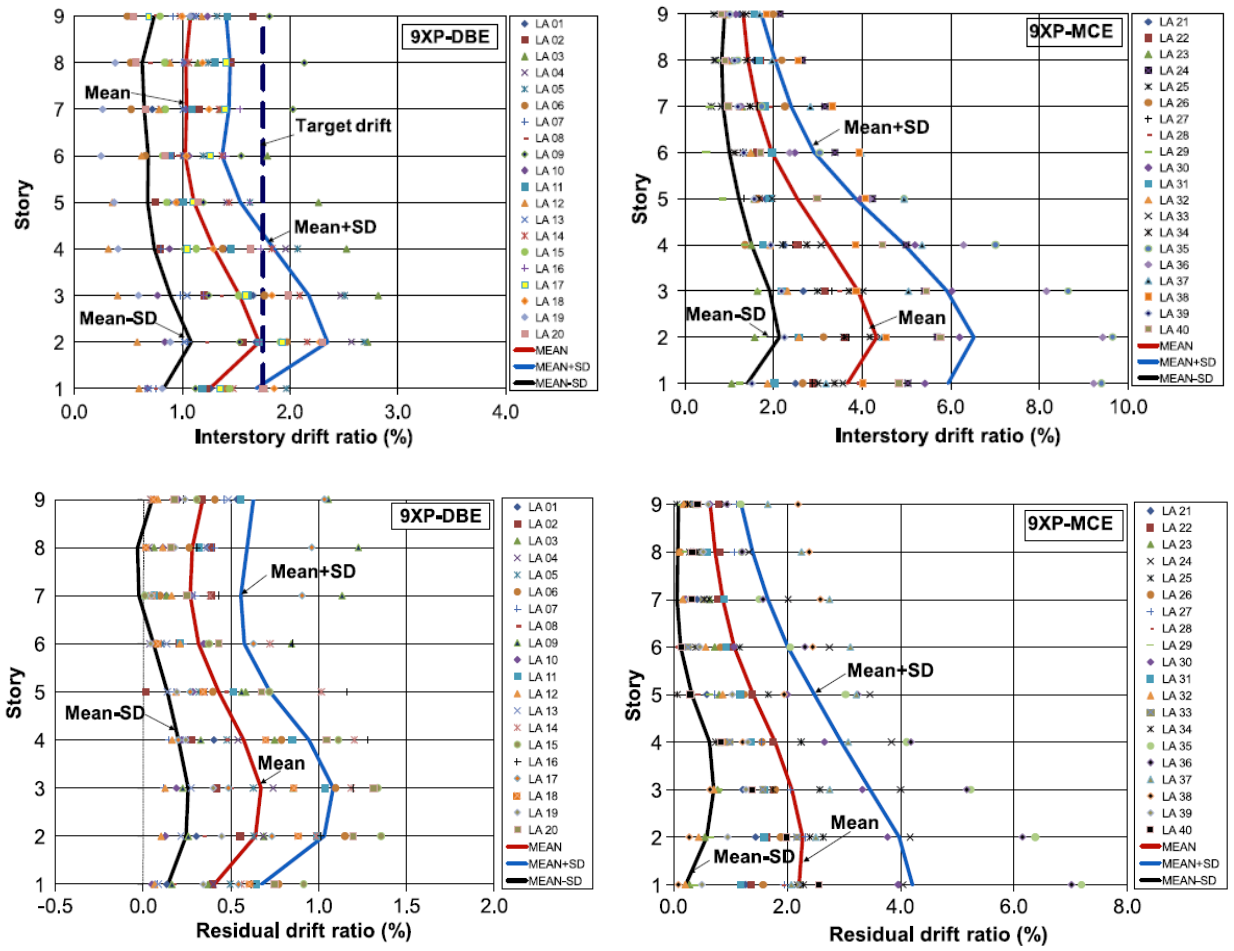

Figure 2.15: Peak and residual inter-storey drift of a 9-storey BRBF designed with the PBPD method outlined in (Sahoo, *et al.*, 2010) (figure from the same reference).

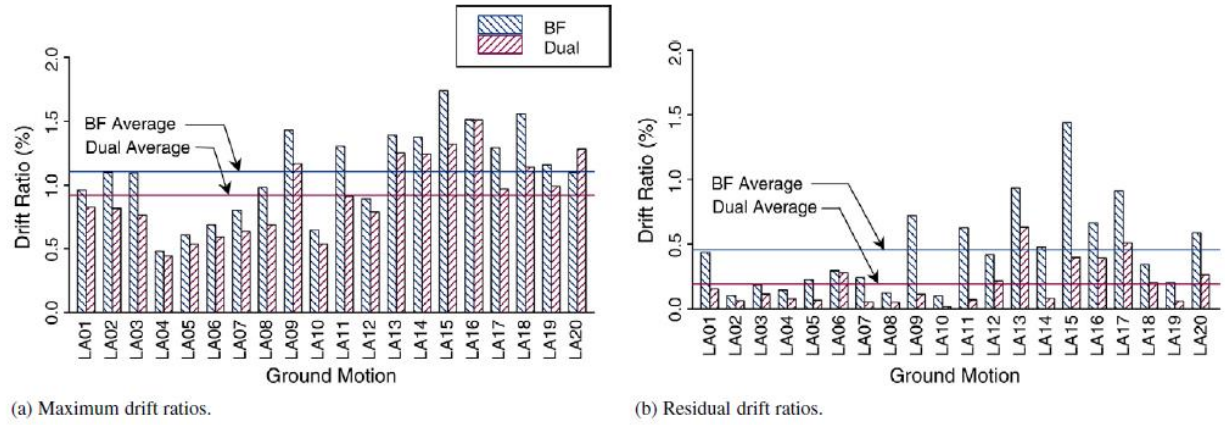

(a) Maximum drift ratios. (b) Residual drift ratios.

Figure 2.16: Maximum and residual drift ratio in 6-storey BRBF and BRBF+MRF dual systems, (Kiggins, *et al.*, 2006).

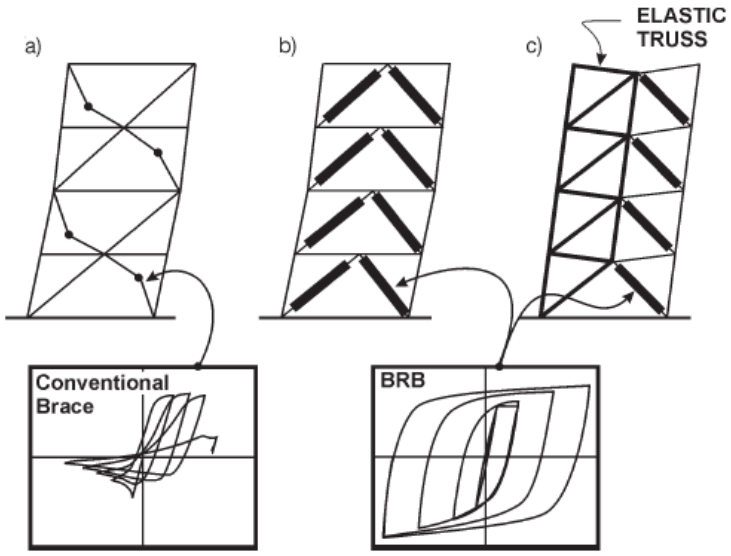

Figure 2.17: Conventional CBF, BRBF, and BRBF + elastic truss dual systems studied in (Tremblay, *et al.*, 2007).

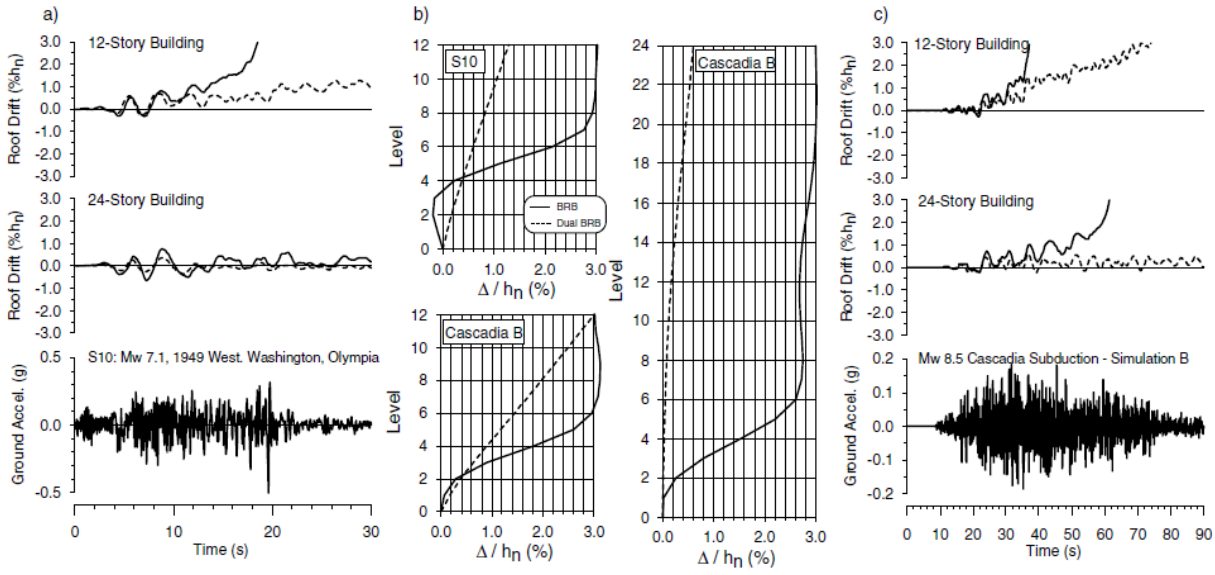

Figure 2.18: Comparison between inter-storey drift profile of bare BRBF and dual BRBF with elastic truss, (Merzouq, *et al.*, 2006).

2.2.4 Qualification testing and acceptance criteria

Building codes require that the performance of BRB members must be qualified under full-scale cyclic test. In Canada, S16 refers to AISC 341 standard for the qualification procedure. This

procedure is outlined in Section K3 of the AISC 341. According to this standard, individual BRB and BRB subassembly should be tested under a certain loading sequence. This loading history is applied as a sequence of two symmetrical cycle of displacement amplitude at Δ_{by}, $0.5\Delta_{bm}$, $1.0\Delta_{bm}$, $1.5\Delta_{bm}$, and $2.0\Delta_{bm}$, where Δ_{by} and Δ_{bm} are displacement corresponding to the first significant yield of test specimen and the design story drift, respectively. Additional cycles at $1.5\Delta_{bm}$ displacement are required to accumulate, at least, inelastic axial deformation 200 times the yield deformation of the brace specimen. AISC 341 stipulates that the design story drift must not be taken less than 1% the story height for the purpose of calculating Δ_{bm}. When the Canadian design standard is followed, $\Delta_{bm}/\Delta_{by} = R_o R_d / I_E$ where I_E is the building importance factor which varies between 0.8–1.5 depending upon the expected use and occupancy after the design earthquake. In NBCC 2010, R_o= 1.2 and R_d = 4.0 are prescribed for the BRBFs. According the U.S. design practice, $\Delta_{bm}/\Delta_{by} = C_d/I$ in which C_d and I are the deflection amplification and occupancy importance factors, respectively. ASCE 7-10 (ASCE, 2010), stipulates C_d = 5.0 for BRBFs. Based on these, for buildings with standard importance, I_E = I = 1.0, Δ_{bm} would be between 4.8–5 times Δ_{by}. This is to say that the maximum ductility amplitude imposed by this protocol, at storey level, would be 9.6–10. AISC permits other loading sequences that could be demonstrated to have equal or greater severity than the prescribed loading sequence both in terms of maximum and cumulative inelastic deformation. At least one individual BRB and one BRB subassemblage must be tested. As the acceptance criteria, AISC 341 requires that:

- the tested specimens must exhibit stable and repeatable hysteresis response with positive incremental stiffness,
- no fracture, brace instability, or brace end connection failure is permitted,
- ratio of the maximum compression force to the maximum tension force must not exceed 1.3.

AISC 341 is silent on the loading rate(s) that should be used in the qualification testing protocol. AISC 341 also points out that the cumulative demand required by this protocol is significantly higher-than-expected for the design basis earthquake and needs to be revisited in light of new research (AISC, 2010, p. 331). The AISC 341 protocol is shown in Figure 2.20. Although the process for development of this protocol is not documented, such as the ones for MRFs (Krawinkler *et al.*, 2000) and EBFs (Richards *et al.*, 2006), the AISC 341 loading sequence currently serves as an international BRB loading standard and has been employed in many studies (Merritt *et al.*, 2003;

Chou *et al.*, 2010; Eryaşar, *et al.*, 2010; Tsai *et al.*, 2014; Metelli *et al.*, 2016). The current AISC loading protocol along with the testing procedure and acceptance criteria was first recommended in Sabelli (2004). Apparently, this protocol was based on the observations made in another analytical study (Sabelli, *et al.*, 2003). Numerical BRBF models in the reference analytical study were designed for site class D (firm soil) with system response modification factors of R = 6 and 8. Models were then subjected to three sets of 20 records corresponding to 50%, 10% and 2% rate of exceedance of seismic hazard in downtown Los Angeles, California. The maximum deformation amplitude of this protocol approximately corresponds to the mean deformation demand in the worst case model, i.e. 3-storey with R = 6, under 10% in 50 years record set. On the other hand, the required cumulative inelastic deformation is 200 which is more than mean-plus-two-standard deviations of the reported values in the extreme case, 6-storey with R = 8, under 10% in 50 years set. In one particular study, (Fahnestock, *et al.*, 2007b) suggested that the maximum amplitude of the AISC loading protocol, $2.0\Delta_{bm}$, should be increased for reflect the expected inelastic demand on BRBs during MCE event. This study suggests ~$4.8\Delta_{bm}$ as the maximum testing displacement amplitude. On the other hand, (Razavi Tabatabaei *et al.*, 2014) showed that when the NTHA demand history is subjected to cycle counting and peak-to-peak response is considered, the AISC loading protocol is overly conservative and the maximum amplitude would be $1.5\Delta_{bm}$. Based on comparison between low cycle fatigue analysis results of numerical models, Hoveidae, *et al.* (2015) concluded that the current AISC 341 loading sequence is conservative. In multi-storey BRBFs, the *storey design drift* term is also not clear and could be interpreted in different ways. According the building codes, *storey design drift* is obtained by amplifying the elastic storey drift using $R_o R_d / I_E$ factor in NBCC, or C_d / I factor in ASCE7. In braced frames, both column and brace deformation contribute to the lateral deflection. Contribution from axial elongation of brace members is nearly constant along the height but columns contribution is accumulative and can become significant at upper storeys. As a result, under design earthquake loads, elastic storey drift at the upper levels can be much higher than the lower storeys. A question may arise, in order to compute *storey design drift*, whether the total elastic storey drift should be amplified or only the elastic drift due to brace elongation? For medium-rise and tall BRBFs, this would make a significant difference in the intensity of the loading protocol. Concerns have been raised that by imposing overly conservative and irrelevant loading protocols, deformation capacity of structural and non-structural components can be significantly underestimated which may lead to costly or even unfeasible designs (Gatto *et*

al., 2003; Mergos *et al.*, 2014). In other words, ultimate deformation capacity of components and their failure modes is not independent of the amplitude, number of cycles, and sequence of the testing protocol.

For Canadian applications, Tremblay, *et al.* (2002) proposed a set of non-symmetrical cyclic loading protocols for testing of ductile bracing members including BRBs for different type of earthquakes. These protocols were generated based on response of 2, 4 and 8 story steel braced frames with short ductile fuses which were designed for generic "soft rock" sites in east and west of Canada and subjected to four ensembles of ground motion records reflecting: 1) west Canada crustal and in-slab events; 2) east Canada crustal earthquake; 3) near-fault impulsive ground motions; and 4) Cascadia-region megathrust earthquakes. Energy dissipation rate concept was introduced to determine the duration of each protocol and arrange the sequence of deformation excursions. The largest deformation excursion, and the cumulative inelastic deformation of the west crustal loading history was nearly 1.5 and 2 times the east Canada loading, respectively.

Model properties			Maximum response quantities Mean and (Mean+1σ) of worst-case story or worst-case brace for suite of ground motions)						
								Brace Ductility	
Model	R	Hazard (% in 50 years)	% Elastic Drift under Design Loads	Max. Drift	Max. Drift/ Elastic Drift	Residual Drift	Column Rotation	Max. Brace Ductility	Cum. Brace Ductility
3vb	6	10%	0.20	1.5	7.8	0.6	0.9	10.6	38
3- story				(2.2)	(11.5)	(1.1)	(1.1)	(15.3)	(59)
3vb2	8	10%	0.19	1.4	7.6	0.5	0.8	9.7	39
3- story				(2.1)	(10.9)	(1.0)	(1.1)	(13.6)	(63)
6vb	6	10%	0.28	1.6	5.7	0.6	1.0	10.7	88
6- story				(1.9)	(7.0)	(1.0)	(1.3)	(12.8)	(132)
6vb2	8	10%	0.24	1.6	6.7	0.7	1.0	10.7	83
6- story				(2.2)	(9.1)	(1.1)	(1.4)	(14.5)	(135)
6vb2	8	50%	0.24	1.0	4.0	0.4	0.6	6.6	45
6- story				(1.2)	(5.0)	(0.5)	(0.9)	(8.2)	(71)
6vb2	8	2%	0.24	4.5	18.4	2.2	3.0	17.4	139
6- story				(6.6)	(27.0)	(3.2)	(4.6)	(25.1)	(185)
6vb3	8	10%	0.24	1.5	6.0	0.6	0.9	8.9	56
Stiff Beam				(2.1)	(8.5)	(1.0)	(1.3)	(12.9)	(92)

Figure 2.19: Statistics of the demand on BRBFs studied in (Sabelli, *et al.*, 2003).

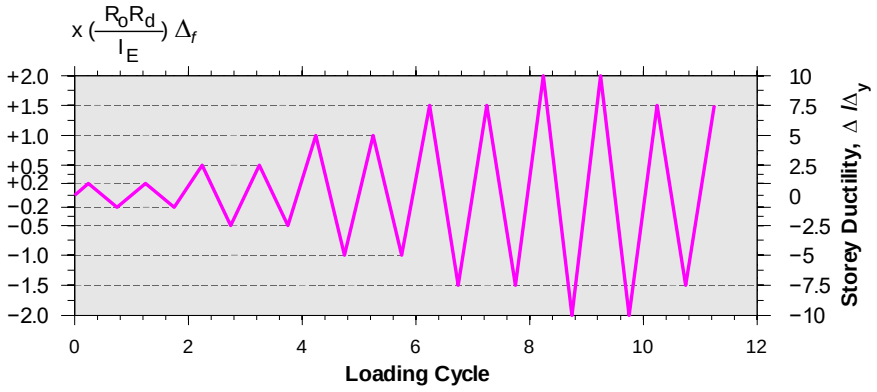

Figure 2.20 AISC-341 loading protocol for seismic qualification of BRBs.

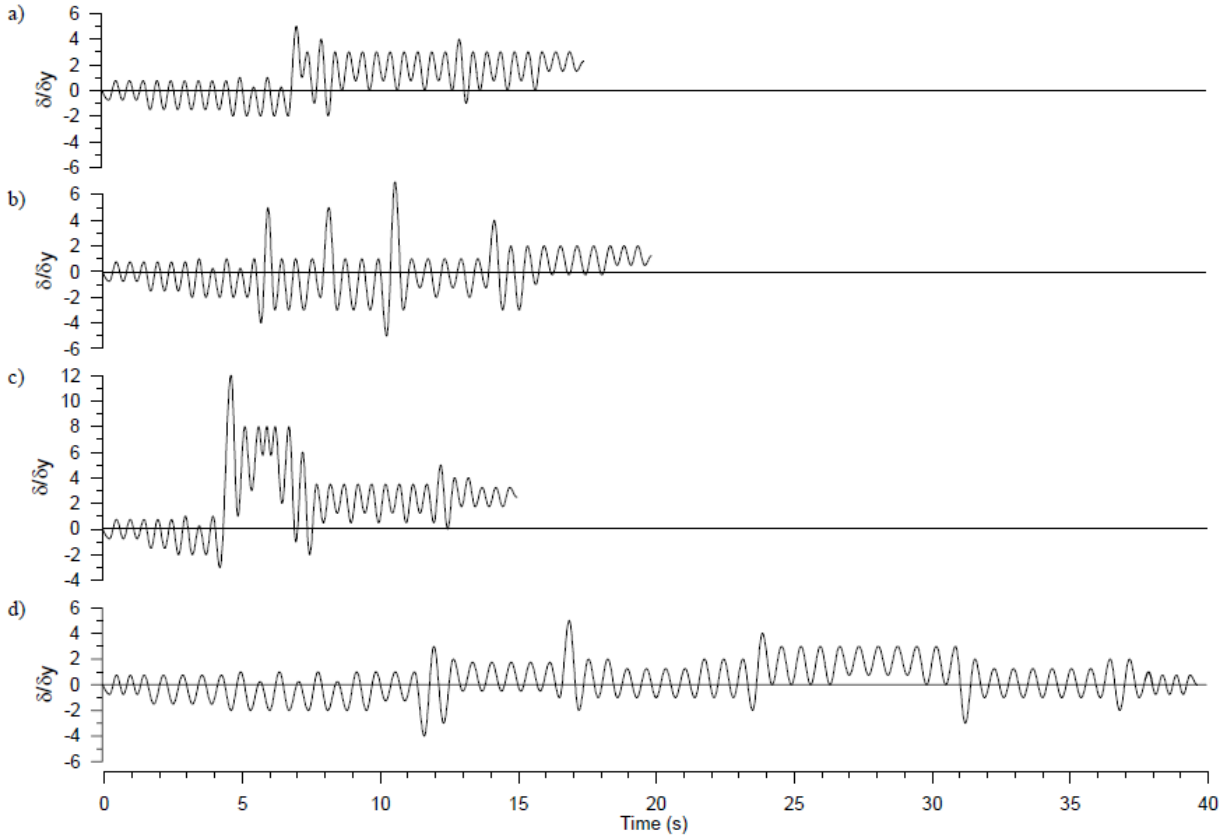

Figure 2.21: Loading histories proposed by (Tremblay, *et al.*, 2002): a) East, crustal events at distance; b) West, crustal events at distance; c) West, near-field events; and d) West, subduction events.

2.3 Design of restrainer

In order to achieve stable and complete hysteresis response under large inelastic displacements, restrainer has to be designed for global stability, and the normal thrust due to core inelastic high-mode buckling.

2.3.1 Global stability design

Ratio between brace Euler buckling load and yield resistance of the core member, P_e/P_y, is typically used as the global stability index for stiffness design of restrainer (Uang, *et al.*, 2004). The brace Euler critical load is computed assuming pin-pin boundary condition at the ends of BRB:

$$P_e = \frac{\pi^2 EI_r}{L^2} \tag{2.3}$$

where EI_r is the unit flexural stiffness of the restrainer, and L measures the effective BRB length. Different interpretation of L exist in the literature. Workpoint-to-workpoint length (Bolduc, *et al.*, 2003), and length between gusset plates (Tadokoro *et al.*, 2009; Chou, *et al.*, 2010) has been assumed as the effective buckling length. Several stability criteria based on P_e/P_y concept has been recommended. Watanabe *et al.* (1988) tested four unbonded brace subassemblies with P_e/P_y ratios between 0.55 and 3.8. Cyclic displacement loading with drift angle amplitudes between 0.25% and 2% were applied. Based on the geometry of the specimens, the largest drift angle was supposed to generate 1.2% core strain. Specimen with $P_e/P_y \geq 1.0$ showed stable hysteresis response in the entire loading. Other specimens globally buckled before reaching the core yield strength in compression. Based on the test results, and the effects of brace initial out-of-straightness, $P_e/P_y \geq 1.5$ was recommended. Wada *et al.* (2004) included initial imperfection and yield bending moment of restrainer in a second-order stability analysis and recommended the following expression:

$$\frac{P_e}{P_y} \geq 1 + \frac{\frac{\pi^2}{2}\frac{E}{F_{y,r}}\frac{\delta_o}{L}}{\left(\frac{L}{D}\right)} \tag{2.4}$$

where D is the minimum dimension of the encasing tube. Usami, *et al.* (2008) proposed an expression for safety factor against global buckling of brace that account for various parameters such as core-restrainer gap, initial out-of-straightness of restrainer, and axial load eccentricity. The proposed safety factor obtained from second-order analysis of a deflected pin-pin beam-column subjected to uniform transversal load and an eccentric axial load. This factor is expressed as the ratio between maximum expected compressive load, $P = \beta\omega R_y F_{ysc} A_{sc}$, and core yield strength:

$$\nu_F = \frac{P}{P_y} = \frac{1}{\frac{P_y}{P_e} + \left(\frac{P_y L}{M_{y,r}}\right)\frac{(a+d+e)}{L}} \tag{2.5}$$

where the parameters of this equation are shown in Figure 2.22. Four all-steel BRBs designed with ν_F range between 1.59 and 3.9 (P_e/P_y between 2.1 and 6.9) and tested under an intense cyclic loading with largest core strain equal to 2.8%. Specimen designed with $\nu_F \geq 3.0$ ($P_e/P_y \geq 4.46$) showed stable hysteresis response without global buckling. Based on this observation, $\nu_F \geq 3.0$ was proposed.

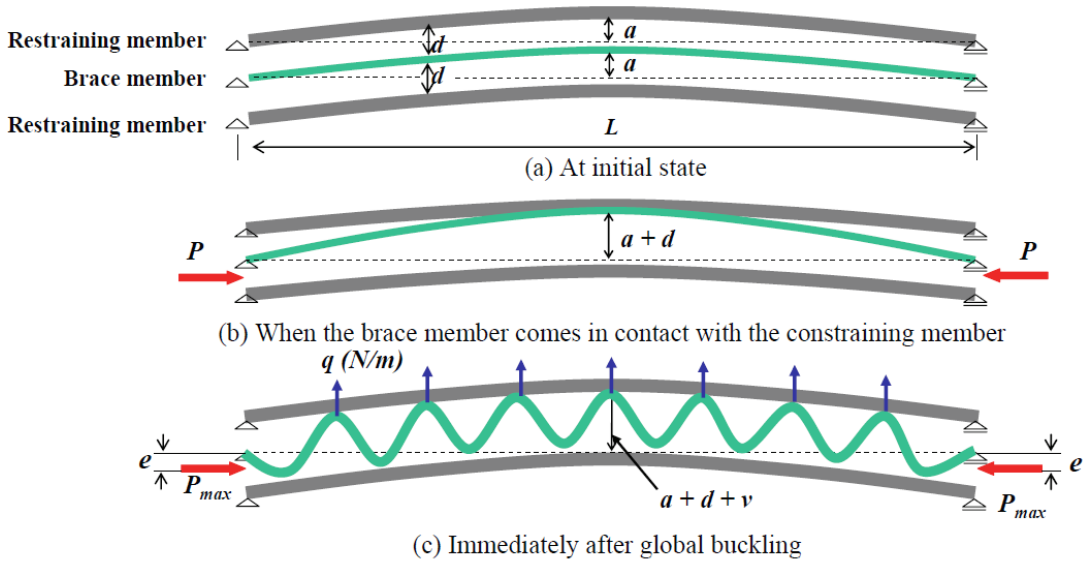

Figure 2.22: Combined global and local buckling in BRB (Usami, *et al.*, 2008).

(Chou, *et al.*, 2010) followed the global stability analysis proposed by (Usami, *et al.*, 2008) and tested 4 BRBs with P_e/P_y between 1.4 to 6.4. Specimens having $P_e/P_y \geq 2.5$ showed stable

cyclic response under loading with maximum core strain of $\epsilon_c = -2.1\%$ to -2.6%. Specimen with $P_e/P_y \geq 1.4$ showed stable responses before buckling globally at $\epsilon_c = -1.6\%$. Based on the results $P_e/P_y \geq 2.5$ proposed. Tremblay, *et al.* (2006) tested concrete-filled and all-steel BRBs with $6.3 \leq P_e/P_y \leq 7.3$ where P_e was calculated based on brace length between gusset plates. The concrete-filled specimen, $P_e/P_y = 7.3$, sustained core strain of $\sim -3.5\%$. Dusicka *et al.* (2012) developed an ultra-light restraining system for an aluminum core BRB using pultruded glass fiber-reinforced polymer (GFRP) tubes that are wrapped with GFRP fabric. Finite element simulation of the developed concept showed that, in absence of frame action bending demand, $P_e/P_y \geq 2.0$ is required to achieve stable cyclic performance. When 50% of the expected bending moment demand was imposed, restrainer stiffness had to be increased 25% to avoid global buckling and fulfil the performance goals under standard loading protocol. In addition to the classic global buckling, lack of sufficient strength at the non-yielding segment has resulted in localized yielding and premature failure of BRB (see Figure 2.23). (Takeuchi *et al.*, 2014) elaborated an analytical method to estimate the plastic collapse load of a BRB subjected to simultaneous in- and out-of-plane loading. To confirm the proposed stability analysis, six full-scale subassembly tests, having range of gusset plate stiffness and non-yielding segment strength, was carried out. In addition to the in-plane loading, an out-of-plane storey drift of 1% was maintained in course of test. Good agreement between the predicted collapse axial loads and the laboratory observation were reported.

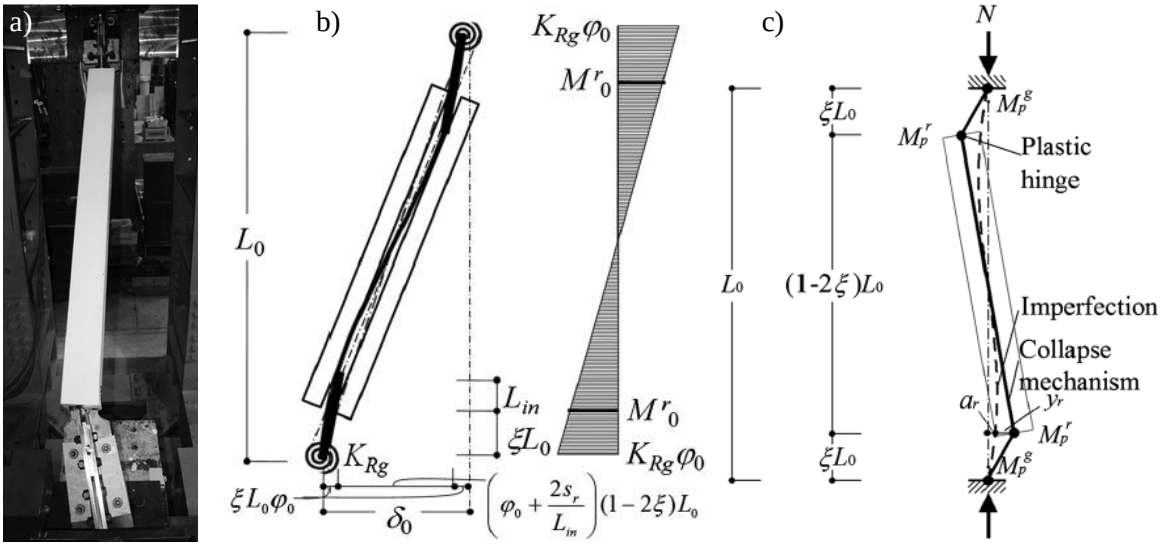

Figure 2.23: a) Global buckling of BRB due to plastic hinge formation at the non-yielding segment; b) additional bending moment due to out-of-plane movement; c) assumed collapse mechanism with plastic hinges at gusset plate ends, (Takeuchi, *et al.*, 2014).

2.3.2 Normal thrust analysis

When core buckling is restrained, it imparts a lateral reaction on the restraining system. Precise estimation of this normal thrust force is of great importance as the restrainer may fail under the imposed demand leading to significant strength degradation. Past studies have suggested that this normal thrust would be complex function of several factors:

- imposed axial shortening,
- gap between core and restrainer,
- core slenderness,
- frictional characteristics at the core-restrainer interface,
- core material mechanical properties (yield strength, stiffness, cyclic hardening),
- stiffness and strength of the restraining system.

The principal step in the core normal thrust analysis is to estimate the core buckling wavelength, or the number of waves, and the buckled configuration (shape). Buckling and post-buckling of a beam (or column) confined inside a frictionless containment has been studied analytically and experimentally in (Domokos *et al.*, 1997; Chai, 1998; Pocheau *et al.*, 2004; Tzaros *et al.*, 2011). In

literature, this problem is typically denoted as "bilaterally constrained buckling" problem. These studies were mostly theoretical with limited applicability to practical engineering problems such as BRBs. However, these studies collectively revealed that the bilaterally constrained buckling phenomenon is a rich bifurcation problem and more importantly, from the theoretical stand point, under certain loading condition a unique solution may not exist. This is to say under the same axial shortening, different buckled configuration may exist with quite distinct normal thrust on the restraining system. Chai (1998) studied experimentally and analytically elastic buckling of narrow flexible polycarbonate sheet confined between two parallel rigid walls (see Figure 2.24). This study developed analytical solutions to express the relation between most important response parameters, i.e. number of modes, axial force, axial shortening, and normal thrust, using small and large displacement hypothesis. Analytically, it was shown the buckling load in not unique and it depends on the relative length of the flat segment (variables a, b, and c in Figure 2.25d). However, it was shown that the buckling load is theoretically bounded between two deformed configurations: lower bound $a = b = 0$; and 2) upper bound $a = b = c$. This was expressed mathematically as follows:

$$\begin{aligned} 1 + 2n \leq \zeta \leq 1 + 4n, \\ \zeta = \frac{kL_0}{2\pi}, k^2 = \frac{P}{EI} \end{aligned} \tag{2.6}$$

where n is the mode number. Chen *et al.* (2016) extended Eq. (2.6) to inelastic buckling by simply replacing the Young modulus with tangent modulus $E_t = 0.02E$ to estimate the buckling wavelength of steel BRBs under inelastic loading:

$$\frac{L_0}{\text{int}\left(\frac{1}{2}\sqrt{\frac{3PL_0{}^2}{\pi^2 E_t b_c t_c{}^3}} - \frac{1}{2}\right)} \leq \ell_w \leq \frac{L_0}{\text{int}\left(\frac{1}{4}\sqrt{\frac{3PL_0{}^2}{\pi^2 E_t b_c t_c{}^3}} - \frac{1}{4}\right)} \tag{2.7}$$

where $\text{int}(\cdot)$ is the integer operator, and L_0 measures the core length. Post-test measurement suggested that the buckling length was better predicted by the lower bound value, i.e. the left hand side of Eq. (2.7). Depending on the maximum testing strain amplitude, experimentally-measured wavelength were −2% to +22% different from the lower bound values (positive means larger length from experiment). The larger differences were observed for the smaller testing strains. In (Chai,

1998) analytical developments, lateral constraint was assumed rigid. In a more recent study, Katz *et al.* (2015) was extended the Chai equations to the case of flexible constraint.

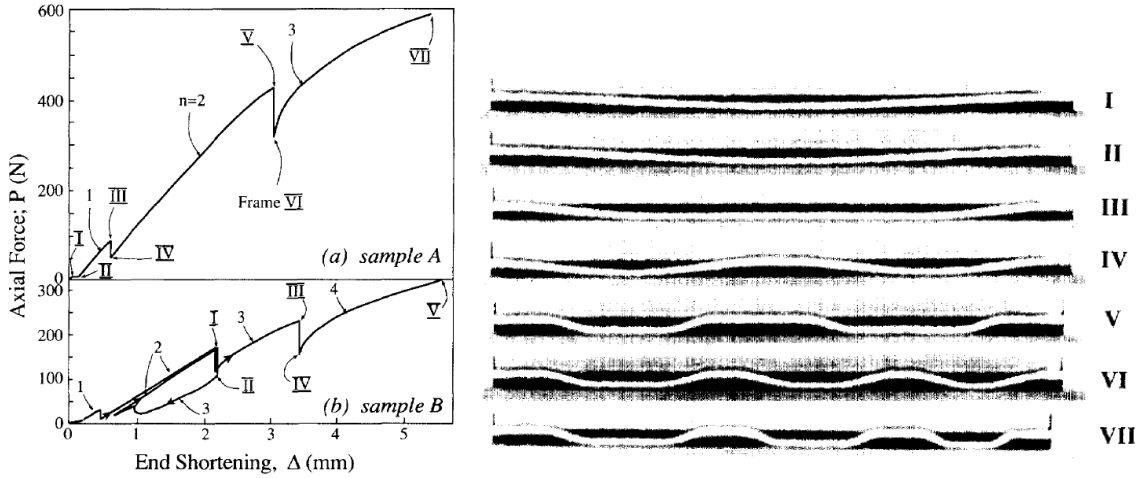

Figure 2.24: Load-displacement response and snapshots of the deformed configuration during at bifurcation points (mode transitions) (sample A), (Chai, 1998).

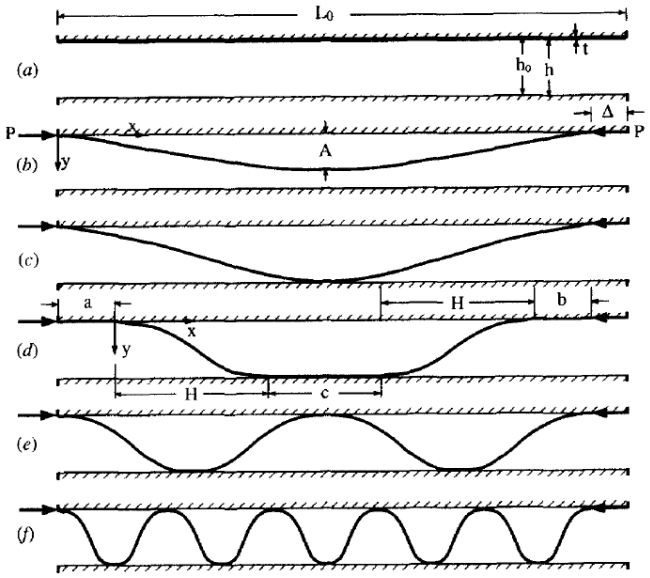

Figure 2.25: Buckling sequence of a bilaterally constrained column, (Chai, 1998).

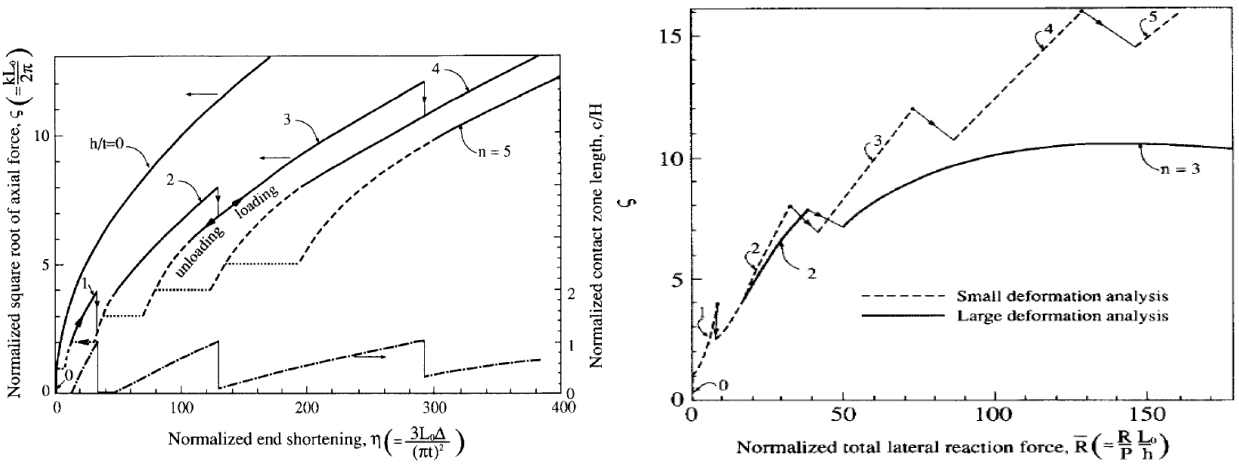

Figure 2.26: a) Relation between loading and response parameters of a bilaterally-constrained elastic beam subjected to end shortening: a) axial force vs shortening; b) axial force vs normal thrust, (Chai, 1998).

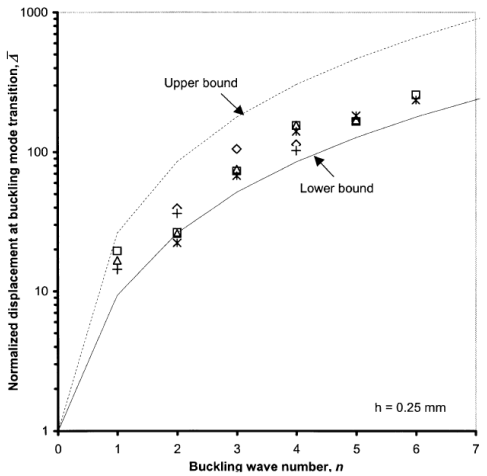

Figure 2.27: Statistical variation in number of modes at the given axial shortening, (Chai, 2002).

Korzekwa (2009) studied buckling of a BRB core that is bilaterally constrained by a frictionless encasing having elastic restraining stiffness K_e as shown in Figure 2.28. Using energy method, closed-from expressions for the critical system load and corresponding mode and total normal thrust was developed. Following waveform models were considered:

- Discrete with point contact (Figure 2.28a);
- Continuous with point contact (Figure 2.28b);
- Discrete with flat segment (Figure 2.28c);

– Continuous with flat segment (Figure 2.28d).

In the discrete models, it was assumed the flexural strain energy is only stored in hypothetical hinges at the folding points of the wave. In the continuous models, flexural strain energy is distributed and core was assumed to follow a sine deformed shape with clamped-clamped boundary condition at the core ends. Waveform in the last two models was mix of inclined and flat segments as seen in number of past experiments. The developed analytical expressions by Korzekwa (2009) are summarized in Table 2.1. In this table, P_y is the core yield strength, EI is the core unit flexural stiffness, $P_{cr,e}$ is the critical load of the system, m_{cr} is the number of buckling waves under the critical load, $m = \text{int}(m_{cr})$ where $\text{int}(\cdot)$ is the integer operator, $P_{cr,K}$ is the elastic critical load of the restraining system, and Δ_b is the gap opening. The total normal thrust could then be computed as $F_{K_e} = \Delta_b K_e$. The remaining parameters are defined in Figure 2.28. The critical system load was then employed to extend the elastic solution to the ultimate inelastic load carrying capacity. Then the minimum required restraining stiffness to develop a given level of compressive force in the system, without instability, was obtained. This stiffness is denoted by $K_{e,\lambda=0.25}$ where $\lambda = (P_y/P_{cr,e})^{1/2}$. It was shown that the normal thrust does not have a unique solution and its magnitude depends on the selected waveform. In the other words, for a given system, there exists many solutions that all satisfy the minimum potential energy principle but may result in different critical loads. Results of detailed 3D inelastic finite element model was used to validate the analytical solution. Model "d" was proposed to estimate the minimum required stiffness, i.e. $K_{e,\lambda=0.25}$, and model "b" was suggested to estimate the imparted normal thrust. Results of FE model that was subjected to cyclic loading up to ~1% shortening confirm the adequacy of the proposed design method. The proposed method was not experimentally verified. FE analysis also showed that providing lower-than-required restraining stiffness may result in less buckling waves (see Figure 2.29). This may imply that the BRBs encased with low restraining stiffness, may also perform satisfactory if enough strength is provided to ensure elastic response.

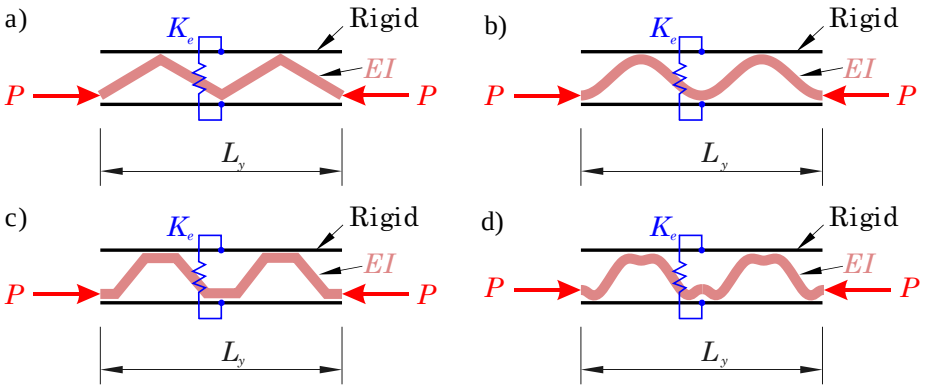

Figure 2.28: Buckling waveforms considered in the analytical development by Korzekwa (2009). Note: only two buckling waves are shown, i.e. m = 2.

Table 2.1: Analytical expressions developed by Korzekwa (2009).

Models	Discrete with point contact (Figure 2.28a)	Continuous with point contact (Figure 2.28c)	Discrete with flat segment (Figure 2.28b)	Continuous with flat segment (Figure 2.28)
$K_{e,\lambda=0.25}$	$\frac{512P_y^{\,2}L_y}{\pi^2 EI}$	$\frac{16P_y^{\,2}L_y}{\pi^2 EI}$	$\frac{256P_y^{\,2}L_y}{\pi^2 EI}$	$\frac{8P_y^{\,2}L_y}{\pi^2 EI}$
m_{cr}	$\frac{1}{2}\sqrt[4]{\frac{K_e L_y^{\,3}}{\pi^2 EI}}$	$\frac{1}{2}\sqrt[4]{\frac{2K_e L_y^{\,3}}{\pi^4 EI}}$	$\frac{1}{2}\sqrt[4]{\frac{K_e L_y^{\,3}}{8\pi^2 EI}}$	$\frac{1}{2}\sqrt[4]{\frac{K_e L_y^{\,3}}{4\pi^4 EI}}$
$P_{cr,e}$	$\sqrt{\frac{K_e \pi^2 EI}{2L_y}}$	$4\sqrt{\frac{K_e EI}{L_y}}$	$\sqrt{\frac{K_e \pi^2 EI}{L_y}}$	$4\sqrt{\frac{2K_e EI}{L_y}}$
$P_{cr,K}$	$\frac{K_e L_y}{4m^2}$	$\frac{2K_e L_y}{m^2\pi^2}$	$\frac{K_e L_y}{8m^2}$	$\frac{K_e L_y}{m^2\pi^2}$
δ	$\frac{4P\Delta_0 m^2}{L_y K_e - 4m^2 P}$	$\frac{2P\Delta_0 m^2\pi^2}{4L_y K_e - 2m^2\pi^2 P}$	$\frac{8P\Delta_0 m^2}{L_y K_e - 8m^2 P}$	$\frac{P\Delta_0 m^2\pi^2}{L_y K_e - m^2\pi^2 P}$

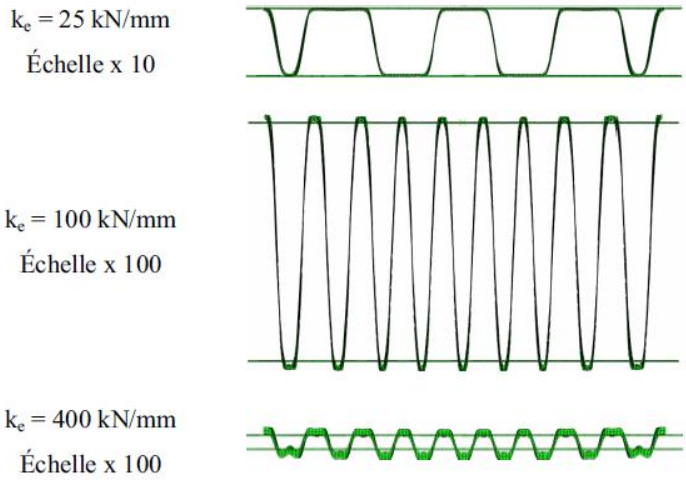

Figure 2.29: Effect of restraining stiffness on the buckling wave number and waveforms, (Korzekwa, 2009).

In another theoretical research with emphasis on BRB problem, Genna *et al.* (2014) studied elastic buckling of the same simple model that was described in (Korzekwa, 2009). Gap between core and restrainer was assumed small to avoid complications arising from large displacement theory and axial shortening due to flexural deformations. Again, it was shown that–theoretically–for a given of axial shortening there exist several alternative buckling configurations which can generate significantly different normal thrust. It was concluded that precise estimation of buckling wave number and shape, and normal thrust is impossible, due to presence of initial imperfections that cannot be defined precisely. It was shown that, mathematically speaking, buckling waveform of a bilaterally constrained beam does not exactly follow the Euler column problem. In fact, normal thrust generated at the point of contact can increase the critical buckling load. The theoretical buckling load of a single wave can be as large as 4 times the Euler critical load of a clamped-clamped column (for the configuration shown in Figure 2.30 (5)). This study presented analytical solution for the buckling wavelength with point and line contact waveforms. As an average buckling configuration, a waveform shown in Figure 2.30 (3) was proposed for the normal thrust calculation. Buckling load of the proposed waveform is 2.25 higher than the clamped-clamped column. Effect of finite restraining stiffness was also studied, and a numerically-obtained solution for the buckling wavelength factor was presented (see Figure 2.31). As this figure implies, the buckling length factor can be larger than the case of rigid restrainer. This may result, under certain condition, in less normal thrust on the restrainer since core buckles with less number of waves.

However, authors proposed using sufficiently rigid restrainer to avoid possible performance complications due to large gap opening. Bregoli, *et al.* (2016) extended the mentioned study to the inelastic buckling domain by replacing elastic modulus with a constant tangent modulus $E_t = 3.85$ GPa (~0.02E). An approximate approach to account for the effect of friction was also proposed along with a method to estimate the available restraining stiffness of a bolted all-steel BRBs. An expression for the minimum required restraining stiffness was also proposed.

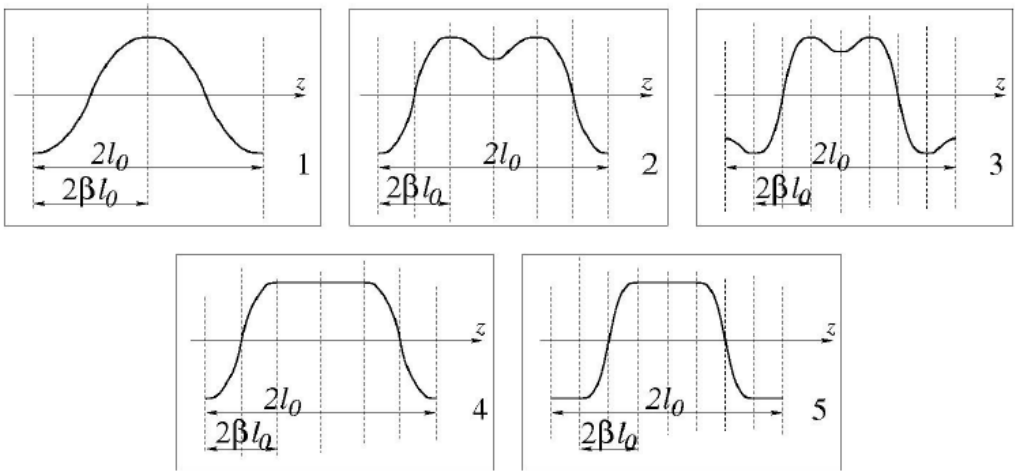

Figure 2.30: Buckling waveforms studied in (Genna, *et al.*, 2014).

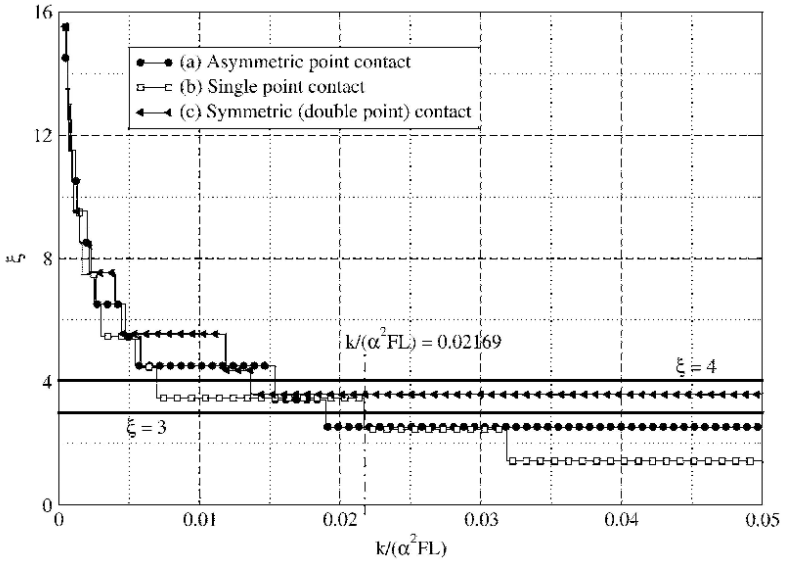

Figure 2.31: Buckling wavelength factor as a function of normalized restraining stiff, (Bregoli, *et al.*, 2016).

For BRBs, other than the mentioned theoretical studies, some other basic engineering approaches can be found, for example, in (Chou, *et al.*, 2010; Wu *et al.*, 2014; Chen, *et al.*, 2016). In these methods, core was supposed to buckle with a periodic multi-wave shape and each wave was assumed as an isolated column with clamped-clamped boundary condition. Length of this column, when buckles elastically, can be computed as:

$$\ell_w = \sqrt{\frac{4\pi^2 EI}{P}} \tag{2.8}$$

where EI is the unit elastic flexural stiffness of the core (about minor-axis), and P measures the axial force acting upon core. This theory is then extended to the case of inelastic buckling by replacing the core material elastic modulus with an inelastic one which is hereinafter referred to by "effective modulus" term. Given the wavelength and shape of the buckled wave, the unit normal thrust at each point of contact was then computed by establishing equilibrium in the deform shape:

$$N_i = \frac{P\Delta + \sum_{i=1,2} M_{i,c}}{\ell_c} \tag{2.9}$$

where Δ is the total gap between core and restrainer, $M_{i,c}$ is the core bending moment at the point of contact that is typically assumed zero, ℓ_c is the lever arm of the normal thrust couple. Generally speaking, difference between these studies lies in the assumed effective modulus in the calculations. Chou, *et al.* (2010) assumed waveform with point contact, i.e. $\ell_c = 0.5\ell_w$ and a constant tangent modulus equal to $E_{eff} = 0.05E$. Tensile yield resistance of the core was assumed as the acting axial load although in reality, at the ultimate condition, core has to carry much larger force. Given the wavelength and shape, the unit normal thrust at each point of contact was computed by establishing equilibrium:

$$f = P_{\max,l} \frac{g}{\ell_w/4} \tag{2.10}$$

Parameters of this expression are shown in Figure 2.32. The initial gap was assumed to remain unchanged given that the restraining stiffness is very high. Bending moment at the points of contact was assumed zero, probably by assuming that is the load carrying capacity of the core section would be entirely exhausted by the axial load.

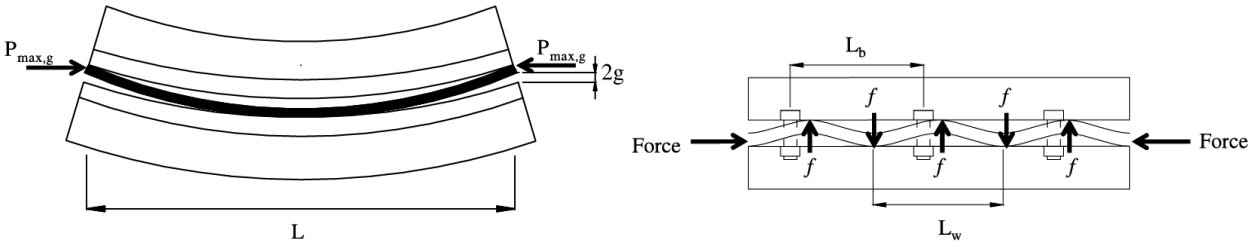

Figure 2.32: Assumed: a) global buckling of brace; and b) local buckled shape of core in (Chou, *et al.*, 2010).

Wu, *et al.* (2014) made the same assumption as in (Chou, *et al.*, 2010) except that the flexural stiffness of section was calculated using reduced or double modulus theory. The underlying assumption was that core section is unloaded on one side while the other side is being loaded. According to (Galambos *et al.*, 2008), reduced modulus of a rectangular section is:

$$E_r = \frac{4EE_t}{\left(\sqrt{E}+\sqrt{E_t}\right)^2} \tag{2.11}$$

(Wu, *et al.*, 2014) suggested to estimate the reduced modulus using $E_t = 0.02E$ and the restrainer was assumed rigid. The proposed calculation led to a minor-axis buckling wave length that is ~11t_c, where t_c is the core thickness. Experimental and finite element simulations were used to validate the proposed method. The maximum wavelength was ~12t_c when core strain was between 1% and 3%. However, for core strain between 3.0% and 4.5%, wavelength reduced to 8t_c–10t_c was observed which may imply the strain-dependent nature of the core inelastic flexural stiffness. (Midorikawa *et al.*, 2016) proposed the following expressions for the core buckling mode:

$$n = \begin{cases} \dfrac{\lambda}{\pi}\sqrt{\dfrac{F_{ysc}(P_c/P_y)}{E}} & P_c/P_y < 1.0 \\ \dfrac{\lambda}{\pi}\sqrt{\dfrac{F_{ysc}}{E}}\left(\sqrt{\dfrac{(P_c/P_y)-1}{E_r/E}}+1\right) & P_c/P_y \geq 1.0 \end{cases} \tag{2.12}$$

where $\lambda = L_y/r$ is the core slenderness, r is the minimum radius of gyration, and P_c is the imposed compressive force. Reduced modulus (Eq. (2.11)) with $E_t = 0.03E$ was suggested. The lower bound corresponds to the elastic buckling mode with clamped-clamped condition. The upper bound mode is the lower bound using $P_c = P_y$ plus the modes that are generated during inelastic buckling.

A good agreement between experimental results and the proposed expression was found. Wu *et al.* (2015) studied evolution of elastic and inelastic buckling mechanism of steel core constrained in a rigid frictionless restrainer under monotonic loading using combination of analytical approach and finite element method. It was shown that buckling waves shape switches back and forth between point and line contact configuration as the loading amplitude increases. Analytical expressions for the maximum normal thrust and bending moment on restrainer were presented. The analytical equations were extended to inelastic buckling problem by replacing E with E_t. Finite element inelastic buckling analysis with linear post-yield hardening, indicated that the actual modulus should be between tangent and reduced modulus. However, at large inelastic strain, number of waves computed by the tangent modulus deemed more accurate.

2.3.3 Interfacial friction

Upon core buckling and contact with restrainer, frictional forces are developed at the core-restrainer interface. This frictional force would be proportional to the normal thrust and can characterized by the coefficient of friction of the surfaces in contact. During compressive loading cycles, friction gradually reduces the core axial force along the sliding path. The reduce force is equilibrated by reaction in the restrainer. Severe friction can create non-uniform distribution of the longitudinal displacement demand along the core length and consequent damage localization and fracture (see Figure 2.33). FE analysis also confirmed this effect (Korzekwa, 2009). As see in Figure 2.34 residual thickness at the core ends was found to be thicker than the middle which is attributed to the differences in the local axial strain demand. The same trend was observed in the full-scale BRB tests with rough interfacial condition (Tremblay, *et al.*, 2006; Chen, *et al.*, 2016). Midorikawa *et al.* (2014) showed, by laboratory measurements, that buckling wavelength were shorter at the core ends compared to the "fixed point". Fixed point is a position along the core that there is no relative slip between core and restraining system. To avoid severe friction, a smooth condition has to be provided at the core-restrainer interface. Typically, this is achieved by gluing low-friction rubber-based layer on the core (Usami, *et al.*, 2008; Tsai, *et al.*, 2014; Chen, *et al.*, 2016) or by lubricating the interface using grease (Razavi Tabatabaei, *et al.*, 2014) or other oil-based products (Wu, *et al.*, 2014). However, the gluing is time consuming as the rubber has to be carefully cut and adhered to the core. In long-term, the grease and oil product may also lose their lubricity as they tend to dry. Therefore, a reliable, practical, and cost-effective smooth interfacial

condition should be devised for all-steel BRBs and its performance should be carefully evaluated through experiment. Tsai, *et al.* (2004) reported test results of six different debonding material and found Silicon rubber as an effective unbonding material.

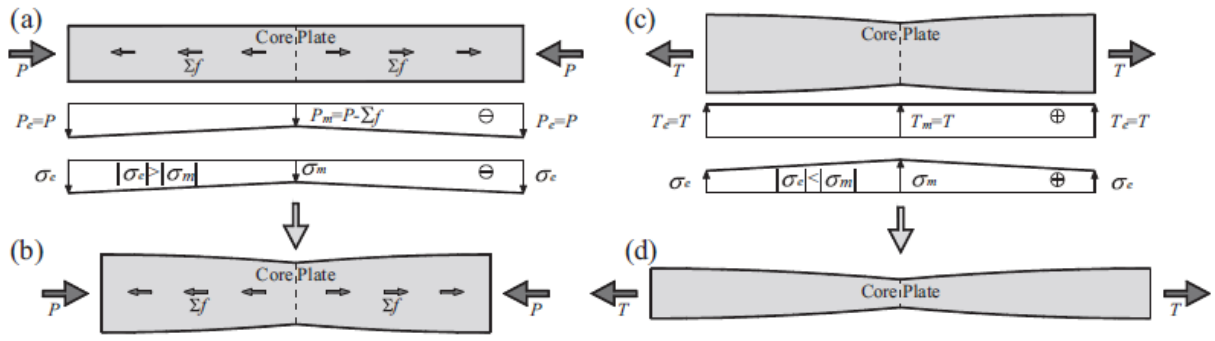

Figure 2.33: Frictional forces in BRB, (Chen, *et al.*, 2016).

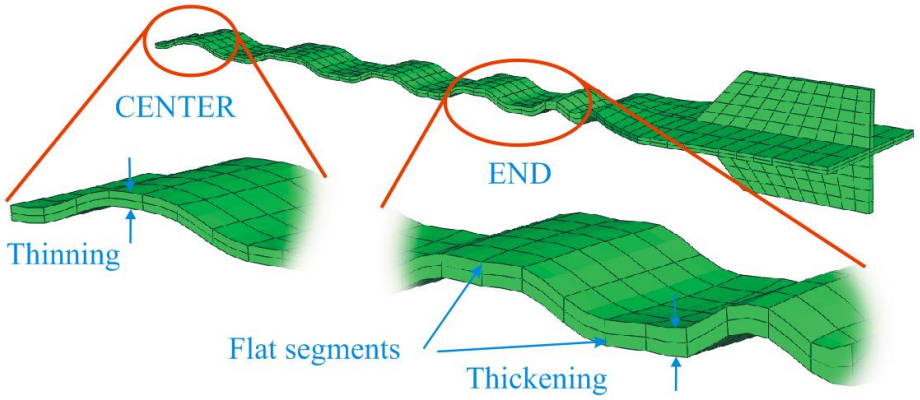

Figure 2.34 Non-uniform distribution of plastic strain of the core subjected to cyclic loads, (Korzekwa, 2009).

CHAPTER 3 METHODOLOGY

3.1 General

In Polytechnique Montréal, research on seismic design and performance of all-steel BRBs started in 2002 with an experimental program that involved testing several full-scale BRB subassemblies (Bolduc, *et al.*, 2003). Observations made in that research raised serious design and performance concerns and thus, further research to understand the behaviour of all-steel BRBs was found necessary. Motivated by this need, Korzekwa (2009) carried out extensive analytical research and developed a design procedure which was confirmed by detailed finite element analysis. However, the proposed method was not experimentally validated and the PhD program of the author was defined to fulfil this gap. Preliminary studies by the author concluded that several issues related to design and performance evaluation of all-steel BRB system are yet to be resolved. In particular, the following essential data for the BRB design are yet to be determined:

- seismic displacement demand on BRBF systems designed according to the Canadian building codes and engineering practice;
- cyclic strain hardening and low cycle fatigue behaviour of BRB core at material level including the effects of cold temperature and rate of loading.

To address these issues and fulfil the main objective of the program, the following research plan was designed:

- designing multi-storey BRBFs according to NBCC 2010 and S16-09, and evaluating the anticipated seismic displacement demand on these buildings through advanced numerical modeling and analysis techniques;
- conducting comprehensive material testing, and extracting the required data for design of BRB's restraining system;
- improving the existing analytical approach to estimate the design forces on the BRB restrainer and conducting more refined finite element simulations in light of the material testing data;
- qualifying the seismic performance of the developed all-steel BRBs concept at full-scale under severe earthquake loading conditions.

A combination of analytical and experimental research was needed to deliver the research objectives. In the following sections, the execution of each major part of the research plan along with the scope of the conducted research activities for each phase are elaborated.

3.2 Literature review

The current level of knowledge about the behaviour of BRBs was determined by reviewing the past research. Special emphasis was given to the Japanese experimental works as the BRB concept has emerged and evolved in this country. Historical data were collected and carefully examined to understand the most critical parameters that control the behaviour of BRBs. In the course of this work, literature review was constantly updated by monitoring the relevant keywords. Findings of new analytical studies, and experimental data were utilized in several steps of this research. In addition to the BRBFs, the literature review also covered several other related subjects such as ground motion selection and scaling, and material plasticity and constitutive laws. A detailed literature review can be found in Chapter 2 of this dissertation.

3.3 Ground motion selection and scaling

Preliminary nonlinear time history analysis (NTHA) was conducted using various sets of scaled ground motion records that were compiled using conventional methods such as that prescribed by ASCE-7 (ASCE, 2010). These analyses showed large statistical variations in the obtained results. Furthermore, in some cases, code-conforming models reached near-collapse conditions. Further investigation showed that the large variations and the severe structural demands were directly related to the selected and scaled ground motion records. Conventional scaling methods were found to produce unrealistic, high-intensity records as they do not account for each individual ground motion's frequency content. Drawbacks of the conventional methods are discussed in more details in Chapter 4. The need for more practical and rational methods was demonstrated. An alternative method of selecting and scaling ground motion records for NTHA was developed. Special emphasis was given to establishing a method that reduces the artificial uncertainty associated with the conventional methods. The developed method accounts for the local site seismic hazard deaggregation and statistical distribution of various ground motion intensity measures. In the record scaling method, special attention is given to the frequency content of the expected ground motions. Several suites of ground motion records were compiled according to the considered site

locations and soil classes. To evaluate the effect of record selection and scaling, several other sets of scaled records were put together using the most common practice such as the method outlined in ASCE7 building code (ASCE, 2010), and Conditional Mean Spectrum (CMS) (Baker, 2011).

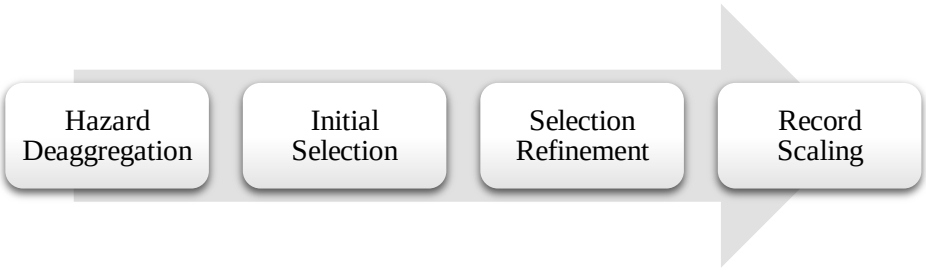

Figure 3.1: Process of selection and scaling of ground motion.

3.4 Estimation of displacement demands on BRBFs in Canada

3.4.1 Background

As a standard lateral seismic force resisting system, BRBFs were recently introduced in the Canadian building design codes. As a results, there was no specific data on the seismic performance of buildings with BRBFs that are designed and detailed according to the Canadian new regulations. Most available research on BRBFs were limited to the U.S. code-conforming prototype buildings which may not be representative of Canada due to differences between the American and the Canadian building codes and design practices. These facts motivated a thorough study of BRBFs that are designed according to the Canadian design standards.

3.4.2 Design of code-conforming BRBFs

Several multi-storey BRBF building prototypes were designed according to the latest edition of the Canadian standards, i.e. NBCC 2010 and S16-09. The chosen prototype represents a typical office building with a generic 56 m×36 m rectangular plan that is illustrated in Figure 3.2. The lateral stiffness and strength is assumed be provided by BRBFs situated at the exterior face of the building. Buildings were designed for 2% in 50 years seismic hazard in hypothetical locations in Victoria, BC and Montréal, QC. These are two densely populated areas with significant seismic hazard in western and eastern Canada, respectively. For both locations, 3- to 15-storey buildings were designed and two generic site soil classes were considered: 1) class C (soft rock); 2) class E (soft

soil). Typical gravity loads are presented in Figure 3.2. More details on design of these buildings can be found in Chapter 5.

To find the most efficient bracing pattern, several diagonal and chevron with Split-X, V, and Inverted-V braces were included in the design. The yielding segments of the chevron and the diagonal BRB were assumed to be 50% and 70% of the brace work-point length, respectively. The designed chevron and diagonal configurations are depicted in Figures 3.4 and 3.5, respectively. For both systems, two different braced bay arrangements were considered: 1) separated (C1 to C6 in Figure 3.4, and D1 to D6 in Figure 3.5); 2) back-to-back (C4 to C6 in Figure 3.4, and D5 to D8 in Figure 3.5). The "separated" layout has four columns in each braced axis that need to be designed and detailed for seismic loads. The "back-to-back" layout has one less seismically-loaded column which may be advantageous for having less column tonnage. In addition, in the "back-to-back" layout there is a shared column between the left and the right braced bays which will be subjected to a relatively small seismic axial force as the capacity forces of the concurrent braces nearly counterbalance each other. Tensile and compressive strengths of BRBs are nearly the same, and thus the out-of-balance capacity forces would be minimum in comparison with the conventional concentrically braced frames. To facilitate the design process, a tool was developed in Microsoft Excel that conducts full structural analysis and design for building with BRBFs. This program computes the capacity design forces for sizing beam and column members in BRBFs for various bracing configurations and arrangements. A snapshot of this program is provided in Figure 3.6. The column design worksheet of this computer program in shown in Figure 3.7. Column design is executed with a macro that determines the lightest possible column section which satisfies the strength and compactness requirements. In obtaining the upper bound of demand, having the least possible column size would be important as the continuous columns in a braced bay can contribute to demand redistribution along the building height. For the 3- to 9-storey prototypes in Victoria site class C, a comparative study was conducted to find the most efficient bracing pattern when the capacity design principles are applied. These frames were then redesigned for gravity-only loads and the required steel tonnage was estimated. For each considered bracing form, the seismic tonnage is then normalized to the gravity-only value to obtain a quantitative index. Only steel tonnage of the braced bay was considered for this calculation. Based on this analysis, configuration C6, i.e. Split-X pattern with "back-to-back" arrangement, was found to be the most efficient chevron bracing configuration when capacity design rules are enforced. This configuration

provides the most direct load path for the seismic actions and has three seismically-loaded columns in each braced axis. Among the studied diagonally braced systems, configuration D1 (with converging diagonals in a "separated" arrangement) resulted in the highest steel tonnage.

3.4.3 Inelastic modeling and analyses

Among the designed framing systems, configurations C6 and D1 were selected for seismic demand estimation using advanced inelastic analyses. C6 and D1 represent the BRBFs with the lightest and heaviest steel tonnage for the framing components, respectively. 2D numerical models of these buildings were built in SAP2000 computer program (CSI, 2010). The braced axis along the longer dimension of the building plan, i.e. east-west direction, was considered in the modeling. Symmetry was assumed to exist with respect to the principal axes of the building plan. Inelastic axial behaviour of BRB core was modeled using Bouc-Wen hysteresis law. Model parameters were calibrated based on the experimental data reported in (Tremblay, *et al.*, 2006). The algorithm elaborated in (Charalampakis *et al.*, 2008) was employed for the identification of the Bouc-Wen model parameters. Beams and columns were modeled using elastic frame elements and beam-brace-column joints that account for the gusset in-plane stiffness were incorporated in the model. Columns in the braced bays were assumed continuous and gravity columns were supposed to have shear-only splices (pin connection) in every other storey. More details on the Bouc-Wen model and the modeling technique can be found in Chapter 5.

Nonlinear static analysis (pushover), was first conducted using inverted triangular loading pattern on the Split-X models. In the next step, direct integration NTHA were carried out using the Newmark-β method. Rayleigh damping coefficients were tuned to obtain 3% critical damping ratios in the fundamental vibration mode and in the mode exceeding 98% of the accumulated modal mass. Stiffness proportional damping was not assigned to the bracing elements to avoid artificial forces that are generated upon fast-rate yielding of BRBs. This approach has shown to be accurate and effective in mitigating the fictitious viscous forces that could be generated in the course of large scale yielding of inelastic elements (Zareian *et al.*, 2010).

3.4.4 Post-processing analysis results

The results of the NTHA were employed to compute several seismic demand parameters that could be useful in performance evaluation of BRBFs at storey and brace level. For the most important

demand parameters sets of performance limits were defined. Statistical distribution of the seismic demands was used to estimate the conditional probability of exceeding the performance limits under the code-prescribed seismic hazard intensity. The demand indices were assumed to have lognormal probability distribution.

The response of the analyzed models at frame level was studied by means of the following demand parameters:

1) Storey drift ratio, θ
2) Amplification of design storey drift, $\Lambda = \Delta/(R_o R_d \Delta_f)$ in which Δ is the history of storey drift obtained from NTHA, and Δ_f is the storey drift computed from elastic analysis of the frame under design base shear
3) Residual storey drift ratio, θ_r
4) Roof drift ratio $\theta_{\text{roof}} = \Delta_{\text{roof}}/h_N$, where Δ_{roof} is the roof displacement history and h_N is the roof height with respect to the ground
5) Drift concentration factor defined as $\text{DCF} = \theta/\theta_{\text{roof}}$, where θ is the time history of drift ratio of a given storey
6) The difference between maximum and minimum storey drift ratios, $\theta_{\max} - \theta_{\min}$
7) Accumulated storey plastic drift angle, $\sum \theta_p$
8) Sorted sequence of plastic drift angle ranges, $\Delta\theta_p^i$ obtained from cycle counting of the history of the plastic drift ratio of the storeys
9) Absolute interstorey velocity, v
10) Column net chord rotation between two consecutive storeys, $\phi = \theta_{i+1} - \theta_i$
11) Dynamic overstrength at the base of the structure, $\Omega_d = V/V_{NBCC}$ where V is the NTHA base shear and V_{NBCC} is the NBCC-prescribed strength-design base shear.

Effective ranges of parameter Λ were computed using the Rainflow cycle counting method (ASTM, 2005) together with the corresponding number of cycles. These ranges are referred to as $\Delta\Lambda_{RF}^i$ in which i represents the sequence of ranges in a descending order.

Items number 7 and 8 require the plastic storey drift which could not be directly exported from the analysis results. To extract the plastic drift, the elastic stiffness matrix of the frame was recovered using the principal of the modal analysis:

$$\boldsymbol{K}_e = \mathbf{M}\Phi\Omega^2\Phi^{-1} \tag{3.1}$$

where $\boldsymbol{K}_e$ is the elastic stiffness matrix of frame; $\mathbf{M}$ is the diagonal storey mass matrix; and Φ and Ω^2 are matrices of eigenvectors and eigenvalues of the first n lateral displacement modes of the frame, where n is the number of storeys. The obtained stiffness matrix includes the global shear and flexural stiffness of the frames, and accounts for the effects of initial gravity stresses if second-order modal analysis is conducted. This matrix was then inverted and multiplied by the storey force history to recover the time history of the elastic storey displacements. The plastic component of drift in each step of analysis was obtained by subtracting the elastic component from the total drift.

The following demand indices were defined to evaluate the seismic demand on the BRBF floor diaphragms:

1) Maximum absolute of floor acceleration, $a_{\max} = \max(|a_f|)$,
2) Maximum ratio of floor acceleration to peak ground acceleration, $a_{\max}/\mathrm{PGA}$,
3) Number of occasions that the design acceleration has been crossed (level crossing), where design level acceleration is prescribed by NBCC 2010,
4) Duration of the diaphragm overload, where overload is assumed to exist when floor acceleration exceeds the design value prescribed by NBCC,
5) The ratio of overload duration to the significant duration of ground motion at the base of the structure.

Seismic demands on the BRBF floor diaphragms are discussed in more details in (Dehghani *et al.*, 2017a).

The response at the brace level was evaluated using deformation history of the BRB elements. Since stiffness of the non-yielding segments was included in the element model, the net ductility demand in the core had to be recovered as:

$$\mu = \frac{\delta - \delta_e}{\delta_{yc}} = \frac{\delta}{\gamma\ \epsilon^*_{yc}\ L_{br}} - \frac{\eta\chi}{\gamma}\frac{P}{P_{yc}} \tag{3.2}$$

where δ is the computed axial deformation in the brace element; δ_e is the elastic deformation of the non-yielding segment; δ_{yc} is the yield deformation of the core; ϵ^*_{yc} is the probable yield strain of the brace element modified for the isotropic strain hardening effect; η is the ratio of the core cross-sections in the yielding and the non-yielding segments; P is the brace axial force history; and $P_{yc} = R_y F_{yc} A_{sc}$ is the probable yield strength of the BRB core. The histories of parameter μ were converted to peak-and-valley data and the following demand parameters were computed:

1) Maximum absolute core ductility, $\mu_{\max}$
2) Sequence of large plastic ductility excursions, $\Delta\mu_p^i$
3) Largest shift in ductility, $\mu_{\max} - \mu_{\min}$
4) Cumulative plastic ductility, $\sum \mu_p$
5) Number of significant excursions, N_f
6) Normalized plastic work in the yielding segment, $W_{pn} = \sum(P\delta_c)/(P_{yc}\delta_{yc})$, where δ_c is the deformation history of the core yielding segment,
7) Rate of the i^{th} large plastic excursions, $\dot{\mu}_p^i$
8) Ductility ranges and corresponding number of cycles obtained from the Rainflow cycle counting method (ASTM, 2005) and sorted in descending order, $\Delta\mu_{RF}^i$ and n_{RF}^i
9) Low cycle fatigue damage, D_{LCF} (see Eq. (3.3))
10) Maximum amplification of brace design displacement, $\xi = \delta/\delta_d$ where δ is the NTHA response of the brace displacement, and δ_d is the expected brace inelastic design displacement as per Eq. (3.4)
11) Sorted effective ranges of ξ obtained from the Rainflow cycle counting, $\Delta\xi_{RF}^i$

The rainflow cycle counting results of μ were employed to estimate the low cycle fatigue damage state of the BRB cores (item number 9). This was achieved through combination of Manson-Coffin

low cycle fatigue equation and Miner's linear damage accumulation rule as elaborated in (Krawinkler et al., 1983):

$$D_{LCF} = 115 \sum_{i=1}^{N} n_{RF}^{i} (\epsilon_{yc} \Delta\mu_{RF}^{i})^{2.5} \tag{3.3}$$

According to this model $D_{LCF} \geq 1.0$ means failure. The coefficient and the exponent of the low cycle fatigue damage model were calibrated against experimental results of commercial grade BRBs.

Parameter δ_d in item number 10 was computed based on the specifications and geometry of the BRB, and the response modification factors of the system:

$$\delta_d = \frac{R_o R_d}{I_E} \frac{1}{\gamma + \eta\chi} \frac{P_{br} L_{br}}{E A_{sc}} \tag{3.4}$$

where R_d = 4.0 and R_o = 1.2 are, respectively, the ductility- and overstrength-related force modification factors as prescribed by NBCC 2010 for BRBFs; P_{br} is the brace axial load obtained from elastic analysis of the frame under the design base shear; I_E is the building importance factor as defined by NBCC; $\gamma = L_{sc}/L_{br}$ and $\chi = L_e/L_{br}$ in which L_{sc}, L_{br} and L_e are the yielding segment, work-point (total), and elastic non-yielding segment lengths of the BRB member, respectively (see Figure 3.9); and E is the Young's modulus of the core section.

Conceptually, parameter ξ is similar to the core ductility μ but it can better reflect the design assumptions. It indicates how the expected design value would be amplified as a result of inelastic dynamic effects.

The NTHA histories of the BRBF columns' axial forces and bending moments were employed to assess the seismic performance of these members. The following demand parameters were defined:

1) Demand/capacity ratio as per S16 column interaction equation (see Eq. (3.5)), CDC
2) Normalized axial force demand, $C_{fn} = C_f/C_r$. In this expression, C_f is the column axial force demand, and C_r is the column factored axial resistance (see Eq. (3.6))

3) Normalized bending moment demand, $M_{fn} = M_f / M_{pc}$ where M_f is the history of column bending moment (maximum of column ends' values), and M_{pc} is the column plastic bending capacity in the absence of axial stress
4) Moment gradient factor, κ defined as the ratio of smaller to larger bending moment demand at the opposite ends of the column
5) Bending moment amplification factor U_1 as defined by Eq. (3.9)
6) Axial load eccentricity, $e_c = M_f / C_f$
7) Normalized axial load eccentricity, $e_{cn} = e_c / h_c$ where h_c is the column depth in bending.

As per S16-09, the column demand/capacity ratio is computed as:

$$\text{CDC} = \frac{C_f}{C_r} + \frac{\beta U_1 M_f}{M_r} \tag{3.5}$$

where C_r is the column factored axial resistance:

$$C_r = \phi A F_y (1 + \lambda^{2n})^{-1/n} \tag{3.6}$$

where ϕ is resistance factor (0.9 for columns); A is the column cross-sectional area; F_y is the column yield stress; n = 1.34 for hot-rolled structural sections; and λ is the square root of the ratio of the column yield stress to the Euler buckling stress:

$$\lambda = \sqrt{F_y / F_e} \tag{3.7}$$

The Euler buckling stress of column is obtained as:

$$F_e = \frac{\pi^2 E}{(KL/r)^2} \tag{3.8}$$

where r is the minor-axis radius of gyration of the column; and KL is the column effective length (the storey height). U_1 is the moment amplification factor that is defined as:

$$U_1 = \frac{\max(0.6 - 0.4\kappa, 0.4)}{1 - C_f/C_e} \tag{3.9}$$

In the above equation, C_f is the axial force; C_e is the Euler buckling load; and κ is the moment gradient factor which is defined as the ratio of the smaller to the larger bending moment demands at the opposite ends of the compressive member. By definition, this factor is positive if the member is subjected to double curvature bending profile and negative in the opposite case. Coefficient β is defined as:

$$\beta = 0.6 + 0.4\lambda \tag{3.10}$$

Using the NTHA results, the effects of several design parameters such as site class, bracing patterns, core material grade, and vertical distribution of the lateral strength is investigated. A procedure is established to account for the uncertainty associated with ground motion selection and scaling. Parameters of the statistical distributions were updated based on this procedure and the probability of exceeding the performance limits were adjusted for ground motion selection and scaling uncertainty. This procedure is discussed in Chapter 5.

The computed displacement demands were subjected to extensive statistical post-processing to develop sets of dynamic loading histories for testing BRBs that are designed for various locations in Canada. These loading histories are discussed in (Dehghani *et al.*, 2012b).

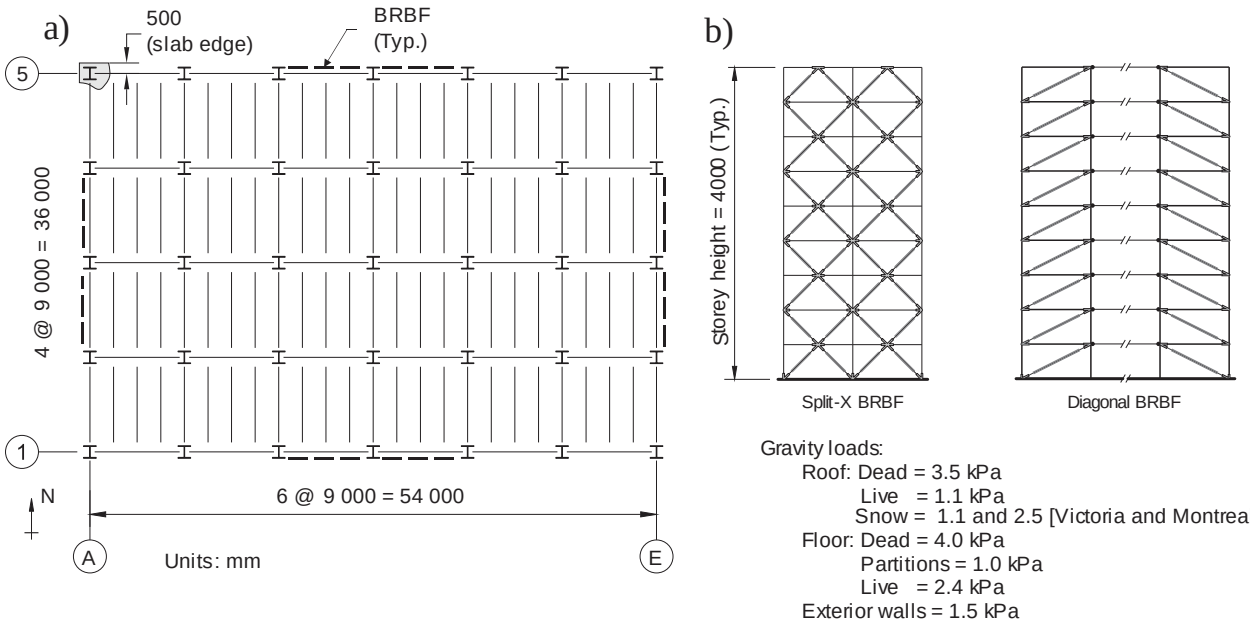

Figure 3.2: a) Plan of the studied building prototype (back-to-back brace bay arrangement is shown); b) Elevation view of the braced bays (only system with "back-to-back Split-X" chevron and "separated diagonal" braced panels are shown).

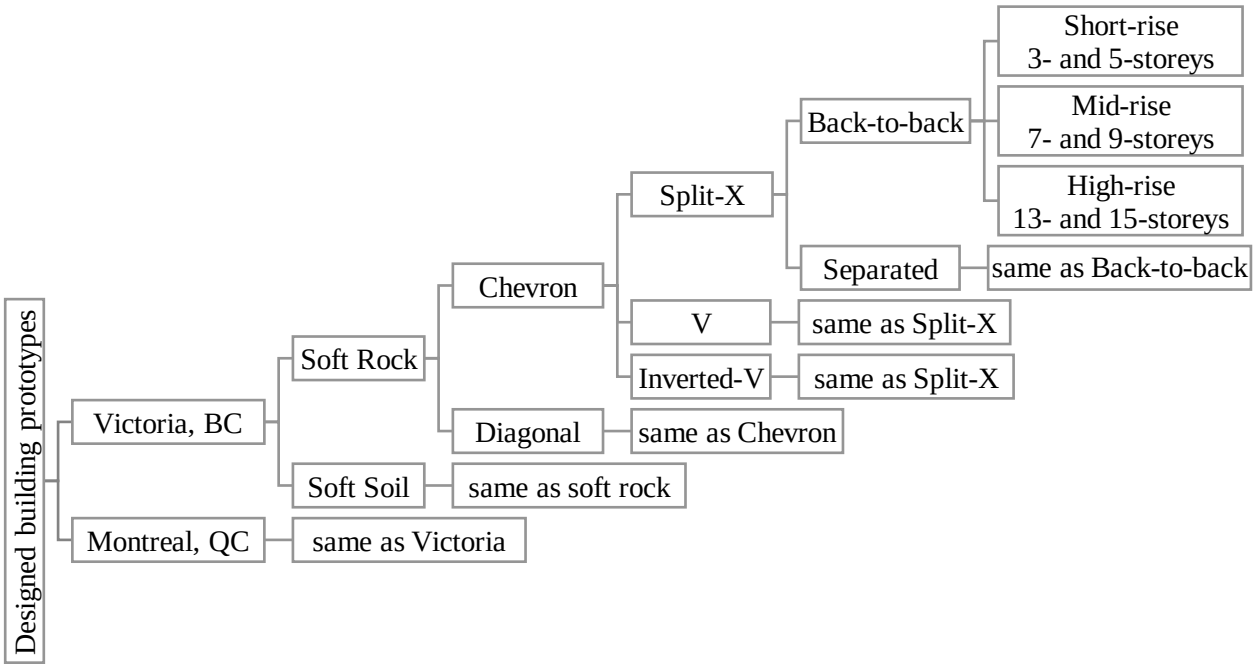

Figure 3.3: Designed building prototypes.

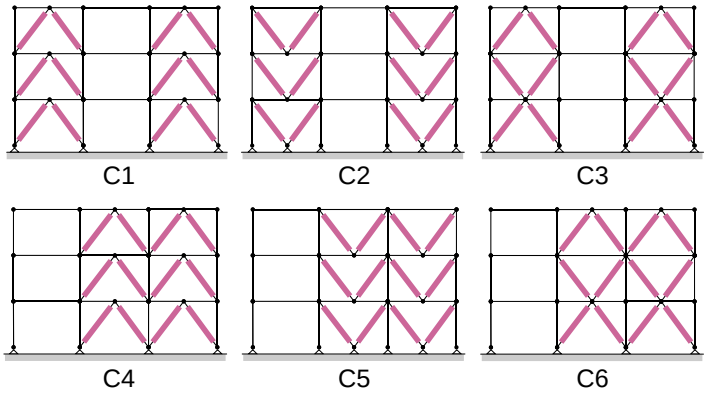

Figure 3.4: Considered chevron BRBF configurations.

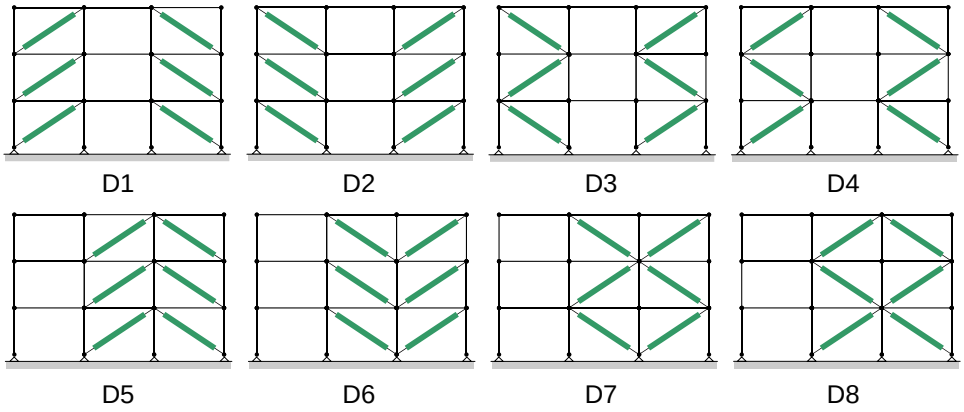

Figure 3.5: Considered diagonal BRBF configurations.

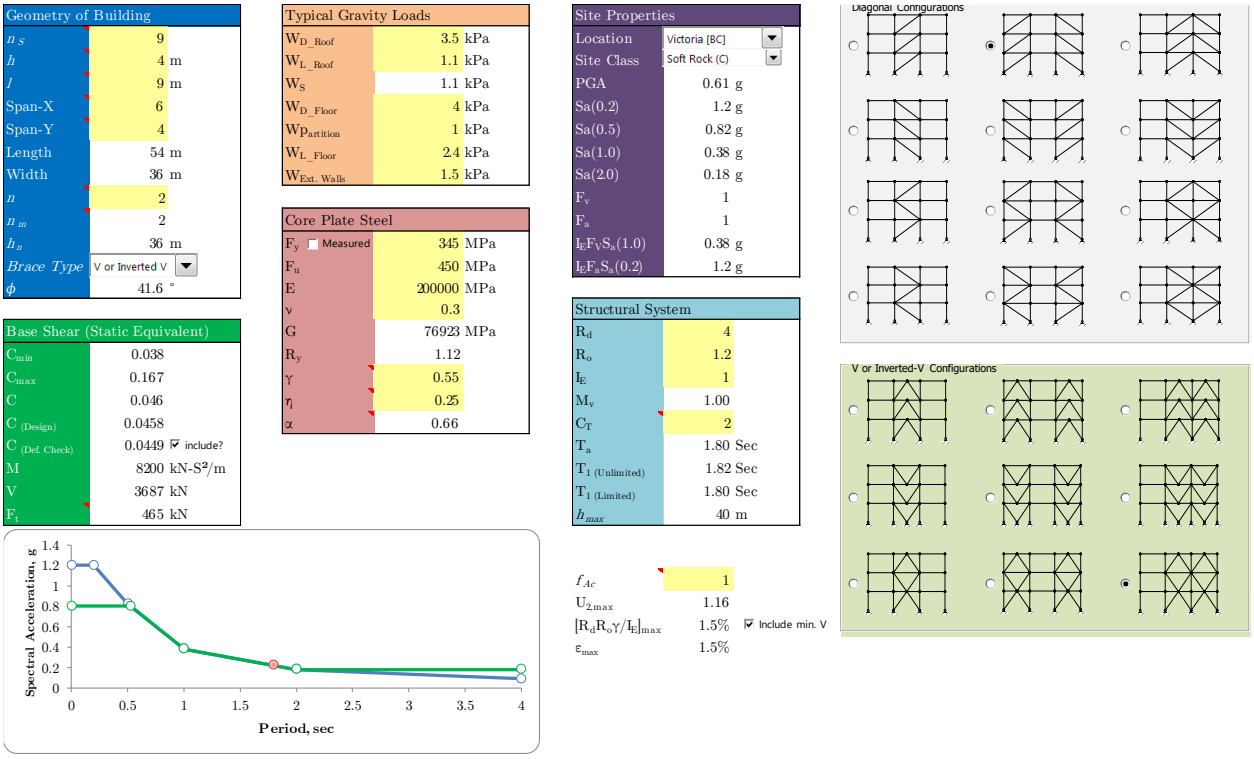

Figure 3.6: Snapshot of the Excel tool developed for seismic design of BRBFs according to NBCC 2010 and S16-09.

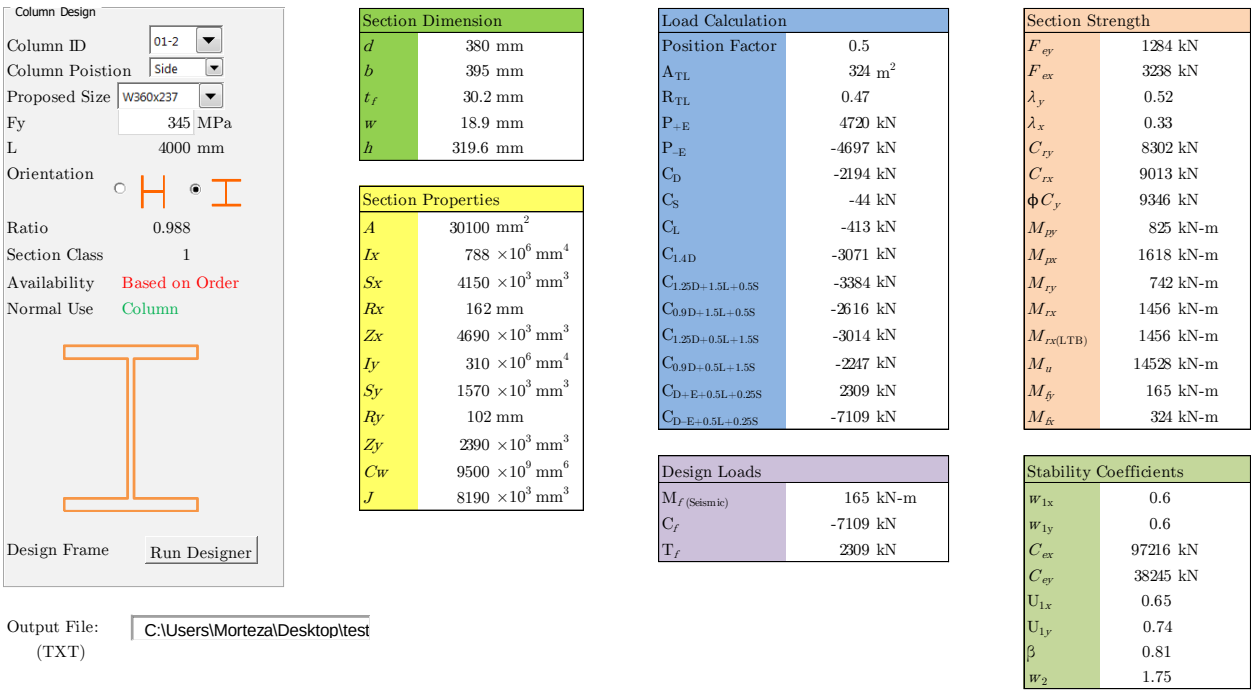

Figure 3.7: Snapshot of the Excel worksheet for automatic design of BRBF columns.

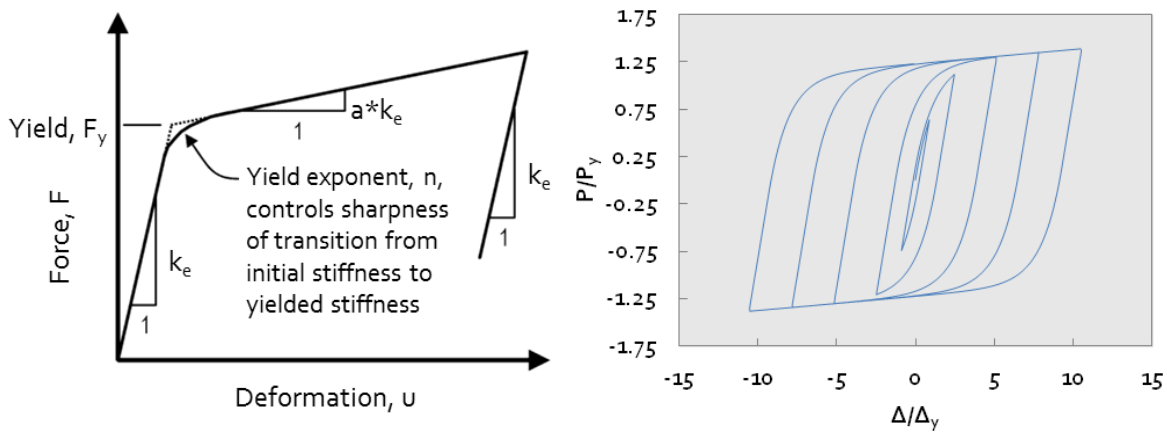

Figure 3.8: Bouc-Wen model: a) General description of force-displacement relation; b) hysteresis response under symmetric displacement-controlled step loading.

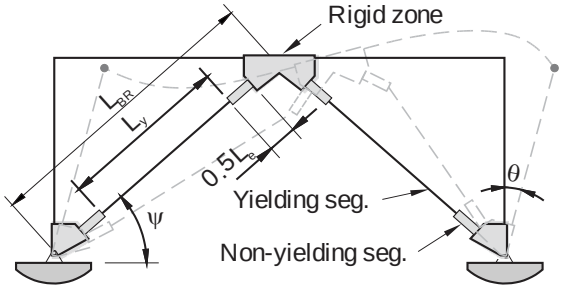

Figure 3.9: Schematic view of chevron BRBF storey.

3.5 Experimental material characterization of 350WT steel

3.5.1 Introduction

An extensive material testing program was designed and executed to characterize the most important mechanical features of CSA G40.21 350WT steel. This steel grade was chosen for the BRB core due to its ductility, and enhanced low temperature toughness. The test matrix is shown in Figure 3.10. These tests are essentially required for restrainer design and evaluating the BRB core fracture life under cyclic loading. Tests were performed at room and subfreezing temperatures to investigate the possible impacts of cold condition on ductility of mild structural steel under fast and large inelastic deformations. Target temperature of −40 °C was defined for the subfreezing tests. This is the designated service temperature for design of bridges in very cold regions of Canada (CSA, 2006). Experiments for characterization of 350WT steel were carried out at the Structural

Engineering Laboratory of Polytechnique Montréal. Some complementary room temperature tests were also performed at the Structural Engineering Laboratory of Laval University, Québec City using a 500 kN MTS 322.41 load frame (Beaumont *et al.*, 2016). Charpy impact test using V-notch specimens (Figure 3.25) was done at +24 °C, −40 °C, and −50 °C in a commercial laboratory in Montréal, Québec.

3.5.2 Specimens

Small-scale round and smooth specimens (see Figure 3.11) were subjected to uniaxial monotonic tensile and cyclic loadings as described in Figure 3.10. Specimens were machined from the coupons that were cut along the rolling direction of a single 1-1/4" (31.75 mm) thick steel plate conforming to the 350WT Category 4 requirements. Precise numerically-controlled tools were used in the machining process with special attention to avoid undercuts at the base of the shoulders. Surface roughness of the specimens were measured at the Virtual Manufacturing Research Laboratory of Polytechnique Montréal using Mitutoyo surface roughness tester model SV-3100W8 (see Figure 3.12). The measured average surface roughness, R_a, of the as-received specimens was ~1 µm. These specimens were not polished after machining given that surface preparation was not expected to have significant effects on the fatigue life of specimens subjected to large strain amplitudes. Few circumferentially-notched specimens were also subjected to monotonic and cyclic loadings at room and subfreezing temperatures. Notch geometry in these specimens was designed to create a relatively mild stress triaxiality condition that may exist at the transition area between yielding and non-yielding segments of BRB core.

3.5.3 Test setup, instrumentations, and execution

Testing at Polytechnique Montréal was performed in an Instron 8806 four-column load frame. This is a closed-loop servo-hydraulic uniaxial testing frame that has static and dynamic force capacities of 1500 kN and 1000 kN, respectively. This fatigue-rated load frame is mainly for testing structural-scale components and to test small-scale specimen a special fixture was required. The fixture parts, shafts, couplers, clamping system, and jam nuts were machined from AISI 4140 HT steel using numerically controlled precision fabrication tools. The stages of specimen insertion in the load frame are shown in Figures 3.16 and 3.17. The test fixtures and the specimen installation process were designed so that the best possible alignment could be achieved. Alignment of the test

setup was verified according to ASTM E1012 (ASTM, 2012) using an instrumented specimen as shown in Figure 3.13. Bending deformations were limited to 5% of the total deformation in the elastic domain. Tensile tests were carried out on round specimens in accordance with ASTM E8 (ASTM, 2009). In the tensile tests, a relatively wide range of strain rates was considered, i.e. between 0.005%/s and 10%/s. Fracture of specimen tested under 10%/s rate at room temperature is shown in Figure 3.19. In addition to the slender specimens (ϕ12.5×50 mm), tensile tests at 0.1%/s strain rate were conducted on stocky specimens (ϕ15×25 mm).

In the tensile subfreezing tests, the specimens and a large portion of the test fixture were placed into a Cincinnati Sub-Zero environmental chamber (model TT-3.3-.75-H/AC) where they were cooled to the target temperature of −40° C using cold air stream generated by the chamber's refrigeration compressor (see Figure 3.20). The chamber temperature along with the temperature at different locations of the fixtures were continuously monitored using isolated thermocouples. It was not possible to attach thermocouples directly on the surface of the specimens' gage area due to the presence of the clip-on extensometer. However, the specimen surface temperature next to the gage area was continuously monitored. A dummy piece with an inserted thermocouple was also fabricated and hung near the test specimens inside the chamber. This dummy piece did not have a conductive heat exchange path and was used to evaluate the cooling rate of the specimens due to convective heat transfer. Testing started 30 minutes after the cold air temperature around the specimen was stabilized at the target temperature. The temperature readings at the vicinity of the gage region were used to determine when the gage area attained the desired temperature of −40 °C. The cold air temperature was then maintained constant through the test.

At the trial stage of cyclic testing it was realized that the lateral stiffness of the load frame was not sufficient to prevent the relative lateral deformations of the specimen ends at compressive strains larger than 2% (see the failure mode shown in Figure 3.18a). The load frame sway buckling mode incurred additional strains in the specimens leading to a premature failure. To prevent this behaviour, the load frame lateral stiffness was increased by adding horizontal lateral bracing in both orthogonal directions at the actuator's lower end and at the crosshead level (see Figures 3.14 and 3.15). The bracing eliminated sway buckling failure mode up to 8% maximum compressive cyclic strain amplitude applied in the tests. As shown in Figure 3.18b, when this lateral bracing was added, the specimen could sustain large compressive strains without lateral out-of-plane movement.

A second set of fixtures with reduced length was used to achieve a stable response in compression. A small in-house insulated box was fabricated and attached to the environmental chamber (see Figure 3.21). This insulated box is referred to as “annex”. The cold air stream was directed to the annex using a funnel-shaped guide. As shown, the instrumented dummy piece was placed in the annex to monitor the air temperature and thermocouples were still used on the test specimens next to the gauge area. Due to the more complex geometry, it was more difficult to reach the desired temperature for the cyclic tests. Depending on the case, the measured annex temperature varied between −42 °C and −65 °C.

3.5.4 Loading

Strain-controlled cyclic tests were divided into tests with constant- and variable-amplitude loading. The former were conducted according to ASTM E606 (ASTM, 2004) practice. A wide range of strain amplitudes, applicable to earthquake engineering domain, was chosen for the constant-amplitude experiments. The chosen amplitudes for the constant-amplitude tests were between ±1.0% to ±8.0%. A fixed gage strain rate of 0.1%/s was employed for the constant-amplitude cyclic tests. In the trial stage of these tests, a sharp load drop were observed upon the first yielding of specimens. To avoid this situation, the first quarter of the first loading cycle was performed at a 10 times slower rate, i.e. 0.01%/s. This practice was found to have literally no effect on the hysteresis response of the specimen (see Figure 3.22). In the cyclic subfreezing tests, the main challenge was to prevent lateral buckling due to the long length of the required test fixtures.

Different variable-amplitude loading histories were designed and applied. This includes real-time seismic loading patterns from three distinct type of ground motion records, and symmetrical and asymmetrical step-wise patterns. Seismic loading patterns were designed using structural response to ground motions from ordinary far-field, impulsive near-field, and subduction interface megathrust earthquakes. The selected ground motion records are described in Table 3.1. Spectral acceleration and kinetic energy built-up of the selected ground motion records are shown in Figure 3.24. These records were scaled to match the NBCC 2010 design spectrum in Victoria, BC and used in inelastic dynamic analysis of numerical multi-storey building models with BRBFs. To design the seismic loading histories, deformation of the BRB members were extracted and converted to strain. More details on the seismic loadings can be found in Chapter 6. Few cyclic

tests were also carried out under asymmetric stress-controlled loading condition to evaluate ratcheting response of the 350WT steel. Results of these tests are briefly discussed in Chapter 9.

Table 3.1: Ground motion records employed to design the seismic loading histories.

Signal Type	**Event name**	**M** [(a)]	**Stat.** [(b)]	**Cmp.** [(c)]	$\mathbf{R_{hyp}}$[(d)]	$\mathbf{R_{cd}}$[(d)]	**PGA**[(f)]	$\mathbf{T_m}$[(g)]	$\mathbf{D_{5\text{-}95}}$[(h)]	**SF** [(i)]
Ordinary	Loma Prieta, 1999	6.9	BRAN	0	20	11	0.48	0.46	9.0	1.5
Impulsive	Chi-Chi, 1999	7.6	TCU031	Fault-normal	80	30	0.11	2.00	24.1	2.7
Subduction Interface	Tohoku, 2011	9.1	FKS005	East-West	145	39	0.45	0.33	92.4	1.7

(a) Moment magnitude

(b) Recording station

(c) Component of ground motion

(d) Hypocentre distance in km

(e) Closets distance to fault rupture in km

(f) Peak ground acceleration in g

(g) Mean period of ground motion acceleration in seconds

(h) Significant duration in seconds

(i) Scaling factor to match the NBCC 2010 2% in 50 years design spectrum of Victoria, BC.

3.5.5 Test data analysis

Material testing results were subjected to extensive post-processing. Special emphasis was put on understanding the cyclic hardening behaviour and characterizing the low cycle fatigue life of 350WT steel. Parameters of the most common strain-based and energy-based low cycle fatigue damage models were calibrated based on the test results. Effectiveness and efficiency of these damage models in predicting fracture life under variable-amplitude inelastic loading patterns was evaluated. Nonlinear regression analysis was conducted to establish a simple prediction model for

the basic features of the cyclic strain hardening behaviour. The effect of cold temperature on fracture strain and low cycle fatigue life of 350WT steel was studied and quantified. The combined effect of fast rate loading and low temperature condition was evaluated. More details on the test results are given in Chapter 6. A thermal analysis finite element model was created in ABAQUS (SIMULIA Inc., 2012) to estimate the gauge area temperature in the subfreezing tests. FE model was calibrated using thermocouple readings attached to the fixture and dummy piece.

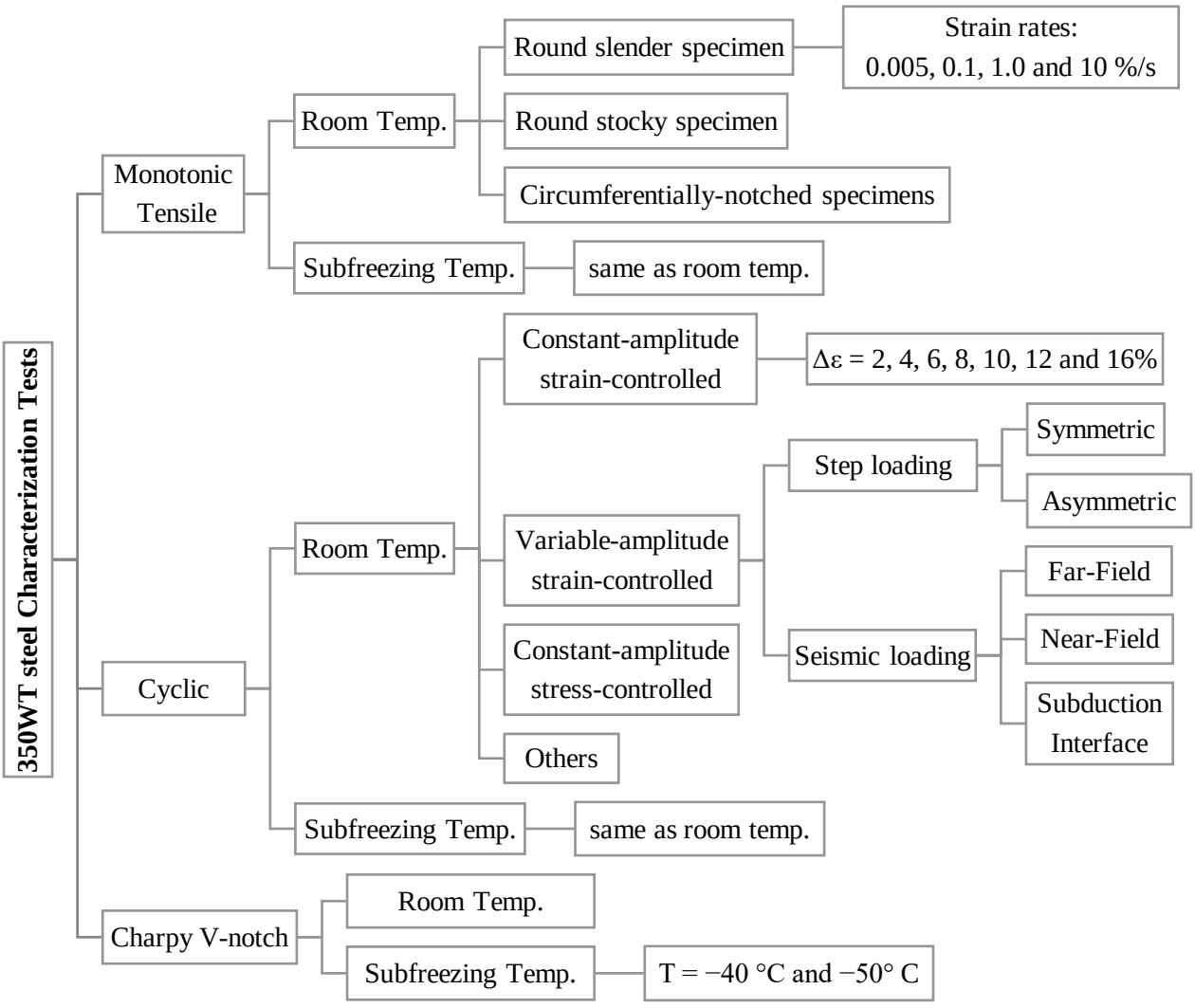

Figure 3.10: Test matrix for 350WT steel material characterization.

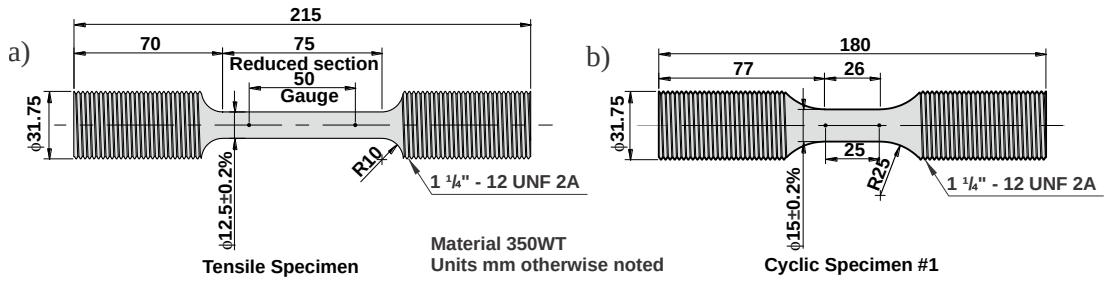

Figure 3.11: Geometry of specimens: a) Tension; b) Cyclic.

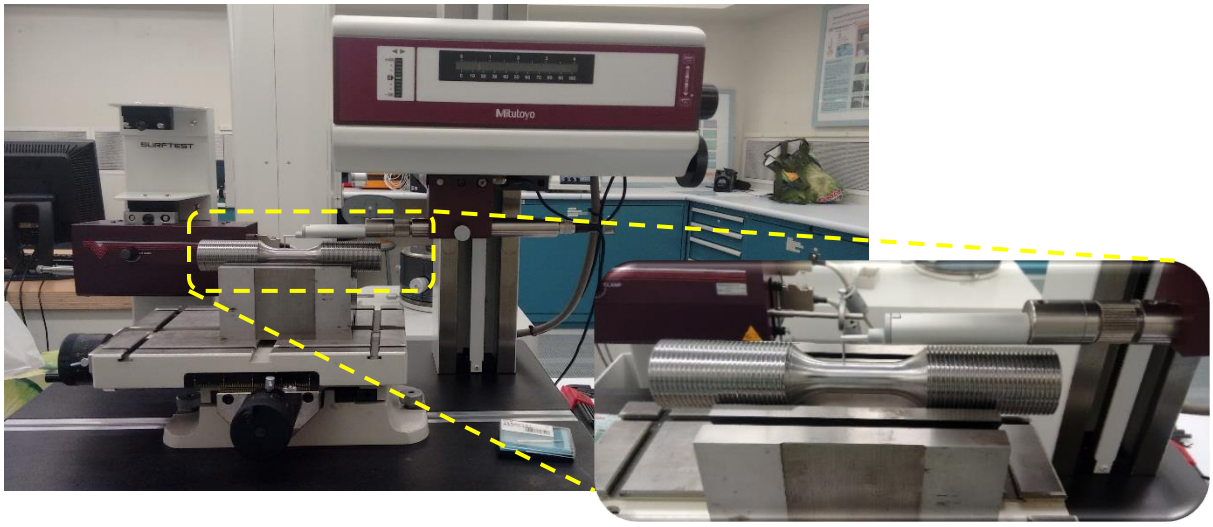

Figure 3.12: Measuring surface roughness of a specimen.

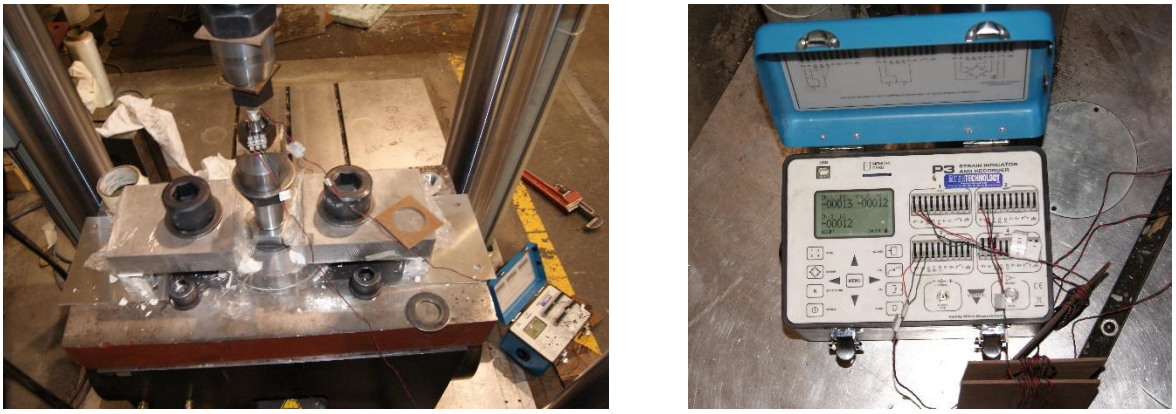

Figure 3.13: Verification of setup alignment using an instrumented specimen.

Figure 3.14: Lateral bracing of load frame: a) actuator end; b) crosshead.

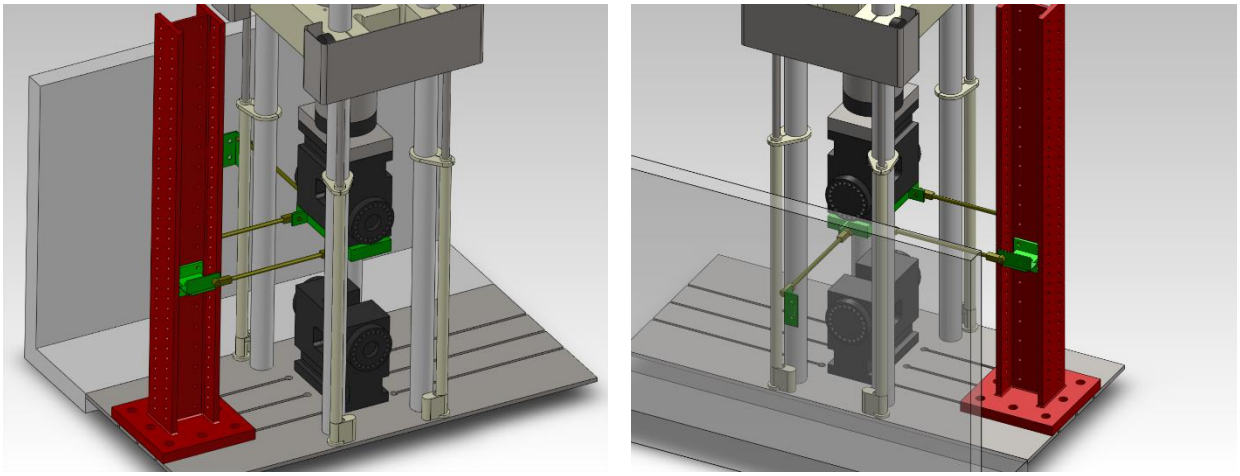

Figure 3.15: Schematic view of the lateral bracing of the load frame actuator (illustrations courtesy of Martin Leclerc).

Figure 3.16: Installation stages of the assembled specimen into the load frame (1/2): a) assembled specimen; b) connecting to the top platen; c) clamping to the top platen; d) inserting the adjustment disk; e) pouring fast-curing mortar between base and adjustment disk; and f) moving down the assembled specimen until a small force is registered.

Figure 3.17: Installation stages of the assembled specimen into the load frame (2/2): a) pouring fast-curing mortar on the supports of the clamping system; b) placing the clamping system; c) clamping; and d) the final setup.

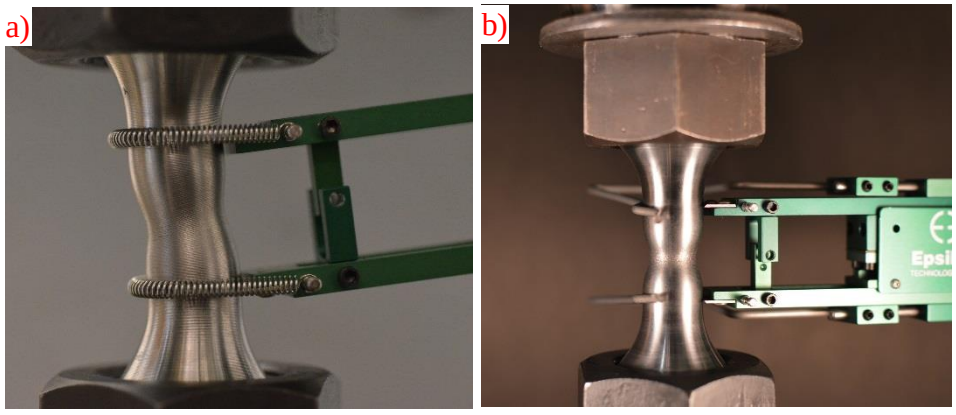

Figure 3.18: a) Deformed shape of specimen under large compressive strain when: a) there is no lateral bracing; b) the load frame is laterally braced (Specimens C107 *vs* C79).

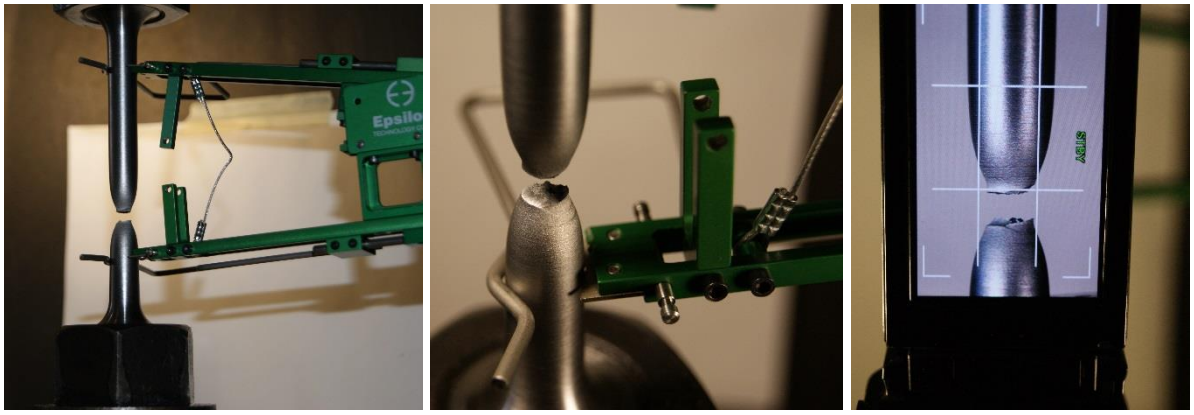

Figure 3.19: Fracture mode of under fast monotonic tension. Gauge strain rate is 10%/s (Specimen M4 tested at room temperature).

Figure 3.20: Test setup for monotonic tensile under subfreezing condition (Specimen M17).

Figure 3.21: The overall view of the test setup for cyclic tests at subfreezing temperature (Specimen C43).

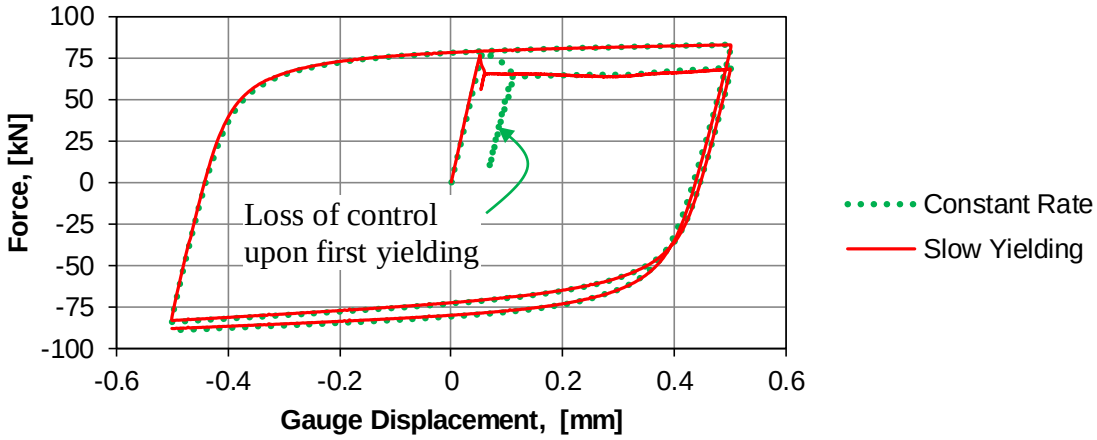

Figure 3.22: First-cycle hysteresis responses when strain rate was kept constant and when the first quarter cycle was conducted at a slow rate. Tests were done at room temperature.

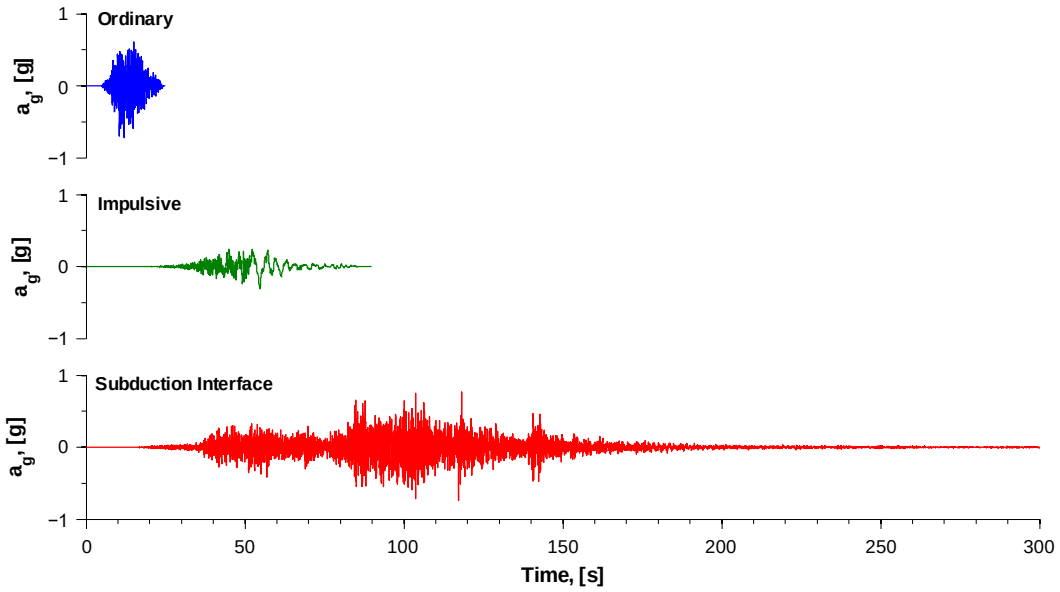

Figure 3.23: scaled ground motion acceleration of the selected records for design of the seismic loading patterns.

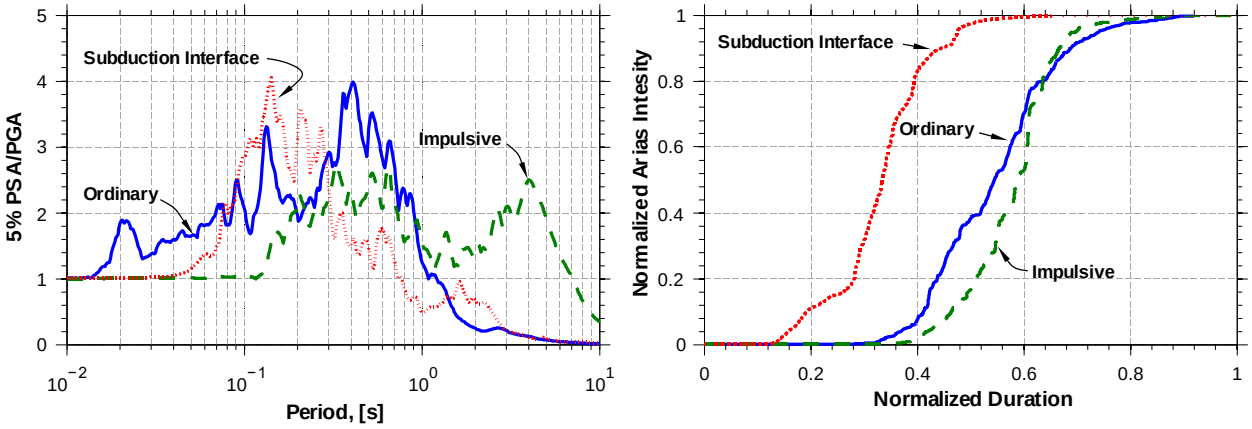

Figure 3.24: Characteristics of the selected records: a) spectral response (ratio of 5% spectral acceleration to the PGA of record); b) Arias intensity built-up.

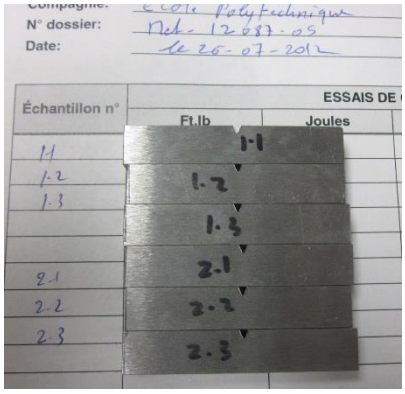

Figure 3.25: Charpy V-notch specimens.

3.6 Analytical estimation of normal thrust

In BRBs, appropriate estimation of the normal thrust forces on the restrainer is very importance for achieving stable inelastic response. These reaction forces are generated when BRB core buckling under large inelastic deformations is constrained by restrainer. As discussed in Chapter 2, there are several parameters that control BRB core response and the generated normal thrust force.

In this phase of research, a practical analytical approach to estimate the core's normal thrust on the restrainer was developed and validated using experimental data and finite element simulation results. The proposed method was utilized to design all-steel restrainer mechanism for full-scale BRB specimens that were tested in the final stage of this research. This method accounts for several important factors that control the core high-mode buckling response. In particular, effects of cyclic strain hardening, friction, and restraining stiffness as well as the Poisson's effect were included in the proposed approach. Prediction accuracy of the proposed analytical approach was validated using the available experimental data. The proposed method requires the constraining stiffness of the restrainer as an analysis input. A simple method to estimate the minimum required constraining stiffness was proposed and validated by experimental data. To further validate the proposed analytical method, a 3D BRB numerical model was created in ABAQUS finite element analysis computer program. Core inelastic behaviour was reproduced with an advanced nonlinear plasticity material model as outlined in (Chaboche, 1989). The chosen material model can simulate nonlinear isotropic and kinematic hardening behaviour. Parameters of this material constitutive law was calibrated using the results of the material testing stage of this research. Accuracy of the developed FE model in prediction of axial force, normal thrust, and buckling mode was validated using the

available experimentally-measured data. The effects of various finite element analysis assumptions such as mesh size, element formulation, and contact settings were investigated. Analyses were conducted using quasi-static implicit and dynamic explicit analysis techniques. The developed analytical approach and the finite element simulations are discussed in Chapter 7.

3.7 Experimental qualification of full-scale all-steel BRBs

To qualify the developed BRB concept, twelve full-scale subassemblies were designed, prepared and instrumented. These specimens were designed to assess the effects of various influential design parameters on the overall brace performance with particular emphasis on the restrainer's functionality. The restrainer's global stiffness, bolt arrangement, gap size, interfacial condition, and loading pattern were among the considered test variables. Test specimens were fabricated by Lainco Inc. located in Terrebonne, Québec. Tests were conducted at the Structural Engineering Laboratory of Polytechnique Montréal. Specimens were tested in a vertical load frame schematically shown in Figure 3.36.

3.7.1 BRB specimens

The BRB specimens had approximately 6.0 m length between the work-points. The core geometry of the BRB specimens is shown in Figure 3.26. The core section (19.05 mm × 150 mm) is the required brace size at the first storey of a 9-storey building with back-to-back Split-X BRBFs. The building was designed for 2% in 50 years chance of exceeding seismic hazard on a generic soft rock site in Victoria, BC. The loading and design of this building was carried out as per NBCC 2010 and S16-09. The building plan and the braced bay elevation are shown in Figure 3.2. The core was plasma-cut from two plates conforming to G40.21-350WT Category 4 steel with minimum yield strength of 350 MPa. Six coupons, with the specifications shown in Figure 3.27, were cut from the core plate and machined to create specimens for tensile testing. The tensile test results were used to design the test setup.

A simple-to-fabricate restrainer system was selected for the developed BRB. It consisted of a pair of bolted built-up steel sections. These sections comprised of a flat plate and a HSS member as shown in Figure 3.29. The HSS and the flat plate were welded together using an intermittent pattern. The restrainer half-sections were bolted together using 15.9 mm (5/8") pretensioned ASTM A325 bolts. At both ends of the braces, the bolts in the last two transversal lines connect to the

long-slotted holes in the non-yielding segment of the core (see Figure 3.26). These bolts were left in the snug-tight condition to allow relative longitudinal movements between the restrainer system and the core.

To manage the frictional actions at the interface of core and restrainer, several practical low-friction materials were evaluated. The selected materials are divided to two types: 1) self-adhesive polymer liners; and 2) dry lubricants. The materials shown in Figure 3.30 were applied to a steel surface and the smoothness of the surface were compared qualitatively. Of the evaluated material, three were chosen for the testing stage based on the surface quality, ease of application, and supply cost. Among the polymers, virgin PTFE and UHMW-PE liners, item 3 and 6 in Figure 3.30 respectively, manufactured by Green Belting Company were selected. Graphite-based dry lubricant with the commercial brand of "SLIP plate No. 1" was selected from the evaluated dry lubricant materials. Before application of the self-adhesive liners, the steel surface was wire-brush cleaned, soap-washed, air-dried, and finally wiped down with a methyl ethyl ketone solvent as shown in Figure 3.32. This procedure was put in place to ensure maximum bond strength between the liners and steel surfaces. Polymer liners were manually applied to the cleaned surfaces and gently pressed to create a better bonding strength (see Figure 3.34). The graphite-based dry lubricant was roller-painted to the core and restrainer surfaces, and then finished by latex glove covered-hands (see Figure 3.33). The applied graphite coating typically becomes dry and solid in 24 hours. Once the coated surface was dried another coating was applied in the same manner. At the stiffened region of the core, a tiny spacer sheet was placed between the core and the restrainer's face plate to mitigate generation of localized bending demand. In some experiments, the counterface of this spacer sheet was coated with Molybdenum disulphide dry lubricant spray as shown in Figure 3.41. This was found necessary to avoid severe friction at this region.

3.7.2 Test setup and instrumentations

The tested BRB members were assumed to be part of a V-bracing configuration. The installed BRB specimen in the load frame is shown in Figure 3.39. As shown in this figure, the test setup represented half the span of a 9.0 m wide and 4.0 m high bracing panel. Several instrumentations were designed and installed to capture the global and local behaviour of the specimens. The core's yielding segment deformation was monitored by a set of two string potentiometers that were attached to the stiffened segment of the core as shown in Figure 3.37. The average reading of these

two sensors were taken as the core yielding segment deformation. The restrainer section was strain-gauged at various locations to trace the bending moment profile and longitudinal distribution of the frictional forces (see Figure 3.31). The instrumented sections were located at the ends and the mid-length of the restrainer. For each instrumented section, 6 strain gages were installed and protected to avoid damage during specimens' installation. An instrumentation schemes was designed and implemented to track sliding of the restrainer and in-plane rotation of the hinge connection. This was done by installing two pairs of LVDTs on the top and at the bottom of restrainer ends as shown in Figure 3.38. On one side these LVDTs were fixed to the gusset plate and on the other side they were attached to the restrainer. Two sets of sensors were utilized to monitor the global in-plane and out-plane flexural deformation of specimens. A three-dimensional triangulation with string potentiometers was designed to trace the spatial position at the mid-length of the brace and at the horizontal edge of the top gusset plate. The spatial position data was then translated into relative in-plane and out-of-plane displacements at mid-length of the restrainer.

An instrumentation scheme was designed to trace the core transversal deformation at its mid-length. As shown in Figure 3.40, pairs of LVDTs were fixed to both sides of the restrainer. Holes were drilled at the mid-thickness of the side shim plates to allow the LVDTs' shaft to pass through. The core's normal thrust was estimated by a combination of readings from the instrumented bolts and the finite element model of the bolted joints. Ten in-house instrumented bolts were fabricated by inserting a special-purpose strain gage into a tight central hole drilled in the 5/8" A325 bolt shank. The hole was then filled with epoxy resin and the instrumented bolts were placed in the oven at a specific temperature for certain amount of time to cure the epoxy resin. The schematic view of the instrumented bolt is shown in Figure 3.42. Each instrumented bolt was calibrated using 3 cycles of 50–90 kN tensile loading (see Figure 3.44a) in a test setup shown in Figure 3.43. Maximum calibration load, i.e. 90 kN, is 5% more than the standard pretension load for 5/8" A325 bolts (~85 kN). The bolts showed nearly perfect linear response and the calibration factors were found to be identical in the loading and unloading paths. An example of bolt response to the described loading history is shown in the plots of Figure 3.45. The instrumented bolts were reused in the subsequent BRB tests and they were recalibrated before each test using 3 cycles of tensile loading between 20–45 kN. During the installation, pretension of the instrumented bolts was verified using the strain gage readings. Only Specimens 9 to 11 were instrumented with these bolts. The arrangement of the instrumented bolts in these specimens is shown in Figure 3.46. Data Image

Correlation (DIC) system was employed to measure local strains on the restrainer exterior surface, and on the top surface of the knife-plate hinge at the fixed end of specimens. The required preparations for using DIC system are shown in Figure 3.47 and Figure 3.34b. The designated areas were painted matte white and then speckled using small black dots. In the course of the test these areas are filmed from two angles to trace the position of the speckles.

3.7.3 Loading protocols

In addition to the conventional step-wise cyclic loading, two seismic loading patterns from the expected type of earthquakes in the west coast of Canada were designed. This includes typical far-field crustal earthquake, and long duration strong ground motions due to earthquakes at the interface of the two plates in the subduction zone. To design the megathrust earthquake loading histories, twenty single-degree-of-freedom systems (SDOFs) having elastic period between 0.5 and 3.0 seconds were designed for 2% in 50 years seismic hazard in a hypothetical soft rock site in Victoria, BC according to the NBCC 2010 design response spectrum. Ductility of these SDOFs was assumed as $R_o R_d$ = 1.2×4.0 = 4.8 which corresponds to the NBCC's prescribed values for BRBFs. Inelastic behaviour of these SDOFs was reproduced by "Giuffré-Menegotto-Pinto model with isotropic strain hardening" as discussed in (Mazzoni *et al.*, 2006). 44 ground motion records were selected from the main shock of the 2011 **M**9.1 Tohoku earthquake. These records were corrected for baseline and low frequency noise, and then scaled to match the NBCC 2010 design spectrum at the given SDOF elastic period. These SDOFs were then subjected to the selected and scaled records and the inelastic response history was computed numerically. Spectra of the peak and cumulative plastic ductility of these SDOFs are shown in Figure 3.48. The east-west component of the record from station FKS005 caused the largest demand both in terms of peak and accumulated plastic deformation. The largest demand was registered for the SDOF having elastic period of ~1.0 second. This period corresponds to the fundamental mode of a 5-storey back-to-back Split-X BRBF that was designed for Victoria, BC soil site class C. To match this record to the site design spectrum scale factor of 1.7 was needed. Inelastic numerical model of this multi-storey BRBF model was subjected to the most demanding record, i.e. FKS005-EW, and response at storey levels were computed. This record caused maximum drift of 2.5% and 2.2% in the first and last storey, respectively. Accumulated inelastic response at the last storey was nearly 3 times

more than that of the first storey due to the higher mode effects. For this reason, the drift response at the last storey was chosen as the megathrust loading history for the testing program.

3.7.4 Test data analysis

Full-scale BRB subassembly tests were conducted. The test results were processed to assess the specimens' performance in detail. Tensile and compressive strength adjustment factors, core cumulative inelastic ductility, and the response of hinge connection were extracted from the tests results. More details on the specimen testing and the performance can be found in Chapter 8.

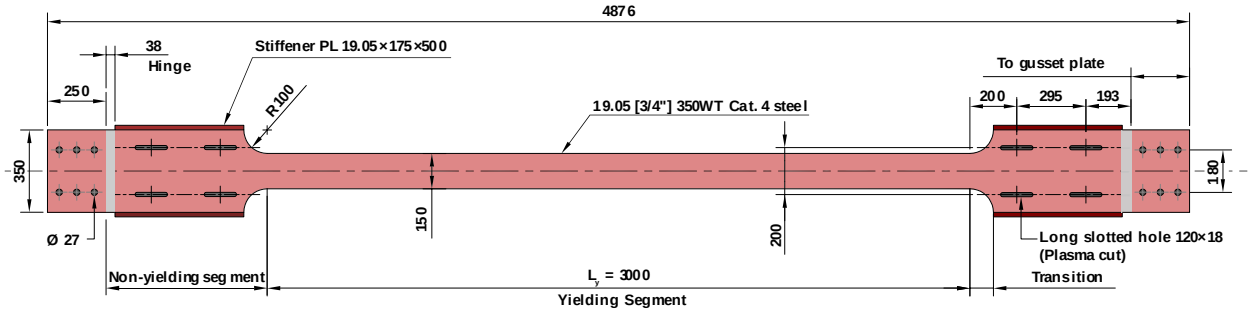

Figure 3.26: Nominal geometry of the core.

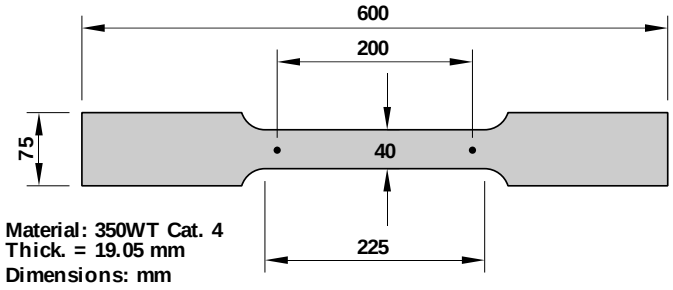

Figure 3.27: Nominal geometry of the coupons machined from the core plates.

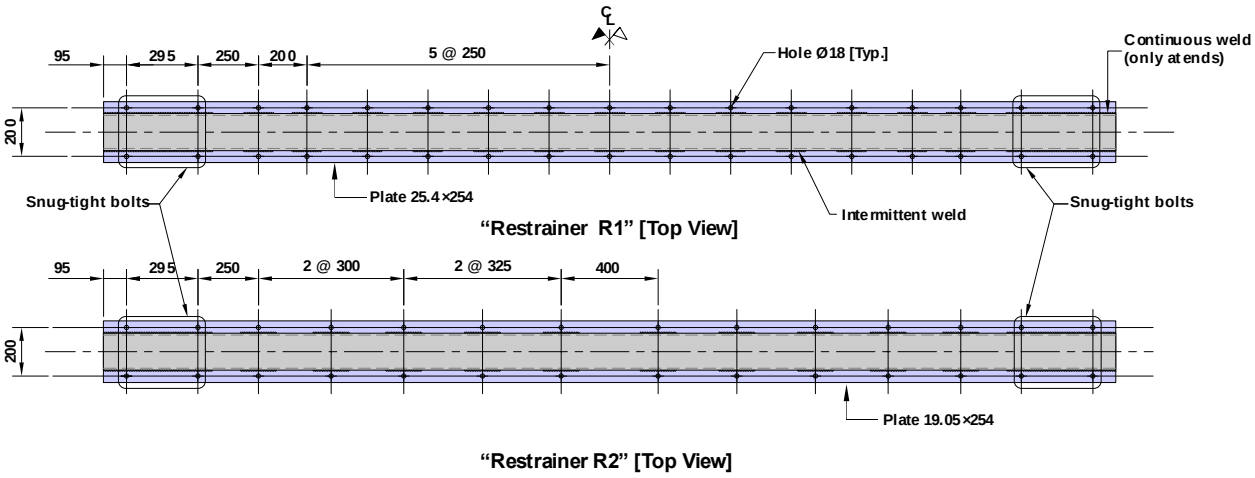

Figure 3.28: Nominal geometry of the two restrainer systems.

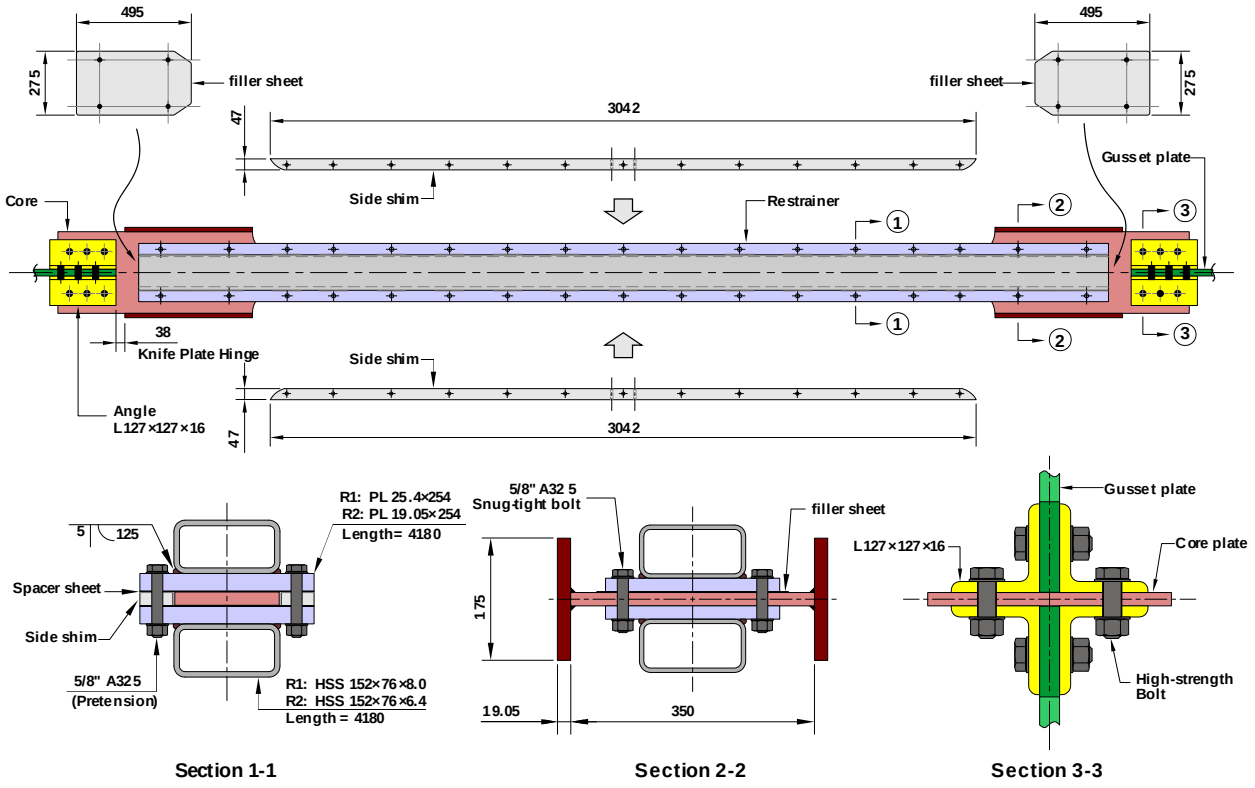

Figure 3.29: Assembled BRB specimen.

Figure 3.30: Low-frictional material evaluated for the debonding layer between the core and the restrainer: (1) 3M™ 5453 PTFE Glass Cloth Tape; (2) 3M™ 5181 Skived PTFE Tape; (3) Green Belting 150-5S High Modulus PTFE Tape; (4) DuraSurf ™ ETA UHMW-PE Tape; (5) 3M™ 5430 Squeak Reduction UHMW-PE Tape; (6) Green Belting 130-10A UHMW Polyolefin Tape; (7) DuraSurf ™ STS Silicone threated surface UHMW; (8) Dow Corning Molykote® D-321 R Anti-Friction Coating (Molybdenum disulphide MoS_2); and (9) SLIP Plate® No. 1 graphite dry lubricant.

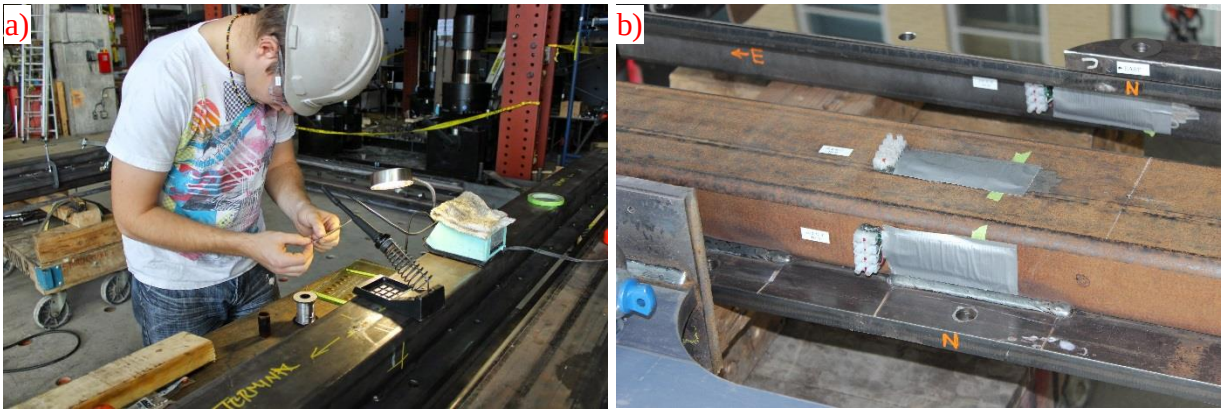

Figure 3.31: Longitudinal strain gages installed on the restrainer exterior surface (R2).

Figure 3.32: Preparation of restrainer R1 for the testing Specimen 2: a) surface cleaning by methyl ethyl ketone; b) application of UHMW-PE self-adhesive liner.

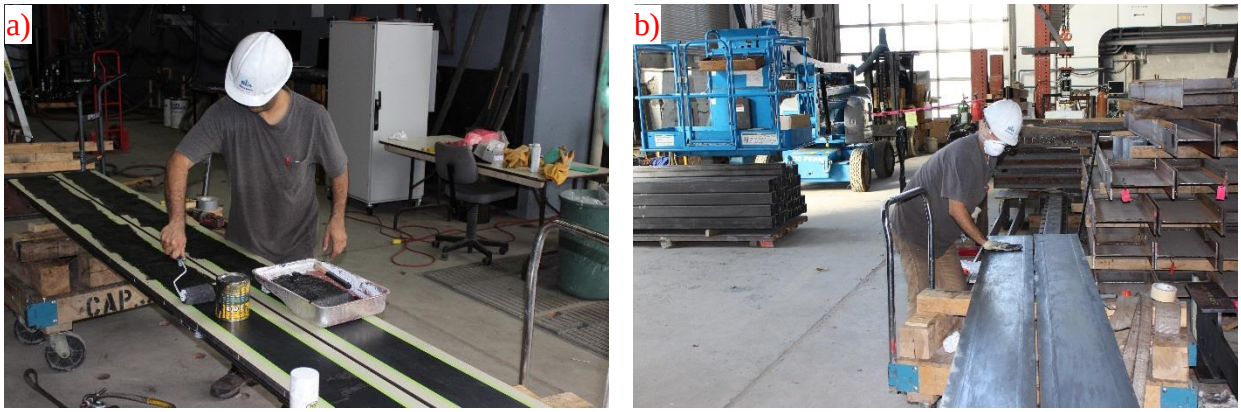

Figure 3.33: Application of graphite dry lubricant on the counterface of restrainer R1 for the testing Specimen 3.

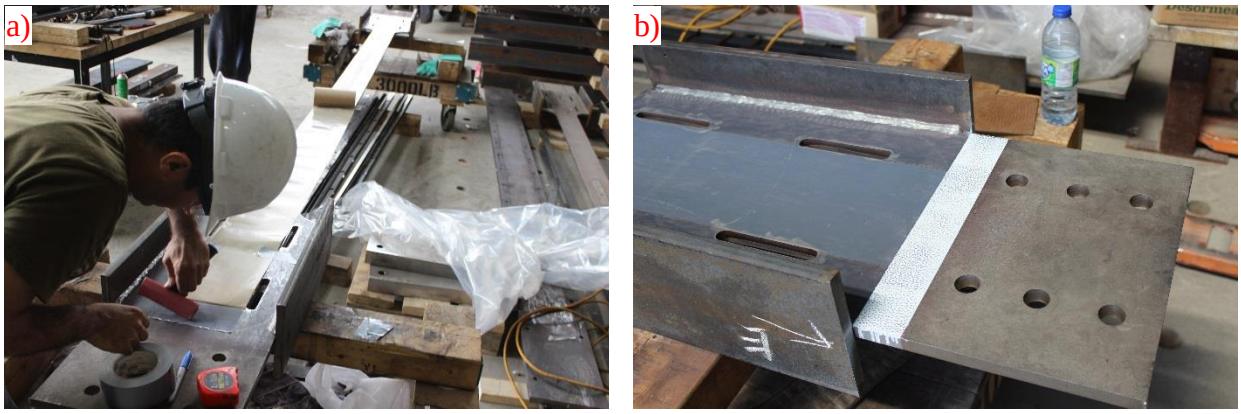

Figure 3.34: Application of PTFE self-adhesive liner on the core of Specimen 11; b) spackled knife-plate hinge to measure the local strains using Data Image Correlation system.

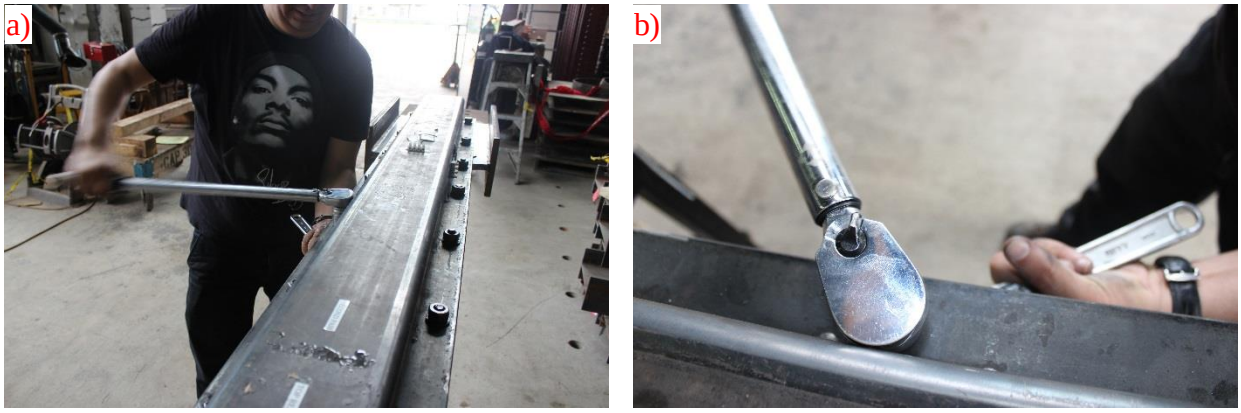

Figure 3.35: Application of bolt pretension using calibrated wrench.

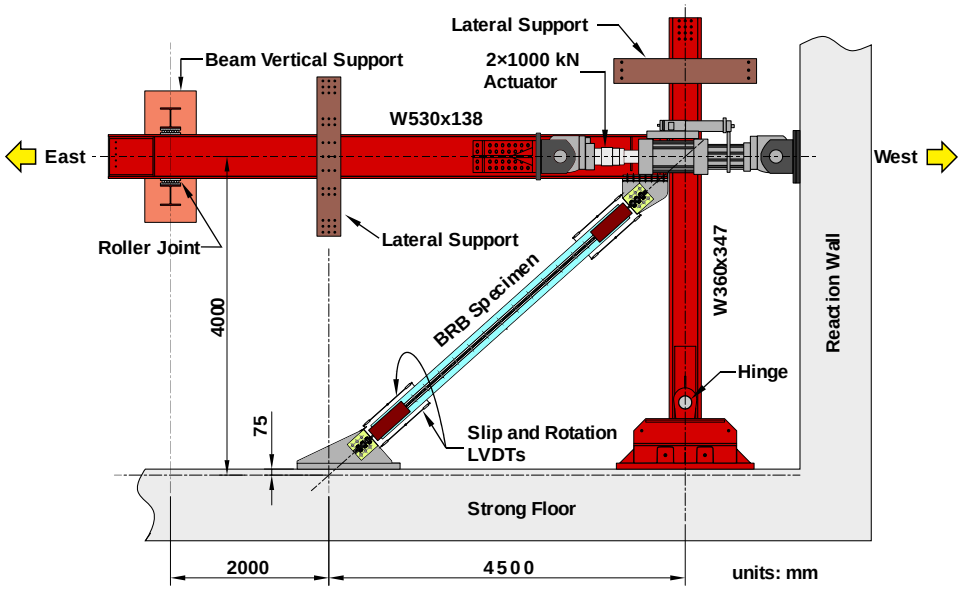

Figure 3.36: Schematic view of the BRB test setup.

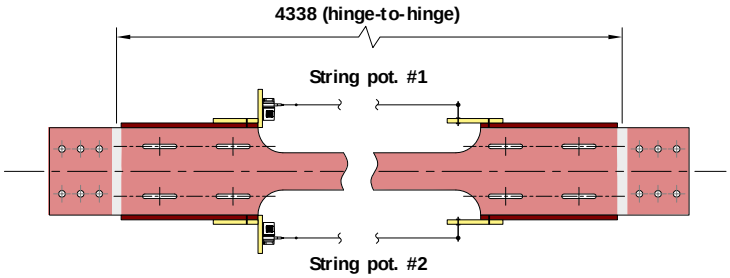

Figure 3.37: String potentiometers for measuring the average axial deformation in the yielding segment of the BRB core.

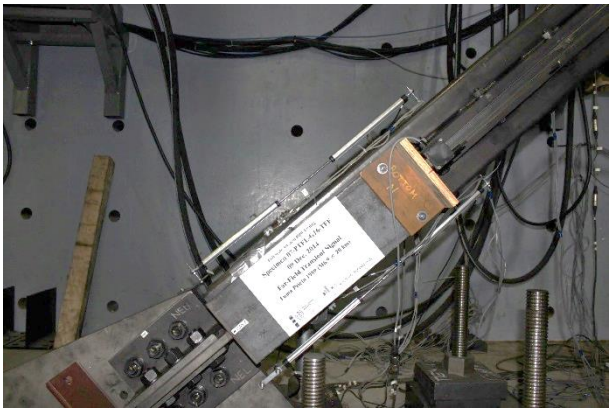

Figure 3.38: LVDTs for measuring the restrainer movement and the knife-plate hinge rotation at the fixed end of Specimen 7.

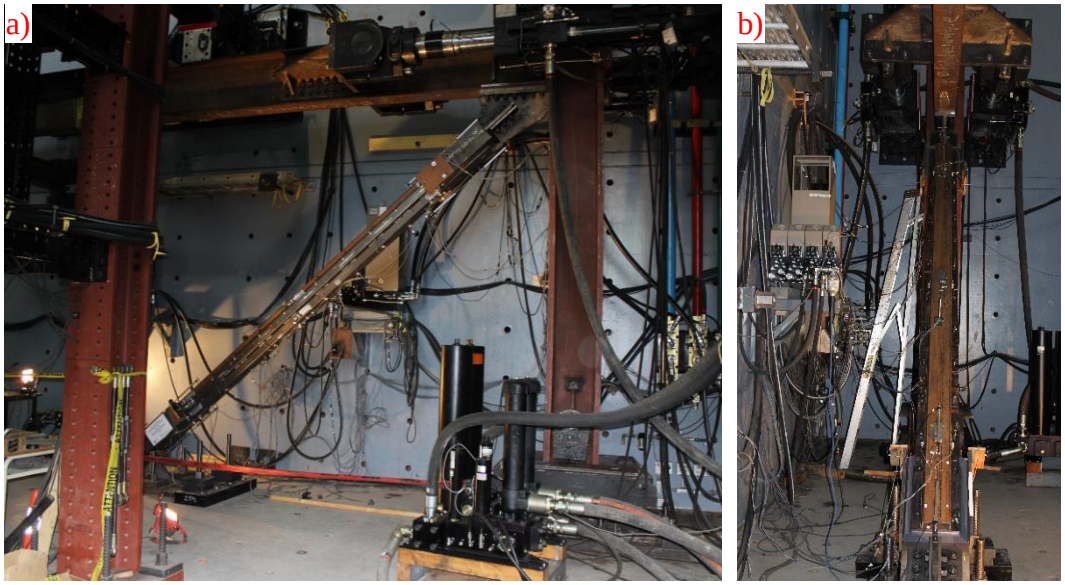

Figure 3.39: Installed BRB specimen in the load frame.

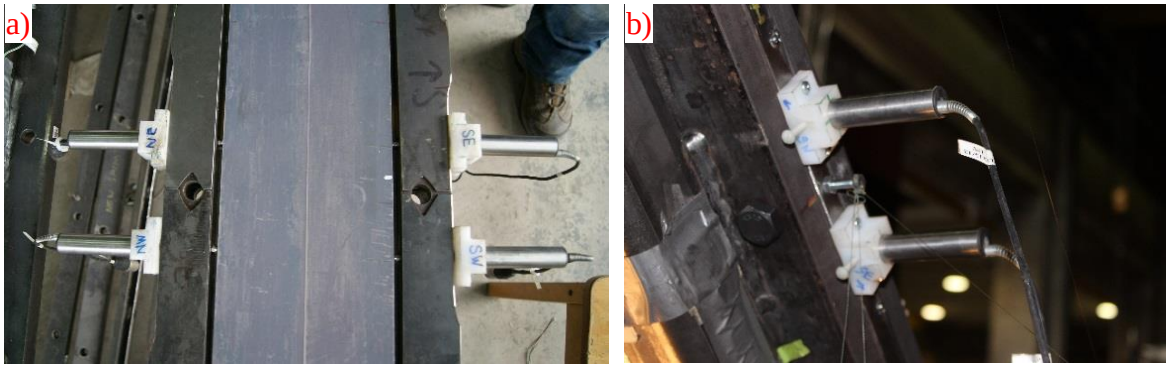

Figure 3.40: Instrumentation for transverse strain measuring: a) plan view (Specimen 7 before closing the restrainer); b) installed specimen (Specimen 11).

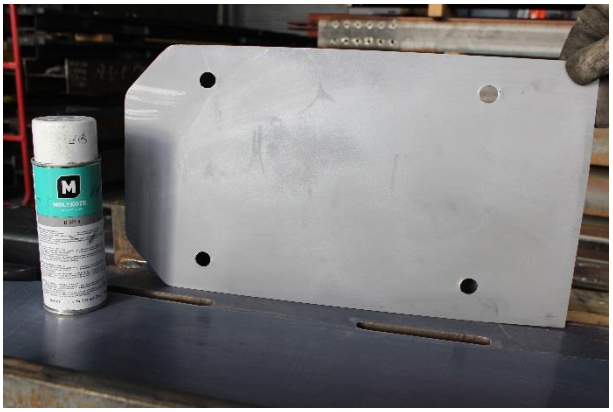

Figure 3.41: Lubrication of the end spacer's counterface using Molybdenum disulphide dry lubricant spray (Specimen 7).

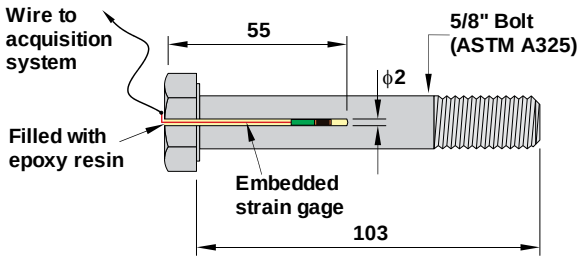

Figure 3.42: Schematic view of an instrumented bolt.

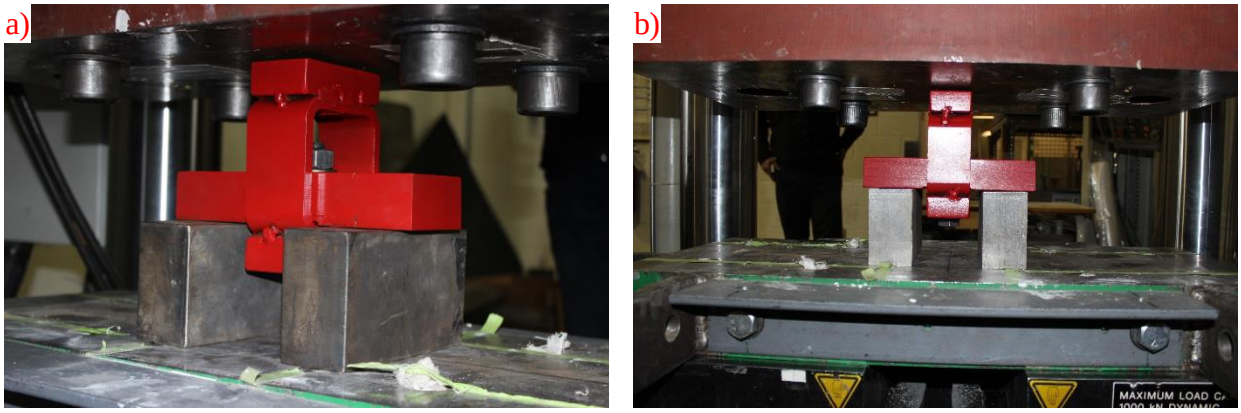

Figure 3.43: Setup for calibration of instrumented bolts.

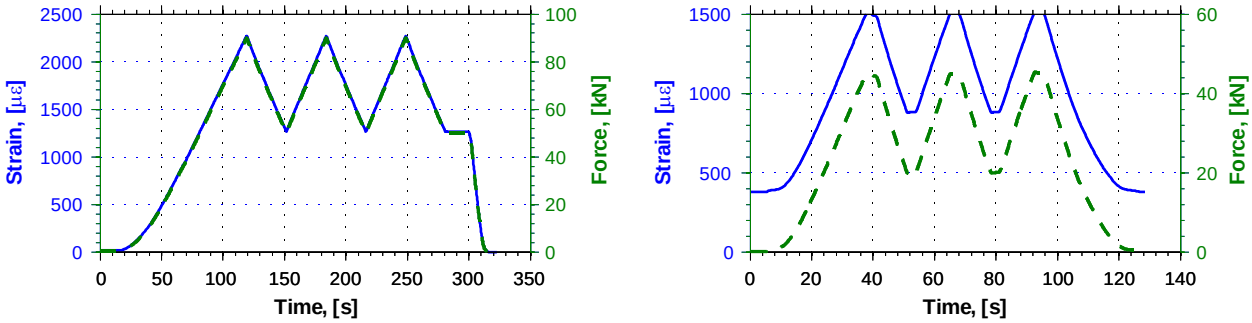

Figure 3.44: a) calibration; and b) re-calibration loading history for instrumented bolts. Note: response of bolt #2 is shown.

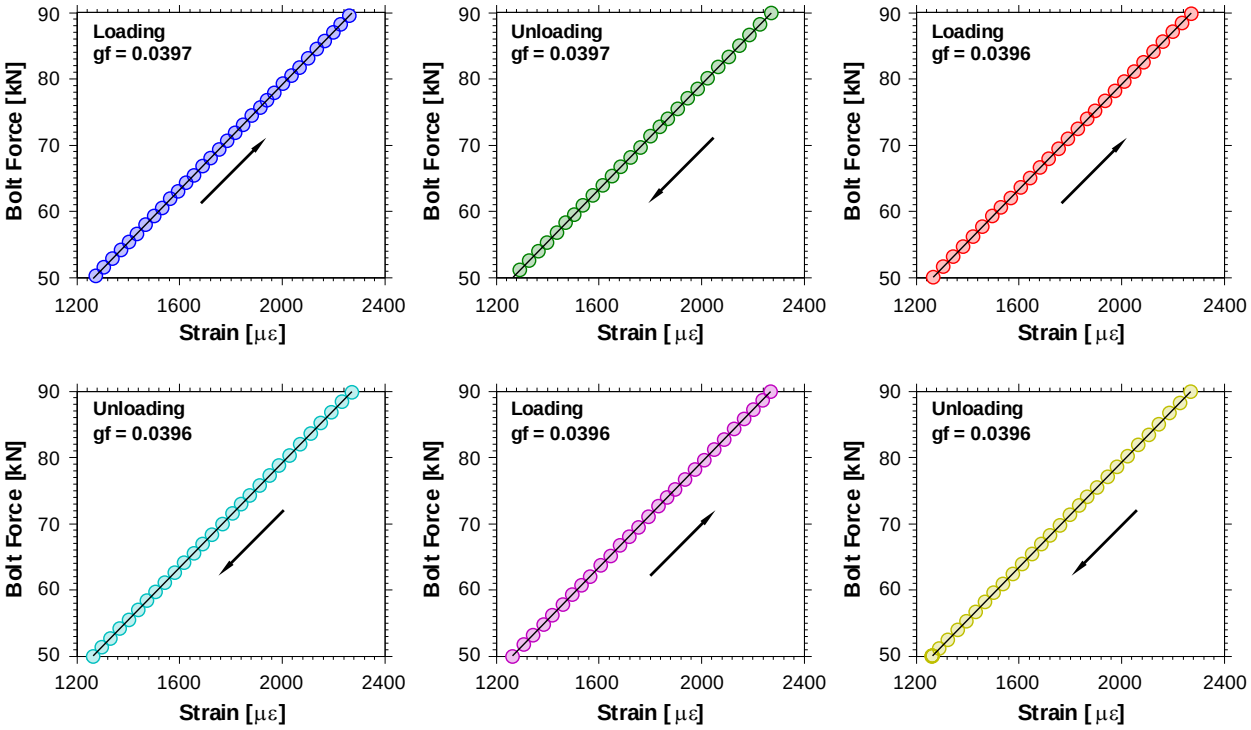

Figure 3.45: Load-strain response of instrumented bolt to the calibration loading history. The bolt gage factor is denoted by "gf" at the right upper corner of each plot.

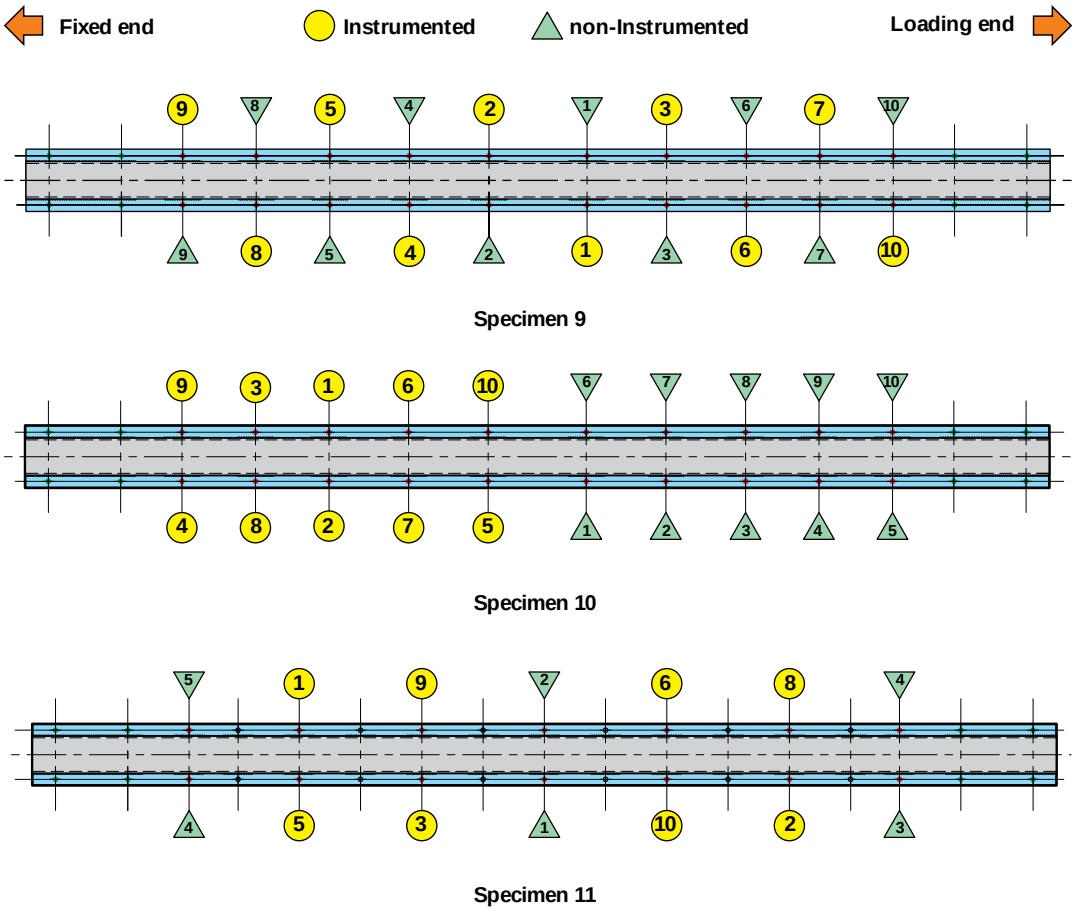

Figure 3.46: Arrangement of the instrumented bolts.

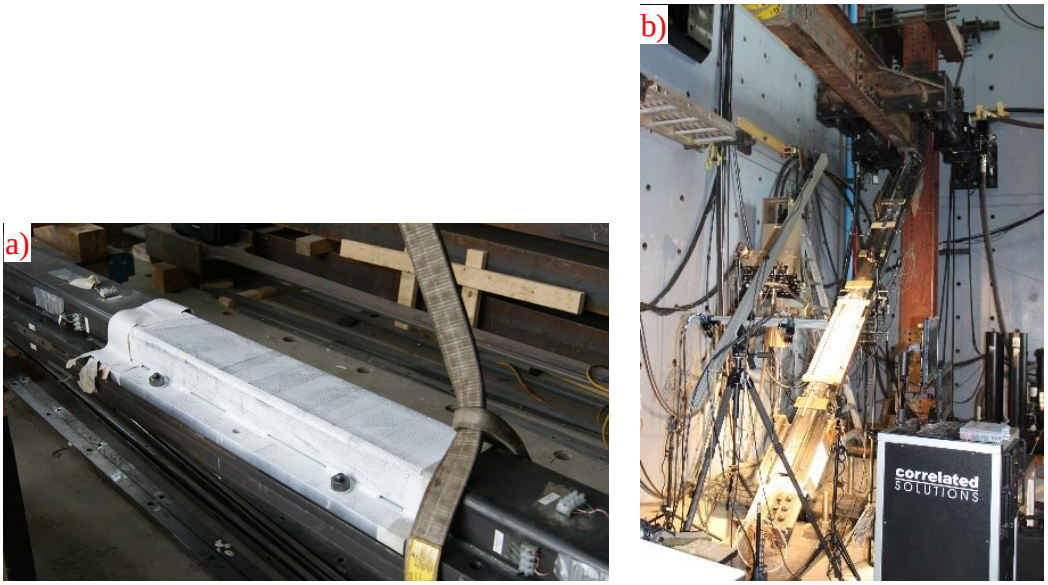

Figure 3.47: The spackled exterior surface of restrainer R1b to monitor local strains.

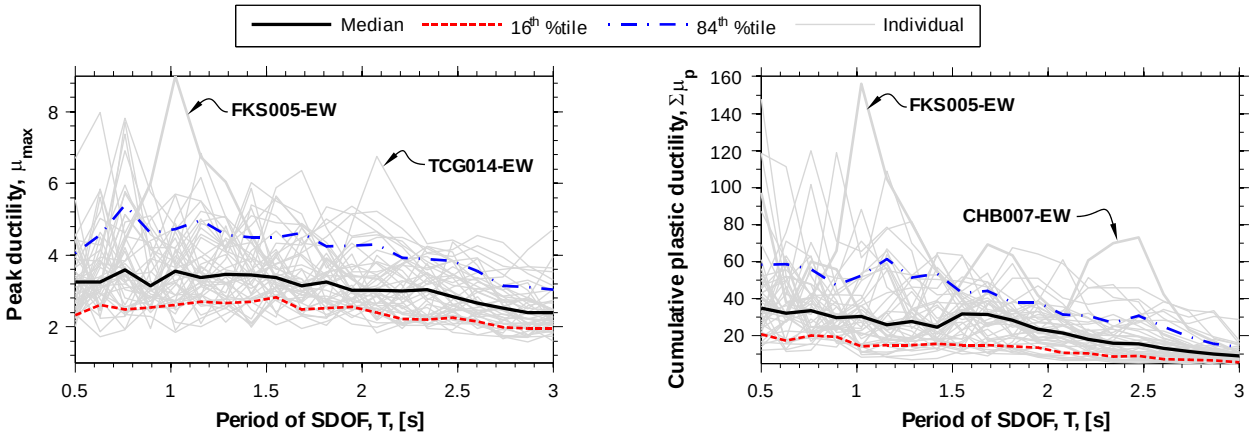

Figure 3.48: Peak ductility and cumulative plastic ductility of the constant strength SDOFs designed for Victoria, BC under 44 ground motion records from **M**9.1 Tohoku megathrust earthquake.

CHAPTER 4 ARTICLE 1 : ROBUST PERIOD-INDEPENDENT GROUND MOTION SELECTION AND SCALING FOR EFFECTIVE SEISMIC DESIGN AND ASSESSMENT

Morteza Dehghani, and Robert Tremblay

Paper published in *Journal of Earthquake Engineering*,
Volume 20, Issue 2, Pages 185-218
DOI: dx.doi.org/10.1080/13632469.2015.1051635
Submitted 7 Aug 2014, Accepted 10 May 2015.

ABSTRACT

A period-independent approach for the selection and scaling of ground motion records aimed at reducing demand variability is proposed for seismic response history analysis. The same set of scaled records can be used to study various structures at the same site regardless of their dynamic characteristics. The statistical robustness of the proposed and current approaches is compared through nonlinear inelastic dynamic analyses performed on single-degree-of-freedom systems and multi-storey braced frames. The proposed approach leads to consistent response predictions with a limited number of records. This is advantageous for day-to-day structural design or assessment against code hazard-based seismic demand levels.

Keywords Dominant Seismic Event; Ground Motion Parameters; Record Selection; Ductility Demand; Record-to-Record Variability

4.1 Introduction

Linear and nonlinear response time history analyses have become an essential tool in modern seismic design and evaluation techniques. One of the important steps in this process is the ground motion selection and scaling which can substantially affect the outcomes as it may represent the largest source of uncertainty and variability in the response estimates (Heo *et al.*, 2011). This process typically includes preliminary scenario-based selection of representative records,

refinement of the selected records to the minimum required number of records, and record scaling to match the expected seismic hazard level. However, methods and criteria are still being discussed and debated in the scientific community and among practicing engineers (Watson-Lamprey *et al.*, 2006; NEHRP Consultants Joint Venture, 2012). Despite the wealth of research, response history analysis remains a challenging task for practising engineers due to the difficulty of selecting and scaling ground records and the sensitivity of the results and conclusions to the assumptions and approaches adopted in this process. In nonlinear response analysis, variability in ground motion properties and the complexity of the structure response can lead to significant variations and even contradicting trends in the analysis results depending on the ground motion selection and scaling methods. This variability can be managed by applying spectrum matching techniques (Rizzo *et al.*, 1975; Hancock *et al.*, 2006b) which have been shown to give hazard consistent spectra and reduced response variability. However, depending on the method and user's knowledge, they could lead to unintended consequences as a result of frequency content manipulation (Naeim *et al.*, 1995). In most current methods, ground motion records are selected and scaled essentially based on the seismic hazard at the structure fundamental period (Baker, 2011; Heo, *et al.*, 2011; Jayaram *et al.*, 2011). These motions may not sufficiently excite the structure modes at other periods or modes that are altered by nonlinear response. Fundamental period-based record selection and scaling techniques also pose difficulties when the structure period changes as the design evolves towards the final solution or the structure has different periods in both orthogonal directions or the structure has a long period torsional mode as its first mode of vibration. The minimum number of records required to conduct an efficient analysis while achieving statistically reliable and robust results is another challenge faced by practicing engineers and researchers (Hancock *et al.*, 2008; Cimellaro *et al.*, 2011).

There is therefore a strong motivation for developing a robust, yet simple ground motion selection and scaling approach that could lead to consistent seismic demand with limited scatter such that the interpretation of the results becomes easier and more straightforward. The method would desirably give results that have limited dependency on the number of the records. It would also be beneficial that the so-selected and scaled records produce seismic demands compatible with the building code spectrum level over a period range wide enough so that they can be used for multi-mode structures, structures having different periods in each direction or for a number of structures having different periods that are located at the same site.

In this study, ground motion selection and scaling methods are proposed to achieve these objectives. The core idea of the proposed selection method is to retain a limited number of ground motion records among a larger ensemble using a refinement technique based on the damage potential characteristics of the ground motion records. This is achieved by finding the most representative Intensity Measures (IMs) for amplitude, frequency content, and duration of the data through intercorrelation analysis. Then the data set is reduced by retaining the records which are closer to the average of the representative IMs for a given dominant event and discarding the remaining ones. The record scaling technique proposed in this article is a period-independent algorithm where the amplitude of the selected records is linearly adjusted to the amplitude of the target spectrum. The technique finds a narrow frequency bandwidth in which the shape of the un-scaled ground motion spectrum matches that of the target spectrum and then adjusts the amplitude of the record spectrum to the target in that frequency bandwidth. The records are therefore adjusted only in the period range where they likely contribute to the hazard while preserving their original frequency content characteristics.

The proposed techniques for record selection and scaling are respectively described in the first two sections of the paper. The application of the method is illustrated through an example for a hypothetical soft rock (class C) site in the city of Victoria, British Columbia, Canada. Victoria is located at the south end of the west coast of Canada and is expected to experience the most intense seismic demand in this region. The PEER-NGA West strong ground motion database (PEER, 2005) was used to compile all of the required sets of records considered in this study. The outcomes of the proposed method are compared to those from other methods currently in use. In the third part of the paper, the statistical robustness of the proposed methods is examined through series of inelastic response history analysis conducted on single-degree-of-freedom systems and multi-storey steel braced frame prototypes. These models are assumed to be located at the same Victoria site and are designed in accordance with the seismic provisions of the 2010 National Building Code of Canada (NRCC, 2010). The analysis results are used to demonstrate that the proposed methods can lead to consistent peak deformation and accumulated inelastic demands that exhibit smaller scatter compared to other available methods. The analyses also show that the average and maximum response values obtained by the proposed method are not sensitive to assumptions made in the initial selection process and the number of selected records. Based on the results of these

analyses, recommendations are made regarding the appropriate seismic demand estimator that should be used when the proposed selection and scaling approaches are adopted.

4.2 Record Selection

4.2.1 Dominant earthquake scenarios

Ground motion characteristics such as amplitude, frequency content, and duration are strongly related to the magnitude of the seismic event, the site-to-source distance, and the site soil profile (Katsanos *et al.*, 2010). It has been also shown that the seismic demand is well correlated with the ground motion characteristics (Kurama *et al.*, 2003; Ye *et al.*, 2011). Hence, there is a general consensus that the various earthquake event scenarios that dominate the seismic hazard at a site should be reflected in the record selection if statistically reliable results are sought (Bommer *et al.*, 2004; ASCE, 2010; ATC, 2011; NEHRP Consultants Joint Venture, 2012). Therefore, the proposed record selection method starts from the de-aggregation of the seismic hazard at the site to include the likely earthquake events in the process. Seismic hazard de-aggregation is a technique to decompose the contribution of different events to a given intensity of a seismic hazard parameter. This technique, which is performed during the hazard calculation procedure, gives clustered bins of magnitudes and site-to-source distances, with relative contribution of each bin to the given exceedance rate of an intensity measure. Hazard de-aggregation has been recognized as a probabilistically-consistent approach for finding dominant earthquake scenarios (McGuire, 1995; Bazzurro *et al.*, 1999). De-aggregation of the 2% in 50 years probability of exceedance of spectral accelerations for the city of Victoria at periods T = 1.0 and 2.0 s are shown in Figure 4.1.

4.2.2 Selection based on conditional IM

Uniform Hazard Spectra (UHS) are now widely used as design spectra in building codes (ASCE, 2010; NRCC, 2010). The ordinates of an UHS at various periods are computed independently such that all values have the same probability of being exceeded. Therefore, the shape of an UHS does not reflect that of the spectra of real individual ground motions. In the selection process, one must ensure that the selected records have spectra with similar shape to those of the ground motions contributing to the UHS at a given period. This can be achieved by using a Conditional Mean Spectrum (CMS) for the selection of earthquake records, a method that preserves consistency

between the hazard calculations and ground motion selection (Baker, 2011). In this method, the median spectrum from a Ground Motion Prediction Equation (GMPE) for the dominant **M**-R earthquake event is converted into a CMS based on the correlation between spectral accelerations at the period of interest and other periods. The UHS is replaced by a conditioned spectrum which typically has less intensity in periods shorter and longer than the period of interest, and then records with the most similar spectral shapes to the computed conditioned spectrum are selected as described in Jayaram, *et al.* (2011). Typically, the mean magnitude and distance from de-aggregation is taken as the dominant event and the CMS is computed for the structure fundamental period, T_1. The selected records are then scaled such that their amplitude matches the target spectrum at the period T_1. An example of a CMS with exceedance rate of 2% in 50 years for Victoria is used later in the paper for comparison purposes. Additional record sets may be needed if the properties of the structure are not yet defined or if the records are to be used to analyse several structures having different dynamic properties at the same site. In this case, multiple CMSs and an associated record set must be generated at all relevant periods, which may lengthen the analysis and less straight-forward acceptance criteria. When de-aggregation analysis shows that several different magnitude-distance events contribute significantly to the hazard at the site, with possible different effects on the structure studied, as it is shown in Figure 4.1, one can consider developing multiple-event CMS to reflect the demand from these different events (Lin *et al.*, 2013). However, this procedure may lead to higher scatter at periods other than the conditioning period.

CMS considers only spectral ordinates and other important ground motion features such as frequency content and duration could be overlooked in the selection process. To tackle this issue (Bradley, 2010, 2012) proposed a more comprehensive approach, referred to as the Generalized Conditional Intensity Measure (GCIM), which incorporates various measures of amplitude, frequency content and duration intensity that are conditioned to a given IM (denoted by IM_j) using set of relevant GMPEs and correlation functions. Instead of average event, this method considers full de-aggregation of seismic hazard of the IM_j. The records selected using this rigorous approach would reflect spectral intensity as well as other key ground motion characteristics anticipated for the considered hazard level. However, implementing the method requires multiple GMPEs and correlation functions for each considered IM in addition to the detailed de-aggregation of IM_j. User also needs to specify weighting factors of each IM when records are being searched that best match the GCIM distribution. This relies on judgment and may need a number of trials. The information

required for this method may not be readily available to practicing engineers and researchers. Furthermore, as is the case for CMS, GCIM needs combinatorial optimization techniques to find set of records that satisfying conditional properties, which may be computationally expensive depending on the size of the perspective set and the records database.

4.2.3 Proposed selection approach

In this study, a simpler selection approach is presented to achieve the abovementioned objectives. As it will be demonstrated, this approach only requires de-aggregation of hazard and calculated IMs of the available data. Furthermore, the solution is obtained in one step and is unique, hence less computationally expensive and user-dependent. This approach would be practical for cases where a single set of records is to be used for multi-mode structures or several structures having different periods located at the same site, and where single dominant event cannot be clearly identified from the de-aggregation and varies in different segments of the target response spectrum. It was therefore aimed that the selection process be period-independent such that the selected records essentially represent the likely ground motions that are expected at a site, based on hazard de-aggregation only and irrespective of the properties of the structures to be designed or evaluated. This would be similar to defining floor occupancy live loads or ground snow loads for a project. In this context, no possible event with a significant contribution should be overlooked, and a range of frequency content, duration and amplitude levels should be covered with the selected records. Such ranges of IMs ensure that event variability is included in the process and potentially-damaging events are not omitted, regardless of their magnitude and distance. Spectral shapes are expected to be naturally consistent when selecting records compatible with the seismic hazard and conditions at the site.

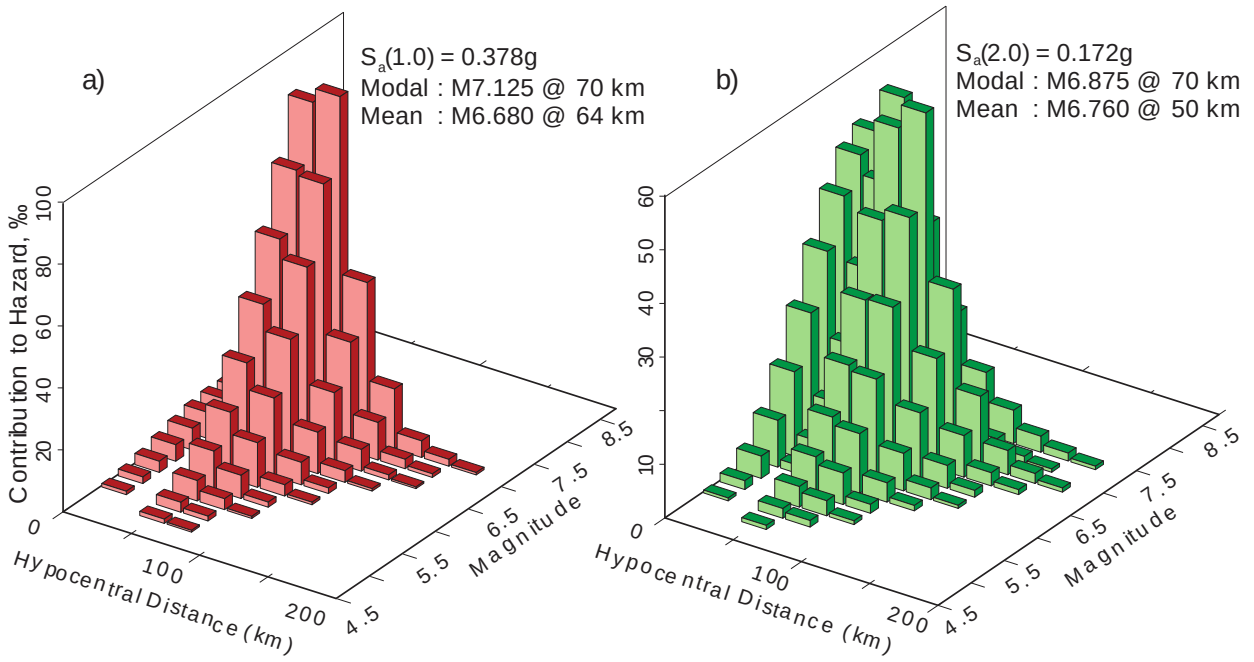

Figure 4.1: Seismic hazard de-aggregation for 2% in 50 years probability of exceedance of spectral accelerations in Victoria at: a) T = 1.0 s; b) T = 2.0 s. (Data provided by Geological Survey of Canada (Halchuk *et al.*, 2007)).

The proposed record selection method involves: 1) identification of the dominant events using de-aggregation, 2) initial selection of records, and 3) refinement of the selection. The following four-step procedure is proposed for the identification of the dominant events:

1. Event data for spectral accelerations at all relevant periods, including **M**, R and the contribution thereof, are combined and sorted in descending order based on their relative contributions;

2. In case of repetitive events from hazard de-aggregation at different periods, i.e. bins with the same **M** and R values, the one with the highest contribution is kept and the remaining ones are discarded;

3. Only the first *n* events are retained, where *n* is the target number of records required for the response history analysis. These are referred to as important events;

4. Dominant events are selected from the important events according to either one of the following four scenarios:

S1: the important bins up to an absolute cumulative contribution of 500 per mil;

S2: the events up to cumulative contribution not less than 50% of the total contribution of the *n* important events;

S3: an arbitrary fraction of important events (e.g., half of them); or

S4: bins of all important events.

In step 1, relevant periods should cover the period range of interest of the structure(s) studied, i.e. from the shortest contributing higher mode periods up to a period exceeding the structure fundamental period to account for inelasticity effects on response. These periods should also be consistent with those considered in the record scaling process as discussed in Section 4.3.2. In step 2, if the same **M**-R event are found for different periods, only the one with the largest contribution is retained because overemphasizing that event could eliminate other less contributing while still relevant or potentially significant events in subsequent steps of the process. In step 3, the number of events is taken equal to the target required number of records in the final set.

Since there is no established method to identify a set of dominant event scenarios from de-aggregation data, four different options are proposed in step 4 of the procedure. These are defined as scenarios S1 to S4. Scenario S1 and S2 are meant to include highly to moderately contributing events. Generally speaking, dominant events obtained by S1 and S2 could be very similar for sites with well-known faults and seismic activities, e.g., western coast of North America continent because limited magnitude-distance pairs are expected. Conversely, they could be different for sites having less defined seismicity sources such as eastern North America. Scenarios S3 and S4 are defined to study the impact of the number of selected events. Obviously, scenario S4 is more inclusive than S3 and would be used when at least one record is sought for each important event to include more variability. Therefore, this scenario is likely to show more scatter compared to the other narrower scenarios. The proposed four scenarios are evaluated throughout the example presented herein and the sensitivity of the outcomes to the chosen scenario is examined later in this paper.

The procedure is applied to the hazard de-aggregation data of Victoria at periods of 0.2, 0.5 and 1.0 and 2.0 s to extract scenarios of the dominant events for this location. Magnitudes and distances of these events together with their contribution are shown in Figure 4.2a. For some of the structures examined later in the paper, the periods exceed 2.0 s and therefore hazard data at longer periods

should have been included in the process. At the time of this study, however, de-aggregation data for Victoria was only available up to 2.0 s and it was assumed that the data at T = 2.0 s was representative of the hazard at longer periods. Ideally, all the available de-aggregation data at relevant periods should be combined to ensure that expected events are included in the process.

For the example, the required number of records in the final set, n, was taken equal to 20. This number has been reported to be sufficient for assessing probability distributions of inelastic structural response (ATC, 2011) and for constructing fragility curves (Cimellaro, *et al.*, 2011). It is also nearly 3 times the required number in ASCE7-10 building code (ASCE, 2010) if average of results are to be used. As shown in Figure 4.2a, the first 6 top contributing events are included in all four scenarios. Scenario S2 must include one more event (7 bins total) to reach at least 50% of the cumulative contribution of the 20 events, while scenarios S3 and S4 respectively include 10 and 20 events for n = 20. Later in the paper, a larger (n = 40) and a smaller (n = 10) sets of records will also be considered to evaluate the robustness of the procedure.

Once the dominant events are found, the number of records assigned to each event has to be determined. The share of each bin can be either: 1) proportional to the contribution; or 2) uniform. The former gives more weight to the more contributing events whereas the latter assumes the same weight for all dominant events. For the example used in this paper, the first scheme is applied to scenario S2 whereas the latter is used for the other three scenarios. Since S1 and S2 are very similar in this example, the effect of the record allocation scheme is examined by comparing the demand imposed by these two particular scenarios. For scenarios S3 and S4, it is logical to use the uniform allocation scheme.

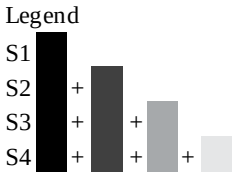

a)

Moment Magnitude	Hypocentral Distance, km				
	10	30	50	70	90
5.875			40		
6.125			51	36	
6.375			61	47	
6.625	34		70	62	
6.875	42		85	83	35
7.125	48	44	103	108	51
7.375	50	58	36		

b)

Moment Magnitude	Hypocentral Distance, km				
	0-20	20-40	40-60	60-80	80-100
5.75-6.00			98		
6.00-6.25			160	216	
6.25-6.50			106	68	
6.50-6.75	4		16	26	
6.75-7.00	8		85	20	20
7.00-7.25	4	10	6	10	6
7.25-7.50	12	30	46		

Figure 4.2: a) Magnitude and distance of the dominant events for scenarios S1 to S4 of the Victoria example. (Contribution of each event to the hazard is reported in thousandths); b) Total number of initially retrieved records for each event from PEER-NGA West ground motion database (lower bound of the ranges is exclusive and upper bound is inclusive).

4.2.4 Initial record selection

As shown in Figure 4.2b, the original resolution of the de-aggregation data is d**M** = 0.25 and dR = 20 km. Past studies have shown that the magnitude has greater impact on spectral shape than the distance and it has been proposed to apply 0.4 and 30 km as the bin's magnitude and distance lengths when records are being searched in databases (Bommer, *et al.*, 2004; Iervolino *et al.*, 2005). However, for simplicity, the original bin sizes were kept unchanged herein and were applied as search criteria to the 6548 records available in the PEER-NGA West database. Site class C was chosen for this example and events were only selected from free field recording stations located at very dense soil and soft rock sites ($360 \leq V_{s30} \leq 760$ m/s), where V_{s30} being the shear wave velocity in the top 30 meters of the site soil deposit. To avoid directivity effects, the closest distance to the fault rupture was set to be always greater than 5 km. This is to comply with the fact that near-fault rupture is not expected in the south west region of British Columbia[3]. It should be noted that regional differences in the expected ground motions characteristics may be disregarded when using a general database of records such as PEER. Ideally, the selection could be limited to the recorded data for regions with similar seismicity. Since data with engineering significance is scarce in case of British Columbia, the authors employed PEER database to demonstrate the approach. Even

[3] G. Atkinson. 2011. Personal communication.

when such a large database is used regional differences could still be taken into account using region-specific GMPEs in the refinement phase as discussed later. Initial selection was performed for all events in the previously defined scenarios S1 to S4. The numbers of initially retrieved records for each event are shown in Figure 4.2b. As this figure shows, the number of initially selected records is as high as 216 in the case of moderate magnitude-long distance events (**M**6.125 at 70 km). The number of records per event will be reduced to the allocated numbers through the selection refinement procedure described in the next sub-section.

For large magnitude events, i.e. **M** ≥ 7.0, the retrieved ground motions are usually very limited due to lack of recorded data, even if a large database such as PEER is searched. To overcome this limitation, one can take advantage of magnitude saturation to increase the possibility of obtaining more records: for crustal earthquakes beyond a certain magnitude level, the magnitude saturation level, some ground motion characteristics such as frequency content and duration are no longer magnitude dependent (Rathje *et al.*, 2004). For instance, Figure 4.3a and b show theoretical and empirical prediction models of the Mean Period of acceleration signals as a frequency content IM (ground motion IMs are reviewed in the next section). Both models indicate that the Mean Period of acceleration becomes independent of the magnitude for **M** ≥ 7.25 while remains linearly distance-dependent. In this study, this observation is taken into account when records for larger-than-**M**7.25 were being selected. To incorporate magnitude saturation concept and retrieve more records, simply the upper bound of magnitude in the bins with the largest **M**7 could then be relaxed in the search process.

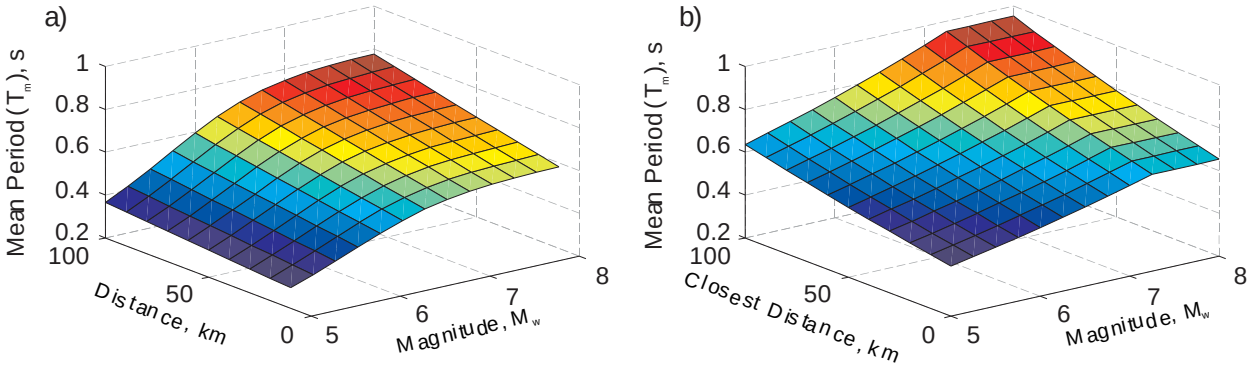

Figure 4.3: Prediction models for Mean Period of acceleration signal: a) Theoretical model (parameters of this model are adopted from (Boore *et al.*, 1997) for generic rock site in western North America); b) Empirical model (coefficients are from regression analysis reported in (Rathje, *et al.*, 2004), forward directivity effects are not included).

4.2.5 Selection refinement

For the initial selection, geophysical metadata such as magnitude, distance and soil profile are generally used as criteria to find event-compatible records from the available databases. When the search criteria are only limited to the mentioned metadata, a large number of event-compatible records may be retrieved, especially in case of moderate magnitude events. This is the case in the example presented herein and a systematic process is needed to reduce the list of initially selected records per event to the allocated number. This process is referred to as record selection refinement. With advancement of the record collection, standard refinement method is essential as it will become more challenging to select few records from a very large batch. For instance, in the recently updated PEER database (NGA-West2 project) more than 7500 horizontal components of recorded ground motions with engineering significance, i.e. $\mathbf{M} \geq 5.5$ and $R \leq 125$ km, are available (Ancheta *et al.*, 2013) which represents 67% increase in the inventory compared to the previous version. Several refinement approaches have been suggested and utilized in research and practice, such as: 1) random selection; 2) adopting more search criteria such as faulting style, basin depth and etc.; 3) implementing optimization techniques to find a set matching average and variance of the given IMs (Kottke *et al.*, 2008); and 4) selecting based on conditioned IMs such CMS (Jayaram, *et al.*, 2011) or GCIM (Bradley, 2012)

Random refinement is suggested in most of the conventional ground motion selection schemes such as ATC-58 (Haselton, 2009; ATC, 2011). This may lead to a high scatter and bias in the computed demand because all of the selected records are given the same chance, regardless of their damaging potential. Imposing more search constraints may result in retrieving fewer-than-required, if nothing, and also needs a database with additional metadata (Bommer, *et al.*, 2004). Finding a set with proper spectral shape using exhaustive search or optimization techniques needs significant computational efforts, especially when the initial set is large (Jayaram *et al.*, 2010). This approach may also lead to multiple different solutions. Applying CMS or GCIM techniques need essential inputs that may not be readily available to practicing engineers and does not guarantee a unique solution. As an alternative to those approaches, the initially selected records can be ranked based on statistical trends of damage-related IMs exhibited by the initial record set. This refinement approach is meant to retain those records which are closer to the central tendency of damage-related IMs and discard those records with exceptional characteristics. The only required input for this technique is the damage-related IMs of the initially selected records. Generally, the damage potential of a ground motion record is attributed to three major classes of IMs: 1) amplitude; 2) frequency content; and 3) duration (Kramer, 1996). These parameters can be easily calculated through simple programming or obtained using commercial software such as SeismoSignal (Antoniou *et al.*, 2012). Various ground motion IMs of the entire records within three major databases have been calculated by the authors and are available for download at the following address: http://www.polymtl.ca/structures/en/. The databases are: 1) PEER-NGA West; 2) Simulated and modified records for east and west of north America (Atkinson, 2009); and 3) Hybrid records for Central and East United States (McGuire *et al.*, 2002). Before going through the detailed instructions of the proposed refinement approach, a quick review of the IMs is given in the following subsection.

4.2.5.1 Ground motion intensity measures (IMs)

Amplitude-related IMs can be calculated from: a) time-domain signal properties such as Peak Ground Acceleration (PGA), -Velocity (PGV) and -Displacement (PGD); or b) spectral parameters such as Spectral Accelerations at selected periods $S_a(T)$, Acceleration Spectrum Intensity, ASI, (integral of acceleration spectrum between 0.1 to 0.5 second). Numerous researches have been carried out to find correlation of the amplitude IMs with seismic damage or demand. A review of

the most popular amplitude-related IMs can be found in (Ye, *et al.*, 2011). That study concluded that none of the considered IMs gives a stable correlation over a wide range of periods. Generally, acceleration- and velocity-based IMs are well-correlated with the demand in stiff (short-period) and flexible (long-period) structures, respectively.

Frequency content IMs can be specified by means of: a) time-domain parameters such as ratio of PGV to PGA; b) frequency-domain parameters such as Mean Period, T_m, i.e. the centre of gravity of the acceleration power spectrum between 0.25 and 20 Hz (Rathje, *et al.*, 2004); or c) spectrum-domain parameters such as Predominant Spectral Acceleration (T_{pSa}) or -Velocity (T_{pSv}), i.e. periods at peak spectral ordinates, or the ratio between spectral accelerations at 0.2 and 2.0 s ($SR_{0.2/2.0} = S_a(0.2)/S_a(2.0)$). Detailed literature review and extensive study on the efficiency of the various frequency content-related IMs can be found in a recent research done by Kumar *et al.* (2011). That research concluded that the Mean Period, T_m, is the most powerful and reliable parameter to express the frequency content.

Duration over which a time-domain amplitude IM is higher than a relative or absolute threshold (e.g., 0.05g or 5% of PGA) has been widely used to define duration-related IMs (Kempton *et al.*, 2006). Among more than 40 definitions of duration in the literature (Bommer *et al.*, 1999), three seem to be more attractive to researchers: 1) Significant Duration ($D_{5\text{-}95}$) which is defined as the time required to build-up between 5 and 95 percent of Arias Intensity index; 2) Bracketed Duration ($D_{\text{Brk.}}$) which is the time between the first and the last specified level of ground acceleration such as 5% of PGA or 0.05g ; and 3) Uniform Duration ($D_{\text{Uni.}}$) which is defined as the total duration in which ground acceleration is higher than a given threshold. Influence of duration on seismic damage is still an ongoing debate (Hancock *et al.*, 2006a).

4.2.5.2 Principal IM

For selection refinement purpose, it is favourable to find an IM that is always well-correlated with seismic demand, regardless of the building's fundamental period or structure type. Despite the wealth of research, there is no single unique IM which can be suitable for all types of structures regardless of their dynamic properties (Riddell, 2007; Ye, *et al.*, 2011). Instead of searching for the best damage-correlated IM of each class, if any, it was decided to find an IM that has the highest average intercorrelation with the other IMs of the same class. This IM is referred to herein as the principal IM. To detect the best inter-parameter harmony, which is reflected by highest average

intercorrelation between sets of random variables with nonlinear relationship, rank correlation is believed to be more efficient than linear correlation (Kottegoda *et al.*, 2008). Rank correlation (Spearman correlation coefficient) is defined as the linear correlation coefficient between the ranked variables:

$$\rho = \frac{\sum_i (x_i - \bar{x})(y_i - \bar{y})}{\sqrt{\sum_i (x_i - \bar{x})^2 \sum_i (y_i - \bar{y})^2}} \tag{4.1}$$

where x_i and y_i are the rank of variables X_i and Y_i. Typical rank correlation matrices for the three classes of IMs are shown in Figure 4.4 for the Victoria example. These rank correlation matrices were calculated for the set of 160 initially selected records for event of **M**6.125 at 50 km in scenarios S3 & S4. In Figure 4.4a, correlation between most of amplitude IMs are relatively high, except for IMs which are formulated based on displacement history of the signals such as PGD. The degree of correlation between duration IMs in Figure 4.4c is more uniform than the one from frequency content IMs in Figure 4.4b. Further analysis showed that the principal amplitude IM of this set is Sustained Maximum Velocity (SMV), which is defined as the 3rd highest cycle in the velocity signal of the record (Ye, *et al.*, 2011). Mean Period, T_m, is deemed to be the most inclusive frequency content IM of this set due to its stronger average correlation with the other frequency IMs. Based on the same concept, Bracketed Duration, $D_{\text{Brk.}}$, can be representative duration IM in this example. Studies performed on the other 19 dominant events (see Figure 4.2) showed that in most cases the Arias Intensity or SVM, Mean Period and Bracketed Duration were the principal IMs.

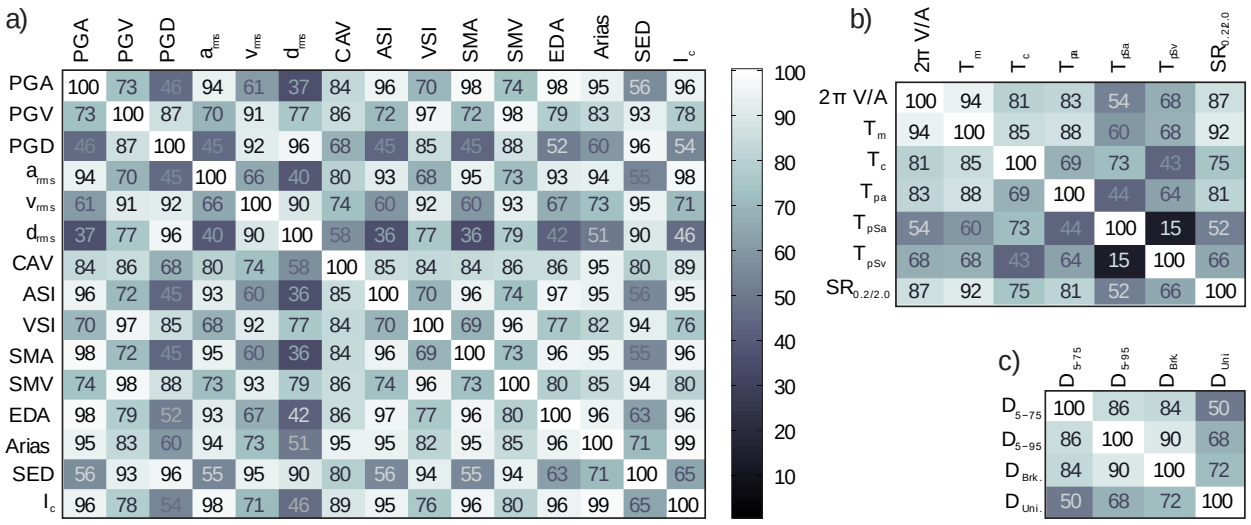

Figure 4.4: Correlation matrices (cell brightness increases with higher correlation coefficient) of: a) Intensity, b) Frequency content; and c) Duration IMs calculated for set of 160 initially selected records for **M**6.125 at 50 km event (absolute value of correlation coefficients (in percent) are shown). For definition of the IMs, refer to (Kramer, 1996; Kempton, *et al.*, 2006; Ye, *et al.*, 2011).

4.2.5.3 Proposed refinement procedure

The proposed record refinement procedure can be summarized in the following steps:

1. The required number of records from a given bin, *m*, is set (this number could be proportional to the contribution of each event or uniform for all events);
2. Ground motion IMs are calculated for the three classes of damage-related IMs:
    a. amplitude IMs, including but not limited to: $S_a(T)$, PGA, PGV, PGD, a_{rms}, v_{rms}, d_{rms}, CAV, ASI, VSI, SMA, SMV, EDA, Arias Intensity, SED, I_c. (see Ye, *et al.* (2011) for definitions);
    b. frequency content IMs, including: 2π V/A, T_m, T_{pSa}, T_{pSv}, $SR_{0.2/2.0}$, among others (see Kumar, *et al.* (2011) for definitions);
    c. duration IMs, including: $D_{5\text{-}95}$, $D_{5\text{-}75}$, $D_{\text{Brk.}}$, $D_{\text{Uni.}}$, etc. (see Kempton, *et al.* (2006) for definitions);

3. Correlation matrix of the IMs of each class is calculated by either linear correlation coefficients or, preferably, rank correlation coefficients;
4. For each class of IM, the IM with the highest average absolute intercorrelation coefficient is selected as the principal IM of that class;
5. Normalized deviation of the principal IMs of each record from the average value of the principal IM, ϵ_i, is calculated for all of the records within each bin:
    a. when the principal IM is normally distributed: $\epsilon_i = (x_i - \mu_X)/\sigma_X$
    b. when the principal IM is log-normally distributed: $\epsilon_i = (\ln(x_i) - \mu_{\ln X})/\sigma_{\ln X}$

    where x_i is the value of the principal IM for the i^{th} record in the bin, μ_X and σ_X are the mean and standard deviation of the principal IM for all of the records respectively, and $\mu_{\ln X}$ and $\sigma_{\ln X}$ are the mean and standard deviation of the natural logarithm of the principal IM of all records, respectively. Alternatively, normalization could be performed using region-specific GMPEs, if available, to reflect regional differences in IMs;
6. For every record, average of ϵ_i for the three classes of IMs is obtained, $\epsilon_{i,\text{avg}}$;
7. Records are ranked based on the $\epsilon_{i,\text{avg}}$ (the record with the minimum $\epsilon_{i,\text{avg}}$ is ranked no. 1); and
8. The ranked records are sorted in an ascending order and the first *m* records are picked as the refined records for a given event.

In the previous section, steps 1 to 4 of the refinement process were applied to identify the principal IMs of the 160 initially selected records of the **M**6.125 at 50 km event. Outcome of steps 5 to 8 of the procedure is shown in Figure 4.5 for a set of 10 records refined from that 160 initially selected records. In this example, for sake of simplicity, $S_a(T)$ of short, moderate and long periods were replaced by PGA, PGV and PGD taking advantage of their high correlation. Note that for the number of IMs (see step 2) there is no limitation in the proposed method and user can specify more IMs if required for better prediction of structural response. In Figure 4.5a to 5c the statistical distribution of the principal IMs of 160 records are shown. These histograms show that the principal IMs have a non-symmetrical skewed type of probability density functions and could be approximated to have log-normal distribution. Principal IM of duration and amplitude have the least and largest coefficients of variation (COV = ratio of standard deviation to average),

respectively. This led to a refined set of records with duration characteristics closer to the central value compared to frequency content and amplitude. The properties of the refined records are circled in the three plots of Figure 4.5d to 5f. It is also shown that records exhibiting values that deviate significantly from the central value of the principal parameters are automatically excluded from the refined set by applying the proposed procedure. In this way, for each scenario, a set of records that have most likely intensity, frequency content, and duration characteristics for the events within that scenario can be obtained. It is noteworthy that IMs of the selected records by this approach could be less intense than the probabilistically calculated IMs for low probabilities. The amplitude of the selected records then needs to be scaled to match the probabilistically calculated values, i.e. target site spectrum. This is elaborated in the next section.

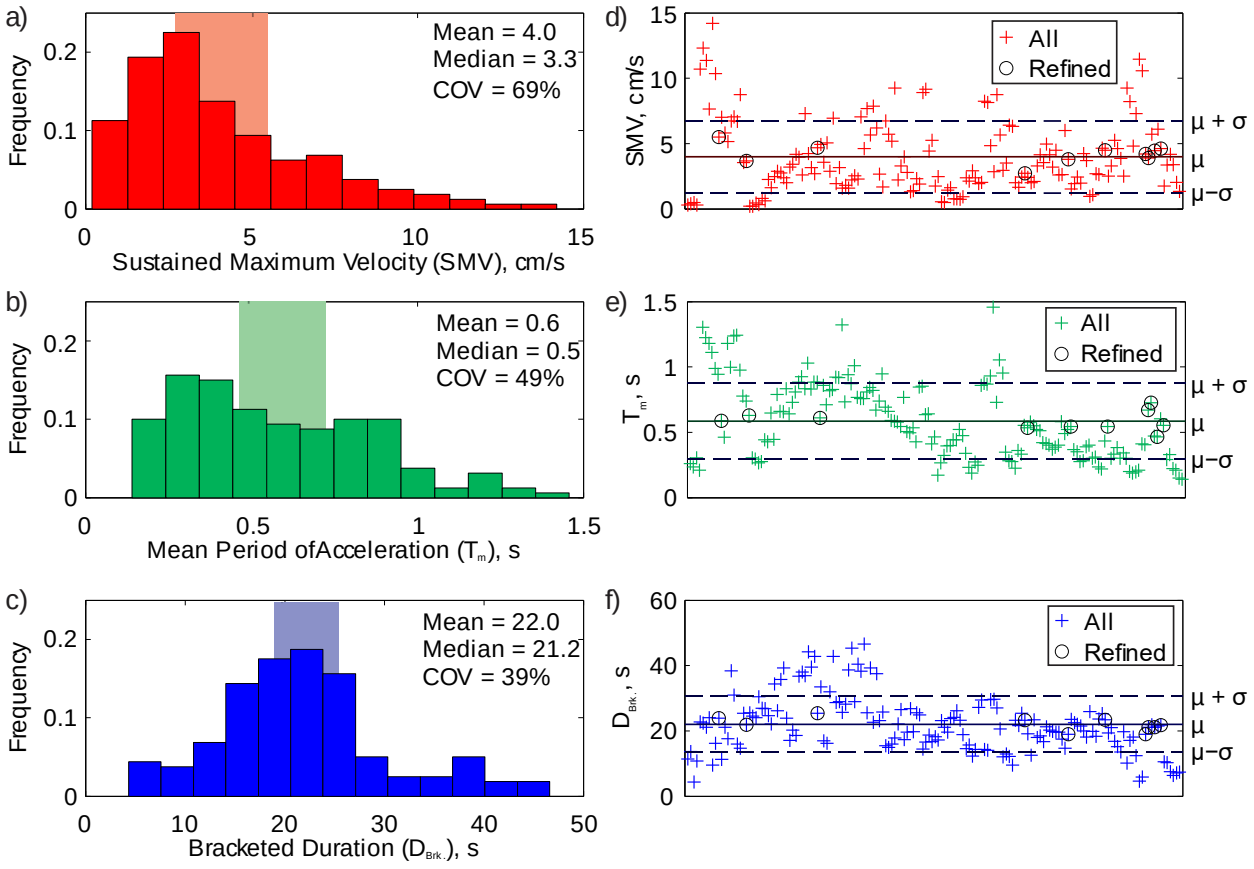

Figure 4.5: Distribution and scatter of principal parameters of 160 records in the bin **M**6.125 at 50 km for: a) and d) Amplitude; b) and e) Frequency content; and c) and f) Duration IMs. Shaded areas in the histograms show the ranges of the principal IMs of the refined set.

The proposed refinement procedure was applied to all events of all four scenarios explained in the example. As mentioned, 20 records were selected for each scenario. Exceptionally, for scenario S1 the number of records was reduced to 18 because this scenario includes only 6 events and the uniform allocation for this scenario resulted in 3 records per event, leading to 18 records instead of 20. The entire process was repeated for n = 10 and 40 records (12 and 36 for scenario S1) to also examine the influence of n. Hence, in total 12 sets of refined records were compiled for scenarios S1 to S4, each scenario having three sets of records which are only different in terms of the number of records.

The quality of the refined record sets can be tested by calculating normalized residual of the spectral ordinates of each record from the median value predicted by a relevant GMPE. This normalized residual is termed epsilon (ε) (Baker, 2011) and can be expressed as:

$$\varepsilon(T) = \frac{\ln S_a^{\text{Record}}(T) - \mu_{\ln S_a}(M,R,T)}{\sigma_{\ln S_a}(M,R,T)} \tag{4.2}$$

where $\ln S_a^{\text{Record}}(T)$ is the natural logarithm of record's spectral acceleration at a given period, $\mu_{\ln S_a}(M,R,T)$ and $\sigma_{\ln S_a}(M,R,T)$ are the predicted mean and standard deviation values, respectively, of the natural logarithm of spectral acceleration at a given period for magnitude and distance of the record. Based on this definition, a positive ε value implies more intensity than expected and vice versa. Figure 4.6 shows the statistical trends of ε for the sets of records that were compiled for scenarios S1 to S4 of the example for the case n = 20 (18 for S1). The GMPE used in the calculation of ε was adopted from (Boore *et al.*, 2008). In this way, it is expected that $\varepsilon(T)$ will be close to zero because the intensity of the selected ground motions represents the considered dominant events. Mean squared error calculation shows that the selected sets for the scenarios S2 and S1 have the least and largest deviations from the predicted average spectral intensity, $\varepsilon = 0$, respectively. This may emphasise the effectiveness of proportional-to-contribution record allocation scheme as the major difference between these two scenarios is the way the records are distributed between the dominant events. Sets from scenarios S2 and S4 have a very similar trend whereas S1 gives relatively weaker-than-expected motions specifically at period longer than 1.5 s. As shown in Figure 4.6b, the average ε of the S2 set is very close to zero for most of the periods and epsilon of the records has the least average variation compared to other sets, and well-centered about zero.

This implies that this set have the most representative records as it was intended by the proposed refinement procedure. As shown, the proposed method converges to a unique solution with least amount of information and judgmental decisions. Further scenario comparisons are performed in Section 4.2.5 of this paper.

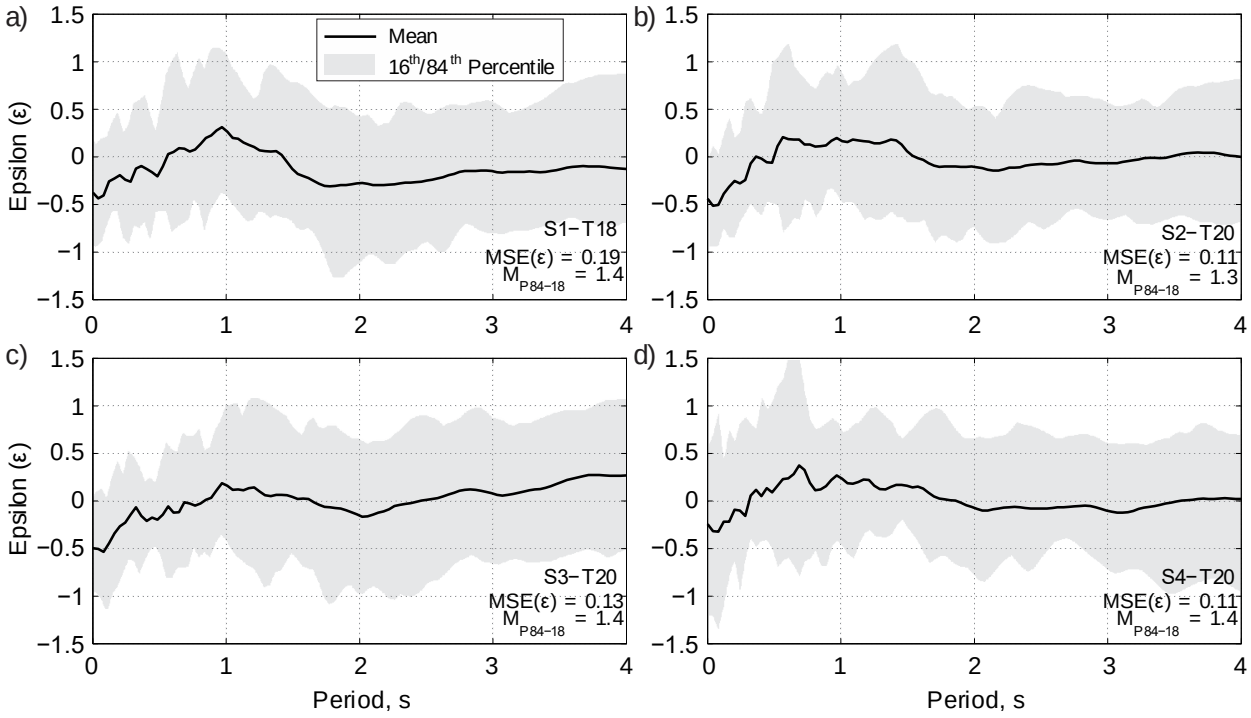

Figure 4.6: Statistical trends of normalized residual of spectral intensity of the refined records, ε, from the expected values as predicted by Boore-Atkinson 2008 GMPE for scenarios a) S1; b) S2; c) S3; and d) S4. (Note: MSE(ε) is the mean squared error between average epsilon of the records and the expected epsilon, i.e. 0, and MP84-16 is the mean of difference between 84th and 16th percentiles of the epsilons).

4.2.5.4 Random selection refinement

In order to compare the outcomes of the proposed refinement technique to a typical conventional record reduction method, sets of records for scenarios S1 to S4 of the example are also compiled using random record drawing technique. This technique simply draws the records randomly for each event, without replacement, from the ensembles of initially selected event-compatible records. In random refinement, virtually the same chance is given to all of the records regardless of their spectral shape and damage potential. Random drawing does not have unique outcome as it may

give another results if it is repeated. Conversely, the proposed trend-based method returns a unique set of records as long as the same input is used.

The randomly-refined sets for this comparative study were compiled from the ensembles of previously initially-selected records of each event. As pointed out earlier, three sets of records were compiled for each scenario using the trend-based approach to investigate the effects of the set size. These sets are different in terms of the number of records but they are mutually inclusive, i.e. the larger sets contain records from the smaller set(s), as it automatically happens when the proposed method is applied. In the case of the randomly-refined sets, the smallest set was first compiled and the number of records was then increased to obtain the larger sets. In this way, the smaller sets are subsets of the larger ones.

The combination of different scenarios (S1 to S4), refinement techniques (trend- and random-based), and the numbers of records makes a total of 24 sets. An 'SX-TY' or 'SX-RY' reference convention was adopted in this paper to designate these sets, where 'X' refers to the scenario number, 'T' and 'R' stand for trend-based and random refinement, respectively, and 'Y' indicates the set size. For instance, 'S2-T20' refers to a set of 20 records which were initially selected for scenario S2 and subsequently refined using the trend-based technique. The comparative study performed with the trend-based and randomly refined sets are presented and discussed later in the paper.

4.3 Record Scaling

4.3.1 Conventional scaling methods

Selected records for response history analysis often need to be scaled or matched to a predefined level of intensity. This can be achieved by linear amplitude scaling or modifying the record in its frequency or time domain (e.g. spectrum matching). In the proposed procedure, linear amplitude scaling is adopted because it does not alter the frequency content and therefore preserves the natural characteristics of the recorded motions or intended frequency content of the synthetic ones. However, as will be shown, linear scaling at a specific period, leads to intensity at other periods higher or lower than the intended values. This limitation is address in the proposed period-independent scaling approach. Currently available options for linear scaling are first critically reviewed in the following subsections.

4.3.1.1 Matching at Fundamental Period scaling method (MFP)

The simplest way of linear scaling is to match, or anchor, the spectral ordinate of a record at the fundamental period T_1 of the structure under study, $S_a^{\text{Record}}(T_1)$, to the intensity of the target spectrum at the same period, $S_a^{\text{Target}}(T_1)$:

$$SF_{MFP} = S_a^{\text{Target}}(T_1) \Big/ S_a^{\text{Record}}(T_1) \tag{4.3}$$

This assures that the structure would undergo an intensity equivalent to the intended level of hazard if the structure was to remain essentially elastic and vibrate predominantly in its first mode, as typically assumed in design. In most earthquake engineering applications, however, the structure response is expected to be also affected by higher modes of vibration having shorter periods and it is anticipated that the structure periods will elongate as a result of inelastic behaviour. Matching at the initial fundamental period of the structure therefore does not guarantee a target-consistent level of input intensity over the range of periods of interest for the structure. Drawbacks of the method can be shown if the spectrum of a relatively high frequency record is being matched to the design spectral ordinate of a flexible structure or vice versa. Figure 4.7 shows scaled spectra of a high and low frequency records from the same event (1994 **M**6.7 Northridge). These motions have been recorded on the same type of soil profile (V_{s30} = 660 and 405 m/s) at similar closest distances from the fault rupture (26 and 32 km). The high and low frequency records are from component 270 Monte Nido Fire Station (NGA 3549) and Playa del Rey - Saran station (NGA 1057), respectively. The high frequency record was matched at a period of 1.8 s corresponding to the fundamental period of a 9-storey Buckling-Restrained Braced Frame (BRBF) and the low frequency one is scaled at period of 0.6 s which is the fundamental period of a 3-storey BRBF. The 9-storey building will experience excessive accelerations in its higher modes (e.g., T_2 = 0.7 s and T_3 = 0.4 s) whereas the 3-storey building will undergo significant accelerations when its fundamental period shifts towards periods longer than T_1 = 0.6 s. Inelastic analysis using these records as scaled resulted in large inter-storey drift ratios: i.e. 4.0% for the 9-storey building and 3.1% for the 3-storey building. Repeating the analysis using properly selected and scaled records gave average peak drift ratio less than 2.0% for these buildings, indicating that unrealistic demand can be obtained with the MFP method. The two records in Figure 4.7 have very different frequency contents, a situation that accentuates the consequences of using the MFP scaling method. Such disparities in ground motion properties will be attenuated when applying the proposed selection refinement method as only the

ground motions with characteristics approaching the central tendency are retained for each dominant event.

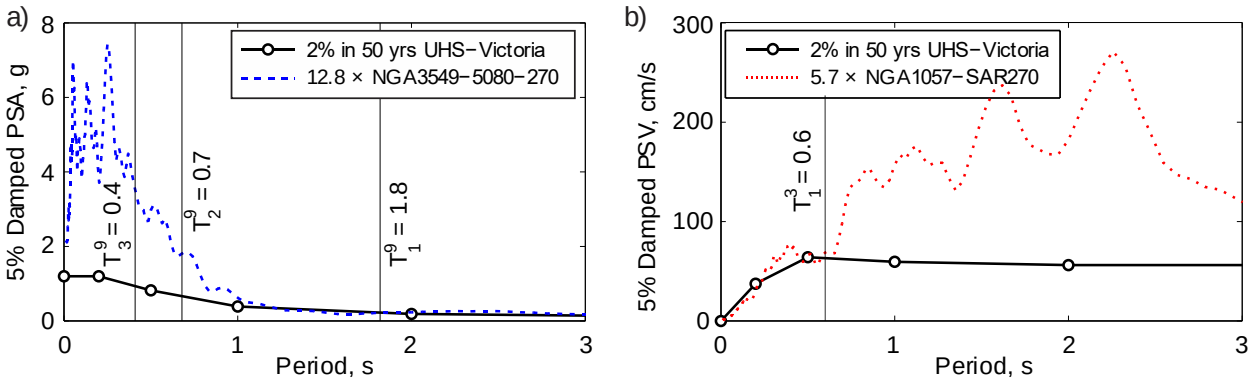

Figure 4.7: Examples of imposing excessive input energy when frequency content of record is neglected in scaling process: a) High frequency record matched at a long period (9-storey building); and b) Low frequency record matched at a short period (3-storey building) (Note: subscripts and superscripts to periods, *T*, indicate mode number and the total number of storeys, respectively).

4.3.1.2 Average Spectral Ratio scaling method (ASR)

To account for higher modes of vibration and elongated periods, average matching can be done over a range of periods centered on the fundamental period of structures. This range has been suggested to start from $0.2T_1$ (higher modes) and end at $1.5T_1$ (elongated period) (ASCE, 2010). One solution is to take the ratio of the average spectral ordinates in this range as the scaling factor (Atkinson, 2009; Baker, 2011):

$$SF_{ASR} = \sum_{0.2T_1}^{1.5T_1} \left[\frac{S_a^{\text{Target}}(T_i)}{S_a^{\text{Record}}(T_i)} \right] \Big/ n_i \tag{4.4}$$

where n_i is the number of period points within the range of interest.

4.3.1.3 Equal Spectral Intensity scaling method (ESI)

In the ESI method, the record is adjusted by a scaling factor such that the area under the record spectrum is equal to the area under the target spectrum. For the $0.2T_1$–$1.5T_1$ period range, the scaling factor of this approach, SF_{ESI}, would be:

$$SF_{ESI} = \sum_{0.2T_1}^{1.5T_1} S_a^{\text{Target}}(T_i) \Big/ \sum_{0.2T_1}^{1.5T_1} S_a^{\text{Record}}(T_i) \tag{4.5}$$

4.3.1.4 Minimum Squared Error scaling method (MSE)

Scaling factors can also be calculated by minimizing the sum of the squared errors (SSE) between the target and scaled spectra in the period range of interest:

$$\text{SSE} = \sum_{0.2T_1}^{1.5T_1} \left[S_a^{\text{Target}}(T_i) - SF_{\text{MSE}} \times S_a^{\text{Record}}(T_i) \right]^2 \tag{4.6}$$

The scaling factor, SF_{MSE}, is obtained by forcing the first derivate of the sum of the squared errors to be zero. The closed-form solution of this process is:

$$SF_{\text{MSE}} = \sum_{0.2T_1}^{1.5T_1} [S_a^{\text{Target}}(T_i) S_a^{\text{Record}}(T_i)] \Big/ \sum_{0.2T_1}^{1.5T_1} [S_a^{\text{Record}}(T_i)]^2 \tag{4.7}$$

4.3.1.5 ASCE 7 scaling method

ASCE 7 selection and scaling approach (ASCE, 2010) is popular in practice and its requirements deemed to be quite simple. In case of 2D analysis, the selected records are scaled so that their average spectrum is always greater than the target in a range between $0.2T_1$ to $1.5T_1$. Although this scaling method seems straightforward at first glance, several different solutions satisfying its requirements can be obtained for a given set of records (Kalkan *et al.*, 2010), which is not desirable for a robust analysis in practice. Since no constraint is placed on the variance of the scaled spectra, the various admissible sets of scaled records can result in very different levels of demand when they are implemented in nonlinear response history analysis. To comply with ASCE 7, scaling factors could be determined either by: 1) adjustment of the average of the un-scaled or scaled spectra; or 2) optimization techniques. In the former method, initial scaling factors obtained from

the closed-form solutions, as discussed previously, are applied to the individual records. Then a unique adjustment factor is collectively applied to all records such that the average spectrum of the set satisfies the code requirement. This factor is simply the minimum ratio of the average scaled spectrum to the target spectrum within the period range of $0.2T_1$ to $1.5T_1$. When applying this technique, at least three solutions exist:

1. Adjusting the average of the un-scaled spectra (initial scale factors of unity). This method preserves the variance of the un-scaled records.

2. Adjusting the average of the matched spectra at T_1. The records are first individually scaled using Equation (4.3) and the average spectrum of the scaled records is then adjusted to satisfy the code requirement. In this way, the scaled spectra will have zero variability at T_1 which may result in less response variability for a structure responding predominantly in its first mode.

3. Adjusting the average of the range-matched spectra. Every record is first scaled using Equations (4.4), (4.5) or (4.7) and scaled records are subsequently adjusted to the target. Since the shapes of the target and the individually scaled record spectra are similar, lower variance in the spectral ordinates may be obtained over a broad range of periods.

When using optimization techniques, an additional constraint is defined and an optimization is conducted to find a set of scaling factors that simultaneously satisfy the code requirement and that extra constraint. Examples of possible extra constraints are:

4. Minimizing the average of squared errors between the average of scaled spectra and the target spectrum. This represents the best constraint if a well-matched average spectrum is sought. However, the scaled spectra may show excessive variance.

5. Minimizing the average of the scaling factors. The obtained set of factors results in the smallest possible scaling values in an average sense which implies less record manipulation by scaling process. However, this extra constraint may not prevent large variance of the spectral ordinates as variance always exists for un-scaled records and may increase when they are scaled, even with the minimum possible scaling factor.

6. Minimizing the average of $S_a(T_1)$. This is another appropriate extra constraint because it forces the average of $S_a(T_1)$ to be as close as possible to the target. Here again, this extra constraint may not be able to restrain the variance of $S_a(T_1)$.

Significant differences between the outcomes of these options can be found when these scaling solutions are applied to a typical set of ground motion records. For instance, the solutions obtained from the 6 abovementioned ASCE 7 scaling methods are presented in Figure 4.8 for a set of 20 records randomly drawn from ensembles of records compatible with **M**7.0–7.5 @ 0–40 km and **M**6.5–7.0 @ 40–80 km events. According to the de-aggregation analysis (see Figure 4.1b), these events correspond to the most contributing earthquakes at period of T = 2.0 s for a class C site in Victoria. This specific scenario is referred to as S5 hereinafter and the associated record set is denoted by S5-R20. Random-based selection is adopted here as ASCE 7 provides limited guidance for selection. Later in the paper, these records with 6 different sets of scaling factors will be utilized in response history analysis of a 9-storey model to examine potential consequences of ASCE 7 scaling method. The fundamental period of the model is T_1 = 1.8 s, therefore the period range of interest for scaling is from 0.36 to 2.7 s as shown in Figure 4.8. In Figure 4.8a, approach 4 gave the best-fitted average spectrum but the resulting maximum spectral ordinates in Figure 4.8b have the highest intensity around and beyond T_1. This shows that reaching the best-fitted average spectrum could have some unintended consequences in terms of variability. Approach 2 resulted in excessive average spectral ordinates in the short period range while its variance at T_1 is zero, which may imply that a trade-off between average and variance is required to obtain a reasonable scaled spectrum. For most approaches, the average of the scaled spectra overshot the target, especially in the short period range. In the case of the maximum of spectra, which could be used as the indicator of variability, approach 3 gave the least intense solution in a wide range of periods while the other approaches resulted in significantly higher intensities.

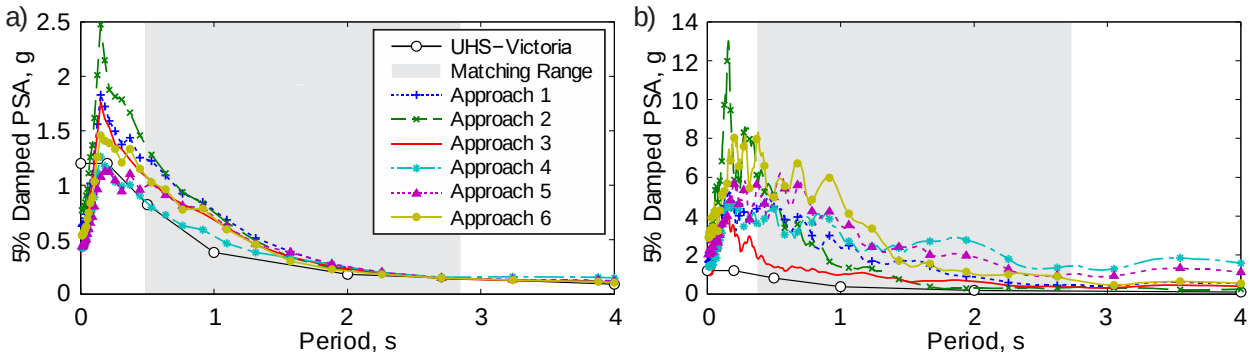

Figure 4.8: Spectra from 6 possible solutions of the ASCE 7 record scaling method: a) Average of scaled spectra; b) Maximum of scaled spectra. (Note: records of set S5-R20 are used in the calculations).

4.3.2 Least Moving Average (LMA) scaling method

The scaling methods described in the previous sections are performed for a predefined period or range of periods. To calculate scaling factors, the structural dynamic properties of analysis subject must therefore be known, which may not be the case in a typical design process, meaning that scaling may need to be adjusted as the design is updated or modified. Different sets of scaling factors may also be needed when assessing seismic demands on structures located on the same site but having different periods. An example of this situation can be found in industrial plants that are constituted of many processing units with different sizes and structural systems which are all supposed to withstand the same earthquakes in the future. Finding proper scaling factors could also be complicated when three-dimensional analysis is to be conducted on buildings which have distinct dynamic behaviour in each principal axis. Period-dependent techniques can result in counter-intuitive solutions as quite different scaling factors may be required for orthogonal components of a given ground motion. Difficulties could also arise when this scaling approach is used for analysis of torsionally-sensitive structures having long periods associated to torsional modes. Figure 4.9 shows that this situation can result in excessive overshoot of the target spectrum and large variability at periods of the translational modes. In this figure, the spectra of the previously compiled set S5-R20 are compared to the UHS after applying two commonly used period-dependent scaling techniques, i.e. MFP and ASCE7 (approach 3), For this specific example, the average of scaled spectra is 50% to 80% more intense than the UHS ordinate at the first and second translational modes which would lead to unrealistic demands. It is also not uncommon in

earthquake engineering research to investigate the response of a given lateral load resisting system for structures having different number of storeys. For each prototype building, an individual set of scaling factors is required which makes the analysis and assessment process more cumbersome to conduct and less straightforward to evaluate. Even dynamic properties of a single building may not be well-represented by a single period as its structure may behave in multi-mode fashion or its dynamic characteristics can change when response is shifted toward inelastic range. As discussed in the selection process, it is therefore desirable to select ground motions based on the seismic hazard and conditions at the site, not the dynamic characteristics of the structures. This issue has been raised and discussed in (Jayaram, *et al.*, 2010). The same reasoning would apply to ground motion amplitude as there is no reason why the intensity of ground shaking should vary for different structures at a given site or when changing the structure properties. If period-independent selection and scaling techniques were used, only a single set of scaled records would be required for seismic design or assessment projects at a given site. This would greatly simplify the required work in contrast to the period-dependent methods which need separate selection and scaling when period is changed (e.g. Tehrani *et al.* (2014)). Early generations of scaling methods mostly relied on so-called record normalization by means of a specific IM independent of the structure periods such as PGA or PGV (Shome *et al.*, 1998; Kurama, *et al.*, 2003). However, these intensity measures cannot be well-correlated with the expected damage in all types of structures (Kurama, *et al.*, 2003). As a result, damage prediction is biased to the IM used for the record normalization. In addition, site specific design spectrum is neglected when these methods are used. An alternative technique is therefore needed to achieve the desired goal. (Jayaram, *et al.*, 2010) proposed a method where records are selected such that their spectra match a target median and variance spectrum over a range of periods. The records can then be scaled at structure fundamental period. The authors showed that while the procedure can result in reasonable match in some cases, it may also lead to discrepancies in the demand estimates.

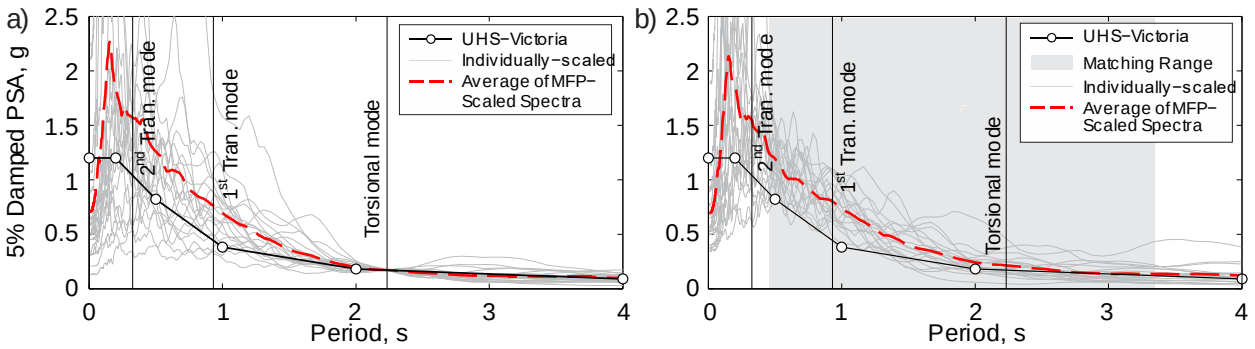

Figure 4.9: Excessive overshooting the target spectrum when conventional period-dependent scaling methods are used for analysis of a 4 storey torsionally-sensitive building by applying: a) MFP method (matched at the torsional mode, T = 2.2 s); b) ASCE 7 (approach 3, matched between $0.45 \leq T \leq 3.35$ s).

As an alternative, it is suggested to scale the record to match the target spectrum in a period range where their spectral shapes are similar. Studies by the authors have shown that by this concept, records are matched to the target in a frequency bandwidth where most of the seismic energy is concentrated. If the selected records cover a sufficient range of frequency contents, this scaling method leads to a consistent average, or envelope spectrum as well as limited spectral ordinates variability. The proposed method herein is denoted as Least Moving Average because it scans all the periods of the spectrum to find a band in which the average difference between the target and record spectra is minimum. This method is a simple convolution technique that smoothens the spectrum of each un-scaled record using average values over a moving window prior to scaling over that window. The minimum scaling factor over the entire period range of interest is kept, meaning that the spectrum of the scaled record matches, on average, the target over one of the windows considered. For each record, the proposed approach can be executed in the following steps:

1. The target 5% damped acceleration spectrum (e.g., UHS) is defined for a sufficiently large number of equally spaced period points in logarithmic space, say 200 period points, over a sufficiently wide range of periods, T_{min} to T_{max}, to cover all meaningful periods for the structure(s) studied, and the period range over which ground motion energy could be located;

2. The 5% damped acceleration spectra of the records are calculated for the same 200 period points, T_i;
3. Spectral ratios, i.e. $\left[S_a^{\text{Target}}(T_i)/S_a^{\text{Record}}(T_i)\right]$, are computed at all periods;
4. An averaging window with either a constant or variable length is defined:
    a. constant: the window is fixed for all periods (e.g., $\Delta T = 0.5$ s);
    b. variable: the window starts at αT_i and ends at βT_i;
5. The first and last center of averaging windows, respectively T_{first} and T_{last}, are computed:
    a. for the constant averaging window: $T_{\text{first}} = T_{min} + \Delta T/2$ and $T_{\text{last}} = T_{max} - \Delta T/2$,
    b. for the variable averaging window: $T_{\text{first}} = T_{min} / \alpha$ and $T_{\text{last}} = T_{max} / \beta$;
6. For each period window, the scaling factor $SF_{LMA,i}$ is obtained from the moving average; it can be either:
    a. arithmetic moving average: $SF_{LMA,i} = \frac{1}{n_{T_i}} \sum \left[S_a^{\text{Target}}(T_i)/S_a^{\text{Record}}(T_i)\right]$; or
    b. geometric moving average: $SF_{LMA,i} = \exp\left(\frac{1}{n_{T_i}} \sum \ln\left[S_a^{\text{Target}}(T_i)/S_a^{\text{Record}}(T_i)\right]\right)$;
7. The scaling factor of the record, SF_{LMA}, is the minimum of the moving average values, and the scaling period, T_{LMA}, is the period T_i associated to the scaling factor.

In step 1, the period range must be sufficiently wide to cover all periods of interest in terms of structural response as well as records' frequency contents. For most structural applications, T_{min} = 0.1-0.2 s can be chosen to capture high spectral accelerations at short periods and T_{max} = 4.0-6.0 s deemed sufficient to include low frequency contents of the most records. T_{max} should also be typically two times greater than longest expected structure period. In that step, a logarithmic scale is suggested such that period intervals expand exponentially as the period is increased, allowing averaging to be performed over longer intervals as the variations in spectral ordinates typically become less pronounced. In step 4, variable averaging windows are proposed for the same reason and values $\alpha = 0.5$ and $\beta = 1.5$ are suggested for the recommended T_{min} and T_{max} values. When a constant window is used, ΔT in the order of 0.5 s is generally adequate.

The results from the proposed method for typical high and low frequency records are shown in Figure 4.10. The calculations were performed using variable averaging windows between T_{min} = 0.1 s and T_{max} = 6.0 s. In this case, the high frequency record is matched to the target at a period near to the Mean Period of the signal, T_m, whereas the low frequency one is matched to the medium-to-low frequency region of the target, close to the predominant period of spectral velocity, T_{pSv}.

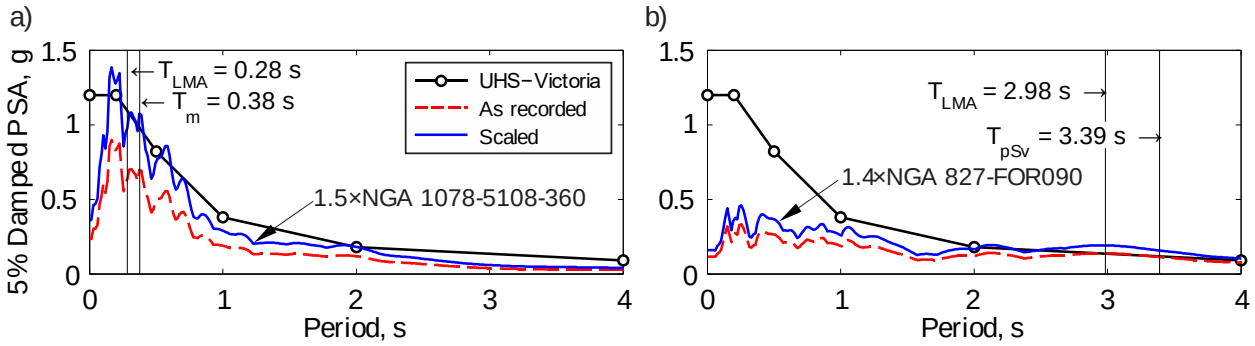

Figure 4.10: Scaling by the Least Moving Average method for a typical: a) High frequency record; and b) Low frequency record (Calculations performed using 400 points over the 0.1-6.0 s period range using variable period windows with α = 0.5 and β = 1.5).

Further analysis shows that the width and shape of the averaging windows can affect the magnitude of the scaling factors. Results of this analysis are shown in Figure 4.11 in which LMA scaling is performed for a set of 266 records. Generally, the magnitude of the scaling factor is directly proportional to the length of the window while the variance of the moving averages is inversely proportional to it. This implies that medium window sizes (e.g., ΔT = 0.5 s or α = 0.5 and β = 1.5) could be appropriate as they give a scaling factor which is calculated with minimum possible variability in the moving averages. Comparing constant and variable averaging windows also shows that the latter gives more stable moving averages. This makes the variable-size averaging window more appropriate and reliable.

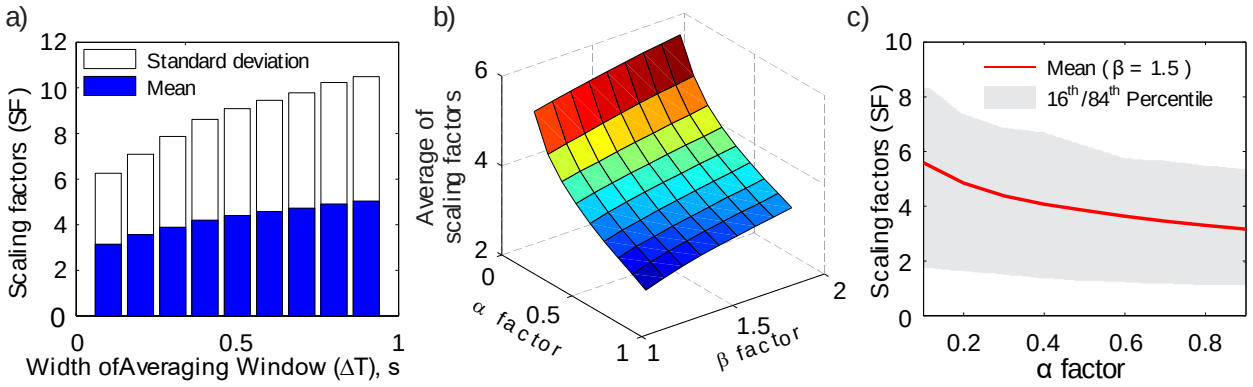

Figure 4.11: Variation of the scaling factors for a set of 266 records calculated by LMA method for different window sizes using: a) Constant averaging window; b) Variable averaging window; and c) Variable averaging window with constant β factor.

Scaling by the proposed LMA technique is done independently from the structure periods and therefore does not necessarily give a fully target-matched spectrum. Instead, each record is adjusted to the target intensity at a period that reflects its frequency content. Scaling to a fully target-matched spectra is shown to give a conservative and biased estimate of seismic demand, especially when the target is UHS (Baker, 2011). The CMS concept discussed earlier was developed as a more probabilistically-consistent target to replace the UHS. Since the CMS is supposed to give more realistic target spectral shapes, the results of LMA are compared to those from the CMS. In Figure 4.12, the CMS of the example Victoria site at periods of T = 1.0 and 2.0 s are compared to the average and 84th percentile spectrum of set S2-T20 (sets are defined in Section 4.2.5.4). The CMS were computed using GMPE for deep in-slab earthquakes in subduction zones, as formulated for soft rock sites by (Youngs *et al.*, 1997), and the inter-period correlation function suggested in (Baker *et al.*, 2008). Mean event for periods of T = 1.0 s and T = 2.0 s are taken as **M**6.7 at 64 km and **M**6.8 at 50 km, respectively (see the de-aggregation results in Figure 4.1). From the figure, the average spectral shape of the scaled records reasonably matches the CMS in a broad range of periods and it stays within the "CMS ± one standard deviation" range. For this example, the proposed LMA scaling algorithm can reproduce a realistic average spectral shape. This can be achieved when records with different frequency content representing the hazard at different periods within the range of interest are included in the set.

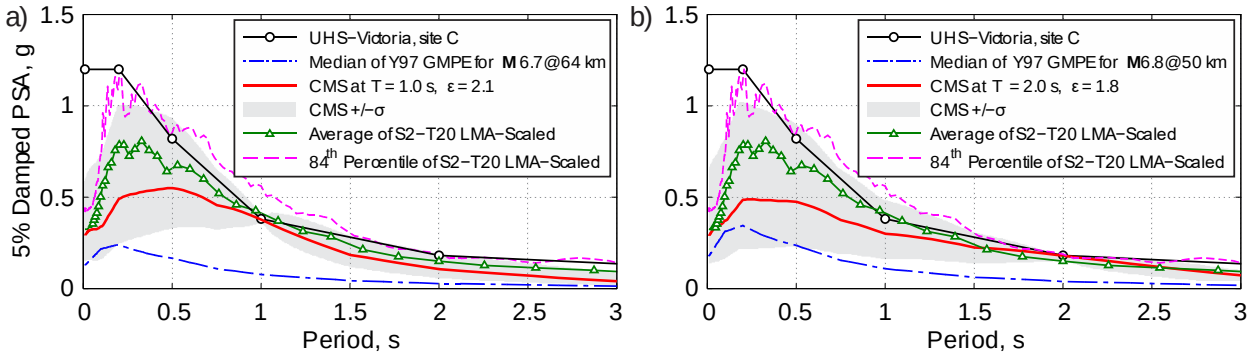

Figure 4.12: Comparison between CMS and the trend of scaled spectra obtained by LMA method for set S2-T20. Conditioning period for CMS is set to a) 1.0 s; b) 2.0 s (Note: For LMA, the records are scaled by variable moving average window within T_{min} = 0.1 and T_{max} = 4.0 s).

4.4 Comparative Studies

The effectiveness of the proposed selection and scaling method is examined using nonlinear response history analyses performed on a series of inelastic single-degree-of-freedom (SDOF) systems and 3- to 15-storey frames. A comparison is also made with conventional selection and scaling methods. In the comparative studies, two seismic demand indices were calculated: 1) peak ductility; and 2) cumulative inelastic ductility. Four scenarios (S1 to S4), two refinement approaches (random-based and trend-based), three set sizes (n = 10, 20 and 40 records, except for scenario S1 for which n = 12, 18 and 36, and three record scaling methods (MFP, MSE and LMA) were also included in the comparative study. Discussion on the selection of the appropriate percentile value for the demand indices is given at the end of this section.

4.4.1 Proposed selection refinement method versus random record drawing

Constant-ductility spectra calculated for ductility of 5.0 are used to compare the robustness of the random drawing and the proposed refinement techniques. Constant-ductility spectrum was chosen as it does not involve record scaling, allowing the effectiveness of the refinement procedures to be qualified without the influence of the scaling process. The Giuffré-Menegotto-Pinto hysteresis material model (Filippou, *et al.*, 1983) was used to simulate inelastic behaviour of SDOF models. This material model is able to reproduce a non-degrading cyclic inelastic response including isotropic and kinematic hardening, and the parameters of the hysteresis law were calibrated using the results from the full-scale bucking-restrained brace frame tests by (Tremblay, *et al.*, 2006). The

post-yield stiffness was set to 0.4% of the elastic stiffness and 5% viscous damping was assumed in the solution. The ductility spectra were calculated for 40 equally-spaced periods ranging from 0.1 to 4.0 s. Figure 4.13a & b plot the mean of base shear ratios (*V*/*M*) and the mean cumulative plastic ductility (CPD) determined with the required base shear, respectively. The sets of scenario S2 were implemented in the calculations. In Figure 4.13a, when compared to the random refinement, the proposed method leads to more stable average results as the required base shear ratio to achieve the target ductility is virtually insensitive to the number of records at all periods. In terms of cumulative plastic ductility (Figure 4.13b) both methods led to almost the same average trend. This demand index is given by an integration process which makes it less sensitive to the input. In general, the trend-based method gives more consistent results with a reduced scatter (lower COVs) over the period range, as shown in Figure 4.13c & d. Similar trends were observed for the other scenarios. However, it was noted that the proposed approach performs better for the sets obtained from scenarios with a smaller number of events, i.e. scenarios S1 and S2.

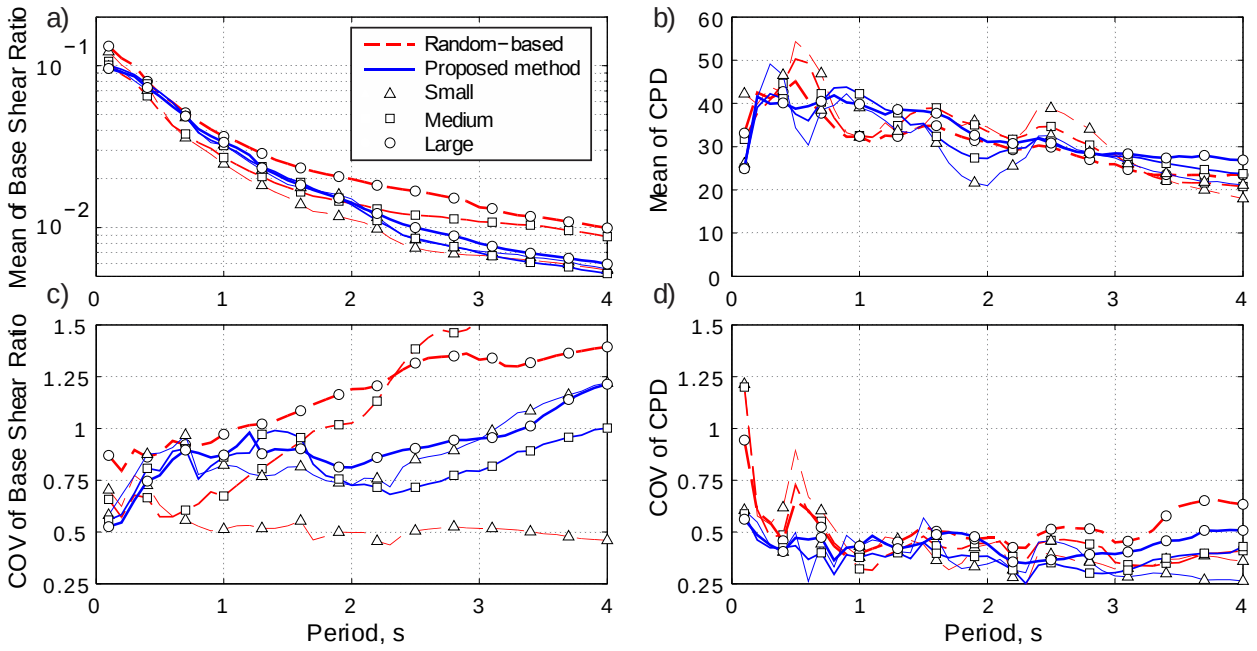

Figure 4.13: Impacts of random- *vs* trend-based selection refinement on mean and coefficient of variation (COV) of: a) & c) Base shear ratio; and b) & d) Cumulative plastic ductility, for a target ductility = 5.0 for scenario S2 with n = 10, 20 and 40 records (line thickness increase with n).

4.4.2 Impacts of earthquake scenario and record allocation

In Figure 4.14, the average and 84th percentile velocity spectra of the trend-based refined and then scaled sets of scenarios S1 to S4 are compared. Spectral velocity is used to better represent the seismic input energy. The records are scaled using the proposed LMA scaling method. As shown, very consistent average and upper percentile (84th) results are obtained, demonstrating the efficiency of the LMA method for reducing the variability in seismic input energy, regardless of the number of records and the scenario being used. Consistency is quantified by measuring mean squared error (MSE) between scaled spectra and the code level spectral intensity between 0.5 to 4.0 seconds. Comparison of MSE values indicates that S2 sets have a better fit and are more consistent as their average MSE is relatively lower and varies less than the other sets. The same observation is valid in case of 84th percentile values. The 84th percentile values also show high consistency and insensitivity as they are minimally affected when scenarios and number of records vary. Overall, comparing the average and 84th percentile spectra in all of the cases shows that the variability of input energy is very low. This result was expected because the variability of input energy is bounded by the trend-based refinement and LMA scaling processes. It is therefore expected to observe low variance in the inelastic demand when response history analysis is conducted, as shown in the next section.

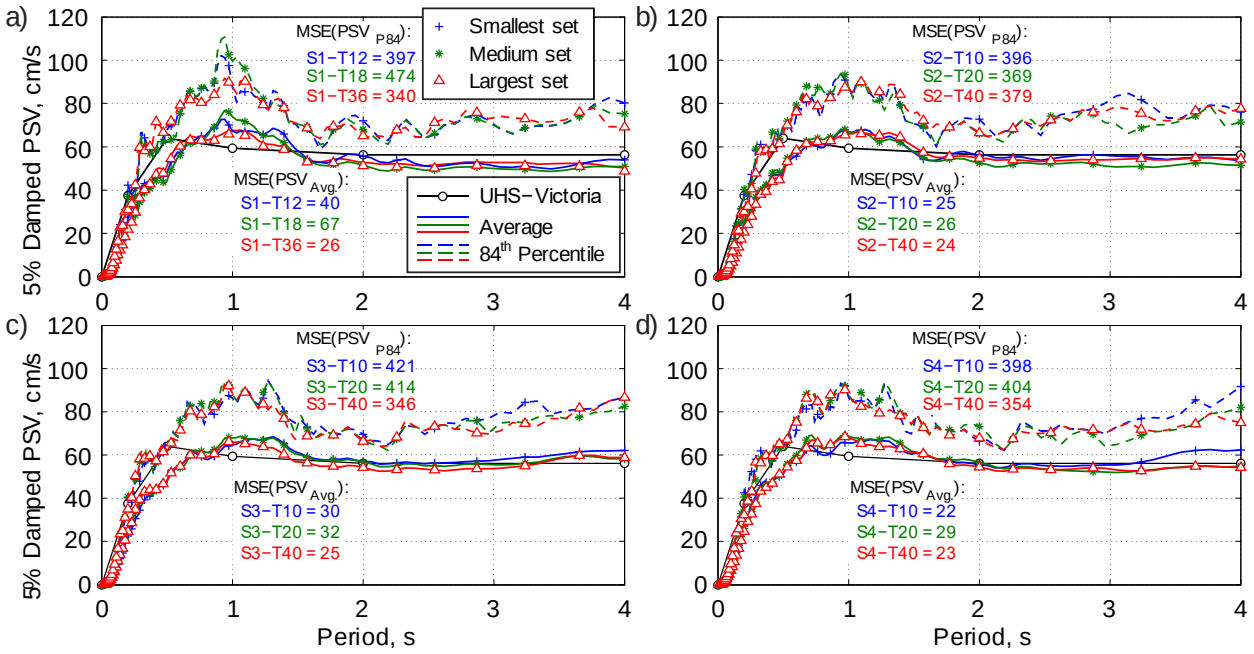

Figure 4.14: Influence of the scenario of dominant events and number of records on the average and 84th percentile spectral pseudo-velocity values calculated for trend-based refined and LMA scaled sets of scenarios: a) S1; b) S2; c) S3; and d) S4. Solid and dashed lines represent the average and 84th percentile values, respectively. (Note: MSE ($PSV_{Avg.}$) and MSE (PSV_{P84}) are the mean squared error between average and 84th percentile spectra, and the 2% in 50 years UHS ordinate, respectively. In MSE calculation, spectral values for range of $0.5 \leq T \leq 4.0$ s are used).

4.4.3 Effect of scaling on inelastic demand of SDOFs

Trend-based refined sets of all scenarios were applied to a series of SDOFs with periods of 0.5, 1.0, 1.5 and 2.0 s. The strength of these systems was determined following the provisions of the NBCC 2010, using the 2% in 50 years UHS values for a site class C in Victoria and a force reduction factor of 4.8. The latter corresponds to the product of the ductility- and overstrength-related force modifications factors, R_d and R_o, specified in the NBCC for the buckling-restrained braced frame (BRBF) system ($R_d \times R_o = 4.0 \times 1.2 = 4.8$). Inelasticity was modelled using Bouc-Wen hysteresis laws (Wen, 1976) which can reproduce stable, symmetrical, and smooth hysteresis response without stiffness and strength degradation such as that from BRBFs. The Bouc-Wen model parameters were calibrated against data from the BRBF tests by (Tremblay, *et al.*, 2006). Viscous damping ratio was set equal to 3% of the critical damping. The records were scaled using

three methods: 1) matched at fundamental period (MFP); 2) minimum average squared error (MSE); and 3) least moving average (LMA). Given that the latter is independent of the elastic period of structure, the same set of scaling factors were used for all four SDOFs when using the LMA method. In total, around 2500 nonlinear response history analyses were required to be carried out.

Figure 4.14 shows the average and standard deviation values of the peak ductility for the different set sizes, scaling methods, and scenarios. In each clustered bars, the number of records increases from left to right (n = 10-20-40, 12-18-36 for scenario S1). The average peak ductility did not change when the basic number of records is doubled or halved. The average results were also very stable regardless of the chosen scenario. However, records of the S3 and S4 sets imposed more demand due to the low frequency records originating from the bins of large magnitude-long distance events. Apparently, the average demand level is affected by the scaling approach. As it was expected, un-scaled records were not able to impose significant inelasticity as they are less intense than the design accelerations of the SDOFs. According to the equal displacement principle (Chopra, 2011), the average anticipated peak ductility for these SDOFs is equal to 4.0 (R_d = 4.0). Analysis results indicated that averages of MFP-scaled sets are very close to this expected level of ductility, i.e. between 3.9 to 4.5, and the variability is moderate, i.e. 29% ≤ COV ≤ 44%. It is also observed that the S2 sets showed the closest match to the target ductility for this scaling method. The MSE approach, which seeks for the closest spectral shape to the target spectrum in a range, resulted in the highest average demands, i.e. between 4.0 to 4.7, and moderate-to-high variability, i.e. 30% ≤ COV ≤ 56%. On the other hand, the LMA scaling method (Figure 4.15d) gives the most robust statistics: the variability is low (23% ≤ COV ≤ 35%), and insensitive to the scenario and number of records. However, the average demand from the LMA method is lower than the others, i.e. between 3.0 and 3.6, because the scaling factors are smaller. For the LMA method, the mean plus one standard deviation of the demand matches very well the anticipated peak ductility value of 4.0. Statistics of the energy dissipated by the SDOF systems are presented for the same parameters in Figure 4.16. The values are normalized to the product of the yield strengths and displacement of the systems. The same trends are observed for this cumulative response parameter, with smaller average and standard deviation values together with reduced sensitivity to the scenario and the number of records when the LMA approach is implemented.

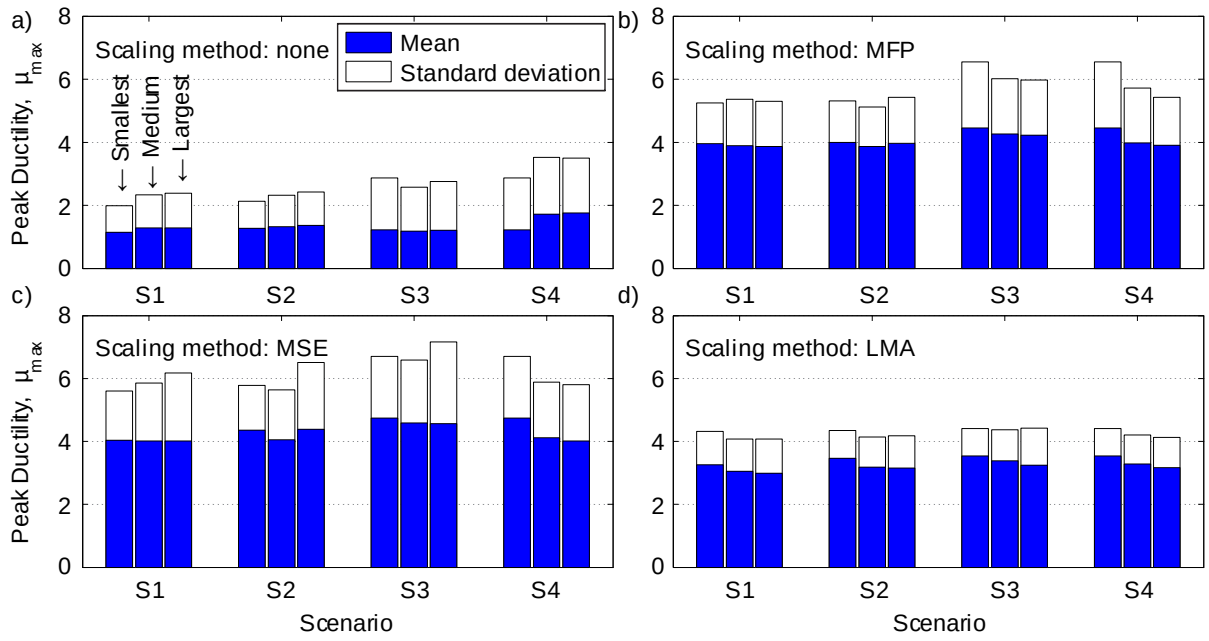

Figure 4.15: Statistics of peak ductility obtained from inelastic response history analysis of SDOFs computed for different scenarios, number of records, and scaling methods: a) Un-scaled; b) MFP; c) MSE; and d) LMA (Note: records are refined using the proposed refinement method).

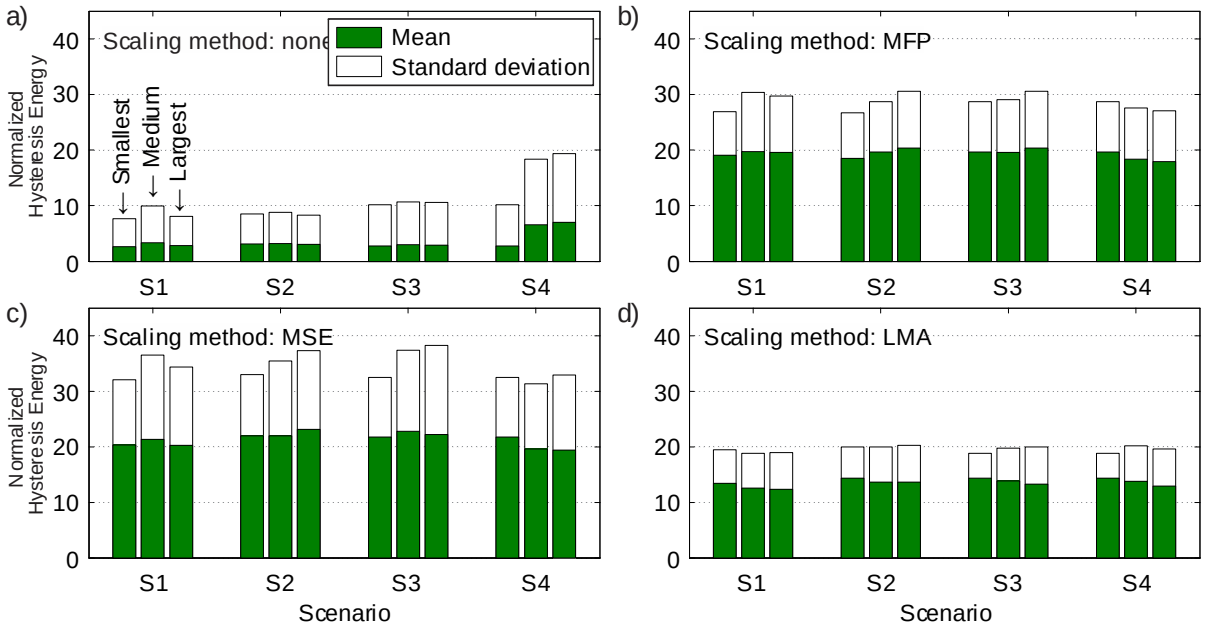

Figure 4.16: Statistics of normalized hysteresis energy obtained from inelastic response history analysis of SDOFs computed for different scenarios, number of records, and scaling methods: a) Un-scaled; b) MFP; c) MSE; and d) LMA. (Note: records are refined using the proposed refinement method).

Figure 4.17 shows the results of the same SDOF analyses but this time using the randomly refined sets that were introduced in Sect. 4.2.5.4. Data analysis showed that the average and upper percentile of the demand are only slightly affected and set size independency is preserved when LMA method is used. On the other hand, MSE scaling method generally resulted in greater variability and increased set size sensitivity comparing to the trend-based refined sets although it predicts almost the same average. This implies that demand estimated using LMA-scaled records could also be less affected by the selection refinement technique. Effectiveness of the proposed trend-based refinement technique in variance reduction could also be demonstrated when standard deviations of the peak ductility demand from the MSE-scaled sets in Figure 4.15c (trend-based) and Figure 4.17a (random-based) are compared.

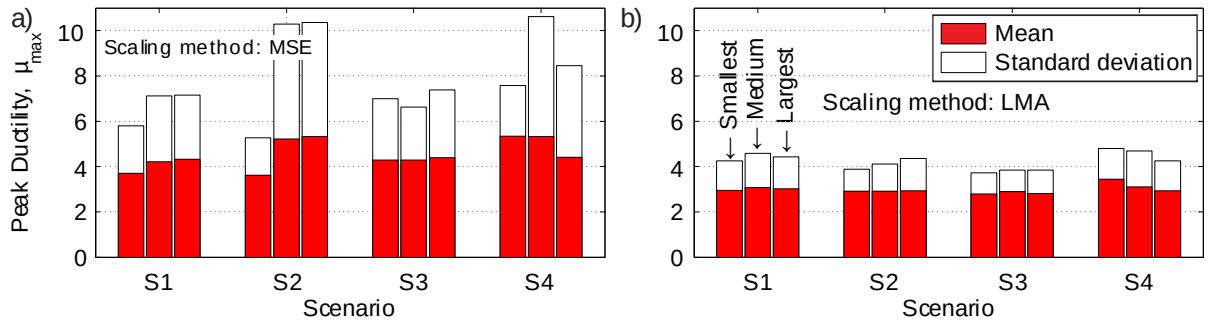

Figure 4.17: Trend of the peak ductility demand of inelastic SDOFs subjected to randomly-refined sets of record from various scenarios and having different set sizes. Scaling is conducted by a) MSE; b) LMA.

4.4.4 Impacts of selection and scaling on response of a multi-storey frame

To reinforce the findings from the previous SDOF studies, impacts of record selection and scaling on peak inter-storey drifts were qualified for a 9-storey office building designed according to the 2010 NBCC and the CSA S16-09 Canadian steel design code (CSA, 2009) for the Victoria class C site. The period of the fundamental vibration mode of this structure is 1.8 s. Selection and scaling was done to compile sets of 20 records for the following three cases: 1) the proposed trend-based selection and LMA scaling; 2) ASCE 7 criteria; and 3) random-based selection and MFP scaling. For the first case (proposed approaches), the records within set S2-T20 were used for this comparative study. For the ASCE 7 method, the record ensemble was a set of 20 records randomly drawn from the most expected events for seismic hazard at period T = 2.0 s (refer to Section 4.3.1.5 for more details), which is close to the prototype fundamental period (1.8 s). The 6 possible sets of scaled records obtained in Section 4.3.1.5, all satisfying the ASCE 7 requirements, were considered in the analysis. The resulting solutions are designated as ASCE 7-X, where X refers to the scaling technique number defined in Section 4.3.1.5. The same set of records was adopted when applying the MFP approach, as commonly done in practice (FEMA, 2009).

Buckling-restrained braced frames (BRBF) was used to resist lateral loads for the prototype building. Although the bracing members exhibit superior hysteretic behaviour compared to the conventional steel braced frames, multi-storey BRBFs may experience concentrations of inelastic deformations due to lack of backup lateral stiffness and P-Delta effects upon brace yielding. Peak inelastic response along the structure height can therefore be sensitive to the intensity and

frequency content of the records. Inelasticity in the brace members of the BRBF prototype was modelled using the same Bouc-Wen hysteresis law with experimentally-calibrated parameters. P-delta effects were considered in the analyses, and mass-and-stiffness proportional damping coefficients were adjusted so that 3% critical viscous damping was achieved in the first and fifth modes. Table 4.1 provides the statistics (mean, standard deviation and COV values) of the scaling factors (SF). The average, 84th, and 96th percentile values of the ratio of the scaled spectra to the site UHS ordinate at three periods (T_1, $0.2T_1$, and $1.5T_1$) are also given for each record set. This parameter which is designated by SR (Spectral Ratio) could be taken as an indicator of relative intensity of the scaled records at important periods of the prototype under study. The bottom part of the table gives the statistics of the peak inter-storey drift ratios, θ_{max}, along with the number of collapse cases observed out of 20 analyses per each scaled set. Strength and stiffness degradation was not included in the hysteresis law and peak response greater than ~5% inter-storey drift ratio was considered as collapse. All six ASCE 7 scaling approaches resulted in some collapse cases and the median demand dramatically varies from one solution to another one (i.e. 0.5% to 2.3% drift ratio). Among the 6 ASCE 7 solutions, approach 2, which has the highest average scale factor and zero variability of $S_a(T_1)$, resulted in the minimum number of collapse cases, the lowest variability and a strong median demand. The ASCE 7-3 approach, which shows the least variations in scaled spectral ordinates, resulted in the highest median and a low variability. These two cases show the importance of the variance of scaled spectral on demand variability. On the other hand, ASCE 7-5 solution, which has the minimum average scaling factor, gave statistically-unreliable storey drift results in view of the much lower median demand and largest COV values. This shows that minimizing the average of scale factor is not a viable solution as it can result in large variability of the scaled spectra. ASCE 7-4 and -6 solutions also resulted in large variability compared to others. Collapse was not observed when the MFP and LMA scaling approaches were implemented. LMA resulted in a smaller mean and scatter compared to MFP. This trend is directly related to smaller scaling factors calculated by the LMA approach. In this example, the maximum peak drift ratio from the LMA-scaled set is 2.4%, which is nearly identical to the average demand from the least variable ASCE 7 scaling solutions (ASCE 7-2 or -3). It is also noteworthy that the 84th percentile of the demand imposed by the LMA set (S2-T20) matches the average of the MFP method.

Table 4.1: Impacts of record selection and scaling on peak inter-storey drift of a 9 storey BRBF[1].

	Name of set	S5-R20						S2-T20	
	Scaling methods	ASCE7-1	ASCE7-2	ASCE7-3	ASCE7-4	ASCE7-5	ASCE7-6	MFP	LMA
Record Scaling	$SF_{Avg.}$	3.1	4.9	4.5	2.4	1.7	2.4	4.1	3.7
	SF_{STD}	0	3.6	3.3	2.2	1.9	1.7	2.8	2.4
	SF_{COV}	0%	74%	72%	93%	107%	72%	68%	66%
	$SR_{Avg.}$ (T = 1.80)	1.3	1.2	1.2	1.3	1.4	1.1	1.0	0.8
	SR_{P96} (T = 1.80)	4.4	1.2	2.9	10.6	8.6	5.4	1.0	1.1
	SR_{Avg} (T = 0.37)	1.5	1.7	1.3	1.0	1.1	1.4	1.5	0.8
	SR_{P96} (T = 0.37)	4.2	5.9	1.9	3.7	5.2	7.0	5.2	1.1
	SR_{Avg} (T = 2.70)	1.0	1.0	1.0	1.0	1.0	1.0	0.8	0.7
	SR_{P96} (T = 2.70)	2.9	2.0	2.3	7.7	5.9	4.6	1.7	1.4
Analysis	Collapse cases	4	2	2	2	4	4	0	0
	$[\theta_{max}]_{P50}$	1.8%	2.2%	2.3%	1.0%	0.5%	0.8%	1.9%	1.5%
	$[\theta_{max}]_{P84}$[2]	4.9%	3.1%	3.1%	1.8%	4.9%	4.4%	2.7%	1.8%
	$[\theta_{max}]_{P96}$[2]	5.0%	4.5%	5.0%	5.0%	5.0%	5.0%	3.4%	2.2%
	$[\ln \theta_{max}]_{STD}$	0.68	0.37	0.44	0.94	1.44	1.03	0.40	0.24
	$[\theta_{max}]_{COV}$	66%	40%	45%	100%	116%	98%	41%	36%

Notes: [1] Avg., STD, COV, P50, P84 and P96 subscripts indicate the average, standard deviation, coefficient of variation, median, 84th and 96th percentile of data, respectively.

[2] In calculation of demand statistics, maximum drift of collapse cases was set to 5% which may undermine the interpretation of the reported values.

4.4.5 Robustness of the proposed method for MDOFs

The proposed approach showed limited sensitivity of the response to the number of records in case of inelastic SDOF systems. In order to verify whether this is true for multi-degree-of-freedom systems, series of 3-, 5-, 7-, 13- and 15-storey BRBFs were designed, modeled and subjected to response history analysis in addition to the previously introduced 9-storey prototype. The fundamental periods of these structures are 0.6, 1.1, 1.4, 2.4, and 2.7 s, respectively. Figure 4.18a shows the average and maximum of the peak inter-storey drift ratios obtained from sets S2-T10, S2-T20 and S2-T40 that were selected and scaled according to the proposed methods. This plot

shows that the average inelastic demand is not sensitive to the number of records. In the worst case, i.e. the 7-storey prototype, the difference between the lowest and highest average demand values is only 16%. In most cases, the coefficient of variation of the demand is around 25% (see Figure 4.18b). This corresponds to a record-to-record variability of 0.24 (standard deviation of the natural logarithm values of the demand), which is low comparing to the values between 0.4-1.4 typically obtained when using conventional selection and scaling approaches (refer to Table 4.1 the row designated by $[\ln \theta_{max}]_{STD}$). The upper percentiles of demand also show a fairly stable trend. In most cases, they are in fact nearly invariant regardless of the number of records.

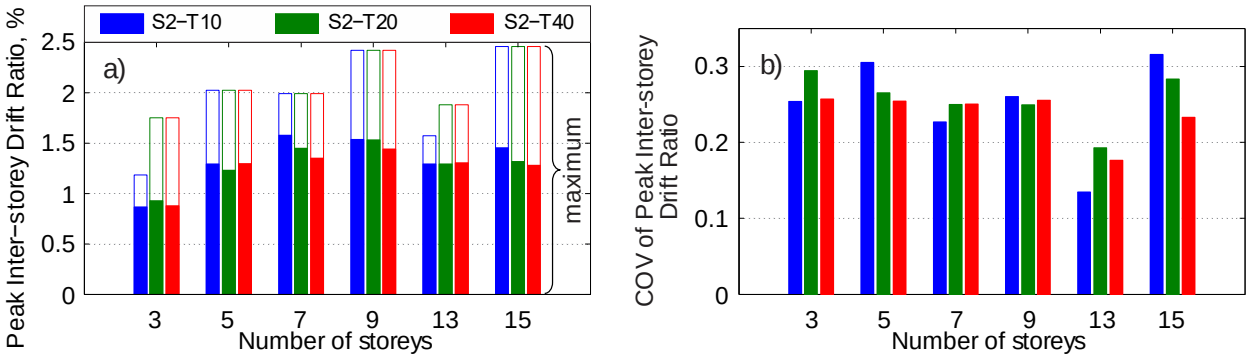

Figure 4.18: Trends of inelastic demand in series of multi-storey buckling-restrained braced frames as the number of records changes. (Note: in 'a' filled bar indicates average, and combination of filled and unfilled bars indicate maximum of the demand).

This example shows the robustness of the proposed selection and LMA methods as the average and upper percentiles of response values do not vary significantly with the number of records that are considered. In fact, the method is expected to give more consistent results when a limited number of records, e.g. 20, are included because the quality of the records decreases as the set becomes larger (the characteristics of the records tend to deviate more and more from the expected central tendency). This represents a clear advantage for day-to-day practice because consistency is naturally achieved without having to increase the population size. A second important observations from Figure 4.18 is that consistent results are generally obtained for the range of building heights (structure periods) considered, which was one of the main features that were sought for the proposed selection and scaling methods. This result suggests that the same set of ground motion records could be used for a structure exhibiting different modes or periods or for different structures

at the same site. In order to compare the robustness of the proposed approach with a recognized benchmark method, 3 sets of records are selected and scaled for the 9-storey model strictly according the CMS method as elaborated in (Jayaram, *et al.*, 2011). Analysis results shows that while the median of response is similar to and almost as stable as the proposed approach, its variability is heavily dependent on the set size and grows as the number of selected records increases as shown in Table 4.2.

Table 4.2: Impacts of selection and scaling technique on stability of responses of 9-storey BRBF with respect to the number of selected records. Peak inter-storey drift ratio is the response metric.

Method	n = 10			n = 20			n = 40		
	Median	STD*	Max.	Median	STD*	Max.	Median	STD*	Max.
Proposed**	1.4%	0.24	2.4%	1.5%	0.24	2.4%	1.3%	0.25	2.4%
CMS	1.5%	0.28	2.0%	1.3%	0.40	3.7%	1.4%	0.54	6.4%

* STD is the standard deviation of the natural logarithm of data.

** Sets prepared for Scenario S2 are employed in this comparative study.

4.4.6 Appropriate percentile of demand indices

Seismic assessment procedures are typically performed to predict the design structural seismic demand. This demand may then be used to design new structures or rehabilitate existing ones. Central values (arithmetic mean, geometric mean, median) or upper percentiles of response parameters have been used as estimators of the demand, depending upon the record selection and scaling scheme as well as the number of records. For instance, the ASCE 7 standard takes the maximum and average values of the response when the ground motion ensemble is composed of 3 to 6 and 7 or more records, respectively. As discussed earlier, the proposed scaling approach will unlikely provide a fully target-matched spectral shape at all structure periods. In addition, the variability of the spectral ordinates of the scaled records is expected to be low when this approach is implemented. As a consequence, the average ductility demand obtained at a given period from LMA-scaled records will typically be lower than the ductility resulting from MFP-scaled records at that period, or the target design ductility as predicted by the equal displacement theory.

This may undermine the appropriateness of this technique when full probability distribution of the response, reflecting the inherent variability and uncertainty in ground motion prediction, is the

main purpose of the analysis. This is shown in Figure 4.19 where the trend of inelastic demands calculated using LMA- and MFP-scaled record sets are compared. To draw statistically-reliable conclusions, a relatively large set of records composed of 266 acceleration time-histories taken from earthquakes of magnitude **M**6.5-7.5 and hypocentral distances between 0 and 80 km was compiled. All of these time-histories were recorded on soft rock profile and none of them include forward directivity effects. Peak ductility spectra were calculated for a series of SDOF systems having elastic periods between 0.5 and 2.5 s varying in 0.2 s increments. These SDOFs were designed for 2% in 50 years spectral acceleration for Victoria in accordance with NBCC 2010 provisions. The ductility and overstrength factors are set to R_d = 4.0 and R_o = 1.2, as was done previously. According to equal displacement principle, it is expected that the systems will undergo average ductility of 4.0 when subjected to the design level of spectral intensity. To verify this assumption, the MFP scaling approach was used to calculate different sets of scaling factors for the ensemble of 266 records at every mentioned period as basis for comparison. An additional set of scaling factors was obtained with the LMA technique for the entire period range. In Figure 4.19, it is shown that the 88th percentile of peak ductility and cumulative plastic displacement ductility calculated from the LMA-scaled set are very similar to the demand imposed by the same set of records scaled by MFP approach at every period. Based on this observation, it is suggested to take an upper percentile value, such as the 84th or even 96th percentile, of the response as an appropriate estimator when the Least Moving Average scaling method is employed. For this example, the results presented in the figure also confirm that LMA scaling can give the same demand as the MFP scaling over a wide period range without having to proceed with record scaling at every period.

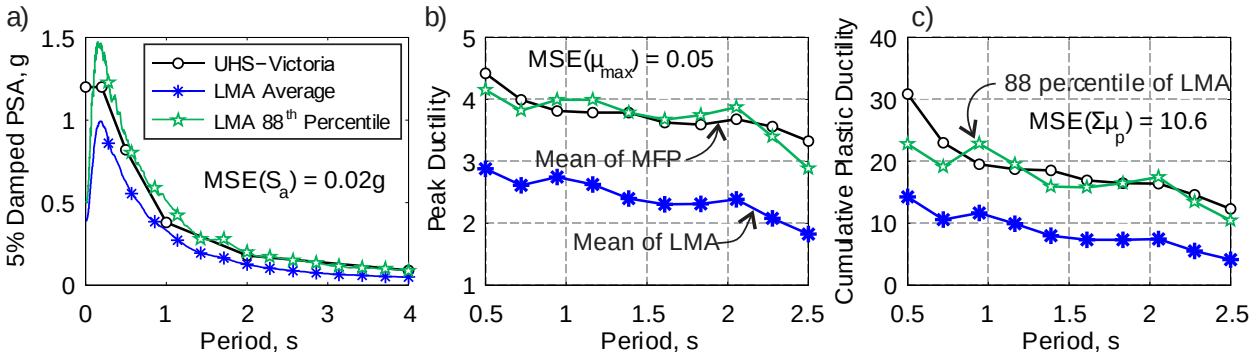

Figure 4.19: a) Trend of acceleration spectra of 266 LMA-scaled records; Comparison between expected theoretical inelastic demand and the mean and upper percentile of demand as imposed by LMA-scaled set of 266 records. Demand indices are: a) peak ductility; and b) cumulative plastic ductility. (Note: MSE(X) is the mean squared error between expected value and the 88th percentile of LMA results, where is X is the spectral intensity or seismic demand).

4.5 Observations and Concluding Remarks

Practical and robust ground motion selection and scaling methods have been presented and their efficiency was qualified throughout nonlinear response history analyses of inelastic SDOFs and multi-storey steel braced frames. In particular, step-by-step instructions have been provided to define the dominant earthquake scenarios, proceeded with an initial selection and then refinement of the selected records; similarly, a detail procedure is suggested to obtain a unique set of scaled records that can be applied over a given period range. The methods were applied and compared to other techniques for a class C site located in Victoria, BC, Canada. The following observations and conclusions are drawn from this study:

a) A procedure is proposed for choosing dominant event(s) from multi-period hazard de-aggregation data. This approach aims at creating a set of dominant events that covers a wide range of ground motion characteristics including frequency content.

b) A standard refinement technique is often required to reduce the retrieved records when only simple geophysical parameters are used for selection from large databases. An approach is proposed that ranks the records based on the likelihood of observing a given anticipated central value of intensity, frequency and duration damage-related IMs for the site.

c) For the three classes of damage-related IMs, the Arias Intensity or Sustained Maximum Velocity, Mean Period, and Bracketed Duration are generally the most representative ground motion IMs. Intercorrelation analysis shows that these IMs have better harmony with the other ones and can represent the damage-related properties of the records when they need to be ranked.

d) For a given design spectrum, de-aggregation data, number of records, and a ground motion database, the proposed selection method gives a unique set of ground motion records in one single step.

e) The possibility of imposing excessive input seismic energy with conventional record scaling methods exists when a high-frequency record is scaled to match the target spectrum in the long period range of the spectrum and vice versa.

f) The proposed LMA (Least Moving Average) scaling technique takes into respect the frequency content of the records (or the shape of their response spectrum).

g) Constant ductility demand spectrum analysis showed that the proposed record refinement approach leads to nearly invariant 'base shear ratio' and less variable 'cumulative plastic ductility' demand compared to the random record refinement when the number of ground motion records changes.

h) The proposed LMA scaling approach can be effective in reducing the variance of scaled spectral ordinates as well as the seismic demand on inelastic SDOF and MDOF systems without altering the frequency content as is the case with spectrum matching techniques. LMA also has the capability of controlling upper percentile of the demand even when records are selected with less sophisticated approaches such as random refinement.

i) Inelastic demand appears to be more sensitive to the scaling approach rather than the selection refinement. However, it is recommended to use the proposed trend-based refinement approach together with LMA scaling technique.

j) The proposed methods applied to inelastic SDOF and MDOF systems resulted in demands not sensitive to the number of records and the chosen earthquake scenario. While CMS also gave stable median demands, it resulted in greater variability compared to the proposed methods.

k) The scaling approach specified in ASCE 7 does not provide a unique solution. In fact, many sets of scaling factors could be obtained that all satisfy the requirements but give structural demands with significantly different average and variability trends. Among the possible solutions, the match-at-fundamental-period and least-average-squared-error-spectra methods (approaches nos. 2 and 3) resulted in the most robust demand statistics. The average demand calculated by these scaling techniques is similar to the maximum demand obtained by the proposed methods.

l) The proposed methods resulted in consistent demand levels over the range of structural periods considered, which represents an important advantage when assessing the response of multi-mode structures or structures having different periods.

m) Since the proposed approach reduces the variability of input seismic energy, it is not recommended to be utilized when full probability distribution of the seismic demand is sought.

n) It is recommended that the upper percentile of the response be retained as the seismic demand estimator when the proposed methods are employed.

Acknowledgment

The financial support provided by the Natural Sciences and Engineering Research Council of Canada (NSERC) for the Canadian Seismic Research Network (CSRN) is acknowledged. Scholarship awarded to the first author by Structural Steel Education Foundation (SSEF) is also acknowledged. Authors are thankful the constructive comments received during review process.

Nomenclature

Symbols

D_{5-95}	:	Significant Duration (a duration intensity measure)
$D_{\mathrm{Uni.}}$	:	Uniform Duration (a duration intensity measure)
$D_{\mathrm{Brk.}}$	:	Bracketed Duration (a duration intensity measure)
$\mathbf{M}$	:	Moment magnitude
$\mathrm{P50}$	:	Fiftieth percentile
$\mathrm{P84}$	:	Eighty-forth percentile

$\mathrm{P96}$	:	Ninety-sixth percentile
R	:	Generic distance from earthquake source to site
R_o	:	Overstrength factor
R_d	:	Ductility factor
S_a	:	Spectral acceleration
$S_a(T)$	:	Spectral acceleration at a period T
$S_a^{\mathrm{Target}}(T)$	:	Target spectral acceleration for scaling at period T
$S_a^{\mathrm{Record}}(T)$	:	Spectral acceleration of as-recorded ground motion at period T
$SR_{0.2/2.0}$	:	Ratio of spectral accelerations at 0.2 and 2.0 seconds
T	:	Period of vibration
T_1	:	Fundamental period of structure (translational or torsional mode)
T_i	:	i^{th} period within the selected period points for LMA method
$T_{\max}$	:	Maximum period included in the LMA process
$T_{\min}$	:	Minimum period included in the LMA process
T_{first}	:	First center of averaging window
T_{last}	:	Last center of averaging window
T_{LMA}	:	Period at which LMA scaling method is performed
T_{pSa}	:	Period corresponding to maximum spectral acceleration
T_{pSv}	:	Period corresponding to maximum spectral velocity
T_m	:	Mean period of ground motion acceleration
V_{s30}	:	Shear wave velocity in the top 30 meters of the site soil deposit
X, Y	:	Random variables
dM	:	Resolution of magnitude in seismic hazard deaggregation data
dR	:	Resolution of distance parameter in seismic hazard deaggregation data
n	:	Target number of records for selection
x_i	:	Ranked (sorted) random variable
ΔT	:	Length of averaging window
$\sum \mu_p$	:	Sum of inelastic displacement an SDOF divided by its yield displacement
α	:	Factor defines the beginning of averaging window
β	:	Factor defines the end of averaging window

ϵ_i : Normalized deviation from central tendency of an intensity measure

$\epsilon_{i,avg}$: Average of normalized deviations

$\epsilon(T)$: Normalized residual from average spectral acceleration predicted by a given GMPE at period T

ρ : Spearman correlation coefficient

$\theta_{\max}$: Peak interstorey drift ratio

$\mu_{\ln X}$: Average of natural logarithm of random variable X

$\mu_{\max}$: Maximum absolute displacement of an SDOF divided by its yield displacement

$\sigma_{\ln X}$: Standard deviation of natural logarithm of random variable X

Abbreviations

ASCE : American Society of Civil Engineers

ASR : Average Spectral Ratio

CMS : Conditional Mean Spectrum

COV : Coefficient of Variation

CPD : Cumulative Plastic Ductility

CSA : Canadian Standard Association

ESI : Equal Spectral Intensity

GCIM : Generalized Conditional Intensity Measure

GMPE : Ground Motion Prediction Equation

IM : Intensity Measure

LMA : Least Moving Average

MFP : Matching at Fundamental Period

MSE : Mean Squared Error

MSE : Minimum Squared Error

NBCC : National Building Code of Canada

NGA : Next Generation Attenuation

PEER : Pacific Earthquake Engineering Research

PGA : Peak Ground Acceleration

PGD : Peak Ground Displacement

PGV : Peak Ground Velocity

SDOF	:	Single Degree-of-Freedom
SF	:	Scale Factor
SMV	:	Sustained Maximum Velocity
SR	:	Spectral Ratio
SSE	:	Sum of Squared Error
STD	:	Standard Deviation
UHS	:	Uniform Hazard Spectrum

References

Ancheta, T. D., Darragh, R. B., Stewart, J. P., Seyhan, E., Silva, W. J., Chiou, B. S., Wooddell, K. E., Graves, R. W., Kottke, A. R., Boore, D. M., Kishida, T., & Dobahue, J. L. (2013). *PEER NGA-West2 Database*: Pacific Earthquake Engineering Reseach Center.

Antoniou, S., Pinho, R., & Bianchi, F. (2012). SeismoSignal (Version 5.0.0): Seismosoft Ltd.

ASCE. (2010). Minimum Design Loads for Buildings and Other Structures (pp. 608). Reston, Virginia: American Society of Civil Engineers.

ATC. (2011). *75% Draft - Seismic Performance Assessment of Buildings* (ATC-58-1). Redwood City, CA: Applied Technology Council.

Atkinson, G. M. (2009). Earthquake time histories compatible with the 2005 National building code of Canada uniform hazard spectrum. *Canadian Journal of Civil Engineering, 36*(6), 991-1000.

Baker, J. W. (2011). Conditional Mean Spectrum: Tool for Ground-Motion Selection. *Journal of Structural Engineering, 137*(3), 322-331.

Baker, J. W., & Jayaram, N. (2008). Correlation of Spectral Acceleration Values from NGA Ground Motion Models. *Earthquake Spectra, 24*(1), 299-317.

Bazzurro, P., & Cornell, C. A. (1999). Disaggregation of seismic hazard. *Bulletin of the Seismological Society of America, 89*(2), 501-520.

Bommer, J. J., & Acevedo, A. B. (2004). The Use of Real Earthquake Accelerograms as Input to Dynamic Analysis. *Journal of Earthquake Engineering, 8*(Special Issue 1), 43-91.

Bommer, J. J., & Martínez-Pereira, A. (1999). The Effective Duration of Earthquake Strong Motion. *Journal of Earthquake Engineering, 3*(2), 127-172.

Boore, D. M., & Atkinson, G. M. (2008). Ground-Motion Prediction Equations for the Average Horizontal Component of PGA, PGV, and 5%-Damped PSA at Spectral Periods between 0.01 and 10.0 *Earthquake Spectra, 24*(1), 99-138.

Boore, D. M., & Joyner, W. B. (1997). Site amplifications for generic rock sites. *Bulletin of the Seismological Society of America, 87*(2), 327-341.

Bradley, B. A. (2010). A generalized conditional intensity measure approach and holistic ground-motion selection. *Earthquake Engineering & Structural Dynamics, 39*(12), 1321-1342.

Bradley, B. A. (2012). A ground motion selection algorithm based on the generalized conditional intensity measure approach. *Soil Dynamics and Earthquake Engineering, 40*(2012), 48-61.

Chopra, A. K. (2011). *Dynamics of structures : theory and applications to earthquake engineering*. Upper Saddle River, NJ: Pearson Prentice Hall.

Cimellaro, G., Reinhorn, A., D'Ambrisi, A., & De Stefano, M. (2011). Fragility Analysis and Seismic Record Selection. *Journal of Structural Engineering, 137*(3), 379-390.

CSA. (2009). CSA S16-09, Limit States Design of Steel Structures. Mississauga, Ontario, Canada: Canadian Standards Association.

FEMA. (2009). *Quantification of Building Seismic Performance Factors* (FEMA P695). Washington DC: Federal Emergency Management Agency.

Filippou, F. C., Popov, E. P., & Bertero, V. V. (1983). *Effects of bond deterioration on hysteretic behavior of reinforced concrete joints* (UCB/EERC-83/19). Berkeley, California: Earthquake Engineering Research Center.

Halchuk, S., Adams, J., & Anglin, F. (2007). *Revised Deaggregation of Seismic Hazard for Selected Canadian Cities.* Paper presented at the Ninth Canadian Conference on Earthquake Engineering, Ottawa, Ontario, Canada.

Hancock, J., & Bommer, J. J. (2006a). A State-of-Knowledge Review of the Influence of Strong-Motion Duration on Structural Damage. *Earthquake Spectra, 22*(3), 827-845.

Hancock, J., Bommer, J. J., & Stafford, P. J. (2008). Numbers of scaled and matched accelerograms required for inelastic dynamic analyses. *Earthquake Engineering & Structural Dynamics, 37*(14), 1585-1607.

Hancock, J., Watson-Lamprey, J., Abrahamson, N. A., Bommer, J. J., Markatis, A., McCoyh, E., & Mendis, R. (2006b). An Improved Method of Matching Response Spectra of Recorded Earthquake Ground Motion using Wavelets. *Journal of Earthquake Engineering, 10*(sup001), 67-89.

Haselton, C. B. (2009). *PEER 2009/01 - Evaluation of Ground Motion Selection and Modification Methods: Predicting Median Interstory Drift Response of Buildings*: Pacific Earthquake Engineering Research Center.

Heo, Y., Kunnath, S. K., & Abrahamson, N. (2011). Amplitude-Scaled versus Spectrum-Matched Ground Motions for Seismic Performance Assessment. *Journal of Structural Engineering, 137*(3), 278-288.

Iervolino, I., & Cornell, C. A. (2005). Record Selection for Nonlinear Seismic Analysis of Structures. *Earthquake Spectra, 21*(3), 685-713.

Jayaram, N., & Baker, J. (2010). *Ground-Motion Selection for PEER Transportation Research Program.* Paper presented at the 7th International Conference on Urban Earthquake Engineering (7CUEE) & 5th International Conference on Earthquake Engineering (5ICEE), Tokyo, Japan.

Jayaram, N., Lin, T., & Baker, J. W. (2011). A Computationally Efficient Ground-Motion Selection Algorithm for Matching a Target Response Spectrum Mean and Variance. *Earthquake Spectra, 27*(3), 797-815.

Kalkan, E., & Chopra, A. K. (2010). *Practical Guidelines to Select and Scale Earthquake Records for Nonlinear Response History Analysis of Structures* (Open-File Report 2010-1068): U.S. Geological Survey.

Katsanos, E. I., Sextos, A. G., & Manolis, G. D. (2010). Selection of earthquake ground motion records: A state-of-the-art review from a structural engineering perspective. *Soil Dynamics and Earthquake Engineering, 30*(4), 157-169.

Kempton, J. J., & Stewart, J. P. (2006). Prediction equations for significant duration of earthquake ground motions considering site and near-source effects. *Earthquake Spectra, 22*(4), 985-1013.

Kottegoda, N. T., & Rosso, R. (2008). *Applied statistics for civil and environmental engineers*: Wiley-Blackwell.

Kottke, A., & Rathje, E. M. (2008). A Semi-Automated Procedure for Selecting and Scaling Recorded Earthquake Motions for Dynamic Analysis. *Earthquake Spectra, 24*(4), 911-932.

Kramer, S. L. (1996). *Geotechnical earthquake engineering*. Upper Saddle River, N.J.: Prentice Hall.

Kumar, M., Castro, J. M., Stafford, P. J., & Elghazouli, A. Y. (2011). Influence of the mean period of ground motion on the inelastic dynamic response of single and multi degree of freedom systems. *Earthquake Engineering & Structural Dynamics, 40*(3), 237-256.

Kurama, Y. C., & Farrow, K. T. (2003). Ground motion scaling methods for different site conditions and structure characteristics. *Earthquake Engineering & Structural Dynamics, 32*(15), 2425-2450.

Lin, T., Harmsen, S. C., Baker, J. W., & Luco, N. (2013). Conditional Spectrum Computation Incorporating Multiple Causal Earthquakes and Ground-Motion Prediction Models.

Bulletin of the Seismological Society of America, 103(2A), 1103-1116.

McGuire, R. K. (1995). Probabilistic seismic hazard analysis and design earthquakes: Closing the loop. *Bulletin of the Seismological Society of America, 85*(5), 1275-1284.

McGuire, R. K., Silva, W. J., & Costantino, C. J. (2002). *Technical basis for revision of regulatory guidance on design ground motions: hazard- and risk-consistent ground motion spectra guidelines* (NUREG/CR-6769). Washington, DC 20555-0001: U.S. Nuclear Regulatory Commission.

Naeim, F., & Lew, M. (1995). On the Use of Design Spectrum Compatible Time Histories. *Earthquake Spectra, 11*(1), 111-127.

NEHRP Consultants Joint Venture. (2012). *Selecting and Scaling Earthquake Ground Motions for Performing Response-History Analysis* (NIST GCR 11-917-15): Engineering Laboratory of the National Institute of Standards and Technology.

NRCC. (2010). National Building Code of Canada, 13th ed. Ottawa, ON.: National Research Council Canada, Institute for Research in Construction.

PEER. (2005). PEER Strong Ground Motion Database. Retrieved 27/03/2012, from http://peer.berkeley.edu/nga/

Rathje, E. M., Faraj, F., Russell, S., & Bray, J. D. (2004). Empirical Relationships for Frequency Content Parameters of Earthquake Ground Motions. *Earthquake Spectra, 20*(1), 119-144.

Riddell, R. (2007). On Ground Motion Intensity Indices. *Earthquake Spectra, 23*(1), 147-173.

Rizzo, P. C., Shaw, D. E., & Jarecki, S. J. (1975). Development of real/synthetic time histories to match smooth design spectra. *Nuclear Engineering and Design, 32*(1), 148-155.

Shome, N., & Cornell, A. C. (1998). *Normalization and Scaling Accelerograms for Nonlinear Structural Analysis.* Paper presented at the 6th U.S. National Conference on Earthquake Engineering, Seattle, Washington.

Tehrani, P., Goda, K., Mitchell, D., Atkinson, G. M., & Chouinard, L. E. (2014). Effects of Different Record Selection Methods on the Transverse Seismic Response of a Bridge in South Western British Columbia. *Journal of Earthquake Engineering, 18*(4), 611-636.

Tremblay, R., Bolduc, P., Neville, R., & DeVall, R. (2006). Seismic testing and performance of buckling-restrained bracing systems. *Canadian Journal of Civil Engineering, 33*(2), 183-198.

Watson-Lamprey, J., & Abrahamson, N. (2006). Selection of ground motion time series and limits on scaling. *Soil Dynamics and Earthquake Engineering, 26*(5), 477-482.

Wen, Y.-K. (1976). Method for random vibration of hysteretic systems. *Journal of the Engineering Mechanics Division, 102*(2), 249-263.

Ye, L., Ma, Q., Miao, Z., Guan, H., & Zhuge, Y. (2011). Numerical and comparative study of earthquake intensity indices in seismic analysis. *The Structural Design of Tall and Special Buildings, 22*(4), 326-381.

Youngs, R. R., Chiou, S.-J., Silva, W. J., & Humphrey, J. R. (1997). Strong Ground Motion Attenuation Relationships for Subduction Zone Earthquakes. *Seismological Research Letters, 68*(1), 58-73.

CHAPTER 5 SEISMIC PERFORMANCE OF CANADIAN CODE-CONFORMING BUCKLING-RESTRAINED BRACED FRAMES

5.1 General

Buckling-Restrained Braced Frames (BRBFs) have been incorporated in the recent Canadian building codes (NBCC 2010 and CSA S16-09) as a ductile seismic force resisting system. This chapter discusses the design issues and investigates the seismic performance of Canadian code-conforming BRBFs. Numerical prototypes of 3- to 15-storey buildings were subjected to ground motions from different types of seismicity sources across the country and the key seismic demand parameters were computed. Effects of site soil, bracing pattern, BRB core grade, and frame stiffness irregularities are investigated using results of nonlinear response history analyses. Sensitivity of the seismic demand to ground motion selection and scaling is also quantified. It is concluded that the performance of the code-conforming BRBFs is generally acceptable except for residual displacement, and diaphragm design forces. The computed brace deformation demand is generally lower than the reported values in the major U.S. case studies. An alternative design parameter for estimation of strain demand in BRB members is introduced. This parameter is shown to be more consistent and robust that the one from S16-09. It is also shown that the NBCC 2010 soft soil site amplification factors for periods longer than 2.0 seconds may need to be revised. Current code requirements on relative lateral stiffness of adjacent storeys is critically reviewed.

5.2 Introduction

Buckling-Restrained Braced Frame (BRBF) is a relatively new lateral load resisting system in North America which incorporates special bracing elements that do not buckle but yield in compressive loading cycles. This bracing element is generally composed of a slender ductile steel core, a buckling-restraining mechanism, and a debonding layer between core and restrainer (Xie, 2005). Plastic deformations take place in Yielding Segment (YS) of the core and the non-yielding core segment is designed to remain elastic under anticipated design forces. Since buckling is prevented, the YS can sustain large compressive inelastic strains without instability which greatly enhances the energy dissipation capacity of the member compared to conventional braces. Numerous past experimental research have confirmed that properly designed BRBs can dissipate

significant amount of energy without strength and stiffness degradation. BRB technology has emerged and evolved in Japan in the mid-80's and was transferred to North America in late 90's (Xie, 2005). Seismic behaviour of BRBFs as a primary lateral force resisting system has been investigated analytically and experimentally in a number of studies (Tremblay, *et al.*, 1999; Sabelli, *et al.*, 2003; Black, *et al.*, 2004; Tremblay, *et al.*, 2006; Fahnestock *et al.*, 2007a; Fahnestock, *et al.*, 2007b; Dutta, *et al.*, 2010; Moni *et al.*, 2016). Past experimental and analytical studies have shown that ductility capacity of BRB members heavily depends on the fabrication details, strength and stiffness of the restraining mechanism, smoothness of core and restrainer interface, and stability of brace-to-frame connections. Full-scale cyclic testing of BRB component and sub-assemblage is required by modern design codes such as AISC/ANSI 341 (AISC, 2010), CSA S16 (CSA, 2009), and EN 15129 (CEN, 2010) to confirm the required ductility capacity. Typically, these standards suggest simple cyclic loading protocols and set of acceptance criteria for the qualification process. A qualified BRB must show certain cumulative ductility capacity and similar hysteresis response in tension and compression.

BRBFs have been recently introduced in the 2010 National Building Code of Canada (NBCC) (NRCC, 2010) and Canadian steel design standard CSA S16-09 (CSA, 2009), as a ductile seismic force resisting system. S16-09 outlines a BRB qualification procedure adapted from the AISC Seismic Provisions (AISC, 2010). This procedure was established from the results of a numerical study conducted on BRBFs designed for a high seismic hazard region in California (Sabelli, 2001). Preliminary studies by the author (Dehghani, *et al.*, 2012b; Dehghani *et al.*, 2012a) and, more recently, by Moni, *et al.* (2016) have indicated that the seismic deformation demand in Canada can be significantly lower than that prescribed by the AISC Seismic Provisions, especially in eastern Canada. This warranted the necessity to assess the inelastic seismic demand on BRBFs designed according to the recently adopted Canadian standards. The assessment had to account for differences in earthquake ground motion characteristics across Canada, local soil effects, braced frame configuration, and stiffness irregularities.

This chapter presents results of a study performed on 3- to 15-storey BRBF buildings designed for Class C (soft rock) and E (soft soil) sites in the east (Montréal, Quebec) and west (Victoria, British Columbia) of Canada using the NBCC 2010 and CSA S16-09 standards. BRBFs with single diagonal and chevron bracing patterns are examined in this study. Important response parameters are computed by nonlinear inelastic time history analyses with suites of site-specific ground motion

records compatible with local seismicity of the mentioned sites. Performance of the models are evaluated by comparing various seismic demand indices with sets of acceptance criteria. Modifications required to account for the ground motion selection and scaling procedures, site effects, brace yielding segment length, and vertical frame irregularity are also discussed. Findings of this study can be used to generate consistent and reasonable loading protocols for testing BRBs.

In the subsequent sections of this chapter, Canadian seismic hazard and design practice will be briefly reviewed first. Then the most important design aspects of BRBFs are discussed and the design results are presented afterward. The next section is dedicated to numerical modeling and ground motion selection and scaling. This is followed by discussions on post-processing of the analyses' results and response assessment. Effects of some important design conditions and assumptions are quantified next. The required adjustment to include uncertainties associated with ground motion selection and scaling are discussed afterward. This chapter concludes with the main findings, observations, and design recommendations.

5.3 Design of prototype models

Basic BRBF prototypes examined here are designed for hypothetical office buildings located in Victoria (British Columbia) and Montréal (Québec). Victoria is exposed to the highest level of seismic hazard in the west coast of Canada, and Montréal faces the highest seismic risk among the populated eastern areas of the country.

5.3.1 Earthquake sources in populated areas of western and eastern Canada

The southwest coast of Canada is the most seismically active region in the country in which three types of earthquake are expected: 1) shallow crustal; 2) subduction deep intraslab; and 3) subduction interface (Atkinson *et al.*, 2003; Cassidy *et al.*, 2010). Return periods, characteristics of seismic waves, propagation path, and attenuation of these earthquakes are significantly different (Atkinson, 2005). Frequency content and attenuation rate of seismic waves of deep intraslab events are expected to be higher and faster than those of the crustal ones. These two types of earthquakes are originated in the oceanic slab and continental plate, respectively, and are collectively denoted hereinafter by "intra–plate" events. Interface of the Cascadia subduction zone is expected to generate very large magnitude earthquakes, i.e. **M**8.0–9.0, which could significantly affect the communities along the west coast of Canada. As a result of long rupture length, these megathrust

earthquakes can generate very long duration and low frequency ground shakings that may cause low cycle fatigue fracture in structural components and impose significant seismic demand on the long period structures such as high-rise buildings and long span bridges. On the other hand, eastern Canada is located in a so-called *stable continental region* with relatively lower rate of seismic activities compared to the west coast. This region has witnessed large and damaging earthquakes in the past (Lamontagne *et al.*, 2008). Seismic waves in this region are believed to be rich in high frequency content and to attenuate with slower rate in comparison to the west coast. As a result, short duration and high frequency strong shakings are anticipated in eastern Canada which could be damaging to short period structures. These high frequency earthquakes can also impose large seismic force demands on high-rise structures as they can excite higher modes of vibration.

Past numerical studies have confirmed that the seismicity source has considerable effect on the structural seismic demand in the east and west of Canada (Tremblay *et al.*, 2001; Tremblay, *et al.*, 2002; Dehghani, *et al.*, 2012b; Koboevic *et al.*, 2012). These studies generally concluded that equally designed buildings in west and east of the country undergo quite different levels of peak and cumulative ductility demand, primarily due to the differences in the frequency content of the expected earthquakes.

5.3.2 Buildings studied

Buildings were assumed to be located on Class C (soft rock and stiff soils) and Class E (soft soil) sites (refer to NBCC 2010 definition of site), respectively. The building plan and design gravity loads are given in Figure 5.1a. Two planer braced frames in each direction were assumed to exist and be located in the exterior faces of the building. In this study, only east-west direction is considered. In this direction, columns were oriented such that their minor axis is perpendicular to the plane of frame. This is to render the most critical condition where the braced bay columns offer the lowest possible contribution to the storey post-yield stiffness and redistribution of inelastic demand along the building height. Basic prototypes have 3, 5, 7 and 9 storeys. The 9-storey buildings are 40 m tall, which corresponds to the height limit currently imposed in the NBCC for BRBFs located in moderate and high seismic regions. For the western Canada site, 13- and 15-storey structures up to 60 m in height were also studied to examine the appropriateness of the code limit. An optimization study was conducted to determine the most effective bracing pattern resulting in least amount of framing steel tonnage in the braced bays (Dehghani, *et al.*, 2012a). This

study showed that column tonnage could be considerably affected, i.e. up to 60%, by the bracing pattern. Split-X configuration (alternative V- and Inverted-V bracing – see Figure 5.1b) was found to give the least tonnage for the framing elements due to its most direct and shortest load path. Hence, Split-X configuration were used as the primary bracing pattern. In addition, 3- to 9-storey west models with single diagonal bracing pattern (see Figure 5.1c) were also considered for a comparative study. This pattern gave the highest steel tonnage for beams and columns of the braced bays.

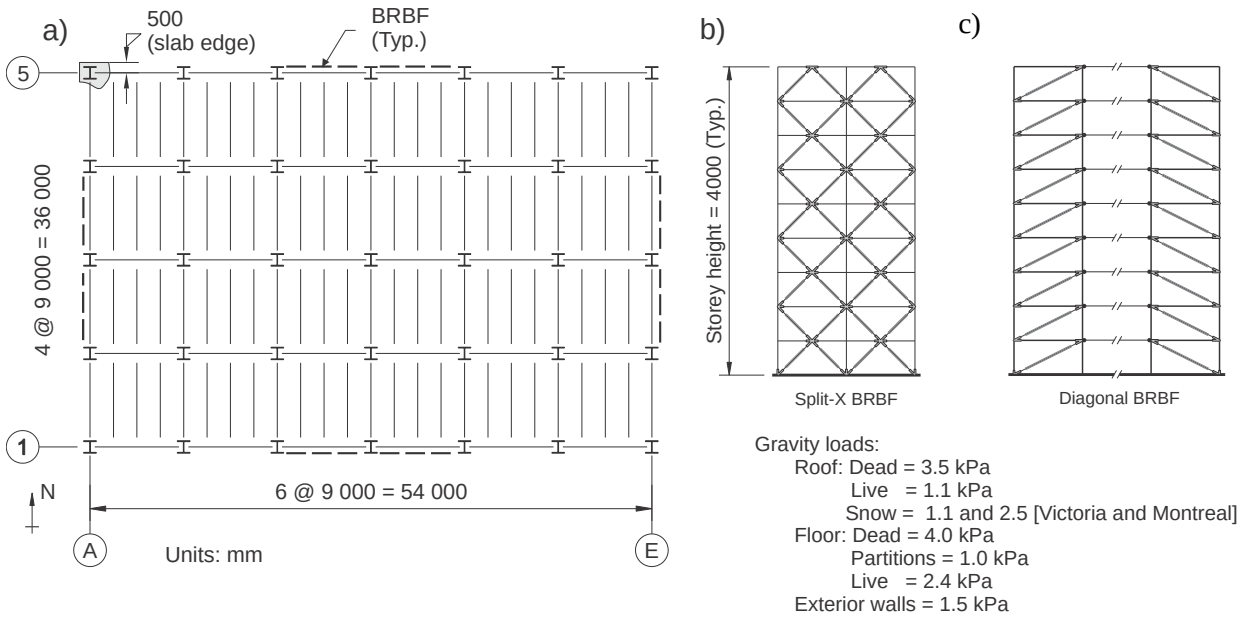

Figure 5.1: a) Typical plan view of the building prototype (only Split-X option is shown); b) and c) Elevation of the 9-storey Split-X and Diagonal bracing patterns.

5.3.3 Seismic design loads

Loading and structural design of the seismic force resisting system (SFRS) were carried out based on the equivalent static force procedure of NBCC 2010 in which the minimum earthquake load V is given by:

$$V = \frac{S(T_a) M_v I_E W}{R_d R_o} \tag{5.1}$$

In this expression, S is the design spectral acceleration at T_a, the structure fundamental period; M_v accounts for higher mode effects on base shear; I_E is the importance factor; W is the seismic weight;

and R_d and R_o are respectively the ductility- and overstrength-related force modification factors. The design spectrum $S(T_a)$ is obtained from uniform hazard spectral ordinates S_a computed at periods of 0.2, 0.5, 1.0 and 2.0 s for a probability of exceedance of 2% in 50 years and modified by site modification factors F_a and F_v. For periods less than 0.2 s, $S(T_a) = F_a S_a(0.2)$. For periods between 0.2 and 4.0 s, $S(T_a)$ is obtained by linear interpolation between the lesser of $F_a S_a(0.5)$ and $F_v S_a(0.5)$, $F_v S_a(1.0)$, $F_v S_a(2.0)$, and $F_v S_a(2.0)/2$ at $T_a = 4.0$ s. For periods longer than 4.0 s, $S(T_a) = F_v S_a(2.0)/2$. M_v is equal to 1.0 for the Victoria site. In Montreal, M_v is equal to 1.0 for $T_a \leq 1.0$ s and 1.5 for $T_a > 2.0$ s, and the product $S(T_a)M_v$ varies linearly between $T_a = 1.0$ and 2.0 s. $S(T_a)$ for both locations and site classes are plotted in Figure 5.5. The NBCC empirical expression for fundamental period of steel braced frames is $T_a = 0.025 h_n$ where h_n is the building height. As permitted in the NBCC, the period from dynamic analysis, T_1, was used for T_a up to 2.0 times the value from the empirical formula. The seismic weight W includes the dead load plus 25% of the roof snow load. The studied buildings were assumed to have normal importance, i.e. $I_E = 1.0$. For BRBFs, ductility and overstrength force modification factors $R_d = 4.0$ and $R_o = 1.2$ are specified in the NBCC. For short period structures, the design base shear need not to be greater than ⅔ $S(0.2) I_E W/(R_d R_o)$. Conversely, for periods longer that 2.0 s, the base shear must be taken equal to V computed with $T_a = 2.0$ s, which implies that base shear ratio (V/W) of tall structures is constant and independent of period.

The prototype buildings did not have any mass or system geometry irregularities. According to the NBCC, however, a seismic force resisting system has vertical stiffness irregularity when lateral stiffness of any storey is: 1) less than 70% of the lateral stiffness of its adjacent storeys; or 2) less than 80% of the average lateral stiffness of the three storeys above or below. Verification after the design showed that the second requirement was not met in the upper storeys of all frames and the frames would therefore classified as structures with vertical stiffness irregularities. Impacts of ignoring that requirement is discussed in Section 5.6.4.

In the NBCC, the design storey drift including inelastic response is equal to $R_d R_o \Delta_f / I_E$, where Δ_f is the storey drift under seismic loads computed with the period T_1. As the current code requires, however, the minimum seismic load corresponding to the base shear at period $T = 2.0$ s was considered for deflection calculations of building having $T_1 > 2.0$ seconds. According to the NBCC, in buildings with normal importance as those examined herein, the design storey drift in any storey must not exceed 2.5% of that storey height h.

In CSA S16-09, for strength design, horizontal notional loads F_{nx} equal to 0.005 of storey gravity loads must be added to the seismic lateral loads to account for effect of storey out-of-plumbness on lateral frame stability. The total member forces including notional load effects must then be amplified at each storey level by the factor U_2 to account for P-delta effects:

$$U_2 = 1 + \frac{\sum C_f}{V_f}\frac{R_d \Delta_f}{h} \tag{5.2}$$

where ΣC_f is the factored gravity loads; Δ_f is as defined earlier; and V_f is the total storey shear force including effects of notional loads. Sufficient lateral stiffness must also be provided so that U_2 factor does not exceed 1.4 in any storey. In the NBCC, the U_2 factor need not be applied when it is less than 1.1. Gravity loads considered in the calculation of the notional loads and P-delta effects are obtained from the code prescribed load combination including gravity dead (D), live (L), snow (S) loads, and earthquake loads (E): D + 0.5 L + 0.25 S + E. Seismic effects must also be amplified to account for in-plane accidental torsion by assuming an eccentricity between the floor center of mass and stiffness equal to 10% of the floor dimension perpendicular to the direction under design. For the structures studied, amplification due to accidental torsion is 1.06.

5.3.4 Design of the prototype BRBFs

Braces are sized first so that their factored axial compression and tensile resistances, $C_r = T_r = \phi A_{sc} F_{ysc}$ exceed the axial loads from combined gravity and lateral loads, where ϕ is the resistance factor (= 0.90), A_{sc} is the cross-section area of the core YS, and F_{ysc} is the minimum specified yield strength of the core (F_{ysc} = 345 MPa was assumed). In CSA S16-09, capacity design must be followed for connections, columns, and beams of BRBFs. These components are therefore designed to resist gravity loads plus forces induced by all braces reaching their probable tensile and compressive axial strengths simultaneously:

$$T_{\max} = \omega R_y F_{ysc} A_{sc} \tag{5.3}$$

$$P_{\max} = \beta \omega R_y F_{ysc} A_{sc} \tag{5.4}$$

where ω and β are the tensile and compressive strength adjustment factors, respectively; and R_y is the ratio of the probable-to-nominal yield strength of the core material, which was taken as 1.12.

Magnitude of ω and β depend on the anticipated deformation demand in the YS of the brace. In CSA S16, these factors must be obtained from results of cyclic test at deformations corresponding to two times the design storey drift. The amplification factor of *two* accounts for non-uniform distribution of inelastic demand across the frame height and uncertainties in seismic deformation demand assessment. In design, the brace axial deformation δ_{br} at two times the design storey drift ($2R_dR_o\Delta_f / I_E$) can be estimated from:

$$\delta_{br} = \frac{2R_dR_o}{I_E}\frac{P_f L_{br}}{EA_{br,eq}} \tag{5.5}$$

where P_f is the brace axial force due to the earthquake loads used to determine Δ_f; L_{br} is the brace total length; E is the steel core Young's modulus; and $A_{br,eq}$ is the cross-section area of an equivalent brace having the same axial stiffness as the actual brace. The area $A_{br,eq}$ is calculated as $A_{sc}/(\gamma + \eta\chi)$, with η being the ratio of the cross-section areas of the core yielding and non-yielding segments; and γ and χ being the ratios of the lengths L_{sc} and L_e to total length L_{br}, respectively (see Figure 5.4b). Equation (5.5) is a simplification as it assumes that all framing members experience the amplified inelastic deformations whereas, in reality, inelastic deformations are expected to develop only in the bracing members. An alternative, more direct interpretation of the code requirement for the calculation of δ_{br} is given in Eq. (5.6):

$$\delta_{br} = \left(\frac{2R_dR_o}{I_E} - \omega\right)\frac{\Delta_f}{\cos\psi} + \omega\frac{P_f L_{br}}{EA_{br,eq}} \tag{5.6}$$

where ψ is the brace angle with respect to the floor. The first term of the equation corresponds to the brace plastic deformation, as member forces are increased by ω when the storey drift reaches the amplified drift, while the second term corresponds to the brace elastic deformation under axial load ωP_f. Contrary to Eq. (5.5), this expression assumes that beams and columns remain elastic under the amplified seismic loads corresponding to brace probable resistances and inelastic deformations concentrate in the braces. It is therefore expected that Eq. (5.6) will give higher δ_{br} values compared to Eq. (5.5), especially in the upper levels because storey drifts from column axial deformations are amplified by 2.0 in the calculations, which is unlikely to be the case in reality. Equation (5.6) can be further simplified by assuming that at the amplified storey design drift, the brace elastic deformation is equal to the factored yield elongation of the brace:

$$\delta_{br} = \left(\frac{2R_d R_o}{I_E} - \omega\right)\frac{\Delta_f}{\cos\psi} + 0.9\omega(\gamma + \eta\chi)\frac{F_{ysc}}{E}L_{br} \tag{5.7}$$

Difference between Eqs. (5.6) and (5.7) would be small when the storey shear forces for strength design and deflection calculation are similar. However, when the analytical period (T_1) is significantly different from the code empirical value (T_a), the strength design and deflection calculation shear forces can be quite different. In this case, elastic analysis brace force could be much lower than the brace yield strength which invalidates the underlying assumption in Eq. (5.7). For design of the studied frames, the Eq. (5.5) was used and the outcome of using Eq. (5.5) *vs* Eq. (5.6) will be discussed later in this chapter when examining the results from nonlinear response history analysis. Having determined δ_{br}, the corresponding shortening or strain in the YS can be obtained from:

$$\epsilon_{YS} = \left(\frac{\delta_{br}}{L_{br}} - \eta\chi\omega R_y \epsilon_{ysc}\right)\Big/\gamma \tag{5.8}$$

where ε_{ysc} is the yield strain of the core material. Using ϵ_{YS}, ω and β can be estimated from the BRB backbone curve. Note that ω in Eq. (5.8) depends on strain ϵ_{YS} and, for this reason, iterations may be required to obtain the solution. For compression brace members, ω in Eq. (5.8) should be replaced by $\beta\omega$; however, this refinement is unnecessary at the design stage and using ω for all braces will result in a slightly conservative YS strain. For design, the ratio γ was taken as 0.55 and 0.7 for BRBs in the Split-X and Diagonal braced frame models, respectively, and parameters χ and η were assumed to be 0.25 and 0.45, respectively. With these values, $A_{br,eq}$ = 1.51A_{sc} and 1.23A_{sc} was obtained for the Split-X and Diagonal braced frame models, respectively. The tri-linear BRB backbone curve proposed in (Dutta, *et al.*, 2010) was used to estimate ω and β. In that backbone, β = 1.1 and for intermediate YS strains and ω can be linearly interpolated between 1.0 and 1.25 at ductility ($\epsilon_{YS}/\epsilon_{ysc}$) of 1 and 10, respectively.

As per CSA S16-09, columns in the BRBFs were designed for simultaneous effects of a factored axial loads from earthquake load combination and an additional bending moment equal to 20% of the column plastic moment capacity. That flexural demand is mainly induced by non-uniform

storey drifts developing in adjacent levels. In S16, the column bending moment is amplified by the factor of U_1 to account for moment gradient and second-order effects:

$$U_1 = \frac{\omega_1}{1 - C_f/C_e} \quad \text{with: } \omega_1 = \max(0.6 - 0.4\kappa, 0.4) \tag{5.9}$$

where ω_1 is the equivalent uniform bending moment coefficient; C_f is the factored axial force; C_e is the column Euler buckling load; and κ is the moment gradient factor which is defined as the ratio of smaller to larger factored bending moment demand at the opposite ends of the compressive member. By definition, κ is positive if the column is subjected to double curvature bending and negative when bending is single curvature. In the Commentary to CSA S16-09, it is suggested to use $\kappa = -1.0$ assuming that both ends of the column at a level will be subjected to the same magnitude of bending moment in a single curvature mode. However, for the buildings studied, κ was taken equal to zero given the susceptibility of BRBFs to large drift concentration in a single storey, a situation that is likely to result in large bending moments only at one column end. This assumption, together with the S16 additional bending moment requirement, will be verified later using the results of nonlinear response history analyses.

Braced bay beams were designed for combination of axial forces and moments due to gravity loads and brace forces corresponding to brace adjusted strengths T_{max} and C_{max}. Beams were assumed to be appropriately restrained against lateral-torsional buckling.

5.3.5 Design results

The design involved successive iterations until convergence on periods T_a for base shear, period T_1 for drifts, Δ_f for P-delta effects, and brace strain demands for ω was reached. Table 5.1 gives the computed periods of the buildings in their first two modes T_1 and T_2, the empirical period T_a, the strength-design base shear ratio V/W, as well as maximum design storey drift ratios, maximum U_2 factor, and maximum YS strain demand across all the storeys. The latter was computed with δ_{br} from Eq. (5.5).

5.3.5.1 Summary of important design values

As shown in Table 5.1, buildings in Victoria were designed for larger lateral loads resulting in larger elastic stiffness and, thereby, tend to have shorter vibration periods in comparison with the

corresponding buildings in Montréal. This is also the case for the buildings designed for the soft soil site E compared to site C. For the same building height, diagonally braced frames are more flexible due to their longer brace core yielding segment (γL_{br}) and steeper brace angle (ψ). The design base shear ratio, *V/W*, is constant when $T_a \geq 2.0$ seconds. For the designed buildings, the maximum design storey drift ratio was less than the NBCC's limit (2.5% of the storey height). As a general trend, the design storey drift ratios in the west site buildings were considerably greater than those designed for the east site. For the west site buildings, storey drift ratio varies between 1.0% and 2.1% while it did not exceed 0.7% in those of the east site. As a typical pattern, the maximum storey drift ratio happened to be always at the last storey. The distribution of the design storey drift ratio, $R_o R_d \Delta_f / h$, along the building height is plotted in Figure 5.2a for the 9-storey building designed for Class C site in west and east. In general, the effects of U_2 factor were found to be more significant in the taller buildings as they are more flexible and carry heavier gravity loads. The U_2 factor had also more pronounced effects on the east site buildings because of the lower specified design earthquake loads which resulted in having less lateral stiffness in comparison with the corresponding west site buildings. Effects of notional loads and P-delta amplification are respectively plotted in Figures 5.2b & 5.2c for the 9-storey Split-X BRBFs that were designed for Class C site in east and west. Amplification due to the notional loads and P-delta effects is more intense in the east site building. In the final design, when Eq. (5.5) were used to compute the brace elongation δ_{br}, the YS strains obtained from Eq. (5.8) varied between 0.7% and 1.6%. For F_{ysc} = 345 MPa, these strains correspond to the YS ductility of μ = 3.5 and 8.5. These strains gave ω values ranging from 1.09 to 1.24 according to the employed backbone curve. YS strains along the building height are plotted in Figure 5.2d for the mentioned 9-storey Split-X BRBFs. In this figure, strains obtained from brace elongation determined from Eq. (5.6) are also plotted for comparison purpose. When Eq. (5.5) is used to calculate δ_{br}, the YS strains are nearly uniform over the frame height, varying between 1.2%–1.5%, and 0.8%–0.9% in the west and east site buildings, respectively. Conversely, the values obtained from Eq. (5.6) vary more significantly over the frame height, between 1.3%–2.4%, and 0.9%–1.3% in the west and east site buildings, respectively. This is directly attributed to the contribution of the columns to frame lateral deflections which is cumulative along the building height.

Table 5.1: Design values of the studied buildings.

Location	Site Class	Bracing Pattern	Design Values	Number of storey					
				3	5	7	9	13	15
Victoria (West)	C	Split-X	T_1 [s]	0.63	1.07	1.40	1.82	2.46	2.70
			T_2 [s]	0.26	0.43	0.54	0.68	0.87	0.94
			T_a [s]	0.60	1.00	1.40	1.80	2.46	2.70
			V/W [g]	0.153	0.079	0.063	0.046	0.038	0.038
			$R_o R_d/I_E$ (Δ_f/h) [%]	1.0	1.1	1.2	1.3	1.6	1.8
			ε_{YS} [%]	1.5	1.5	1.5	1.5	1.5	1.4
			U_2	1.06	1.10	1.13	1.16	1.21	1.23
		Diagonal	T_1 [s]	0.77	1.32	1.69	2.24	-	-
			T_2 [s]	0.31	0.51	0.63	0.49	-	-
			T_a [s]	0.60	1.00	1.40	1.80	-	-
			V/W [g]	0.153	0.079	0.063	0.046	-	-
			$R_o R_d/I_E$ (Δ_f/h) [%]	1.2	1.3	1.5	1.7	-	-
			ε_{YS} [%]	1.1	1.1	1.0	1.1	-	-
			U_2	1.07	1.13	1.14	1.20	-	-
	E	Split-X	T_1 [s]	0.64	0.82	1.03	1.25	1.94	2.24
			T_2 [s]	0.26	0.32	0.39	0.47	0.68	0.78
			T_a [s]	0.60	0.82	1.03	1.25	1.94	2.24
			V/W [g]	0.150	0.150	0.136	0.121	0.070	0.065
			$R_o R_d/I_E$ (Δ_f/h) [%]	1.0	1.2	1.4	1.7	1.8	2.1
			ε_{YS} [%]	1.6	1.6	1.6	1.6	1.4	1.5
			U_2	1.06	1.06	1.07	1.09	1.14	1.17
Montreal (East)	C	Split-X	T_1 [s]	1.03	1.68	2.15	2.68	-	-
			T_2 [s]	0.44	0.69	0.85	1.00	-	-
			T_a [s]	0.60	1.00	1.40	1.80	-	-
			V/W [g]	0.058	0.029	0.024	0.018	-	-
			$R_o R_d/I_E$ (Δ_f/h) [%]	0.5	0.6	0.6	0.7	-	-
			ε_{YS} [%]	0.7	0.8	0.7	0.9	-	-
			U_2	1.07	1.14	1.16	1.23	-	-

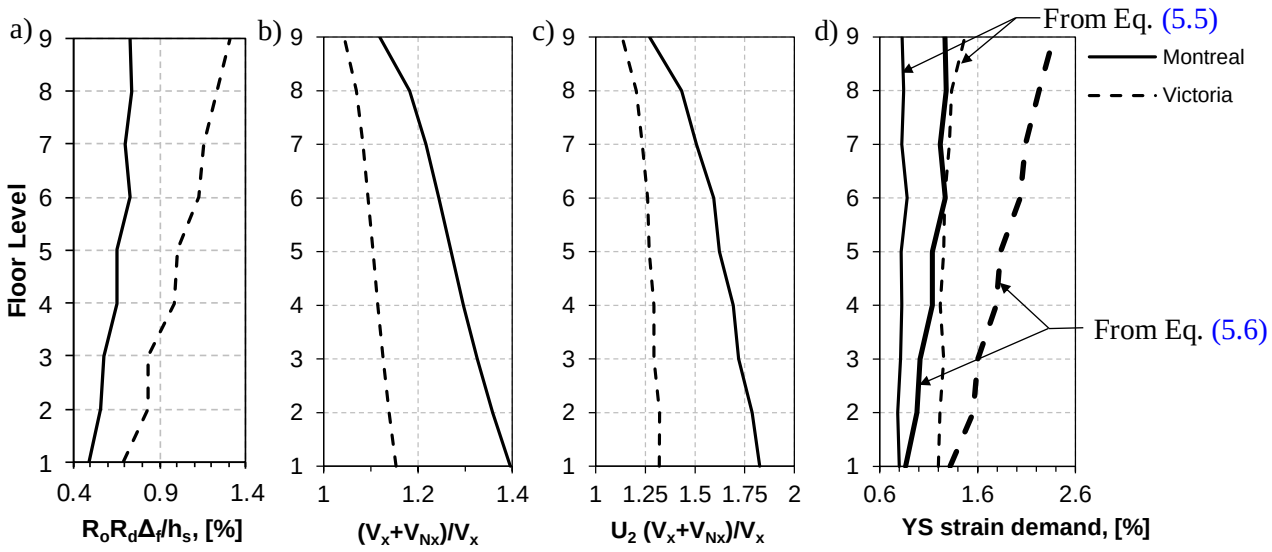

Figure 5.2: Stability related design parameters for the 9-storey Split-X BRBFs in Victoria (west) and Montréal (east): a) Storey design drift ratios; b) storey shear force amplification due to notional loads; c) total amplification factor of design storey shear force; and d) yielding segment strain demand.

5.3.5.2 Empirical vs analytical periods

The empirical expression for the period T_a in the NBCC is supposed to be a lower-bound value for steel concentrically braced frames (CBFs) in regions with low-to-moderate seismicity (Tremblay, 2005). Compared to BRBFs, steel CBFs are designed for higher seismic loads (lower R_d values) and have higher overstrength impacting the design of beams and columns. It is therefore expected that BRBFs will be more flexible and have longer periods than CBFs in an equivalent design condition. The computed and empirical periods, T_1 and T_a, of the designed Split-X BRBFs are plotted against buildings' heights in Figure 5.3. It should be noted that in addition to the buildings whose properties are shown in Table 5.1, some other cases were also designed to include a wider range of building height and site soil class especially for east Canada site. These extra models were only studied to obtain the relation between periods T_a and T_1. As shown in Figure 5.3a for the Victoria site, calculated T_1 for the buildings in west Class C site is in a close agreement with the upper-bound of the code equation, $T_a = 0.05h_n$. For buildings taller than 9-storey the relation between height and period becomes slightly nonlinear as result of using constant base shear ratio after period of 2 seconds. For the east site buildings (Figure 5.3b) analytical periods are generally

longer than the upper-bound of the code prescribed values except for the 13- and 15-storey cases that were designed for soft soil site. Since Victoria has the most intense UHS ordinates in Canada, the soft soil west prototypes may represent the case with the highest possible design base shear (and lateral stiffness) for standard occupancy (I_E = 1.0) in the country. Values of T_1 for these prototypes are consistently longer than the lower-bound for T_a (0.025 h_n), which suggests that the lower bound period estimate for T_a could probably be relaxed to a higher value, say T_a = 0.035 h_n, for BRBFs. For design of BRBFs in the moderately seismic active regions of Canada, i.e. east of Rocky Mountains, $T_a = c_x h_n^{0.8}$ is suggested in which c_x varies between 0.1 and 0.15.

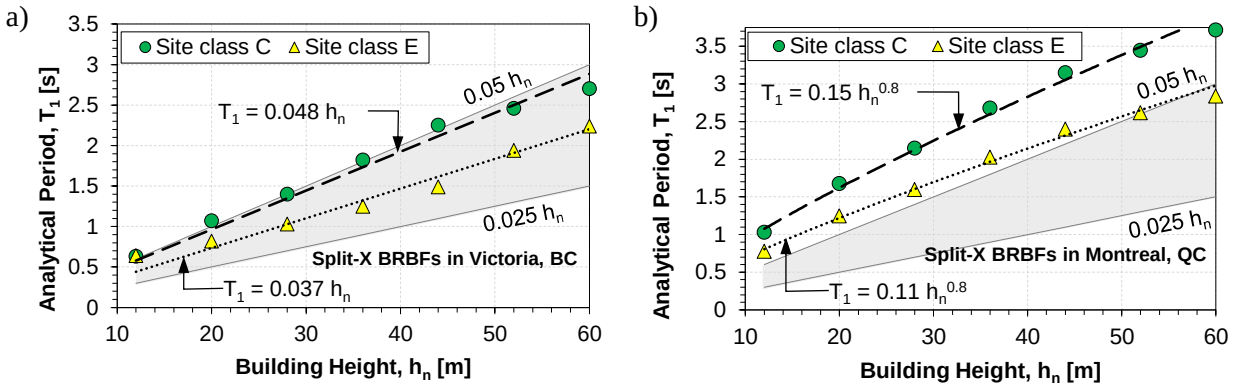

Figure 5.3: Comparison between first mode analytical BRBF periods (T_1) and the NBCC 2010 empirical periods of the buildings designed for: a) Western; and b) Eastern Canada sites.

5.4 Numerical models and ground motion records

5.4.1 Modelling assumptions

Two-dimensional numerical models of the discussed prototypes were built in SAP2000 structural analysis program (CSI, 2010). BRB cores were modelled as nonlinear inelastic elements using the Bouc-Wen hysteresis model (Wen, 1976). Bouc-Wen model can reproduce cyclic response of ductile elements with stable and smooth hysteresis behaviour. This is the case for a typical BRB member since no strength and sharp stiffness degradation (pinching) is expected to happen. Although this model cannot simulate isotropic hardening and has issues such as displacement drift and force relaxation (Charalampakis, *et al.*, 2009), it has been successfully implemented to simulate real-time dynamic excitations and displacement-controlled cyclic test results of BRB members (Black, *et al.*, 2004). The restoring force in the model is expressed as:

$$F = aku + (1-a)ku_y z \tag{5.10}$$

where *a* is the ratio of the post-yielding stiffness to the initial elastic stiffness; *k* is the initial elastic stiffness; *u* is the deformation time history; u_y is the yield deformation; and *z* is the hysteresis parameter obtained by solving the following differential equation:

$$\dot{z}u_y = \dot{u}[1 - |z|^n(\beta_{BW}\,\mathrm{sgn}(\dot{u}z) + \gamma_{BW})] \tag{5.11}$$

where *n* is the yield exponent that controls the transition between initial and post-yield stiffness; β_{BW} and γ_{BW} are the factors to control the shape of hysteresis loops; sgn is the Signum function; and dot denotes time derivative. Comparison with the full-scale BRB test results reported in (Tremblay, *et al.*, 2006) showed that $\beta_{BW} = \gamma_{BW} = 0.5$ (i.e. the same loading and unloading slope), $n = 2.0$, and $a = 0.02$ would be appropriate model parameters. It should be noted that in reality the post-yield ratio (*a*) is not constant and degrades as the plastic deformation increases and accumulates. The implemented value in this study would be appropriate up to a certain ductility levels, e.g. 10 as expected from design, above which it would overestimate the post-yield stiffness. Since isotropic hardening cannot be simulated directly by this model, yield deformation of the element was modified to approximately adjust the hysteresis law as proposed in (Black, *et al.*, 2004):

$$u_y = [1 + a(\mu_{exp} - 1)]R_y F_{ysc} A_{sc}/k \tag{5.12}$$

where μ_{exp} is the maximum expected ductility demand in the YS. In this study, the yield deformation was multiplied by an adjustment factor of 1.18, assuming $\mu_{\text{exp}} = 10$. This adjustment increases the system overstrength and as a result, the inelastic deformation could be slightly underestimated. Ideally, successive trial and error has to be conducted until convergence between assumed μ_{exp} and the maximum ductility response, μ_{max}, is reached. Prior to analyzing the frames, this was done for single-degree-of-freedom models and it was found that convergence could be achieved mostly after a few trials. It was also observed that the need for trial and error can be eliminated, with a reasonable accuracy, if the response from the first trial is simply adjusted as follows:

$$\mu(t) = [1 + a(\mu_{exp} - 1)]/[1 + a(\mu_{max} - 1)]\,\mu_{ini}(t) \tag{5.13}$$

where $\mu(t)$ is the adjusted YS ductility history; and $\mu_{\max}$ and $\mu_{ini}(t)$ are the maximum ductility and ductility history of the YS that were calculated in the first trial based on the initial setting of the model.

Conceptual modeling of the brace elements is illustrated in Figure 5.4a. The yielding and non-yielding segments of the core are modelled together as a single element with an equivalent stiffness to reduce the analysis time:

$$k = \frac{1}{(\gamma + \eta\chi)} \frac{EA_{sc}}{L_{br}} \tag{5.14}$$

Past experimental investigations have shown that a fully-restrained connection between BRB and gusset plate can impose large flexural demand on the non-yielding segments as well as on the framing components (López *et al.*, 2002; Tsai *et al.*, 2008). This bending moment can destabilize the brace-to-gusset connection, impose severe out-of-plane distortion or cause premature fracture (Fahnestock, *et al.*, 2007a). To avoid these failure modes, the gusset plate and non-yielding segment of the core can be connected by a knife plate having low flexural stiffness and strength as illustrated in Figure 5.4d. This detail caps the maximum transferable bending moment to the knife plate plastic moment capacity. Based on this detail, connections between the non-yielding segment and gusset plate were assumed to have partially fixity which was modelled using an inelastic rotational spring. To avoid excessive bending moments on brace-beam-column joints as a result of gusset plate edge constraints, a single-edge gusset plate detail is assumed in the models as shown Figure 5.4d. In this detail, the gusset plate edge is only connected to the beam and the beam has a simple shear connection to the column with a negligible rotational stiffness. This allows the column and beam to rotate almost independently, preventing generation of excessive in-plane bending moments. Pin connections were therefore assumed between beams and columns in the model. In the numerical models, beam and column members were modelled as linear elastic elements, assuming that they behave elastically consistent with the capacity design approach. Another reason for using elastic column models is to track the force demand in case it exceeds the design values. P-delta effect is considered and modeled by means of leaning columns carrying floor gravity loads.

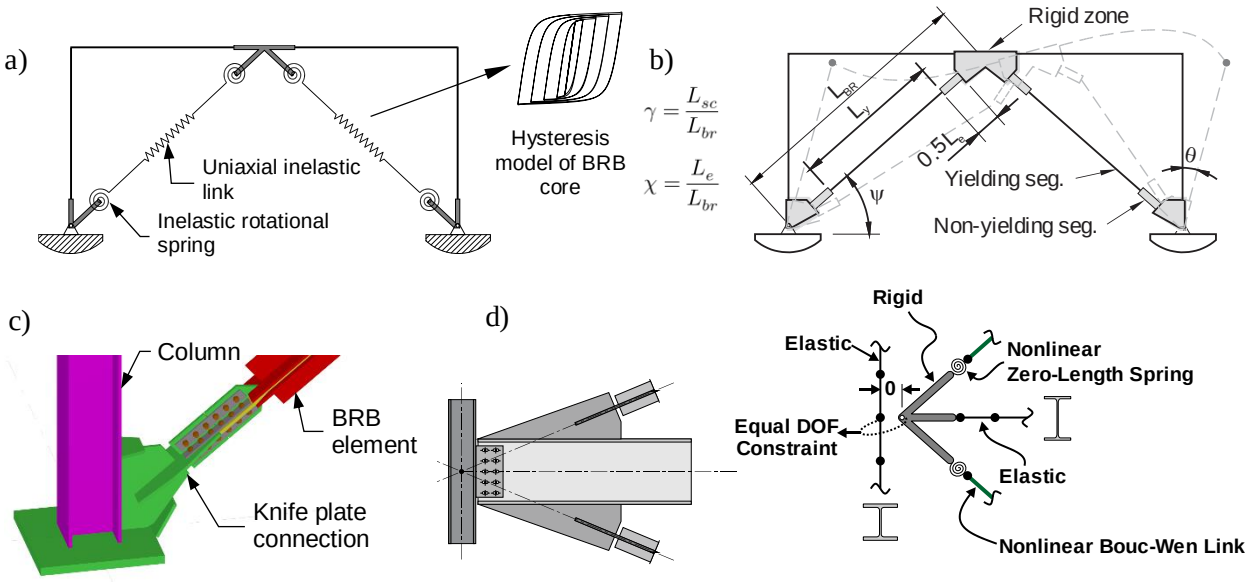

Figure 5.4: a) conceptual modelling of BRBF; b) graphical definition of brace geometry; c) modelling of beam-and-brace-to-column hinge connection; and d) pin brace-to-gusset plate connection.

The numerical models are designated by the number of storeys followed by W or E (for west and east, respectively). The bracing pattern is specified next (X for Split-X and D for Diagonal), and at end the site class is denoted by letters C or E. For instance, 9W-X-C refers to the 9-storey prototype with Split-X bracing pattern designed for a generic 'soft rock' site in Victoria.

5.4.2 Ground motion selection and scaling

Ground motion selection and scaling have been shown to have substantial impact on the response history analyses outcomes. Specific to BRBFs, two separate studies (Sabelli, *et al.*, 2003) and (Fahnestock, *et al.*, 2007b) reported 30% different deformation demand for nearly identical prototypes designed for the same site but subjected to different ground motion records scaled with the same approach. In this study, selection and scaling was performed using a statistically robust approach introduced in (Dehghani *et al.*, 2016c). This approach leads to a mean and variance that are nearly constant regardless of the number of records, and to less variance of demand compared to conventional approaches. It was applied to create three basic sets of ground motion records representing the following events: 1) intra–plate in west; 2) intra–plate in east; and 3) inter–plate

in west coast of Canada. The first two, and the last basic sets contain 20 and 10 records, respectively.

PEER-NGA West ground motion database (PEER, 2005) were utilized to build the set of records representing the west intra–plate events. This database is only suitable for regions with shallow crustal activities such as west of North America. Due to lack of historically recorded earthquakes for eastern Canada, a combination of hybrid and simulated earthquake records were used. To this end, the following ground motion databases were utilized: 1) hybrid ground motions for Central and East of the United States (CEUS) (McGuire, *et al.*, 2002); and 2) simulated ground motions for Eastern North America (ENA) (Atkinson, 2009). Records for the west inter–plate event were collected from: 1) database of stochastically simulated, and modified subduction interface records (Atkinson *et al.*, 2009); 2) database of simulated inter–plate events for Cascadia subduction zone (Atkinson, 2009). The Least Moving Average (LMA) technique (Dehghani, *et al.*, 2016c) was used as the basic scaling method to match the intensity of the records to that of relevant target spectrum.

Mean and 16–84th percentile band of the scaled spectra of the selected records for the west and east intra–plate events are compared with the NBCC 2010 2% in 50 years design spectrum for Victoria and Montréal in Figures 5.5a & 5.5b, respectively. Since inter–plate source was not included in the probabilistic hazard spectrum of the NBCC (Adams *et al.*, 2003), records from this source were scaled with respect to the Cascadia deterministic spectrum (see Figure 5.5d) as reported in (Halchuk *et al.*, 2003). Record-to-record (RTR) variability rendered by the standard deviation of natural logarithm of scaled spectra (σ_{lnSa}) is also given in the figure. Impacts of ground motion selection and scaling on the demand statistics will be discussed later in this chapter. For the reasons that are elaborated in (Dehghani, *et al.*, 2016c) upper tail of the computed demand parameters, i.e. 84th percentile, will be used as the basis for performance assessment.

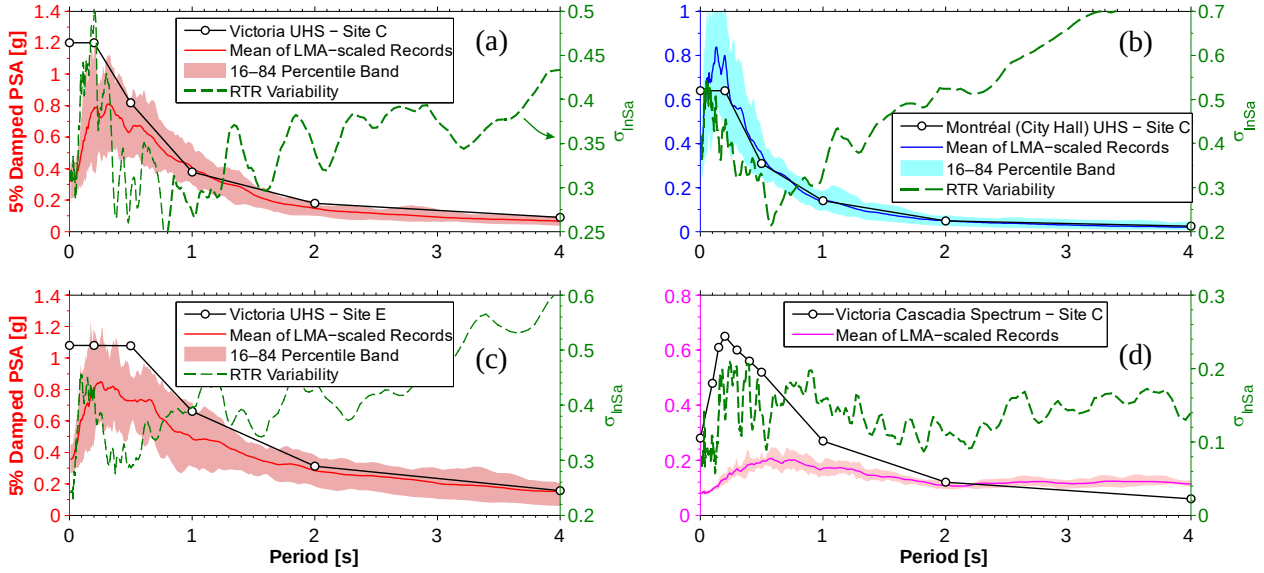

Figure 5.5: Spectra of scaled records for: a) Victoria intra–plate; b) Montréal Intra–plate; c) Victoria Intra–plate in soft soil; and d) Victoria Inter–plate.

5.4.2.1 Alternative sets

To investigate effects of ground motion selection and scaling on seismic demand estimation, an alternative set of 20 records and two conventional record scaling methods were considered for the west prototypes subjected to intra–plate earthquakes. The alternative set was compiled using relatively stronger records compared to the basic set. Plots in Figure 5.6 illustrate the frequency content and duration intensity measures of the basic and alternative sets. In general, the basic set contains records with lower frequency content and longer duration in comparison with the alternative one.

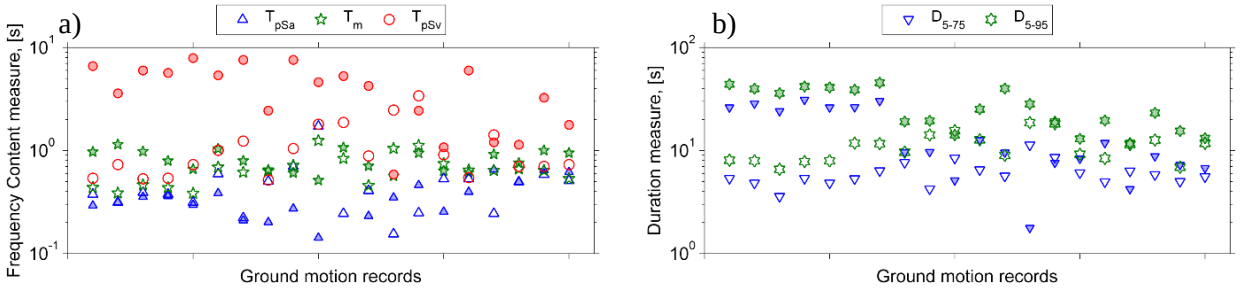

Figure 5.6: Frequency content and duration of the basic and alternative sets. Colour-filled and unfilled markers represent values from the basic and alternative set, respectively. For definitions of the measures see (Dehghani, *et al.*, 2016c).

In addition to the LMA basic scaling method, two other popular techniques were examined for the alternative set: 1) matching at fundamental period (T_1), MFP; and 2) matching between $0.2T_1$ and $1.5T_1$, MSE. In the MFP technique, spectrum of an as-recorded motion is anchored to the design spectrum at T_1 period. In the MSE method, minimum squared error optimization is conducted to find the scale factor which gives the best fit to the design spectrum in the mentioned period range. Details of this scaling techniques are discussed in (Dehghani, *et al.*, 2016c). Record-to-record (RTR) variability of spectral acceleration is known as the main source of response variability. RTR is typically rendered by standard deviation of natural logarithm of the scaled spectra of the selected records. MFP and MSE techniques are prone to produce unrealistic RTR variability unless records are normalized to an intensity measure prior to scaling (see appendix A in (FEMA, 2009)). Quantitative comparison between RTR variability of the records employed in this study can be found in Figure 5.5 and Figure 5.7 (dash line).

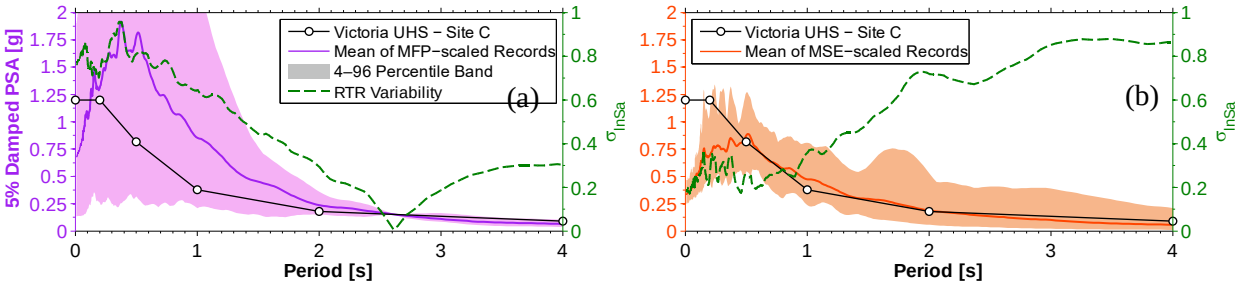

Figure 5.7: Examples of scaled spectra of the alternative set: a) scaled by MFP method for the 15-storey model; b) scaled by MSE method for the 7-storey model.

Since both MFP and MSE are first-mode period dependent, for each prototype a specific set of scale factors were calculated. Analysis results using the alternative set are discussed in Section 5.7.

5.5 Analysis setting, results and post processing

Direct integration nonlinear time history analyses (NTHA) were conducted using Newmark-beta method. Rayleigh damping coefficients were tuned to obtain 3% critical damping ratios in the fundamental vibration mode and in the mode with 98% of the accumulated modal mass. Stiffness proportional damping was not assigned to the bracing elements to avoid the artificial viscous forces that are typically generated upon yielding in inelastic elements (Charney, 2008). This approach has shown to be accurate and effective to eliminate these fictitious viscous forces (Zareian, *et al.*, 2010). Results of the NTHA were subjected to uniform post processing in order to calculate various global (at frame level) and local (at BRB yielding segment level) seismic demand indices. In both levels and for the most important demand indices, sets of performance limits are defined. Then the probability of exceeding these limits, when ground motions are scaled to the code prescribed intensity, are calculated assuming that the demand is lognormally distributed. Mean and standard deviation of the probability density function (PDF) of demand were computed from the most critical value across all storeys in each ground motion. Later, these PDFs will be adjusted to account for the uncertainties associated with ground motion selection and scaling.

In addition to the NTHA, all prototype buildings were subjected to nonlinear static analysis (pushover) with an inverted triangular load pattern. Roof target displacements were set to 2% and 1% of the building's height in the west and east prototypes, respectively. These values approximately represent twice the corresponding anticipated seismic displacements from Table 5.1. Pushover capacity curves for the "soft rock" Split-X west and east prototypes are plotted in Figure 5.8a & c, respectively. Figure 5.8b & c show the post-yield stiffness ratio that is computed by dividing the tangent stiffness to the elastic stiffness of the models. This parameter can be used as a seismic lateral stability criterion. The tangent stiffness is obtained at the drift corresponding to the roof design displacement, $R_o R_d \delta_{roof}$. These design values are shown by filled dots in the Figure 5.8a & c. In general, the post-yield ratio varies in a nonlinear fashion with the first mode period (or the building height). For the same building height, soft soil models have higher post-yield ratios since their elastic stiffness is larger than the "soft rock" counterparts. This larger stiffness is attributed to the higher design base shear ratios for the soft soil models. Downward

trend in the post-yield ratio of the "soft rock" west models ceased around period of 2.0 s (T_1 of the 9W-X-C model is 1.82 s). As discussed earlier, according to the NBCC, the design base shear ratio after 2.0 s is constant and this resulted in lower ratios of gravity loads to lateral strength for models taller than 9 storeys. Stabilization of post-yield ratio after 2.0 s may imply that the concept of using minimum base shear ratio could be effective in reducing the chance of collapse for high-rise buildings. Models 9W-X-C and 9E-X-C showed the least post-yield ratios among the west and east Split-X prototypes, respectively. In particular, model 9E-X-C lost more than 50% of its lateral strength at the design roof displacement and subsequently collapsed (reached to zero base shear) at 0.8% roof drift ratio as a result of concentration of lateral deflection in the first storey. This may indicate the vulnerability of medium-to-high rise BRBFs in east of Canada to collapse if they are exposed to strong ground motions with low frequency content. Nevertheless, in east Canada, chance of exposure to this type of ground motions may be very low. The choice of the target displacement for computing tangent stiffness may result in significantly different seismic stability metrics for models with low V/W ratios. Re-evaluation of the post-yield ratio of the east models at displacement corresponding to $0.01h_n$ revealed the sensitivity of this parameter to the target displacement. As shown in Figure 5.8d using $0.01h_n$ as the target displacement resulted in significantly lower post-yield ratios for 3- to 7-storey models. Meanwhile, re-computing the post-yield ratios for the west models at $0.02h_n$ roof drift resulted in negligible changes.

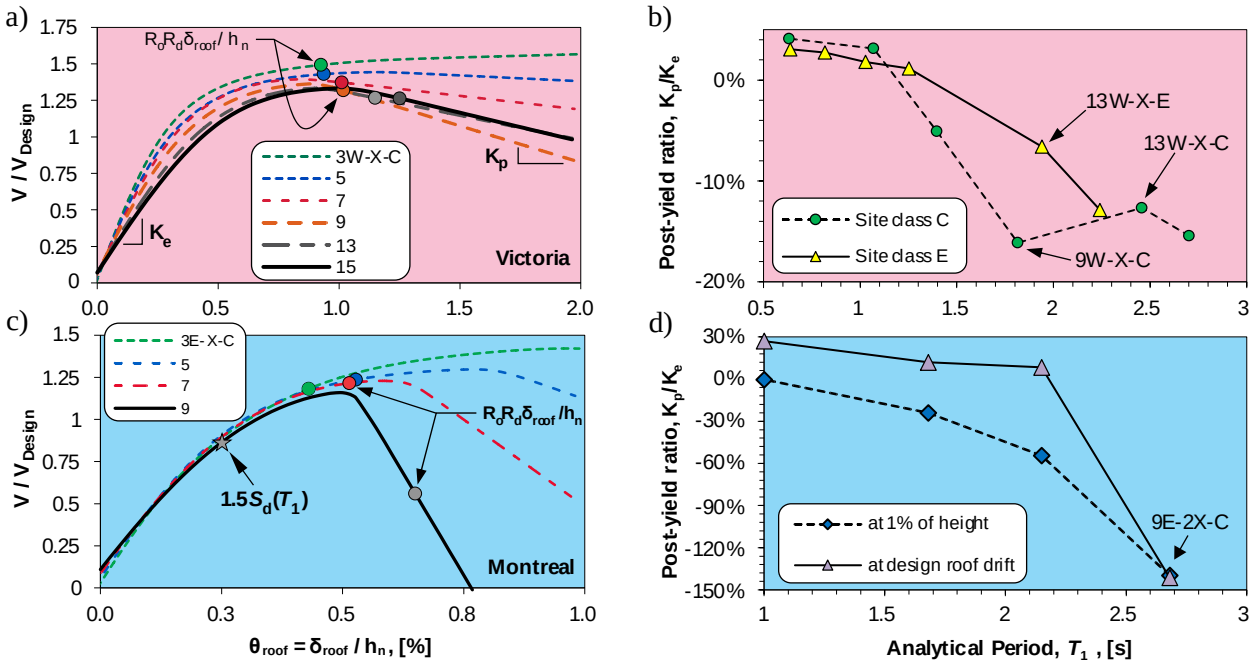

Figure 5.8: a) and c) normalized base shear ratio from pushover analysis of the west and east Split-X prototypes on "soft rock" site; b) and d) relation between first mode analytical period and post-yield stiffness of models in west and east.

5.5.1 NTHA global demand (at frame level)

Response of the studied models at frame level is studied by computing the following global demand parameters: 1) maximum storey drift ratio, θ_{max}; 2) maximum amplification of design storey drift, $\Lambda_{\max} = [\Delta / R_o R_d \Delta_f]_{\max}$ in which Δ is the history of storey drift from NTHA; 3) residual drift, θ_r; 4) peak roof drift ratio, θ_{roof}; 5) maximum drift concentration factor, DCF_{max} = max (θ/θ_{roof}), where θ is the history of drift ratio of a given storey; and 6) maximum absolute storey acceleration, a_{max}. In addition to these, other secondary demand parameters are also calculated: 7) difference between maximum and minimum storey drift ratios; [$\theta_{max} - \theta_{min}$]; 8) accumulated storey's plastic drift angle, $\Sigma\theta_p$; 9) sequence of large plastic drift angles, $\Delta\theta_p^i$; 10) maximum interstorey relative velocity, v_{max}; 11) maximum net column chord rotation between two consecutive storeys, ϕ_{max}; and 12) dynamic overstrength, Ω_d, that is the ratio of maximum lateral base shear to the strength-design base shear. Effective ranges of histories of parameter Λ are computed using the Rainflow cycle counting method (ASTM, 2005) together with the corresponding number of cycles. These ranges are designated by $\Delta\Lambda^i_{RF}$, in which i represents the sequence of ranges in a descending order.

In addition to the mentioned demand parameters, maximum demand/capacity ratio of the column members are also calculated using the interaction equations of CSA S16-09. Some of the global demand parameters required the plastic storey drift ratio which could not be directly exported from the analysis results. To extract the plastic drift angles, the elastic stiffness matrix of the frames were recovered using principles of modal analysis:

$$\boldsymbol{K}_e = \mathbf{M}\Phi\Omega^2\Phi^{-1} \tag{5.15}$$

where $\boldsymbol{K}_e$ is the elastic stiffness matrix of the frame; $\mathbf{M}$ is the diagonal storey mass matrix; and Φ and $\boldsymbol{\Omega}^2$ are matrices of eigenvectors and eigenvalues of the first n lateral displacement modes of the frame, where n is the number of storeys. The obtained stiffness matrix includes global shear and flexural stiffness of the frame, and accounts for effects of initial gravity stresses if second-order modal analysis is conducted. This matrix was then inverted and multiplied to the storey force history to recover the history of elastic storey displacements. Plastic component of the drift angle in each step of analysis was obtained by removing the elastic component from the total drift angles.

Table 5.2 summarizes the most critical statistics of the global demand parameters in the models with Split-X bracing pattern that were designed for the "soft rock" sites. As a prevailing trend, the west models subjected to the intra–plate events underwent the highest demand both in form of peak and cumulative deformation demand.

In the following subsections, performance of the studied prototypes for the principal demand parameters are discussed in detail.

Table 5.2: Different percentile levels of the global demand parameters (for each percentile level the highest values across all models are reported).

Global demand Parameters	West Intra–plate Events			East Intra–plate Events			West Inter–plate Events		
	50th	84th	96th	50th	84th	96th	50th	84th	96th
θ_{max} [%]	1.6	1.9	2.4	0.8	1.0	1.1	0.8	0.9	1.2
Λ_{max}	1.4	1.7	3.1	1.5	2.2	2.4	0.8	1.3	1.7
θ_r [%]	0.7	1.1	2.1	0.3	0.6	0.7	0.4	0.8	1.0
θ_{roof} [%]	0.7	0.9	1.0	0.4	0.5	0.5	0.6	0.6	0.6
DCF_{max}	2.6	4.2	6.9	3.5	5.2	7.3	1.5	1.6	1.9
a_{max} [g]	0.46	0.57	0.68	0.23	0.4	0.48	0.27	0.28	0.29
$\theta_{max} - \theta_{min}$ [%]	2.3	2.7	3.0	1.2	1.4	1.6	1.2	1.3	1.5
$\Sigma\theta_p$ [rad.]	0.118	0.176	0.220	0.049	0.096	0.153	0.226	0.238	0.255
$\Delta\theta_p^1$ [%]	1.2	1.5	1.8	0.5	0.7	0.9	0.3	0.4	0.5
$\Delta\theta_p^2$ [%]	0.8	1.0	1.3	0.3	0.4	0.6	0.2	0.3	0.3
v_{max} [cm/s]	34	40	42	22	29	38	15	17	18
ϕ_{max} [%]	1.1	1.4	2.0	0.7	1.1	1.3	0.3	0.3	0.4
Ω_d	1.4	1.5	1.5	1.2	1.3	1.4	1.3	1.4	1.4

5.5.2 Storey drift ratio

Figure 5.9 shows the statistics of the peak and residual storey drifts in the east and west prototypes under relevant intra– or inter–plate events. West prototypes subjected to the intra–plate events underwent the most significant drift demand compared to the cases. As a typical pattern, displacement demands were concentrated at the first and the top storeys as shown in Figure 5.10. The most critical drift concentration was found in prototype 9W. The same prototype showed the

lowest post-yield stiffness ratio among the west models under pushover analysis (see Figure 5.8b). For models subjected to the west intra–plate earthquakes, both peak and residual displacement demand showed an increasing trend until 9-storey model which experienced the most severe demand. In the worst case, the first storey of this model experienced 2.4% drift angle under a ground motion with low frequency pulses. For the west intra–plate case, the difference between peak and residual drift seemed to be nearly constant, $\theta_{max} - \theta_r \approx 1.0\%$ across all the models. Similar observation has been made in another study related to BRBFs (Erochko, *et al.*, 2011). For the short-rise models, the computed peak roof drifts were similar to the design values as predicted by $R_o R_d \delta_{roof}$ in which δ_{roof} is the roof displacement under design base shear (computed with the period T_1). This trend was not observed in the 7- to 15-storey models in which the estimated roof drifts were 20%–45% less than the expected design values. On the other hand, the 84th percentile of the roof drift in all models can be predicted well by the first mode design spectral displacement, $S_d(T_1) = 3/2\ S_a(T_1)\ T_1^2/4\pi^2$. In this expression, the 3/2 factor is to approximately map the displacement at the effective height of building to the roof level. This observation indicates that the displacement predicted by the force-based design method would not be as robust and accurate as the one from displacement-based approach.

Displacement demands under the west inter–plate, long duration mega-thrust earthquakes were always lower than those from the intra–plate earthquakes. This trend is attributed to the spectrum that was used as the target for record scaling. The deterministic Cascadia spectrum of Victoria is less intense than the probabilistically calculated Uniform Hazard Spectrum (UHS) (see Figure 5.5a & d), particularly in the short period range. Since the structures were designed based on the UHS, they showed considerable overstrength when subjected to records scaled to the Cascadia deterministic spectrum. As a result, limited inelasticity was observed in the low-rise prototypes. For this hazard source, the maximum storey drift ratio happened to be at the first storey of prototype 9W (1.2%). However, the maximum accumulated damage was observed at the top storey of the same prototype and it was approximately equivalent to 30 fully-reversed yield cycles.

Displacement demands on the east Canada prototypes were less than those on the west frames. In the worst case, θ_{max} reached 1.2% (at the top storey of 5E-X-C) which is well below the NBCC's limit of 2.5%. As discussed earlier, east intra–plate earthquakes are expected to be rich in high frequency content and as a result they are less likely to impose large inelastic deformations to flexible structures. In addition, NBCC 2010 requires that the base shear for the east buildings to be

amplified for higher mode effects through M_v factor. This extra amplification results in additional system overstrength when compared with the west prototypes. This observation may imply that a separate and less strict set of design and qualification rules for BRBFs in east of Canada should be considered. Prototype 9E was found to be the model with the largest drift concentration factor. This could be described by the considerably negative post-yield stiffness ratio of this model (see Figure 5.8c). Predicted roof design drifts were only achieved in the 3-storey frame; for the rest of the east structures, the NTHA-estimated roof drifts were 25%–40% less than the predicted design values. As was the case for the west models, the 84th percentile of NTHA's roof drifts was closely predicted by the projected first mode design spectral displacement. When comparing peak storey drifts in the west and east prototypes under intra–plate earthquakes to the reported values in the U.S. case study by Sabelli, *et al.* (2003), 15% and 50% decrease, respectively, are observed.

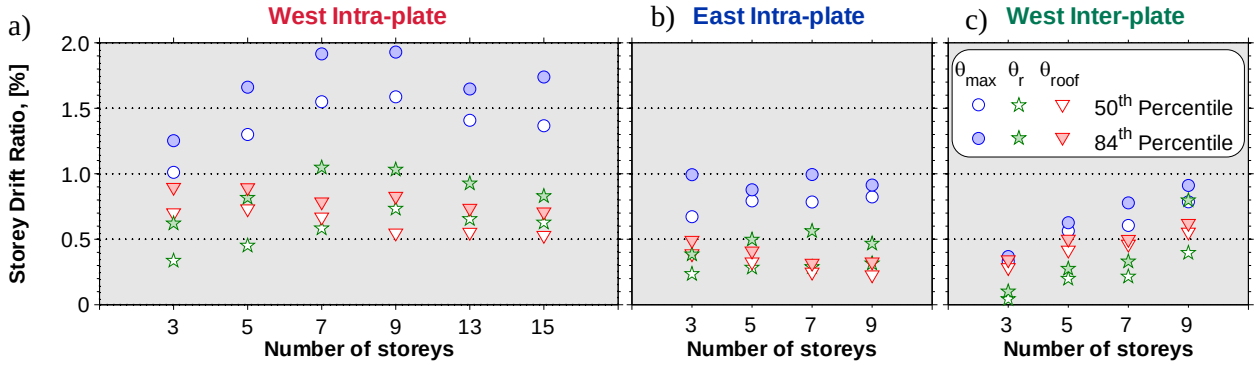

Figure 5.9: Peak, and residual storey drift, and peak roof drift ratio demand in the: a) west prototypes under intra–plate events; b) west prototypes under inter–plate events; and c) east prototypes under intra–plate events. Note that the filled and unfilled markers represent the 50th and 84th percentile of the results, respectively.

In the plots of Figure 5.10, NTHA θ_{max} values are compared with the design and two-times design drift ratios. The latter was used in Eq. (5.6) for the calculation of brace axial deformations under two times the design storey drift. In the 9-storey model, the predicted design drift ratios are always less than the NTHA's median values (except in the last storey) while at the 84th and 96th percentile levels, the predicted design values are exceeded in 50% and 100% of the storeys, respectively. Nearly the same trend can be seen in the case of the 3-storey model. For the 15-storey buildings, the design values were only exceeded at the 96th percentile level only at the lower and upper storeys.

Overall, these observations suggest that the expected design storey drift can be exceeded in some cases. On the other hand, two-times the design storey drifts were only exceeded at the 96th percentile level and this trend was limited to the lower storeys of the high-rise models. Based on this, it can be concluded that the likelihood of exceeding two-times the design storey drifts in all storeys at the same time is very low. A more representative value for amplification of design drifts will be presented in Section 5.7.2 after adjusting the NTHA results for ground motion selection and scaling uncertainty.

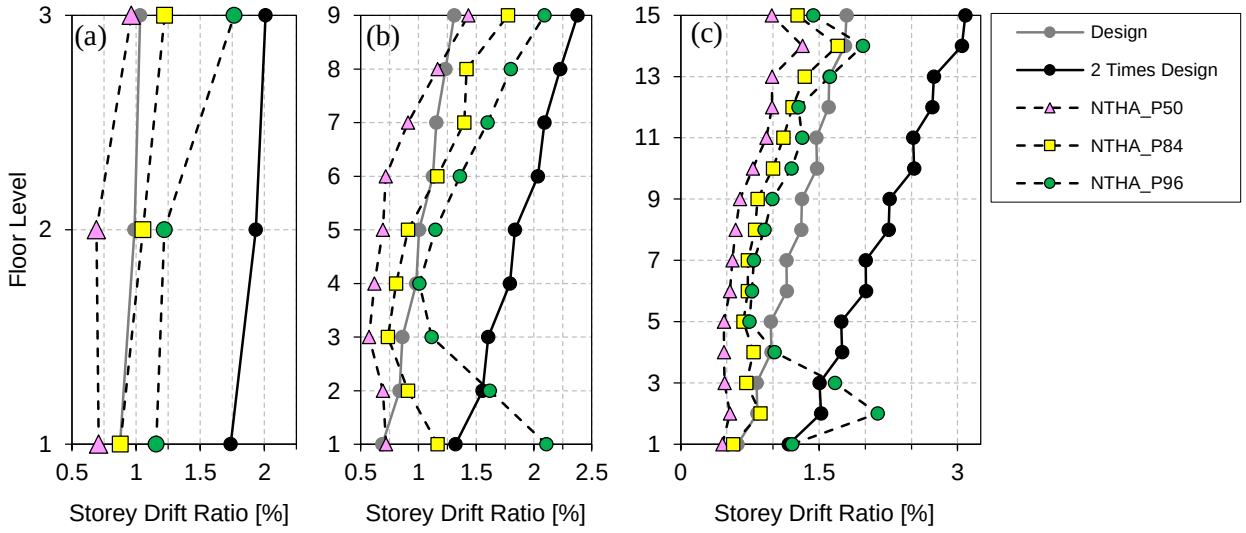

Figure 5.10: Comparison between design drift ratio and NTHA results: a) 3W-X-C; b) 9W-X-C; and c) 15W-X-C models.

5.5.2.1 Floor accelerations

Accurate estimates of peak floor accelerations are important for the design of diaphragms and non-structural components. NBCC 2010 specifies separate design floor forces, or accelerations, for non-structural components and for diaphragms. The former is a linear acceleration profile that starts from 30% of the short period design ground acceleration, S(0.2s) at the ground and reaches to 3.0 times this value at the roof level. According to the NBCC, the maximum of the following cases must be taken as the diaphragm design forces:

1) Storey forces obtained from Equivalent Static Force Procedure (ESFP) or Response Spectrum Analysis (RSA) which are increased to reflect the lateral capacity of the system,

2) Forces obtained by dividing the total base shear (from ESFP or RSA) to the number of diaphragms (= V/N).

Generally speaking, forces obtained from RSA are more accurate than the static method since RSA includes the higher mode effects. The force corresponding to the lateral capacity of frame is typically obtained as the difference between shear resistances of adjacent storeys. To calculate this capacity, tensile and compressive adjustment factors, ω and β, should be included. Typically, capacity-based storey force becomes significant at top floor since the difference between storeys' shear resistance is more considerable. Requirement no. 2 assumes constant acceleration profile across building height. For some of the studied prototypes, NBCC's design acceleration, i.e. design force divided by storey mass, for non-structural element and diaphragms are plotted in Figure 5.11. In this figure accelerations are normalized by the relevant elastic design acceleration, $S(T_1)$. The median and 84th percentile of the peak floor accelerations computed from NTHA are also presented in Figure 5.11 for comparison purpose.

As a general trend, the peak acceleration was nearly constant over the frame height and it was capped at the roof level by the shear resistance of the last storey. NBCC's design floor accelerations are systematically lower, by a large margin, than the computed responses from NTHA. For models subjected to the intra–plate events, the 84th percentile of the peak floor accelerations were as large as 3.5 times the design acceleration, $S(T_1)$. That maximum ratio was observed in the 13W-X-C model. Results from NTHA indicate that NBCC fails to predict the diaphragms' design forces at all levels but the roof. Such an underestimation may lead to undesirable failures in diaphragm components such as collectors, chords, and drag members which are supposed to remain essentially elastic under the design level earthquakes. These large and unprecedented diaphragm forces are mainly attributed to: 1) time lag between brace response in adjacent storeys; and 2) higher mode effects. The former is dominant when braces in one storey are fully yielded while braces in the adjacent storey are still responding elastically or loaded in the opposite direction.

NBCC design accelerations for non-structural elements are not consistent either with the NTHA acceleration results. For the west intra–plate events, the NBCC simple formula tends to overestimate the accelerations at all levels of the short-rise structures. Conversely, the computed peak accelerations in the lower levels (below 20–40% of the building height) of medium-to-high rise buildings exceed the code prescribed values.

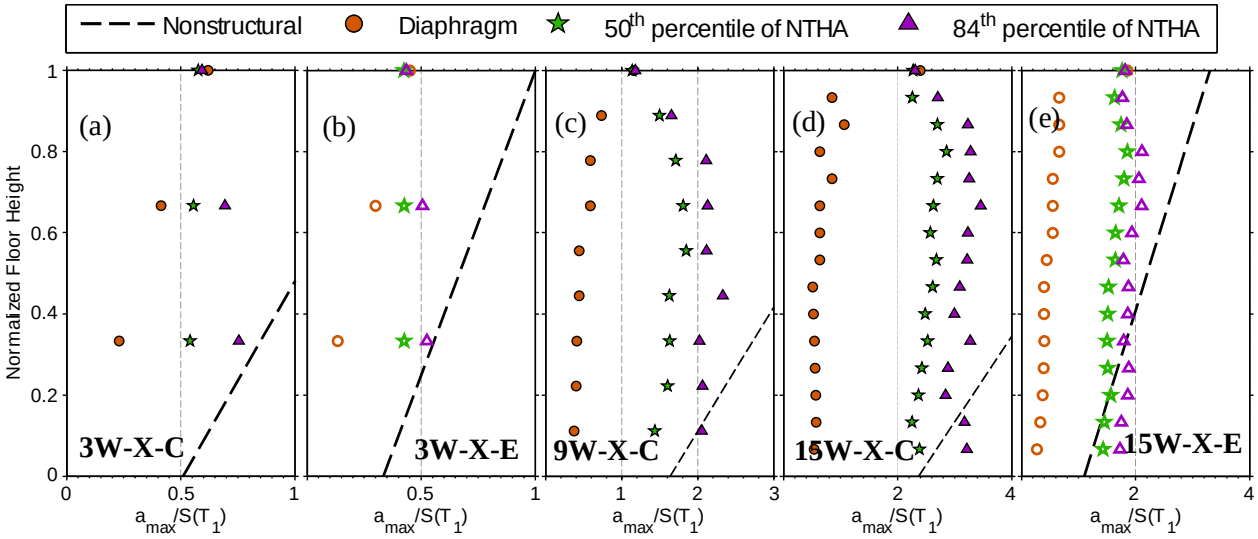

Figure 5.11: Comparison between NBCC 2010 design accelerations for diaphragm and non-structural elements, and the results of nonlinear time history analysis. In some plots, the line representing the design acceleration of non-structural elements is not fully shown to put more emphasis on the diaphragm accelerations.

5.5.2.2 Acceptance criteria and performance at global level

Computed probabilities of exceeding set of prescribed performance limits are given in Table 5.3 for the Split-X structures on "soft-rock" sites subjected to all considered ground motions. Demand parameters θ_{max}, θ_r, and Λ_{max} were utilized for the evaluation of the system performance at the frame level. Their statistics were checked against a deterministic set of performance limits. These limits are 2.5%, 1.0%, and 2.0 for the peak storey drift (θ_{max}), the residual drift (θ_r), and the amplification of storey design drift (Λ_{max}), respectively. It must be noted that the presented values in Table 5.3 are the probabilities of exceeding some performance level when the design earthquake occurs, which is different than total collapse or failure probabilities that are estimated from fragility curves as defined in (Zareian *et al.*, 2007). For the west intra–plate hazard, the values are generally low and tolerable except for the residual drifts for which probabilities as high as 27% were obtained in the case of the west 9-storey structure. In the worst case, the chance of observing storey drift larger than two-times the design value is around 11%. For the west intra–plate events, the calculated probabilities are adjusted later in this chapter to reflect the uncertainties associated with the ground motion record selection and scaling process. For the other seismicity sources, the chance

of exceeding the aforementioned limits are very low except for the parameter Λ_{max} in 3E-X-C prototypes.

In NBCC 2010, the maximum allowable storey drift is limited to 2.5% of the storey height but the code does not prescribe any limits for residual drift. In order to maintain building functionality after an earthquake, McCormick, *et al.* (2008) has proposed an acceptable residual drift angle of 0.5%. However, in this study 1% drift angle limit is set as the maximum acceptable level of residual displacement given that the NBCC 2010 performance objective for standard occupancy (I_E = 1.0) is life safety which may imply that building functionality after the design earthquake would be of a secondary importance. This justifies using 1% residual drift angle as a less strict performance limit in lieu of the proposed value of 0.5% because immediate occupancy of buildings is not the primary performance objective of the current code. Furthermore, given the prescribed force reduction factor of $R_o R_d$ = 4.8 for the studied structures, a permanent displacement equal to 3.8 times the storey yield displacement is expected for BRBFs. Given the BRB specifications and the storey aspect ratio that are assumed in this study, i.e. F_{ysc} = 345 MPa, γ = 0.55, η = 0.45, χ = 0.25 and ψ = 46°, a ductility of 3.8 will result in a permanent drift angle equal to ~0.9% of the storey height. This is close to the assumed performance limit of 1% residual drift angle. CSA S16-09 requires the framing components to be capacity-designed for the forces corresponding to the probable BRB axial resistances at 2.0 times the design storey drift. For consistency, the performance limit for Λ_{max} corresponding to the ratio between NTHA and design storey drift was taken equal to 2.0.

Table 5.3: Unadjusted probability of exceeding global performance limit computed for the "soft rock" Split-X frames (probabilities are shown in percent).

Seismicity Source	Demand Parameter	Performance limit	Number of storeys					
			3	5	7	9	13	15
West Intra–plate	θ_{max}	2.5%	0.03	0.2	1.9	1.2	0.06	0.6
	θ_r	1.0%	6.1	7.7	16.2	25.7	16.3	18.9
	Λ_{max}	2.0	0.8	5.4	8.4	11.1	0.3	1.5
East Intra–plate	θ_{max}	2.5%	1×10^{-3}	1×10^{-6}	5×10^{-4}	1×10^{-8}	–	–
	θ_r	1.0%	2.0	1.1	2.1	0.1	–	–
	Λ_{max}	2.0	19.0	5.4	8.7	0.02	–	–
West Inter–plate	θ_{max}	2.5%	nil*	nil	2×10^{-13}	1×10^{-5}	–	–
	θ_r	1.0%	8×10^{-7}	3×10^{-3}	0.1	6.7	–	–
	Λ_{max}	2.0	nil	nil	3×10^{-9}	0.6	–	–

* calculated value is nearly zero.

As mentioned earlier, for a given prototype, the most critical demands among all storeys were chosen to compute the parameters of the probability density function (PDF) of the demand indices. PDF gives the statistical distribution of a given variable, e.g. peak storey drift ratio, from which the probability of exceeding a certain value, e.g. a performance limit or an acceptance criterion, can be calculated. PDF of a log-normally distributed variable is typically characterized by the mean and standard deviation of the sample. Using another approach to establish the sample size for constructing the PDFs may significantly affect the computed probabilities. As a general rule, increasing the sample size results in more low-magnitude demand values in the data set, which typically leads to reduced central tendencies and increased dispersions. For instance, as Table 5.3 shows in the case of the 9-storey model, the probability of exceeding 1% residual drift ratio is ~26%. When residual drift ratios of all storeys are included in the PDF for this structure, the probability of exceedance reduces to ~11% (see Figure 5.12b). Conversely, as shown in

Figure 5.12d, when the largest residual drifts across all storeys of all prototypes are chosen to construct the PDF, the probability of exceedance increase to ~43%. If all data from all considered prototypes are implemented, the probability would be as low as ~7%.

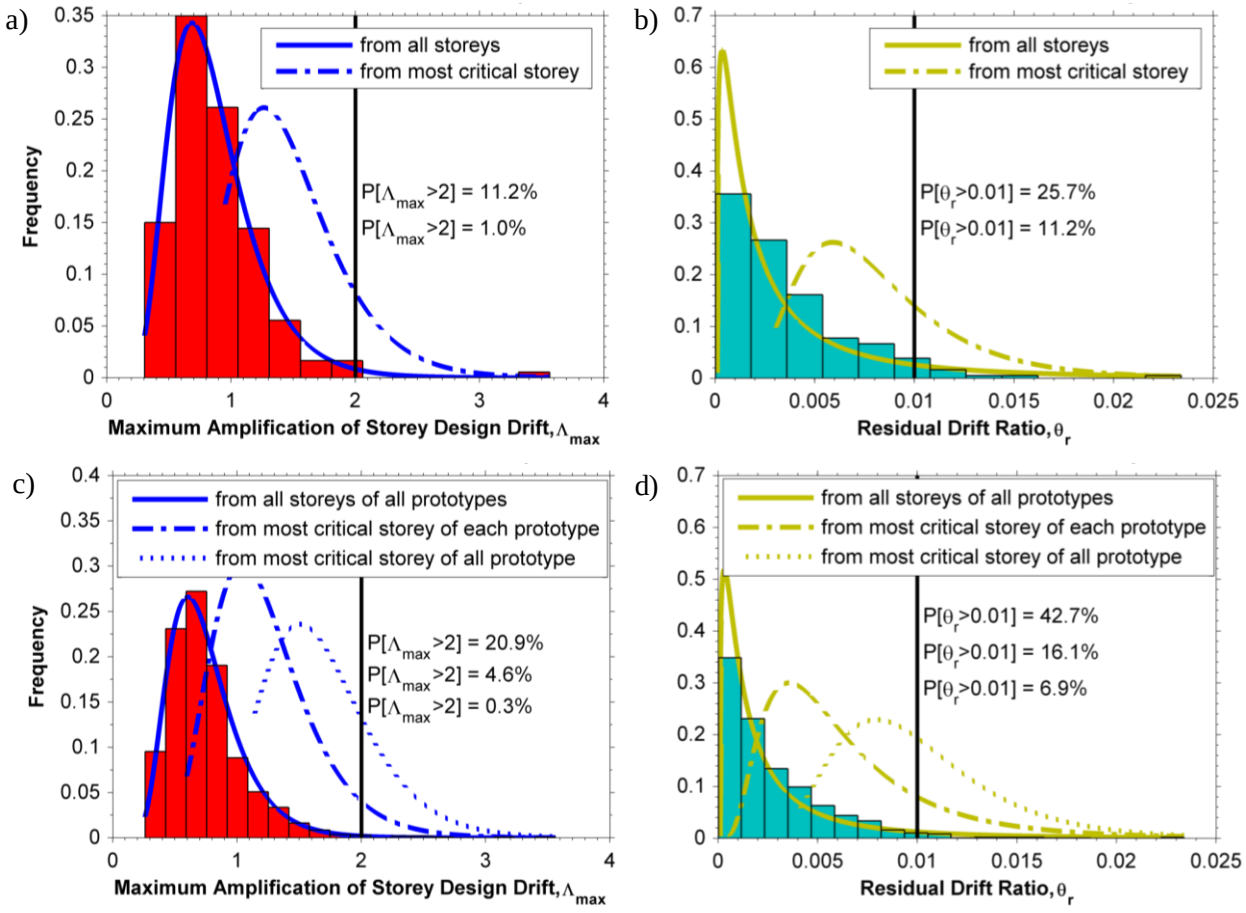

Figure 5.12: Effect of data treatment on the computed probability of exceedance of certain performance limit for a) and b) 9W-X-C model; c and d) all west "soft rock" Split-X models combined (3 to 15 storey).

5.5.3 NTHA local demand (at brace level)

Response at the brace level was evaluated using the deformation histories of the BRB elements. Since the stiffness of the non-yielding segment was included in the element model, the net ductility demand in the core YS had to be recovered as:

$$\mu = \frac{\delta - \delta_e}{\delta_{y,YS}} = \frac{\delta}{\gamma\ \epsilon^*_{ysc}\ L_{br}} - \frac{\eta\chi}{\gamma}\frac{P}{P_{ysc}} \tag{5.16}$$

where δ is the computed brace element elongation from NTHA; δ_e is the elastic elongation of the non-yielding segment; $\delta_{y,YS}$ is the yield elongation of the yielding segment; ε^*_{ysc} is the probable yield strain of the brace element modified for isotropic strain hardening effect; P is the brace axial force history from NTHA; and P_{ysc} is the probable yield strength of the YS segment. Ductility histories were then converted to peak-and-valley data from which the following demand parameters were computed: 1) peak ductility, $\mu_{\max}$; 2) sequence of large plastic excursions, $\Delta\mu_p^i$; 3) maximum shift in ductility, ($\mu_{\max} - \mu_{\min}$); 4) cumulative plastic ductility, $\sum \mu_p$; 5) number of significant excursions, N_f; 6) plastic work normalized to yield work, W_{pn}; 7) rate of i^{th} large plastic excursions, $\dot{\mu}_p^i$; and 8) ductility ranges and their corresponding number of cycles obtained from Rainflow cycle counting (ASTM, 2005) sorted in descending order, $\Delta\mu_{RF}^i$ and n_{RF}^i. Rainflow cycle counting results were then employed to estimate the low cycle fatigue damage state. This was achieved by the combination of the Manson-Coffin low cycle fatigue equation and the Miner's linear damage accumulation rule as elaborated in (Krawinkler, *et al.*, 1983):

$$D_{LCF} = 115 \sum_{i=1}^{N} n_{RF}^i (\epsilon_{ysc} \Delta\mu_{RF}^i)^{2.5} \tag{5.17}$$

According to this model, $D_{LCF} \geq 1.0$ means failure. The damage state parameters were calibrated against experimental results of commercial grade BRBs.

In addition to the YS ductility, another demand parameter defined as the amplification of brace design elongation was investigated:

$$\xi = \frac{\delta}{\delta_d}, \qquad \text{where } \delta_d = \frac{R_o R_d}{I_E}\frac{1}{\gamma + \eta\chi}\frac{P_f L_{br}}{E A_{sc}} \tag{5.18}$$

This parameter is similar, in concept, to the YS ductility but it can reflect better the design assumptions by indicating by how much the expected design values are amplified as a result of inelastic dynamic effects. The maximum value of ξ is designated by $\xi_{\max}$. The Rainflow cycle counting procedure was also applied to histories of ξ in order to obtain sorted effective ranges of this parameter which is symbolized by $\Delta\xi_{RF}^i$. The most critical statistics, i.e. largest percentiles

among all considered models, for some of the computed demand parameters are shown in Table 5.4.

Table 5.4: Percentile levels of seismic demands on BRB core YS in the most critical prototypes subjected to the basic set of ground motion records.

Local Demand Parameter		**West Intra–plate Events**			**East Intra–plate Events**			**West Inter–plate Events**		
		50th	**84th**	**96th**	**50th**	**84th**	**96th**	**50th**	**84th**	**96th**
Amplitude or Range	μ_{max}	9.6	11.0	12.2	6.3	7.1	7.6	6.0	6.8	7.0
	ξ_{max}	2.5	2.9	3.7	2.9	3.4	3.6	1.7	1.9	2.2
	$\Delta\mu_p^1$	5.6	7.0	8.8	3.2	4.8	5.5	1.5	2.1	2.4
	$\Delta\mu_p^2$	4.2	4.9	6.3	1.9	2.6	3.1	1.3	1.5	1.6
	$\Delta\mu_p^3$	3.3	4.1	4.8	1.5	2.3	2.7	1.0	1.1	1.2
	$\Delta\mu_p^4$	3.1	3.9	4.2	1.0	1.6	2.4	0.9	1.0	1.0
	$\mu_{max} - \mu_{min}$	10.1	11.3	13.2	5.7	6.7	7.0	5.9	6.4	7.9
Cycles	$\Sigma\mu_p$	41	54	71	9	16	47	6	10	10
	N_f	23	30	37	6	11	31	7	10	11
	W_{pn}	35	43	59	8	13	33	12	15	16
	D_{LCF} [%]	1.04	1.43	1.97	0.23	0.39	0.92	0.61	0.73	0.77
Rate	$\dot{\mu}_p^1$ [s^{-1}]	16	21	23	11	13	18	3	4	5
	$\dot{\mu}_p^2$	13	17	22	7	10	11	3	4	4
	$\dot{\mu}_p^3$	11	14	17	6	8	11	3	3	4
	$\dot{\mu}_p^4$	10	13	16	5	7	10	2	3	4

The comparison shows that the YS ductility demand in the west models is almost 50% higher than in the east models. However, the maximum amplification of the brace design deformation, ξ_{max}, in the east models are ~20% more than in the west models. This can be explained by the difference between the empirical and analytical periods in the east and west models. As shown in Table 5.1, the analytical periods of the east models were considerably lower than the code empirical values. As permitted by NBCC 2010, storey drifts can be computed using seismic loads obtained from the analytical period T_1 instead of T_a (see Eq. (5.1)). Since the BRB core YS segments are designed for P-delta amplified axial forces from T_a base shears, consequently the brace design elongation would be considerably lower than the yield elongation as a result of the differences between T_a and T_1. Values of the parameter μ_{max} in the west and east models were approximately 30% and 50% less than the reported values in (Sabelli, *et al.*, 2003), respectively. For the worst case, only 2% of the available low cycle fatigue life (LCF) was exhausted in the west models. The reason for such a low fatigue demand is due to the large cumulative plastic ductility (CPD) capacity of the commercial grade BRBs used to calibrate the LCF life model (Eq. (5.17)). For instance, BRBs tested by Merritt, *et al.* (2003) exhibited a CPD capacity of 1025 under cyclic strains amplitudes as large as ±3.0% while the maximum CPD demand obtained from NTHA in this study was less than 100. Although the duration of the west inter–plate records was much longer than the intra–plate ones, the cumulative plastic ductility imposed by the latter set was much higher. As mentioned earlier, this is attributed to the lower spectral intensity that was used as the target for scaling the inter–plate records (see Figure 5.5a & d). Comparing μ_{max} and ($\mu_{max} - \mu_{min}$) indicates that the response at the brace level was highly asymmetric. As a consistent trend, a negative correlation was found between rate of deformation in the core YS and the YS deformation range. This is attributed to the fact that the rate of deformation mainly follows the natural period of the structure, which is relatively constant under design level earthquakes.

5.5.3.1 Qualification deformation

In the plots of Figure 5.13 the estimated core YS deformation demand at two times the design storey drifts from brace axial deformations computed with Eqs. (5.5) & (5.6) are compared to the NTHA results for three of the studied structures in the west. In the plots of Figure 5.13, values of the estimated qualification ductility, i.e. the strain amplitude divided by the yield strain, are compared to NTHA results for the 3-, 9- and 15-storey, Split-X frames on “soft-rock” in the west.

The NTHA results presented in this figure are the 84th percentile estimates of the largest ductility range obtained by Rainflow cycle counting, i.e. $\Delta\mu^{1}_{RF}$, which is divided by two for conversion from range to amplitude. The NTHA demands presented in the plots of Figure 5.13 were adjusted for uncertainties associated to ground motion selection and scaling according to a procedure that will be discussed in Section 5.7.2. As mentioned earlier, the deformation demand on the BRB core YS must be estimated for the qualification testing of BRB elements. Qualification involves full-scale, fully-reversed cyclic testing with the maximum target deformation amplitude corresponding to two times the design storey drift.

As shown in Figure 5.13, the method using brace axial deformations from the simpler Eq. (5.5) predict the maximum strain demand in the core YS better than the method using Eq. (5.6). In the case of the 15-storey building, Eq. (5.6) suggests a ductility amplitude of 14, or core YS strain of ±2.5%, for the cyclic testing of BRBs at the 14th storey. This is more than two times the predicted value by NTHA and represents an unrealistic deformation demand for qualification testing. As Eq. (5.17) implies, the low cycle fatigue life is reduced exponentially as the strain amplitude is increased linearly. For instance, by doubling the strain amplitude, the fracture life of a component decreases by a factor of five or more. The deformations predicted by Eq. (5.6) could result in premature failure of the tested components and, thereby, higher fabrication costs for a BRB that could sustain such a large strain demand. For this reason, caution should be exercised when Eq. (5.6) is used to predict brace deformation at the design stage. The brace inelastic demand derived from Eq. (5.5) shows good agreement with the NTHA results. Hence, simply multiplying design brace axial deformations by 2.0 seems to achieve the objective of the S16 standard, i.e. to predict the maximum expected strain demand in the brace core YS.

More accurate estimation of the strain demand could perhaps be obtained by assuming a lateral deflection pattern that more realistically reflects drift concentration scenarios along the building height. If this avenue was to be explored, the NTHA results show that at least two drift concentration scenarios should be considered: 1) concentration at lower levels, which typically occurs under strong ground motions with rich low frequency content; and 2) concentration at top floors as results of higher modes effects when the frequency content of the record is close to the higher mode frequencies of the building.

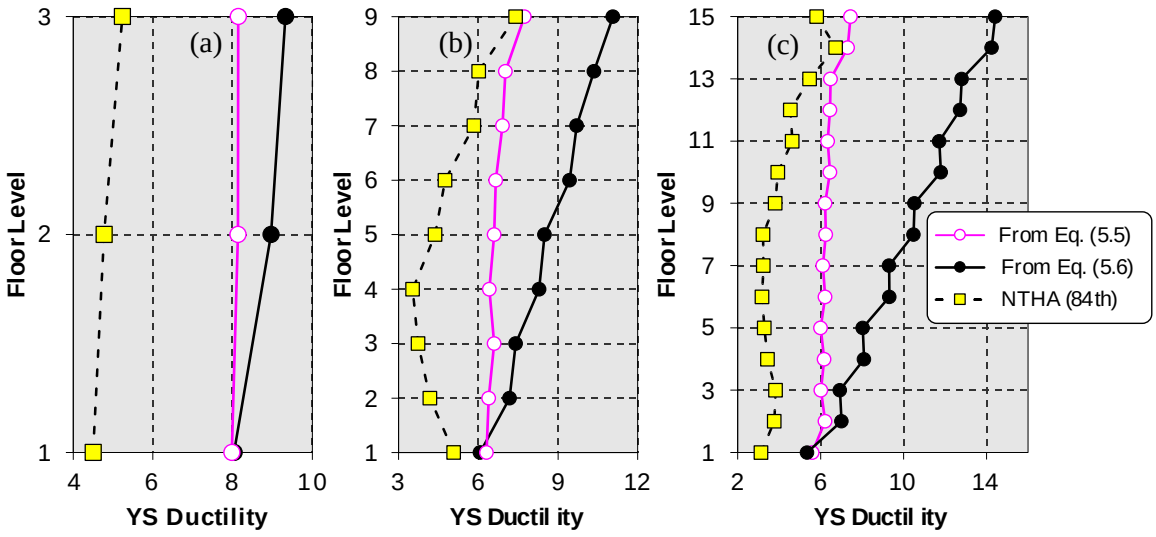

Figure 5.13: Comparison between estimated ductility demand at design stage and 84th percentile robust estimate of YS ductility amplitude, i.e. $½\Delta\mu^{1}_{RF}$, computed from NTHA results of a) 3W-X-C; b) 9W-X-C; and 15W-X-C models.

5.5.3.2 Acceptance criteria at the brace level

Demand parameters $\mu_{\max}$ and D_{LCF} were considered as the main performance evaluation indices at the brace level. Typically, BRB members can accommodate large inelastic strains in tensile excursions but experimental observations have shown that excessive forces can be generated at compressive strains equal to or larger than 3–4% as a result of contact between the brace restrainer and the core non-yielding segment. This contact activates the axial stiffness of restrainer which is much larger than that of the core, which leads to high resistance against further axial shortening. This large force can result in BRB buckling, connection failure, or column overstress. Based on this, the maximum accepted ductility amplitude was assumed to be 15 which approximately corresponds to 3% strain in the core YS when the core is made from 345 MPa steel. For the low-cycle fatigue demand, D_{LCF}, the performance limit was chosen equal to 0.5 assuming that BRB members should have at least 50% reserved fracture life after occurrence of the design level earthquake to avoid catastrophic failure under possible aftershocks. Probabilities of exceeding the limit states associated to maximum ductility amplitude and LCF were calculated as explained previously and the results show that the probability of observing $\mu_{\max} > 3\%$ is less than 0.2% for the most extreme case studied. Meanwhile, the probability of exceeding 50% of the available LCF

life is lower than 1.5×10^{-7}, which suggests that low cycle fatigue fracture is not an issue for BRBs designed in accordance with current Canadian code provisions.

In the past, Cumulative Plastic Ductility (CPD) has been employed as a cyclic performance indicator. Currently, AISC 341 and CSA S16 require that any qualified BRB should be capable of undergoing CPD of 200 without failure. This value could then be used a performance limit. However, CPD may not be directly used for performance evaluation purposes since it only denotes the accumulated inelastic deformation without accounting for the inelastic ranges being applied in the deformation cycles. In other words, a BRB can achieve a very large CPD capacity without fracture when subjected to a large number of small amplitude inelastic cycles but the same BRB may fail prematurely when subjected to large amplitude inelastic cycles. For this reason, CPD was not considered herein for performance evaluation.

5.5.4 Performance of the columns

In BRBFs, inelastic actions should be limited to the brace members and other framing elements such as beams and columns should remain essentially elastic under gravity loads plus maximum expected earthquake induced loads. To achieve this, CSA S16 requires that the braced bay columns be sized according to the capacity design principles. In addition, a minimum additional bending moment equal to 20% of the plastic moment capacity of column, M_{pc}, has to be considered in design to account for moments induced by variations of storey drifts along the frame height. All columns in the frames studied are oriented such that this bending demand develops about the weak axis of the columns. As explained in Section 5.4.1, the braced bay columns were modeled continuously using elastic beam column elements, allowing to monitor both the axial and flexural demands imposed on the columns. In order to evaluate the performance of the columns, NTHA histories of the axial force and simultaneous end bending moments were input to the S16-09 column interaction equation:

$$\mathrm{CDC} = \frac{C_f}{C_r} + \frac{\beta_c U_1 M_f}{M_r} \tag{5.19}$$

where C_f and M_f are the axial force and bending moment acting at column ends at a given time step of analysis, respectively; C_r and M_r are the factored axial and bending strength, respectively; U_1 is

a factor that accounts for bending moment gradients and member second-order effects (see Eq. (5.9)) and the β_c coefficient is defined as:

$$\beta_c = 0.6 + 0.4\lambda, \text{ where}$$
$$\lambda = \sqrt{\frac{F_y}{F_e}} \tag{5.20}$$

where F_y is yield stress of column section (= 345 MPa); and F_e is the column elastic buckling stress computed by Euler weak-axis buckling load of a pin-pin W shape member. Parameter U_1 had to be updated at each time step as it is a function of the ratio of smaller to larger factored moment at the opposite ends of column. As discussed in Section 5.4.1 this ratio is denoted by κ and it is recalled that $\kappa > 0$ implies double curvature bending.

For each time step of NTHA, largest of the demand/capacity ratio at two ends of column was taken as the CDC value. Histories of the CDC were then computed for each column member and the maximum value of each history was designated as CDC_{max} and the computed CDC_{max} values for the columns of the Split-X frames are discussed herein. In all cases, the force demand remain below the code-based factored capacity from Eq. (5.19). Among the west models the most critical CDC_{max} was found to be 0.92 which was recorded at the 11th storey of the 15W-X-C model. Scatter of CDC_{max} in the 15-storey structure is plotted in Figure 5.14a. The last storey columns were excluded from this plot because these columns only carry gravity loads in a Split-X pattern. In this plot, the color of the circles indicate the storey number for the data. In addition, the relative magnitude of the normalized bending moment demand at the time of CDC_{max} is indicated by the size of the circles. The normalized bending demand, designated hereinafter by M_{fn}, is defined as the ratio of the largest column end bending moment to the plastic moment capacity of the column cross-section assuming zero axial force. As a typical trend, CDC_{max} of the most critical columns showed a fairly uniform distribution among the ground motion records with an inter-event variability as low as 4%. As a general tendency, the largest force demand was imposed on the first storey columns of the low rise models (3- and 5-storey), mid-height columns of the medium-rise models (7- and 9-storey), and columns located at the 2/3 height of the high-rise models (13- and 15-storey). Detailed analysis of the results showed that the most critical storey in the high-rise models, in terms of column axial demand, is at the position of the maximum frame curvature along the building height. At this

position, the frame is subjected to significant overall bending and, as a result, the columns undergo considerable elongation and shortening resulting in large axial force demand. As it could be noticed from Figure 5.14a, the bending demand on the columns is more intense at the bottom and top storeys (the color of the larger dots is either very dark or very light referring to the bottom and top storeys, respectively according to the color bar shown on the right side of the plot), and the columns at intermediate storeys are mainly controlled by axial force demand. These relatively large bending demands in those specific locations are driven by soft-storey mechanism in the lower storeys and higher mode lateral displacement profile at the top levels. For instance, the significant drift concentration at the 2nd and 3rd storey of the 15W-X-C structure (see Figure 5.10) resulted in a large bending demand on the columns at those storeys. Column axial forces in such a condition is not significantly high because only the BRBs in a few storeys reach their maximum axial resistances. In the top levels, higher mode response induces reversed storey shears and drifts in adjacent storeys, which generates large localized flexural demands on the continuous columns. These columns are typically subjected to double curvature moment gradients, $\kappa \geq 0$, at the time of CDC_{max}. Concomitant seismic column axial forces are however small due to opposite directions of floor accelerations.

In the east buildings, the 1st storey columns of the 3-storey frame faced the highest force demand with a largest computed CDC_{max} value of 0.89. Among the east buildings, the most critical storeys, in terms of CDC_{max}, were found to be two levels below the roof. Again, the inter-event variability of CDC_{max} of the most critical columns was low (~5%). Based on this evidence it is concluded that the columns remained elastic and performed satisfactory. This also validates the assumption made in the column modeling.

Statistical analysis of column responses of all Split-X frames show that the bending moment and axial force demands have a rather weak and negative correlation (~ −30%). This implies small probability of having simultaneous large axial force and large bending demand. For instance, the largest bending demands, i.e. $M_{fn} \geq 0.3$, coincide with relatively low normalized axial compression demands, $C_{fn} \leq 0.5$ (the normalized axial force demand is the ratio of the applied axial force to the column nominal axial compressive strength). This observation is not in accordance with the basic assumptions of the capacity-based design approach prescribed for columns in S16. In case of BRBFs, S16 requires that the column resist the effects of an axial force from all BRB members reaching their probable maximum resistances simultaneously plus a uniform bending moment

equal to 20% M_{pc} over the full column height. In Figure 5.14b, fitting a lognormal distribution function to the NTHA results shows that in the worst case, i.e. 9W-X-C building, there would be only 0.5% probability that M_{fn} exceeds 0.2 M_{pc} when axial demand is significant, i.e. $C_{fn} \geq 0.65$. Based on this, it can be concluded that the CSA S16 requirement for the additional design bending moment is conservative for BRBFs. A more reasonable estimate of this design bending demand would be $0.1M_{pc}$ which has around 5% probability of exceedance when axial force demand is large, i.e. $C_{fn} \geq 0.65$.

As mentioned earlier, a value of zero was used at the design stage for the moment gradient factor, κ, assuming that the moments at the opposite ends of the columns are $0.2M_{pc}$ and zero. This assumption was verified by extracting the values of κ factor from NTHA, i.e. the ratio of the smaller to the larger end moments, of each column. The trend of κ factor is plotted versus CDC_{max} for the 15W-X-C model in Figure 5.14a. Last storey columns are not shown in this plot since their κ is always zero (pin condition at the roof level). The plot indicates that there is no specific trend in the κ factor as it varies between −1.0 (single curvature) and 1.0 (double curvature) with a significant cluster between −0.5 and 0.5. This trend in κ factor was also observed in the other prototype frames. While almost zero correlation was found between axial demand and κ, there was around +20% linear correlation between bending demand and κ. The latter implies that at occasions of high bending demand, the columns are more likely subjected to double curvature moment gradient with end moments having opposite signs. Based on this observation, it can be concluded that $\kappa = 0$ could be an appropriate value for design purposes. A robust estimate of design κ and M_{fn} will be presented later in this chapter after adjusting the NTHA results for the uncertainty related to ground motion selection and scaling.

Using capacity design often results in very large design axial forces in the lowers storeys. This is directly related to the underlying assumptions of the method: frame lateral displacement profile follows the first elastic mode shape and all fuse elements (BRBs in this context) reach their maximum probable resistances at the same time. However, this assumption is not entirely valid in mid- and high-rise frames due to dynamic effects. Figure 5.14c shows the trend of C_{fn} for the first-storey of the west Split-X frames. In this figure, the geometric mean of C_{fn} of each frame is connected by a line to highlight the trend in the average NTHA axial force demand. Note that a value of 0.8 for C_{fn} approximately corresponds to the design axial load knowing that a resistance (ϕ) factor of 0.9 and a moment of 0.2 M_{pc} are considered in design. This value is reached in NTHA

for the low-rise buildings. As this plots shows, in the west "soft rock" Split-X models, the average NTHA axial demand constantly decays as the number of storeys is increased from 5 to 13 and drops to 80% of the 3-storey value in case of the 15-storey model. This suggests that capacity design may overestimate column axial force demands in the lower storeys of high-rise braced frames located in "soft rock" sites.

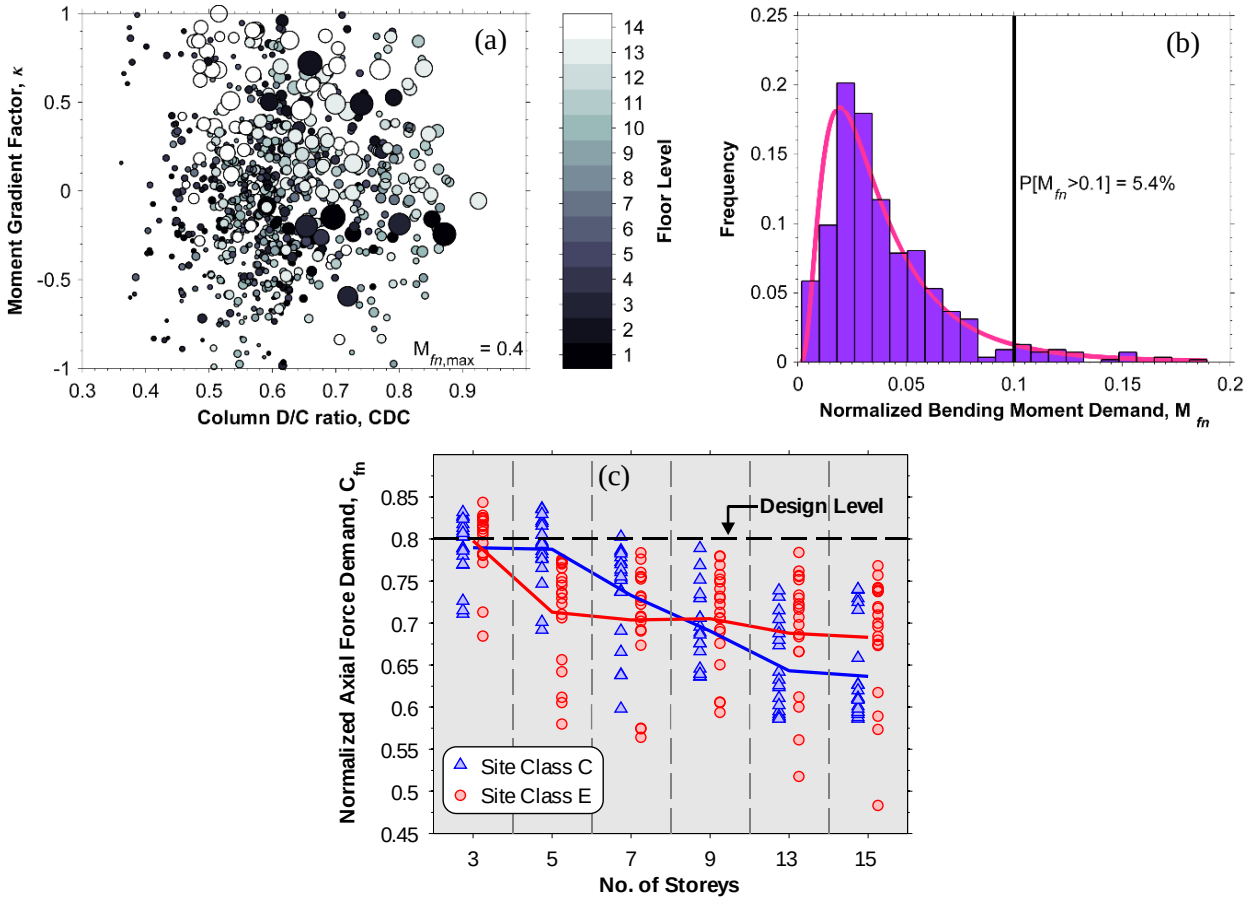

Figure 5.14: a) Trends in maximum column demand/capacity ratio (CDC_{max}) and corresponding κ factor of 15W-X-C model, relative size of circles indicate the intensity of normalized bending moment demand (M_{fn}) and their colour indicate the floor level; b) Distribution of normalized bending moment demand on critical columns of the 9W-X-C model at all instants of high axial load, i.e. $C_{fn} \geq 0.65$; c) Trend of normalized axial force demand on the first storey columns of Split-X frames on site classes C and E in western Canada.

5.6 Effects of important design parameters

5.6.1 Site effects

When seismic stress waves pass through soft soil layers, their amplitude, frequency content, and duration can be significantly altered. NBCC 2010 accounts for the site effects by adjusting the design spectrum using a set of empirical amplification or de-amplification factors. In order to investigate the possible impacts of soft soil site on the seismic demand on BRBFs, the previously introduced prototypes were redesigned for a typical site class E ($V_{s30} \leq 180$ m/s, V_{s30} being the average shear wave velocity in the top 30 meter layers of the site). This resulted in stiffer models because the frames were proportioned for a higher level of lateral loads (see Table 5.1). Numerical models of these prototypes were subjected to set of 20 soft soil ground motion acceleration histories. For the west, records representing the expected west intra–plate earthquakes were retrieved from the PEER ground motion database. A set of records for generic class E site in east was compiled from the simulated soft soil ground motions by Atkinson (2009).

Inelastic demand spectra of the 'soft soil' and 'soft rock' sets were compared to develop some insight into the influence of the site class on the seismic demand. Spectra of maximum ductility (μ_{max}) and cumulative plastic ductility ($\Sigma\mu_p$) were calculated for inelastic single-degree-of-freedom systems that were designed for 2% in 50 years spectral acceleration in Victoria and Montréal with force modification factor $R_d R_o = 4 \times 1.2 = 4.8$. The records were scaled by the LMA technique (see Figure 5.5c) and 5% critical damping was assumed in the analyses. Inelasticity in these SDOFs was simulated using the Giuffré-Menegotto-Pinto mixed hardening model (Filippou, *et al.*, 1983). Constant-strength demand spectra for the intra–plate event in Victoria and Montréal are shown in Figure 5.15. For Victoria, these spectra reveal that in a wide range of periods the 'soft soil' set imposes more demand than the 'soft rock' one. This is more evident at a period of around 2.0 seconds which corresponds to the first-mode period of the 9- and 13-storey prototypes in sites C and E, respectively. On the contrary, in case of Montréal, the site does not have a notable impact on both maximum and cumulative demand indices.

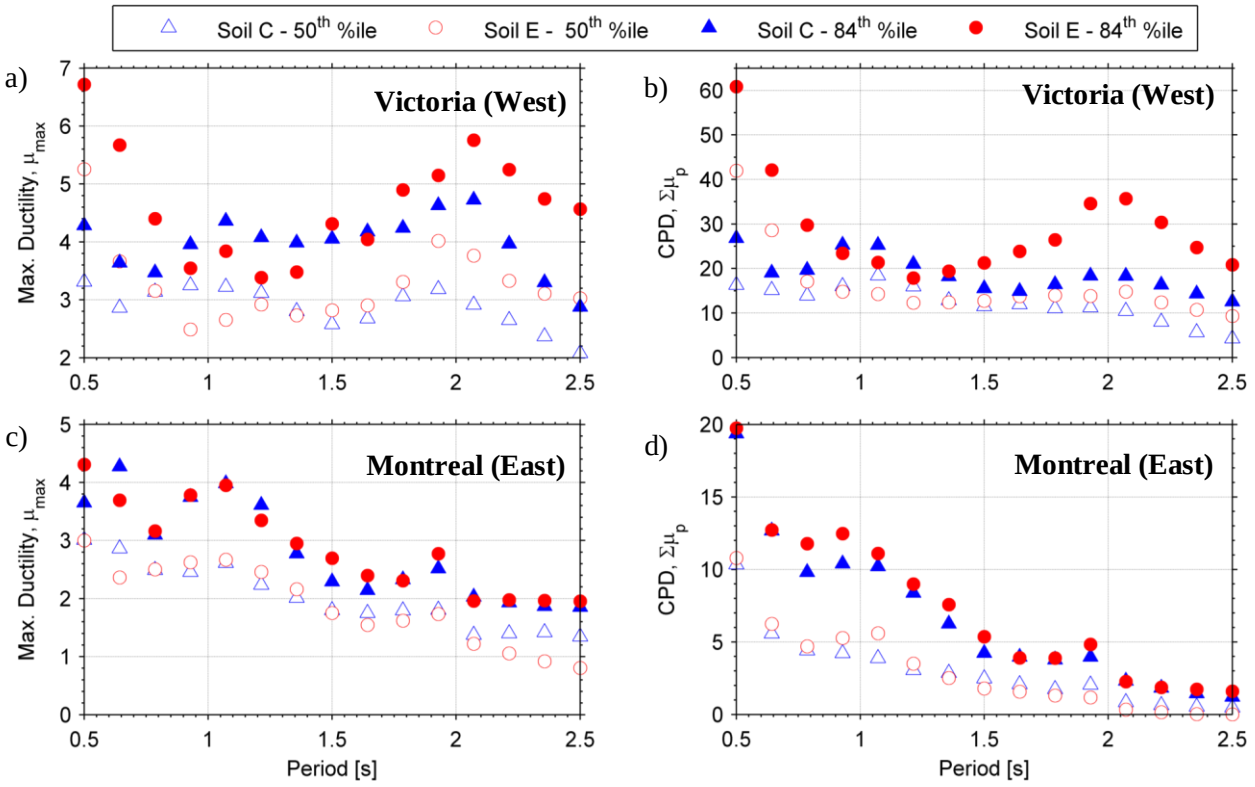

Figure 5.15: Demand spectra for 'soft soil' and 'soft rock' ground motion record suites compiled for intra–plate hazard in: a) and b) Victoria (west Canada); c) and d) Montréal (east Canada).

Because the SDOF analysis indicated insignificance of soft soil effects for the east site, the NTHA procedure of multi-storey buildings was only conducted for the 3- to 15-storey Split-X frames designed for a class E site in Victoria (west). NTHA results from these analyses confirmed the trends observed in the constant-strength spectra of the relevant SDOFs (see Figure 5.16). The median and 84th percentile values of the maximum ductility for the 'soft soil' prototypes are higher in case of the shortest and tallest frames. While the medians are in the same order, differences between the upper tail of maximum ductility for the 'soft soil' and 'soft rock' models become substantial for the prototypes taller than 9 storeys. Percentiles of important global and local demand parameters can be found in Table 5.5.

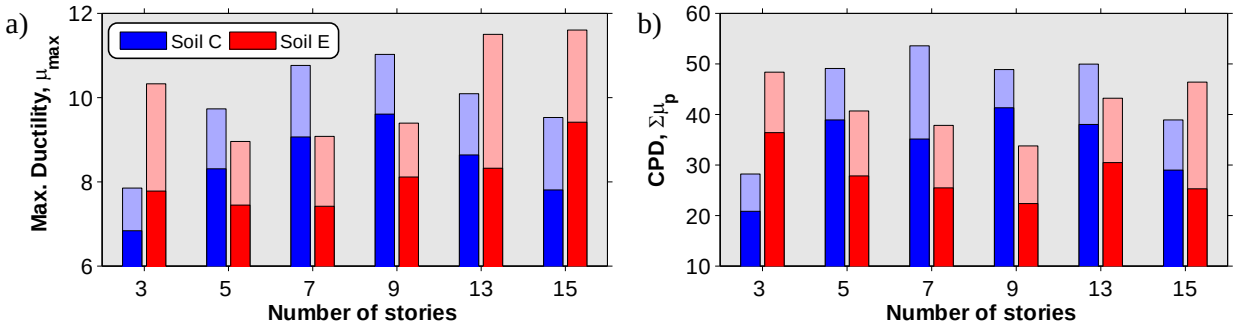

Figure 5.16: Comparison between demand parameters obtained from analysis of Split-X prototypes designed for site soil class C and E in Victoria (Prototypes were subjected to ground motion set representing intra–plate hazard).

Columns of the frames located on soft soils behave similarly to the ones of the "soft rock" prototypes. The largest CDC_{max} is equal to 1.02 and is recorded in the 1st storey column of 3-storey model (3W-X-E). As a distinctive pattern, the axial load demand on the first-storey columns of the soft soil buildings did not reduce significantly as it did in the case of the "soft rock" models (see Figure 5.14c). This could be attributed to the relatively longer duration of the strong pulses in the "soft soil" records compared to the "soft rock" motions. This increases the likelihood of simultaneous yielding of the braces along the frame height and, as a result, increases the accumulated axial loads in the lower storeys. Correlation between important column design parameters, i.e. axial force, bending moment, and moment gradient, is nearly the same regardless of the site conditions (C and E).

Table 5.5: Different percentile levels of important global and local demand parameters of 3 to 15 storey Split-X prototypes designed for class E sites (soft soil) and subjected to intra–plate earthquakes.

Percentile level	**Global Demand Parameter**							**Local Demand Parameters**						
	θ_{max} **[%]**	Λ_{max}	θ_r **[%]**	DCF_{max}	$\theta_{max} - \theta_{min}$ **[%]**	$\Sigma\theta_p$ **[rad.]**	a_{max} **[g]**	μ_{max}	$\Delta\mu^1_{RF}/2$	ξ_{max}	$\Delta\xi^1_{RF}/2$	$\mu_{max} - \mu_{min}$	$\Sigma\mu_p$	N_p
50th	1.8	1.7	0.9	2.2	2.6	0.122	0.60	9.4	5.1	2.5	1.4	10.5	36	45
84th	2.4	2.8	1.5	2.7	3.1	0.179	0.71	11.6	6.3	3.3	1.8	13.0	48	66
96th	3.4	4.3	3.0	3.4	4.4	0.243	0.83	15.5	9.5	4.3	2.7	19.0	79	107
100th	3.4	4.4	3.0	3.6	4.6	0.268	0.86	15.6	10.2	4.3	2.9	20.3	86	122

Fitting lognormal cumulative probability function to the analysis results for the 15-storey prototype shows that the probabilities of observing storey drift ratios greater than 2.5% and storey residual drifts larger than 1.0% under the design intensity are approximately 17% and 40%, respectively (see Table 5.6). Those may be considered as excessive and unacceptable. This observation may imply that the site amplifications factors, especially for periods longer than 2.0 s, need to be revised to achieve acceptable and more uniform collapse risk.

Table 5.6: Unadjusted probabilities of exceeding global performance limits for Split-X frames on soft soil in the west subjected to intra–plate earthquakes (probabilities are shown in percent).

Seismicity Source	Demand Parameter	Performance Limit	Number of storeys					
			3	5	7	9	13	15
West Intra–plate	$\theta_{\max}$	2.5%	3.7	1.1	0.6	0.3	11.4	16.6
	θ_{r}	1.0%	11.4	10.0	7.9	1.0	40.6	40.4
	$\Lambda_{\max}$	2.0	20.1	4.1	1.9	0.7	33.4	34.1

5.6.2 Effect of bracing pattern or length of YS

Another important issue in the estimation of the inelastic demand in BRB members is the bracing pattern of the frame. Analytically, it can be shown that for equally-designed BRBFs, the core YS ductility is mainly affected by the yielding length ratio (γ) and is almost independent of other parameters such as brace angle, bracing pattern, and core material grade. In the preceding sections, the demands on BRBFs were estimated using the results of Split-X prototypes which, for the same storey aspect ratio, can have smaller γ compared to other popular bracing pattern, that is, the diagonal configuration. In line with the mentioned hypothesis, core YS ductility in BRBs with arbitrary γ ratios can be simply estimated by applying a factor $0.55/\gamma$ to the results of the Split-X models presented in the preceding sections of this chapter. This hypothesis was examined by conducting time history analyses on 3- to 9-storey diagonally braced frames using the basic set of scaled ground motion records from west intra–plate earthquakes. These frame models were designed for a 'soft rock' site in Victoria, BC. The length of the core YS of the BRB members is assumed to be 70% of the brace center length dimensions, i.e. γ = 0.7. Comparison between statistics of the major local demand parameters obtained from post-processing of the 3- to 9-storey Split-X and Diagonal models is made in Table 5.7. Analysis results indicate that the demand is less intense in the 'equivalent' Diagonal braced frames. Ratios of the demand parameters are close to the predicted value, i.e. 0.55/0.7 = 0.78. These ratios are also nearly invariant with respect to the percentile levels. Comparison between parameters $\mu_{\max}$ and ($\mu_{\max} - \mu_{\min}$) indicate that the response of the Diagonal frames tend to be more symmetrical than the corresponding Split-X model. Based on these observations, one may generalize the ductility demand computed from the studied Split-

X prototype for BRBFs with an arbitrary γ using scale factor of $0.55/\gamma$. However, estimating the demand on BRBFs with extremely short yielding segment ratios, e.g. $\gamma \leq 0.20$, by the proposed scale factor may give overly conservative values. For such cases, a more accurate analysis is required to account for the contribution of non-yielding segments to the total deformation.

Comparing the demand amplitude predicted by the parameters μ and ξ, it is shown that both parameters have the same degree of accuracy for predicting the demand when μ is adjusted according to the proposed solution. By definition, the parameter ξ includes all the basic properties of BRB member (A_{sc}, F_{ysc}, γ, η, χ, and ψ) as well as the basic parameters related to the design of the lateral load resisting system (R_o, R_d, and I_E). Thus, it was expected that the demand estimated by ξ would be the same for both Split-X and Diagonal frames. On the other hand, the parameter μ only includes F_{ysc} and the brace angle (ψ). As a result, the computed demand in terms of μ under the same ground motion would not necessarily be the same when the basic design parameters are changed. In other words, the parameter ξ is supposed to be more robust than the core YS ductility as it does not need modification to account for other possible combinations of design parameters. However, in terms of cumulative plastic demand and low cycle fatigue damage, using the parameter μ would be more straightforward as it reflects the pure strain demand on the core YS of the brace.

Table 5.7: Ratio between local demand parameters in the 3- to 9-storey Diagonal and Split-X BRBFs designed for "soft rock" site in Victoria, BC (west of Canada).

Percentile level	**Demand Parameters**								
	μ_{max}	$\Delta\mu^1_{RF}$	$\Delta\mu^2_{RF}$	ξ_{max}	$\Delta\xi^1_{RF}$	$\Delta\xi^2_{RF}$	$\mu_{max} - \mu_{min}$	$\Sigma\mu_p$	N_f
50th	0.56	0.85	0.78	0.72	1.13	1.00	0.77	0.59	0.65
84th	0.59	0.80	0.75	0.83	1.03	1.05	0.80	0.65	0.67
96th	0.60	0.80	0.73	0.75	1.00	0.92	0.77	0.54	0.59
100th	0.61	0.81	0.71	0.69	1.06	0.93	0.79	0.53	0.58

It was also observed that the columns of the Diagonal BRBFs sustained slightly higher force demands than the Split-X models. In the most extreme case, CDC_{max} = 1.06 was obtained for the 5th floor column of the 7W-D-C model. The bending moment demand in the columns of the

Diagonal frames was also larger compared to that observed in the Split-X models, especially in the top storeys. As shown in Figure 5.17, bending moments as large as $0.5M_{pc}$ were imposed on one of the last storey columns of the 7W-D-C model. However, at the time of this bending moment, the axial force was nearly zero (see Figure 5.17). As it was the case for the previously studied models, the correlation between axial forces and bending moments was weak and negative, and no correlation was found to exist between the κ factor and axial forces. The critical CDC_{max} for the low-rise models (3- and 5-storey) occurred at the first level whereas the floor levels in the upper third of the building height were found to be critical for the columns of the medium-rise (7- and 9-storey) frames.

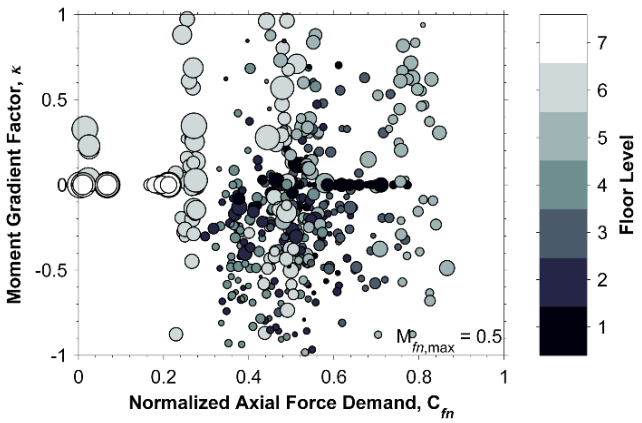

Figure 5.17: Normalized axial force demand versus κ factor in the columns of the 7W-D-C building.

5.6.3 Effect of core material grade

In the previous sections of this chapter, inelastic demand was estimated based on NTHA of prototypes incorporating 345 MPa steel BRB cores. In practice, BRB members with lower grade material for the core would be beneficial when code drift limits are not met with BRB built with higher strength steel cores. However, under the same storey drift, BRBs with lower steel grade core undergo larger ductility demand in comparison to those with higher grade core as a result of having lower yield deformation. When two BRBFs are designed to have the same T_1 with different grades of core steel; it can be shown that the ductility demands would be almost proportional to square root of their core grade ratio. For instance, if the core of these hypothetical BRBFs are made from 225 and 345 MPa steels, the ductility demand on the lower grade core would be $(345/225)^{½} \approx 1.25$

times higher than the ductility on the higher grade core. In theory, these frames are supposed to experience the same displacements since their periods are same. Given that the periods are the same, the ½ exponent accounts for difference in their stiffness since the elastic period is proportional to the square root of the elastic stiffness. This implies that the ductility demand computed in the preceding sections needs to be adjusted for the effect of core steel grade.

To investigate the possible effects of steel core grade on the core YS ductility demand, the results of time history analysis of the most damage prone prototype in the west (9W-X-C) are compared to those of an 11-storey BRBF designed for the same site but with a core grade of 225 MPa. The 11-storey model was chosen because its first-mode period, i.e. T_1 = 1.88 s, is almost equal to that of the 9W-X-C model so the hypothesis presented above could be verified. The same ground motion records with identical scaling factors were used in the nonlinear time history analysis of these two prototypes.

Table 5.8 summarizes the ratios between key demand parameters for the two frames. Most global demand parameters are found to be lower for the 11-storey model except for the maximum floor accelerations. At the 84th percentile level, storey drift-related parameters for the 11-storey model are 80% lower than the corresponding ones for the 9-storey model. This is attributed to the ratio between the heights of the 9- and 11-storey models which is 36 m / 44 m = 0.81. If these model experienced the same roof displacements and drift concentration factors, storey drift ratios in the 11-storey frame would be 81% of the drifts observed in the 9-storey frame. On the other hand, the core YS ductility-related demand parameters are higher for the 225 MPa core of the 11-storey BRBF compared to the 345 MPa core of the 9-storey model by a factor close to, in an average sense, the predicted amplification factor of 1.25 ($\approx \sqrt{345/225}$). Based on this observation, one may estimate the core YS ductility demand in BRBFs with an arbitrary core steel grade using the results of this study and adjusting them by factor $(345/F_{ysc})^{½}$.

Table 5.8: Ratio between demands computed from an 11-storey frame with F_{ysc} = 225 MPa and a 9-storey frame with F_{ysc} = 345 MPa. (Both frames have a Split-X bracing pattern and were designed for "soft rock" site in Victoria in west Canada).

Percentile level	Global Demand Parameter							Local Demand Parameters				
	θ_{max}	Λ_{max}	θ_r	DCF_{max}	$\theta_{max} - \theta_{min}$	$\Sigma\theta_p$	a_{max}	μ_{max}	ξ_{max}	$\mu_{max} - \mu_{min}$	$\Sigma\mu_p$	N_p
50th	0.76	0.92	0.69	0.91	0.80	0.88	1.14	1.20	1.23	1.14	1.20	1.17
84th	0.80	0.90	0.93	0.91	0.79	0.97	1.18	1.16	1.23	1.24	1.23	1.17
96th	0.72	0.80	0.66	1.03	0.87	1.20	1.16	1.20	1.08	1.26	1.16	1.16
100th	0.70	0.79	0.62	1.05	0.86	1.19	1.16	1.24	1.05	1.28	1.11	1.15

5.6.4 Effects of frame vertical irregularity

In NBCC 2010, structural system irregularities are classified into 8 types and response spectrum analysis may be required, in some circumstances, if a building structure is prone to these system irregularities. In this study only vertical stiffness/strength irregularity is discussed and it is assumed that the other irregularities will not affect the seismic demand as long as the code requirements for those systems are met. Tremblay *et al.* (2005) studied the effects of severe mass irregularity on the seismic performance of 8-storey concentrically braces frames using NTHA. This study concluded that mass irregularity had negligible impacts on the seismic demand when the design forces were calculated using response spectrum analysis. The NBCC 2010 definition for vertical stiffness irregularity reads as follows:

> "Vertical stiffness irregularity shall be considered to exist when the lateral stiffness of the seismic force resisting system in a storey is less than 70% of the stiffness of any adjacent storey, or less than 80% of the average stiffness of the three storeys above or below".

For steel braced frames, to the author experience, the first irregularity criterion (stiffness difference between two adjacent storeys) can be avoided in most cases. Conversely, the second criterion is generally met in the upper levels (structure has vertical stiffness irregularity) unless overdesigned

braces and columns are used in these levels. This extra overstrength may cause concentration of inelastic demand in the lower storeys since the upper storeys will undergo less inelasticity, if any, owing to their more-than-required shear strength. This indicates that attempting to avoid vertical stiffness irregularity may have adverse effects on the structure seismic performance. For BRBFs, this shortcoming might be overcome by adjusting the length of the core YS in the upper levels to achieve uniform stiffness while keeping the core YS cross-sections to the minimum required to resist the design storey shear. In this study, this option was not considered, however, but the second criteria on relative stiffness between storeys was intentionally ignored in the design of the prototypes.

In practice, it often happens in BRBF design to use the same core section for two or three consecutive storeys to facilitate the process of fabrication and installation. This practice also increases the frame stiffness and overstrength which may cause additional concentration of inelastic demand on a few storeys and, as a consequence, increase the probability of structural collapse. To quantify the impacts of this practice, the most critical prototype, i.e. 9W-X-C, was rearranged so that the core YS cross-sections are only changed at every: 1) two storeys; and 2) three storeys. These prototypes are denoted by moderately irregular (MI) and severely irregular (SI) models. Response spectrum analysis of these models resulted in minimal changes for the required storey shear strength in comparison with the equivalent static force method. In accordance with the capacity design principles, the braced bay columns were resized based on the adjusted strength of the modified core YS cross-sections. Since storey heights and braced bay spans are identical at all levels, storey shear strengths only change at every two or three levels of the MI and SI models, respectively. The mentioned design practice often results in sudden changes in the profile of the total storey stiffness (see Figure 5.18a) which may cause soft storey effect. NTHA were conducted on these models using the basic set of scaled records for the west intra–plate earthquakes. In Figure 5.18b, statistics of the peak storey drift ratios of the regular and irregular models are compared. This figures shows that the displacement demand was increased at the first floor and decreased at the adjacent levels when the frame becomes more irregular. In the most severe case, the displacement demand increased by factor of 2 at the 7^{th} storey of the severally irregular frame, where the most abrupt change in shear stiffness was present (see Figure 5.18a). However, the mean and 96^{th} percentile of the maximum response only show increases of 1.13 and 1.22 for the MI and SI models, respectively. As a rule of thumb, the amplification factor due to this

practice can be estimated by the ratio between the provided storey shear strength and the design storey shear. This simplified estimation is not valid for the last storey. The observed behaviour may emphasis on the importance of avoiding excessive storey overstrength and on the fact that using elastic response spectrum analysis may not be sufficient to prevent unwanted response.

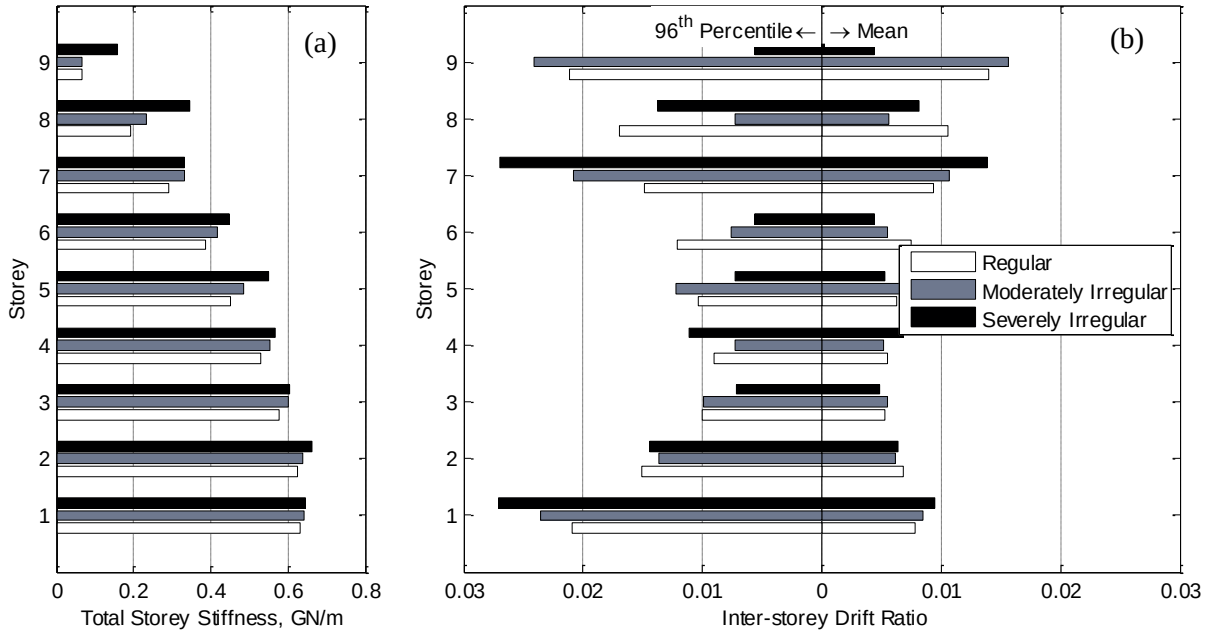

Figure 5.18: Vertical frame irregularity in prototype 9W-X-C and its impact on: a) storey stiffness; b) storey drift ratios.

5.7 Robust estimate of the demand

5.7.1 Results of the alternative ground motion sets

Nonlinear time history analyses were repeated for the west prototypes under the alternative ground motion record sets (see Section 5.4.2.1). Statistics of major local demand parameters for the most critical prototypes are presented in Table 5.9. While the median demand from the LMA-, MFP-, and MSE-scaled alternative sets are comparable, there is a notable difference in the upper tail of the demand. This difference is mainly attributed to the differences in variability that result from each scaling method (Dehghani, *et al.*, 2016c). In some cases, the MFP-and MSE-scaled sets resulted in large drift ratios (around 4–5%) that could be interpreted as failure to comply with code requirements. In general, the MFP-scaled set imposed the most severe demand to the high-rise

models. In contrast, the MSE-scaled set was more critical in case of the low-rise prototypes. This trend is directly attributed to the RTR variability profile associated to each scaling method. The MFP method tends to produce greater RTR in the short period range of the response spectrum (see Figure 5.7a), which can result in a larger contribution from higher modes. On the other hand, the MSE method typically gives higher RTR at longer periods of the spectrum. This can produce significant displacement demand on low-rise building when its fundamental period is elongated due to inelastic actions (see Figure 5.7b). Analysis results showed that the MSE-scaled set imposed a roof drift that was nearly two times the expected design value ($R_o R_d \delta_{roof}$), and the MFP-scaled set resulted in a significant cumulative inelastic ductility demand at the roof level of the 13-storey model.

Table 5.9: Statistics of demand parameters in the Split-X west prototypes subjected to intra–plate earthquakes of the alternative suites of ground motions scaled using three scaling techniques.

Percentile Level	**Scaling method**											
	LMA				**MFP**				**MSE**			
	Λ_{max}	ξ_{max}	μ_{max}	$\Sigma\mu_p$	Λ_{max}	ξ_{max}	μ_{max}	$\Sigma\mu_p$	Λ_{max}	ξ_{max}	μ_{max}	$\Sigma\mu_p$
50th	1.2	2.4	9.2	37	1.8	3	10.6	73	1.9	2.6	9.8	47
84th	1.6	3	10.7	48	3	3.5	12.5	110	2.9	3.5	13.3	61
96th	2.9	3.3	11.9	55	4.4	4.6	14.7	170	6.3	5.9	21.1†	97
Critical*	9	9	9	9	9	15	15	13	5	5	7	5
Ratio**	1.2	1.1	1.1	0.9	2.7	1.5	1.3	2.2	2.0	1.5	1.4	1.6

† Analysis resulted in one case of storey drift ratio greater than 5%.

* Storey with the most severe demand at most of the percentile levels.

** Ratio between computed demand from alternative and basic sets (evaluated at the 84th percentile)

5.7.2 Adjustment for record selection and scaling uncertainty

As the comparative study of the previous section showed, there is considerable uncertainty in the estimated demand parameters which is mainly rooted in the record scaling, and partially in the record selection. Since there is no universally accepted record selection and scaling method, the associated uncertainty to this process may be treated as an epistemic or systematic source of uncertainty. A simple approach to treat such a source of uncertainty would be to take a weighted average of the outcomes of the different possible options for a procedure. By applying this approach, one can adjust the estimated value of a demand parameter at any given percentile by using weighted percentiles of that parameter which was obtained from different selection and scaling techniques:

$$\tau_{x^{th}} = 0.5\ \tau_{x^{th}}^{LMA} + 0.25\ \tau_{x^{th}}^{MFP} + 0.25\ \tau_{x^{th}}^{MSE} \tag{5.21}$$

where $\tau_{x^{th}}$ is the robust or adjusted estimate of the x^{th} percentile of the generic demand parameter τ. The proposed weighting factors were assigned based on the ability of various scaling techniques in maintaining the RTR variability of the spectral accelerations to a reasonable level. Table 5.10 shows the robust estimate for different percentile levels of the key global and local demand parameters obtained from NTHA using the alternative record set which was scaled by three different scaling methods. Depending upon the percentile level, this adjustment procedure resulted in 110% to 150% increase in the estimated demand calculated from the ‘LMA-scaled basic set’.

Table 5.10: Robust (adjusted) estimate of some important global and local demand indices obtained from NTHA results of 3- to 15-storey west Split-X models subjected to intra–plate source.

Percentile level	Global Demand Parameter						Local Demand Parameters							
	θ_{max} [%]	Λ_{max}	θ_r [%]	DCF_{max}	$\theta_{max} - \theta_{min}$ [%]	$\Sigma\theta_p$ [rad.]	μ_{max}	ξ_{max}	$\Delta\mu_p{}^1$	$\Delta\mu_p{}^2$	$\Delta\mu_p{}^3$	$\mu_{max} - \mu_{min}$	$\Sigma\mu_p$	N_p
50th	1.6	1.4	0.7	2.9	2.5	0.119	10	2.6	6	5	4	11	45	22
84th	2.1	2.3	1.3	4.0	3.0	0.163	12	3.1	9	7	5	13	63	30
96th	2.7	3.8	2.5	5.7	4.0	0.222	14	4.2	12	9	7	17	83	34
100th	2.9	4.2	2.8	6.3	4.2	0.231	14	4.4	13	11	7	18	87	35

For any given demand parameter, the probability of exceeding performance limit at the global and local levels were also adjusted by using a weighted probability density function with the following weighted mean and variance:

$$\hat{\mu}_w = \sum_i w_i \hat{\mu}_i \tag{5.22}$$

$$\sigma_w^2 = \sum_i w_i \sigma_i^2 + \sum_i w_i \hat{\mu}_i^2 - \left(\sum_i w_i \, \hat{\mu}_i \right)^2 \tag{5.23}$$

where, $\hat{\mu}_i$ and σ_i^2 are the mean and variance of any given demand parameter (in logarithm scale) computed using i^{th} 'record set and scaling method', and w_i are the weight factors assigned to each 'record set and scaling method' as shown in Eq. (5.21). It should be noted that the so-obtained weighted average PDF would not be necessarily lognormal. Theoretically speaking, the weighted average results should follow Gaussian mixture type of PDF (Kottegoda, *et al.*, 2008). However, given that the average results of the studied 'record sets and scaling methods' were fairly similar, it is assumed that the weighted demand parameters follow lognormal distribution. Results of this

study confirmed that the difference between the cumulative distribution of the assumed lognormal model and the theoretical one, i.e. the Gaussian mixture model, is insignificant. Implementing lognormal distribution model also simplifies generalization of the proposed uncertainty treatment procedure to the other cases for which the impacts of record selection and scaling is not assessed directly. The adjusted probabilities of exceeding certain performance limits for the west prototypes under intra–plate earthquakes are shown in Table 5.11. In terms of θ_{max} and μ_{max}, the probabilities are still acceptable after adjustment. However, the probability of observing excessive residual drifts is high.

Table 5.11: Adjusted probabilities of exceeding performance limits for the Split-X west prototype located on "soft rock" sites and subjected to intra–plate earthquakes (values are in percent).

Demand Parameter	**Performance Limit**	**Number of storeys**						
		3	**5**	**7**	**9**	**13**	**15**	**Median**
θ_{max}	2.5%	2.7	3.4	6.1	6.5	2.1	4.2	3.8
θ_{r}	1.0%	9.4	12.9	23.8	30.8	23.4	27.8	23.6
Λ_{max}	2.0	15.1	18.9	20.4	25.8	6.3	9.3	17.0
μ_{max}	15	0.3	0.6	1.2	1.0	0.2	0.6	0.6

Plots in Figure 5.19 show the adjusted cumulative distribution functions (CDF) of important demand parameters at global and local levels. One important implication of these weighted distributions is to compare the robustness or stability of similar demand parameters. This could be done by computing inter-prototype variability using geometric coefficient of variation (Kottegoda, *et al.*, 2008 - p. 216) of the weighted standard deviations. For instance, at the global level, inter-prototype variability of θ_{max} was slightly less than Λ_{max}, which implies that the 'maximum storey drift ratio' would be more stable predictor of displacement demand than the 'maximum amplification of design storey drift'. The same comparison at the local level reveals that ξ_{max} was slightly more stable than μ_{max}. Similar trend was also observed for the unadjusted demand

parameters indicating that the proposed adjustment procedure did not alter the relative stability of the studied demand parameters.

As mentioned earlier, current CSA S16 requires to amplify the storey design drift of BRBFs by factor of 2.0 to estimate the strain amplitude expected in BRB members. This strain demand would then be the largest amplitude of the cyclic test which needs to be performed on full-scale BRB members in order to qualify their performance. Brace strength adjustment factors ω and β are also obtained from testing at this target strain demand. Findings of the current study shows that the design brace axial deformation (δ_d in Eq. (5.18)) would be a more stable and consistent parameter for estimating strain demands in brace members in comparison with the storey drift ratio. NTHA results also indicated that the ξ_{max} index has better correlation with the core YS ductility (μ_{max}) in comparison with Λ_{max}. Inter-prototype variability of the parameter ξ_{max} (4.8%) was also lower than the one from Λ_{max} (8.6%), which may imply that the ξ_{max} is a more robust parameter for seismic demand estimation than Λ_{max}.

Figure 5.19c shows the adjusted CDF of the largest amplitude of the parameter ξ that was obtained after Rainflow cycle counting. It should be noted, for the purpose of strain amplitude estimation, that dividing cycle counted ranges of ξ by two is more consistent than using half of ξ_{max}. The former index accounts for any degree of response asymmetry while the latter is only valid when response is fully symmetric. Based on the adjusted probability function, it is suggested to estimate the brace strain amplitude by amplifying the design brace axial deformation, not the design storey drift, by a factor of 2.0. The mean probability of exceeding the suggested value across all the frames studied (after removing the outlier model, i.e. 3W-X-C), and in the most critical prototype (9W-X-C) are 8% and 12%, respectively. Removing the outlier model from the probability calculations gives a more conservative outcome as the 3-storey model has the lowest ξ_{max} values among the studied structures. In the probability calculations, only the results of the critical storey over the frame height and under each ground motion was employed. Alternatively, if the response from all storeys are collectively implemented in the probability fitting procedure, the mean probability of observing $½\Delta\xi^{1}_{RF} \geq 2.0$ reduces to 0.7% which denotes a very small likelihood. In this data treatment approach, there would be 10% chance of exceeding 1.65 times the brace design deformation. The latter approach is deemed to be more consistent with the behaviour of BRBFs since this system is vulnerable to soft storey mechanism as the NTHA results showed drift concentration factor, DCF_{max}, of 4.1±0.4 at 10% probability of exceedance. Based on this, the likelihood of reaching a

large strain demand in braces of all storeys would be very low (see Figure 5.10). One practical design approach would be to make a distinction between floor levels that are susceptible to soft storey mechanism and those that are not. Then, an amplification factor of 2.0 would be used for strain estimation of braces located in the 'soft storey-susceptible' levels. For braces in the remaining storeys, an amplification factor of 1.65 could be implemented. NTHA results showed that for low- to medium-rise (3 to 7 levels), storeys located below 1/3 of the building height are susceptible to soft storey mechanism. For taller BRBFs (9 to 15 levels), soft-storey is expected in the lower 1/8 of the frame height.

Λ_{max} is an important demand parameter which could be used in design and evaluation of drift-sensitive non-structural elements such as windows. Accordingly, an appropriate amplification factor of this parameter may be needed for this purpose. To avoid catastrophic failure of the drift-sensitive non-structural elements and components, a stricter probability exceedance criterion can be imposed compared to the design brace deformation. Assuming a tolerable probability of exceedance of 5%, the results show that the design storey drifts would need to be amplified by factors of 2.6 and 1.65 in the 'soft storey-susceptible' levels and the remaining storeys, respectively.

When compared to the study by Sabelli, *et al.* (2003), robust estimates of maximum ductility and cumulative inelastic ductility, parameters μ_{max} and $\Sigma\mu_p$, showed 25% and 50% reduction, respectively. Comparison is made at the 84^{th} percentile level of the demand in the most critical prototype under the design level earthquake intensity. Currently, U.S. and Canadian steel design codes require reaching at least 200 cumulative inelastic ductility at the end of qualification testing. At 10% probability of exceedance, the robust estimate of the cumulative inelastic ductility of the studied "soft rock" Split-X models was found to be around 75.

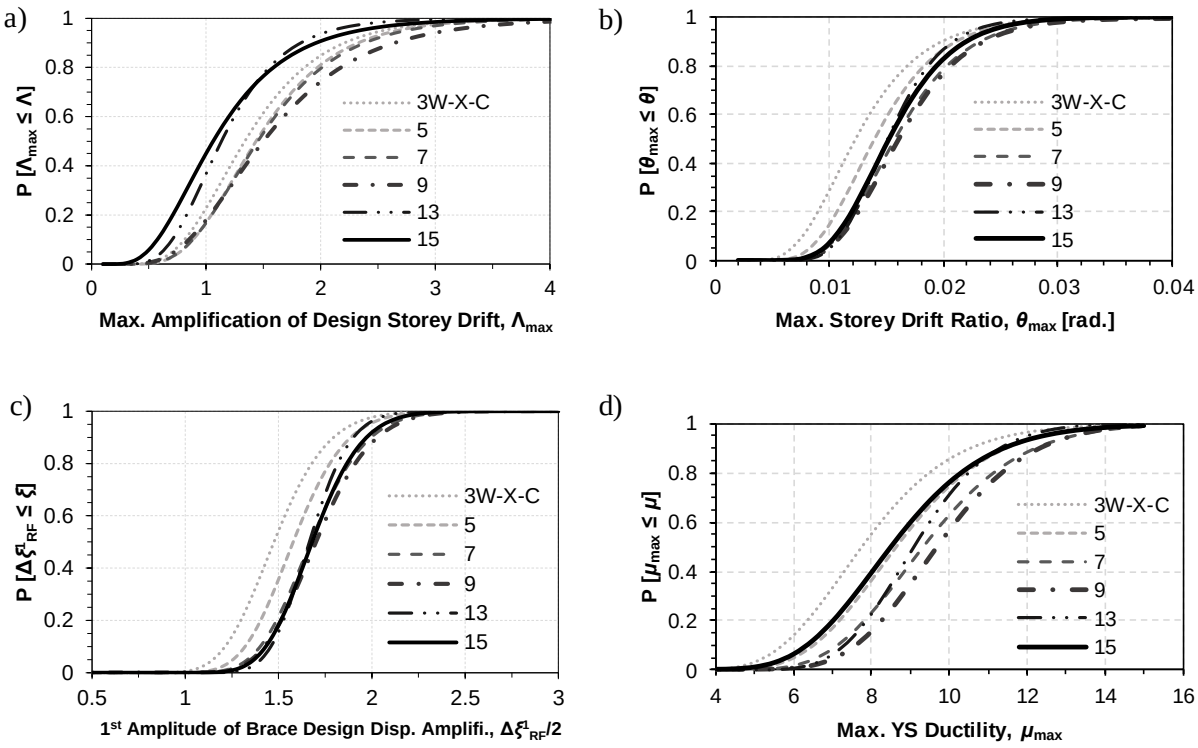

Figure 5.19: Adjusted cumulative distribution function of various important global and local demand parameters for Split-X models under west intra–plate source.

The abovementioned procedure for the evaluation of ground motion selection and scaling impacts on the response estimation was limited to the case of west prototypes under intra–plate source. To adjust the exceedance probabilities for the east prototypes, the log-transformed mean and standard deviation of the demand parameters obtained for the east prototype under the basic ground motion set and LMA scaling were amplified. The amplification factors were obtained by comparing the basic and adjusted statistics of the west Split-X prototypes under the intra–plate earthquakes. It was assumed that record selection and scaling had similar impact on the statistical distribution of the seismic demand regardless of the seismic hazard source. Further calculations on these indirectly adjusted results suggest to use design displacement amplification of 2.1 for the BRBFs designed for east of Canada. The average probability of exceeding this amplification factor would be same as the one for the west Canada BRBFs, i.e. 10%. Table 5.12 summarizes the amplification factors of the design parameters for the studied BRBFs in east and west of Canada. In this table, the values shown in the brackets are computed based on the statistics of the demand parameters from

maximum response of all storeys while the values shown before the brackets are based on the results of the most critical storey.

Comparing to the "soft rock" sites, design storey drifts for the soft soil BRBFs should be amplified with a larger factor. This is directly related to the increased vulnerability of BRBF systems to soft-storey mechanism when they are subjected to low frequency content of the soft soil strong ground motions. This vulnerability is more dominant for the models taller than 9 storeys (having periods longer than 2.0 seconds). If the 13- and 15-storey prototypes are removed from statistical analysis, the recommended amplification factor of design storey drift would be reduced to 2.5 which is similar to the recommended factor for the west Canada "soft rock" sites. As a general design recommendation, using BRBFs as stand-alone lateral system in high-rise buildings, e.g. more than 9 storeys, on soft soil sites should be avoided. For such buildings, BRBFs can be placed in parallel with other systems that have proper self-centring capability to reduce the likelihood of soft-storey mechanism.

Table 5.12: Suggested amplification factor of two important BRBF design parameters.

Design Parameter	**Tolerable Probability of Exceedance**	**West Intra–plate**		**East Intra–plate**
		Site Class C	**Site Class E**	**All site classes**
Brace displacement, (see Eq. (5.18))	10%	2.0 [1.65]*	2.1 [1.70]	2.0 [1.70]
Storey drift, $R_o R_d \Delta_f / I_E$	5%	2.6 [1.65]	3.6 [1.90]	2.7 [1.80]

* Numbers before bracket are suggested for design of the levels that are vulnerable to soft-storey mechanism (typically lower ones) and the value inside brackets is recommended for design of other storeys.

The adjusted CDF of design parameters related to the braced bay columns are shown in Figure 5.20. The mentioned adjustment process indicates that the probability of exceeding demand/capacity ratio of 1.0 would be as low as 2%. It also implies that there is approximately 7% chance that the

normalized bending moment demand, M_{fn}, would exceed 20% of the column plastic moment, M_{pc}. To achieve 10% probability of exceedance, the design bending moment could be reduced from 20% to 15% of M_{pc}. As it was indicated, there is no specific trend for the bending moment gradient factor, κ, as this factor was found to vary between −1.0 and 1.0. However, the adjusted probability models indicate that the chance of having $\kappa \leq -0.5$ at the time of maximum demand/capacity ratio or at all occasions of large axial demand ($C_{fn} \geq 0.65$) would be below 13%. It is recalled that using the current recommended value $\kappa = -1.0$ for column design represents the most conservative assumption (single curvature uniform bending profile that has the largest moment amplification factor). Based on this observation, it is suggested to relax this requirement by proposing to design columns of BRBFs for simultaneous effects of an axial force corresponding to the probable resistances of the BRB members and end bending moments equal to $0.15M_{pc}$ and $0.075M_{pc}$ in a single curvature mode ($\kappa = -0.5$).

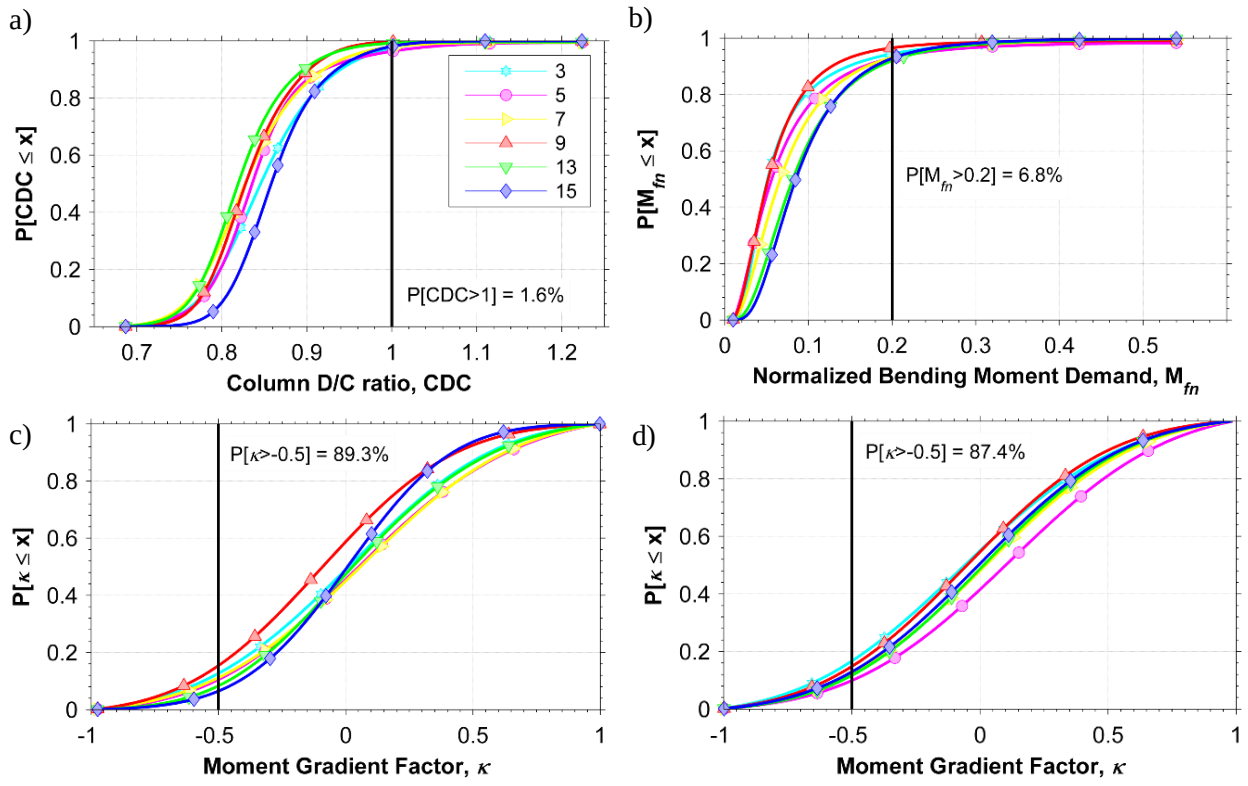

Figure 5.20: Adjusted CDF of: a) maximum column demand/capacity ratio, CDC_{max}; b) normalized bending moment demand on columns at the time of CDC_{max}; c) moment gradient factor at time of CDC_{max}; and d) moment gradient factor at all occasions of large axial forces (i.e. $C_{fn} \geq 0.65$).

5.8 Observations and conclusions

The inelastic seismic response of buckling-restrained braced frames was quantified using nonlinear time history analysis (NTHA) for multi-storey buildings located in two earthquake-prone regions of Canada: Victoria, British Columbia, along the Pacific coast in western Canada, and Montréal, Quebec, in eastern Canada. The structures were designed in accordance with the NBCC 2010 and CSA S16-09 standards. Different site-representative earthquake scenarios were considered in the ground motion record selection to account for the uncertainties related to ground motion selection and scaling. The following observation and conclusions can be made from this study:

- For all buildings, seismic strength requirements governed the design of the frames and drift limits did not impact the design. Notional loads and P-delta effects had more influence on the structures located in eastern Canada where the specified seismic loads are lower.
- The NBCC empirical expression for the first mode period of braced frames tends to underestimate the actual period of the BRBFs studied, especially in east Canada. A modification to this expression for BRBFs is suggested.
- Storey drifts were found to be non-uniform along the building height of the studied frames, especially in case of west intra–plate design earthquakes. This is mainly due to formation of soft-storey mechanism at some specific levels. Analysis results showed that in BRBFs having 7 storeys of less, storeys located below 1/3 of building height are susceptible to soft-storey mechanism. For taller BRBFs, soft-storey was observed in the lower 1/8 of the frame height.
- Ground motion scaling has considerable effects on seismic demand estimates and the results from conventional scaling approaches may require adjustments to account for an artificially high record-to-record variability resulting from these scaling approaches. A simple statistical procedure is proposed to treat the uncertainties associated with the ground motion selection and scaling. As a result of the proposed procedure, the median and standard deviation (in log scale) of the results was increased by factors of 1.1 and 1.35, respectively. Subsequent conclusions given herein are drawn from the results obtained using that proposed approach.

- For the western site, inter–plate earthquakes at long distance imposed less inelastic deformation demands compared to crustal events at closer distances. The inelastic demand in the west was also higher than that induced by earthquakes with richer high frequency content anticipated in east Canada. On average, the brace inelastic deformations and the cumulative inelastic demand in the west prototypes caused by inter-plate and crustal earthquakes was nearly 2 and 4 times larger than the ones obtained for the east frames, respectively.

- The seismic demand on BRBFs designed for "soft soil" condition in west Canada is more than the corresponding system on "soft rock" sites. NTHA results from soft soil ground motion records suggested that the foundation factors for periods shorter than 0.5 and longer than 2.0 seconds may need to be revised to ensure uniform performance and collapse risk. For the time being, caution should be exercised when using BRBFs as single lateral force resisting system for buildings taller than 40 m and located on soft soil sites in the west.

- Force demands on braced bay columns did not exceed the columns' factored resistances. Demand/Capacity ratios of critical columns were dominated by axial forces induced by simultaneous yielding of braces in storeys above the level under consideration. Maximum bending moment demands on columns generally occurred in single curvature and did not coincide in time with peak axial force demands. In general, the correlation between axial forces and bending moments was found to be weak and negative. The moment gradient factor, κ, and the axial force are also deemed to be uncorrelated. The axial force demand computed from capacity design approach are deemed to be conservative for the lower storeys of buildings taller than 5-storeys, especially in case of "soft rock" sites. For high-rise BRBFs (13-storey and taller), the design column forces from capacity design could be reduced in the lower storeys.

- The ductility of the core yielding segment is shown to be the most robust parameter for estimating the seismic demand at the brace level. However, this parameter depends on the length and material grade of the brace core yielding segment. Simple adjustment approaches are suggested to account for the effect of these variables on the estimated response. The suggested adjustments were validated using comparative NTHA studies.

Adjusted yielding segment ductility can serve as the amplitude parameter of qualification testing protocols for BRBs having arbitrary yielding segment lengths and material grades.

- The NBCC criteria on minimum storey stiffness relative to storeys below to avoid vertical stiffness irregularity can lead to uneven distribution of inelastic response and soft-storey response in the structure. It is recommended that the minimum storey stiffness requirement relative to storeys below be deleted for braced steel frames. It was also observed that a common design practice consisting of providing larger-than-required brace sizes may introduce a vertical frame irregularity that is sufficient to increase the displacement demand, cause greater demand concentration, and promote further soft-storey mechanisms.
- NBCC's design accelerations for diaphragms and non-structural elements attached to floor were found to be systematically lower than the demand computed by NTHA. A more consistent design approach will need to be developed. The time delay between brace forces in adjacent storeys has been identified as a possible parameter affecting floor acceleration levels.

The response of the frames subjected to intra–plate hazard in the west was found to be more critical. The following conclusions are based on the robust estimate of the seismic demand for these frames:

- The seismic response of code-compliant BRBFs was found to be generally satisfactory. The probability of exceeding the NBCC drift limit (2.5% of storey height) under the design earthquake was found to less than 5%. However, the mid- and high-rise west prototypes sustained large residual drifts. For a 10% probability of exceedance under the design earthquake level, residual drifts of buildings taller than 5 storeys are found to be around l.5% of the storey height.
- The current CSA S16 requirement that qualification testing protocol and estimation of adjusted brace strengths be based on 2.0 times the seismic design storey drift was found to give conservative estimation of the strain demand on the yielding segment of BRB members, especially in the building top storeys. An alternative criterion based on the design brace axial deformation has been introduced and its accuracy and statistical robustness have been validated. For qualification testing purposes, the study showed, that a design brace axial deformation amplified by a factor of 2.0 has a 10% probability of being exceeded

under the design earthquake level. For the storeys that are less prone to significant soft-storey mechanism this amplification factor may be reduced to 1.65.

- The maximum ductility and inelastic cumulative ductility demands were found to be 25% and 50% lower, respectively, than the reported values in the study by Sabelli, *et al.* (2003) for BRBFs in California. The U.S. and Canadian code minimum requirements for cumulative inelastic ductility are deemed to be overly conservative. The estimated cumulative inelastic ductility demand from the present study is approximately 60% less than the minimum specified value.
- Based on 10% probability of exceedance under the design earthquake level, it is recommended to design the braced bay columns for the simultaneous effects of capacity-based axial forces and an additional end bending moments equal to 15% of the column plastic moment, M_{pc}. That design moment is less than the CSA S16 current design moment of $0.2M_{pc}$. It was shown that the κ factor could be taken equal to zero in design with no adverse effects on the column response. However, to reduce the risk of column failures $\kappa = -0.5$ is recommended.
- Analysis results showed that approximately only 5% of the low cycle fatigue life of well-proportioned BRB yielding segments is expected to be exhausted under the design earthquake level. Assuming that the BRB members were capable of sustaining 2.0 times the design storey drift, the low cycle fatigue fracture of the yielding segments would not be a critical limit states.

The magnitude of residual drift is highly dependent on modeling assumptions, e.g. hysteresis law, and duration of strong shaking (Ruiz-García et al., 2006). Further studies are needed to better assess the residual drifts using more refined models reflecting actual strain hardening response. More refined models should also account for contribution of gravity system to lateral stability.

References

Adams, J., & Atkinson, G. M. (2003). Development of seismic hazard maps for the proposed 2005 edition of the National Building Code of Canada. *Canadian Journal of Civil Engineering, 30*(2), 255-271.

AISC. (2010). ANSI/AISC 341-10, Seismic Provisions for Structural Steel Buildings. Chicago, IL: American Institute of Steel Construction, Inc.

ASTM. (2005). E1049 − 85(2005) Standard Practices for Cycle Counting in Fatigue Analysis. West Conshohocken, PA: ASTM International.

Atkinson, G. M. (2005). Ground Motions for Earthquakes in Southwestern British Columbia and Northwestern Washington: Crustal, In-Slab, and Offshore Events. *Bulletin of the Seismological Society of America, 95*(3), 1027-1044.

Atkinson, G. M. (2009). Earthquake time histories compatible with the 2005 National building code of Canada uniform hazard spectrum. *Canadian Journal of Civil Engineering, 36*(6), 991-1000.

Atkinson, G. M., & Boore, D. M. (2003). Empirical Ground-Motion Relations for Subduction-Zone Earthquakes and Their Application to Cascadia and Other Regions. *Bulletin of the Seismological Society of America, 93*(4), 1703-1729.

Atkinson, G. M., & Macias, M. (2009). Predicted Ground Motions for Great Interface Earthquakes in the Cascadia Subduction Zone. *Bulletin of the Seismological Society of America, 99*(3), 1552-1578.

Black, C., Makris, N., & Aiken, I. (2004). Component Testing, Seismic Evaluation and Characterization of Buckling-Restrained Braces. *Journal of Structural Engineering, 130*(6), 880-894.

Cassidy, J., Rogers, G., Lamontagne, M., Halchuk, S., & Adams, J. (2010). Canada's earthquakes: 'The good, the bad, and the ugly'. *Geoscience Canada, 37*(1).

CEN. (2010). EN 15129:2010 Anti-seismic devices: European Committee for Standardization.

Charalampakis, A. E., & Koumousis, V. K. (2009). A Bouc–Wen model compatible with plasticity postulates. *Journal of Sound and Vibration, 322*(4–5), 954-968.

Charney, F. A. (2008). Unintended Consequences of Modeling Damping in Structures. *Journal of Structural Engineering, 134*(4), 581-592.

CSA. (2009). CSA S16-09, Limit States Design of Steel Structures. Mississauga, Ontario, Canada: Canadian Standards Association.

CSI. (2010). Integrated software for structural analysis & design SAP2000 (Version 15.0.1). Berkeley, CA: Computers and Structures, Inc.

Dehghani, M., & Tremblay, R. (2012a). *Development of standard dynamic loading protocol for buckling-restrained braced frames.* Paper presented at the 7th International Conference on Behaviour of Steel Structures in Seismic Areas - STESSA 2012, Santiago, Chile.

Dehghani, M., & Tremblay, R. (2012b). *Standard Dynamic Loading Protocols for Seismic Qualification of BRBFs in Eastern and Western Canada.* Paper presented at the 15th World Conference on Earthquake Engineering, Lisbon, Portugal.

Dehghani, M., & Tremblay, R. (2016c). Robust Period-Independent Ground Motion Selection and Scaling for Effective Seismic Design and Assessment. *Journal of Earthquake Engineering, 20*(2), 185-218.

Dutta, A., & Hamburger, R. O. (2010). Case study of a 40-storey buckling-restrained braced frame building located in Los Angeles. *The Structural Design of Tall and Special Buildings, 19*(1-

2), 77-93.
Erochko, J., Christopoulos, C., Tremblay, R., & Choi, H. (2011). Residual Drift Response of SMRFs and BRB Frames in Steel Buildings Designed according to ASCE 7-05. *Journal of Structural Engineering, 137*(5), 589-599.
Fahnestock, L. A., Ricles, J. M., & Sause, R. (2007a). Experimental Evaluation of a Large-Scale Buckling-Restrained Braced Frame. *Journal of Structural Engineering, 133*(9), 1205-1214.
Fahnestock, L. A., Sause, R., & Ricles, J. M. (2007b). Seismic Response and Performance of Buckling-Restrained Braced Frames. *Journal of Structural Engineering, 133*(9), 1195-1204.
FEMA. (2009). *Quantification of Building Seismic Performance Factors* (FEMA P695). Washington DC: Federal Emergency Management Agency.
Filippou, F. C., Popov, E. P., & Bertero, V. V. (1983). *Effects of bond deterioration on hysteretic behavior of reinforced concrete joints* (UCB/EERC-83/19). Berkeley, California: Earthquake Engineering Research Center.
Halchuk, S., & Adams, J. (2003). *Fourth generation seismic hazard maps of Canada: Values for over 650 Canadian localities intended for the 2005 National Building Code of Canada* (Open File 4459). Ottawa, ON: Geological Survey of Canada.
Koboevic, S., Rozon, J., & Tremblay, R. (2012). Seismic Performance of Low-to-Moderate Height Eccentrically Braced Steel Frames Designed for North American Seismic Conditions. *Journal of Structural Engineering, 138*(12), 1465-1476.
Kottegoda, N. T., & Rosso, R. (2008). *Applied statistics for civil and environmental engineers*: Wiley-Blackwell.
Krawinkler, H., & Zohrei, M. (1983). Cumulative damage in steel structures subjected to earthquake ground motions. *Computers & Structures, 16*(1–4), 531-541.
Lamontagne, M., Halchuk, S., Cassidy, J. F., & Rogers, G. C. (2008). Significant Canadian Earthquakes of the Period 1600–2006. *Seismological Research Letters, 79*(2), 211-223.
López, W. A., Gwie, D. S., Saunders, C. M., & Lauck, T. W. (2002). *Lessons Learned From Large-Scale Tests of Unbonded Braced Frame Subassemblages.* Paper presented at the 71st annual convention of SEAOC, Sacramento, CA.
McCormick, J., Aburano, H., & Ikenaga, M. (2008). *Permissible residual deformation levels for building structures considering both safety and human elements.* Paper presented at the 14th World Conference on Earthquake Engineering, Beijing, China.
McGuire, R. K., Silva, W. J., & Costantino, C. J. (2002). *Technical basis for revision of regulatory guidance on design ground motions: hazard- and risk-consistent ground motion spectra guidelines* (NUREG/CR-6769). Washington, DC 20555-0001: U.S. Nuclear Regulatory Commission.
Merritt, S., Uang, C.-M., & Benzoni, G. (2003). *Subassemblage Testing of Corebrace Buckling-Restrained Braces* (TR-2003/01): Department of Structural Engineering, University of California, San Diego.
Moni, M., Moradi, S., & Alam, M. S. (2016). Response modification factors for steel buckling restrained braced frames designed as per the 2010 National Building Code of Canada. *Canadian Journal of Civil Engineering, 43*(8), 702-715.
NRCC. (2010). National Building Code of Canada, 13th ed. Ottawa, ON.: National Research Council Canada, Institute for Research in Construction.
PEER. (2005). PEER Strong Ground Motion Database. Retrieved 27/03/2012, from http://peer.berkeley.edu/nga/
Ruiz-García, J., & Miranda, E. (2006). Residual displacement ratios for assessment of existing

structures. *Earthquake Engineering & Structural Dynamics, 35*(3), 315-336.

Sabelli, R. (2001). *Research on Improving the Design and Analysis of Earthquake-resistant Steel-braced Frames* (The 2000 NEHRP Professional Fellowship Report). Oakland, California: Earthquake Engineering Research Institute.

Sabelli, R., Mahin, S., & Chang, C. (2003). Seismic demands on steel braced frame buildings with buckling-restrained braces. *Engineering Structures, 25*(5), 655-666.

Tremblay, R. (2005). Fundamental Periods of Vibration of Braced Steel Frames for Seismic Design. *Earthquake Spectra, 21*(3), 833-860.

Tremblay, R., & Atkinson, G. M. (2001). Comparative Study of the Inelastic Seismic Demand of Eastern and Western Canadian Sites. *Earthquake Spectra, 17*(2), 333-358.

Tremblay, R., Bolduc, P., Neville, R., & DeVall, R. (2006). Seismic testing and performance of buckling-restrained bracing systems. *Canadian Journal of Civil Engineering, 33*(2), 183-198.

Tremblay, R., & Bouatay, N. (2002). *Loading Protocols for the Seismic Testing of Ductile Bracing Members in Concentrically Braced Steel Frames.* Paper presented at the 12th European Conference on Earthquake Engineering, London, UK.

Tremblay, R., Degrange, G., & Blouin, J. (1999). *Seismic Rehabilitation of a Four-Storey Building with a Stiffened Bracing System.* Paper presented at the 8th Canadian Conference on Earthquake Engineering, Vancouver, BC, Canada.

Tremblay, R., & Poncet, L. (2005). Seismic Performance of Concentrically Braced Steel Frames in Multistory Buildings with Mass Irregularity. *Journal of Structural Engineering, 131*(9), 1363-1375.

Tsai, K.-C., Hsiao, P.-C., Wang, K.-J., Weng, Y.-T., Lin, M.-L., Lin, K.-C., Chen, C.-H., Lai, J.-W., & Lin, S.-L. (2008). Pseudo-dynamic tests of a full-scale CFT/BRB frame - Part I: Specimen design, experiment and analysis. *Earthquake Engineering & Structural Dynamics, 37*(7), 1081-1098.

Wen, Y.-K. (1976). Method for random vibration of hysteretic systems. *Journal of the Engineering Mechanics Division, 102*(2), 249-263.

Xie, Q. (2005). State of the art of buckling-restrained braces in Asia. *Journal of Constructional Steel Research, 61*(6), 727-748.

Zareian, F., & Krawinkler, H. (2007). Assessment of probability of collapse and design for collapse safety. *Earthquake Engineering & Structural Dynamics, 36*(13), 1901-1914.

Zareian, F., & Medina, R. A. (2010). A practical method for proper modeling of structural damping in inelastic plane structural systems. *Computers & Structures, 88*(1–2), 45-53.

CHAPTER 6 ARTICLE 2 : FATIGUE FAILURE OF 350WT STEEL UNDER LARGE-STRAIN SEISMIC LOADING AT ROOM AND SUBFREEZING TEMPERATURES

Morteza Dehghani, Robert Tremblay, and Martin Leclerc

Paper submitted to *Construction and Building Materials,*

Submitted on 2 Aug 2016

ABSTRACT

Due to its high ductility, weldability and toughness at low temperature, CSA G40.21-350WT steel in Canada is primarily used in bridge construction, ship building, and seismic energy dissipation systems. The article presents uniaxial tensile tests and constant- and variable-amplitude cyclic testing performed on 350WT steel at room and subfreezing temperatures. The variable-amplitude tests include common step-loading patterns as well as tests under strain signals obtained from the brace response in building structures subjected to three different types of earthquakes. The ductility of 350WT steel from monotonic tensile tests is essentially same at room and low temperatures (−40 °C). The cyclic test results revealed that cold temperatures as low as −35 °C did not have adverse effects on the low cycle fatigue life of 350WT steel. The benchmark constant-amplitude tests were employed to predict fatigue life under different large-strain variable-amplitude loading patterns both for room and subfreezing temperature conditions. In addition to the common strain-life approach, the adequacy of two well-established energy-life models for predicting fatigue life under variable-amplitude loading was evaluated. The strain-life approach generally performed better than the energy-life methods, particularly for step-loading histories. Comparison between predictions and laboratory observations showed that the fatigue failure life under large strain seismic loading can be accurately estimated, especially at room temperature.

Keywords: extremely low cycle fatigue, seismic loading, cold temperature, random strain path, mean strain effect

6.1 Introduction

Earthquake-induced fracture failure of steel structures has been observed and reported in post-event reconnaissance reports (Tremblay *et al.*, 1995; Tremblay *et al.*, 1996; Clifton *et al.*, 2011). In several cases, failure was attributed to localized fatigue damage caused by large cyclic plastic strains in regions with complex states of stress. Such fractures in critical elements, which occur in a few cycles, can lead to catastrophic failure of engineered structures. In fatigue engineering, materials are studied in two distinctive regimes, namely high cycle and low cycle fatigue (HCF and LCF). In the LCF regime, i.e. less than 10^3–10^4 cycles to failure, plastic strains dominate compared to elastic ones. LCF is more relevant to earthquake engineering applications as the intense seismic vibrations are typically very short in duration and energy-dissipating structural components are subjected to few large plastic deformation cycles, i.e. less than 10-20. Failure under this condition is commonly referred to as extremely- or ultra-low cycle fatigue (ELCF or ULCF) failure and has received more attention in the past decade. Nucleation, initiation and growth of fatigue cracks in this regime is fundamentally different from typical LCF problems where limited plasticity exists. Kamaya (2010) showed that cracks under large plastic strains initiate inside the specimen and then propagate to the surface. Kuroda (2002) argued that under large plastic strains, fatigue damage is dominated by exhaustion of ductility rather than crack propagation; he proposed a new damage accumulation theory. (Kanvinde *et al.*, 2005; Kanvinde *et al.*, 2014) developed and implemented an uncoupled continuum-based fatigue damage model to predict initiation of failure in energy-dissipating members of structural systems under large strain seismic demand. This model, which employs accumulated plastic strain and state of stress as damage parameters, needs to be calibrated against results of cyclic tests on notched specimens. Fundamental to any ELCF damage model is the uniaxial behaviour under large cyclic strains. In this context, Dusicka *et al.* (2007) studied uniaxial fatigue life of five types of structural steel plates, ranging from very low yield point to high performance steel, under axial strain amplitudes up to ±7.0% and reported their cyclic hardening and fatigue life parameters. The tests showed that the overall fatigue life of all steel plates was similar and strain rate did not have appreciable effects on their hysteresis behaviour. Nip *et al.* (2010) compared the low and extremely low cycle behaviour of three types of structural carbon and stainless steels under axial strain amplitude up to ±7% and surface bending strains as large as ±15%. The materials studied showed similar fatigue resistance although their fracture ductility from tensile tests was different.

There has been ever-increasing demand for building sustainable infrastructures in cold regions of the world subjected to subfreezing temperature. These regions are often seismically active and need special considerations for design and construction. Steel, due to its unique features, is a viable construction material in such a complex and harsh climate. ASTM A709 (ASTM, 2011) and CSA G40.21-350WT (CSA, 2004) steels are commonly used for bridge structural applications due to their enhanced fracture toughness at low temperature. The 350WT steel is a low carbon, ductile and weldable structural quality steel with a minimum yield strength of 350 MPa. This steel is supplied in 5 categories depending upon the required toughness. According to the standard, category 4 must have a minimum Charpy V-notch (CVN) toughness of 27 J energy at −45 °C. In Canada, this grade is widely used in ship building industry, bridge construction, and heavy mining equipment operating in cold regions. The superior toughness of this steel allows applications in cold marine environments such as ship hull susceptible to brittle facture due to cold water and impact loadings (e.g. ice collision). The Canadian bridge design code CSA S6 specifies high toughness steels with minimum CVN of 40 J at −40 °C in fracture-critical elements of bridges in regions with very low service temperature (−40 °C and below). This steel was also experimentally verified for critical seismic force-resisting elements for building structures that must dissipate earthquake energy by undergoing large cyclic plastic deformations without strength and stiffness degradation (Tremblay, *et al.*, 2006). Full-scale tests indicated that 350WT steel can sustain large cyclic plastic strains. High cycle fatigue behaviour of this steel at room and cold temperatures has been the subject of few past studies. Taheri *et al.* (2003) investigated the HCF crack propagation of 350WT steel under constant- and variable-amplitude loadings using standard fracture mechanic procedure at −40 °C. Chen *et al.* (2005) compared the 350WT Category 4 and ASTM A709 HPS grade 485W steels and concluded that LCF resistance, crack propagation, and low temperature toughness properties of these two steels were similar. Josi *et al.* (2010) reported the crack initiation life of flat specimens made of 350WT steel tested between ±0.1% and ±0.6% axial strain amplitudes. Hamdoon *et al.* (2014) conducted LCF testing of this steel at room and low temperatures (−30 °C). In tests up to strain amplitudes of 0.24% it was remarked that the fatigue life of 350WT was superior at low temperature.

The available information on fatigue response of 350WT steel is limited to small plastic strain regime, which is not applicable in earthquake engineering applications. Possible effects of cold temperatures on the fatigue performance of this steel under large deformations are not documented

either. This data is essential to properly design exposed steel structures with steel energy-dissipative components, such as bridge, mining, and pipeline structures located in cold and seismically active regions such as Alaska, the northern part of the conterminous United States, and subarctic territories of Canada. There was a need to investigate the performance of this specific steel grade at both room and subfreezing temperature conditions. The applicability of common fatigue damage models and damage accumulation rules under variable-amplitude loadings induced by strong earthquakes also needed to be studied. To this end, an extensive experimental program was conducted on 350WT steel under constant-amplitude and different variable-amplitude loading histories. Variable-amplitude histories included common step-loading signals as well as real-time strain histories obtained from the nonlinear response of energy dissipating elements in steel building structures subjected to three different types of earthquakes. Tests were performed at both room and subfreezing temperatures. The paper describes the experimental program and presents the test results. Constant-amplitude test results are used to determine the parameters of commonly used strain-life and energy-life fatigue models for the two temperature conditions. Test results under the variable-amplitude tests are presented and discussed. This data set is then used to verify the capacity of the different fatigue models to accurately predict fatigue failure under complex cyclic inelastic seismic demands.

6.2 Experimental Program

6.2.1 Test Matrix

The experimental program included uniaxial cyclic testing of round 350WT steel specimens at room (+24°C) and subfreezing (−40 °C) temperatures. As ancillary tests, uniaxial monotonic tensile and V-notch Charpy tests at room and subfreezing conditions were also included in the program. Tensile tests were carried out on round specimens in accordance with ASTM E8 (ASTM, 2009). The test matrix is summarized in Table 6.1. Cyclic experiments were strain-controlled and divided into constant- and variable- amplitude tests. The former were conducted according to ASTM E606 (ASTM, 2004) practice and included seven fully-reversed strain amplitudes ranging from 1 to 8%. The variable-amplitude tests were performed using step- and seismic-loading strain patterns. Step-loading patterns included low-high and low-high-constant sequences that were applied at moderate strain rates with and without mean strains. Seismic-loading patterns were

constructed from the response of building structures to three types of earthquake ground motions. Seismic-loading blocks were applied at real-time deformation rates and repeated until failure of specimens took place. The experiments were carried out at the Polytechnique Montréal structural engineering laboratory. Results from complementary room temperature tests performed at Laval University were also used when analysing the data.

Table 6.1: Test matrix

Test class	Test description		Temperature (° C)	Strain rate (% strain/s)	No. of specimens
Cyclic	Constant-amplitude		+24, −40	0.1	23
	Variable-amplitude	Step-loading	+24, −40	0.1	11
		Seismic-loading	+24, −40	Variable	11
Ancillary	Monotonic tensile		+24, −40	0.005	3†
	Charpy V-notch		+24, −40, −50	–	13

† Two specimens for room and one specimen for subfreezing temperature.

6.2.2 Test Specimens

Round specimens were machined from the coupons that were cut along the rolling direction of a single 1-1/4" (31.75 mm) thick steel plate conforming to the 350WT Category 4 requirements. Two different specimen sizes were designed and fabricated for the tensile and cyclic tests and details are shown in Figure 6.1. Precise numerically-controlled tools were used in the machining process with special attention to avoid undercuts at the base of the shoulders. The stockier specimens with diameter to gage length ratio of 0.6 were used in the cyclic testing to avoid buckling. The measured average surface roughness, R_a, of the as-received specimens was ~1 μm. These specimens were not polished after machining given that surface preparation was not expected to have significant effects on the fatigue life of specimens subjected to large strain amplitudes (Stephens *et al.*, 2000). For the same reason, stress relieving procedure was not conducted either after machining. The round-ended specimens in Figure 6.1c were utilized for the complementary tests at Laval University. The gage length of these specimens were manually polished using in sequence grade 360 and 500 sand papers.

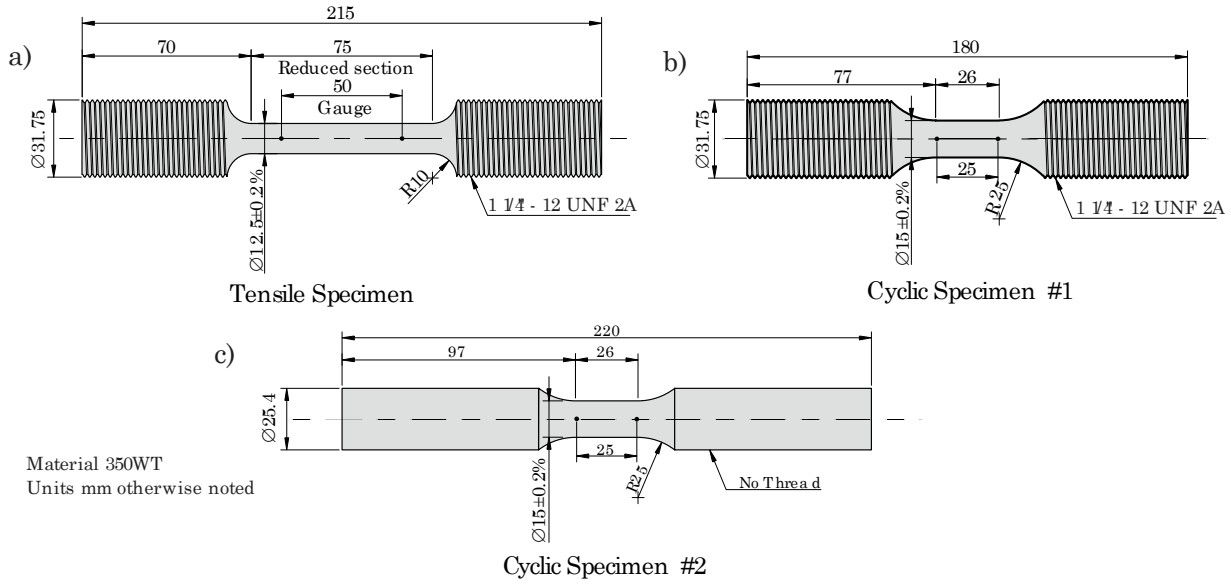

Figure 6.1: Specimen geometry used in: a) tensile; b) cyclic; and c) complementary cyclic tests at Laval University (dimensions in mm).

6.2.3 Cyclic loading protocols

6.2.3.1 Constant-amplitude

Fully-reversed, strain-controlled constant-amplitude loading is the basic standard test protocol used to characterize the fatigue properties of engineering materials. In this study, constant-amplitude loading tests were conducted at 1, 2, 3, 4, 5, 6, and 8% engineering strain amplitudes. These tests were carried at a constant gage strain rate of 0.001 s^{-1} using ramp-type waveforms.

6.2.3.2 Variable-amplitude step-loading

In a step-loading pattern, strain amplitudes are gradually incremented in successive steps each consisting of a series of constant amplitude cycles. Step-loading protocols are widely used in qualification testing of seismic energy dissipating structural components (AISC, 2010). In this research, step-loading with two sequence patterns were investigated: 1) Low-High (LH); and 2) Low-High-Constant (LHC), as shown in Figure 6.2a. In the LH pattern, strain range has a gradually-increasing pattern with minimum strain range $\Delta\epsilon$ = 1.0%. After four cycles, the strain range is increased to a higher level that was maintained until failure. The LH pattern was applied in symmetrical (fully-reversed) and asymmetrical formats. In the asymmetrical case, the minimum

strain in each cycle was set to zero and the specimen was always subjected to tensile (positive) straining. In this paper, the symmetrical and asymmetrical patterns are symbolized by R = −1 and R = 0 tags, respectively, placed in brackets after the pattern name. The LHC pattern consisted of successive pairs of symmetrical cycles, i.e. R = −1, at 0.5%, 1.0%, 2.0%, 3.0% and 4.0% strain amplitudes, followed by constant-amplitude cycles at ±2.0% strains ($\Delta\epsilon$ = 4%) until specimen failure. All step-loading tests were conducted in strain-controlled mode at a constant strain rate of 0.001 s^{-1}, i.e. same as in the constant-amplitude tests.

6.2.3.3 Seismic-loading

Response of building structures to earthquakes is a highly random process and earthquake-induced deformations in structural components do not follow a unique pattern. Typical engineering structures are also expected to respond inelastically during strong earthquakes to dissipate the induced seismic energy. This results in large inelastic deformation cycles with rates that are much faster than what is typically used in standard fatigue testing. For these reasons, strain histories in the energy-dissipating components of structures exhibit complex random sequence patterns with fast-rate large-amplitude cycles. In this study, the strain signals for the seismic-loading patterns were constructed using axial deformation demands on buckling-restrained braces (BRBs) of multi-storey building structures subjected to design-level earthquakes obtained from nonlinear inelastic time history analysis. BRB members are designed to yield in tension and compression, without buckling. Detail on the building numerical models and seismic analyses can be found in (Dehghani *et al.*, 2017b). The test signals were developed using axial strain histories in the cores of the BRB members assuming uniform strain distribution along the yielding core segments. The so-obtained strain responses were corrected to by removing the low intensity end portions, high frequency noises, and baseline offsets.

Three different types of earthquake ground motions were considered in the building analyses: 1) Ordinary (OR) motions; 2) Pulse-Like (PL) motions; and 3) motions from Subduction Interface (SI) earthquakes. These ground motions have distinctive features in terms of frequency content and duration which significantly affect the dynamic response of buildings. “OR” ground motions are recorded at moderately far distance (e.g. 30–60 km) from the source of the earthquake and have various duration and energy discharge rates depending upon their magnitude and distance. These ground motions contain a mix of strong amplitudes at both low and high frequency motions. “PL”

ground motions are recorded at shorter distances (less than 20 km) from the earthquake rupture zone and often have rupture directivity effects in their fault-normal component. The rupture directivity is characterized by an impulsive double-sided velocity cycle. The rate of energy discharge in PL signals is much higher than in the OR motions. Consequently, very fast deformation rates are expected in bracing members of structures exposed to this type of ground motion. In subduction zones, an oceanic plate forces itself under a continental plate over long distances such that an enormous amount of energy is released upon failure of the locked zone between the colliding plates, which results in large magnitude events. Due to the large ruptured areas, SI earthquakes are also characterized by long duration of ground shaking, which can cause low-cycle fatigue damage and other duration-dependent undesirable phenomena to structures. The OR ground motion in this study was recorded at the BRAN station during the 1989 Loma Prieta earthquake. Fault-normal recording at station TCU031 in 1999 Chi-Chi earthquake was chosen as the PL motion. For the Subduction Interface seismic event, the east-west component of the ground motion recorded at station FKS005 (Haramachi) during the **M**9.1 Tōhoku earthquake of 2011 was selected. The resulting strain history test signals are plotted in Figure 6.2b. For the PL signal, it was found impractical to apply the computed brace axial strain response due to its large permanent end offset that was large enough to exhaust the stroke capacity of the load frame actuator in a few passes. The end offset was removed by joining a complementary signal at the end of the original response. The complementary signal was obtained by mirroring the original response about the time axis and then shifting its amplitude by the offset value. The original-plus-complementary PL signal was then applied as a single loading history. In some seismic-loading tests, block signals were amplified or de-amplified to create a separate experiment.

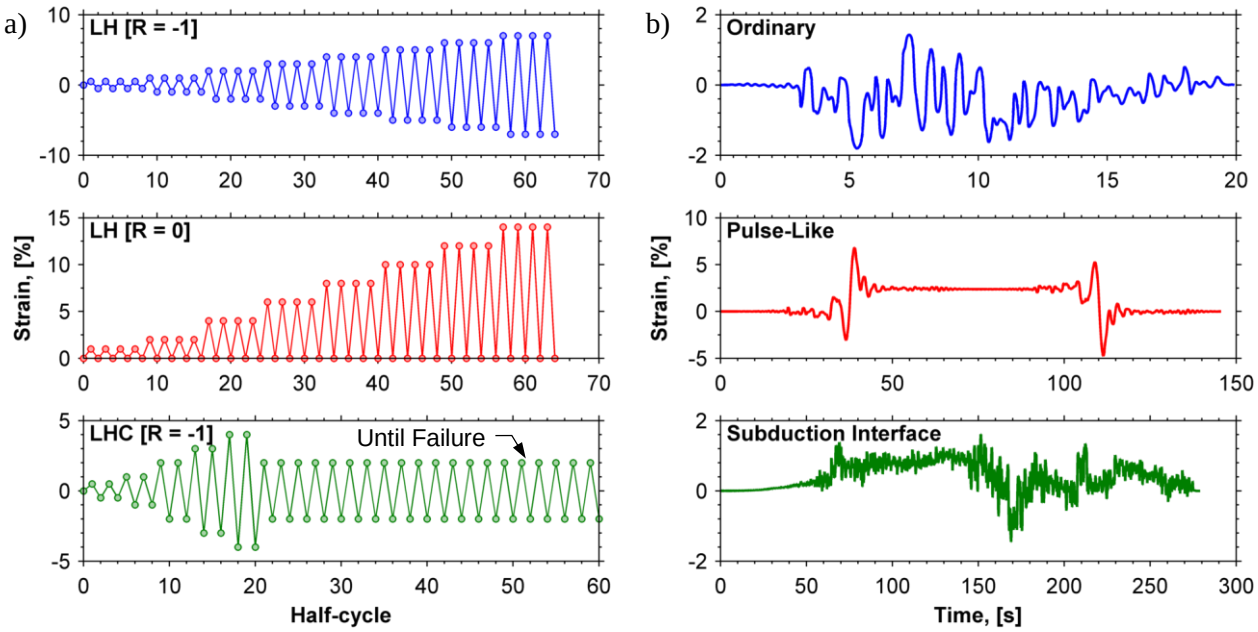

Figure 6.2: Variable-amplitude loadings: a) step-loading histories; b) seismic-loading blocks.

6.2.4 Test Set-up

Testing at Polytechnique Montréal was performed in an Instron 8806 four-column load frame. This is a closed-loop servo-hydraulic uniaxial testing frame that has static and dynamic force capacities of 1500 and 1000 kN, respectively. This load frame was designed for testing structural-scale components and the special fixtures shown in Figure 6.3a were required to adapt the small-scale fatigue specimens to the load frame platens. The fixture parts, shafts, couplers, clamping system, and jam nuts (see Figure 6.5), were machined from AISI 4140 HT steel using precision numerically-controlled fabrication tools. Alignment of the test set-up was verified according to ASTM E1012 (ASTM, 2012) using an instrumented specimen. Bending deformations were limited to 5% of the total deformation in the elastic domain. At the trial stage of cyclic testing it was realized that the lateral stiffness of the load frame was not sufficient to prevent relative lateral deformations of the specimen ends at compressive strains larger than 2%. This load frame sway buckling mode resulted in additional strains in the specimens that led to premature failure. To prevent this behaviour, the load frame lateral stiffness was increased by adding horizontal lateral bracing in both orthogonal directions at the actuator's lower end and at the crosshead level. The bracing eliminated sway buckling failure mode up to 8% maximum compressive cyclic strain amplitude applied in the tests. In Figure 6.3b and c unloaded deformed shapes of two identical

specimens tested in the unbraced and braced load frame are compared. Under ±4.0% constant amplitude cyclic strains, the first specimen failed after 14 cycles whereas the specimen tested in the braced frame could sustain 35 cycles prior to failure. Failure of the first specimen was affected by localized flexural strains resulting from frame lateral displacements and the measured failure life did not represent the actual material fatigue resistance under uniform strain. The lateral bracing system was employed in all cyclic tests. Complementary tests at Laval University were performed in a 500 kN MTS 322.41 load frame with the actuator lateral displacement restrained in two orthogonal directions (Beaumont, *et al.*, 2016).

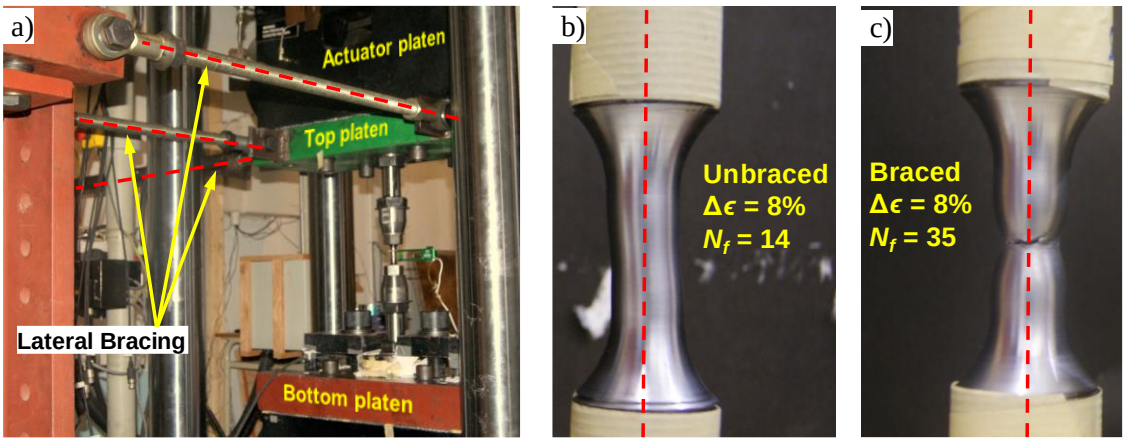

Figure 6.3: a) Lateral bracing of the actuator, b) and c) deformed shape of specimens tested in the laterally unbraced and braced load frame conditions, respectively (specimens tested under cyclic constant ±4% strains at room temperature).

Amplitude and rate of deformation at the gage length were controlled by feedback from clip-on extensometer. Gage lengths of 25 and 50 mm were respectively used in the cyclic and tensile tests. Loads were measured by a dynamic force transducer located at the top of the load train. Lateral deformations at the actuator's end was continuously recorded at two perpendicular directions using string potentiometer transducers.

6.2.4.1 Temperature condition

In the tensile subfreezing tests, the specimens and a large portion of the test fixture were placed into a Cincinnati Sub-Zero environmental chamber (model TT-3.3-.75-H/AC) where they were cooled to the target temperature of −40° C using cold air stream generated by the chamber

refrigeration compressor (Figure 6.4a). The chamber temperature along with the temperature at different locations of the fixtures were continuously monitored using isolated thermocouples. It was not possible to mount thermocouples directly on the surface of the specimens' gage area due to presence of the clip-on extensometer. However, the specimen surface temperature next to the gage area was continuously monitored (Figure 6.4b). A dummy specimen with an inserted thermocouple was also fabricated and hung near the test specimens inside the chamber. This dummy specimen did not have conductive heat exchange path and was used to evaluate the cooling rate of the specimens due to convective heat transfer. Testing started 30 minute after the cold air temperature around the specimen was stabilized to the target temperature. The temperature readings at the vicinity of the gage region were used to determine when the gage area attained the desired temperature of −40 °C. The cold air temperature was then maintained constant through the test.

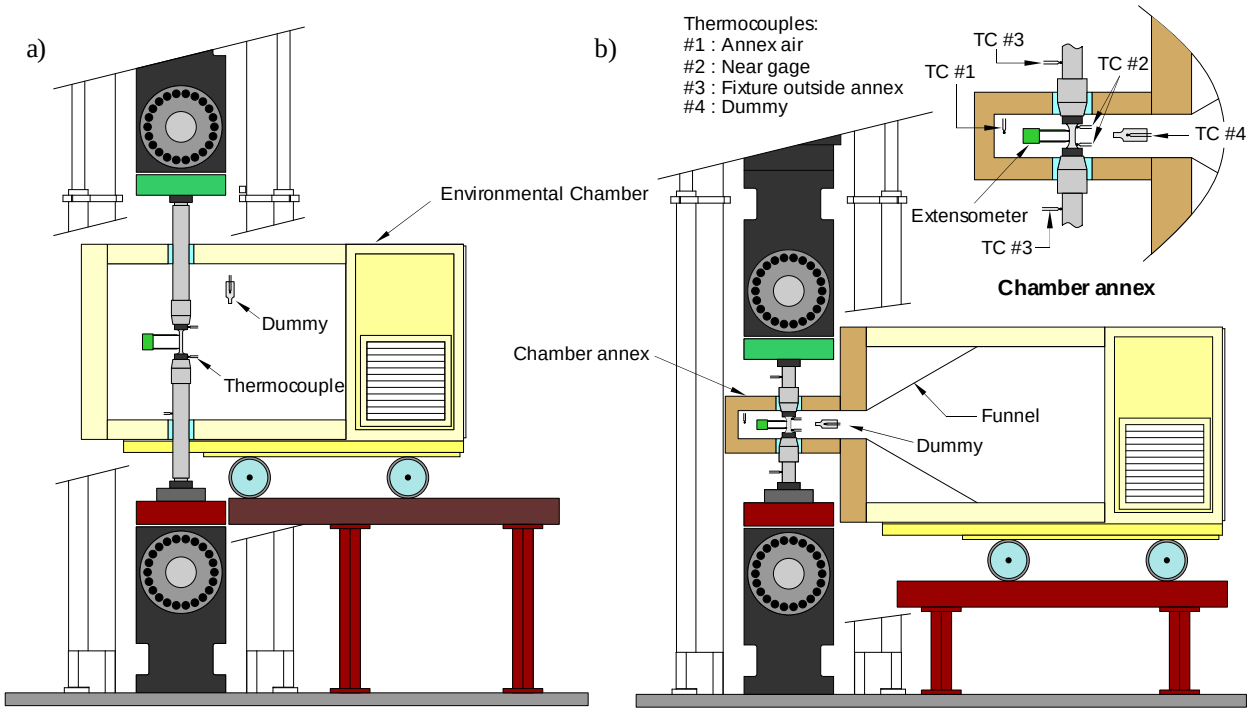

Figure 6.4: Cold temperature test set-up for: a) tensile tests; and b) cyclic tests (lateral bracing system is not shown).

In the cyclic subfreezing tests, the main challenge was to prevent lateral buckling due to long length of the required test fixtures. A second set of fixtures with reduced length was used to achieve stable

response in compression and a smaller in-house insulated box was fabricated and annexed to the original chamber (Figure 6.4b and Figure 6.5a). The cold air stream was forced to the annex using a funnel-shape guide. As shown, the instrumented dummy specimen was placed in the annex to monitor air temperature and thermocouples were still used on the test specimens next to the gage area. Due to the more complex geometry, it was more difficult to reach to the desired temperature for the cyclic tests. Depending on the case, the measured annex temperature varied between −42 °C and −65 °C. After completion of the test program, it was realized that heat transfer due to conductivity of the test fixtures likely influenced the temperature of the specimen gage region. To examine this effect, finite element heat transfer analysis was conducted for each subfreezing cyclic tests and the temperature of the gage region was computed numerically. The entire fixture including the end platens were modelled in ABAQUS finite element software (version 6.11) and a transient heat transfer analysis was carried out using a 2D axisymmetric model with typical thermal properties of low carbon structural steel. Both conduction and convection heat transfer modes were included in the model. The surface of the test fixture inside the chamber annex was modelled as a film exposed to a temperature sink equal to the history of air temperature near the specimen surface. Cooling rate of the dummy specimen was utilized to calibrate the convective heat transfer coefficients of the film. The numerical models were validated against the thermocouple readings at different locations on the test fixtures. This analysis showed that the entire gage area was uniformly cooled to the desired temperature in the tensile tests. Thermal analysis of the cyclic test fixture, indicated significant differences up to approximately 30°C between cold air and gage area temperatures, as a result of continuous heat flow from the fixture extremities to its centre. This higher heat exchange was due to a relatively short length of the fixtures that was exposed to cold air stream inside the annex. The analyses showed that the steady-state temperature of the gage region varied between −15 to −35 °C before tests were started, were depending on the annex air temperature and other specific set-up conditions such as thermal insulation of the fixture shaft outside of the annex. Hence, the cyclic tests were not conducted under strictly uniform temperature conditions. For this reason, the test temperature for the cyclic tests will be collectively referred to by “subfreezing temperature” term. This shows that setup used for this type of test must be carefully designed to achieve target temperatures in the gage area of the specimens and temperature conditions be carefully monitored during the experiment.

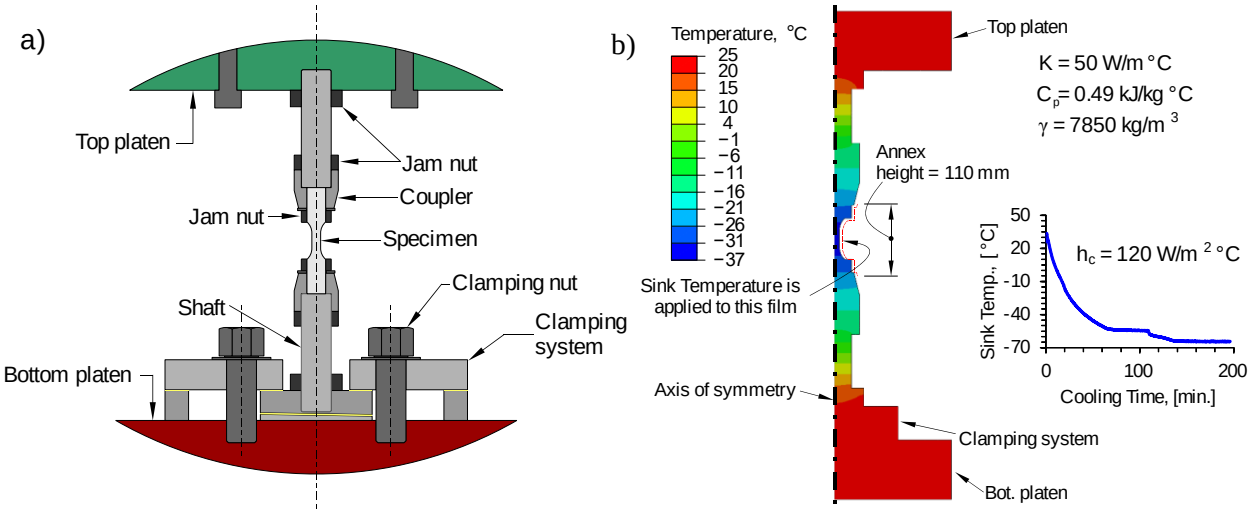

Figure 6.5: Cyclic test setup: a) Test fixture; b) distribution of temperature in the testing fixture at steady state conditions from heat transfer finite element analysis (the plot shows the measured annex temperature history applied as the film temperature to a part of the fixture model inside the annex K is the coefficient of thermal conductivity, C_p is the specific heat, γ is the density, and h_c is the convective heat transfer coefficient).

6.3 Test Results and Discussions

6.3.1 Ancillary tests

Results of tensile tests conducted on the slender specimens (Figure 6.1a and 2-4a) with the gage length of 50 mm are presented in Table 6.2. In this table $F_{y,0.2\%}$ and $F_{y,Upper}$ are the upper and lower yield stresses, and F_u is the ultimate tensile stress. $F_{y,0.2\%}$ was obtained by 0.2% offset. Engineering strain at F_u and true strain at fracture are referred to as e_{pD} and ϵ_f, respectively. Reduction in cross-section (RA) and elongation (EL) after fracture are also given in the table. A constant strain rate of 5.0×10^{-5}/s was applied throughout the experiment.

Table 6.2: Average tensile properties of 350WT steel at room and subfreezing temperatures

Testing Condition	E (GPa)	$F_{y,0.2\%}$ (MPa)	$F_{y,Upper}$ (MPa)	F_u (MPa)	e_{pD} (%)	RA† (%)	EL†† (%)	ϵ_f (mm/mm)
Room (+24 °C)	210	353	400	469	17.7	75	37	1.4
Subfreezing (−40 °C)	213	363	429	506	19.5	75	37	1.4

† Reduction in cross-section area after fracture.

†† Elongation on gage of 50 mm after fracture.

All strength-related parameters increased at cold temperature. $F_{y,Upper}$ and F_u were found to be more sensitive to the cold temperature than $F_{y,0.2\%}$. On average, $F_{y,Upper}$ and F_u at −40 °C showed 8% increase with respect to the room temperature tests. Ductility of 350WT steel, as measured by gage elongation or area reduction at fracture, was not reduced in tests at −40 °C compared to room temperature tests. As seen in Figure 6.6 the rate of strength degradation after peak load was faster under cold temperature conditions.

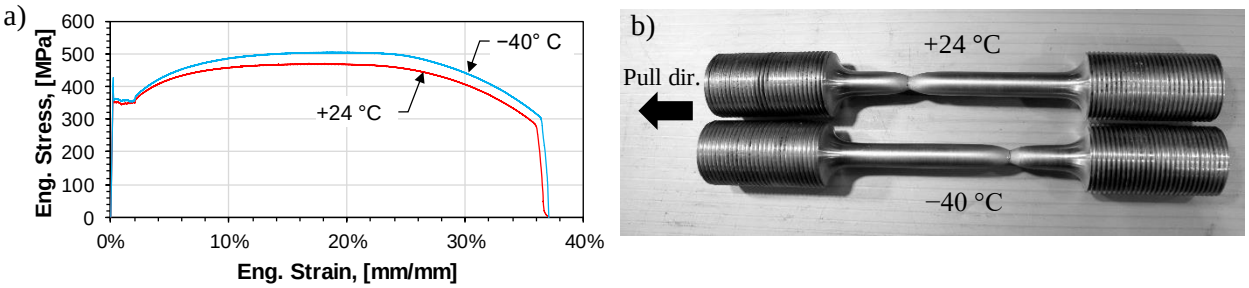

Figure 6.6: Comparison of tensile response of 350WT steel at room and subfreezing condition (−40 °C).

Series of Charpy impact tests were also conducted on V-notch specimens at +24, −40, and −50 °C. Tests were performed in a commercial laboratory according to ASTM E23 (ASTM, 2007). Results of these tests are summarized in Table 6.3. Tests at −50 °C showed a brittle fracture mode with low energy absorption. On the other hand, specimens tested at −40 °C fractured in a relatively more ductile manner with a significantly higher toughness than the −50 °C tests, suggesting that the ductile-brittle transition temperature of the tested material was between -40 and −50°C, which is consistent with findings by Chen, *et al.* (2005) on the same steel grade. Typical fracture mode of the tested specimens is shown in Figure 6.7.

Table 6.3: Results of Charpy V-notch impact tests

Source	Number of specimens	Energy (J)	Temperature (°C)
Mill report	3	357 ± 20[†]	−40
This study	6	18 ± 10	−50
This study	6	155 ± 62	−40
This study	1	>353	+24

[†] 95% confidence interval of mean

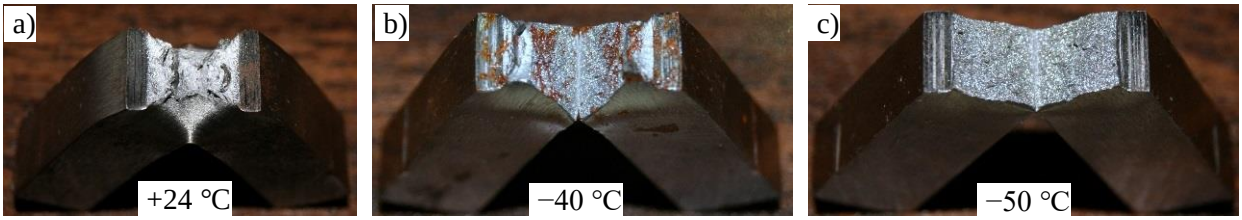

Figure 6.7: Fracture mode of the Charpy V-notch specimens tested at: a) room (+24 °C); b) −40 °C; and c) −50 °C.

6.3.2 Constant-amplitude tests

The constant-amplitude tests were conducted at 1, 2, 3, 4, 5, 6 and 8% engineering strain amplitudes both at room and subfreezing temperature and loading continued until failure happened. Failure was assumed to have occurred when the tensile resistance at any load reversal instant had reduced to less than 50% of the maximum tensile strength recorded in the preceding load reversal instants, according to the load drop criterion of ASTM E606. Constant-amplitude tests were repeated at 1, 3 and 4% strain amplitudes to quantify the variability of the results. The coefficient of variation (CoV) of the failure life was found to be between 5 to 15%. Specimens tested beyond 3% strain experienced necking which was detected by negative post-yield slopes at the end of tensile loading cycles. In the largest strain tests, i.e. ±8.0%, necking started as early as the second cycle and both room and subfreezing specimen failed after 15.5 reversals. As an important observation, the fatigue life of specimens at subfreezing temperature were found to be comparable to the room temperature tests (detail is given in Section 6.4.1). Specimens at subfreezing temperature even showed

relatively higher number of cycles to failure. This is consistent with observation made by Stephens *et al.* (1982) who studied low cycle fatigue crack propagation of a similar structural steel, ASTM A572 Grade 50, at room and −45 °C. As stated before, in this test program, specimen temperature in the subfreezing cyclic tests varied between −15 and −35 °C. Specimens tested at subfreezing temperature exhibited higher level of cyclic strain hardening. On average, cyclic strain hardening at subfreezing was ~4% more than at room condition. In both conditions, Young modulus degraded gradually. At the stable cycle, the elastic stiffness degraded between 10 to 20% depending upon the strain amplitude. Higher degradation was measured in the tests with larger strain.

6.3.3 Variable-amplitude test

6.3.3.1 Step-loading patterns

The LH tests were conducted both at room and subfreezing temperatures. Testing temperature condition is denoted by plus (+) or minus (−) prefixes for room and subfreezing conditions, respectively. In all LH tests, necking became visible in the 8% strain range cycles and failure occurred in the 5^{th}, 6^{th}, 5^{th}, and 5^{th} half-cycle of the 14% strain range cycles for the specimens subjected to +LH [R = –1], –LH [R = –1], +LH [R = 0], and –LH [R = 0] loading conditions, respectively. Failure modes are shown in Figure 6.9a–d. Conversely, necking was not observed prior to failure in the LHC tests, with maximum strain range $\Delta\epsilon$ = 8%, (Figure 6.9e). For every strain ranges, the asymmetrical LH test showed greater hardening than the symmetrical one, meaning that, for the same displacement range, more energy was dissipated in the asymmetrical LH loading pattern. However, the difference between stress ranges became less pronounced as the strain range was increased. In the first cycle of the asymmetrical LH test at low temperature, i.e. −LH [R = 0], the specimen was pulled to 4% instead of 0.5% due to a control problem. The rest of the loading history was same as in the LH test at room temperature. No replication was attempted for the LH tests but the testing with LHC pattern was repeated seven times. These LHC tests were conducted at room temperature at Laval University using the round-ended specimens of Figure 6.1c. These specimens all failed in the ±2% constant amplitude segment of the loading. In these tests, the CoV of failure life was ~6% which implies low and acceptable variability for typical structural engineering applications.

6.3.3.2 Seismic-loading patterns

The seismic-loading strain patterns OR, PL, and SI were applied to specimens at room and subfreezing condition. Plus (+) and minus (−) prefixes imply room or subfreezing test conditions, respectively. The failure life, expressed as the number of applied passes causing failure, along with the basic intensity-related features of the seismic-loadings are described in Table 6.4. In some seismic-loading tests, block signals were amplified or de-amplified to create a separate experiment. In Table 6.4, the amplitude scaling factors are given in brackets after the block name. Each strain block was repeated, with no pause between passes, until failure of the specimen took place. Failure is defined as the point where the tensile strength degraded to less than 50% of the maximum recorded tensile resistance. Some experiments were repeated to verify the variability of failure life and other response parameters. In all cases, similar failure lives were observed indicating a high and reliable repeatability. The PL block has the most intense strain range compared to the others, i.e., two half-cycle of $\Delta\epsilon$ = 10% with a strain rate of ~5% s^{-1}. The hysteresis response of +PL [1.0X] experiment is plotted in Figure 6.8a. The shortest and longest durations belong to the OR and SI signals with 20 and 278 seconds, respectively. The SI block has more than 500 zero force crossings, i.e., load alternations, and several hundreds of small elastic half-cycles.

Table 6.4: Intensity measures of the loading signals in the seismic-loading tests

Block Name	Applied Passes	Intensity metrics measured in a single pass of loading									Heat Generation	
		No. of force zero-crossing	$\Sigma(\mathrm{d}\epsilon_p)$ (mm/mm)	$\epsilon_{\max}$ (%)	$\Delta\epsilon_{\max}$ (%)	ϵ_{rms} (%)	σ_{rms} (MPa)	ϵ_m (%)	σ_m (MPa)	W_p (MJ/m^3)	ΔT (°C)	$\Delta T_{\max}$ (°C)
+OR [1.0X]	86.1	61	0.354	2.0	2.7	0.8	272	−0.6	53	131	–‡	–‡
+OR [1.0X]	84.7	81	0.362	1.8	2.7	0.6	271	−0.3	2	139	20.0	1.0
−OR [1.0X]	100.1	74	0.345	1.8	2.7	0.6	285	−0.3	2	140	27.0	2.0
−OR [0.6X]	223.2	77	0.208	1.2	1.8	0.4	250	−0.2	7	79	7.0	0.3
+PL [1.0X]	12.3	151	0.534	6.8	10.0	1.9	255	1.2	11	243	5.0	1.5
−PL [1.0X]	13.1	142	0.508	6.7	9.8	1.9	260	1.2	18	244	3.0	1.0
−PL [0.6X]	46.0	176	0.247	3.9	5.7	1.1	226	0.7	13	117	2.0	0.6
+SI [1.0X]	43.8†	512	0.597	1.6	1.9	0.6	216	0.4	−18	220	–‡	–‡
+SI [1.5X]	21.9	515	1.420	2.4	2.8	0.9	255	0.6	2	536	–‡	–‡
−SI [1.5X]	26.0	523	1.343	2.3	2.8	0.9	257	0.6	−2	526	12.0	9.0
−SI [1.5X]	24.7	540	1.347	2.3	2.8	0.9	261	0.6	−4	532	11.0	8.0

† This specimen deemed to fail earlier than it should (see discussions of test results)

‡ Not measured or problematic measurement

The shortest and longest fatigue lives were respectively observed under the PL and OR loading blocks. The specimens under the OR [1.0X] signal sustained 88 and 100 loading passes for room and subfreezing temperature conditions, respectively. Given that each pass of the applied loading represents the response to a severe design earthquake, the results show that 350WT steel has

significant cyclic energy-dissipation capacity. As shown in Figure 6.9g–i, strains in the PL experiments were large enough to cause necking after a few passes. Failure life at subfreezing temperature was always slightly higher than at room temperature tests. The specimens at subfreezing temperature however exhibited sharp crack opening before failure and sudden loss of strength. This failure mode is shown in Figure 6.9m for one of the –SI [1.5X] experiments.

In test +SI [1.0X], reading from the lateral displacement monitoring sensors showed that the alignment of test set-up gradually degraded. As shown in Figure 6.9j, the specimen fracture pattern at the bottom of the gage area, near the extensometer knife, indicates significant bending that likely reduced the fatigue life of the specimen. The evolution of the "energy dissipated per pass" is plotted in Figure 6.8b. As a general trend, it started to decline considerably a few passes before failure due to damage experienced by the specimen. However, the results from +SI [1.0X] test showed a different pattern as the energy-per-pass constantly rose during the final passes, which is not theoretically possible. Increases in the inter-pass stress range and differences between lowest and highest stress amplitudes in one pass were also observed. Since the gage area was fully strain-hardened in previous passes, an increase in the energy-per-pass or inter-pass stress range, can only happen if the specimen underwent a larger displacement range, which suggests that specimen sustained axial deformations over the gage area larger than the extensometer reading during the last passes. For this reason, it is estimated that this specimen failed earlier than it should. A similar behaviour, although less pronounced, was also seen in +SI [1.5X]. Results from the other tests are deemed to better represent the actual fatigue resistance of the material under the applied loading.

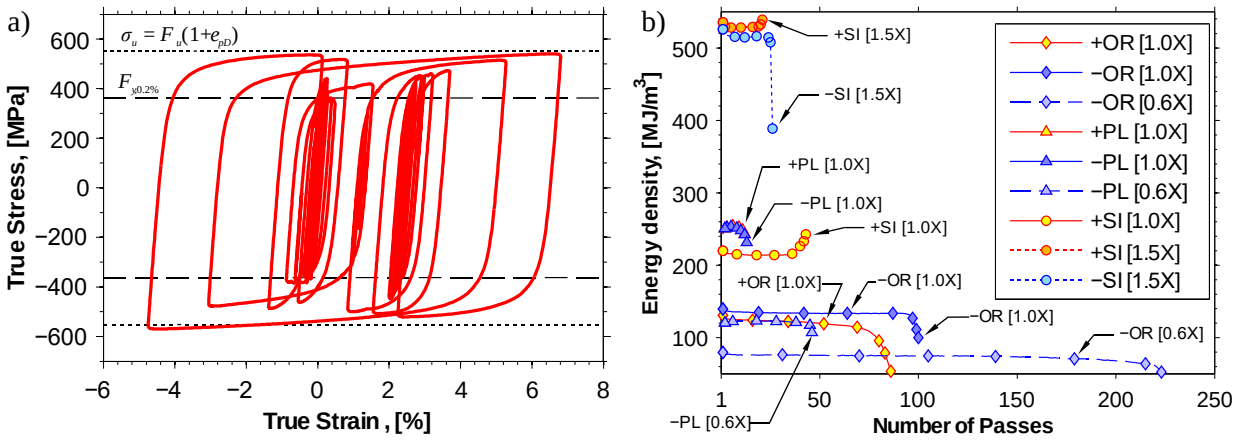

Figure 6.8: a) Hysteresis response in +PL [1.0X] experiment; b) trend of dissipated energy per pass in the seismic-loading tests.

Temperature rises from heat generation during the seismic-loading tests were measured by the thermocouples mounted near the gage area. The measured temperatures are available in Table 6.4: ΔT is the temperature change between beginning and end of test whereas $\Delta T_{\max}$ is the maximum increase in temperature over a single pass. The most significant amount of heat built-up was during the OR tests in which temperature rises of ΔT = 20 and 27 °C were registered under room and subfreezing conditions, respectively. The marked temperature changes under the OR earthquake are attributed to the fact that the majority of the large cycles causing plastic deformations are concentrated in a short time period in the loading signal, which resulted in limited time for heat exchange with the surrounding environment during that time period. Under the SI motion, significant heat was generated by the large number of inelastic cycles during the strong motion portion of the signal but the remaining time periods containing only elastic cycles were long enough to allow heat dissipation and moderate temperature increases after every pass. The highest heat generation rate in a single pass occurred in the –SI [1.5X] tests in which 9 °C temperature rise was recorded near outside of the gage.

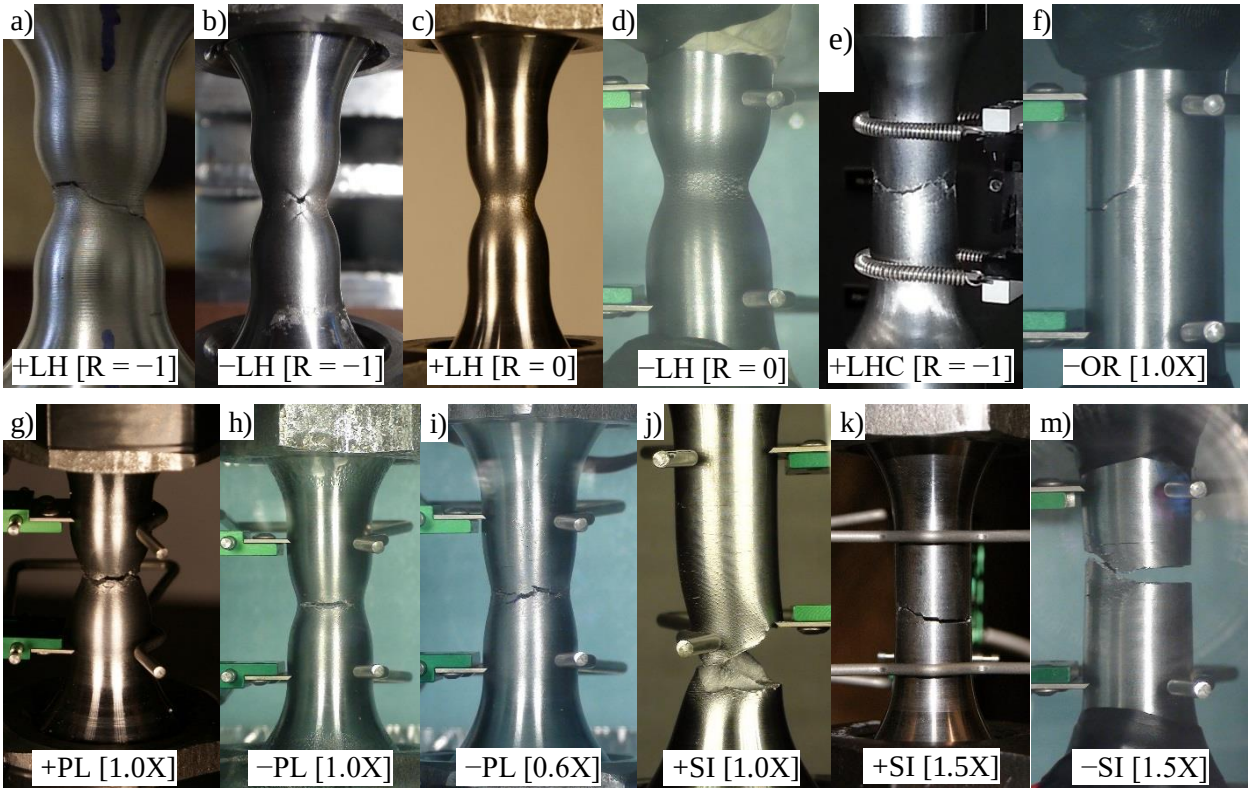

Figure 6.9: Failure under variable-amplitude loadings.

6.4 Fatigue Damage models

Two general frameworks for fatigue damage under uniaxial loading condition are examined in this section: 1) strain-life; 2) energy-life. For each framework, the basics of the fatigue damage model is explained and the empirically calibrated model parameters are reported.

6.4.1 Strain-life models

In the strain-life framework, fatigue damage parameters are based on a combination of elastic and plastic strains. The Manson–Coffin–Basquin models is the most prominent strain-life model in practice. According to this model, amplitude of the total applied strain is related to the number of reversals, $2N_f$, to failure in a double term power-law form (Manson *et al.*, 2006):

$$\frac{\Delta\epsilon}{2} = \frac{\sigma'_f}{E}(2N_f)^b + \epsilon'_f(2N_f)^c \tag{6.1}$$

where $\Delta\epsilon$ is the total applied strain range (elastic + plastic); N_f is the number of cycles to failure; σ'_f and ϵ'_f are the fatigue strength and ductility coefficient, respectively; and, b and c are the fatigue strength and ductility exponents, respectively. The first and second terms on the right-hand side of Eq. (6.1) can be interpreted as elastic and plastic strain amplitudes, respectively. For loading with large plastic strains, the elastic component can be ignored, which leads to a simplified model commonly used in extremely low cycle fatigue calculation (Ohji *et al.*, 1966; Tateishi *et al.*, 2007; Kamaya, 2010):

$$\frac{\Delta\epsilon}{2} = \epsilon'_f(2N_f)^c \tag{6.2}$$

The parameters of the abovementioned models where obtained by regression analysis of the results of all constant-amplitude tests. Logarithmic strain and true stress terms were used in the regression analysis. Simplified strain-life fatigue models of Eq. (6.2) fitted to the experimental data are shown in Figure 6.10a for both temperature conditions. According to these models, failure life at small strains is longer under the subfreezing condition but this difference reduces as the applied strain becomes larger. The best-fit parameters for both the full and simplified strain-life models are presented and compared with those from other studies on similar steels in Table 6.5. The intercept of strain-life fatigue models, ϵ'_f, is highly dependent on the range of strains considered in the test program. Models fitted to tests at small plastic strains give much smaller ϵ'_f and, thereby, shorter life under large strains in comparison to models based on results at large plastic strains. Caution should then be exercised when results of small plastic strain cyclic tests are used in failure prediction under large plastic strains.

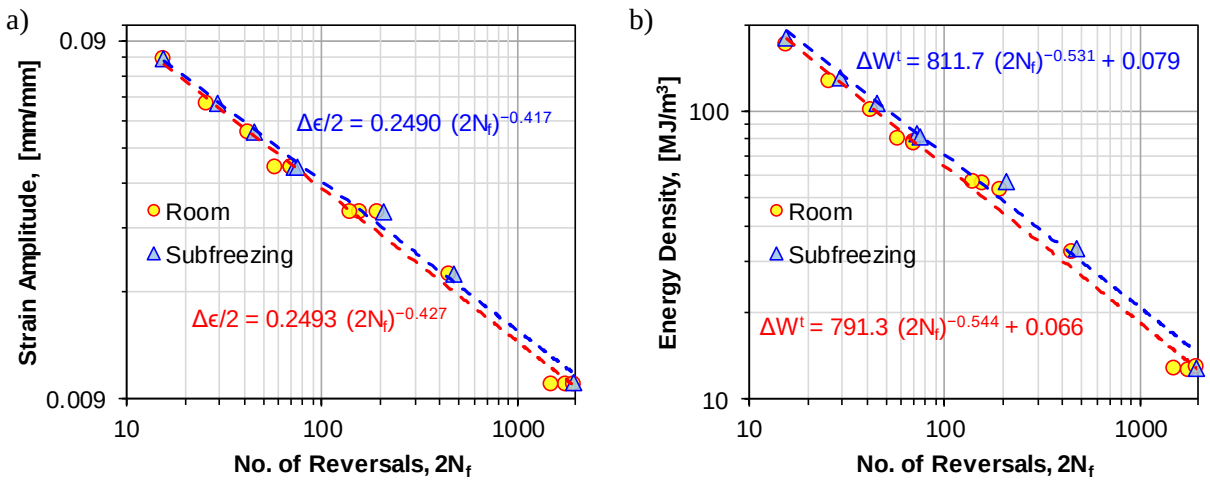

Figure 6.10: Fitted test results to fatigue life models: a) simplified strain-life; and b) energy-life (total strain energy density).

Table 6.5: Parameters of strain-life fatigue damage models for 350WT steel.

	Testing Conditions		Strain-life models					
			Full (Manson–Coffin–Basquin)				Simplified	
	Strain amplitudes	Temperature	σ'_f (MPa)	b (–)	ϵ'_f (%)	c (–)	ϵ'_f (%)	c (–)
This study	1–8%	Room	955	−0.093	27.95	−0.475	24.93	−0.427
		Subfreezing	1050	−0.094	27.77	−0.462	24.90	−0.417
(Josi, *et al.*, 2010)	0.1–0.63%	Room	569	−0.072	12.41	−0.429	5.38	−0.286
(Hamdoon, *et al.*, 2014)	0.1–0.24%	"	76	−0.017	1.84	−0.215	1.41	−0.176

6.4.2 Energy-life models

As the name implies, energy-life fatigue damage is expressed in form of energy. In this framework, it is hypothesized that fatigue failure takes place when absorbed cyclic energy, in excess of some non-damaging threshold, is accumulated to a critical level. Reviews of energy-based theories can be found in (Morrow, 1965) and (Ellyin, 2012). Energy-based approaches have wide practical implications in fatigue life calculation, especially under complex non-proportional multiaxial loading paths. Energy-life models employ different definitions of energy among which plastic energy and total strain energy have shown to be efficient in prediction of fatigue life under complex

loadings (Ellyin, 2012). In the model based on plastic energy (Ellyin *et al.*, 1984), it is assumed that a linear relation exists in log-log coordinates between the number of load reversals to failure and the plastic energy density in a loading cycle:

$$\Delta W^p = \kappa_p (2N_f)^{\alpha_p} \tag{6.3}$$

where ΔW^p is the plastic strain energy density per cycle that corresponds to the area under the stress-strain loop at the half-life cycle (stabilized cycle); and κ_p and α_p are the coefficient and exponent of this damage model. Golos *et al.* (1988) have shown that by accounting for elastic energy and fatigue limit, the accuracy of this plastic energy model could be improved upon, especially when loading involves mean stress. In the improved model, the plastic energy density is replaced by the total strain energy density per cycle ΔW^t and the term ΔW_0^t portraying the strain energy corresponding to the fatigue limit is added:

$$\Delta W^t = \kappa_t (2N_f)^{\alpha_t} + \Delta W_0^t \tag{6.4}$$

In this equation, κ_t and α_t are the coefficient and exponent of the total strain energy model. For structural steel, this energy density could be approximated using the empirical relationship between the fatigue limit stress, σ_{FL}, and the engineering tensile stress, F_u, obtained from monotonic tension tests:

$$\Delta W_0^t = 0.5\sigma_{FL}^2/E \approx 0.5(F_u/3)^2/E \tag{6.5}$$

In Eq. (6.4) , ΔW^t is the summation of the plastic and elastic strain energy densities. The elastic energy component is only accounted for when the loading cycle involves tensile stresses. In uniaxial loading case, ΔW^t can be obtained from:

$$\Delta W^t = \Delta W^p + \Delta W^{e+} = \int_{Cycle} \sigma \mathrm{d}\epsilon_p + \frac{\sigma_{\max}^2}{2E} \tag{6.6}$$

where $\sigma_{\max}$ is the maximum stress is a hysteresis loop.

The energy terms in Eqs. (6.3) and (6.4) were computed from engineering stress and strain histories of the half-life cycle of the constant-amplitude tests and implemented in the regression analysis to

find the parameters of the energy-life models. The results of these regression analyses are presented in Figure 6.10b and Table 6.6.

6.4.2.1 Cyclic strain-hardening curve

To quantify the cyclic hardening behaviour, transitions between the linear segments of stable hysteresis loops from constant-amplitude tests can be represented with a Ramberg-Osgood functional form:

$$\frac{\Delta\epsilon}{2} = \frac{\Delta\epsilon_e}{2} + \frac{\Delta\epsilon_p}{2} = \frac{\Delta\sigma}{2E} + \left(\frac{\Delta\sigma}{2K'}\right)^{1/n'} \tag{6.7}$$

where $\Delta\epsilon_e$ and $\Delta\epsilon_p$ denote the elastic and plastic strain ranges, respectively, $\Delta\sigma$ is the stress range, and K' and n' are the cyclic strength coefficient and cyclic hardening exponent, respectively. When the ascending and descending branches of the hysteresis loops can be described by the cyclic stress-strain curve magnified by a factor of 2, the material is assumed to exhibit "Masing" behaviour. In such cases, if the stable hysteresis loops of various strain amplitudes are transferred to a common origin, e.g. the largest compressive stress, the ascending branch of these loops would follow the same curved path. For this type of behaviour, the plastic energy density can be obtained in a closed-form solution for a given $\Delta\epsilon_p$ and $\Delta\sigma$ at a given cycle:

$$\Delta W^p = \frac{1-n'}{1+n'}\Delta\sigma\Delta\epsilon_p \tag{6.8}$$

Ellyin, *et al.* (1984) have shown that for materials not following the "Masing" behaviour, which is common in carbon steels, the plastic energy is better quantified by a "master" curve which has the same functional form as the cyclic hardening curve except that a different origin is used for superimposing the hysteresis loops so that their ascending half-cycle responses form a unique curve:

$$\Delta\epsilon^* = \frac{\Delta\sigma^*}{E} + 2\left(\frac{\Delta\sigma^*}{2K^*}\right)^{1/n^*} \tag{6.9}$$

where n^* and K^* are the parameters of the "master" curve that could be obtained as instructed in (Ellyin, 2012). By employing this concept, plastic energy density for "Masing" and "non-Masing" materials can be obtained as:

$$\Delta W^p = \frac{1-n^*}{1+n^*}\Delta\sigma\Delta\epsilon_p + \frac{2n^*}{1+n^*}\delta\sigma_0\Delta\epsilon_p \tag{6.10}$$

where n^* is the exponent of the "master" curve and $\delta\sigma_0$ is a stress term computed from the difference between the "master" and cyclic strain hardening curves:

$$\delta\sigma_0 = \Delta\sigma - \Delta\sigma^* = \Delta\sigma - 2K^*\left(\frac{\Delta\epsilon_p}{2}\right)^{n^*} \tag{6.11}$$

Examination of the stable hysteresis loops from the constant-amplitude tests indicated that the 350WT steel studied herein is a non-Masing type of material. Values of the parameters of the cyclic hardening and master curves that best reproduce the test results for that steel are presented in Table 6.6.

Table 6.6: Fitted parameters of energy-life models and cyclic hardening and master curves of the 350WT steel

	Energy-life fatigue models				Cyclic hardening and master curve			
	Plastic		Total					
Temperature Condition	κ_p (MJ/m^3)	α_p (–)	κ_t (MJ/m^3)	α_t (–)	K' (MPa)	n' (–)	K^* (MPa)	n^* (–)
Room	802.6	−0.550	791.3	−0.544	923	0.142	517	0.027
Subfreezing	823.1	−0.536	811.7	−0.531	1001	0.153	620	0.058

6.5 Fatigue failure prediction

Fatigue damage under variable-amplitude loading were computed using the strain-life and energy-life models. As a typical process, the loading history is first broken down into series of partial damage events, e.g. strain half-cycles or hysteresis energy loops. For the i^{th} partial damage event, the number of cycles to failure, $N_{f,i}$, is computed from the strain- or energy-life fatigue damage model, as applicable. The fatigue damage induced by the event is then computed as the ratio of the

event's number of cycles to the $N_{f,i}$. Finally, the so-computed fatigue damage is integrated over all events considering linear damage accumulation hypothesis (Miner, 1945) to estimate the total fatigue damage:

$$D = \sum_{i=1}^{N} n_i / N_{f,i} \tag{6.12}$$

According to this model, failure occurs when D reaches 1.0. For seismic-loading, the number of passes to failure is predicted as the inverse of the accumulated fatigue damage in one loading pass. The predicted number of passes to failure under seismic-loading obtained from the various discussed fatigue models are reported in Table 6.7. Details of calculations and discussions on the results for both seismic- and step-loading protocols are presented in the next subsections.

6.5.1 Strain-life approach

In the strain-life fatigue failure estimation, the fatigue life is defined as function of applied strains (Eq. (6.1) or (6.2)). The simplified strain-life equation (Eq. (6.2)) will be used as the main fatigue model for the calculations. Differences between the predictions from the simplified and full strain-life models are presented at the end of this subsection. To compute damage, the recorded gage strain history was subjected to the rainflow cycle counting method (ASTM, 2005) and only strain ranges larger than 50% of the fatigue limit, i.e. $\Delta\epsilon < \sigma_{FL}/E \approx F_u/3E$, were considered in the damage calculation. When mean stress or strain effects could be ignored, combining Eqs. (6.2) and (6.12) gives the accumulated damage directly as follows:

$$D = 2(2\epsilon'_f)^{1/c} \sum_{i=1}^{N} n_i \, (\Delta\epsilon)_i^{-1/c} \tag{6.13}$$

where $(\Delta\epsilon)_i$ and n_i are the strain range and the corresponding number of cycles for the i^{th} damaging event, respectively. The parameters ϵ'_f and c are the values reported in Table 6.5. The effect of mean stress was accounted for using the Morrow's approach as explained in (Dowling, 2009). In this approach, the number of cycles to failure is first computed from the zero-mean stress strain-life equation and subsequently modified according to:

$$N^*_{f,i} = N_{f,i}\left[1 - \frac{\sigma_{m,i}}{\sigma'_f}\right]^b \tag{6.14}$$

Where, N^*_f is the number of cycles to failure under presence of mean stress, $\sigma_{m,i}$ is the average of the stresses at the beginning and end of the i^{th} counted half-cycle, and parameters σ'_f and b can be found in Table 6.5. According to this model, a tensile mean stress reduces the fatigue life whereas a compressive mean stress has the opposite effect. Calculations showed that the mean stress effect becomes significant when the loading block comprises a large number of elastic cycles. Similarly, the mean strain effect was taken into account by using the model proposed by Ohji, *et al.* (1966). In such a case, the simplified strain-life equation (Eq. (6.2)) was replaced by the following equation which was solved to find the failure life N_f for the given half-cycle event with mean strain:

$$\frac{\Delta\epsilon}{2} = (1-R)\epsilon'_f\left[\frac{(4N_f-1)}{2(1-R)^{1/c}} + \frac{1}{2^{1+1/c}}\right]^c \tag{6.15}$$

where R is the ratio of the smaller to larger strains (the comparison is based on the absolute value of the peak strains) in the half-cycle under consideration. In the mentioned theory the tensile and compressive mean strains are assumed to be equally damaging. This equation is downgraded to Eq. (6.2) when the mean strain is zero, i.e. $R = \epsilon_{\min}/\epsilon_{\max} = -1$. Parameters ϵ'_f and c are from regression analysis of the constant-amplitude tests with zero-mean strain (see Table 6.5). Calculations showed that the mean strain did not have detrimental effects for strain ranges less than 5%. The predicted fatigue life under the step- and seismic-loading patterns using the simplified strain-life model are compared to measured values in Figure 6.11.

For the LH patterns, the predicted failure life is overestimated by 10 to 26%. The calculations resulted in $D < 1.0$ while specimen failure was observed in the laboratory. The least and highest errors were respectively obtained for the +LH [R = −1] and −LH [R = 0] patterns. Accounting for the effect of mean strain using Eq. (6.15) improved the prediction and the calculated fatigue damage under symmetrical and asymmetrical patterns became comparable. Failure life in the LH tests at room temperature were better predicted compared to that in the subfreezing tests. This difference may be due to the variations in specimen's temperatures in the subfreezing tests. In the −LH [R = 0] test, the bending strains (see Figure 6.9d) may have contributed to the relatively higher (26%) overestimated fatigue life. On the other hand, the life under the LHC loading pattern was

consistently underestimated with an average error of 41% ± 8%. This relatively high error can be explained by the fact that the LHC tests were conducted on polished specimens that likely had relatively longer fatigue life. In general, errors in fatigue life predictions for the step-loading patterns are mainly attributed to the damage accumulation rule employed in the calculations. (Fatemi *et al.*, 1998) have shown that the Miner's linear damage accumulation rule overestimates the fatigue life under low-high loading sequences and underestimates it when the high amplitude loading is followed by a less intensive history.

The observed numbers of passes under seismic-loading are compared to the values predicted by the various models, i.e. $1/D$, in Table 6.7. The observed values are also plotted against the corresponding predictions in Figure 6.11b. For the majority of the cases, the failure life is predicted with less than +12% error (the error in the figure is defined as 1.0 minus the ratio between observed and predicted lives). The most precise prediction was obtained for the +OR [1.0X] and +PL [1.0X] cases with +2% error. In the case of the long duration SI pattern, the failure life is overestimated by 23 to 48%. As mentioned before, strain readings over the gage area in the SI loading tests were likely less than reality, which may explain the relatively higher life overestimation obtained for these tests. The adverse effects of bending strains in the +SI [1.0X] experiment can partially explain the relatively larger error for this specific experiment. As a general trend, the predicted fatigue life is relatively more accurate in the room condition tests than in the subfreezing ones. For instance, failure life under the OR signal is estimated within +2.0% and +12.0% for tests at room and subfreezing conditions, respectively. This difference can be attributed to the higher temperature of the specimens due to the greater heat built-up generated by the fast loading rate applied in the seismic tests compared to the lower rate of the benchmark quasi-static constant-amplitude tests used to determine the fatigue model parameters at subfreezing condition. The parameters obtained from the benchmark tests may be representative of the conditions that prevail under dynamic seismic-loading.

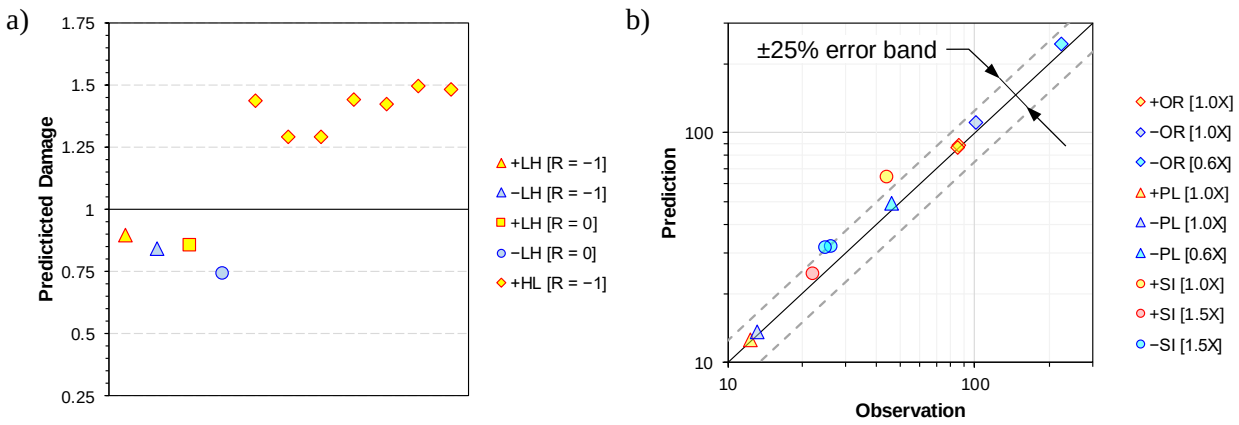

Figure 6.11: Prediction of fatigue damage (or failure life) using strain-life model for: a) Step-loading patterns; and b) Seismic-loading patterns.

When the full strain-life model of Eq. (6.1) is used in the calculations, the accuracy of the predictions was generally reduced. Differences between the full and simplified models become less pronounced as the strain intensity is increased. The least and largest differences between fatigue life values from the two models were for the −PL [0.6X] and +SI [1.0X] tests, respectively. For the latter case, the full model gives 50% more error than the simplified one. This is attributed to the large number of small strain cycles in this loading block. The fatigue life is likely overestimated because the model was fitted for strain amplitudes between 1 and 8% and then extrapolated to smaller strains. The slope of the full model at large strains, c, starts to change at 1.0% strain and gradually increases to much higher values at smaller strains. This results in a longer life, or lower damage, for a given strain compared to the simplified model which has a constant slope. As a results of this difference, predictions from the two models start to deviate considerably starting at 0.5% strain amplitude. From these observations, it can be concluded that the simplified strain-life model of Eq. (6.2) would be more efficient for large strain demands encountered in earthquake engineering applications. The full strain-life model of Eq. (6.1) could be equally accurate if the calibration includes test results at small strain amplitudes, e.g. $\Delta\epsilon/2 < 1.0\%$.

Table 6.7: Observed and predicted numbers of passes to failure in the seismic-loading experiments (numbers are rounded to nearest integer for clarity)

		Ordinary				Pulse-Like			Subduction Interface			
		+OR [1.0X]	+OR [1.0X]	−OR [1.0X]	−OR [0.6X]	+PL [1.0X]	−PL [1.0X]	−PL [0.6X]	+SI [1.0X]	+SI [1.5X]	−SI [1.5X]	−SI [1.5X]
Observations		86	85	100	223	12	13	46	44	22	26	25
Predictions	Simplified strain-life	88	86	112	244	13	14	49	65	25	32	32
	Full strain-life	99	94	128	323	13	14	48	100	31	42	44
	Ellyin[†]	104	96	118	315	13	15	52	111	32	42	42
	Lagoda-Macha	95	111	146	395	13	16	56	61	18	26	26

[†] Results of total strain energy model are presented

6.5.2 Energy-life approach

Two phenomenological energy-based damage models for fatigue failure prediction under variable-amplitude loading were examined: 1) Ellyin (2012); and 2) Lagoda-Macha (Lagoda, 2001).

6.5.2.1 Ellyin method

As described in the previous section, this method takes the plastic or total strain energy density of a cycle (Eq. (6.6)) as the fatigue damage parameter. In the first step, the full stress-strain response under variable-amplitude loading is broken down into hysteresis loops and the fatigue life for each loop is calculated using Eq. (6.3) or (6.4). These loops can be detected using rainflow cycle counting of the strain signal. For each variable-amplitude tests, this procedure was followed using the recorded stress and strain data. As indicated, loops with energy density lower than 50% of the fatigue limit energy (Eq. (6.5)) were ignored in damage calculations. If the history of stress is not available, energy densities can be approximated by implementing a realistic stress-strain relationship with an appropriate strain hardening law to simulate the stress response. Alternatively, master and cyclic strain hardening curves from Eqs. (6.7) to (6.11) can be employed to compute

the plastic energy assuming either Masing or non-Masing behaviour. As noted, the experimental results showed that the 350WT steel does not follow the Masing rule.

The predictions made with the Ellyin method are compared to the experimental observations in Table 6.7 and Figure 6.12. The Ellyin and strain-life approaches give comparable accumulated damage for the step-loading patterns. These approaches also had the same trend in terms of sequence effect. However, as opposed to the strain based models, the Ellyin approach predicts the same damage for fully-reversed LH tests at room and subfreezing tests. For seismic loading, applying the Ellyin method results in predictions with +9 to +153% errors compared to test values. The lowest and highest errors were obtained for the +PL [1.0X] and +SI [1.0X] experiments, respectively. The prediction error by the Ellyin method is substantially higher than the strain-life method. However, both approaches converge to nearly the same results at very large strains, e.g. PL [1.0X], and would diverge significantly when the loading block consists of many elastic cycles, e.g. SI [1.5X]. Given the effort required to extract the hysteresis loops and associated energies, and its lower accuracy, this approach is deemed less effective than the strain-life model.

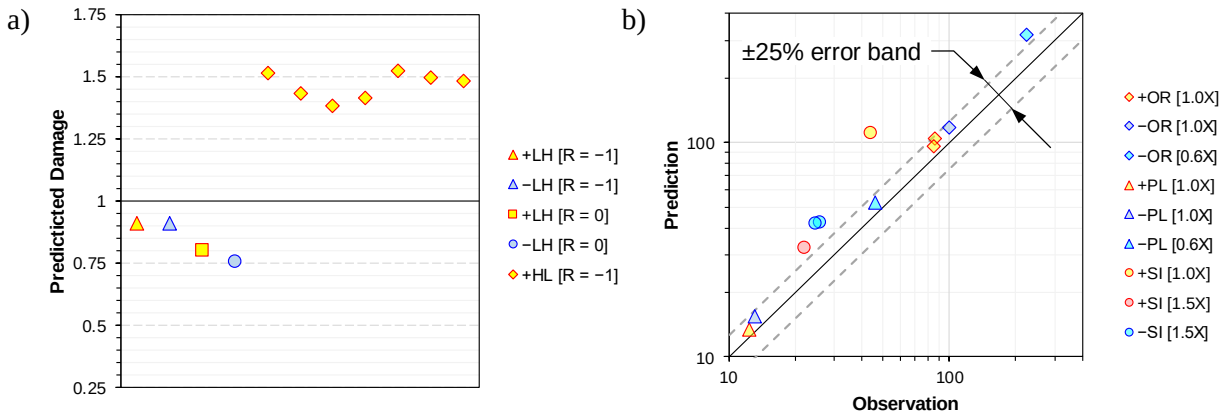

Figure 6.12: Prediction of fatigue damage (or failure life) using the Ellyin energy-life model for: a) Step-loading; and b) Seismic-loading patterns.

6.5.2.2 Lagoda-Macha method

Lagoda (2001) proposed a fatigue damage term which employs histories of both stresses and strains in the following form:

$$W(t) = \frac{1}{2}\sigma(t)\epsilon(t)\left[\frac{\mathrm{sgn}\big(\sigma(t)\big) + \mathrm{sgn}\big(\epsilon(t)\big)}{2}\right] \tag{6.16}$$

where t denotes time and $\mathrm{sgn}(x)$ is the Signum function which is defined as:

$$\mathrm{sgn}(x) = \begin{cases} 1 & x > 0 \\ 0 & x = 0 \\ -1 & x < 0 \end{cases} \tag{6.17}$$

In this model, damage is counted when stresses and strains have the same signs. To compute the fatigue life, the energy history obtained from Eq. (6.16) is first decomposed in damaging events by a cycle counting method, e.g. rainflow. Then, for each event, the following equation is solved to obtain the number of cycles to failure:

$$W_a = \frac{(\sigma'_f)^2}{2E}(2N_f)^{2b} + 0.5\epsilon'_f\sigma'_f(2N_f)^{b+c} \tag{6.18}$$

where W_a is the amplitude of the given half-cycle event. Material constants on the right-hand side of Eq. (6.18) is obtained by fitting the constant-amplitude tests results to the Manson-Coffin-Basquin strain-life model as described by Eq. (6.1) (see Table 6.6). Eq. (6.18) is a two-term power-law expression that does not have a closed form solution. For any given energy amplitude, the failure life can be obtained by a general nonlinear solver such as Newton-Raphson. Manson, *et al.* (2006) proposed an approximate non-iterative solution for this type of equation which can facilitate calculations. The failure life can then be computed by integrating the fatigue damage due to each counted significant event obtained by solving Eq. (6.18) for the given energy amplitude. Life calculation results for the step- and seismic-loading histories based on the Lagoda-Macha model are given in Table 6.7 and plotted in Figure 6.13. For the LH step-loading pattern, the fatigue damage predictions are less accurate than those obtained from the other models with maximum error of 57% in case of –LH [R = 0]. However, this method showed better prediction capabilities for the LHC patterns. In general, the average error of the Lagoda-Macha approach for failure prediction under step-loading is comparable to the other methods.

Prediction errors with the Lagoda-Macha approach for seismic-loading are between −19% to +77% with the majority being within the ±25% band. The smallest absolute error was obtained for +PL [1.0X] and –SI [1.5X] experiments for which the predicted life is only 2% different from the

laboratory observations. Unlike the other models, the largest prediction error was observed in case of the −PL [0.6X] loading. Contrary to previously discussed models which overestimated fatigue life in all cases, the Lagoda-Macha method underestimated the fatigue life in one case, i.e. +SI [1.5X], by a 19% margin. Although, the Lagoda-Macha approach tends to perform better than the Ellyin model, its prediction ability is still found less accurate than the strain-life method.

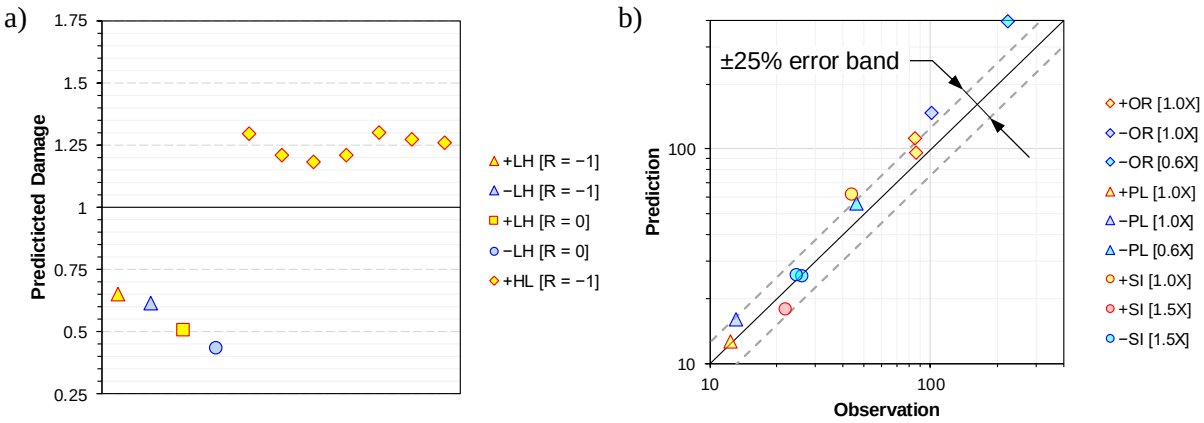

Figure 6.13: Prediction of fatigue damage (or failure life) using Lagoda-Macha energy-life model for: a) Step-loading; and b) Seismic-loading patterns.

6.6 Conclusions

Uniaxial tensile and low cycle cyclic tests were conducted on round specimens from 350WT Category 4 steel at room and subfreezing temperatures. The cyclic tests were performed under constant amplitude, step loading, and seismic loading patterns that corresponded to three different types of earthquakes. It was observed that the monotonic tensile ductility of the steel studied was not reduced by cold temperatures as low as −40°C. The low-cycle fatigue life under constant- and variable-amplitude loading histories at subfreezing temperatures between −15°C and to −35°C was found to be equal or slightly higher than values measured at room temperature. Lateral stiffness of the loading frame is also shown to be an important factor in the fatigue life under large strains. Test results were used to obtain the parameters of popular strain-life and energy-life fatigue damage models, as well as cyclic strain hardening curves. Fatigue failure life under various uniaxial variable-amplitude loading patterns were calculated using three fatigue life models and linear damage accumulation rule, and compared to the laboratory measurements. All life prediction models were found to be accurate for seismic loading, especially when the loading history

contained large strain cycles. Among all models, the simplified strain-life model from Eq. (6.2) showed superior performance in terms of the prediction accuracy and numerical efficiency for high strain demands. The fatigue life predictions were generally more accurate at room temperature, likely because the temperature conditions in the constant-amplitude tests used to determine the model parameters and those prevailing in the seismic loading tests were different. The linear damage accumulation rule seems to under- and overestimate fatigue life under low-high and low-high-constant step-loading strain patterns, respectively. To improve the prediction accuracy, more uniform testing conditions and wider range of applied strains may be required.

Acknowledgment

The authors express their gratitude to the technical staff of the Structural Engineering Laboratory at Polyetchnique Montreal for their assistance and input in the experimental program. The assistance of summer intern Mr. Xavier Lachapelle-Trouillard is appreciated. Sincere thanks are also extended to graduate student Éric Beaumont and Professor Charles-Darwin Annan from Laval University for conducting the complementary tests and sharing their data. Financial support for this project was provided by the Natural Sciences and Engineering Research Council of Canada (NSERC) for the Canadian Seismic Research Network (CSRN). The first author acknowledges the scholarship awarded by the Structural Steel Education Council of the Canadian Institute of Steel Construction. The strong ground motion records used in this study were obtained from PEER strong motion database (http://peer.berkeley.edu/) and Japanese strong-motion seismograph networks K-Net and Kik-Net (http://www.kyoshin.bosai.go.jp/).

Nomenclature

Symbols

C_p	:	specific heat
D	:	fatigue damage
E	:	Young modulus
EL	:	elongation at fracture
$F_{y,0.2\%}$	:	lower yield stress measured by 0.2% offset method
$F_{y,Upper}$	:	upper yield stress

F_u	:	ultimate tensile stress
K	:	coefficient of thermal conductivity
K'	:	cyclic strength coefficient
K^*	:	coefficient of master curve (for non-Masing materials)
N_f	:	number of cycles to failure
R	:	ratio of minimum to maximum strain in a half-cycle
RA	:	area reduction at fracture
R_a	:	average surface roughness
W_a	:	amplitude of energy density term
W_p	:	total plastic work in a single loading pass
b	:	fatigue strength exponent
c	:	fatigue ductility exponent
h_c	:	convective heat transfer coefficient
n'	:	cyclic hardening exponent
n^*	:	exponent of master curve (for non-Masing materials)
n_i	:	number of cycles of damaging events for a given intensity
ΔT	:	total temperature changes during test
$\Delta T_{\max}$	:	maximum temperature changes in one single pass of seismic-loading
ΔW_0^t	:	strain energy corresponding to the fatigue limit
ΔW^{e+}	:	elastic strain energy of tensile stress in one cycle
ΔW^p	:	plastic strain energy density in one cycle
ΔW^t	:	total strain energy density in one cycle
$\Delta\epsilon$	:	strain range
$\Delta\epsilon_{\max}$	:	largest strain range in the strain signal
$\Delta\epsilon_e$	:	elastic strain range
$\Delta\epsilon_p$	:	plastic strain range
$\Delta\sigma$	:	stress range
$\Sigma(\mathrm{d}\epsilon_p)$	:	sum of plastic strain increments (absolute values)
α	:	exponent of energy-life fatigue models
γ	:	density

$\epsilon_{\max}$: maximum strain amplitude

ϵ_f : true stress at fracture

ϵ'_f : fatigue ductility exponent

ϵ_m : average of strain signal

ϵ_p : plastic strain

ϵ_{pD} : elongation at maximum force

ϵ_{rms} : root mean-square of the strain signal

κ : coefficient of energy-life fatigue models

σ_{FL} : fatigue limit stress (endurance stress)

$\sigma_{\max}$: maximum amplitude of tensile stress in one cycle

$\sigma_{m,i}$: average of stresses at the beginning and end of the i^{th} counted half-cycle

σ_m : average stress signal

σ_{rms} : root mean-square of the stress signal

σ'_f : fatigue strength coefficient

Abbreviations

2D : two-dimensional

BRB : Buckling-Restrained Brace

BRBF : Buckling-Restrained Braced Frame

CoV : Coefficient of Variation

CVN : Charpy V-Notch

ELCF : Extremely Low Cycle Fatigue

LCF : Low Cycle Fatigue

LH : Low-High (a loading sequence)

LHC : Low-High-Constant (a loading sequence)

OR : Ordinary (a type of seismic loading history)

PL : Pulse-Like (a type of seismic loading history)

SI : Subduction Interface (a type of seismic loading history)

ULCF : Ultra Low Cycle Fatigue

References

AISC. (2010). ANSI/AISC 341-10, Seismic Provisions for Structural Steel Buildings. Chicago, IL: American Institute of Steel Construction, Inc.

ASTM. (2004). E606 − 04e1 Standard Practice for Strain-Controlled Fatigue Testing. West Conshohocken, PA: ASTM International.

ASTM. (2005). E1049 − 85(2005) Standard Practices for Cycle Counting in Fatigue Analysis. West Conshohocken, PA: ASTM International.

ASTM. (2007). E23 - 07ae1 Standard Test Methods for Notched Bar Impact Testing of Metallic Materials. West Conshohocken, PA: ASTM International.

ASTM. (2009). E8/E8M − 09 Standard Test Methods for Tension Testing of Metallic Materials. West Conshohocken, PA: ASTM International.

ASTM. (2011). A709/A709M – 11 Standard Specification for Structural Steel for Bridges. West Conshohocken, PA: American Society for Testing and Materials,.

ASTM. (2012). E1012 −12 Standard Practice for Verification of Testing Frame and Specimen Alignment Under Tensile and Compressive Axial Force Application: ASTM International.

Beaumont, E., & Annan, C.-D. (2016). *Cyclic Response of Structural Stainless Steel Plate Under Large Inelastic Strains*. Paper presented at the Annual Conference of the Canadian Society for Civil Engineering, London, Ontario.

Chen, H., Grondin, G. Y., & Driver, R. G. (2005). *Fatigue Resistance of High Performance Steel* (Structural Engineering Report No. 258). Edmonton: University of Alberta.

Clifton, C., Bruneau, M., MacRae, G., Leon, R., & Fussell, A. (2011). Steel structures damage from the Christchurch earthquake series of 2010 and 2011. *Bulletin of the New Zealand Society for Earthquake Engineering, 44*(4), 297-318.

CSA. (2004). G40.20-04/G40.21-04 (R2009) General Requirements for Rolled or Welded Structural Quality Steel/ Structural Quality Steel: Canadian Standards Association.

Dehghani, M., & Tremblay, R. (2017b). Seismic Performance of Canadian Code-Conforming Buckling-Restrained Braced Frames. (under preparation).

Dowling, N. E. (2009). Mean stress effects in strain–life fatigue. *Fatigue & Fracture of Engineering Materials & Structures, 32*(12), 1004-1019.

Dusicka, P., Itani, A. M., & Buckle, I. G. (2007). Cyclic response of plate steels under large inelastic strains. *Journal of Constructional Steel Research, 63*(2), 156-164.

Ellyin, F. (2012). *Fatigue damage, crack growth and life prediction*: Springer Science & Business Media.

Ellyin, F., & Kujawski, D. (1984). Plastic Strain Energy in Fatigue Failure. *Journal of Pressure Vessel Technology, 106*(4), 342-347.

Fatemi, A., & Yang, L. (1998). Cumulative fatigue damage and life prediction theories: a survey of the state of the art for homogeneous materials. *International Journal of Fatigue, 20*(1), 9-34.

Golos, K., & Ellyin, F. (1988). A total strain energy density theory for cumulative fatigue damage. *Journal of pressure vessel technology, 110*(1), 36-41.

Hamdoon, M., Zamani, N., & Das, S. (2014). Effect of Combined Cold Temperature and Fatigue Load on Performance of G40. 21 Steel. *Materials Performance and Characterization, 3*(1), 49-64.

Josi, G., & Grondin, G. (2010). *Reliability-based management of fatigue failures* (SER 285). Edmonton, Alberta, Canada: University of Albetra.

Kamaya, M. (2010). Fatigue properties of 316 stainless steel and its failure due to internal cracks in low-cycle and extremely low-cycle fatigue regimes. *International Journal of Fatigue, 32*(7), 1081-1089.

Kanvinde, A. M., & Deierlein, G. G. (2005). *Continuum Based Micro-Models for Ultra Low Cycle Fatigue Crack Initiation in Steel Structures.* Paper presented at the Structures Congress 2005, New York, New York.

Kanvinde, A. M., Marshall, K., Grilli, D., & Bomba, G. (2014). Forensic Analysis of Link Fractures in Eccentrically Braced Frames during the February 2011 Christchurch Earthquake: Testing and Simulation. *Journal of Structural Engineering, 141*(5), 04014146.

Kuroda, M. (2002). Extremely low cycle fatigue life prediction based on a new cumulative fatigue damage model. *International Journal of Fatigue, 24*(6), 699-703.

Lagoda, T. (2001). Energy models for fatigue life estimation under uniaxial random loading. Part I: The model elaboration. *International Journal of Fatigue, 23*(6), 467-480.

Manson, S. S., & Halford, G. R. (2006). *Fatigue and Durability of Structural Materials*: ASM International.

Miner, M. A. (1945). Cumulative damage in fatigue. *Journal of applied mechanics, 12*(3), 159-164.

Morrow, J. (1965). Cyclic plastic strain energy and fatigue of metals *Internal friction, damping, and cyclic plasticity*: ASTM International.

Nip, K. H., Gardner, L., Davies, C. M., & Elghazouli, A. Y. (2010). Extremely low cycle fatigue tests on structural carbon steel and stainless steel. *Journal of Constructional Steel Research, 66*(1), 96-110.

Ohji, K., Miller, W. R., & Marin, J. (1966). Cumulative Damage and Effect of Mean Strain in Low-Cycle Fatigue of a 2024-T351 Aluminum Alloy. *Journal of Basic Engineering, 88*(4), 801-810.

Stephens, R. I., Fatemi, A., Stephens, R. R., & Fuchs, H. O. (2000). *Metal fatigue in engineering*: John Wiley & Sons.

Stephens, R. I., Lee, S. G., & Lee, H. W. (1982). Constant and variable amplitude fatigue behavior and fracture of A572 steel at 25°C(77°F) and −45°C(−50°F). *International Journal of Fracture, 19*(2), 83-98.

Taheri, F., Trask, D., & Pegg, N. (2003). Experimental and analytical investigation of fatigue characteristics of 350WT steel under constant and variable amplitude loadings. *Marine Structures, 16*(1), 69-91.

Tateishi, K., Hanji, T., & Minami, K. (2007). A prediction model for extremely low cycle fatigue strength of structural steel. *International Journal of Fatigue, 29*(5), 887-896.

Tremblay, R., Bolduc, P., Neville, R., & DeVall, R. (2006). Seismic testing and performance of buckling-restrained bracing systems. *Canadian Journal of Civil Engineering, 33*(2), 183-198.

Tremblay, R., Filiatrault, A., Bruneau, M., Nakashima, M., Prion, H. G. L., & DeVall, R. (1996). Seismic design of steel buildings: lessons from the 1995 Hyogo-ken Nanbu earthquake. *Canadian Journal of Civil Engineering, 23*(3), 727-756.

Tremblay, R., Filiatrault, A., Timler, P., & Bruneau, M. (1995). Performance of steel structures during the 1994 Northridge earthquake. *Canadian Journal of Civil Engineering, 22*(2), 338-360.

CHAPTER 7 ARTICLE 3 : AN ANALYTICAL MODEL FOR ESTIMATING RESTRAINER DESIGN FORCES IN BOLTED BUCKLING-RESTRAINED BRACES

Morteza Dehghani, and Robert Tremblay

Paper submitted to *Journal of Construction Steel Research*,

Submitted on 22 Nov 2016

ABSTRACT

This article presents an analytical model that is proposed to predict the normal thrust force to be considered for the design of the restraining system of all-steel buckling restrained bracing members. Compared with previous similar models, the model accounts for Poisson's effects on core cross-section properties, flexibility of the restraining system, longitudinal frictional forces and variation of the axial load along the core yielding segment. It is shown that the strain distribution along the core is non-uniform when friction at the interface of the core and restrainer becomes significant. Kinematic and isotropic strain hardening of the core steel material under cyclic loading are also incorporated in the model and the analysis is performed for the largest anticipated compression excursion in a test protocol or from response history seismic analysis of a frame. The buckled shape of the core and the resulting normal thrust forces are evaluated along the length of the brace core yielding segment. The model predicts the maximum compression axial load resisted by the brace, which is used to estimate the tensile and compressive strength adjustment factors in the braced frame design. Guidance is also given on the restrainer minimum stiffness required to achieve stable core inelastic response under the maximum compression force. The model is validated against the results from physical tests and three-dimensional finite element analyses for two different buckling restrained bracing members tested in previous experimental programs.

Key words: Buckling modes, cyclic strain hardening, confined buckling, friction, restrainer, wavelength

7.1 Introduction

Buckling restrained braces (BRBs) represent a very effective means of resisting lateral loads and dissipate seismic input energy for building structures. The cyclic inelastic response of BRB members in structures subjected to strong earthquake events heavily depends on the buckling restraining system used for the braces. All-steel restraining mechanisms have been proposed in the last decade to achieve robust hysteretic response. These systems typically consist of a pair of steel profiles connected together by two longitudinal rows of bolts regularly spaced along the brace length. One such system is illustrated in Figure 7.1a. In this example, the BRB core is a flat plate and each restraining half is a built-up section made of a plate welded to a rectangular HSS. Shim plates are placed on each side of the core to complete the confinement. A gap is left around the core to permit expansion of the cross-section due to Poisson's effect under compression. A debonding material is generally used between the core and the restrainer to minimize friction when the core slips relative to the restrainer under axial straining.

The restraining system must possess sufficient flexural stiffness and strength to prevent overall buckling of the brace under compression. It must also constrain local buckling of the yielding segment (YS) of the core about both its weak and strong axes when subjected to large compressive strains. Weak axis buckling typically dominates the core response and the restraining system must resist the normal outward forces imposed by the buckled core (Figure 7.1b). The amplitude of the normal forces depends on the core axial compression load, the length of the buckling waves, the gap size, and the flexibility of the restraining system. The buckling wavelength is a function of the core axial load and the tangent modulus of the core steel material. Longitudinal frictional forces develop between the core and the restrainer as the core is pushed inside the restrainer and compressive axial load and strains in the core decrease towards a fixed point along the core length where there is no slip between the core and the restrainer (Figure 7.1b). Core buckling, frictional forces, and Poisson's effects are therefore more severe at the ends of the core yielding segment, which further accentuates the variation of the compressive axial load and strains along the core length. Upon load reversal, the amplitude and distribution of the tension force and tensile strains along the core depend on the conditions present at the end of the preceding compression excursion. Thus, larger tensile strains typically develop near the core fixed point due to the lower compression strains and smaller cross-section dimensions (less Poisson's effects) at this location. Core inelastic

buckling and yielding is also significantly influenced by isotropic and kinematic strain hardening of the steel material upon cyclic loading (Figure 7.1c). Inelastic cyclic response of BRB members including low-cycle fatigue life can be improved by reducing these variations in core axial strains, which can be achieved by minimizing the normal thrust forces and resulting longitudinal frictional forces in compression. A simple model that can reliably predict these forces and variations in core axial strains is therefore needed to properly design the restraining system and develop effective brace response.

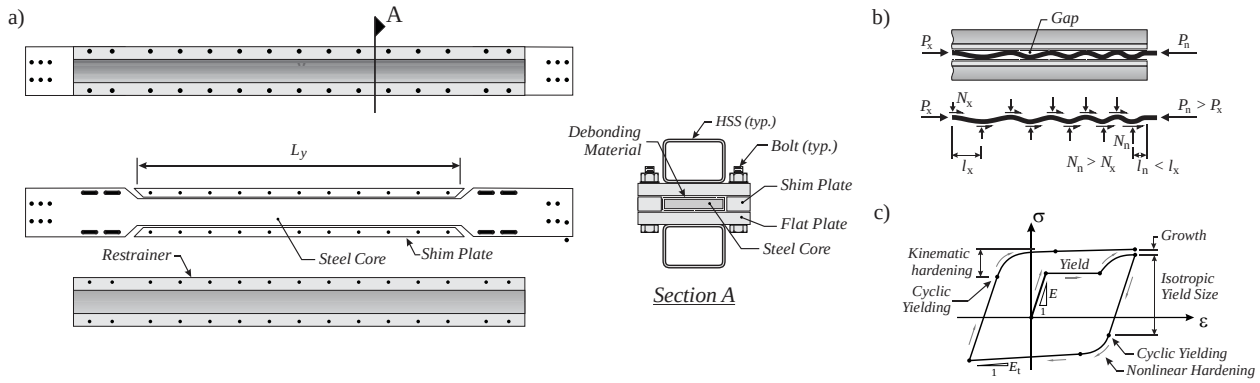

Figure 7.1: a) Typical steel-encased BRB member; b) Weak axis local buckling of the core and longitudinal friction under axial compressive strains; and c) Stress-strain response of steel under cyclic inelastic loading.

Past tests on steel encased BRBs have shown that restraining systems with insufficient strength and/or stiffness can lead to excessive compression forces, premature core failure due to low-cycle fatigue, and failure of restrainers (Tremblay, *et al.*, 2006; Chou, *et al.*, 2010; Lin *et al.*, 2012; Della Corte *et al.*, 2015; Dehghani *et al.*, 2016b; Midorikawa, *et al.*, 2016). Most useful insight on the complex nonlinear response of steel BRB members has been obtained from those and other experimental programs, as well as finite element studies performed in past studies (Korzekwa *et al.*, 2009; Genna *et al.*, 2012b; Genna *et al.*, 2012a; Midorikawa *et al.*, 2012; Wu *et al.*, 2012; Hoveidae *et al.*, 2013; Genna, *et al.*, 2014; Midorikawa, *et al.*, 2014; Razavi Tabatabaei, *et al.*, 2014; Tsai, *et al.*, 2014; Wu, *et al.*, 2014; Jiang *et al.*, 2015; Wu, *et al.*, 2015; Bregoli, *et al.*, 2016; Chen, *et al.*, 2016; Metelli, *et al.*, 2016). In particular, (Genna, *et al.*, 2012b; Genna, *et al.*, 2012a) provided experimental and numerical data on the normal forces imposed by core local buckling on the restraining system, including the effect of initial gap size. The variation of the axial load along

the yielding segment of BRB cores at peak compressive deformations was measured in (Midorikawa, *et al.*, 2014). The influence of the restrainer flexibility on thrust and frictional forces has been investigated in (Korzekwa, 2009; Genna, *et al.*, 2014; Metelli, *et al.*, 2016). Several analytical models have been proposed to predict the required minimum strength of steel BRB restraining systems. However, most available models ignore the variation in core axial loads due to friction when determining the buckling wavelength, number of waves and core strain demands, which may underestimate the maximum core strain demands and the normal force demands on restrainers near the core ends. Also, the buckling wavelength and number of buckling waves are generally determined assuming a unique value for the steel tangent modulus, without consideration of the actual strains along the core length and hardening conditions of steel material resulting from previously sustained cyclic inelastic deformations.

This article presents an extension to existing models to predict design forces for the BRB restraining system. The model proposed herein can be used to determine the core axial loads and strains along the length of a brace subjected to a compressive deformation excursion with consideration of longitudinal frictional forces. The normal thrust forces to be resisted by the restrainer are also determined along the core length together with the axial compression force that must be applied to reach the deformation imposed to the brace. Tensile and compressive strength adjustment factors for the brace can then be estimated. In the model, the core is discretized into buckling half-wave segments and the core axial forces and strains are evaluated for every segment considering the longitudinal frictional forces that develop at the contact points between the core and restrainer. Cyclic hardening of the core steel material and Poisson's effect are also taken into account in the calculation of the core stresses and strains. The length of each buckling half-wave segment is adjusted as a function of the core axial load and steel modulus properties. The method therefore requires iterations to achieve geometric compatibility and force equilibrium, which can be easily done in a spreadsheet environment. The calculations are typically performed for the largest compression excursion but can also be done for every cycle of a loading protocol to trace the evolution of the brace axial compression force and the history of the strain demand. The influence of the restrainer stiffness and friction between core and restrainer on the brace response can be assessed and the model can be used to optimize the design of a BRB member for a target brace hysteretic response. The first section of the paper introduces the proposed analysis method. The model is then validated against the results from physical tests and three-dimensional finite

element analyses for two buckling restrained bracing members that have been tested in previous experimental programs.

7.2 Proposed Model

7.2.1 Buckling wavelength and normal thrust force

The main objective of the proposed method is to estimate the normal thrust imposed on a steel BRB restrainer by weak-axis buckling of the core subjected to an axial compressive deformation. The method was developed to account for the effect of longitudinal friction between core and restrainer on the axial load carried by the core as well as the flexibility of the restrainer on the amplitude of the core buckling waves. The core is assumed to have a rectangular cross-section. The axial deformation u_x induces an average longitudinal strain, $\bar{\epsilon} = u_x/L_y$, where L_y is the length of the yield segment (YS) of the core (see Figure 7.1a). In this article, shortening and compressive forces have positive sign. The core deformation u_x is applied at the end of the core and slip displacement between the core and restrainer is maximum at this point referred to herein as SP. Typically, a fixed point (FP) is created at mid-length of the core YS by using a stopper that prevents relative longitudinal movement between core and restrainer. In that case, the brace deformation is imposed symmetrically at both ends of the core and the BRB has a slip length ratio λ, defined as the ratio of the distance between FP and SP and the length L_y equal to 0.5. If the stopper is located at one of the core ends, the distance separating SP and FP corresponds to L_y and λ is equal to 1.0.

7.2.2 Core buckled shape and forces

The brace response in compression is studied over the slip length λL_y and the core is divided in buckling half-wave segments as shown in Figure 7.2a and b. Assuming the core section is fully yielded when the final core local buckling pattern is developed, the length of the i^{th} buckling half-wave is obtained from:

$$\ell_i = \xi\pi\sqrt{\frac{E_{eff,i}\ I_{c,i}}{P_{i-1}}} \tag{7.1}$$

where ξ is the buckling length factor shown in Figure 7.2c-g; $E_{eff,i}$ is the effective flexural modulus of the core cross-section; $I_{c,i}$ is the weak axis moment of inertia of the core section; and P_{i-1} is the axial force carried by the core in the i^{th} buckling half-wave (as shown in Figure 7.2b, P_i is the core axial load applied at the SP end of the i^{th} buckling half-wave).

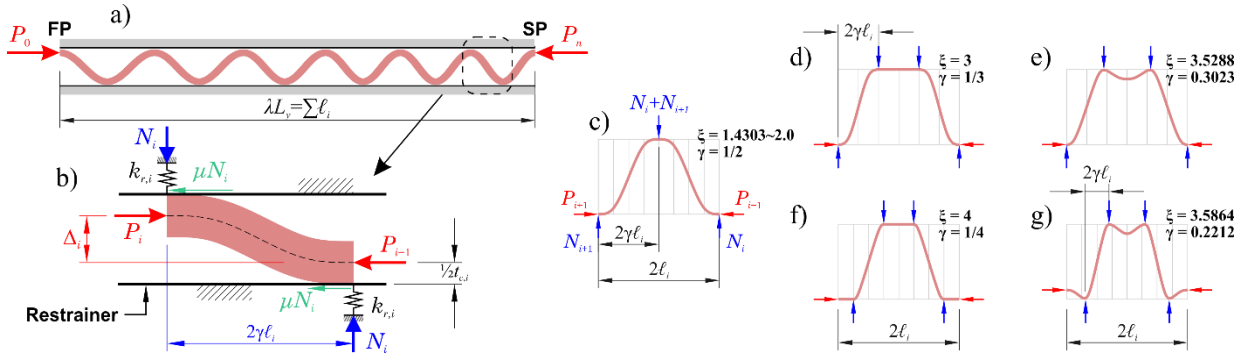

Figure 7.2: a) Core buckling between FP and SP along the core; b) Forces acting on the inclined portion of a single buckling half-wave; and c) to g) some possible waveforms (adopted from (Bregoli, *et al.*, 2016)).

The buckling length factor ξ and effective modulus E_{eff} are discussed in the next sections. In Figure 7.2b, it is assumed that the moments in the core are small and can be ignored at the contact points between core and restrainer. From equilibrium, the core axial loads at both ends of the inclined portion of the i^{th} buckling half-wave can be related as follows:

$$P_i = \frac{2\gamma\ell_i + \mu\Delta_i}{2\gamma\ell_i - \mu\Delta_i} P_{i-1} \tag{7.2}$$

where γ is the buckling shape factor (see Figure 7.2c-g); μ is the coefficient of friction between core and restrainer; and Δ_i is the total gap size including the outward deformation due to the flexibility of the restraining system (gap opening) and change in the thickness of the core:

$$\Delta_i \approx \Delta_0 - 0.5 t_c \epsilon_i + \delta_i \tag{7.3}$$

In this expression, Δ_0 is the initial total gap between core and restrainer, ϵ_i is the average axial compressive strain over the core cross-section; and δ_i is the gap opening computed with:

$$\delta_i = \frac{2N_i}{k_{r,i}} \tag{7.4}$$

where N_i is the normal thrust at the point of contact; and $k_{r,i}$ is the local stiffness of the restrainer against opening at the point of contact. When the longitudinal bolt spacing is uniform, the local stiffness against gap opening at the i^{st} half-wave can be approximated as a fraction of the total stiffness of the restrainer against opening, K_e:

$$k_{r,i} = \frac{2\ell_i}{L_y} K_e \tag{7.5}$$

Recommended minimum values for the stiffness K_e are discussed at the end of this section. The normal thrust induced by the inclined portion of the i^{th} buckling half-wave is the solution of the quadratic equation obtained by the combination of Eqs. (7.2) to (7.4):

$$\left(\frac{2\mu}{k_{r,i}}\right) {N_i}^2 + \left(\frac{2P_{i-1}}{k_{r,i}} + \mu\Delta_0 - 2\gamma\ell_i\right) N_i + P_{i-1}\Delta_0 = 0 \tag{7.6}$$

The selection of the buckling wave shape (γ factor) is discussed later in the paper. If the restrainer is infinitely stiff, i.e. $K_e \to \infty$, and the core buckles with a single contact point pattern, i.e. $\gamma = 1/2$, (see Figure 7.2c), Eq. (7.6) reduces to a linear equation that gives the half-wave thrust force directly:

$$N_i = \frac{P_{i-1}\Delta_0}{\ell_i - \mu\Delta_0} \tag{7.7}$$

Longitudinal shortening of the i^{st} buckling half-wave resulting from material straining and the buckled deformed shape can be approximated as:

$$dL_i = \ell_i\epsilon_i + \frac{\pi^2 {\Delta_i}^2}{8\ (2\gamma\ell_i)} \tag{7.8}$$

7.2.3 Cyclic strain hardening of steel and Poisson's effect

Examination of the hysteretic stress-strain response of steel under cyclic inelastic loading shows that isotropic hardening is dominated by the strain range $\Delta\epsilon$ in the largest cycles previously

sustained by the material. As shown in Figure 7.3a, the strain range is the difference between peak compressive and tensile strains reached in a cycle, $\Delta\epsilon = \epsilon_c - \epsilon_t$. Since BRB members are typically designed to exhibit satisfactory response under loading histories that contain repeated symmetrical cycles at stepwise incremented deformation amplitudes, it is assumed in the model that the core material has already experienced previous symmetrical cycles with a strain range $\Delta\epsilon$ equal to two times the peak axial compressive strain reached at the end of the compressive deformation excursion under examination. At this point, the average stress σ_i in the core section at the crest of the i^{st} buckling half-wave can then be obtained from:

$$\sigma_i = E_{t,i}\left(2\epsilon_i + \frac{\sigma_{yc,i}}{h_i}\right) \tag{7.9}$$

where $E_{t,i}$ is the tangent modulus at peak compressive strain ϵ_i; $\sigma_{yc,i}$ is the cyclic yield stress; $h_i = E\,E_{t,i}/(E - E_{t,i})$ is the hardening modulus; and E is the steel Young modulus (= 200 GPa). As shown in Figure 7.3a, the tangent modulus is defined as the hardening slope at the end of the compressive excursion and the cyclic yield stress is the stress value at the intersection between elastic and tangent slopes. In the figure, the effective modulus $E_{eff,i}$ is defined as the hardening slope at the point of yielding in compression.

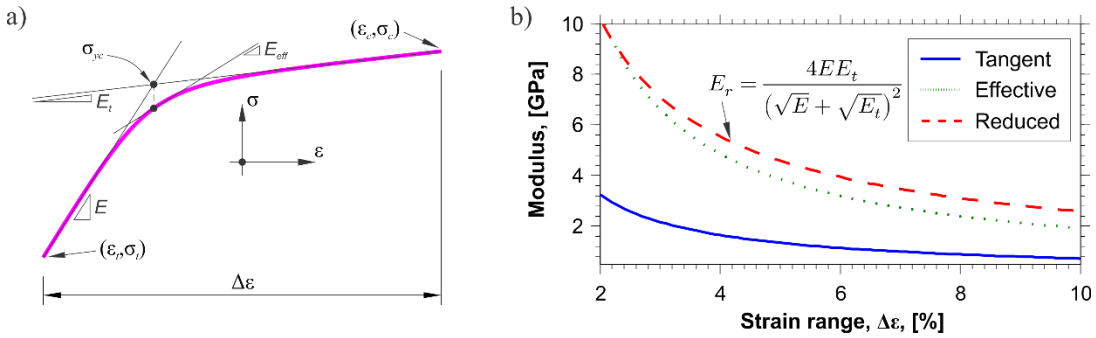

Figure 7.3: a) Tangent and effective steel moduli, and cyclic yield resistance in a compression loading half-cycle (from cyclic test on a stocky specimen); b) Comparison between tangent, effective, and reduced moduli (values for 2nd cycle of loading is shown, n_c = 2). Note: Reduced modulus is computed for a rectangular section.

Values of $E_{t,i}$, $E_{eff,i}$, and $\sigma_{yc,i}$ can be estimated from the following empirical model:

$$\frac{E_{t,i}}{E} = a_1 \left(\frac{\epsilon_i}{\epsilon_y} - 1\right)^{-0.839} \tag{7.10}$$

$$\frac{E_{eff,i}}{E} = a_2 \left(\frac{\epsilon_i}{\epsilon_y} - 1\right)^{-0.950} \tag{7.11}$$

$$\frac{\sigma_{yc,i}}{R_y F_y} = a_3 \left(\frac{\epsilon_i}{\epsilon_y} - 1\right)^{0.169} \tag{7.12}$$

where $\epsilon_y = R_y F_y / E$ is the expected yield strain of the core; a_1 and a_2 are the cyclic hardening degradation coefficients; and a_3 is the cyclic yield strength growth coefficient. These coefficients are estimated from the following expressions:

$$a_1 = 0.0746[1 + (n_c - 1)^{0.155}]^{-0.465} \tag{7.13}$$

$$a_2 = 0.2943[1 + (n_c - 1)^{0.07}]^{-0.528} \tag{7.14}$$

$$a_3 = 0.715[1 + (n_c - 1)^{0.37}]^{0.169} \tag{7.15}$$

where n_c is the number of cycles of same amplitude including the cycle under consideration. Values for the parameters of this empirical model have been obtained from a regression analysis of the results of constant amplitude cyclic experiments conducted on round specimens of CSA G40.21-350WT steel with strain amplitude between 1 to 8% (Dehghani *et al.*, 2016d). Variations of $E_{t,i}$, $E_{eff,i}$, and $\sigma_{yc,i}$ from this empirical model are illustrated in Figure 7.4.

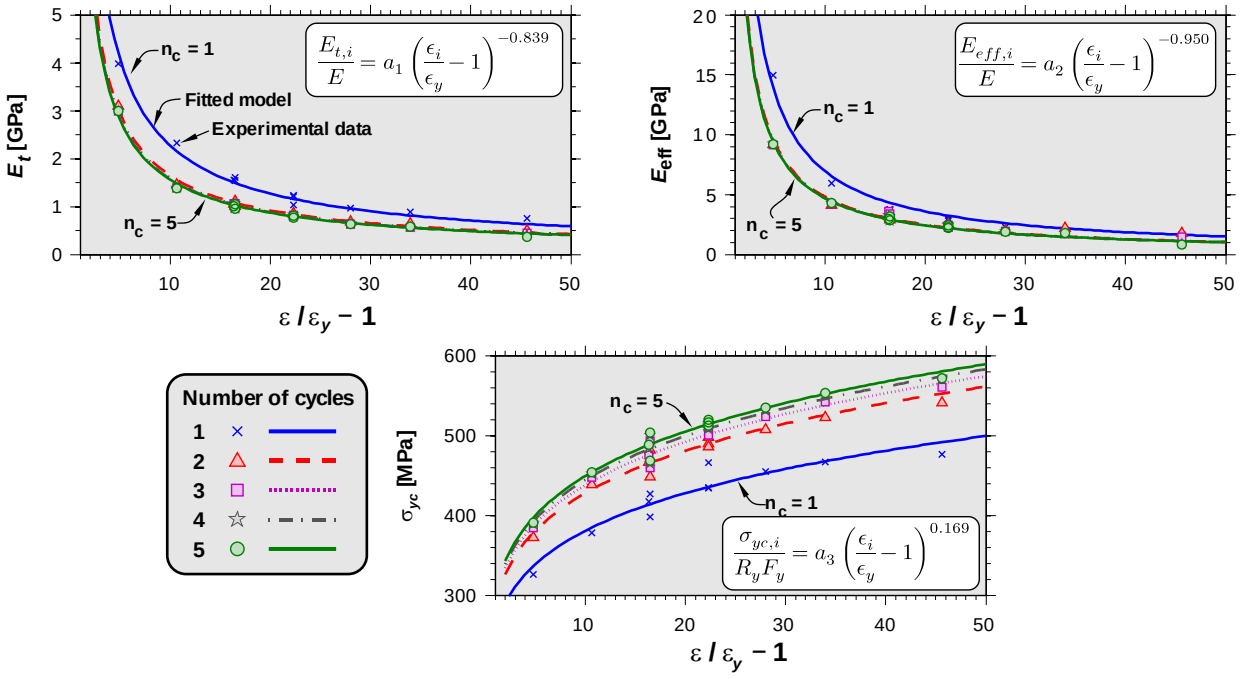

Figure 7.4: Variation of the tangent modulus, effective modulus, and cyclic yield stress (R_yF_y = 361 MPa).

The choice of the steel modulus to determine the core flexural stiffness in Eq. (7.1) to calculate the buckling half-wave length ℓ_i is a critical aspect of the method. According to inelastic column buckling theory, unloading is not expected across the member cross-section while it buckles if axial shortening develops at a higher rate than flexural deformations. For such a condition, the flexural stiffness of the core section is proportional to the tangent modulus of the steel material, i.e. the slope of the stress-strain curve, which is a function of strain amplitude and number of cycles experienced. This situation prevails for typical BRB members with a small gap and sufficiently stiff restrainer as the amplitude of the buckling waves is limited. An exception to this is when a new wave is being formed upon loading in compression. In this case, the rate of sectional curvature can be faster than axial shortening due to snap-through nature of core buckling. This condition is maintained until contact between the core and restrainer is fully established and further flexural deformations are restrained.

When a buckling wave is formed, a portion of the core cross-section is subjected to unloading and the core flexural stiffness tends towards the value corresponding to the reduced steel modulus (Galambos, *et al.*, 2008). Depending on the material hardening response and core cross-section

geometry, this value typically surpasses the tangent modulus by a large margin. Hence, as core buckling develops in compression, its flexural stiffness fluctuates between values determined with the tangent and reduced moduli. Experimental and finite element analysis results indicate that a reasonably good compromise is to use the effective modulus concept, i.e. the material stiffness when cyclic yielding is initiated in compression (see Figure 7.3a). As shown in Figure 7.3b for 350WT steel studied by (Dehghani, *et al.*, 2016d), the effective modulus E_{eff} leads to a sectional flexural stiffness that lays between the lower and upper bound values respectively obtained by tangent and reduced moduli. Although the effective modulus has no physical significance, it is deemed to reflect well the core flexural stiffness as buckling waves form when the core axial load approaches yielding in compression. Upon applying further plastic strains in compression, the modulus tends towards the tangent modulus but the numerical simulation shows that the core buckling mode (number of waves and waves lengths) obtained with E_{eff} remains essentially unchanged. This is an area where the method proposed herein could be further refined in the future.

For a given average core compressive strain, ϵ_i, the core sectional area and weak-axis inertia must be updated to account for lateral expansion due to the Poisson's effect:

$$A_{c,i} = b_c t_c (1 + 0.5\epsilon_i)^2 \approx b_c t_c (1 + 2\epsilon_i) \tag{7.16}$$

$$I_{c,i} = \frac{b_c t_c^3}{12}(1 + 0.5\epsilon_i)^4 \approx \frac{b_c t_c^3}{12}(1 + 4\epsilon_i) \tag{7.17}$$

7.2.4 Iterative procedure and design forces

An iterative procedure is needed to determine the strain value in each buckling half-wave. The solution starts with a trial strain $\epsilon_1^{\text{trial}}$ for the first buckling half-wave at the FP (i = 1). At this point, the core axial load P_0^{trial} is computed from Eqs. (7.9) and (7.16):

$$P_0^{\text{trial}} = \sigma_1^{\text{trial}} A_{c,1}^{\text{trial}} = E_{t,1}^{\text{trial}} \left(2\epsilon_1^{\text{trial}} + \frac{\sigma_{yc,1}^{\text{trial}}}{h_1^{\text{trial}}} \right) b_c t_c (1 + 0.5\epsilon_1^{\text{trial}})^2 \tag{7.18}$$

This load is inserted into Eq. (7.1) to compute the buckling half-wave length ℓ_1^{trial}, the thrust force N_1^{trial} from Eq. (7.6), the gap opening δ_1^{trial} from Eq. (7.4), the total gap size Δ_1^{trial} from Eq. (7.3), the longitudinal shortening dL_1^{trial} from Eq. (7.8), and the axial load in the adjacent buckling half-

wave P_1^{trial} from Eq. (7.2). The calculation is then propagated to the other half-waves along the slip length and the parameters ℓ_i^{trial} and dL_i^{trial} are computed until $\sum_i \ell_i^{\text{trial}} \geq \lambda L_y$, where $0.5 \leq \lambda \leq 1.0$ is the slip length ratio as previously defined. The total shortening of the core along the slip length is obtained by summing the trial shortenings over that length. The corresponding trial average axial strain is then determined from:

$$\bar{\epsilon}^{\,\text{trial}} \approx \frac{\sum_i dL_i^{\text{trial}}}{\lambda L_y} \tag{7.19}$$

Iteration on the trial strain of the first half-wave, $\epsilon_1^{\text{trial}}$, is conducted until the absolute difference between $\bar{\epsilon}^{\,\text{trial}}$ from Eq. (7.19) and the applied external strain $\bar{\epsilon}$ from the applied axial deformation becomes less than a given tolerance, e.g. 10^{-5}. In each of these trials, an inner iterative process is also performed to determine the $\epsilon_i^{\text{trial}}$ values required to obtain equilibrium between strain induced stress from Eq. (7.9) and the stress computed from the axial core buckling load, $\sigma_i^{\text{trial}} = P_i^{\text{trial}}/A_{c,i}^{\text{trial}}$. For the hypothetical frictionless case (μ = 0), no inner iteration is required because the core axial load does not vary along the slip length.

Once convergence is reached, the total normal thrust on the restraining system is obtained as:

$$N = \frac{\sum_i N_i}{\lambda} \tag{7.20}$$

and the average tension on the bolts connecting the two restrainer halves can be estimated as:

$$T_b = \frac{N}{n_b} \tag{7.21}$$

where n_b is the number of bolts along the core YS. When friction exists, the normal thrust is larger at the SP and this increases the demand on the bolts located at the end of the core YS when compared to those near the brace mid-length. In that case, assessment of the bolt tension forces along the core can be obtained by performing an elastic analysis of a continuous Timoshenko beam with vertical supports at every bolt position when subjected to the local normal forces N_i. This is illustrated in the example presented in the next section.

If required, the total accumulated frictional force at the FP is calculated from:

$$P_f = \sum_i F_i = 2\mu \sum\nolimits_i N_i \tag{7.22}$$

This equation assumes Coulomb friction. If necessary, a more sophisticated frictional law can be incorporated in the calculation.

For frame design, the compression strength adjustment factor can be estimated as the ratio between the axial load at SP and the maximum tensile resistance including cyclic strain hardening effect:

$$\beta = \frac{P_n}{T_{\max}} \tag{7.23}$$

where $T_{\max}$ is the maximum tensile force that can be estimated by Eqs. (7.9) and (7.12) using the applied external strain $\bar{\epsilon}$ assuming that the core is subjected to an equal displacement amplitude in compression and tension:

$$T_{\max} \approx E_t(\bar{\epsilon}) \left(2\bar{\epsilon} + \frac{\sigma_{yc}(\bar{\epsilon})}{h(\bar{\epsilon})}\right) b_c t_c (1 - 0.5\bar{\epsilon})^2 \tag{7.24}$$

7.2.5 Determination of the buckling wavelengths and shapes

Selection of the buckling wavelength factor ξ and wave shape factors γ, is the most critical part of this simplified analysis method. These parameters were introduced in (Genna, *et al.*, 2014) (note: β is used instead of γ in that reference). Parameter ξ constitutes the number of buckling waves in the slip length. It is analogous to the inverse of the column effective length factor for a given single buckling wave. Parameter γ determines the length of the inclined portion of the buckling half-wave. For a given wavelength and core axial load, a smaller γ results in a larger normal thrust. In the column analogy, the effective length factor of the inclined portion of the buckling wave is determined as $1/(2\xi\gamma)$.

Parameters ξ and γ can take a range of values dictated by initial geometrical imperfections of core, the deformation history, and the stiffness of the restrainer. Genna, *et al.* (2014) studied the elastic buckling response of a beam encased in a frictionless restrainer under monotonic loading and concluded that precise estimation of the buckling wavelength and shape is practically impossible. For an infinitely stiff restrainer, i.e. $K_e \to \infty$, it is shown that under the same amount of axial shortening, buckling waves can follow various patterns depending upon initial imperfection. The

authors showed that theoretically, in case of a rigid restrainer, parameter ξ can take any value between 1.4303 and 4.0. However, when bending moment vanishes at the points of contact, ξ tends toward 2.0, 3.0, and 4.0 for the cases of a single contact point (Figure 7.2c), asymmetric (Figure 7.2d), and symmetrical double contact points (Figure 7.2f) buckling waveforms, respectively. Since $\gamma = 1/\xi$, the corresponding values of γ are respectively γ = 1/2, 1/3, and 1/4. This is to say that, for the mentioned cases, the effective length factor of the inclined portion of the buckling waves are equal to 0.5.

According to (Genna, *et al.*, 2014; Bregoli, *et al.*, 2016), a reasonably accurate practice when $K_e \rightarrow \infty$ is to use $\xi = 1/\gamma = 3$. When the restrainer is flexible, the estimation of ξ becomes more complicated. Theoretically, when restrainer is too flexible, it is shown that ξ can take values even larger than 4.0 and γ tends toward 1/2. This condition does not typically prevail in BRB application. Based on the results of the current study, which will follow, $\xi = 1/\gamma = 2$ is recommended when the restrainer is sufficiently stiff and the axial shortening is larger than 1.5% of the core length. The recommended combination of ξ and γ implies a periodic buckling waveform that has single point contact pattern and bending moment at the points of contact are vanished (see Figure 7.2c). In actual response, parameters ξ and γ may not be constant along the core, i.e. wave is not periodic, especially when friction is significant.

7.2.6 Restrainer stiffness

When using the method to initiate the design of the BRB restrainer system, a trial value is needed for the restrainer stiffness K_e to start the iterative process. An arbitrary value can be used which can then be adjusted to achieve the desired BRB response. Alternatively, the restrainer stiffness required to stabilize the core response under maximum anticipated compression load P_n and control gap opening can be used. A conservative estimate of that stiffness can be obtained from elastic buckling theory assuming uniform axial load and material properties along the core length, neglecting longitudinal frictional forces, and adopting a simple core buckling deformed shape $v(x)$ consisting of n buckling waves of amplitude $\Delta = \Delta_0 + \delta$ over the length L_y:

$$v(x) = \frac{\Delta}{2}\left\{1 - \cos\left(\frac{2n\pi x}{L_y}\right)\right\} \tag{7.25}$$

The total potential energy of the system, Π, is given by:

$$\Pi = U + V \text{ where: } U = \int_0^{L_y} EI_c \frac{(v'')^2}{2} dx \; + \; K_e \; \frac{(\Delta - \Delta_0)^2}{2} \; ; \qquad V = -\int_0^{L_y} P \frac{(v')^2}{2} dx \tag{7.26}$$

The elastic critical buckling load $P_{cr,e}$ can be obtained by minimizing Π and setting Δ_0 = 0:

$$P_{cr,e} = \frac{4n^2\pi^2 EI_c}{L_y^2} + \frac{2K_e L_y}{n^2\pi^2} \tag{7.27}$$

The first term on the right-hand side of this equation is the contribution of the core to the critical load. That contribution can be ignored when determining the restrainer required minimum stiffness and $K_{e,min}$ is then obtained by setting $P_{cr,e} = P_n$:

$$K_{e,\min} = \frac{n^2\pi^2 P_n}{2L_y} \tag{7.28}$$

Given the provided stiffness, the gap opening δ as a function of the initial gap Δ_0 is obtained as:

$$\frac{\delta}{\Delta_0} = \frac{K_{e,\min}/K_e}{1 - K_{e,\min}/K_e} \tag{7.29}$$

To limit gap opening δ to the initial gap size, i.e. $\delta/\Delta_0 \leq 1.0$, K_e should therefore be taken at least equal to two times the value of $K_{e,\min}$. In some cases, when the initial gap is large or the friction is high, a larger value of K_e may be needed to achieve satisfactory BRB response, i.e. limited axial compression P_n and thrust force N. The procedure presented in this article should be followed to verify the BRB behaviour.

At the beginning of the design stage, P_n is not known and it can be taken equal to $\omega\beta A_c R_y F_y$, where ω and β are compression and tension strength adjustment factors for which values reported in the literature or target values can be used. In Eq. (7.28), a conservative (large) number of buckling waves $n = L_y/(2\ell_i)$ can be assumed where ℓ_i is determined from Eq. (7.1) with $\xi = 2$, $E_{eff,i}$ is estimated from Eq. (7.11) for the anticipated core shortening ($\epsilon_i = \bar{\epsilon}$) and number of

cycles n_c, and $P_{i-1} = P_n$. As indicated, this first trial value of K_e can be modified as necessary in subsequent design iterations to reach the desired brace response.

When evaluating the behaviour of a given brace, K_e can be determined from simple analysis of the restraining system accounting for the flexural stiffness of the restrainer components along both orthogonal directions in series with the bolt axial stiffness. A more refined value can be obtained from a finite analysis of the brace restrainer system under a unit normal force simulating the action of the buckled core on the restrainer. This is illustrated in the next section.

7.3 Application and validation of the proposed method

The proposed approach is applied to two BRB members that have been tested in previous experimental programs. In both cases, the predictions from the proposed model are compared to the available test data. Detailed three-dimensional finite element (FE) analysis of the two specimens is also performed to generate additional data on the brace response for the conditions investigated in the tests. For one specimen, other conditions not considered in the test programs are also examined with the finite element model. These additional numerical results are also used to verify the proposed analytical method. The finite element simulations are first verified against the physical test data.

The FE model is built in ABAQUS (SIMULIA Inc., 2012). In this model, only weak-axis buckling of the core is considered and the restrainer is modeled using two analytically rigid planes that are connected by an elastic spring which represents the stiffness against gap opening, K_e. This simplified restrainer model allows more direct comparison between the FE results and the proposed analytical approach that replaces a continuous restrainer with a lumped elastic spring. Hence, only the core YS was incorporated in the model. The core was constructed using 8-node reduced integration continuum elements C3D8R. Longitudinal and transversal mesh sizes were one-quarter of the core thickness and four elements were employed through the thickness. Mesh size and element type were selected after conducting a sensitivity study. Inelastic material properties including combined nonlinear kinematic and isotropic hardening were defined for the core member. The employed material constitutive law is elaborated in (Lemaître *et al.*, 1990). This model assumes von Mises yield criterion and incorporates multi back stresses to model nonlinear kinematic hardening. In this model, isotropic hardening is a nonlinear asymptotic function of the

accumulated plastic strains. Hard contact behaviour, i.e. no penetration, was specified between the core and restrainer. Node-to-Surface type of discretization was chosen for the contact pairs and the Lagrange multipliers method was chosen to enforce the contact constraints in the normal direction. Coulomb friction behaviour enforced by penalty method was chosen in the direction tangent to the contact interface.

Core initial imperfections were modeled with a half-sine arc that had a maximum amplitude equal to 3/10000 of the core length. The BRB core response can be classified as a severely discontinuous type of problem with convergence difficulty since it involves contact, plasticity, and local instability (buckling). This demands a special consideration when finite element simulation of BRB is attempted. Static implicit analysis method was used with a displacement controlled loading scheme. To improve the convergence rate and stabilize the solution, artificial mass-proportional viscous damping was added to the model. The maximum ratio of viscous to internal energy (elastic and plastic) was limited to 2.5% to ensure that the solution is not distorted by this artificial damping. Time-averaged ratio of viscous to internal energy was also kept lower than 0.5%. To further cross-check the validity of the static implicit analysis results, series of dynamic explicit analysis with slow loading rate and smooth displacement history was also conducted. Since convergence is not an issue in dynamic explicit analysis, no damping was required to obtain the solution. The computed results from static and dynamic explicit methods showed very similar trends. For cyclic loading, dynamic explicit analysis was found computationally 2–3 times more expensive than the static analysis. The results presented herein are from static analysis.

7.3.1 Case study I

The presented analytical approach is first validated against the experimental results of Specimen 2Dcs0.46 reported in (Metelli, *et al.*, 2016). The test specimen consisted of a 560×50×5 mm steel core (length × width × thickness) and an all-steel bolted restrainer. The authors estimated K_e between 414 and 552 kN/mm (see Table 5 in (Metelli, *et al.*, 2016) and Table 4 in (Bregoli, *et al.*, 2016)). A stopper was used at mid-length of the core, hence $\lambda = 0.5$. A total gap of 2×0.46 = 0.92 mm was provided between core and restrainer. The specimen was subjected to the AISC standard cyclic loading protocol for testing BRBs (AISC, 2010) which consists of two symmetric cycles of displacement amplitude equal to ±0.95, 2.8, 5.6, 8.4, and 11.2 mm (0.2, 0.5, 1.0, 1.5, and 2.0% of the core length). Based on the reported axial and normal thrust forces, the coefficient of friction is

estimated as 0.15. Data on cyclic response of the core material was not provided by the authors, hence the predictive model for 350WT steel introduced in Eqs. (7.10) to (7.15) was used instead. The results of the proposed analytical calculations are compared to the experimentally measured quantities in Table 7.1 for two cyclic amplitudes, i.e. $\bar{\epsilon}$ = 1.5% and 2.0%. Results at the maximum amplitude of the 2nd cycle of loading are compared. In this validation, the total normal thrust, number of buckling waves and their length, and the axial forces are examined. In the analytical calculations, ξ and γ were assumed to be 2.0 and 0.5, respectively. While the axial force predicted closely, the proposed method overestimates the thrust by 24% to 44%, depending on the strain amplitude. This could be attributed to the approximation in the effective modulus that tends to give wavelengths shorter than the experimentally measured values. Given the complexity of the core behavior and simplifications in the proposed method, this conservative margin of error would be reasonably insignificant for most engineering applications. Further analysis showed that for $\bar{\epsilon} <$ 1.5%, assuming $\xi = 1/\gamma = 3$ gives more accurate results.

Table 7.1: Comparison between experimental results of specimen 2Dcs0.46 reported in (Metelli, *et al.*, 2016), the proposed analytical method, and finite element analysis.

Basic design parameters	$\bar{\epsilon}$ (%)	Results	$n^{\dagger}$ (–)	$2\ell^{\ddagger}$ (mm)	N (kN)	P_n (kN)	β (–)
L_y = 560 mm A_c = 50×5 mm R_yF_y = 300 MPa Δ_0 = 0.92 mm K_e = 552 kN/mm μ = 0.15 λ = 0.5 n_c = 2	1.5	Experiment	6	–*	34	101	1.05
		Analytical	8	59.2–71.8	49	104	1.06
		Finite Element	7	59.8–109.9	52	100	1.07
	2.0	Experiment	8	39.7–96.5**	66	110	1.10
		Analytical	10	46.8–63.2	82	113	1.10
		Finite Element	7	59.5–107.2	73	107	1.11

† number of buckling waves

‡ buckling wave length

* value not reported

** values estimated from plot of Fig. 11 in (Metelli, *et al.*, 2016)

The finite element model was validated against the test results for the same specimen and same two loading cycles. The kinematic component of the core strain hardening was modelled using three back stresses with hardening moduli C_1 = 75, C_2 = 30, and C_3 = 3.3 GPa and saturation rates γ_1 = 7500, γ_2 = 900 and γ_3 = 33. For the isotropic hardening, a maximum saturation stress Q_∞ = 10 MPa and a saturation rate b = 2.5 were specified. For the kinematic and isotropic components, the same initial yield size σ_0 = 290 MPa was defined. These parameters were obtained by fitting the material model to the plotted hysteresis responses of the BRBs tested in (Metelli, *et al.*, 2016). The FE simulated hysteresis response of the core axial force and normal thrust are shown in Figure 7.5a. In these plots, negative deformation values imply core shortening and core tension

forces are positive. The hysteretic response is stable, as was observed in the test. The thrust *vs* core strain plot shows that the thrust gradually increases in each compressive excursion. Additional thrust develops when the same cycle is repeated, as was also observed in the test. In the proposed model, this behavior is accounted for by the parameter n_c which reduces the inelastic core stiffness and leads to shorter buckling waves and larger thrusts. The sudden drops in this plot indicate local instability occurring when a new buckling configuration is being established. As shown, during the largest excursion, the final buckling pattern formed early as assumed in the analytical model, which supports the use of E_{eff} instead of E_t to establish buckling wavelengths. The deformed shapes of the core at the end of the 1.5% and 2.0% strain amplitudes are given in Figure 7.5b and c, respectively. As shown, the waveform is a combination of single point contact (Figure 7.2c) and symmetric double point contact (Figure 7.2g). As predicted by the analytical model and observed in the test, the wavelengths are shorter near the core ends and become longer towards the FP at the middle of core length. In Table 7.1, good agreement between the test results and the FE model is generally observed. While the axial force is predicted accurately, the normal thrust is over-predicted by ~10% and ~50% in the last cycle of $\bar{\epsilon}$ = 2% and 1.5%, respectively. This difference can be attributed to several factors such as the lack of the actual core material cyclic properties, the simplified restrainer representation assumed in the FE model, and the simple frictional Coulomb's law used in the FE analysis. Nevertheless, the analytical model gave reasonably accurate results for $\bar{\epsilon}$ = 2%, which generally represents the maximum strain level for BRB qualification in typical applications (Genna, *et al.*, 2012a; Tsai, *et al.*, 2014; Metelli, *et al.*, 2016).

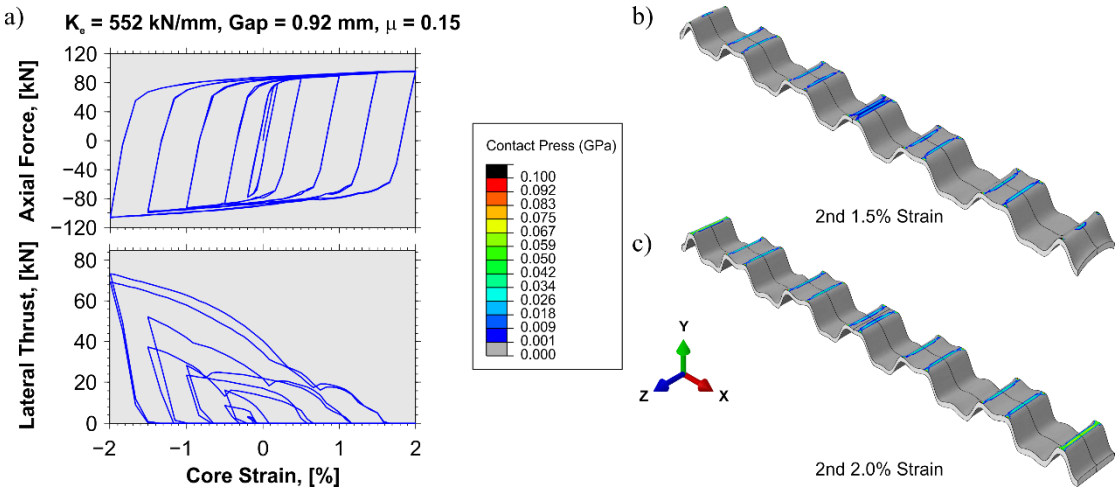

Figure 7.5: Finite element simulation results of specimen 2Dcs0.46 in (Metelli, *et al.*, 2016): a) Hysteresis of axial force and normal thrust; b) and c) Deformed shapes of the core and contact pressure contour at 1.5% and 2.0% axial strains, respectively (Y-axis deformation is magnified by factor of 25).

In Figure 7.6a, the FE model predicts uniform axial strain along the core length for small shortening values ($\bar{\epsilon}$ = 0.5%). When the brace deformation demand increases, distribution of the core local strain becomes increasingly non-uniform with much higher strain amplitude towards SP. In the $\bar{\epsilon}$ = 2.0% cycle, the maximum strain at the core end is nearly 3 times the average applied strain. This behaviour is reflected in the hystereses at FP and SP that are plotted in Figure 7.6b. Although the imposed axial strain is symmetrical, the local strain responses are highly non-symmetric: at SP, strains gradually shift towards compression whereas the inverse takes place, although at a slower rate, at mid-length of the core (FP). One of the key parameters governing the BRB response is strain hardening of the core material, which is predominantly controlled by the imposed strain range rather than the strain amplitude. In Figure 7.6b, the FE computed local strain ranges in the last compressive excursion are 0.045 and 0.035 at SP and FP, respectively. The corresponding values in the analytical model are 0.053 and 0.032, which is can be deemed satisfactory in view of the complexity of the problem.

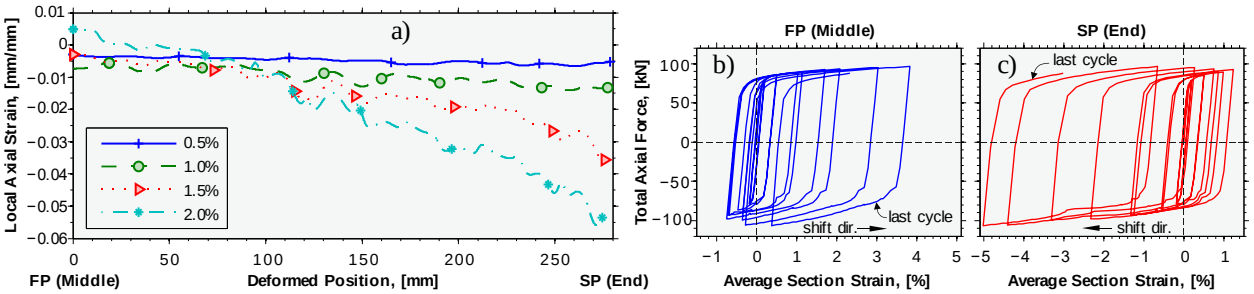

Figure 7.6: FE analysis of specimen 2Dcs0.46 in (Metelli, *et al.*, 2016): a) Distribution of axial strain between SP and FP at the end of the compressive excursion of the 2nd cycle with amplitudes of 0.5, 1.0, 1.5, and 2.0% strain; b) and c) Hysteresis responses at FP and SP, respectively.

For the specimen studied, the required minimum stiffness $K_{e,\min}$ is calculated from Eq. (7.28) to sustain two cycles at $\bar{\epsilon}$ = 2.0%. Using $\bar{\epsilon}$ = 2.0% and n_c = 2, on obtains E_{eff} = 3.7 GPa and P_n = 115 kN from Eqs. (7.10) to (7.15). The calculations result in n = 10 buckling waves which, when inserted in Eq. (7.28), gives $K_{e,\min}$ = 101 kN/mm. The contribution of the core flexural stiffness to the total critical load (first term in Eq. (7.27)) is less than 4%. This justifies omitting this contribution when estimating $K_{e,\min}$ with Eq. (7.28). For the studied specimen, (Metelli, *et al.*, 2016) reported a gap opening δ = 0.16 mm at the end of the second $\bar{\epsilon}$ = 2.0% loading cycle. Given the provided restrainer stiffness K_e = 552 kN/mm and the initial total gap Δ_0 = 0.92 mm, Eq. (7.29) predicts δ = 0.21 mm, which represents ~30% difference compared to the measured value. When the laboratory measured restrainer stiffness and number of waves are used, i.e. K_e = 414 kN/mm and n = 8, Eq. (7.29) exactly predicts the laboratory measured gap opening of δ = 0.16 mm. This implies that the proposed method for estimating the gap opening can be more accurate when more realistic estimates of the number of buckling waves and the restrainer stiffness are available.

7.3.2 Case study II

In the second verification case, BRB Specimen 9 tested in (Dehghani, *et al.*, 2016b) and illustrated in Figure 7.7 is examined. The core yielding segment has L_y = 3000 mm and A_c = 150×19.05 = 2858 mm^2. It is fabricated from CSA G41.20-350WT steel with a measured yield strength $R_y F_y$ = 385 MPa. As shown in Figure 7.7b, the restrainer comprises of two built-up sections that were

joined by pre-tensioned bolts. The restrainer stiffness of this specimen was evaluated using the 3D finite element model shown in Figure 7.8a. The FE model predicted K_e = 2400 kN/mm when the bolts pretension load is 85 kN. A combination of stainless steel sheet and Polytetrafluoroethylene (PTFE) liner was employed at the core-restrainer interface for debonding purpose and to obtain smooth sliding conditions. The measured through-thickness gap between the core and restrainer was 0.9 mm after accounting for the flexibility of the debonding layer. The coefficient of friction μ of the interface is estimated to be between 0.15 and 0.2 (Bondonet *et al.*, 1997). A slip length ratio λ = 0.5 is assumed although no stopper mechanism was implemented in that specimen and the slip length can vary between $0.5L_y$ and L_y.

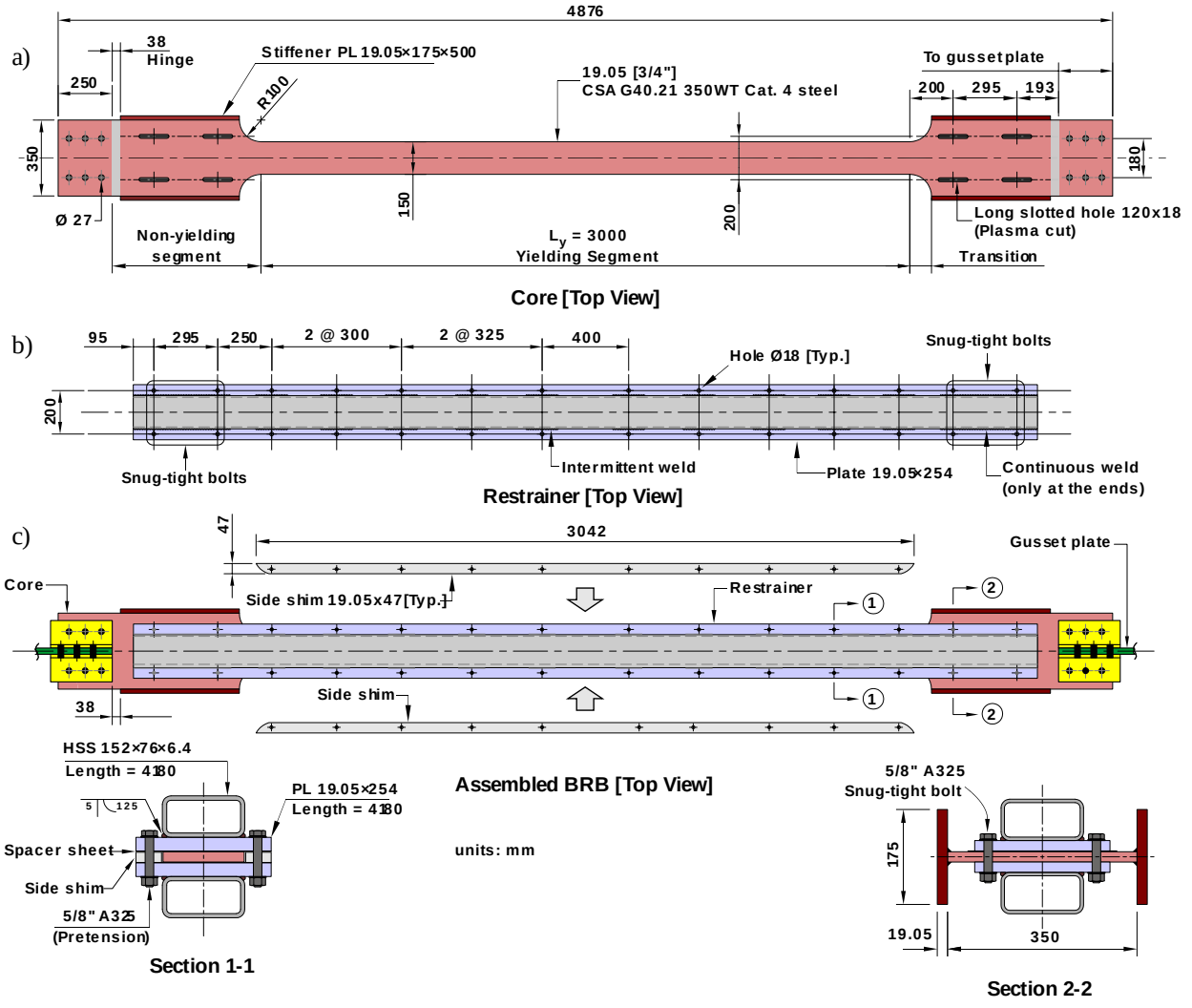

Figure 7.7: Geometry and specification of Specimen 9 tested in Dehghani, *et al.* (2016b).

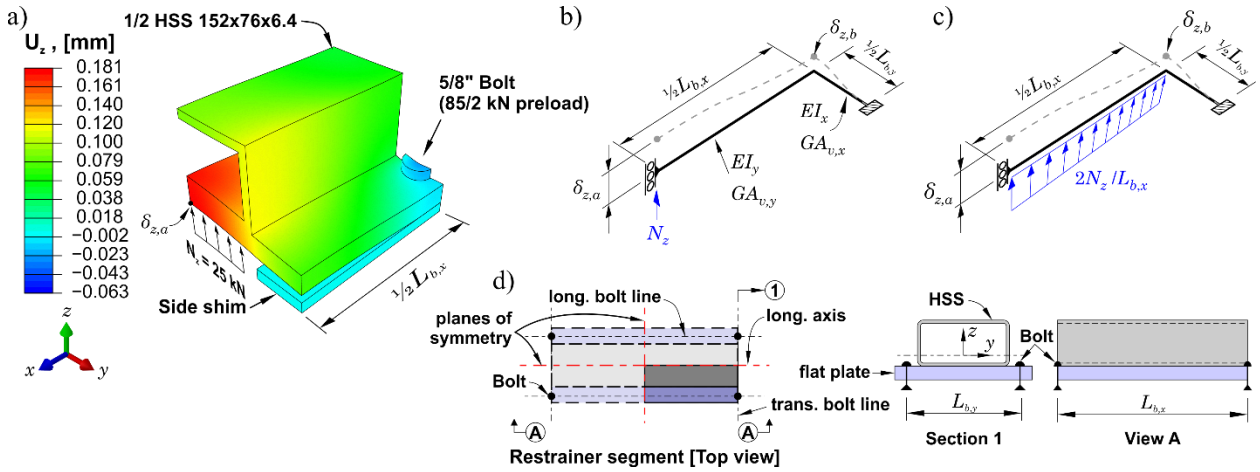

Figure 7.8: Models for estimating the restrainer stiffness: a) 3D finite element model of a restrainer segment (one- quarter of segment is modelled); b) and c) Simple models with 1-dimentional elastic beam elements; and d) plan, cross-section, and elevation views of the restrainer segment.

The analytical model and FE analysis are applied for the three sets of design parameters shown in Table 7.2. The first two sets represent the following hypothetical conditions: Set 1 is an ideal case of infinitely stiff restrainer with a frictionless interface whereas Set 2 is a case where the restrainer stiffness is the actual value (K_e = 2400 kN/mm) and the interface is still frictionless. Set 3 represents the actual conditions: K_e = 2400 kN/mm and the lower bound for the coefficient of friction μ = 0.15.

Table 7.2: Comparison between the proposed analytical method and finite element analysis (values in brackets are from finite element analysis).

General design parameters	Specific design parameters		Loading	Analysis results				
	Set	Design parameters	$\bar{\epsilon}$ (%)	n (–)	2ℓ (mm)	N (kN)	β (–)	P_n (kN)
L_y = 3000 mm A_c = 150×19.05 mm R_yF_y = 385 MPa Δ_0 = 0.9 mm λ = 0.5 n_c = 2	1	$K_e = \infty$ μ = 0.0	2	13 [**12**]	214.6 [**178–386**]	258 [**276**]	1.04 [**1.04**]	1499 [**1540**]
			3	17 [**15**]	168.8 [**125–271**]	403 [**454**]	1.06 [**1.07**]	1626 [**1657**]
	2	K_e = 2.4 MN/mm μ = 0.0	2	13 [**12**]	214.6 [**182–384**]	308 [**316**]	1.04 [**1.04**]	1499 [**1540**]
			3	17 [**16**]	168.8 [**119–270**]	564 [**530**]	1.06 [**1.07**]	1626 [**1656**]
	3	K_e = 2.4 MN/mm μ = 0.15	2	13 [**14**]	238.0–205.6 [**177–265**]	308 [**346**]	1.06 [**1.05**]	1520 [**1564**]
			3	17 [**15**]	157.6–180.6 [**168–255**]	566 [**682**]	1.09 [**1.10**]	1667 [**1708**]

In the experimental program, the BRB was tested using a sequence of two symmetrical cyclic axial deformations in the core YS with amplitudes of 6, 15, 30, 45, 60, and 90 mm. In the FE analysis, the core was only subjected to the last four cycles of the mentioned history, i.e. two cycles of 60 and 90 mm axial deformations ($\bar{\epsilon}$ = 2% and 3%) with the loading starting at the end of the previous tension excursion. The FE model is same as in Case Study I except that the material strain hardening was modelled with different sets of parameters. Kinematic hardening was defined with C_1 = 30 GPa, γ_1 = 300, C_2 = 2 GPa, and γ_2 = 20, whereas isotropic hardening was modelled using Q_∞ = 50 MPa and b = 1.5. The initial yield size σ_0 = 385 MPa was specified for both hardening

components. These parameters were obtained by calibration against the experimental cyclic tests data for 350WT steel in (Dehghani, *et al.*, 2016d). The full length of the core was considered in the FE model. To comply with the assumption λ = 0.5, which implies reflective symmetry in the buckling waveform w.r.t. core mid-length, the same displacement loading history with inversed signs was imposed at each end of the core.

The FE computed axial force and normal thrust hysteretic responses as a function of the applied strain are plotted in Figure 7.9 for Sets 1 to 3. A stable hysteresis is obtained for Set 3, as was observed in the experiment. The results show that the normal thrust tends to increase as the restrainer flexibility and friction are incorporated in the model. Opening of the gap due to restrainer deformability increases the lever arm of the core axial load, which requires a larger normal thrust for equilibrium. Friction also increases the thrust as a larger force P_n must be applied compared to the load for frictionless condition. An increase in axial load only occurs when friction is considered. Nevertheless, as shown in Figure 7.9, the additional axial load due to friction is much less significant compared to the additional generated thrust. The axial load in Sets 1 and 2 are same, indicating that core shortening was dominated by material straining rather than core flexural deformation corresponding to the second term in Eq. (7.8), owing to the small gap size and high restrainer stiffness. Had core bending deformations been more important, the axial load for a given total core shortening would have been reduced as the core would have been less axially strained.

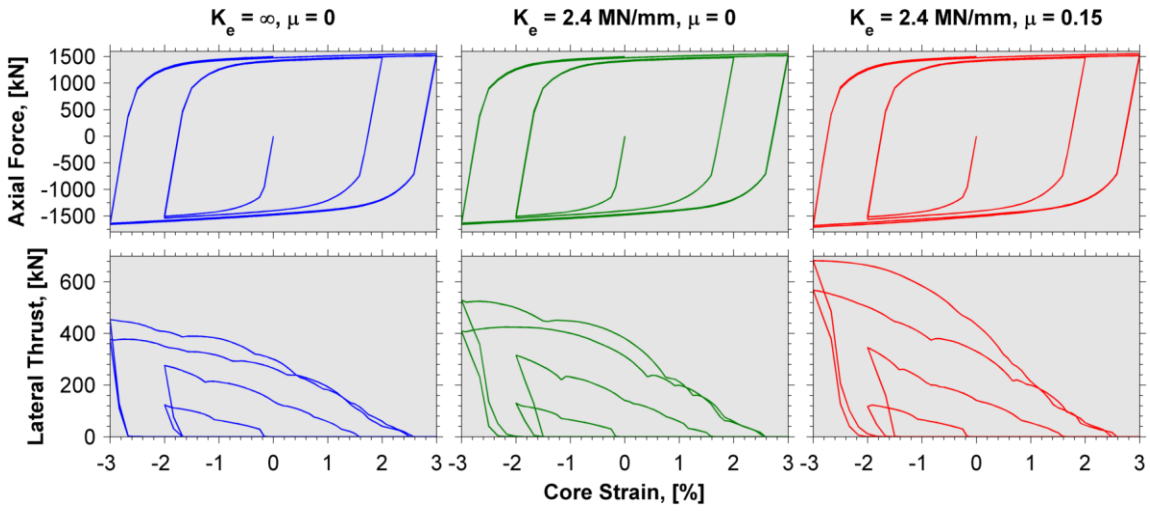

Figure 7.9: Axial force and normal thrust hysteresis from FE analysis for Sets 1, 2, and 3.

The buckling configurations of the core from FE models at the end of the second excursions at $\bar{\epsilon}$ = 2% and 3% are shown in Figure 7.10. At 3% shortening, the buckled shape is mainly characterized by waves with single contact point (Figure 7.2c), which is consistent with the assumption made in the analytical model. Contact pressure contours indicate that, at 2% shortening, several waves are not in full contact with the restrainer and contact is limited to the exterior edges of the waves' crests. In general, the buckled shapes exhibited full reflectional symmetry w.r.t to core mid-length. An exception is Set 1 under $\bar{\epsilon}$ = 3% (see Figure 7.10d), for which the waves on either side of the core mid-length are slightly different. In theory, when friction does not exist, formation of new buckling waves should happen at the same time as the axial load is the same for all existing buckling waves. This expected behaviour was not observed in the simulation of Sets 1 and 2. The same observation was made in the models analyzed with the dynamic explicit method. The longitudinal variation in the core thickness along the core length is noticeable when friction is added to model (see Figure 7.10c and f). This is an indicator of a non-uniform distribution of longitudinal strains when considerable friction exists.

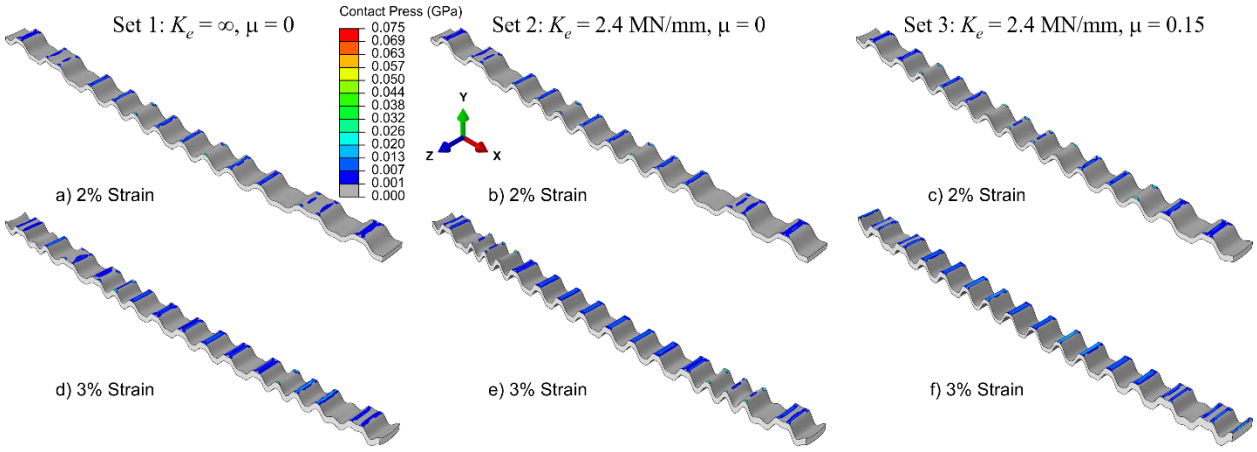

Figure 7.10: Deformed shapes and contours of contact pressure from FE analysis of Sets 1, 2, and 3 at the end of the 2nd cycle of loading at the given strain amplitude (Displacements along Y-axis are magnified by a factor of 75).

Comparison between the FE analysis results and the proposed analytical method is given in Table 7.2. Analytical results are obtained by assuming $\xi = 1/\gamma = 2.0$ and λ = 0.5. Good agreement is generally observed. In all except one case, the FE analysis predicted a larger normal thrust compared to the analytical model. The differences between the computed normal thrusts were in

the −17% to +6% range, where a negative sign indicates a lower value from the analytical method. As shown earlier, in the FE validation against test results reported in (Metelli, *et al.*, 2016), the simple FE model tends to overestimate the laboratory measured normal thrust. For Set 3, the laboratory measured core axial loads and normal thrust forces at the end of the 2nd 3% compression excursion were respectively 1866 kN and 500 kN (Dehghani, *et al.*, 2016b). The axial loads predicted by the analytical and FE models are ~10% less than the measured values. These models over-predicted the normal thrust by 13% and 36%, respectively. As mentioned before, a lower bound of frictional behaviour was considered by assuming λ = 0.5 and μ = 0.15. The same reference, i.e. (Dehghani, *et al.*, 2016b), showed that for the tested specimen, core response was not symmetric w.r.t the middle of core and the frictional forces tend to have a one way path between core ends. This was attributed to having no stopper between core and restrainer. When the analytical calculations is repeated with λ = 1.0 and μ = 0.2 (upper bound value), at the end of second 3% excursion, the difference between the measured and predicted axial force reduced to 7% while the predicted normal thrust remained nearly unchanged. This imply that the frictional characteristics, i.e. coefficient of friction and friction path, should be properly estimated to have a more precise analysis.

For the core geometry studied and properties given in Table 7.2, E_{eff} = 3.2 GPa and P_n = 1815 kN is obtained from Eqs. (7.10) to (7.15) given that $\bar{\epsilon}$ = 3.0% and n_c = 2. From Eq. (7.28), the minimum restrainer stiffness $K_{e,\min}$ = ~1100 kN/mm. In this calculation, the compressive strength adjustment factor β was set to 1.15. Calculations indicates that core bending contribution to the total critical load was less than 10%. As mentioned before, the available restraining stiffness K_e for Specimen 9 was 2400 kN/mm which implies $K_e/K_{e,\min} \approx 2.2$. According to (Dehghani, *et al.*, 2016b), this specimen exhibited stable inelastic response under the described loading history. In addition, this specimen sustained two more intense loading histories and reached to more than 800 cumulative inelastic ductility before core low-cycle fatigue failure occurred. For this particular brace, following the generally recommended practice of maintaining a ratio of 2.0 for $K_e/K_{e,\min}$ was sufficient to achieve adequate inelastic response, as demonstrated by the test and suggested by the results from the proposed method and the FE analysis. As noted earlier, this may not be the case for situations where high friction or a large initial gap is present.

Minimum strength requirements for the restrainer to prevent yielding of the restrainer's components, failure of bolts or welds, etc. must be always be verified in addition to satisfying stiffness requirement. In their tests, Dehghani, *et al.* (2016b) studied other BRB specimens (Specimen 12) that had the same core specifications as Specimen 9 discussed herein but with a different initial gap, restrainer section, and bolt spacing. For Specimen 12, the measured net initial gap was 2.8 mm after accounting for the flexibility of the debonding liner. The restrainer was identical to that of Specimen 9 except that heavier half-sections were used that we made from a plate 25.4×254 mm welded to an HSS 152×76×8 mm but the pre-tensioned bolts along the yielding segment of the core were longitudinally spaced at ~500 mm, longer than for Specimen 9. For this restrainer, the stiffness K_e was estimated as 2300 kN/mm using 3D FE analysis. Although $K_e/K_{e,\min}$ was still greater than 2, failure of the restrainer due to fracture of bolts occurred. The analysis showed that the normal thrust resulting from the larger gap exceeded the tensile resistance of the bolts. This confirms that strength requirements can govern the design although the provided restrainer stiffness seems sufficient.

7.3.3 Estimation of stiffness and force demand on restrainer

To estimate the total available stiffness against gap opening K_e, one may build a simple model with one-dimensional elements as shown in Figure 7.8b and c using Timoshenko beam (with bending and shear flexibility) or a detailed three-dimensional finite element model (Figure 7.8a). In both methods, the restrainer is first discretized into segments having a length equal to the longitudinal bolt spacing L_{bx}. Making use of the symmetry, only half a segment is modelled that spans from one bolt to the segment mid-length and comprises only the half-width of one half-section of the restrainer, as illustrated for the 3D FE model in Figure 7.8a. Appropriate boundary conditions must be considered to reflect the bi-directional response of the complete restrainer. The normal thrust is applied at mid-distance between the longitudinal bolts, i.e. at the free end of the segment. This loading condition implies having one buckling wave per each segment with the crest of wave being at the segment mid-length. This condition would give a lower bound estimate of the restrainer stiffness; an upper bound may be obtained by imposing a uniformly distributed load over the entire length of the model.

If beam elements are used, one beam is used to reproduce the stiffness of the restrainer along the length of the brace and one beam is used to reproduce the stiffness of the restrainer in the transverse

direction. When pretensioned bolts are employed, the bolts can be assumed infinitely stiff. On the contrary, bolt axial deformation must be considered when it is snug-tight as discussed in (Bregoli, *et al.*, 2016). Hence, all elements are considered as elastic springs that act in series. Typically, when ratio of the longitudinal to transversal bolt spacing is larger than unity, the overall segment rigidity is dominated by the deformations in the longitudinal direction as the transversal one is much larger. This also depends on the relative stiffness of the restrainer component. In typical application, the mentioned longitudinal to transverse bolt spacing ratio is close to or smaller than 1.0 (Chou, *et al.*, 2010).

Although the beam model is simple and convenient, it may not be accurate enough when the deformations in the transverse direction become significant as it is difficult to properly estimate the properties that must be assigned to the beam simulating transverse flexibility. In addition, the effect of bolt pretension cannot be directly seen in a beam model as it may affect the stiffness over an area surrounding the bolt and provide additional restraint against opening of the gap. Bolt pretension is generally adopted for BRB because of this beneficial effect and the resulting more stable inelastic brace response compared to snug-tight conditions (Eryaşar, *et al.*, 2010). For these reasons, the 3D finite element modeling approach was implemented to estimate the restrainer stiffness for the BRB restrainer of case study II.

For the case study II, the three-dimensional model of the quarter of the restrainer half-section segment was created in ABAQUS finite element code. Symmetry was enforced along the length of the segment by specifying zero rotation along the transversal bolt line and mid-span of the full segment. Vertical displacement was not restrained at these two locations. Bolt head and half-length of the bolt shank were included in the model and the bolt pretension was imposed using thermal initial conditions. Half thickness of the side shim plate was also considered in the model to resist the contact pressure from bolt pretension. Symmetry was also achieved in the transverse direction by specifying zero rotation about the brace longitudinal axis along at mid-width of the restrainer. 3D 8-node continuum element with incompatible formulation, denoted by C3D8I in the software, was employed to construct the mesh for the restrainer, shim plate, and bolt. Normal force N_z was applied as a uniformly distributed edge pressure at the mid-length of the segment. For a given bolt spacing, the longitudinal and transversal stiffness of each segment, $k_{e,l}$ and $k_{e,t}$, respectively, are computed as:

$$k_{e,l} = \frac{4N_z}{\delta_{z,a} - \delta_{z,b}} \tag{7.30}$$

$$k_{e,t} = \frac{4N_z}{\delta_{z,b}} \tag{7.31}$$

where N_z is the applied normal edge load; and $\delta_{z,a}$ and $\delta_{z,b}$ are the nodal vertical displacement of the free and clamped ends of the model, respectively (see Figure 7.8). These displacements are at the nodes located on the underside of the face plate along the assumed longitudinal plane of symmetry. In the equations, the factor of 4 is to account for the symmetry in the model (one-quarter of segment is modelled). Given that the longitudinal and transversal stiffness are in series, the total restraining stiffness of each segment is:

$$k_e = [1/k_{e,l} + 1/k_{e,t}]^{-1} \tag{7.32}$$

The total restrainer stiffness is then obtained by summation of the segmental stiffness:

$$K_e = \sum k_e/2 \tag{7.33}$$

In this equation, k_e is divided by 2 to account for the flexibility of the other restrainer half-section not incorporated in the model. As mentioned, the FE analysis predicts $K_e = 2400$ and 2300 kN/mm for the restrainer used in Specimens 9 and 12, respectively. If the bolts were in the snug-tight condition (~20% of the bolt nominal tensile resistance), K_e would have reduced to 1800 and 1600 kN/mm for the same two specimens, which corresponds to 25–40% reduction in stiffness that may affect the BRB response. Large bolt pretension is found to provide a boundary condition similar to fully-restrained rotational support.

Using the value of K_e, the solution can be found for the buckled core yielding at the end of the largest compression excursions and the normal forces obtained from the core analysis can be applied to the restrainer to determine the stress demand on the restrainer components and bolt forces. This is done by means of a simple analysis of the restrainer acting as a continuous beam, as shown in Figure 7.11. Using symmetry w.r.t. to the longitudinal plane, the stiffness of only one restrainer half-section may be considered in the model. Timoshenko beam elements with flexural

and shear flexibilities should be used as shear deformations can be significant due to the small length-to-depth ratios. Vertical supports are specified at bolt locations. Alternatively, the transversal segment stiffness $k_{e,t}$ can be assigned to support springs at the bolt locations. Normal thrust forces and longitudinal frictional forces from the analytical method are then applied as point loads to the beam. When a stopper is provided at mid-length of the core, half-length model as shown in Figure 7.11 can be used as both loading and geometry are symmetrical. The computed support reactions from the analysis are the tension forces in the bolts. These bolt forces account for the variation of by the normal forces and core buckling wave length along the core and would therefore represent a more realistic estimates of the actual demand compared to the average bolt force from Eq. (7.21). Depending on the joint geometry, bolt tension forces from the beam analysis may need to be amplified for prying action. Stresses in the restrainer components due to normal thrust and frictional forces should be combined with the anticipated stresses induced by global bending of the restrainer under the maximum axial compression load, as described in (Dehghani, *et al.*, 2016b).

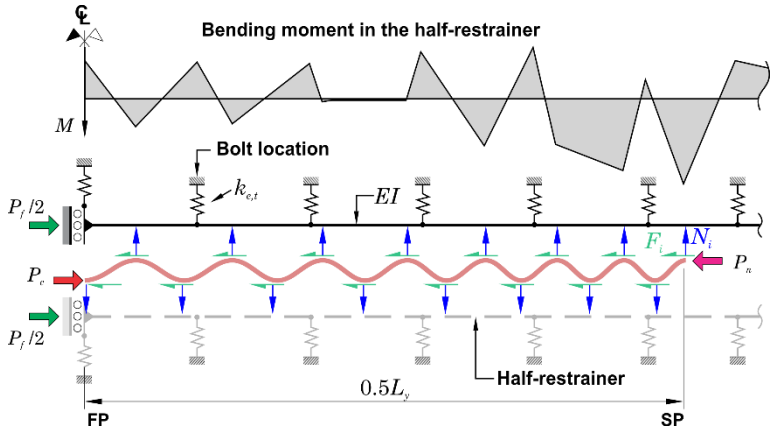

Figure 7.11: Continuous beam concept to estimate internal action in restrainer.

7.4 Summary and conclusions

This article presents an extension to existing models for predicting design forces on the restrainer system of buckling-restrained braces subjected to large compression deformation excursions. The proposed iterative approach accounts for cyclic hardening behaviour of steel core, section expansion due to Poisson's effect, longitudinal frictional forces and variation of the core axial load and strains along the core length, and flexibility of the restrainer. A simple predictive model for

cyclic hardening of structural steel was presented. The method proposes minimum values for the restrainer stiffness and can be used to predict the brace compression and tension adjustment factors for frame design. The method was validated against experimental data and finite element analysis for two different BRB members. In general, good agreement was found between test, finite element analysis and analytical results and core axial loads, normal thrust forces, and buckling wavelength were predicted with reasonable accuracy sufficient for most engineering applications. Comparison with the finite element analysis results showed that the proposed method can predict the asymmetric nature of the local strain demand along the core. It was shown that the required minimum restrainer stiffness can serve as a simple design criteria when strength requirements do not govern. A finite element method to estimate the available restraining stiffness was introduced to account for bolt pretension in addition to the longitudinal and transversal restrainer flexibilities. The analysis showed that pretensioned bolts can increase the restraining stiffness by 25% to 40% compared to bolts used in the snug-tight condition. Finally, an analysis technique was suggested to estimate internal design actions on the restrainer and anticipated bolt tension forces.

As proposed, the approach is only valid under small displacement condition which requires small initial gap sizes and sufficient restraining stiffness to prevent excessive gap opening. The method could be improved upon by considering a distributed restraining stiffness rather than a lump stiffness model. Although the analytical model accounts for variable buckling wavelengths, it assumes the same buckling configuration for all waves along the core length. Further work could be performed to develop criteria that would regulate the waveforms under a given loading condition. Finally, the proposed model could be extended to track the history of core strain in tension and compression for a brace subjected to a given cyclic loading protocol such that low-cycle fatigue can be verified. Core bending strains would then need to be added to axial strains for fatigue assessment. The computed strains would also lead to a better estimation of the Poisson's effect along the core length.

Acknowledgements

Financial assistance for this project was provided by the Natural Sciences and Engineering Research Council (NSERC) of Canada. The scholarship awarded to the first author by the Structural Steel Education Foundation of the Canadian Institute of Steel Construction is acknowledged.

References

AISC. (2010). ANSI/AISC 341-10, Seismic Provisions for Structural Steel Buildings. Chicago, IL: American Institute of Steel Construction, Inc.

Bondonet, G., & Filiatrault, A. (1997). Frictional Response of PTFE Sliding Bearings at High Frequencies. *Journal of Bridge Engineering, 2*(4), 139-148.

Bregoli, G., Genna, F., & Metelli, G. (2016). Analytical estimates for the lateral thrust in bolted steel buckling-restrained braces. *Journal of Mechanics of Materials and Structures, 11*(2), 173-196.

Chen, Q., Wang, C.-L., Meng, S., & Zeng, B. (2016). Effect of the unbonding materials on the mechanic behavior of all-steel buckling-restrained braces. *Engineering Structures, 111*, 478-493.

Chou, C.-C., & Chen, S.-Y. (2010). Subassemblage tests and finite element analyses of sandwiched buckling-restrained braces. *Engineering Structures, 32*(8), 2108-2121.

Dehghani, M., & Tremblay, R. (2016b). Design and Full-Scale Experimental Evaluation of a Seismically Resilient Steel Buckling Restrained Brace System. *Earthquake Engineering and Structural Dynamics* (submitted).

Dehghani, M., Tremblay, R., & Leclerc, M. (2016d). Fatigue failure of 350WT steel under large-strain seismic loadings at room and subfreezing temperatures. *Construction and Building Materials* (submitted).

Della Corte, G., D'Aniello, M., & Landolfo, R. (2015). Field Testing of All-Steel Buckling-Restrained Braces Applied to a Damaged Reinforced Concrete Building. *Journal of Structural Engineering, 141*(1), 1-11.

Eryaşar, M. E., & Topkaya, C. (2010). An experimental study on steel-encased buckling-restrained brace hysteretic dampers. *Earthquake Engineering & Structural Dynamics, 39*(5), 561-581.

Galambos, T. V., & Surovek, A. E. (2008). *Structural stability of steel: concepts and applications for structural engineers*: John Wiley & Sons.

Genna, F., & Bregoli, G. (2014). Small amplitude elastic buckling of a beam under monotonic axial loading, with frictionless contact against movable rigid surfaces. *Journal of Mechanics of Materials and Structures, 9*(4), 441-463.

Genna, F., & Gelfi, P. (2012a). Analysis of the Lateral Thrust in Bolted Steel Buckling-Restrained Braces. I: Experimental and Numerical Results. *Journal of Structural Engineering, 138*(10), 1231-1243.

Genna, F., & Gelfi, P. (2012b). Analysis of the Lateral Thrust in Bolted Steel Buckling-Restrained Braces. II: Engineering Analytical Estimates. *Journal of Structural Engineering, 138*(10), 1244-1254.

Hoveidae, N., & Rafezy, B. (2013). Global Buckling Prevention Condition of All-Steel Buckling Restrained Braces. *Journal of Theoretical and Applied Mechanics, 51*(4), 891-902.

Jiang, Z., Guo, Y., Zhang, B., & Zhang, X. (2015). Influence of design parameters of buckling-restrained brace on its performance. *Journal of Constructional Steel Research, 105*, 139-150.

Korzekwa, A. (2009). *Simulation numérique du comportement inélastique et conception parasismique d'un système de diagonales ductile confinées construit uniquement en acier.* École Polytechnique de Montréal, Montréal. (in French).

Korzekwa, A., & Tremblay, R. (2009, August 16-20). *Numerical simulation of the cyclic inelastic behaviour of BRBs.* Paper presented at the 6th International Conference on Behavior of

Steel Structures in Seismic Areas – STESSA 2009, Philadelphia, Pennsylvania.

Lemaître, J., & Chaboche, J.-L. (1990). *Mechanics of solid materials*. Cambridge: Cambridge University Press.

Lin, P.-C., Tsai, K.-C., Wang, K.-J., Yu, Y.-J., Wei, C.-Y., Wu, A.-C., Tsai, C.-Y., Lin, C.-H., Chen, J.-C., Schellenberg, A. H., Mahin, S. A., & Roeder, C. W. (2012). Seismic design and hybrid tests of a full-scale three-story buckling-restrained braced frame using welded end connections and thin profile. *Earthquake Engineering & Structural Dynamics, 41*(5), 1001-1020.

Metelli, G., Bregoli, G., & Genna, F. (2016). Experimental study on the lateral thrust generated by core buckling in bolted-BRBs. *Journal of Constructional Steel Research, 122*, 409-420.

Midorikawa, M., Hishida, S., Iwata, M., Okazaki, T., & Asari, T. (2016). Bending Deformation of the Steel Core of Buckling-Restrained Braces *Geotechnical and Structural Engineering Congress 2016* (pp. 613-623): American Society of Civil Engineers.

Midorikawa, M., Iwata, M., Wakayama, T., Iizuka, R., Okazaki, T., & Asari, T. (2014). *Buckling-mode Number and Compressive-to-Tensile Strength Ratio of Buckling-Restrained Braces.* Paper presented at the 10th U.S. National Conference on Earthquake Engineering, Anchorage, Alaska.

Midorikawa, M., Wakayama, T., Iizuka, R., Asari, T., Murai, M., & Iwata, M. (2012). Experimental Study on Buckling-Restrained Braces using Steel Mortar Planks-Evaluation of the buckling mode number, compression-to-tension strength ratio and friction force. *Journal of Structural and Construction Engineering (Transactions of AIJ), 77*(681), 1763-1771 (in Japanese).

Razavi Tabatabaei, S. A., Mirghaderi, S. R., & Hosseini, A. (2014). Experimental and numerical developing of reduced length buckling-restrained braces. *Engineering Structures, 77*, 143-160.

SIMULIA Inc. (2012). *ABAQUS Analysis User's Manual Version 6.12-1*.

Tremblay, R., Bolduc, P., Neville, R., & DeVall, R. (2006). Seismic testing and performance of buckling-restrained bracing systems. *Canadian Journal of Civil Engineering, 33*(2), 183-198.

Tsai, K.-C., Wu, A.-C., Wei, C.-Y., Lin, P.-C., Chuang, M.-C., & Yu, Y.-J. (2014). Welded end-slot connection and debonding layers for buckling-restrained braces. *Earthquake Engineering & Structural Dynamics, 43*(12), 1785–1807.

Wu, A.-C., Lin, P.-C., & Tsai, K.-C. (2014). High-mode buckling responses of buckling-restrained brace core plates. *Earthquake Engineering & Structural Dynamics, 43*(3), 375-393.

Wu, B., & Mei, Y. (2015). Buckling mechanism of steel core of buckling-restrained braces. *Journal of Constructional Steel Research, 107*, 61-69.

Wu, J., Liang, R. J., Wang, C. L., & Ge, H. B. (2012). Restrained Buckling Behavior of Core Component in Buckling-Restrained Braces. *Advanced Steel Construction, 8*(3), 212-225.

CHAPTER 8 ARTICLE 4 : DESIGN AND FULL-SCALE EXPERIMENTAL EVALUATION OF A SEISMICALLY RESILIENT STEEL BUCKLING RESTRAINED BRACE SYSTEM

Morteza Dehghani, and Robert Tremblay

Paper submitted to *Earthquake Engineering and Structural Dynamics Journal*,

Submitted on 14 Nov 2016

ABSTRACT

This paper presents the results of 12 full-scale tests on buckling-restrained brace (BRB) specimens. A simple-to-fabricate all-steel encasing that is joined by high strength bolts was employed as the buckling-restrainer mechanism. Steel BRBs offer significant energy dissipation capability through non-degrading inelastic response of an internal ductile core. However, seismic performance of BRBs is characterized by interaction between several factors. In this experimental study, the effects of core-restrainer interfacial condition, gap size, loading history, bolt spacing, and restraining strength are evaluated. Tested specimens with bare steel contact surfaces exhibited satisfactory performance under the AISC qualification test protocol. BRBs with friction-control self-adhesive polymer liners and a graphite-based dry lubricant displayed larger cumulative inelastic ductility under large-amplitude cyclic loading, exceeding current code minimum requirements. The BRB system is also examined under repeated typical fast-rate seismic deformation history. Furthermore, performance is qualified under long-duration loading history from subduction megathrust type of earthquake. A simple hinge detail is introduced at the brace ends to reduce the flexural demand on the framing components. Internally imposed normal thrust on the restrainer is measured using series of instrumented bolts. Weak- and strong-axis buckling responses of the core are examined, and higher post-yield stiffness was achieved when the latter governed. This could be advantageous to the overall seismic response of braced frames incorporating BRBs.

Keywords: Buckling-restrained braced frames; friction; debonding; seismic loading; megathrust earthquake

8.1 Introduction

Buckling-Restrained Braced Frames (BRBFs) have become a viable choice for seismic lateral force resisting systems in buildings and other types of structures. BRBFs are equipped with special brace members that play the fuse role by dissipating earthquake energy through axial plastic deformations in a stable manner. The buckling restrained brace (BRB) members are typically composed of a slender core metallic element and an encasing (restrainer) system to prevent lateral buckling of the core. Typically, a small gap is provided and a low-friction debonding material is employed to ensure free relative sliding at the core-restrainer interface. Since the core is prevented from buckling, it can be axially compressed far beyond yield capacity without strength degradation and this behaviour provides significant source of energy dissipating capacity.

BRB technology was developed in the 1980's in Japan as a supplemental damping device for steel moment resisting frames (Watanabe, *et al.*, 1988). Two decades later, this technology was adapted as a braced frame system in North America after experimental verification programs (Tremblay, *et al.*, 1999; Black, *et al.*, 2004). The stiffness of the restrainer, the core-restrainer interface gap and frictional characteristics, and strain hardening of the core are the major parameters that control the behavior of a typical BRB member under large plastic strain cyclic loading (Tremblay, *et al.*, 2006; Genna, *et al.*, 2012b). Conventionally, the restrainer system is made of a concrete- or mortar-filled steel tube. As an alternative, the restrainer can be fabricated entirely out of steel to eliminate the time and efforts required for concrete casting and curing procedures. This also offers more design and fabrication options since many configurations would be possible by joining different available steel sections (Eryaşar, *et al.*, 2010). Some all-steel BRB could also be as low as 40% lighter than an equivalent mortar-filled BRB (Usami, *et al.*, 2008). Potentially, bolted all-steel BRBs can be disassembled for damage inspection after earthquake which represents an advantage over the conventional BRBs (Wu, *et al.*, 2014).

For all-steel BRB members, the main challenge is to design a restraining system that provides a uniformly stiff lateral support for the core as can be easily achieved with a concrete-filled tube system. Seismic performance of all-steel BRBs have been subject of numerous past research that dates back to early 90's in Japan. Imai *et al.* (1991) is among the first experimental studies on behaviour of all-steel BRBs which investigated stability of a BRB that comprised of an outer tube as the core and an inner tube as the restrainer. Tremblay, *et al.* (2006) tested all-steel BRB

subassemblies with different yielding segment length under quasi-static and dynamic loadings. It was concluded that, when friction is severe, strain distribution along the core would not be uniform and local buckling is more concentrated at the core ends. To improve the performance, it was suggested to employ a debonding material, stiffer restrainer and minimum possible gap between core and restrainer. Eryaşar, *et al.* (2010) experimentally verified performance of several fully-steel restraining mechanism details including rolled and built-up sections that were joined by bolts or weld. It was reported that the BRBs with snug-tight bolted restrainer showed lower performance than the ones having pretensioned bolts. Usami, *et al.* (2008) experimentally studied stability and energy-dissipating capacity of all-steel BRBs with built-up bolted restrainers. It was shown that to prevent global buckling under large axial deformations, combined effects of axial force, P-delta bending moments, and normal thrust due to local buckling of core must be considered in design. Genna, *et al.* (2012a) conducted experimental studies and complementary finite element analysis to evaluate the normal thrust on a fully steel restrainer. It was found that the thrust force increases as a deformation cycle is repeated. In a number of past research, premature failure has been observed due to insufficiency of the buckling restraining system (Tremblay, *et al.*, 2006; Eryaşar, *et al.*, 2010; Razavi Tabatabaei, *et al.*, 2014; Della Corte, *et al.*, 2015).

In this paper, results of the experimental qualification of a BRB system with a bolted fully steel encasing are presented. The proposed patent-free BRB member is simple to fabricate and install. Key parameters affecting the seismic performance of the BRB member were investigated through twelve full-scale cyclic tests. In particular, the member performance is verified and compared with different restrainer-core interfacial conditions. Performance of the proposed BRB system under repeated fast-rate seismic loading as well as long-duration loading history from megathrust type of earthquakes are verified. The BRB specimens were tested in a planer load frame to investigate the flexural demand imposed by frame action. A simple end connection detail is introduced to limit that demand and its response is qualified under different loading conditions.

8.2 Test Program

8.2.1 BRB specimens

Twelve full-scale BRB specimens with nominally identical cores were tested. Details of the specimens are given in Figure 8.1. The yielding segment (YS) of the BRB core is 150 mm wide by

3.0 meters long. It approximately covers 50% of the workpoint-to-workpoint length of the brace member in the test frame. The core width at the end is increased to 350 mm to preclude yielding outside of the reduced section and net section tension failure at the end bolted connections in the gusset plate. Between the end bolted connections and the core YS, the wider core segment is stiffened by means of two flange plates to form I-sections. In this stiffened core segment, long-slotted holes are used to connect together the core and the restrainer system and accommodate the free relative movement between them. In a braced frame, the core would be oriented such that weak-axis buckling of the core occurs in the plane of the frame. The core would be connected to the frame gusset plates using 2 pairs of angles and a short (38 mm) length is left between the ends of the angles and the stiffened core segments to create a flexible low-strength plastic hinge for limiting in-plane bending moments induced by frame action. This hinge detail is discussed further later. The brace cores were plasma-cut from ¾" (19.05 mm) thick plates conforming to CSA G40.21-350WT category 4 steel with minimum yield strength of 350 MPa. The measured properties of the core steel are given in Table 8.1. Coupon tests were performed at a quasi-static rate of 1.0×10^{-6} s^{-1}. Given the core YS section dimensions (19.05×150 mm) and the material yield strength, the nominal and actual axial yield resistances of the BRB core are 1000 and 1100 kN, respectively. Nominal axial elastic stiffness of the YS is 200 kN/mm and the core axial stiffness between gusset plates is 175 kN/mm.

Table 8.1: Average mechanical properties of core plate

Elastic Modulus	**Upper Yield Stress**	**Yield Stress**	**Ultimate Tensile Stress (UTS)**	**Strain at UTS**	**Elongation on 200 mm gauge**	**Reduction in area at fracture**
(GPa)	(MPa)	(MPa)	(MPa)	(%)	(%)	(%)
210	412	385	509	16	28	60

The BRB restraining system consists of a pair of bolted built-up steel sections. These sections comprised of a flat plate and a HSS member (see Figure 8.1c). Two different restrainer designs denoted R1 and R2 were utilized in the experimental program. Restrainer R1 was proportioned to avoid global buckling of the brace member and resist the internal normal thrust demand imposed by the core undergoing two cycles of 4% axial elongation or shortening of the core YS. A reduced

target core axial strain of 3% was considered for restrainer R2. As shown in Figure 8.1c, compared to restrainer R2, restrainer R1 was fabricated with a thicker HSS and thicker plates and had more closely spaced connecting bolts. Except for these differences, the two restrainer systems were identical. In both cases, the restrainer half-sections were bolted together using 15.9 mm (5/8") pretensioned ASTM A325 bolts. The nominal tensile strength of these bolts is 120 kN but mill test data indicated that the actual strength was 150 kN, i.e. 22% overstrength. At both ends of the braces, the bolts in the last two transversal lines connect to the long-slotted holes in the non-yielding segment of the core. These bolts were left in the snug-tight condition to allow relative longitudinal movements between the restrainer system and the core. The long-slotted holes were sized to accommodate 4% elongation or shortening of the core YS.

Core and restrainer were not longitudinally locked together anywhere along the length, i.e. no stopper, and the restrainer was free to slide with respect to the core. Out-of-plane (strong-axis) buckling of the core YS is restrained by a pair of 47 mm wide shim plates placed on either side of the core YS and held in place by the longitudinal restrainer bolted connections. The side shims used in most of the specimens were cut from the same plate as the core, thus had the same thickness as the core. However, side shims in few specimens were prepared from a different 19.05 mm (¾") plate that was slightly thicker than the core plates. Gaps were left on the four sides of the YS core to accommodate transverse core expansion due to the Poisson's effects under compression. The through-thickness gap was provided by thin steel sheets acting as spacers attached on top and/or bottom of the shim plates. The required gaps along the core sides were achieved when placing the shim plates.

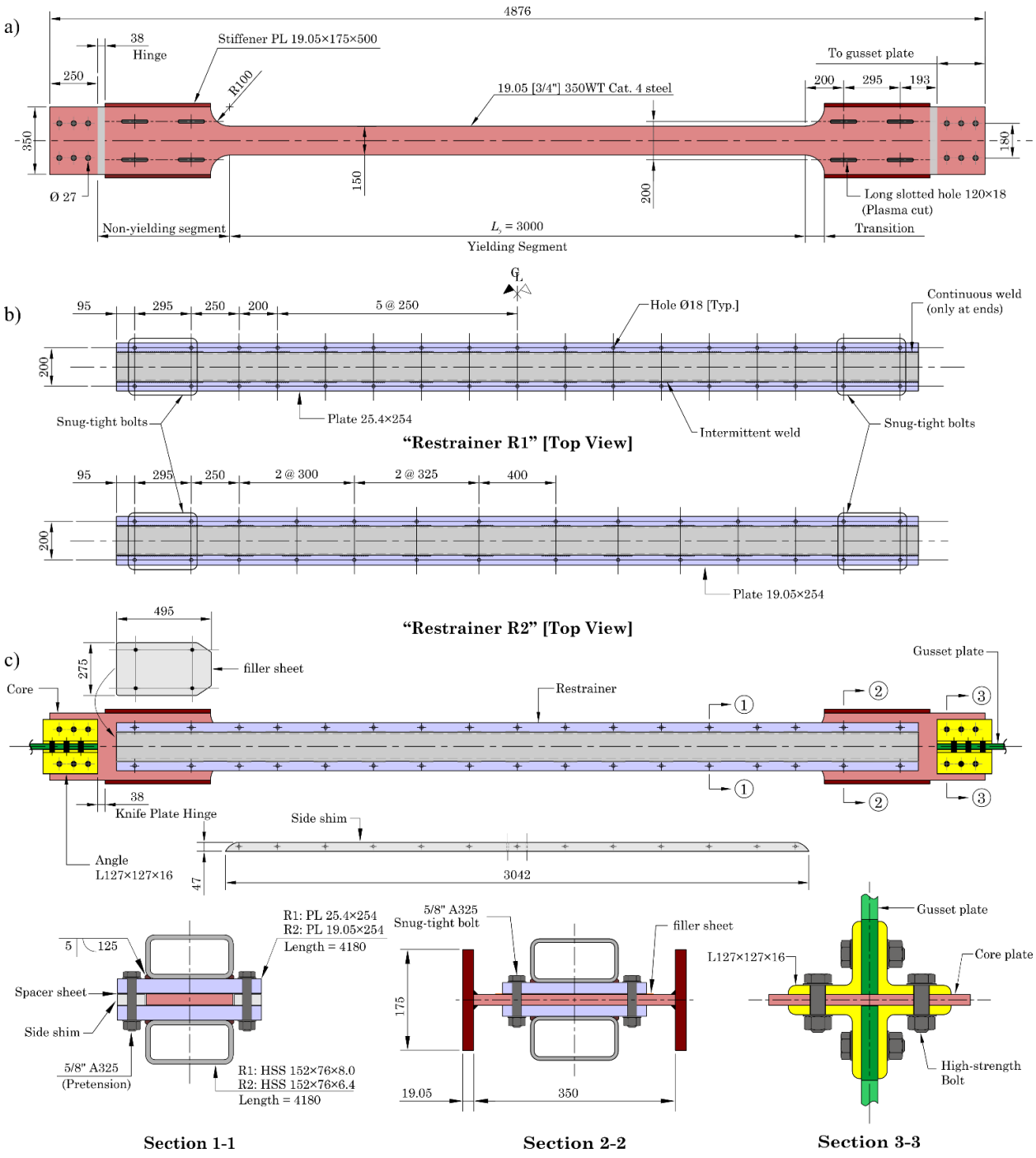

Figure 8.1: a) Geometry of the BRB core; b) and c) Restrainer R1 and R2; and c) Plan view of the assembled BRB with restrainer R1.

8.2.2 Knife plate hinge (KPH) detail

Past research has shown that frame action can induce flexural demand on the BRB and its end connections (Lin *et al.*, 2015; Zhao *et al.*, 2016) that can be damaging to the brace and other framing components (López, *et al.*, 2002; Takeuchi, *et al.*, 2014). This adverse effect can be controlled by using gusset plates connected to beams only and a knife plate brace-to-gusset connection exhibiting low flexural stiffness and strength. The detail is illustrated in Figures 8.2a and b for the test setup used in this test program where the tested BRB members were assumed to be part of a V-bracing configuration. As shown, the test setup represented half the span of a 9.0 m wide by 4.0 m high bracing panel. The BRB specimens had approximately 6.0 m length between work-points. At their bottom end, the BRB specimen was connected to a gusset plate simulating the connection to the floor beams that was anchored in the laboratory strong floor. At their upper end, the gusset plate was connected under the beam. The beam-to-column connection was a simple bolted double-angle joint with long-slotted holes in the angle legs to accommodate the relative rotation between the beam and the column. Slots were cut in both gusset plates to accommodate the ends of the brace core and allow simple field-bolted connections with four angles. With this connection detail, both gusset plates remain nearly horizontal during an earthquake, and rotations at the brace ends are limited to those caused by the relative horizontal displacement between brace ends due to storey drift. That rotation is to take place in the knife plate hinge (KPH) in the net distance left between the end of the connecting angles and the stiffened portion at the ends of the core (Figures 8.1c and 8.2b).

The KPH must resist the brace maximum compressive force $P_{\max}$ while forming plastic hinges when the frame attains the target storey drift. The force $P_{\max} = \beta\omega R_y F_y A_c$ where ω and β are the tensile and compressive strength adjustment factors that account for cyclic hardening, and friction and core expansion, respectively, $R_y F_y$ is the actual yield strength of the core plate material, and A_c is the cross-section area of the core YS. The KPH length must then be short enough to prevent instability while being sufficiently long so that inelastic rotations do not lead to low cycle fatigue fracture. For the latter, the relation between the KPH rotation θ and the storey drift ratio Δ/h for the test setup studied can be expressed as:

$$\theta = \frac{\Delta}{h}\frac{\sin^2\psi}{a_h} \tag{8.1}$$

where ψ is the brace angle with respect to floor, and a_h is the ratio of hinge-to-hinge distance to the work-point length of the brace (see Figure 8.2c). Under an axial load P, the yield curvature in the KPH with rectangular cross-section is:

$$\phi_y = \frac{2(1 - P/P_{y,k})\epsilon_y}{t_c} \tag{8.2}$$

where ϵ_y and t_c are the yield strain and thickness of the KPH, and $P_{y,k}$ is the axial yield strength of KPH. On average, when the BRB is stretched or compressed, the normalized axial stress could be estimated as:

$$\frac{P_{\text{avg}}}{P_{y,k}} = \frac{\omega(1+\beta)}{2}\eta \approx \omega\beta\eta \tag{8.3}$$

where η is the ratio of A_c to the knife plate cross-section. For the specimens in this study, η = 150/350 = 0.43 (see Figure 8.1a) . Integrating the yield curvature over the KPH length gives the joint yield rotation:

$$\theta_{y,k} = \int_{\text{hinge}} \phi_y dx = 2r(1 - P_{\text{avg}}/P_{y,k})\epsilon_y \tag{8.4}$$

where r is the length-to-thickness ratio of the KPH. Axial strain in the extreme fiber of the knife-plate is then:

$$\epsilon_k = \frac{\theta}{\theta_{y,k}}\epsilon_y = \frac{\theta}{2r(1 - P_{\text{avg}}/P_{y,k})} \tag{8.5}$$

By substituting Eq. (8.1) into Eq. (8.5), strains in the extreme fiber of the KPH can be directly related to storey drift:

$$\epsilon_k = \frac{1}{2r(1-\omega\beta\eta)}\frac{\sin^2\psi}{a_h}\frac{\Delta}{h} \tag{8.6}$$

The number of cycles to failure can be estimated by implementing the strain-life fatigue model relating strain to fatigue life model proposed by Dehghani, *et al.* (2016d) for the 350WT core steel material. Magnitude of ω and β mainly depend on the anticipated deformation demand on the YS at the target storey drift and BRB specifications such as core material, gap size, and severity of friction at the core-restrainer interface. Given the geometry of the brace and test frame, the axial elongation or shortening in the BRB YS nearly corresponds to the target drift angle. This is to say that, for example, storey drift angle of Δ/h = 2% would induce strain of ϵ_c = 2.0% in the core YS. For design purpose, ω = 1.18–1.47 for ϵ_c = 1.0% to 4.0% was obtained from cyclic testing of small-scale round specimens of 350WT steel (Dehghani, *et al.*, 2016d). Parameter β = 1.04~1.2 was estimated from core buckling normal thrust analysis assuming an appropriate coefficient of friction. For the test frame studied, ψ = 41.6° and a_h = 0.75, and using r = 1.0 gives 1700, 250, 70 and 25 cycles to failure when Δ/h = 1.0, 2.0, 3.0 and 4.0% of the storey height, respectively. When r = 2.0, the failure life increase to 9000, 1300, 350, and 125 cycles for the mentioned range of storey drifts. Given that the employed fatigue model was obtained from testing smooth specimens and strain concentration was expected in the KPH, a conservative value r = 2.0 (= 38 mm, see Figure 8.1a) was adopted in the test program. An even larger r value could have been selected to further reduce the strain demand in the hinge but stability could have become an issue. As will be presented later, the tests showed that r = 2.0 was appropriate.

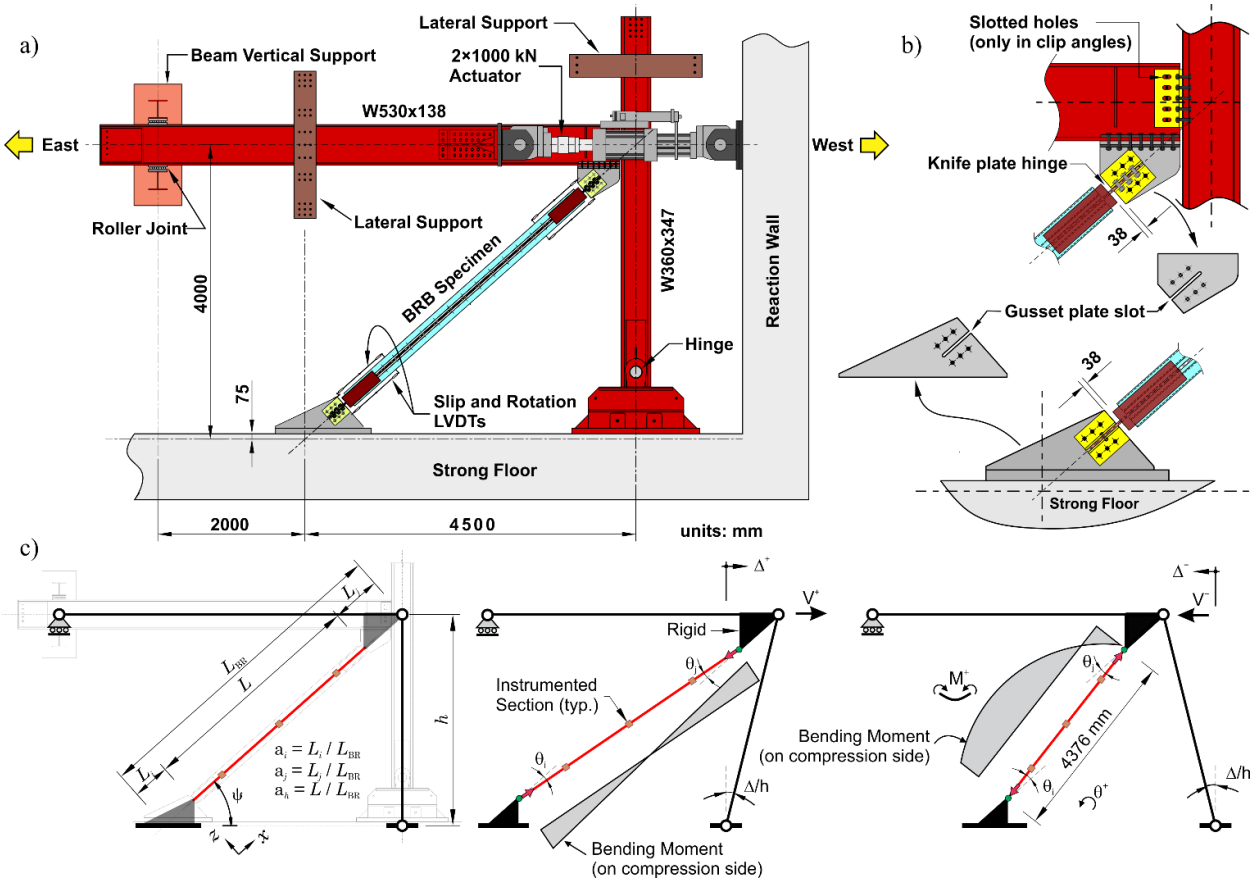

Figure 8.2: a) Elevation of the test setup; b) Beam-brace-column joint, and top and bottom gusset plates prior to connecting the BRB specimens; c) End rotations and bending moment demand induced by storey drifts.

8.2.3 Design of restrainer

The restrainer is designed to develop stable global response as well as satisfactory local behaviour. Global stability is verified in accordance with the Canadian CSA S16 steel design standard (CSA, 2014) which recommends that compressive members be braced so that their initial imperfection δ_0 is not amplified by more than two times when subjected to the design loads. For BRB systems, deflection amplification under the maximum compressive load $P_{\max}$ can be estimated as:

$$\frac{\delta}{\delta_0} = \frac{1}{1 - P_{\max}/P_e} \leq 2.0 \tag{8.7}$$

where $P_e = \pi^2 E I_r / L^2$ is the Euler elastic buckling load of the BRB; E is the Young modulus of the restrainer material; I_r is the minor-axis moment of inertia of the restrainer; and L is the effective brace length taken as the distance between the knife plate hinges (see Figure 8.2b). Sectional properties and design values for restrainers R1 and R2 are given in Table 8.2. In computing I_r, the built-up restrainer was assumed to act as a composite member given that the bolts are pretensioned. The verification was performed at 3% drift angle and maximum δ/δ_0 = 1.7 was estimated for Specimens 1 to 8 and 11 and 12 that employ restrainer R1. This ratio with restrainer R2 was 2.0 and 2.2 for drift angles of 2% and 3%, respectively. Eq. (8.7) is equivalent to $P_e/P_{\max} \geq 2.0$, which can serve as a criterion for stiffness design of restrainer system. Among the specimens, the lowest estimated $P_e/P_{\max}$ ratio was 2.0 for restrainer R2 in Specimens 9 and 10.

In addition to Eq. (8.7), adequate global response including stability effects requires that the restrainer remains elastic when the brace is developing the load $P_{\max}$. In particular, longitudinal axial stresses induced by axial load and flexure must be verified. When the brace is subjected to compression, weak-axis buckling of the core generates longitudinal frictional forces at the core-restrainer interface inducing axial compression in the restrainer. In the proposed BRB system, the restrainer is free to slide with respect to the core and frictional forces may accumulate in the restrainer from both ends towards the brace mid-length or from one end to the other end where they are transferred back to the core by the end bolts. In both cases, the anticipated total accumulated frictional force in the restrainer can be obtained from:

$$P_f \approx \omega(\beta - 1 - 2|\epsilon_c|)P_y \tag{8.8}$$

where ϵ_c is the applied compressive strain to the core YS at the target storey drift; and $P_y = R_y F_y A_c$ is the yield resistance of the core member. Effect of core section lateral expansion due to the Poisson's effect is included in Eq. (8.8) assuming that the core section expands by a factor $(1 + 2 \times 0.5|\epsilon_c|)^2 \approx 1 + 2|\epsilon_c|$. For the verification of the restrainer against longitudinal axial stresses, the first frictional force transfer scenario was considered with the axial load P_f acting at the center of the brace length, where the moments due to global flexural response, M_r, are maximum:

$$M_r \approx \frac{P_{\max}\delta_0}{1 - P_{\max}/P_e} \tag{8.9}$$

The equation assumes that the moment M_k develops in the knife-plate hinges (see Eq. (8.12) and Figure 8.2c) have no significant effect on the global flexural demand near the brace mid-length. In addition, axial load was assumed to have no eccentricity with respect to the brace centerline. The total maximum longitudinal stress in the restrainer is then obtained by combining stresses from friction-induced axial load and stresses due to global and local bending of the restrainer components:

$$\sigma_{\max} = \frac{P_f}{A_r} + \frac{M_r}{S_r} + \sigma_{NT} \leq \frac{F_{yr}}{\text{S. F.}} \tag{8.10}$$

where A_r and S_r are the restrainer cross-sectional area and modulus of section, respectively; $F_{yr}/\text{S. F.}$ is the restrainer yield stress divided by a safety factor to ensure fully elastic response; and σ_{NT} is the stress caused by local bending of restrainer due to core normal thrust. This normal thrust is generated when core buckling is constrained by the restrainer stiffness. The normal thrust is estimated using the method proposed in Dehghani *et al.* (2016a) for the critical weak-axis buckling mode of the core illustrated in Figure 8.3d. The method is based on the approach outlined in Midorikawa, *et al.* (2012). It also accounts for the effects of cyclic strain hardening, restraining stiffness, longitudinal frictional forces, and Poisson's effects on core cross-section. Longitudinal stress calculations are presented in Table 8.2 for two basic design cases under ϵ_c = –3%: 1) restrainer R1 with nominal gap g_z = 1.52 mm, restraining stiffness K_e = 6500 kN/mm, and core-restrainer's coefficient of friction μ = 0.2 (Specimens 1 to 4); and 2) restrainer R2 also with μ = 0.2, g_z = 0.91 mm, and K_e = 2400 kN/mm (Specimen 9). Note that K_e represents the constraining stiffness against gap opening provided by the restrainer flexural rigidity between the bolt lines. For both cases, frictional forces were assumed to have reflective symmetry w.r.t the middle of brace (see Figure 8.15a). This assumption will be verified later using the test results. For the two mentioned cases, calculation resulted in ω = 1.4 and β = 1.12. As shown, the maximum total longitudinal stresses were equal to 13% and 21% of the restrainer yield stress F_{yr} (= 345 MPa). In addition to the basic cases, specimens with larger gap size (Specimen 5) and more severe frictional conditions (Specimen 6) were also considered in the test program. In these specimens, the force

demand on the restrainer was expected to be higher than the basic cases. The restrainer was sized so that the maximum stress demand remains below 35% of F_{yr} so that when combined with residual stresses no early yielding occurs. In Table 8.2, design values corresponding to non-composite action in the restrainer are also presented. Bolt pretension to achieve composite action was deemed necessary as the global stability index δ/δ_0 exceeds the code recommended limit when restrainer is assumed non-composite. Bolt pretension was also required to limit the stress demand, and to increase the constraining stiffness against core local buckling. In general, more robust and reliable behaviour is expected when bolts of all-steel BRBs are pretensioned (Eryaşar, *et al.*, 2010).

As illustrated in Figure 8.1c, each restrainer half is made of an HSS welded to a flat steel plate. The HSS was selected to achieve the required flexural stiffness in Eq. (8.7) and control overall bending moment M_r in Eq. (8.9). The plate thickness was selected essentially to constrain the local buckling response. A rectangular HSS was chosen to cover most of the distance separating the two rows of bolts connecting together the restrainer components while minimizing the overall depth of the BRB.

The regularly spaced pretensioned bolts along the restrainer were designed to resist the tension due to the anticipated maximum normal force generated by weak-axis buckling of the core as well as the longitudinal shear due to global flexural response. The former is also obtained from the model developed by Dehghani, *et al.* (2016a). For the two aforementioned basic design scenarios, the maximum anticipated tension is equal to 39 kN and 27 kN, respectively. When gap was increased to 3.05 mm maximum tension of 113 kN was predicted by the analytical model. This exceeds the bolt factored design strength, i.e. T_r = 98 kN, and is nearly equal to the nominal bolt tensile resistance T_u = 122 kN.

The maximum longitudinal shear, including stability effects, can be estimated from:

$$V(x) = \frac{P_{\max}\delta_0}{1 - P_{\max}/P_e}\frac{\pi}{L}\cos\left(\frac{\pi x}{L}\right) + \frac{2M_k}{L} \tag{8.11}$$

where M_k is the plastic moment capacity of the knife-plate including effect of axial stress. Equation (8.11) assumes that the knife-plate joints have insignificant rotational restrain, and the brace member has a sinusoidal initial geometric imperfection with maximum in-plane amplitude of δ_0 at its mid-length. The former assumption will be verified later in this paper. The second term in Eq.

(8.11) is the shear due to plastic hinging of the knife-plate joints. For a knife-plate with rectangular section, the plastic hinge capacity is estimated as:

$$M_k = \left[1 - \left(\frac{P_{\max}}{P_{y,k}}\right)^2\right] R_y M_{p,k} \tag{8.12}$$

where $M_{p,k}$ is the nominal plastic moment of the knife plate in absence of axial stress; R_y is the ratio of actual to nominal yield stress; and $P_{y,k}$ is the yield axial strength of the KPH. For the two cases discussed here, shears on each bolt are respectively equal to 36 and 45 kN. These forces are resisted by the friction between the two restrainer halves obtained from the pretensioned bolts. The connection is therefore designed as a slip-critical connection subjected to combined tension and shear. Note that local buckling of the core about its strong axis also induces shear forces in these bolts, which was estimated as 10 kN. This shear was adopted in design of the bolted joints and in strength design of the side shim plate. As will be shown later, strong axis buckling of the core is a possibility and must be properly considered in the design of the restrainer.

In the BRB end regions, longitudinal stiffeners were welded along both edges of the widened core to form a stiff I-shaped section to ensure that the BRBs will remain straight so that relative slip between the restrainer and the core in this region occurs with limited resistance. Sung-tight bolts with slotted holes in the core are used in this region to maintain together the core and restrainer while allowing sliding. As shown in Figure 8.3b, tension can be imposed in these bolts due to out-of-plane movement of the stiffened core allowed by gap g_z. In the test BRB specimens, a filler sheet with standard hole size was employed at both ends of the core. As the filler sheet prevents the mentioned response, the tension in the bolts was ignored in the design. The end bolts were however designed for the shear P_f due to longitudinally accumulated frictional forces along the core length. This would occur when the longitudinal movement of the restrainer relative to the core will reach the point where the bolts come in contact against the ends of the long slotted holes. To account for this possible load transfer scenario, the innermost two snug-tight bolts were designed to resist the entire force P_f from Eq. (8.8).

Table 8.2: Restrainers' sectional properties and summary of the design results at the target storey drift angle of 0.03 rad.

Rest-rainer	Section components	A_r (mm^2)	$I_{r,y}$ ($10^6\,mm^4$)	$I_{r,z}$ ($10^6\,mm^4$)	W † kg/m	P_e/P_{max} (–)	P_e/P_y (–)	δ/δ_0 (–)	σ_{max}/F_{yr} * (%)	P_f (kN)	$V_{f,b}$ ** (kN)
R1	PL25.4×254 + HSS 152×76×8.0	19343	47.2	87.0	166	2.8 [1.7]‡	4.4 [2.8]	1.6 [2.3]	11 [28]	50	35
R2	PL19.05×254 + HSS 152×76×6.4	14957	32.3	67.0	132	2.0 [1.4]	3.0 [2.2]	2.0 [3.6]	17 [49]	33	44

† weight per unit length.
‡ values in the brackets obtained by assuming non-composite action between restrainer halves.
* ratio of maximum stress demand to restrainer nominal yield stress.
** maximum shear force on the pretensioned bolts ($P\delta$ shear force (Eq. (8.11)) + normal thrust from core strong-axis buckling)

The snug-tight bolts in the restrainer-to-core connections with slotted holes at the brace ends must also be designed to resist the combined tension and shear forces that are induced when the brace is subjected to compression. The lever arm of this normal thrust can be taken as the distance from end of the restrainer to the onset of the core YS, where first buckling wave becomes in contact with the restrainer. To minimize the generated tension in the snug-tight bolts, a filler sheet can be inserted between restrainer and core, at the stiffened segment, as shown in Figure 8.1c. Past experience shows that if this gap is left unfilled, excessive gap opening can take place which may result in an unwanted brace response (see S1-1 behavior described in (Tremblay, *et al.*, 2006)). Available plastic moment capacity of the stiffened core section was also verified against the required moment transfer capacity to precluded the S-shape failure mechanism described by Takeuchi, *et al.* (2014). To transfer the expected bending moment, the most critical position along the stiffened segment is at the ends of the restrainer after sliding has occurred. For buckling in the plane of the frame, the moment transfer capacity is verified using:

$$M_{p,t} \geq \frac{\delta_t P_{\max}}{1 - P_{\max}/P_e} - (1 - 2\xi)M_k \tag{8.13}$$

where δ_t is the initial imperfection at the point of moment transfer; $\xi = L_t/L$; and L_t is the distance from moment transfer point to the gusset plate (see Figure 8.3c).

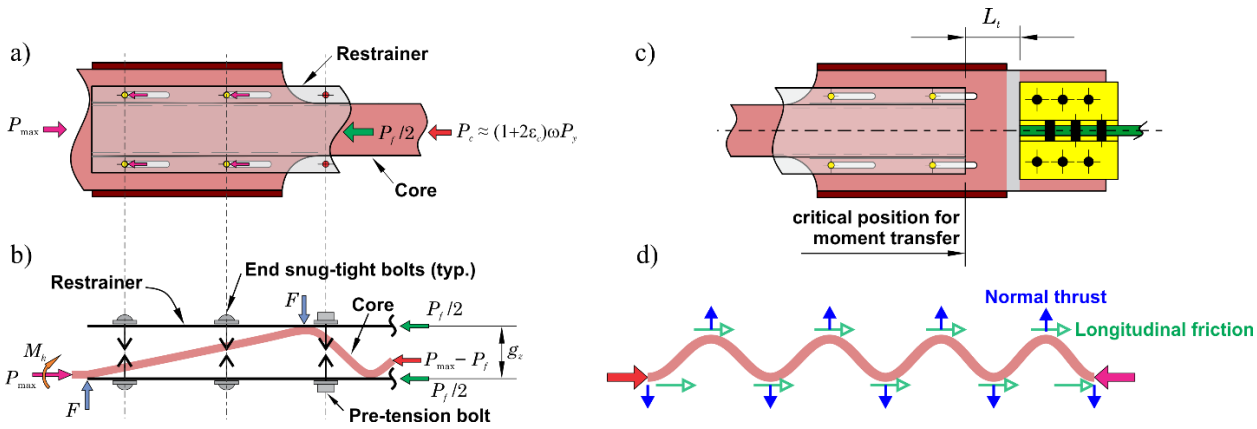

Figure 8.3: a) and b) Shear and tensile force demands on the snug-tight bolts, respectively; c) Distance between point of moment transfer and gusset plate (see Eq. (8.13)); d) Normal thrust and frictional force due to core buckling.

8.2.4 Interfacial conditions

Frictional forces are generated as result of relative sliding between the buckled core and the restrainer. The magnitude of these forces depends on the frictional characteristics at the interface of the two components and the normal thrust due to core buckling. This frictional resistance increases the energy dissipation capacity of the brace at the cost of an elevated demand on the force-controlled structural elements such as framing members and connections. High friction also causes non-uniform distribution of deformation along the yielding segment of the core, which results in localization of plastic strains and, consequently, reduced fatigue life for the BRB member. Tremblay, *et al.* (2006) reported tests results of all-steel BRBs with bare steel–steel interfacial condition and concluded that excessive frictional forces can have adverse effects on the performance of BRBs. The significance of frictional actions in BRBs are typically measured as the ratio of compressive to tensile resistances, β, at the instant of load reversal. In most available BRBs, the core is debonded from restrainer by means of a low-friction material generally denoted as debonding layer. In case of all-steel BRBs, materials such as butyl rubber (Usami, *et al.*, 2008), Polytetrafluoroethylene (PTFE) based synthetic paste (Genna, *et al.*, 2012a), penetrating oil lubricant (WD-40) (Wu, *et al.*, 2014), and ceramic paste (Razavi Tabatabaei, *et al.*, 2014) have been tested as the debonding layer at the core and restrainer interface. In this research, five interfacial conditions were examined: 1) PTFE–SS, 2) UHMW–SS, 3) Graphite–Graphite, 4) BS–UHMW, and 5) BS-BS. Properties of the debonding materials employed at these interfacial

conditions are presented in Table 8.3. PTFE, also known as Teflon, is a smooth and flexible polymer that is widely popular in friction control applications. A notable PTFE structural engineering application is in sliding bridge bearings (Dolce *et al.*, 2005). In this study, unfilled (virgin) PTFE was used against mirror-finished AISI Type 304 stainless steel (SS) with yield resistance of 215 MPa. The coefficient of friction for this interface is reported to be between 0.05 and 0.15 depending upon the normal stress and rate of sliding (Bondonet, *et al.*, 1997). UHMW (Ultra-High-Molecular-Weight) polyethylene is another polymer that has better wear resistance than PTFE but its coefficient of friction is relatively higher (0.08 to 0.2) (Thorp, 1986; Samyn *et al.*, 2006). In this research, both PTFE and UHMW were supplied on the form of pressure-sensitive self-adhesive tapes that greatly facilitated their installation. The tapes were applied on the core plate except for Specimen 2 in which UHMW tape was placed on the restrainer counterface. Before the application, the steel surface was wire-brush cleaned, soap-washed, air-dried, and finally wiped down with a methyl-ethyl ketone solvent. This procedure was put in place to achieve maximum bond strength between the tape and steel surfaces. The supply cost of UHMW tape was ~60% less than that of the PTFE. Adhesives for the PTFE and UHMW tapes were silicone- and acrylic-based, respectively. According to the manufacturer catalog, the bond strength of the UHMW tape to clean steel surface was ~2.5 times that of the PTFE. Tensile strength and break elongation of the UHMW tape were also higher than the PTFE values. The stainless steel was provided in form of thin sheets (0.9 and 1.5 mm thick) placed against the restrainer flat plates (see Figure 8.6a). Graphite as a solid lubricant also provides an effective option for debonding purpose due to its high lubricity, low cost, endurance, and easy application. An industrial-grade dry film graphite lubricant (45% solids synthetic graphite) was roller-painted to the core and restrainer surfaces, and then finished by latex glove covered-hands. The applied graphite coating typically becomes dry and solid in 24 hours and does not absorb dirt and dust, as typical liquid lubricant or gel greases would do, which could degrade the lubricity of the debonding layer. BS stands for bare steel condition, meaning mill-finish quality without any additional debonding material.

Table 8.3: Typical properties of the debonding materials verified in this study

Debonding Material	Thickness of Applied Layer (mm)	Elastic Modulus (GPa)	Yield Resistance (MPa)	Coefficient of Friction [b] (–)
PTFE	0.18 [a]	0.5	20	0.05–0.15
UHMW	0.33 [a]	0.8–1.5	19–23	0.08–0.2
Graphite	0.23	–	–	0.1–0.2

[a] total thickness of tape (backing (tape film) + adhesive)

[b] reported static coefficient of frictions for sliding against polished steel surface

8.2.5 Test setup and instrumentations

An elevation of the test setup is illustrated in Figure 8.2a. A general view is given in Figure 8.4 together with connection details. Lateral displacements were applied at the beam of the test frame with a pair of 1000 kN high performance dynamic actuators. Out-of-plane deformation of the test frame was restrained by friction-less sliding guides. The clear distance between the gusset plate and the column face was set to prevent binding between the gusset plate vertical edge and the column flange up to a storey drift ratio of 0.04 rad. (Figure 8.4b). The load frame was therefore expected to provide little lateral stiffness and resistance. This was verified by applying large amplitude cyclic deformations to the load frame without BRB. The measured maximum lateral resistance was around 10 kN, which represents less than 1% of the nominal yield resistance of the BRB members. As shown in Figure 8.4c, the lower gusset plate was bolted directly to the laboratory strong floor. Both gusset plates were designed to remain completely elastic during the testing program. As described, the BRB specimens were connected to the gusset plates using the long slots.

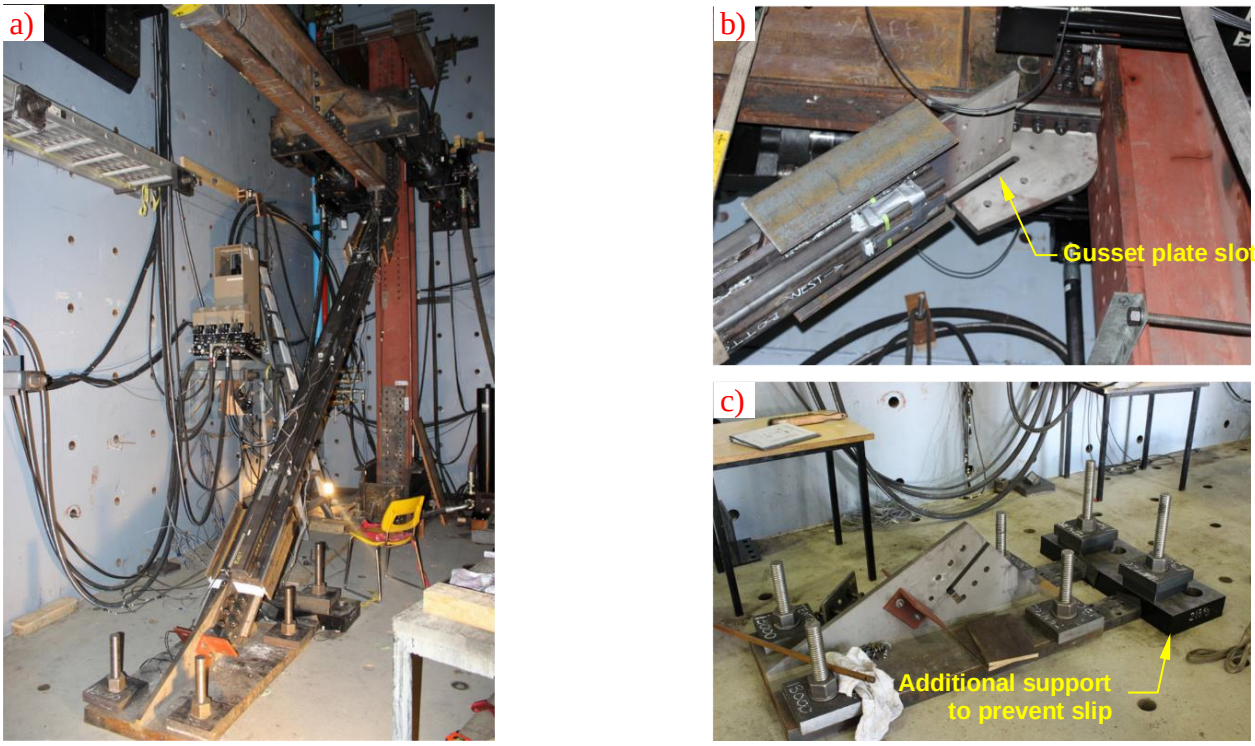

Figure 8.4: a) General view of the test setup (Specimen 6); b) Insertion of BRB into the upper gusset slot; and c) Anchorage of the lower gusset plate to the laboratory strong floor.

At each brace end, pairs of LVDTs were placed between the gusset plates and the restrainer ends to track the longitudinal movement (sliding) of the restrainer. These sensors were also utilized to monitor the relative in-plane rotations between the brace core and the gusset plates at the knife plate hinges. Three-dimensional triangulation with string potentiometers was used to trace the spatial position at the brace mid-length and at the horizontal edge of the top gusset plate. The spatial position data was then translated into relative in-plane and out-of-plane displacements at mid-length of the restrainer. For Specimens 7, 10, 11 and 12, a pair of LVDTs were attached to the exterior face of the side shim plates, at the mid-length of the restrainer, to continuously track the change in the YS width (see Figure 8.5b and c). Shaft of these LVDTs passed through 10 mm holes that were drilled at mid-thickness of the side shims. For other specimens the YS width was measured by the depth probe of a digital caliper that was inserted in the side shim holes at the end of each loading stage once the brace was unloaded to zero force. The measurements were then compared to the registered values before testing to estimate the localized transversal strains. Changes in the YS width can reflect the intensity of the longitudinal strains sustained by the section,

a technique that could be used as a quick non-destructive test to verify the state of damage in a BRB after an earthquake without dismantling it. These access holes can also allow in-situ core hardness measurement after an earthquake. Hardness has been shown as an appropriate indicator of plastic damage and remnant fracture life (Ferguson *et al.*, 2013).

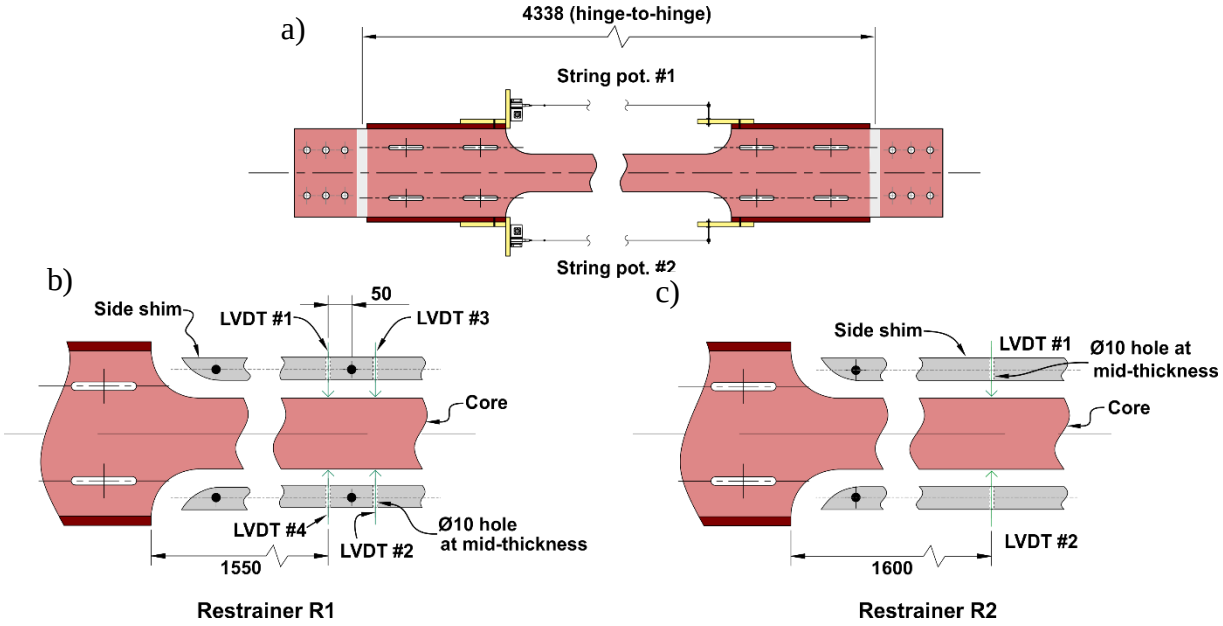

Figure 8.5: Instrumentation: a) to monitor displacement in the yielding segment of the specimens; and b) and c) tracing transverse deformation of core.

Internal actions in the restrainer were estimated using the readings from 18 strain gauges installed at the restrainer ends and mid-length. The location and position of these sensors are shown in Figure 8.6b. Longitudinal distribution of axial frictional forces in the restrainer, and in- and out-of-plane bending moment profiles along the specimen could then be computed from these readings. Two identical restrainer R1 sets were used in the tests. In restrainer R1a, the extremity strain gauges were installed close to the snug-tight bolts where composite action between the restrainer halves is limited. In restrainer R1b, the extremity strain gauges were installed along the first row of pretensioned bolts.

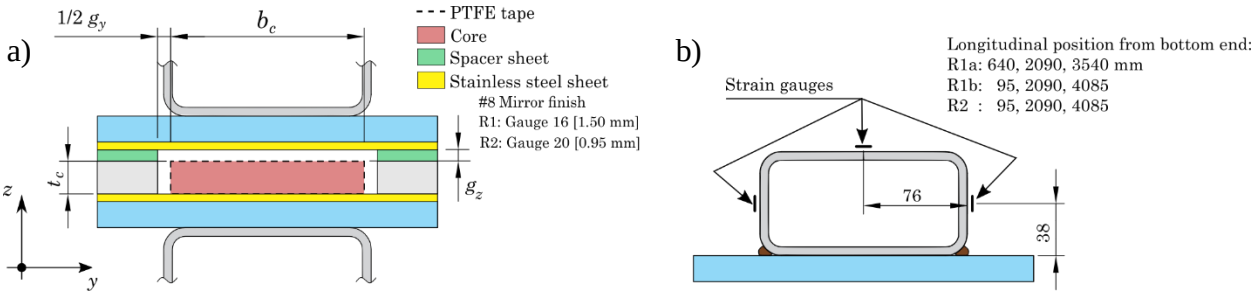

Figure 8.6: a) Schematic view of BRB cross-section (PTFE-Stainless steel interface condition shown); b) location and position of strain gauges to monitor internal actions in the BRB member.

In Specimens 9 to 11, half of the pretensioned bolts, i.e. 10 bolts, were instrumented to monitor the variation of bolts load along the core YS. Schematic view of the instrumented bolt and arrangement of the bolts in Specimen 9 are shown in Figure 8.7a and b, respectively. A 2×55 mm hole (diameter × depth) was drilled at the center of bolt and a special strain gage was embedded inside the hole. The hole was then filled with an epoxy compound. Bolts were subsequently placed into oven to cure the epoxy as instructed by the strain gage manufacturer. The instrumented bolts were all calibrated using 3 cycles of 50–90 kN tensile loading. Maximum calibration load, i.e. 90 kN, is 5% more than the standard pretension load for 5/8" A325 bolts (~85 kN). Bolts showed nearly perfect linear response and the calibration factors were found to be identical in the loading and unloading paths. In the calibration stage, one instrumented bolt was pulled to 110 kN and it showed essentially linear response. The instrumented bolts were reused in the subsequent BRB tests and they were recalibrated before each test using 3 cycle of tensile loading between 20–45 kN. During the installation, pretension of the instrumented bolts was verified using the strain gage readings.

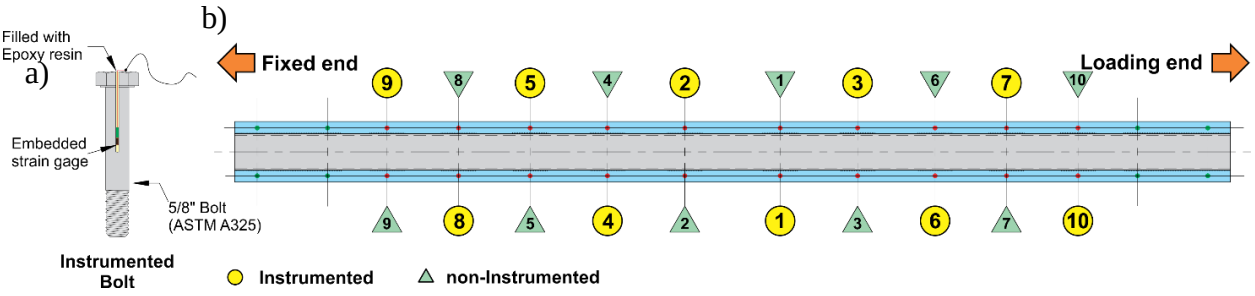

Figure 8.7: Schematic view of an instrumented bolt; b) arrangement of the instrumented bolt in Specimen 9.

8.2.6 Loading histories

Figure 8.8 shows the three-stage cyclic (TSC) loading history expressed as the equivalent uniform axial strain in the brace YS core, ϵ_c. The first stage (P1) is a customized version of the AISC standard loading protocol for qualification of BRBs (AISC, 2010) for a storey design displacement, Δ_{bm}, inducing 1% core strain. As shown, it includes two additional cycles at $\pm 3\Delta_{bm}$. The first stage finishes at strain of -1% ($-\Delta_{bm}$), which represents an likely residual storey drift of 1% for code-compliant BRBFs subjected to the design earthquake level (Erochko, *et al.*, 2011). The second stage (P2) represents the demand from an aftershock earthquake and is centered about the residual displacement from the previous stage. The last excursion of the second stage simulates the response under pulse type motion that can be expected during a very strong aftershock. The third stage (P3) of the protocol consists of a fully reversed constant-amplitude pattern, at $\pm 2\Delta_{bm}$, that was repeated until BRB failure took place. It was applied to estimate the remnant low cycle fatigue life of the BRB specimens after a shock-aftershock sequence. Accumulated inelastic deformation during the first and second stages of the TSC loading are 250 and 180 times the brace yield deformation, respectively. This parameter for the third stage loading is approximately equal to 35/cycle. In the tests under the TSC loading, storey displacements were applied using the axial deformation of the core YS as feedback. YS axial deformations were monitored by the pair of string potentiometers shown in Figure 8.5a. All three stages of TSC were applied at a constant YS axial deformation rate of 0.75 mm/s, which corresponds to a strain rate of 250×10^{-6} s^{-1} in the YS. This is 250 times faster than the rate applied in the coupon tensile tests.

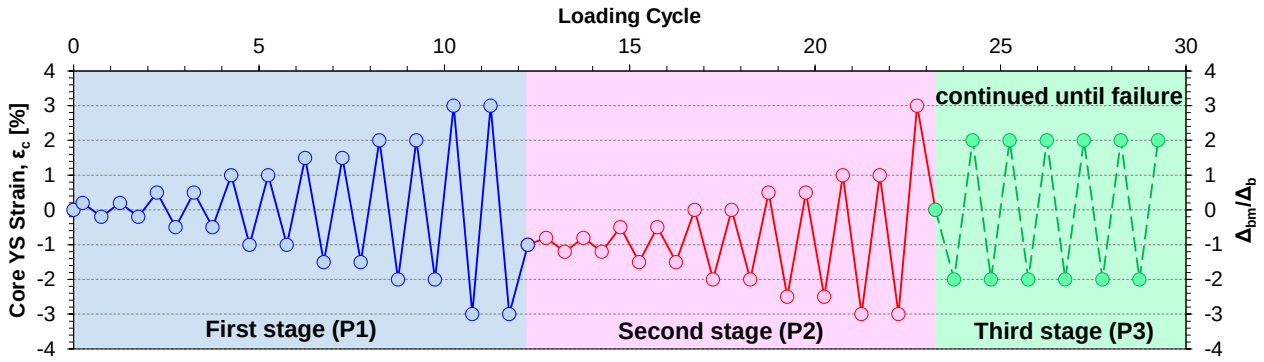

Figure 8.8: Three-stage cyclic (TSC) loading pattern.

In addition to the three-stage cyclic loading history of Figure 8.8, two seismic loading histories were employed that represented the demand anticipated from two types of earthquake ground motions expected in southwest British Columbia (BC) along the west coast of Canada: 1) Far-field intra-plate crustal earthquake; and 2) Subduction interface megathrust earthquake. Far-field intra-plate crustal ground motion records are typically free of rupture directivity effects and have normal strong motion duration. On the other hand, the subduction interface earthquakes generally have long duration of strong shaking which could promote failure mode associated to low cycle fatigue. The far-field (FF) signal was obtained from the response-history analysis of a 9-storey BRBF designed for Victoria, BC, under the NS component of the BRN record during the 1989 Loma Prieta earthquake. A scale factor of 1.5 was applied to the ground motion to match the site-specific spectrum established for a 2% in 50-year probability of exceedance. The scaled record imposed storey drifts varying between −2.2% to +2.0% (−2.2 to +2.0Δ_{bm}) in the prototype structures and cumulative inelastic ductility of 180 in the core YS. The subduction interface (SI) signal is from the storey drift history at the top floor of a 5-storey BRBF subjected to the EW component of the ground motion recorded at the FSK005 station during the 2011 M9.1 Tohoku earthquake. The original signal was 300 s long. It was shortened to 150 s by removing the low amplitude cycles at the beginning and end of the signal. The FF and SI displacement signals was repeated several times in order to evaluate seismic resiliency of the developed BRB system in shock and after-shock earthquake sequences. In the test with the FF and SI signals, the feedback from the actuators displacement was used as the control parameter.

8.2.7 Test matrix

The test matrix is given in Table 8.4. The first specimen served as dummy to verify the test set-up for quasi-static and real-time dynamic seismic loading histories. Specimens 2, 3, 4, and 6 were identical with the exception of the interfacial condition. They were all tested under the TSC loading history. The goal of this phase was to identify the interface condition that would lead to minimum frictional forces at the core-to-restrainer interface. Specimen 6 with no debonding material represents a minimum cost BRB solution and the steel surfaces were left in the as-received condition. In Specimen 2, the steel of the restrainer flat plate was wire-brush cleaned before assembly. In the next round of the test program, the effect of gap size on the brace response indices was explored by comparing Specimens 4 and 5. The two specimens had identical specifications

except that the through-thickness gap, g_z, was approximately doubled by using thicker sheet spacers. Specimens 7 and 8 were used to examine the behaviour of the proposed BRBs under the seismic signals FF and SI, respectively. These two specimens had the same properties as Specimen 4. Specimens 9 and 10 were tested with the lighter restrainer R2 in order to verify simultaneous effects of a more flexible restrainer and tighter gap sizes. Specimen 11 is a replica of Specimen 4 except that larger through-thickness gap was specified and the restrainer bolt spacing was doubled. Specimen 12 was similar to Specimen 11 except that the gap g_z was same as in Specimen 5 and additional loose bolts were placed between the pretensioned bolts to control strong-axis buckling of the core. Specimens 9 to 12 were also used to compare the frictional response of the PTFE–SS and UHMW–SS interface conditions.

Table 8.4: Test matrix.

Specimen	**Width, b_c** [a] (mm)	**Thickness, t_c** [a] (mm)	**Loading** [b]	**g_z** [c] (mm)	**g_y** [d] (mm)	**Debonding layer thick.** [e] (mm)	**Restrainer**	**S_x** [f] (mm)	**Interface condition** [h]
1	150.90	19.01	TSC	1.44	8.45	0.36	R1a	250	PTFE–SS
2	151.21	19.01		1.44	9.61	0.66			BS–UHMW
3	150.26	19.05		1.40	9.97	0.46			Graphite–Graphite
4	151.39	19.00		1.45	7.04	0.36			PTFE–SS
5	150.43	18.96		3.35	7.99	0.36			PTFE–SS
6	150.23	19.05		1.41	10.02	–	R1b		BS–BS
7	150.28	18.92	FF	1.83	7.27	0.36	R1a		PTFE–SS
8	151.23	18.94	SI	1.81	6.27	0.36			PTFE–SS
9	150.12	18.92	TSC	1.08	4.68	0.36	R2	300	PTFE–SS
10	149.35	18.93		1.37	7.49	0.66			UHMW–SS
11	151.49	18.90		2.67	6.71	0.36	R1b	500	PTFE–SS
12	149.20	18.94		3.05	5.27	0.66		500 [g]	UHMW–SS

[a] average of measured values at 5 equally spaced positions along the yielding segment

[b] TSC: Three-stage cyclic loading; FF: Far-field seismic loading; and SI: Subduction interface seismic loading.

[c] total through-thickness gap between core and restrainer (thickness of the debonding layer is not deducted).

[d] average measured total gap between core and side shim plates.

[e] thickness of debonding layer on each side of core.

[f] longitudinal distance between the restrainer pretensioned bolts (at ends of core YS for restrainer R2).

[h] core versus restrainer flat plate.

[g] loose bolts are added between each pretensioned bolt to prevent strong-axis buckling of core.

8.3 Experimental Results

8.3.1 General observations

Key response parameters measured in the tests are presented in Table 8.5. Values of maximum tensile and compressive core strains, $\epsilon^{+}_{c,\max}$ and $\epsilon^{-}_{c,\max}$, and the largest core strain range $\Delta\epsilon_c$ sustained by the specimens are reported, together with the total accumulated inelastic ductility (CID), the maximum values of the force adjustment factors in tension and compression, $\omega_{\max}$and $\beta_{\max}$, respectively, and failure description. For specimens subjected to the TSC loading history, values of the force adjustment factors after completing the second ϵ_c = ±2% (±2.0Δ_{bm}) cycle, $\omega_{2\%}$ and $\beta_{2\%}$, are also given as those would typically be used in design. After testing, the specimens were opened and inspected for failure location and buckling wavelengths measurements. The test on Specimen 1 confirmed the adequacy of the test setup. The yield resistance of the core material showed ~15% increase with respect to the coupon tests. This is attributed to the testing strain rate that was faster (250 times) than in the coupon test. Specimen 1 was also used to fine-tune the control scheme in the real-time seismic loading histories. Damage to the clip angles due to bolt bearing progressively developed during the tests and the clip angles had to be replaced three times in the test program. Hysteretic responses of the specimens are shown in Figure 8.9. For Specimens 7, 9, 11 and 12, the response during the last stage of loading prior to failure is shown in Figure 8.12.

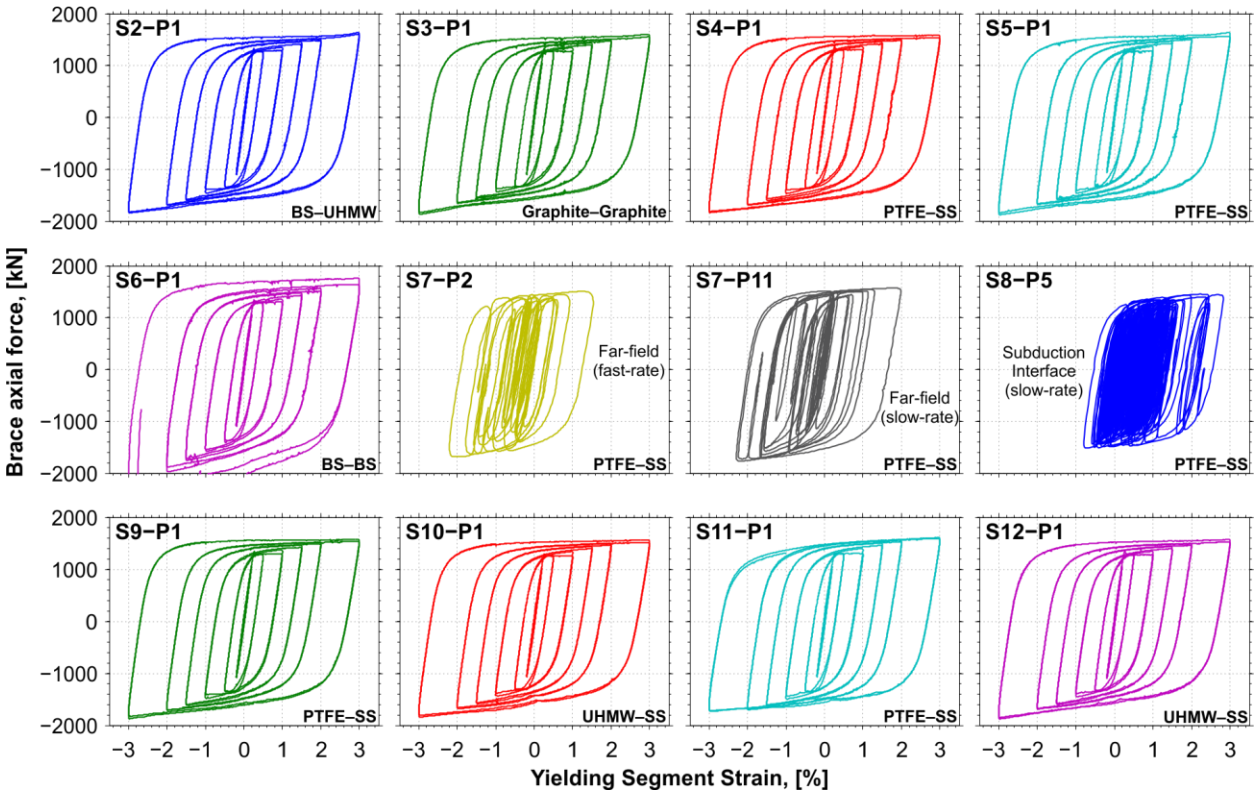

Figure 8.9: Hysteresis response of Specimens 2 to 12 (S*n*-P*m* indicates the response of Specimen *n* to the m^{th} stage of loading; the interfacial condition is specified at the lower right corner of the plots).

Specimens 2, 3, and 4 showed similar behaviour. They all sustained the first (P1) and second (P2) stages of the TSC loading and failed during the 3rd loading stage. Failure occurred in tension without any noticeable damage to the restrainer parts. In Table 8.5, the measured force adjustment factors for all three specimens are comparable. However, Specimen 4 with the PTFE-SS interface sustained the largest number of cycles and exhibited the highest CID value. In testing Specimen 2, the vertical edge of the top gusset plate came in contact with the column flange at the end of the +3% strain excursions and the flexural stiffness of the frame column was engaged. This explains the gradual increase seen in the hardening slope during those excursions (Figure 8.9 S2–P1). Specimen S5 was identical to Specimen S4 except that the through-thickness gap was intentionally increased from 1.45 to 3.35 mm. This change had no significant effect on peak resistance values but the fracture life was considerably reduced. For this specimen, bolt tension failure due to higher normal thrust was expected at the design stage but this response was not observed likely because of the actual bolt strength was higher that the anticipated tension demand (150 *vs* 113 kN).

Specimen 6 with BS-BS interfacial condition showed an acceptable performance up to the end of ϵ_c = ±2.0% cycles. However, a significantly large tensile and compressive resistances (ω = 1.61 and β = 1.47) was generated in the subsequent loading cycles. In the middle of the TSC-P2 loading, the compressive resistance became so high that the capacity of the actuators (2000 kN) was exhausted and the test had to be stopped. Post-test examination showed that the bolts connecting the core and the restrainer in the slotted holes at the core ends had imposed significant inelastic bearing deformations to the 0.76 mm thick filler steel sheet. As described, this filler sheet was placed between core and restrainer, in the non-yielding stiffened core segments (see Figure 8.10a and b), to minimize the bending demand illustrated in Figure 8.3b. During the test, due to high friction between the steel surfaces, the filler sheets obstructed the longitudinal movement of the core relative to the restrainer, which contributed to the large axial resistance exhibited by the specimen. When the test was halted, necking had formed in the core YS (Figure 8.10a) and the specimen was therefore near failure. It had then reached a CID of 323, which exceeds the minimum value of 200 specified in the AISC qualification requirement for BRB members (AISC, 2010). The maximum compressive strength adjustment factor of this specimen at ±2% strain cycles, $\beta_{2\%}$, was 1.25 which is less than the maximum value of 1.3 permitted by the AISC qualification standard. In the subsequent tests, this frictional problem at the interface of core and filler sheets was avoided by lubricating that interface. Ratio of buckling capacity to maximum compressive load, $P_e/P_{\max}$, was 1.9. Although this is slightly lower than the suggested value by Eq. (8.7), Specimen 6 sustained the maximum applied load without noticeable global buckling related deformations. Among the specimens tested with R1 restrainer, Specimen 6 had the smallest measured $P_e/P_{\max}$.

Specimen 7 was subjected to the far-field seismic displacement history. This specimen showed excellent performance and the complete history had to be repeated 13 times before fracture of the core YS occurred. During the first 10 passes of this loading history, displacements were applied at real-time rate. However, the target strain could not be fully reached because the hydraulic power supply of the actuators reached its flow capacity and the actual CID was reduced from 180 to ~120 during these 10 loading passes. In the last three passes, 11 to 13, the loading rate was reduced by a factor of 10 so that the target strain and CID could be fully reached. In total, the yielding segment of this specimen sustained more than 1600 CID before fracture. In the last pass of loading, the test was stopped about two second after a loud fracture sound was heard. This was sufficient for the brace to undergo a reverse-direction excursion. As a result, the fractured segments joined through

contact and the brace started to regain considerable strength in compression (see Figure 8.12 S7-P13). This may imply that even after a complete tensile fracture, in certain circumstances, BRB could still sustain some level of compressive load. Specimens 7 and 4 were identical and the similitudes between the CIDs (1657 *vs* 1228) and force adjustment factors measured in the two tests (ω = 1.42 *vs* 1.46 and β = 1.14 *vs* 1.15) suggest that the cyclic qualification protocols can predict well the BRB fracture life and maximum expected forces under actual seismic demand.

For Specimen 8, which was identical to Specimen S7, the same 1/10 reduced loading rate, was used to fully impose the strain history induced by the subduction interface earthquake. The specimen sustained without failure 9 passes of this long duration seismic history. It was then subjected to ϵ_c = 0 to +0.03 cycles and failure occurred in the 30th cycle. In total, this specimen accumulated more than 3700 inelastic deformation ductility. This is equivalent to the energy dissipated in more than 200 cycles of storey sway at amplitude of $\pm\Delta_{bm}$. Unlike the other tested specimens for which fracture was observed within the core YS, failure of Specimen 8 occurred at the transition area of the core (see Figure 8.21). In this test, the knife plate hinges at the brace ends performed well without any sign of damage or distortion under the numerous cycles of high axial loads and rotations.

Specimens 9 and 10 were tested using restrainer R2. This lighter restrainer was designed for two cycles of storey drift angle of 0.03 rad. and had lower flexural stiffness and wider longitudinal bolt spacing in the core YS. Relatively tighter through-thickness gap was specified for these specimens. Both specimens survived successfully the 1st and 2nd stages of the TSC loading and failed in the third stage. Specimens 9 could sustain two cycles more than Specimen 10, indicating that the PTFE-SS interface may lead to slightly longer fracture life compared to the UHMW–SS condition. In these two experiments, no visible distortion was observed in the restrainer and the strain gauge readings confirmed that the restrainers behaved elastically. Comparison between Specimens 4 and 9 shows that the restrainer size and number of bolts could be optimized by using properly sized through-thickness gap without compromising the performance. Again, while the measured $P_e/P_{\max}$ for Specimens 9 and 10 was only 1.8, no sign of global buckling initiation was detected.

Specimen 11 and 12 were tested with wider-than-required restrainer bolt spacing to promote undesirable failure modes. Specimen 11 with 500 mm bolt spacing sustained the first loading stage without failure. However, at the end of this stage, the side shim plates were significantly bent and

pushed out of the restrainer at two opposite end sides of the specimen, revealing buckling of the core about its strong axis (Figure 8.11a). Application of additional loading cycles resulted in fracture of one side shim and subsequent bolt fracture in double shear mode. These fractures occurred near the mid-length of the restrainer where the side shim had its weakest shear area due to the 10 mm hole used for monitoring the core width (see Figure 8.5b). When the specimen was pulled after the last −3% excursion, the core started to rupture. The loading direction was then reversed to compression and the tests was finally stopped at $\epsilon_c = -1.0\%$. During this test, the restrainer remained essentially elastic as the damage was concentrated in the side shim plates and the core YS (Figure 8.11b). Remarkably higher tensile post-yield stiffness was observed in Specimen 11 compared to the others (see Figure 8.11 S11-P1). The tensile post-yield stiffness is defined as the slope of the force-displacement curve in a tensile excursion between zero and maximum displacement. During the last +3% strain excursion of the TSC-P1 loading, the tensile post-yield stiffness of Specimen 11 was ~1.4 kN/mm, while Specimen 4 and 9 showed only 0.2 and 0.3 kN/mm post-yield stiffness values, respectively. When Specimen 11 was pulled after a large compressive excursion, plastic deformations probably started earlier due to the core distortion caused by excessive strong-axis buckling. The core was eventually straightened at the end of the tensile excursions and the core material could strain harden similarly to the other specimens. Because yielding started earlier and the total hardening remained the same, the post-yield slope of Specimen 11 was higher compared to the other specimens. Higher post-yield stiffness can be beneficial to the overall seismic response of BRBFs as it can mitigate progressive drifting and excessive residual displacements. This specimen also performed well in terms of the frictional forces as it is characterized by a β factor as low as 1.08. This is also attributed to the strong-axis buckling mode that is characterized by fewer, longer waves, resulting in fewer contact points and smaller normal thrust compared to the case of weak-axis buckling. Although Specimen 11 successfully passed the first stage of loading without any sign of global instability, its fracture life was relatively low because of the premature fracture in the side shim that was weakened by the monitoring hole. This emphasizes the need to properly verify the restrainer for this buckling mode of core member.

In Specimen 12, strong-axis buckling of the core was precluded by adding non-tightened bolts between the pretensioned bolts spaced 500 mm c/c. The non-tightened bolts were entirely loose and did not contribute to restrain the core weak-axis buckling. Specimen 12 sustained the TSC-P1

loading without core strong-axis buckling. In the last compressive cycle of the TSC-P2 loading with $\Delta\epsilon_c$ = 4%, two pretensioned restrainer bolts fractured in tension due to excessive normal thrust generated by the core weak-axis buckling response. Three additional pretensioned bolts fractured in the same manner when the load was reversed to compression after imposing +3% strain. This specimen eventually lost its compressive resistance due to the large amplitude core buckling and inelastic gap opening. When the specimen was unloaded, permanent bending deformation of the restrainer was still appreciable. The deformed shape of the buckled core after removal of the restrainer is shown in Figure 8.11c. The developed model for normal thrust analysis, predicted bolt force larger than 150 kN. Therefore bolt tension fracture for this specimen was expected.

Table 8.5: Summary of test results.

Speci-men	$\epsilon^{+}_{c,max}$ (%)	$\epsilon^{-}_{c,max}$ (%)	$\Delta\epsilon_c$ (%)	CID † (–)	ω_{max} (–)	β_{max} (–)	$\omega_{2\%}$ (–)	$\beta_{2\%}$ (–)	Description of failure
1	2.9	2.9	5.8	1623	1.46	1.15	1.35	1.11	specimen used to check the setup, no failure
2	3.0	3.0	6.0	672	1.48	1.16	1.37	1.11	failure in 8th cycle of TSC-P3
3				965	1.45	1.16	1.36	1.11	failure in 17th cycle of TSC-P3
4				1228	1.46	1.15	1.37	1.12	failure in 23rd cycle of TSC-P3
5				765	1.49	1.14	1.40	1.09	failure in 11th cycle of TSC-P3
6				323	1.61	1.47	1.43	1.25	test stopped at the middle of TSC-P2 due to actuators force capacity
7	1.5 [2.0] *	2.2 [2.3] *	2.3 [3.6] *	1657	1.42	1.14	–	–	tensile fracture in the 13rd pass
8	2.6 [3.2] **	1.65 [0.0] **	2.2 [3.3] **	3707	1.39	1.13	–	–	no failure after 9 passes; failure in subsequent $\epsilon_c = 0$ to 3% cyclic loading (30th cycle)
9	3.0	3.0	6.0	859	1.45	1.19	1.39	1.12	failure in 14th cycle of TSC-P3
10				795	1.43	1.17	1.40	1.13	failure in 12th cycle of TSC-P3
11				412	1.47	1.08	1.43	1.08	strong-axis buckling of the core producing bolt shear failure and fracture of side shims in the 2nd stage (non-standard loading – see Figure 8.12)
12				421	1.43	1.19	1.37	1.14	bolt tension failure resulting in weak-axis core buckling in the TSC-P2

† total cumulative inelastic ductility (sum of plastic deformation increments normalized by core yield displacement) up to failure

* numbers in brackets are from slow rate loading

** numbers in brackets are from low cycle fatigue testing performed after seismic loading test

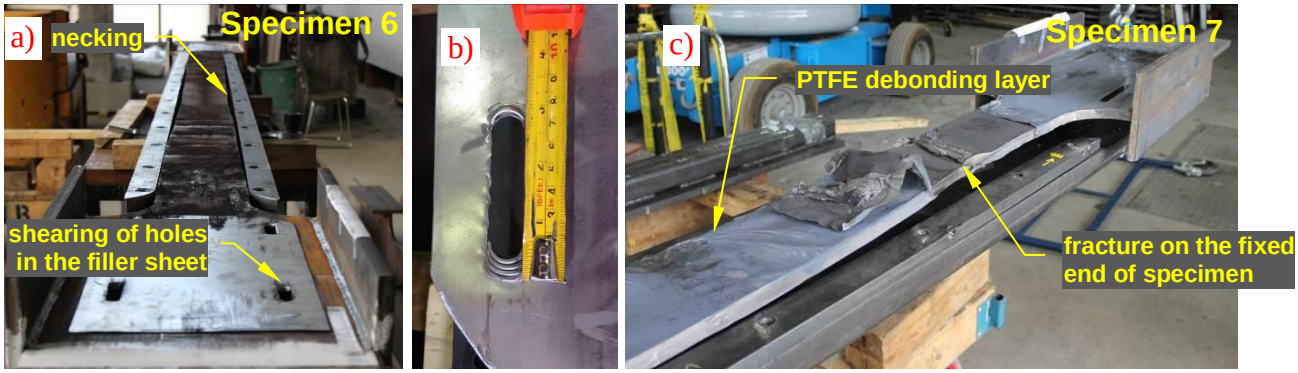

Figure 8.10: a) Deformed shape of Specimen 6 at the end of test; b) Shearing of standard hole in the end filler sheet of Specimen 6; and c) Fractured core of Specimen 7 under FF seismic loading.

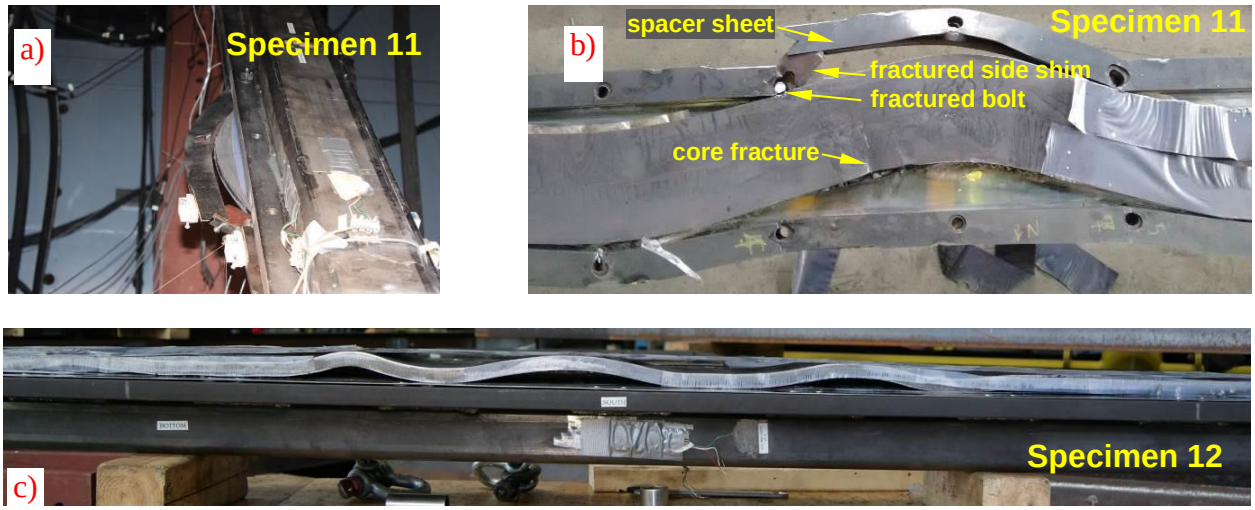

Figure 8.11: a) and b) Strong-axis buckling of the core in Specimen 11; c) Weak-axis buckling of the core in Specimen 12.

In all tests on BRB specimens with the PTFE and UHMW tapes, post-test investigation showed that both materials had good adhesive performance as they detached from the core surfaces only in few locations. In some cases, the tapes were broken locally due to excessive wear or tensile stresses. When subjected to the same conditions, the PTFE film performed slightly better than the UHMW one; however, given the 60% lower supply cost, the UHMW could represent a more effective choice. Graphite-based dry lubricant employed in Specimen 3 also showed a good debonding performance at a relatively lower supply cost compared to the PTFE–SS and UHMW–SS interfaces. Nevertheless, preparation of this debonding layer was longer due to the drying time. Results from Specimens 4, 5 and 9 can be compared to examine the effect of the through-thickness

gap size. Specimen 4 with an intermediate (1.45 mm) gap exhibited a longer fracture life than Specimen 5 with 3.35 mm gap. Specimen 9 with 1.08 mm gap performed similar to Specimen 4 although it had a 20% lighter restrainer and fewer pretensioned bolts. Specimen 11 and 12 had similar condition but their response was dominated by different buckling modes due to the spacing of the bolts. These specimens sustained similar cumulative inelastic ductility but the post-yield stiffness and frictional behaviour of Specimen 11 was superior. In Specimen 11, the restrainer also remained undamaged while it underwent considerable inelastic bending which made it unusable in case of Specimen 12. These observations suggest that promoting a controlled strong-axis core buckling may have potential benefits.

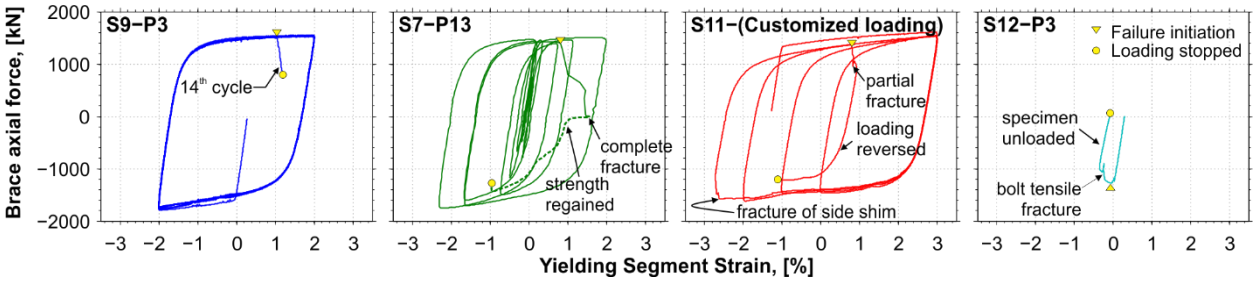

Figure 8.12: Hysteresis response of Specimen 9, 7, 11, and 12 during the last loading stage.

8.3.2 Specific measurements

8.3.2.1 Buckling wavelength

In order to estimate the buckling wavelengths, the deformed shape of the cores was measured after opening the restrainer. For most of specimens, i.e. 8 out of 12, the test was stopped when the core was being stretched in tension and the brace was subjected to a large tensile force. For such specimens no visible trace of buckling waves could be extracted as the core was already straightened by the tensile force. Loading of Specimens 7, and 10 to 12 was terminated while they were being compressed. However, Specimen 7 was already fractured in tension before the last compressive excursion at −28 mm (~1% strain). Specimen 9 also had already lost more than 50% of its tensile resistance due to partial core fracture before it was pushed to −20 mm ($\epsilon_c = -0.67\%$). Among the tested specimens, only the deformed shape of Specimens 11 and 12 could reveal a clear core buckling wave pattern and the measured buckling wave amplitude of these specimens are plotted in Figure 8.13a and b, respectively. Strong-axis buckling was the dominant mode for

Specimen 11. As shown in Figure 8.13a, due to bolt shearing and fracture of the side shim plate (see Figure 8.11b), buckling wave amplitudes are not uniform as bending deformations concentrated where the side shim plate fractured. Weak-axis buckling amplitude of Specimen 12 is also not uniform along YS core length due to bolt fracture and subsequent inelastic gap opening. At the region without bolt fracture and excessive gap opening, i.e. ends of yielding segment, buckling wavelength is ~225–250 mm. Before the final unloading, the YS of this specimen was pushed from +9 mm to −10 mm (+0.3% to −0.33% strain), which resulted in ~1000 kN brace axial compressive force.

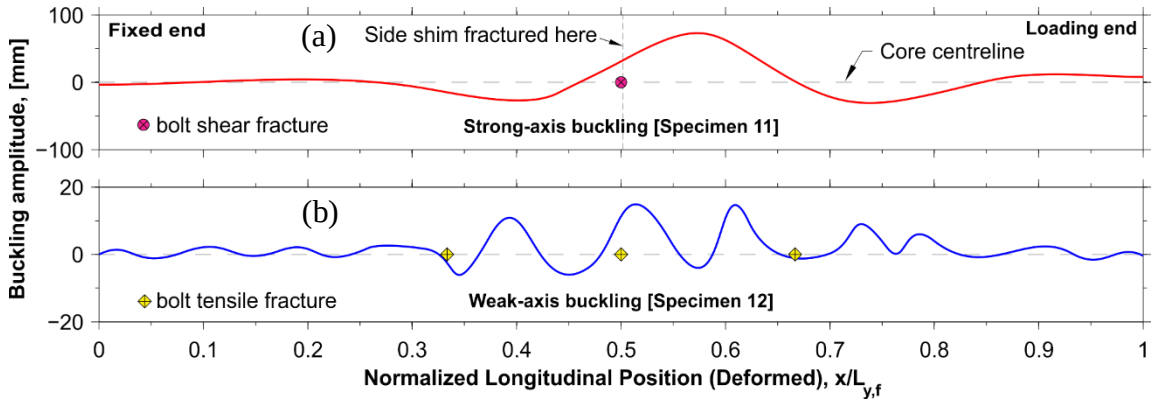

Figure 8.13: Buckling wave amplitude of: a) Specimen 11; b) Specimen 12. ($L_{y,f}$ is the final length of the yielding segment).

8.3.2.2 Response of the knife plate hinges

Moment-rotation response of the knife plates hinges (KPH) of Specimen 9 during the first stage of the TSC loading is shown in Figure 8.14a and b. The KPH bending moments were computed by extrapolation of the bending moments computed at the BRB instrumented sections. KPH rotations were computed from the LVDTs mounted on the top and bottom of the restrainer, as shown in Figure 8.2a. The bending moments are normalized w.r.t. the plastic moment of the knife plate section, $M_{p,k}$. In Figure 8.14a and b, the vertical dash lines indicate the maximum and minimum yield rotations of the KPH predicted by Eq. (8.4). Axial force-bending moment responses of the KPH joints are shown in Figure 8.14c and d. The axial force is normalized w.r.t the yield strength of the knife plate section. In figures c and d, the diamond shape area indicates the elastic response zone while the curved surfaces specify the ultimate capacity of the section under combined axial

and bending demand. Until the cycle at ±1.5% strain, the knife plate response remained essentially inside the elastic zone. Deviation from elastic response started during the −2% strain excursions and considerable yielding took place when the specimen was pushed to −3% strain. Yielding was limited to the compressive excursions and it was bounded by the KPH section capacity. The measured KPH rotations agree well with the predicted values by Eq. (8.1). For the ±3% strain cycle, Eq. (8.1) predicts total rotation of 2×0.0176 = 0.035 rad. and the measured total rotation of the bottom and top KPH joints were 0.034 and 0.037 rad., respectively. The bending moment demand is also well-predicted by Eq. (8.12). In Figure 8.14, the response path for the second cycle of ±3% strain cycle is highlighted by thick continuous lines. Filled and unfilled arrows indicate the tensile and compressive excursion loading paths, respectively. The KPH rotational stiffness shows load path dependency as it is more flexible in the tensile excursions than in the compressive ones. This is attributed to the varying distance between the end of the restrainer and the KPH, designated by d_r in Figure 8.14a and b. In the derivation of Eq. (8.4), the stiffened segment of the core was treated as a flexturally rigid object. However, a portion of the core plate inside the stiffened zone was left uncovered by the restrainer and could deform transversally due to its relatively larger width. This made the joint longer and more flexible. Tracing the history of the restrainer slip shows that d_r does not have a symmetrical pattern during tensile and compressive excursions. In the tensile excursions (from point b to c in Figure 8.14), as the brace was stretched, the restrainer moved away from the KPH which made the joint more flexible. Conversely, during the compressive excursions (from a to b) the restrainer moved towards the joint, which increased the joint stiffness. The loading path dependency of the KPH elastic stiffness is more pronounced in the upper joint, which was attributed to small rotation of the beam-to-column joint.

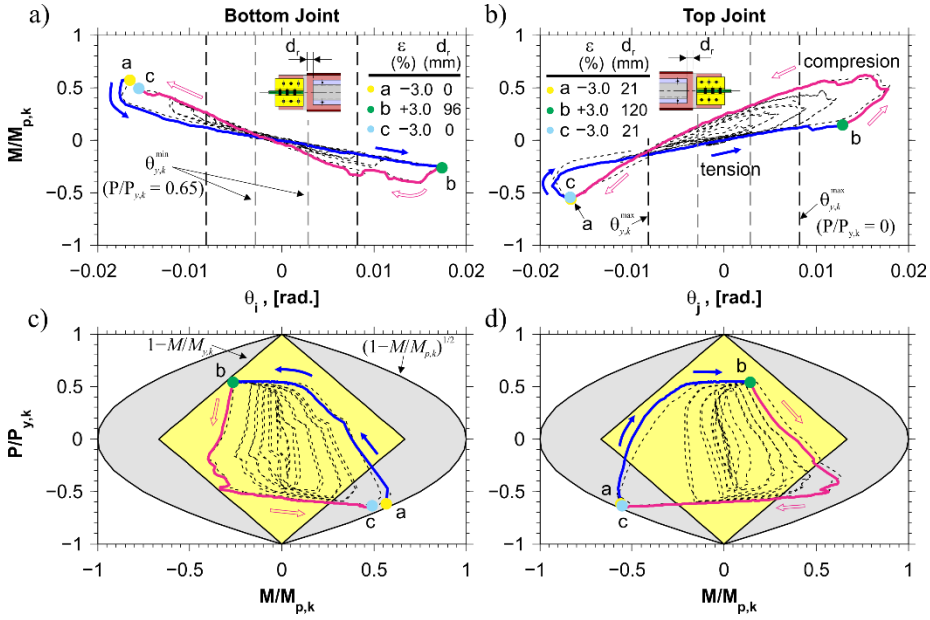

Figure 8.14: a) and b) Moment-rotation response; and c) and d) axial force versus bending moment demand on the bottom and top knife plate hinge, respectively. Tension to compression loading path is indicated by the unfilled arrows.

8.3.2.3 Slip length

To calculate the normal thrust on the restrainer, the engineer must estimate where the frictional forces accumulate along the restrainer length. This position is referred to as the Fixed Point by Midorikawa, *et al.* (2012) and is herein denoted by FP. The distance between the point of maximum slip (SP) (see Figure 8.15) and the FP is hereinafter referred to as the slip length (L_s). At the FP, there is no relative motion between core and restrainer and the FP works as a support that collects the longitudinal frictional forces. As a result, the axial force in the restrainer is maximum at the FP due to the accumulation of the frictional forces from SP to FP. By equilibrium, at any position along the YS, the total compressive axial resistance is shared between the core and the restrainer. At the FP, the core takes only a part of the total axial force and the remainder is resisted by the restrainer. Conversely, at the SP, the entire compressive force is carried by the core. As a result, the shortest and longest buckling wavelengths developed at SP and FP, respectively. For a given condition, the longer slip length means higher frictional forces, smaller buckling wavelengths, larger normal thrust on the restrainer, and more non-uniform distribution of the axial deformations along the YS. Typically, a locking mechanism is implemented along the YS in BRBs to prevent

free sliding of the restrainer (Wang *et al.*, 2012). This mechanism is referred to as "stopper" and is typically employed at the brace mid-length to maximize the low cycle fatigue life of BRBs (Wang, *et al.*, 2012; Wu, *et al.*, 2014), i.e. $L_s = 0.5L_y$ (Figure 8.15a). On the other hand, when the core and restrainer are not locked together by a stopper, the slip length can vary from $0.5L_y$ to $1.0L_y$.

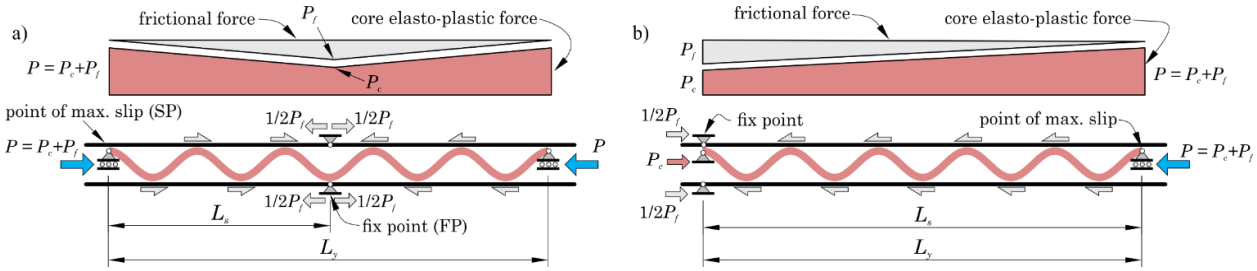

Figure 8.15: Frictional force in a BRB with: a) SLR = 0.5 (stopper at mid-length); and b) SLR = 1.0 (stopper at end).

For ease of fabrication, the BRBs tested in this study had no stopper at their mid-length. As a result, FP could be virtually anywhere along the core and its position could vary during the tests. Histories of the YS deformation and the restrainer sliding were employed to estimate the position of the FP and compute the slip length ratio (SLR), i.e. L_s/L_y. In this calculation, it was assumed that the core axial deformation varied linearly from the loading end (upper end) of the YS and became zero at the fixed end (lower end). In addition, rigid body motion was assumed for the restrainer and its position could be obtained from the measured sliding at the fixed end of the brace. Then, at any given time, the FP position was obtained as the intersection of the restrainer position and the YS axial deformation. The FP would therefore be at the mid-length of the YS when the restrainer sliding is half of the deformation imposed to the YS. In this case, the restrainer movement with respect to the fixed and loading end gusset plates are equal but with opposite signs. Histories of the restrainer movement at the fixed and loading ends of Specimen 9 during the TSC-P1 loading are plotted in Figure 8.16a. The restrainer movements show a reflective symmetrical pattern that implies a SLR close to 0.5. However, tracing the restrainer slip in the compressive excursions indicate that SLR was not constant. At the beginning of excursion, most of the imposed shortening was accommodated by the restrainer slip at the fixed end, i.e. SLR ≈ 1.0. Eventually, restrainer become stuck at lower end when its movement approaches 60 mm. From this point on, the applied shortening was accommodated by sliding at the loading end. The computed SLR of Specimens 2–

5 and 9–10 during the TSC-P1 loading are shown in Figure 8.16b. Note that these values are calculated based on the restrainer position at end of excursion. For Specimens 1, and 3 to 6, when $\epsilon_c \leq \pm 1.5\%$, the FP is generally at the loading end of the YS and, by definition, SLR = 1.0. It is estimated that friction between the restrainer and the core at the stiffened segment was more severe at the loading end of these specimens. The higher friction probably locked the restrainer and core together at that brace end and the total deformation applied to the core was accommodated by sliding of the restrainer at the fixed end of the brace. When the FP is so located at the YS end, the frictional forces accumulate in a non-symmetrical one-way fashion as illustrated in Figure 8.15b. This sliding behaviour however vanished as the loading amplitude became larger and the FP moved towards the mid-length of the YS. After the test on Specimen 6, the end filler sheets in Specimen 9 and 10 were sprayed with Molybdenum disulfide, i.e. a dry lubricant with a coefficient of friction as low as 0.05. This reduced the friction at the end of the restrainer and resulted in a more symmetrical sliding and the smaller SLR values shown in Figure 8.16b. Analysis of the TSC-P3, i.e. constant-amplitude cycles of $\epsilon_c = \pm 2\%$, showed that the asymmetric sliding behaviour was prevailing in this phase of the test and the FP was near the YS end located at the loading end of the brace. This may have contributed to reducing the low cycle fatigue life of the specimens. Implementing a stopper at mid-length of the core could have led to higher performance.

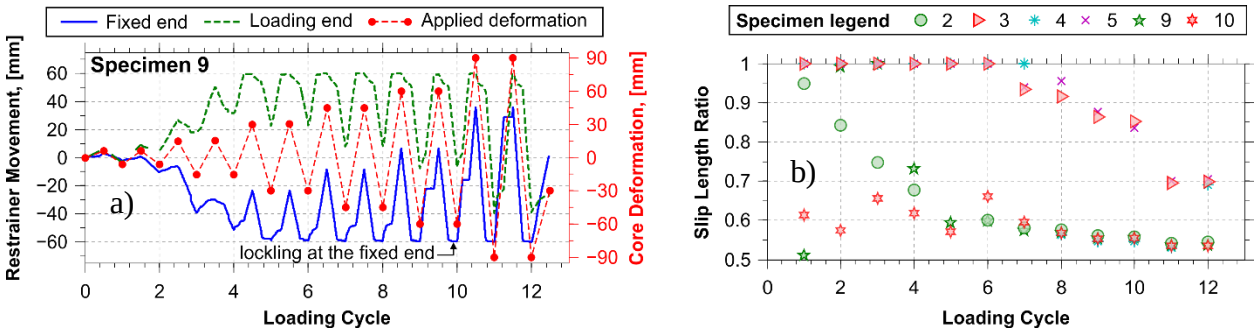

Figure 8.16: a) History of the restrainer movement in Specimen 9; b) Slip length ratios of selected specimens. Note: data in a) and b) are from the TSC-P1 loading.

If friction causes the axial compression force in the core to vary longitudinally, a non-uniform axial strain is also expected as both axial forces and strains are correlated. The core region near the FP would then be subjected to lower strains because the core axial load is minimum at that location. When the loading direction is reversed to tension, the core axial force would revert to uniform as

the friction disappears. Thus, to achieve uniform tension force in the core, the portion of the core near the FP would be subjected to higher tensile strains. Hence, a non-symmetrical local strain history may develop even though the applied displacement loading is symmetrical. The effect of friction on the strain distribution may be shown by continuously tracing changes in the core's width or thickness as the loading protocol is applied. According to solid mechanics, variations of the section width or thickness can be used to assess local axial strains. Upon plastic deformations, volume change for metals is assumed negligible and the ratio between transverse and axial strains can be taken as −0.5. The history of the transverse core strain from core width measurements at mid-length of Specimen 12, during the TSC-P1 loading, is plotted in Figure 8.17. In the figure, the axial strain history computed with this technique is also shown together with the average axial strain obtained by dividing the applied total core deformation by the YS core length (applied strain). Except for the 3rd cycle, the measured transverse strains exhibit a nearly symmetrical pattern and the computed axial strains compare well with the average applied axial strains. However, the pattern becomes non-symmetrical in the ϵ_c = ±3% cycles and the baseline of the computed axial strains is shifted towards positive values, indicating higher local tensile strains near mid-length of the core. For this specimen, the computed axial tensile strains are equal to 2.7 and 3.3% in the last two cycles when the peak applied strain is ϵ_c = +3%. In the previous two cycles both the applied and computed axial strains are equal to, or close to 2%, which indicates that longitudinal friction became significant only when applied deformation exceeded 2% average core strain.

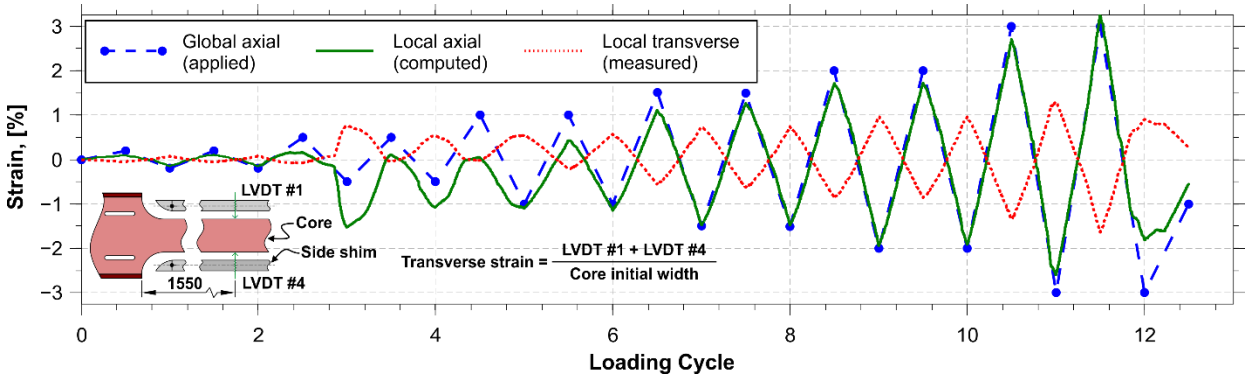

Figure 8.17: Strain at the mid-length of Specimen 12 during the TSC-P1 loading.

8.3.2.4 Bolt forces and estimation of normal thrust

The history of the change in bolt tension for Specimen 9 during the TSC-P1 loading is shown in Figure 8.18. Nearly all bolts eventually lost some tension in the large ±3% strain cycles but this loss was insignificant in most cases. Only bolts nos. 7 and 10, near the loading end, experienced progressive reduction in tension in the first portion of the loading protocol. For bolt no. 10, it is noted that bolt tension slightly increase when applying compressive loads in the two ±2% strain cycles. In the subsequent compressive excursions at −3% strain, the increase in bolt tension becomes more pronounced and the peak tension even exceeded the bolt preload in the last cycle. A similar trend, although less severe, is observed for neighboring bolts nos. 7 and 6. At the end of the last compression to −3% strain (segment a–b on the deformation path in Figure 8.18), the tension in bolts nos. 10, 7 and 6 increased by ~9.6, 3.4, 2.5 kN, respectively. This bolt tension increase can be seen in Figure 8.18b. This behaviour suggests that weak-axis local buckling of the core concentrated at the upper end of the YS and this effect became significant only when applying average core axial strains of 2%, as expected. As discussed in Section 8.3.2.3, halfway through the ±3% excursion, the FP (fixed point) switched from the upper end to the lower end. Accordingly, the upper end of core had to carry the entire applied load resulting in shorter buckling wavelengths and larger normal thrust in comparison with the lower end.

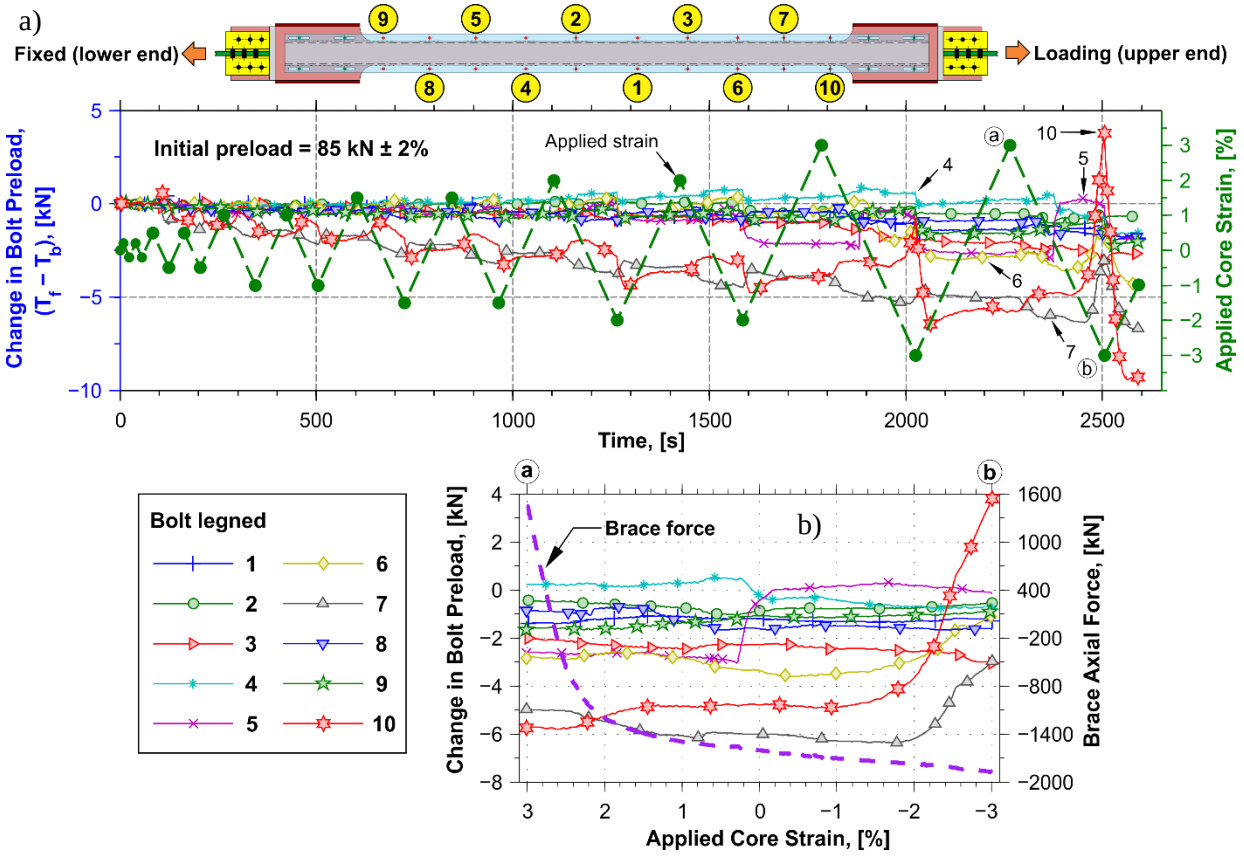

Figure 8.18: Specimen 9 under the TSC-P1 loading: a) Full history of the change in bolt tension (T_f = current tension; T_b = pretension); b) Change in the bolt preload during the last compressive excursion (from +90 to −90 mm).

Due to the pretension in the bolts, it was not feasible to obtain the normal force on the restrainer directly from the bolt tension readings. To estimate the normal force, a three-dimensional detailed finite element (FE) model of the bolted joint was created in ABAQUS (SIMULIA Inc.). As shown in Figure 8.19, assuming symmetry about longitudinal and transversal axes, only one-quarter of the bolted joint, i.e. half-restrainer segment between two consecutive transversal bolt lines, was included in the model. Symmetry in loading and boundary conditions was also assumed to exist with respect to the transversal bolt lines, i.e. zero rotation at the transversal bolt line. Bolt head and shank were included in the model and the bolt pretension was imposed using thermal initial conditions. The normal force was applied as a uniformly distributed edge pressure at the free edge of the model, i.e. one buckling wave per each segment. For each longitudinal bolt spacing, the relation between externally applied normal load and bolt tension was obtained from elastic analysis.

The deformed shape of the FE model and the normal load-bolt tension diagram for bolt nos. 9 and 10 are shown in Figure 8.19. Up until a normal load of ~12 kN, virtually no change in bolt tension is obtained. Using these FE results, it is estimated that the normal load at the locations of bolts nos. 1, 2, and 5 to 10 were respectively equal to ~17, 25, 37, 36, 39, 20, 25, and 51 kN due to core buckling at the end of the last −3% strain excursion (point b in Figure 8.18). Normal forces on bolts nos. 3 and 4 could not be estimated because tensions reading showed negative increments during the last compressive excursion. Excluding bolts nos. 3 and 4 and assuming symmetry in the bolt tension with respect to the longitudinal brace axis, the total normal load at the end of the last −3% strain excursion is estimated as ~500 kN.

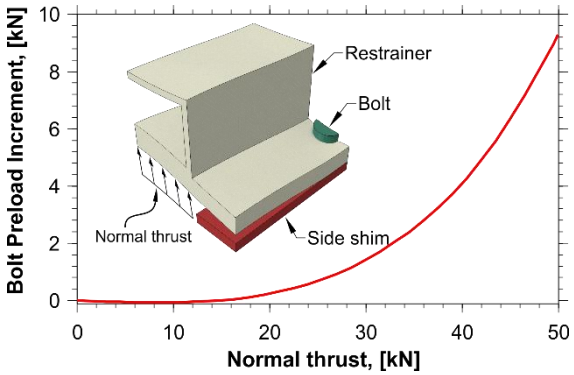

Figure 8.19: Joint diagram obtained from finite element simulation.

8.3.2.5 Final core size

After testing and dismantling the restrainer, the final width and thickness of the core plate along the YS were measured. Changes in core width and thickness with respect to initial values, are plotted in Figure 8.20a and b, respectively. In these plots, large negative values indicate the position(s) where necking took place. The final section sizes may be used to validate the accuracy of finite element models in capturing plastic strain distribution along the YS. For Specimen 6, with BS–BS interface condition exhibiting a high coefficient of friction, the YS expanded at the ends (~5%) while the core section dimensions reduced by ~10% near mid-length. The section reduction indicates that localized longitudinal strains reached a value as large as 20% when the maximum applied elongation was 3% of the YS length. This highly non-uniform and localized strain distribution can increase the likelihood of low cycle fatigue failure and may promote premature fracture as it was observed in previous studies (Tremblay, *et al.*, 2006; Chen, *et al.*, 2016). This

shows clear benefits of reducing friction by adopting smooth condition at the core-restrainer interface. Implementing a stopper mechanism at the middle of core can also contribute to more uniform axial deformations along the core YS and less localized response.

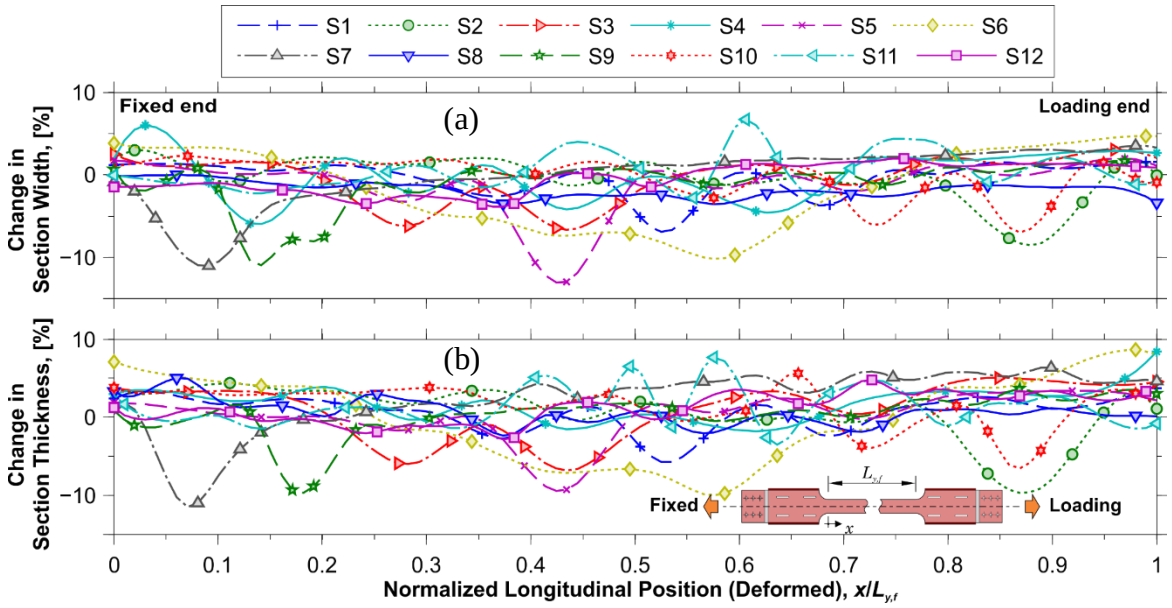

Figure 8.20: Change in the core cross-section size along the yielding segment: a) width; and b) thickness. Note: positive and negative values indicate section budging and shrinkage, respectively.

Locations of core fracture and close-up views of the fractured zone are shown in Figure 8.21 for selected specimens. Except for Specimen 7, all tests were stopped before complete fracture of the core. Fracture typically occurred within the core YS, generally closer to the fixed end of the brace. For Specimen 8 subjected to the Subduction earthquake type of seismic loading, fracture initiated at the boundary of the transition zone at the end of the core YS. In that case, the fracture occurred after apparent necking which suggests a ductile failure. For Specimens 7, 10 and 11, the fractured zone was closed as the specimens were pushed to compression after initiation of fracture.

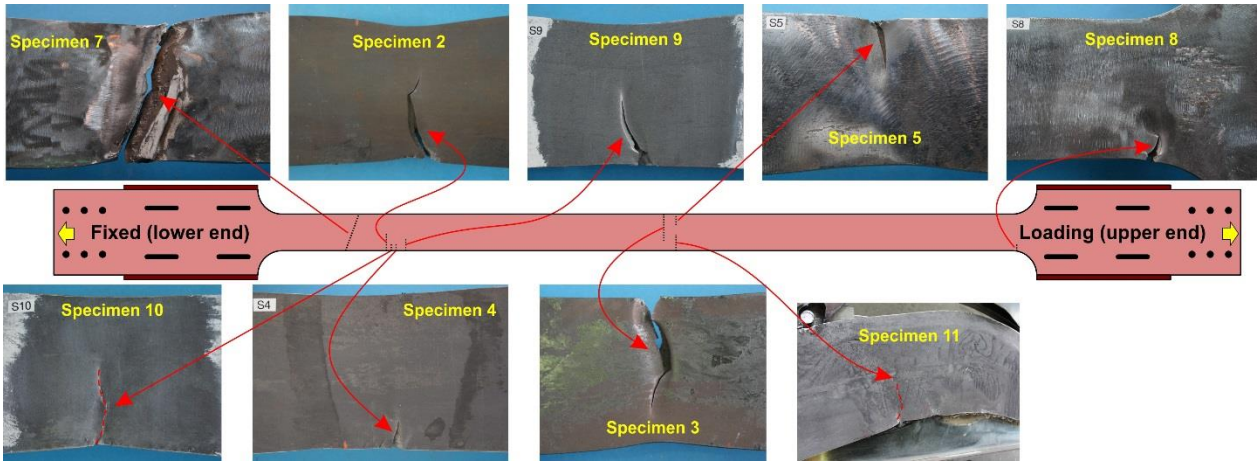

Figure 8.21: Locations of fracture and close-up views of the fractured zone for selected specimens.

8.4 Conclusions

Twelve full-scale buckling-restrained braces with bolted steel restraining systems were tested and the results were presented. Effects of parameters such as core-restrainer interfacial condition, gap size, restrainer stiffness and loading condition were evaluated. In general, the tested BRBs exhibited stable inelastic cyclic response and high cumulative ductility capacities varying from 320 to 3700 depending on the test parameters. The tested BRB system showed excellent performance under repeated seismic loading conditions and demonstrated a significant post-earthquake ductility capacity. The tests showed that the PTFE–stainless steel interface condition was very effective in reducing longitudinal frictional forces and achieving long fracture life. However, the UHMW–stainless steel interface appeared to be an effective alternative as it also provided efficient debonding behaviour at a relatively lower cost. The graphite-based dry lubricant is also deemed a reasonable choice for debonding material given the supply cost and ease of application. The specimen with steel–steel interfacial condition showed acceptable performance up until two times the storey design displacement. For this specimen, improper detailing at the restrainer ends caused additional frictional resistance, which led to excessive compressive strength under larger displacement cycles. This problem could be avoided by lubricating the filler sheet or by employing long-slotted holes, as demonstrated in tests on other specimens. The knife plate hinges implemented at the brace-to-gusset connection successfully limited the flexural demands on the BRB members. No fracture or excessive distortion was noticed in the knife plate hinges, even under

the long duration loading history from subduction zone's megathrust earthquake, which suggests that the proposed design criteria for this hinge connection detail are adequate. Various types of failure mechanisms were observed. Most tested specimen failed due to exhaustion of low cycle fatigue life in core member. This phenomenon was more pronounced when larger gap or rough interface condition was provided. To increase the fatigue life, providing smooth condition at the core-restrainer interface is deemed necessary. However, for regions with low seismic demand, e.g. east of Canada and east north of U.S., steel–steel interfacial condition can be an efficient choice. Adopting a stopper mechanism at the mid-length of core should be considered if longer fatigue life is sough. The results showed that proper through-thickness gap size that allows unconstrained core expansion while minimizing core buckling amplitude is necessary to develop an optimal fatigue life response. Failure of the restrainer due to excessive core buckling about both strong and weak core axes have been observed when insufficient restraining was provided. When strong-axis core buckling was dominant, higher post-yielding axial stiffness in tension was observed, which could be beneficial for the overall response of BRB frames. However, the possibility of reduced low cycle fatigue life due to this buckling mode should be taken into account. More research is recommended to validate the possible benefits of promoting partially constrained strong-axis buckling. More research is also needed for a rigorous measurement of normal forces on restraining systems, and for distribution of longitudinal deformation along the BRB core, buckling wavelengths and waveforms. Detailed characterization of frictional behaviour of the introduced interface conditions may be needed for precise estimation of system behaviour.

Acknowledgements

Funding for this project was provided by the Natural Sciences and Engineering Research Council (NSERC) of Canada. The scholarship awarded to the first author by the Structural Steel Education Foundation of the Canadian Institute of Steel Construction is acknowledged. The core plate material was supplied by Canam-Bridges in Quebec City. Goodco Z-Tech Inc. in Laval, QC, donated the stainless steel sheets, and the specimens were graciously fabricated by Lainco Inc. from Terrebonne, QC. The authors are also grateful to the staff of the Structural Engineering Laboratory of Polytechnique Montréal and the intern students for their assistance.

References

AISC. (2010). ANSI/AISC 341-10, Seismic Provisions for Structural Steel Buildings. Chicago, IL: American Institute of Steel Construction, Inc.

Black, C., Makris, N., & Aiken, I. (2004). Component Testing, Seismic Evaluation and Characterization of Buckling-Restrained Braces. *Journal of Structural Engineering, 130*(6), 880-894.

Bondonet, G., & Filiatrault, A. (1997). Frictional Response of PTFE Sliding Bearings at High Frequencies. *Journal of Bridge Engineering, 2*(4), 139-148.

Chen, Q., Wang, C.-L., Meng, S., & Zeng, B. (2016). Effect of the unbonding materials on the mechanic behavior of all-steel buckling-restrained braces. *Engineering Structures, 111*, 478-493.

CSA. (2014). CSA S16-14, Design of Steel Structures. Mississauga, Ontario, Canada: Canadian Standards Association.

Dehghani, M., & Tremblay, R. (2016a). An Analytical Model for Estimating Restrainer Design Forces in Bolted Buckling-Restrained Braces. *Journal of Constructional Steel Research* (submitted).

Dehghani, M., Tremblay, R., & Leclerc, M. (2016d). Fatigue failure of 350WT steel under large-strain seismic loadings at room and subfreezing temperatures. *Construction and Building Materials* (submitted).

Della Corte, G., D'Aniello, M., & Landolfo, R. (2015). Field Testing of All-Steel Buckling-Restrained Braces Applied to a Damaged Reinforced Concrete Building. *Journal of Structural Engineering, 141*(1), 1-11.

Dolce, M., Cardone, D., & Croatto, F. (2005). Frictional Behavior of Steel-PTFE Interfaces for Seismic Isolation. *Bulletin of Earthquake Engineering, 3*(1), 75-99.

Erochko, J., Christopoulos, C., Tremblay, R., & Choi, H. (2011). Residual Drift Response of SMRFs and BRB Frames in Steel Buildings Designed according to ASCE 7-05. *Journal of Structural Engineering, 137*(5), 589-599.

Eryaşar, M. E., & Topkaya, C. (2010). An experimental study on steel-encased buckling-restrained brace hysteretic dampers. *Earthquake Engineering & Structural Dynamics, 39*(5), 561-581.

Ferguson, W., Nashid, H., Clifton, G., Kral, M., Lopert, S., & MacRae, G. (2013). *The Performance and Remnant Life of Structural Steel in an Earthquake Damaged Building.* Paper presented at the Steel Innovations Conference, Christchurch, New Zealand.

Genna, F., & Gelfi, P. (2012a). Analysis of the Lateral Thrust in Bolted Steel Buckling-Restrained Braces. I: Experimental and Numerical Results. *Journal of Structural Engineering, 138*(10), 1231-1243.

Genna, F., & Gelfi, P. (2012b). Analysis of the Lateral Thrust in Bolted Steel Buckling-Restrained Braces. II: Engineering Analytical Estimates. *Journal of Structural Engineering, 138*(10), 1244-1254.

Imai, K., Wakiyama, K., Tada, M., Kuwahara, S., & Yoneyama, T. (1991). A study on the stiffening effect of the Double Tube : Part 1 The procedure of the longitudinal loading test. *Summaries of technical papers of Annual Meeting Architectural Institute of Japan. Structures II, 1991*, 1281-1282 (in Japanese).

Lin, P.-C., Tsai, K.-C., Wu, A.-C., Chuang, M.-C., Li, C.-H., & Wang, K.-J. (2015). Seismic design and experiment of single and coupled corner gusset connections in a full-scale two-story buckling-restrained braced frame. *Earthquake Engineering & Structural Dynamics, 44*(13),

2177-2198.

López, W. A., Gwie, D. S., Saunders, C. M., & Lauck, T. W. (2002). *Lessons Learned From Large-Scale Tests of Unbonded Braced Frame Subassemblages.* Paper presented at the 71st annual convention of SEAOC, Sacramento, CA.

Midorikawa, M., Wakayama, T., Iizuka, R., Asari, T., Murai, M., & Iwata, M. (2012). Experimental Study on Buckling-Restrained Braces using Steel Mortar Planks-Evaluation of the buckling mode number, compression-to-tension strength ratio and friction force. *Journal of Structural and Construction Engineering (Transactions of AIJ), 77*(681), 1763-1771 (in Japanese).

Razavi Tabatabaei, S. A., Mirghaderi, S. R., & Hosseini, A. (2014). Experimental and numerical developing of reduced length buckling-restrained braces. *Engineering Structures, 77*, 143-160.

Samyn, P., De Baets, P., Schoukens, G., & Van Peteghem, A. P. (2006). Large-scale tests on friction and wear of engineering polymers for material selection in highly loaded sliding systems. *Materials & Design, 27*(7), 535-555.

SIMULIA Inc. (2012). *ABAQUS Analysis User's Manual Version 6.12-1*.

Takeuchi, T., Ozaki, H., Matsui, R., & Sutcu, F. (2014). Out-of-plane stability of buckling-restrained braces including moment transfer capacity. *Earthquake Engineering & Structural Dynamics, 43*(6), 851-869.

Thorp, J. M. (1986). Tribological Properties of Selected Polymeric Matrix Composites against Steel Surface. In K. Friedrich (Ed.), *Friction and wear of polymer composites* (2 ed., Vol. 1, pp. 89-134): Elsevier.

Tremblay, R., Bolduc, P., Neville, R., & DeVall, R. (2006). Seismic testing and performance of buckling-restrained bracing systems. *Canadian Journal of Civil Engineering, 33*(2), 183-198.

Tremblay, R., Degrange, G., & Blouin, J. (1999). *Seismic Rehabilitation of a Four-Storey Building with a Stiffened Bracing System.* Paper presented at the 8th Canadian Conference on Earthquake Engineering, Vancouver, BC, Canada.

Usami, T., Ge, H., & Kasai, A. (2008). *Overall buckling prevention condition of buckling restrained Braces as a structural control damper.* Paper presented at the 14th World Conference on Earthquake Engineering, Beijing, China.

Wang, C.-L., Usami, T., & Funayama, J. (2012). Evaluating the influence of stoppers on the low-cycle fatigue properties of high-performance buckling-restrained braces. *Engineering Structures, 41*(2012), 167-176.

Watanabe, A., Hitomi, Y., Saeki, E., Wada, A., & Fujimoto, M. (1988). *Properties of brace encased in buckling-restraining concrete and steel tube.* Paper presented at the 9th World Conference on Earthquake Engineering, Tokyo-Kyoto, Japan.

Wu, A.-C., Lin, P.-C., & Tsai, K.-C. (2014). High-mode buckling responses of buckling-restrained brace core plates. *Earthquake Engineering & Structural Dynamics, 43*(3), 375-393.

Zhao, J., Lin, F., & Wang, Z. (2016). Effect of non-moment braced frame seismic deformations on buckling-restrained brace end connection behavior: Theoretical analysis and subassemblage tests. *Earthquake Engineering & Structural Dynamics, 45*(3), 359-381.

CHAPTER 9 GENERAL DISCUSSION

9.1 Introduction

In course of the present study, several important issues related to seismic design and performance evaluation of steel buckling-restrained brace (BRB) system were investigated and the essential data for proper design of BRB restraining system were acquired, processed, and implemented. This study was conducted in several phases that all together served the main research objective. In this chapter, the importance and results of each research phase will be discussed.

9.2 Ground motion selection and scaling

Time history analysis has become a standard analytical tool for performance evaluation of structures under effects of ground motion shaking. Selection, and scaling of ground motion records are the two essential steps in order to conduct any time history analysis and they proved to have overwhelming influence on the analysis outcomes. Currently, several techniques are being utilized by researchers and practicing engineers and one of them have been already included in the U.S. national building code, i.e. ASCE 7 (ASCE, 2010). The conventional methods have shown to introduce large uncertainty and bias in the estimated seismic demand, especially when structure responds inelastically. Most conventional selection techniques do not consider deaggregation of seismic hazard and mainly rely on personal judgment and experience of the user. In this study, a record selection method is introduced that considers the local site hazard deaggregation. A simple algorithm to obtain a general perspective of the most expected combinations of magnitude and distance is presented. With the advancement in ground motion instrumentation and record collections, the available data has become extremely large. This has warranted a refinement method that could effectively find the most representative records out of a large batch, for a given site condition and hazard. A refinement technique based on statistical trend of ground motion Intensity Measures (**IM**s) in terms of amplitude, frequency content, and duration is suggested in this study. At first, this method finds the most representative **IM**s, referred to as “principal **IM**s”, using intercorrelation analysis. The average deviation of each record from central tendency of the principal **IM**s is then computed. Records with the least average deviation from the expected value of the principal **IM**s will be retained and the rest are discarded. The presented method has shown

to be effective in selecting records that their spectral intensity is compatible with the predicted values by major GMPEs[4]. For a given combination of target spectrum, deaggregation data, number of records, and a record database, the proposed method gives a unique set of records without any need for iteration. The presented approach is utilized to compile sets of records that could be employed for conducting advanced seismic analysis in major earthquake-vulnerable urban areas in east and west of Canada. This selection method could be easily extended to include GMPEs for predicting the trend of the **IM**s for a given event. This may facilitate the process and improve the robustness of the outcomes as the GMPEs are more inclusive.

Current record scaling methods are overly conservative as they match the intensity of record to the Uniform Hazard Spectrum (UHS), at a single period or in a range of periods. In addition, conventional scaling methods typically ignore the frequency content of record. This may result in unintended consequences when a naturally high-frequency record is scaled in the long period range of the spectrum or vice versa. Frequency content of record is important factor that has to be accounted in scaling. One powerful indicator of the frequency content intensity is the *Mean Period* (T_m) of ground acceleration as introduced by Rathje *et al.* (1998). Effect of frequency content can be shown by conducting elastic and inelastic analysis on SDOFs[5] having wide range of periods. In Figure 9.1, "ratio of inelastic to elastic peak displacement" is plotted against "ratio SDOF period to mean period of ground motion". This plot represents data from a large batch of records (266) having wide range of frequency content, i.e. 0.1 s $\leq T_m \leq$ 1.25 s. These constant strength SDOFs had period range of 0.5 to 5.0 seconds and they were designed for response modification factor of 4.8. According to the equal displacement theory, peak inelastic displacement of flexible buildings, e.g. $T \geq 0.5$ s, is equal to the peak displacement obtained from elastic analysis, i.e. $Sd_i/Sd_e = 1.0$. Interesting trend can be seen in plot of Figure 9.1. This plot indicates that when $T \geq T_m$, i.e. building frequency is smaller than the record frequency content, the average inelastic response could be accurately predicted by an elastic analysis. On the other hand, when building frequency is higher than the ground motion, the average inelastic displacement is much more than predicted value by the elastic analysis.

---

[4] Ground Motion Prediction Equations

[5] Single-Degree-of-Freedom Systems

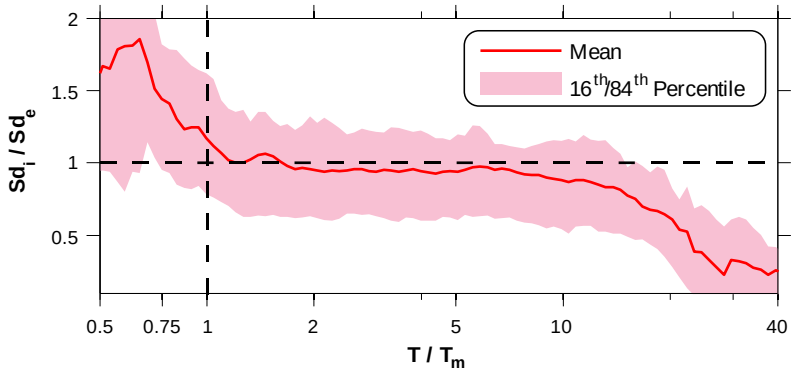

Figure 9.1: Ratio of inelastic to elastic peak displacement *vs* ratio of SDOF period to mean period of ground motion.

As shown by an example in Chapter 4, neglecting frequency content may artificially increase the uncertainty of the predicted response. Level of uncertainty, which is characterized by standard deviation, is of great importance when upper bound of response, or worse case scenarios, are being sought. Development of loading histories for seismic qualification of structural or non-structural systems is a classic example where degree of uncertainly has a direct consequence. As a common practice, upper percentile of response is utilized in loading histories. When large uncertainty exists in the computed building response, using the upper percentiles may give an unnecessary intensive loading history. Excessively intensive loading history may lead to costly or even unfeasible designs as the deformation capacity and failure modes of components are not independent of the imposed loading history.

The current study showed that a most cited scaling method in practice, which is implemented in ASCE 7, does not guarantee a unique set of scaling factors. As the ASCE 7 requirement is open to interpretation, quite different sets of scaling factors can be obtained. When utilized in nonlinear time history analysis, these sets predicted markedly different demand statistics both in terms of median and standard deviation. Such a scatter in the statistical distribution of demand can complicate the seismic assessment and decision making process. To this end, in this study an alternative scaling method is presented with emphasis on robustness of the predicted demand. An algorithmic method for computing scale factor is developed and elaborated. This algorithm seeks a narrow period range in which the shape of record spectra is similar to the target spectrum. Record spectrum is then scaled linearly to the target spectrum in this narrow band. It is shown that this technique is effective in capturing frequency content of records and considering them in the scaling

process. The results show relatively smaller scatter in the spectral intensity of the selected records. Importantly, this method is period-independent which means that one set of scaled records can be used for analysis of structures located on the same site but having different dynamic characteristics. This would be more intuitive compared to the current period-based methods that may give different sets of scale factors for buildings with different period but all located on the same site. In the 3D dynamic analysis of buildings having different orthogonal vibration frequencies, conventional methods can be even confusing as different scale factors for the components of the same record may be required.

Ideally, when time history analysis is conducted with scaled records no correlation should be found between analysis results and scaling factors. In other the words, estimated demand should be independent from the scale factors used in the analysis. According to Luco *et al.* (2007), bias in the estimated response can be computed as the linear coefficient of correlation between a demand parameter and the scaling factors used to adjust the ground motion record intensity. Conventional methods are known to introduce statistical bias to the peak displacement. In Figure 9.2a and b, peak ductility of an inelastic SDOF subjected to 266 ground motion records that were scaled by MFP[6] and LMA[7] methods are compared. MFP is a conventional linear scaling method that anchors the response spectrum of record to the target spectrum at the fundamental period of building and LMA is the method that introduced in this study. As seen in Figure 9.2b no bias is introduced by the LMA method while the peak response under MFP-scaled sets are correlated with scale factors.

NTHA of multi-storey BRBFs showed that the proposed scaling method results in a predicted demand with reasonable variability. Another challenge faced by engineers is the number of records that should be implemented in the analysis. Current techniques tend to increase the uncertainty when more records are included in the analysis. The proposed method was shown to be virtually insensitive to the number of selected records in comparison with a widely popular method, i.e. Conditional Mean Spectrum (CMS) (Baker, 2011).

---

[6] Matching at fundamental period

[7] Least moving average

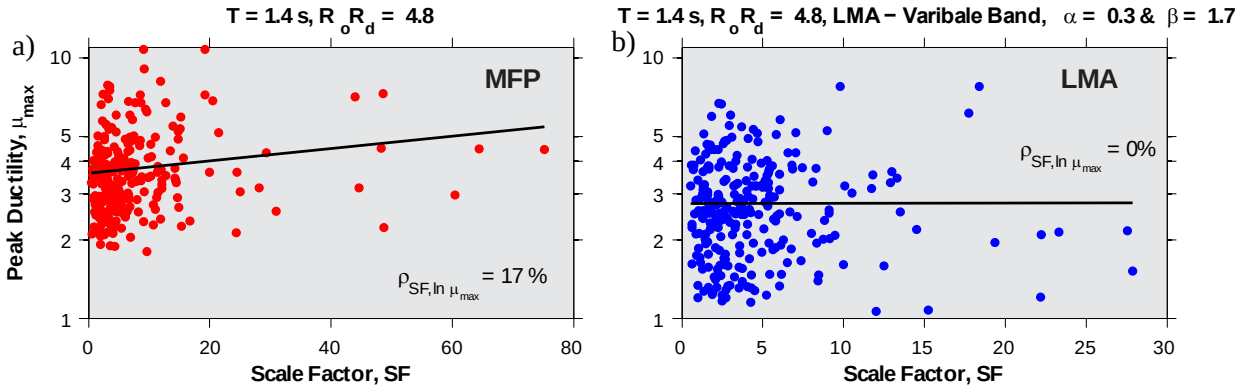

Figure 9.2: Comparison between bias in the estimated response of a SDOF system when ground motions are scaled by: a) MFP (a conventional method), and b) LMA methods. Note: elastic period of SDOF is 1.4 s.

9.3 Seismic design and performance of code-conforming BRBFs

Buckling-restrained braced frames (BRBFs) have been recently incorporated into the Canadian building code and steel design standard. Currently, BRB qualification has to be done in accordance with the U.S. seismic design specification reflected in AISC 341 (AISC, 2010). Due to the differences between design practice and seismic hazard in U.S. and Canada, the current BRB qualification requirements needed to be reconsidered. BRBF response modification in the U.S. code (ASCE7-10) is nearly two times the prescribed value in the Canadian code (NBCC 2010). Consequently, in equal condition, a BRBF designed according to the U.S. code will have much lower lateral strength compared to the Canadian one. Differences between U.S. and Canadian standards regarding design of BRBFs is elaborated in (Tremblay, *et al.*, 2016). Furthermore, seismic design and seismic evaluation in the U.S. are typically done at two distinctively different hazard levels. For instance, ASCE7 stipulates 10% in 50 years probability of exceedance as the basis for seismic design while the seismic evaluation is typically done using 2% in 50 years probability. Naturally, when a building is subjected to a lateral load that is 50% higher than the design load, extremely intense demand should be expected. On the contrary, in Canada design and evaluation are both done at a consistent level of hazard, i.e. 2% in 50 years. Logically, this practice would result in better consistency between expected and predicted demand level.

As a part of this study, and in order to estimate the seismic design displacement demand on BRBs, several multi-storey BRBF building prototypes were designed according to the latest edition of the

Canadian standard, i.e. NBCC 2010 and S16-09. These prototypes included 3- to 15-storey buildings that were designed for two hypothetical locations in west and east of Canada: Victoria, BC and Montréal, QC. Several bracing patterns and two generic site soil classes were considered in the process. The designed building prototypes are discussed in Chapter 5. A comparative study was conducted to find the most effective and efficient bracing pattern for multi-storey BRBFs when S16 capacity design approach is adopted. The studied bracing patterns are shown in Figure 9.3 and Figure 9.4. This study showed that configuration C6 in Figure 9.4, i.e. Split-X pattern with "back-to-back" arrangement, is the most efficient option for chevron bracing. This configuration provides the most direct load path of the lateral loads and has three seismically-loaded columns in each braced axis. According to the capacity design rules of S16-09, columns section must remain constant at least for two storeys. In the Split-X configuration, axial capacity force on the braced bay column is nearly constant for two storeys. By default, the required column sections for these two storeys would be similar as their design force are nearly equal. Gravity loads on these columns would be different but it may not be as significant. Of the studied diagonally braced prototypes, configuration D1 (converging diagonals in "separated" arrangement) resulted in the highest steel tonnage. Configuration D1 to D4 had nearly the same column tonnage but their girders' sizes were different. Braced bay girders in D1 and D2 carry significant axial load as the capacity forces of the connected braces have the same sign. On the other hand, capacity axial force in the braced bay girders of configuration D3 and D4 is nearly zero.

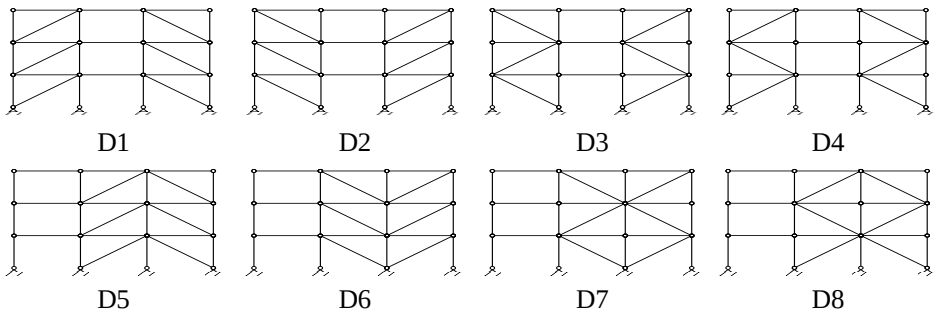

Figure 9.3: Considered diagonal braced frame configurations.

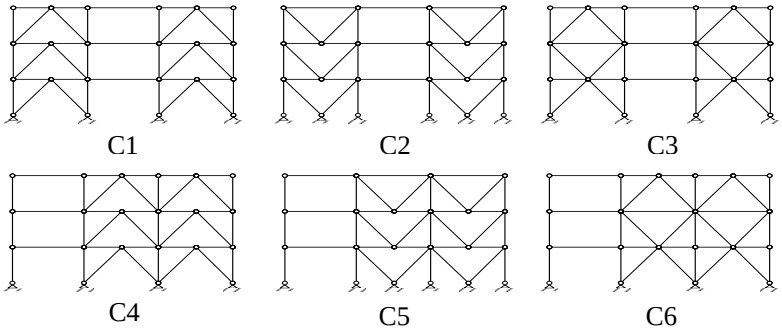

Figure 9.4: Considered chevron braced frame configurations.

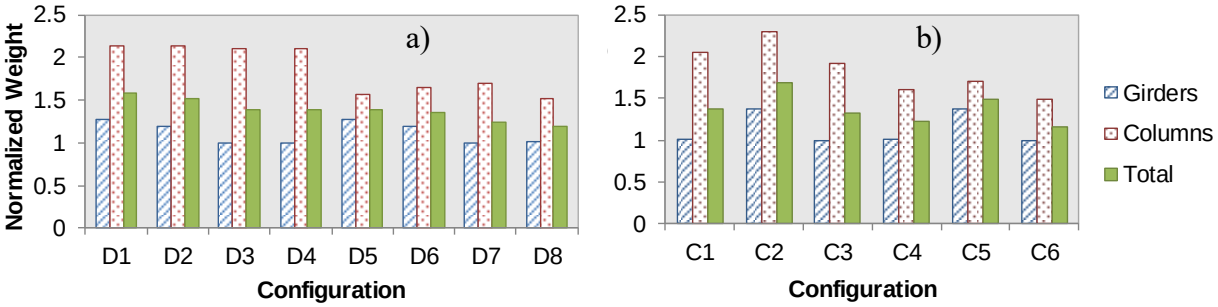

Figure 9.5: Relative steel tonnage-efficiency of different considered braced frame configurations: a) system with diagonally braced panels; b) system with chevron braced panels.

Seismic assessment was carried out using nonlinear static (pushover) and dynamic analyses. Ground motion sets representing the expected earthquake scenarios were compiled for combination of seismicity sources, and site soil classes. Among the designed framing systems, configuration C6 and D1 were selected for seismic demand estimation using advanced inelastic analyses. C6 and D1 represent, respectively, the BRBFs with the lightest and heaviest steel tonnage for the framing components.

Pushover analysis indicated stable inelastic response in case of west Canada prototypes even for building taller than 40 m. On the other hand, medium-rise east Canada models showed poor inelastic response as they tend to become laterally unstable once the design roof displacement approaches the design displacement, i.e. $R_o R_d \delta_{\text{roof}}$. Comparison between pushover response of the 9-storey prototypes in Victoria and Montréal (designed for site class C) can be seen in Figure 9.2. Plot in Figure 9.2c shows the storey response at the lower three storeys. Deformed shapes imply that the vertical distribution of displacement demand is more uniform in the Victoria

prototype. When roof reaches to the design displacement, indicated by dots in the plot, the storey drift angles are more or less similar. On the other hand, in the Montréal model the second and third floor do not participate in the lateral resistance due to excessive softening. The numerical models developed in this study may not represent the upper bound of lateral strength and stiffness as the contribution of gravity system was not considered. Previous studies have shown that there is significant reserved lateral capacity in the gravity system (Elkady *et al.*, 2015; Imanpour *et al.*, 2016a). If this capacity is mobilized, the laterally unstable behaviour in the taller east models may completely change. In addition, the target roof displacement predicted by $R_o R_d \delta_{\text{roof}}$ may be overly conservative, especially for taller buildings. This is discussed in Chapter 5.

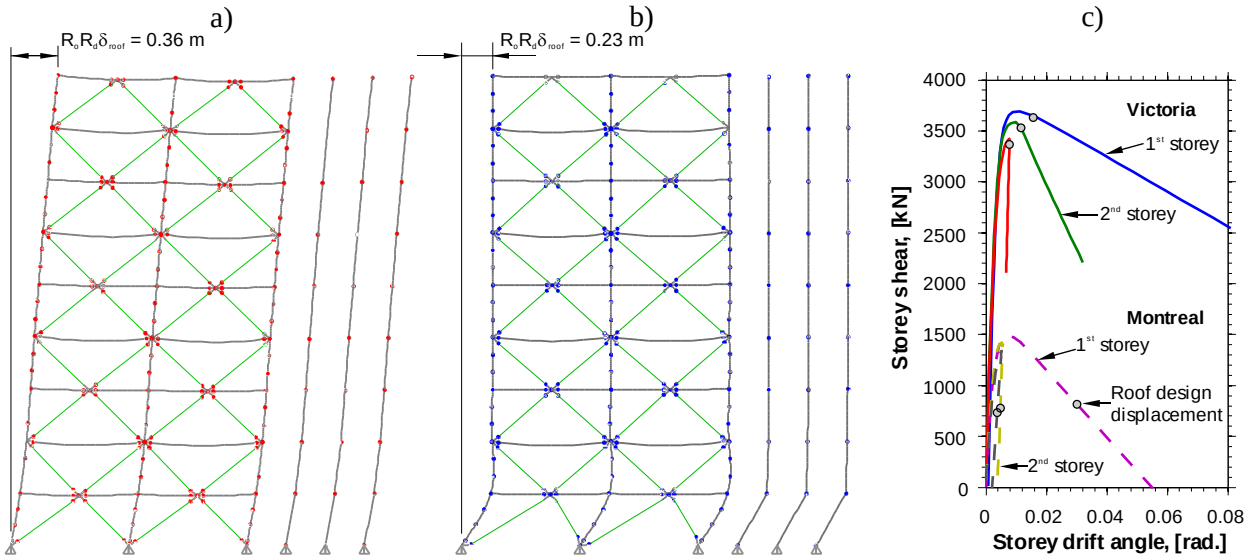

Figure 9.6: Pushover deformed shape of the 9-storey Split-X prototypes at roof design displacement: a) Victoria, b) Montréal, Note: displacement magnified by factor of 10; c) frame response at the first three storeys of the 9-storey Victoria and Montréal models, note: dots indicate the time instant that roof reached to the design displacement.

NTHA analysis showed that, among different seismicity source in Canada, west intra-plate earthquakes are likely to impose the most intense seismic demand on the BRBFs. Interstorey drift ratios were found to be less than the prescribed limit in the NBCC 2010 while the mid- and high-rise buildings were prone to significant permanent residual drift. Large permanent drift may hinder an immediate functionality of building following an earthquake and may impose considerable repair cost. NTHA indicated that the roof displacement predicted by force-based method, i.e.

$R_o R_d \delta_{\text{roof}}$, can be overly conservative for mid- and high-rise models. The predicted roof displacement by the first-mode code-based spectral displacement, i.e. $S_d(T_1) = 3/2\, S_a(T_1)\, {T_1}^2/4\pi^2$ was found to be more accurate. Comparison between NTHA results and these two methods can be found in Table 9.1 and Table 9.2. The 84th percentile of the NTHA results shows that the force-based method was only accurate for 3- and 5-storey models which deform predominantly in shear with little flexure due to column elongation. In the taller models, contribution of column elongation to the roof displacement is significant. To estimate the roof inelastic displacement in the design earthquake, the force-based method suggests to amplify the total frame deflection by factor of $R_o R_d$. In this way, column contribution to the roof displacement is also amplified. This is not totally correct since, in the design earthquake, columns are supposed to remain elastic. At the same percentile level, i.e. 84th, roof displacement predicted by the spectral displacement method matches the NTHA result regardless of the building height. This observation would be important for having a more realistic estimation of target roof displacement to conduct pushover analysis.

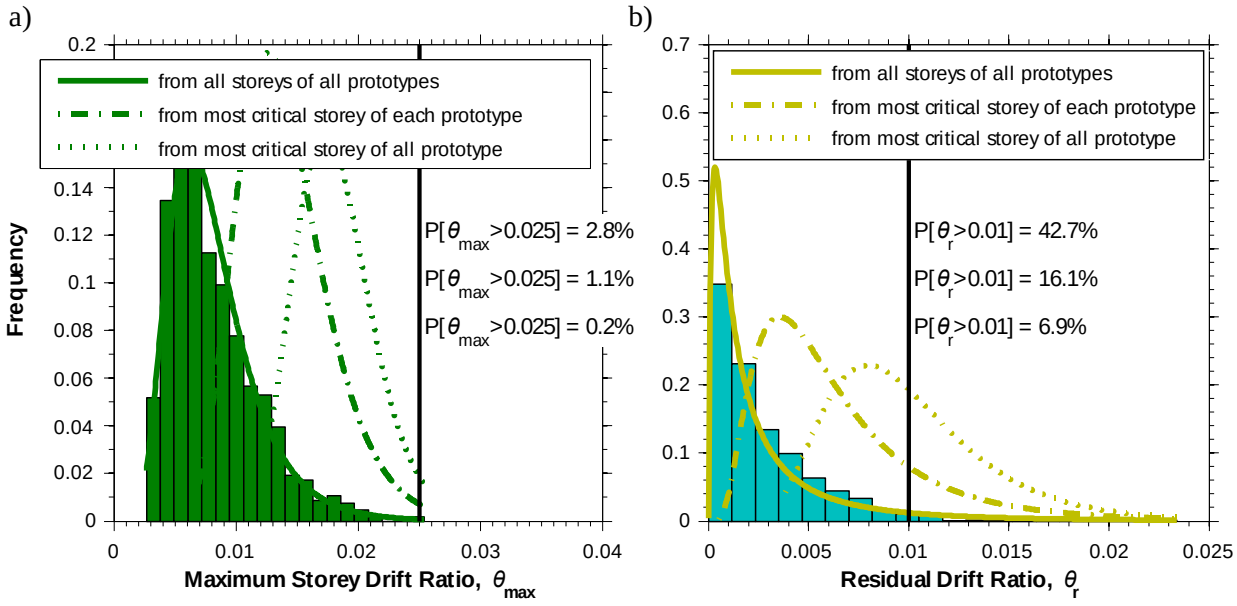

Figure 9.7: Statistical distribution of storey drift demand on 3- to 15-storey Split-X prototypes in Victoria site class C: a) maximum drift, b) residual drift.

Table 9.1: Ratio of roof design drift predicted by R_o R_d δ_{roof} to the NTHA maximum roof drift (Victoria class C site Split-X models).

Percentile level	**Number of storeys**					
	3	**5**	**7**	**9**	**13**	**15**
50	1.32	1.34	1.44	2.04	1.92	2.50
84	1.03	1.04	1.26	1.27	1.64	1.79
96	0.92	0.94	0.92	0.93	1.28	1.25
100	0.84	0.85	0.84	0.93	1.15	1.25

Table 9.2: Ratio of roof design displacement predicted by 3/2 $S_a(T_1)$ $T_1^2/4\pi^2$ to the NTHA maximum roof displacement (Victoria class C site Split-X models).

Percentile level	**Number of storeys**					
	3	**5**	**7**	**9**	**13**	**15**
50	1.25	1.11	1.12	1.48	1.15	1.35
84	0.97	0.87	0.98	0.93	0.99	0.96
96	0.88	0.78	0.71	0.67	0.77	0.67
100	0.80	0.71	0.65	0.67	0.69	0.67

Floor acceleration was also found to be significantly higher than the code prescribed value, especially at lower storeys. This may result in diaphragms being overloaded and subsequent failures in the chord and collector elements. As seen Figure 9.8, the overload was not limited to few occasions. It repeated many times during a design earthquake. Intensity of diaphragm overload can be quantified in different ways. In this study to indices are introduced. Table 9.3 presents the statistics of level crossings occasions, i.e. the number of peaks above the code-prescribed design acceleration. Duration of overload could also be important as a persistent overload pulse can be more damaging. Persistency of the overload occasions can be obtained as the accumulated durations that the diaphragm experiences an acceleration higher than the design values. This

parameter can be then divided to the *Significant Duration*[8] of the ground motion record to have a normalized demand index. In Table 9.4, trend of this normalized overload persistency index is presented. Interestingly, in the taller models, diaphragm overload duration is more than 100% of the earthquake strong shaking duration. This means that the diaphragms were even being overloaded in the very low amplitude shaking time at the beginning and end of ground motion.

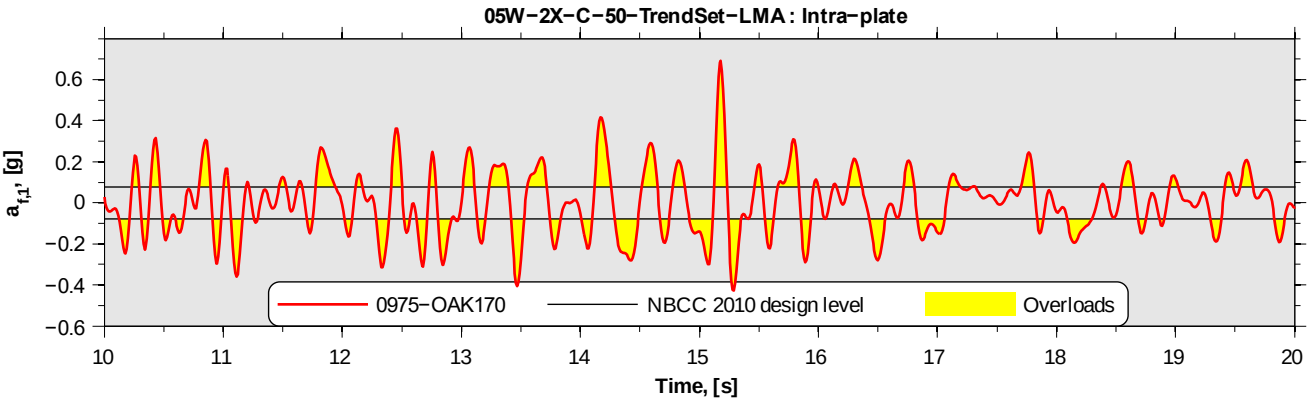

Figure 9.8: Overload occasions of the first storey diaphragm in 5-storey Split-X BRBF designed for soil class C site in Victoria.

Table 9.3: Number of level crossing of the design floor acceleration in Split-X Victoria prototypes.

		site C							site E					
Number of storeys		**3**	**5**	**7**	**9**	**13**	**15**		**3**	**5**	**7**	**9**	**13**	**15**
Percentile level	**50**	22	51	65	83	110	117		40	41	50	59	99	104
	84	27	69	79	96	143	135		58	72	78	104	197	200
	96	39	79	99	110	173	160		85	103	118	166	237	244
	100	43	82	106	114	180	166		91	109	119	171	244	245

[8] see (Bommer, *et al.*, 1999) for the definition

Table 9.4: Ratio of overload to significant duration in Split-X Victoria prototypes (class C site).

Percentile level	**Number of storeys**					
	3	**5**	**7**	**9**	**13**	**15**
50	0.12	0.38	0.57	0.78	1.06	1.17
84	0.21	0.54	0.74	1.04	1.24	1.24
96	0.31	0.67	0.83	1.08	1.36	1.33
100	0.34	0.68	0.85	1.09	1.37	1.36

NTHA showed that the demand on the BRBF columns under simultaneous effect of axial force and bending moment is less than the S16 specified capacity. This may imply satisfactory column response should be expected when the S16 capacity design rules are enforced. Concomitant maximum bending and axial demand on columns would not be the likely case according to the analysis results.

In general, soft soil ground motion records imposed more demand on the studied BRBFs in comparison with the motions recorded on soft rock. Soft soil foundation factor currently prescribed by the Canadian building code may need to be re-evaluated in light of new ground motion data.

Ground motion selection and scaling method was shown to have considerable impact on the estimated demand especially in terms of variability. In this study, a simple statistical framework is implemented to include this effect in the estimated demand. In comparison with a reference U.S. case study, much lower displacement ductility and cumulative inelastic displacement was predicted for the Canadian code-conforming BRBFs, especially in east of Canada. Low cycle fatigue was found to be a rather unlikely failure mode in BRBs.

9.4 Mechanical behaviour of 350WT steel

In BRBFs, seismic energy dissipation takes place in the core member of the brace elements. Therefore, core material has to have enough ductility to absorb the induced energy in a stable fashion without losing stiffness or strength. In this context, low cycle fatigue capacity under large inelastic strains becomes an important issue. For using BRBs in seismic protection of exposed

structures in cold environments, satisfactory performance of core material under combined effects of low temperature and fast loading rates should be experimentally investigated. Accordingly, careful examination of the core material behaviour under different severe loading conditions is an immediate necessity. In addition, cyclic hardening behaviour of core material is a highly contributing factor in estimation of the normal thrust imparted on the restrainer. To this end, a comprehensive testing program was planned and carried out to capture the required data and develop predictive analytical models. Tests were performed at target temperatures of +25 °C (room) and −40 °C (subfreezing). Significant efforts were put forward to enforce a uniaxial loading condition by avoiding flexural deformation and lateral buckling of test specimen. In addition to the basic tensile mechanical properties, crack initiation life of 350WT steel under constant-amplitude cyclic tests was obtained for a relatively wide range of inelastic strain amplitudes, i.e. 1% to 8%. Fatigue tests revealed the importance of providing sufficient lateral stiffness to the loading frame when specimen is tested under large inelastic strains. When lateral stiffness was not adequate, specimens incurred premature fracture due to the generated flexural strains after lateral buckling of specimen.

Experimental observations indicated that subfreezing temperature does not have adverse effect on the low cycle fatigue capacity and on the fracture ductility of 350WT steel. Combined effect of cold temperature and fast rate loading resulted in 45%, and 25%, 16% increase in upper yield, lower yield, and tensile stresses, respectively. This extra resistance should be included in the capacity design of connections and other framing components.

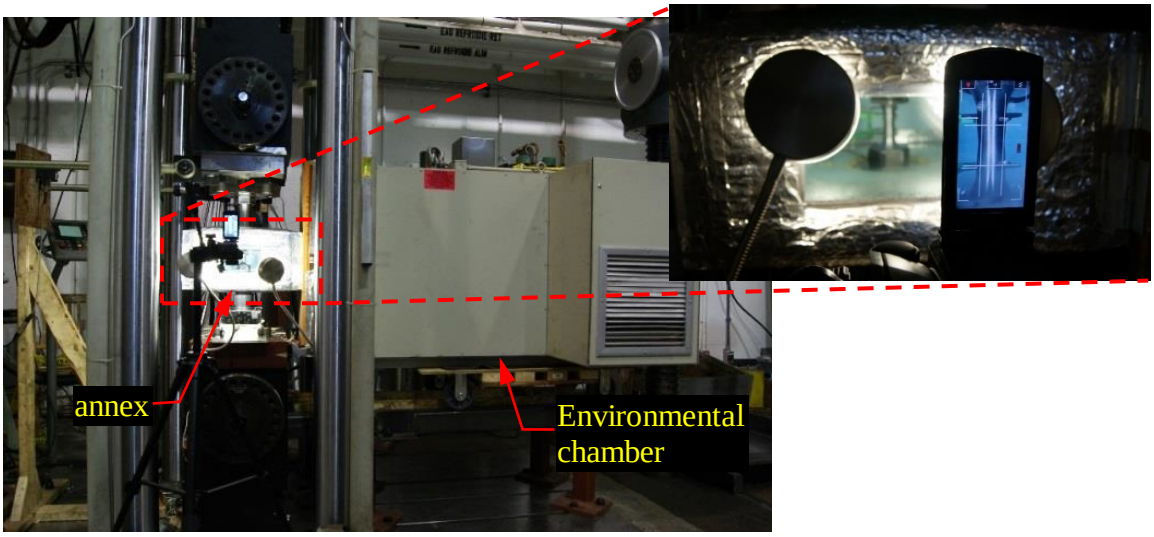

Figure 9.9: Test setup for subfreezing experiments.

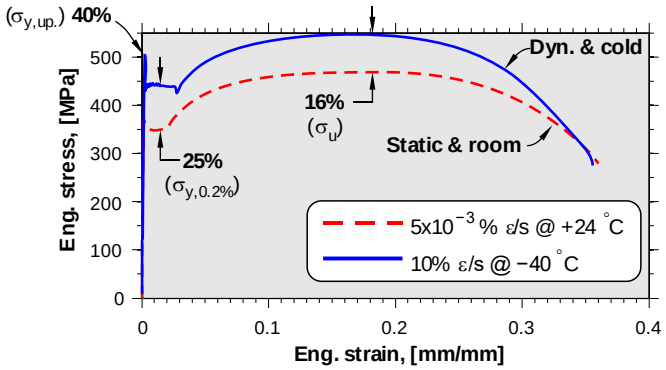

Figure 9.10: Comparison between tensile behaviour under two conditions: quasi-static rate at room temperature, and dynamic rate at subfreezing temperature.

Few tests conducted on circumferentially notched specimen also indicated that the fracture ductility under mild tensile stress triaxiality is not reduced under the subfreezing condition. Experiment indicated that under subfreezing condition larger gage displacement was required to reach the point of fracture in comparison with room temperature condition. Stress triaxiality is defined as the ratio of hydrostatic pressure to von Mises stress. According to (Bridgman, 1944), stress triaxiality of a circumferentially notched specimen with elastic-perfectly plastic material can be obtained as:

$$T = \frac{1}{3} + \ln\left(\frac{D_{NR}}{4R_N} + 1\right) \tag{9.1}$$

where D_{NR} and R_N are the notch root diameter and notch radius, respectively. By definition, stress triaxiality is equal to 1/3 when specimen has no notch. For notch geometry of the tested specimens, i.e. $D_{NR} = R_N = 7.5$ mm, stress triaxiality would be $T = 0.55$.

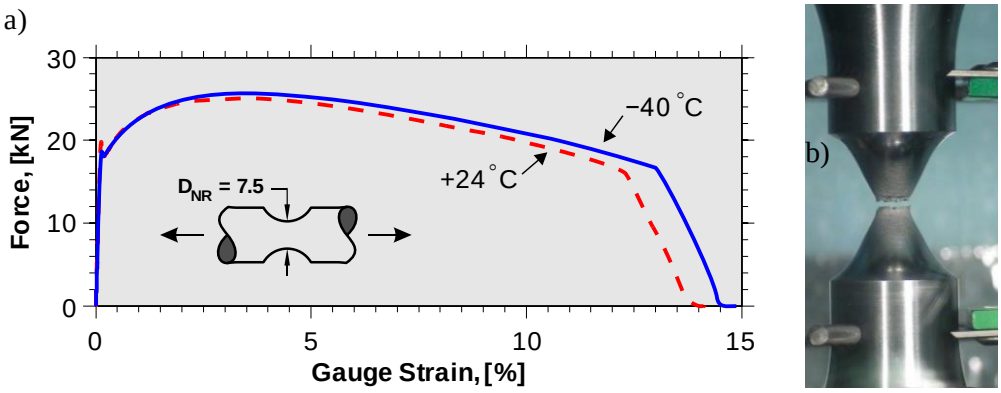

Figure 9.11: Tensile monotonic response of circumferentially notched specimens at room and subfreezing temperature.

Fatigue failure prediction under random loading pattern is of great importance in seismic assessment studies. In this research, several existing fatigue damage model were calibrated based on constant-amplitude cyclic tests. These models then utilized along with linear damage accumulation rule to predict fatigue failure under several variable-amplitude loading patterns including those extracted from response of BRBFs to major type of earthquakes. When the calibrated fatigue damage models employed for life cycle prediction under random-pattern loading, very good results were obtained. Conventional strain-based fatigue damage model was found more efficient than the energy-based methods, especially in case of less intense loadings. However, linear damage accumulation rule (Miner's rule) consistently overestimated the failure life under low-high step-loading patterns. This loading pattern is widely used in cyclic testing protocols for seismic qualification of structural components. Caution should be exercised when Miner's rule is employed to predict fracture under standard testing protocols. Conducting cyclic tests under large inelastic strain is often a challenging task due to problems resulting from buckling of coupons. For this reason, it would be easier to carry out the fatigue tests only at moderate inelastic strains and then extrapolate the fatigue model to larger range. However, comparison with the available 350WT fatigue data reported in (Josi, *et al.*, 2010) and (Hamdoon, *et al.*, 2014) shows that the low cycle

fatigue damage models calibrated based on small inelastic strains tests may not be extrapolated to the larger strains as it would introduce substantial prediction error.

Cyclic hardening equations are central to the energy-based fatigue prediction models. In addition, estimation of tangent modulus and cyclic yield stress is of great importance in the core normal thrust analysis. In this study, in addition to the classic cyclic hardening equations, prediction models for the tangent stiffness and cyclic yield resistance were developed and calibrated based on the constant-amplitude tests' results. For a given strain range and number of loading cycles, these models output tangent stiffness and cyclic yield.

Past experimental and analytical studies have shown that inelastic response of structures to seismic excitation is often not symmetric. It was not well-studied if hardening rules calibrated under symmetrical loadings can be extended to asymmetric displacement loading paths. Based on few tests conducted in the current study, it was seen that neither low cycle fatigue nor kinematic hardening of 350WT is significantly affected by asymmetry of the loading pattern. Plots in Figure 9.12 show the symmetric and asymmetric step-wise displacement histories and the response of specimens to these patterns of loading. Asymmetric loading resulted in slightly higher total stress range and the fracture time was almost the same.

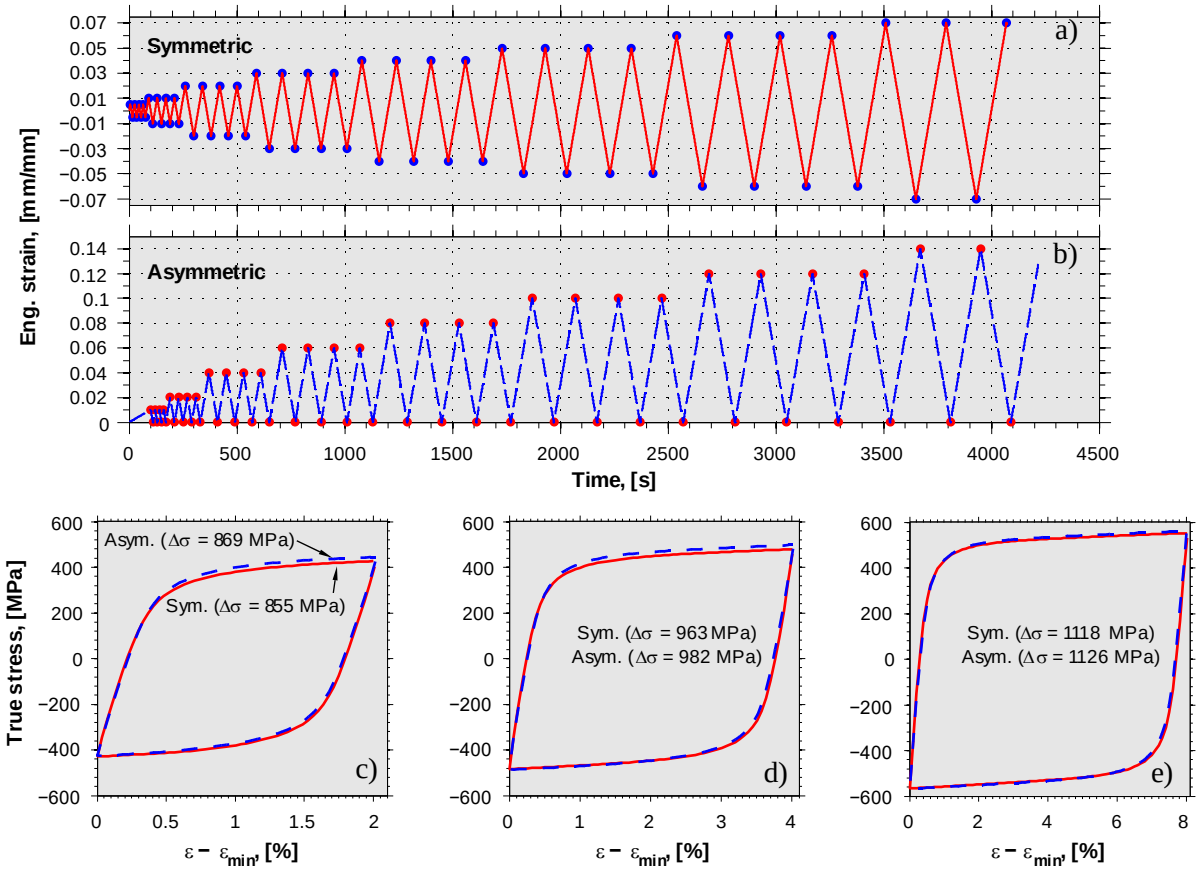

Figure 9.12: Response of 350WT steel to symmetric and asymmetric strain loading.

Strain hardening is typically decomposed into isotropic, and kinematic components. Latter component is directly linked to the strain amplitude and the isotropic hardening is typically expressed as a monotonic asymptotic function of accumulated plastic strain. For this reason, to estimate the isotropic yield at the given loading time, history of previously applied inelastic deformations is important as it conveys the amount of accumulated plastic strain. In this study, effect of loading history was investigated by comparing response of material to a given strain amplitude under symmetric step-wise and constant-amplitude loadings. Response of 350WT round specimens under these loadings for strain amplitude of 1% to 4% is shown in Figure 9.13. Symmetric step-wise loading (Figure 9.12a) was applied in one continuous test and each amplitude was repeated four times. Constant amplitude tests were carried out in separate experiments until failure of specimen. In plots of Figure 9.13, hysteresis loops corresponding to the second cycle of loading at a given strain amplitude are compared. The hysteresis loops are nearly identical and the difference between total stress range obtained from these two types of loading is around 1%.

Material showed slightly more hardening under step-wise loading which could be attributed to the larger accumulated plastic strains in that loading. Nevertheless, material hardens to the same level regardless of the loading history. This observation implies that, under symmetric cyclic condition, history of previously applied deformations has little impact on the isotropic and total hardening of 350WT steel. In other words, hardening is mainly controlled by the strain range. This observation has an important implication for calibration of cyclic hardening models. One symmetric step-wise loading that covers a relatively wide range of applicable strains would be sufficient for calibration purpose as the hardening is strongly controlled by the strain range rather than the accumulated plastic strain.

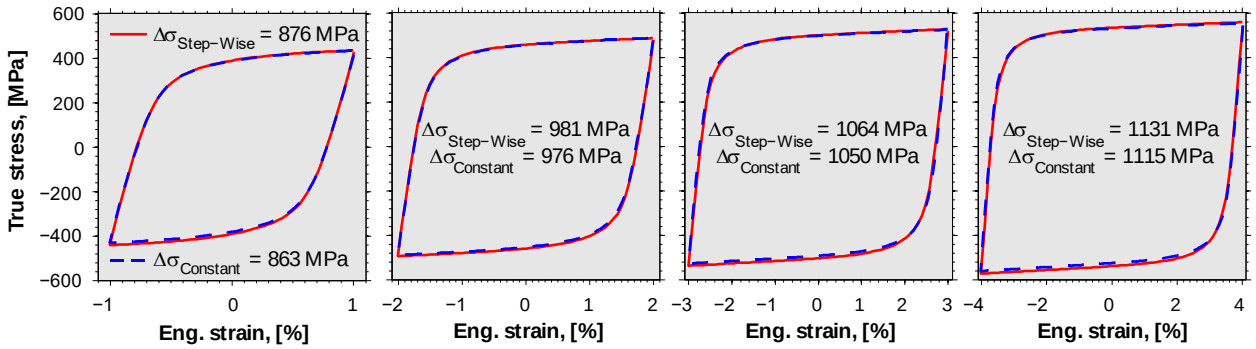

Figure 9.13: Comparison between hardening behaviour under step-wise and constant amplitude tests.

Shear response of storeys to earthquake excitation is not necessarily symmetric. When steel is subjected to asymmetric stress cycles, strain progressively ratchets toward the direction of mean stress. This "ratcheting" phenomenon is typically characterized by testing under asymmetric stress-controlled cyclic loading. For a given material, rate of ratcheting depends on the range of stress and mean stress value. Figure 9.14 shows the ratcheting response of 350WT steel under an asymmetric stress loading with stress range $\Delta\sigma = 650$ MPa and mean stress $\sigma_m = +65$ MPa. In 1000 cycles under this loading condition, strain increased from 2% to ~4.75%. Ratcheting phenomenon is attributed to difference between kinematic hardening in the loading and unloading directions. To capture the ratcheting effect in numerical simulation, constitutive material model must adopt special nonlinear kinematic hardening rule. Plot in Figure 9.15 shows the response of steel02 uniaxial material model to 25 cycles of asymmetric stress loading with $\Delta\sigma = 650$ MPa and $\sigma_m = +65$ MPa. "steel02" is a material model that has been implemented in OpenSees software

framework and is widely popular in earthquake engineering community. As it can be seen, steel02 predicts a reversed-direction ratcheting in comparison with the test results. This problem may lead to significant error in prediction of residual drift under earthquake loading.

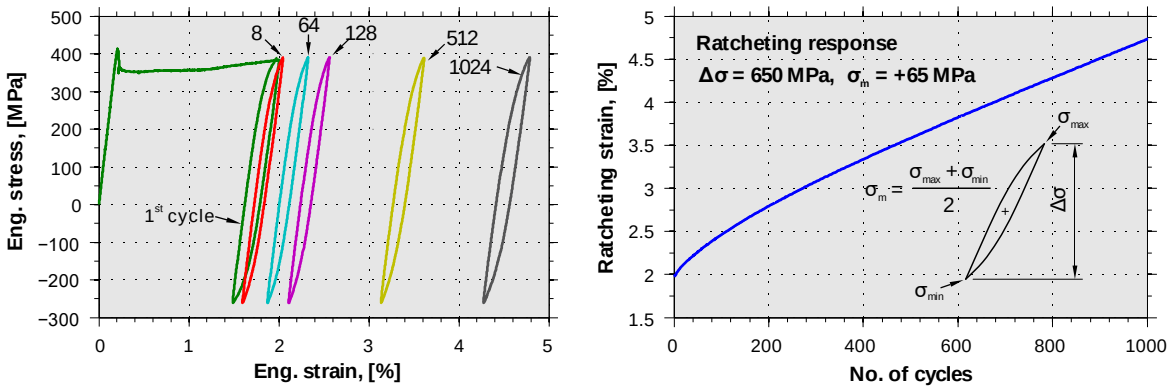

Figure 9.14: Response of 350WT steel under asymmetric stress cycles.

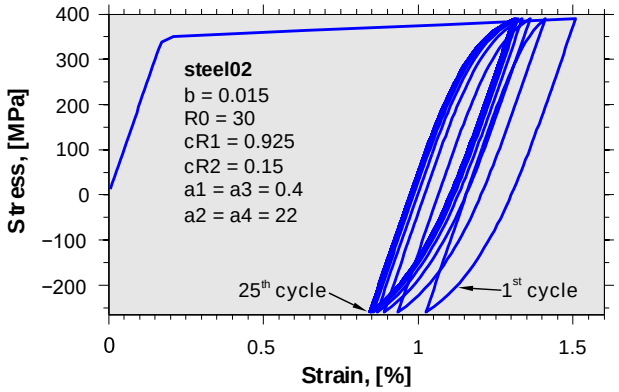

Figure 9.15: Response of steel02 model to asymmetric stress cycles

9.5 Analysis of normal thrust

When buckling of core is restrained, a lateral reaction will be imparted upon the restraining system. Seismic design of restraining system without proper estimation of this normal thrust would be an incomplete task. Lack adequate capacity against this normal thrust can give rise to premature failure modes. Failure of restrainer has been observed in several experimental studies both in conventional and all-steel BRBs. Magnitude of the core normal thrust depends on several factors including imposed axial shortening, core slenderness, gap between core and restrainer, cyclic hardening behaviour of the core material, number of loading cycle, restraining stiffness, frictional

characteristics of the core-restrainer interface, initial imperfection of the core member, and flow path of the frictional forces. There are only a few available methods that have been proposed to predict core normal thrust forces and most these methods only account for some of the influencing parameters. Furthermore, simplifying assumptions made in these methods may lead to mix of conservative or un-conservative estimations depending on the loading condition. In particular, current methods, suggest rather arbitrary values for the core inelastic flexural stiffness that may only be valid for a limited range of loading condition. In this study, a more comprehensive solution was developed to estimate the normal thrust that is essential for seismic design of BRB restraining mechanism. The method accounts for the most important measurable factors that control the inelastic buckling behaviour of the core member. Inelastic core flexural stiffness properties are determined using tangent material stiffness considering cyclic hardening of the core material based on a realistic model that was developed by the acquired data from the material testing stage of this research. Furthermore, current methods presume periodic buckling waveform while several experimental observations have shown that the core buckling is not periodic and considerable differences may exist between wavelengths and waveforms at different positions along the core. This is mainly attributed to the magnitude of frictional forces and their flow path. Unlike the current methods, in this study these two factors were directly considered so that the buckling wavelengths and normal thrust would be predicted with more precision. Currently, BRB encasing is often assumed to provide infinite restraining stiffness and no clear boundary between this infinite stiffness and a practical value that should be provided is drawn. The method presented in this study accounts for the flexibility of the restrainer and its subsequent impacts on the gap augmentation and normal thrust. Due to Poisson's effect, upon compressive deformation, core section expands laterally and this phenomenon reduces the effective gap between core and restrainer. Current methods typically ignore this effect, but in this study Poisson's effect was incorporated and was found to be important when ratio of gap to core thickness is small.

For a given BRB axial compression deformation, the method requires iterations to achieve force equilibrium and deformation compatibilities. In design, the stiffness of the restraining system will be adjusted until satisfactory response will be achieved. The method proposes a minimum restrainer stiffness based on the analytical results presented in (Korzekwa, 2009) that can be used to initiate the design process. In practice, the proposed method can be readily implemented in a spreadsheet and be used in lieu of a more sophisticated tool such as finite element analysis which can be

computationally very expensive. Accuracy of this approach was verified against available experimental data and finite element analysis results. In both cases promising results were obtained and the developed method was found capable for predicting normal thrust, buckling mode, and axial resistance with a sufficient accuracy for most engineering applications.

For validation purpose, both 3D and 2D finite element BRB models were created and analyzed. In the 2D model, the core was constructed by plane stress elements and continuum elements were used in the 3D model. In the 3D model strong-axis buckling of core was prohibited by applying an appropriate constraint. Surprisingly, significant differences were found between responses from the 2D and 3D models. This is illustrated in Figure 9.16 for one of the BRB specimens examined in by (Metelli, *et al.*, 2016). Figure 9.16a and b show the deformed shapes of the 2D and 3D core models under 6% axial shortening, respectively, and the plot in Figure 9.16c compares the evolution of the normal thrust from these two models. At 6% shortening, the 2D model predicts a normal thrust that is nearly 2.5 times larger than that of the 3D model. The number of buckling waves and their shapes are also different. It must be noted, however, that the axial force predicted by these models were almost the same, as shown in Figure 9.16d. Tracing of buckling wave formation in the 3D model indicated that, at a given wave crest, contact between core and restrainer is first established at the core edges. Contact zones would then gradually spread to the center of section if the applied axial deformation is sufficiently large. This implies that the buckled plate has two orthogonal curvatures, i.e. longitudinal and transversal, which can increase the core flexural stiffness and its buckling load. Comparison with the experimental results reported in (Metelli, *et al.*, 2016) indicate that the normal thrust and number of waves are closely predicted by the 3D model. The same observation was made by (Bregoli, *et al.*, 2016).

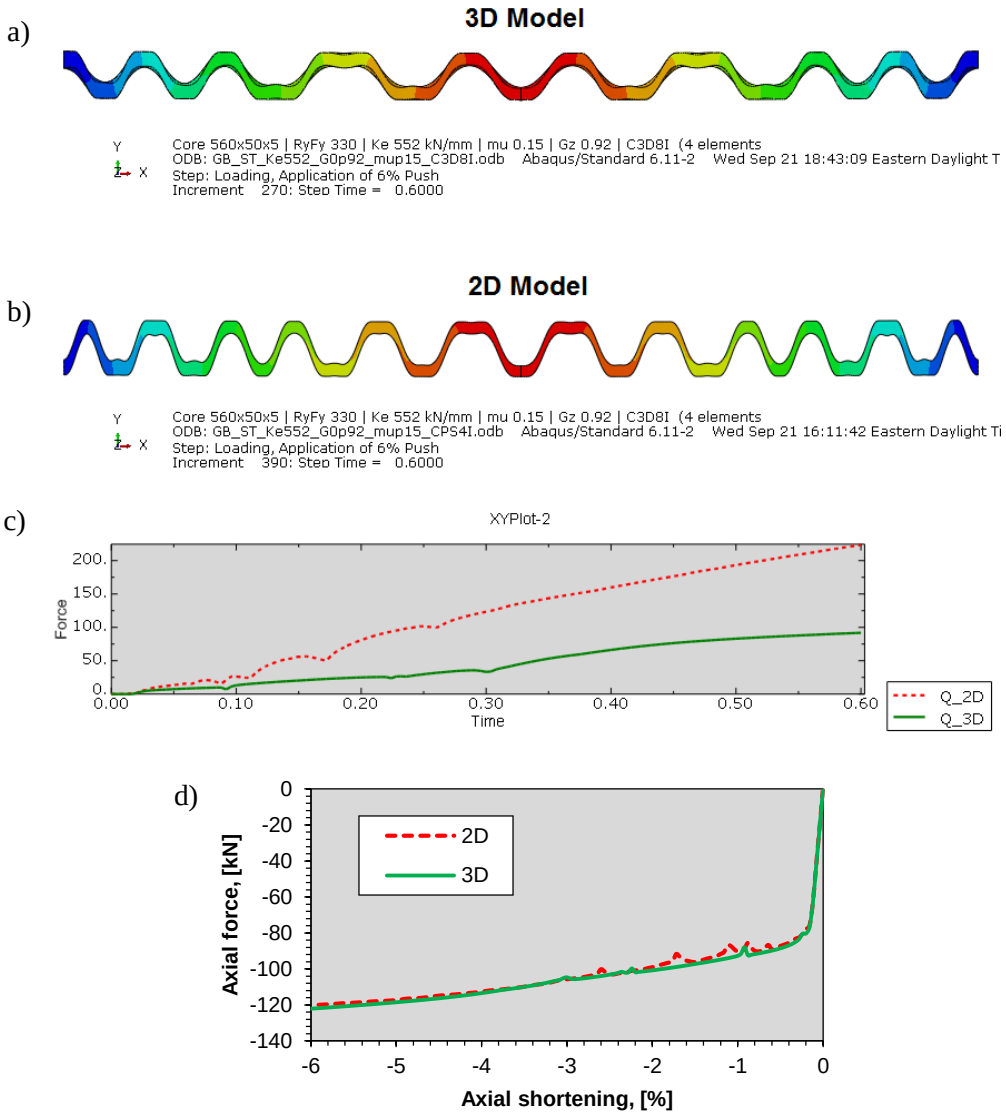

Figure 9.16: Deformed shape of a BRB core at 6% shortening: a) 3D (continuum), and b) 2D (plane stress) model; c) total normal thrust as a function of analysis time; d) axial force *vs* axial shortening.

9.6 Experimental qualification

This research aimed at developing a patent-free all-steel BRB that would be simple enough for fabrication and assembly in a regular steel fabrication shop. Restrainer of this BRB is composed of two built-up steel sections that are joined together by high strength pretensioned bolts. Ideally, in this system, core-restrainer interface should be debonded by simple high performance material to

minimize the adverse effects of friction. For this purpose, several options for core-restrainer debonding were included in the qualification program. Finding a proper through-thickness gap that is small enough to minimize the normal force demand on the restrainer, and large enough to allow unconstrained through-thickness core expansion is a major design challenge. In the qualification program a relatively wide range of through-thickness gap sizes, i.e. from 1.1 mm to 3.6 mm, were considered to investigate the gap effect and finding the minimum practical size that could be achieved. Different components of the developed all-steel BRB concept are shown in Figure 9.17. A graphical representation of the assembled BRB is depicted in Figure 9.18a.

Special attention was given to reducing the potentially damaging effects of the frame action-induced bending moments. To this end, the specimens were tested in a vertical loading frame and a simple low-constraint brace end connection detail was conceived and utilized. This brace-to-gusset plate connection was achieved by a compact bolted joint where only one edge of the gusset plate was fixed to the frame beam and 25 mm clearance was left between vertical edge of the gusset plate and the column flange (see Figure 9.18b). In addition to the standard S16 quasi-static loading protocol, satisfactory performance had to be also demonstrated under fast rate seismic loading and long duration loading representing demand from megathrust earthquakes. To serve this purpose, two seismic loading patterns were designed from response of code-conforming multi-storey BRBFs to the earthquake scenarios expected in south west of British Columbia. Lateral response of the test frame without BRB specimen is shown in Figure 9.19 and very small lateral resistance was measured, even at large drift angles.

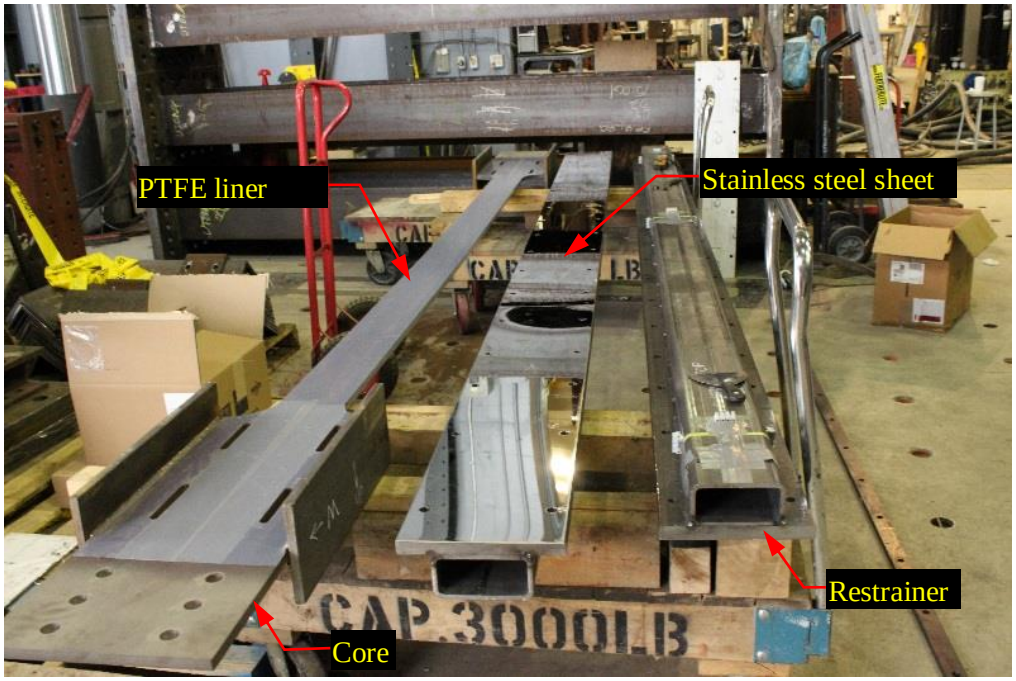

Figure 9.17: BRB specimen with stainless steel–PTFE interfacial condition.

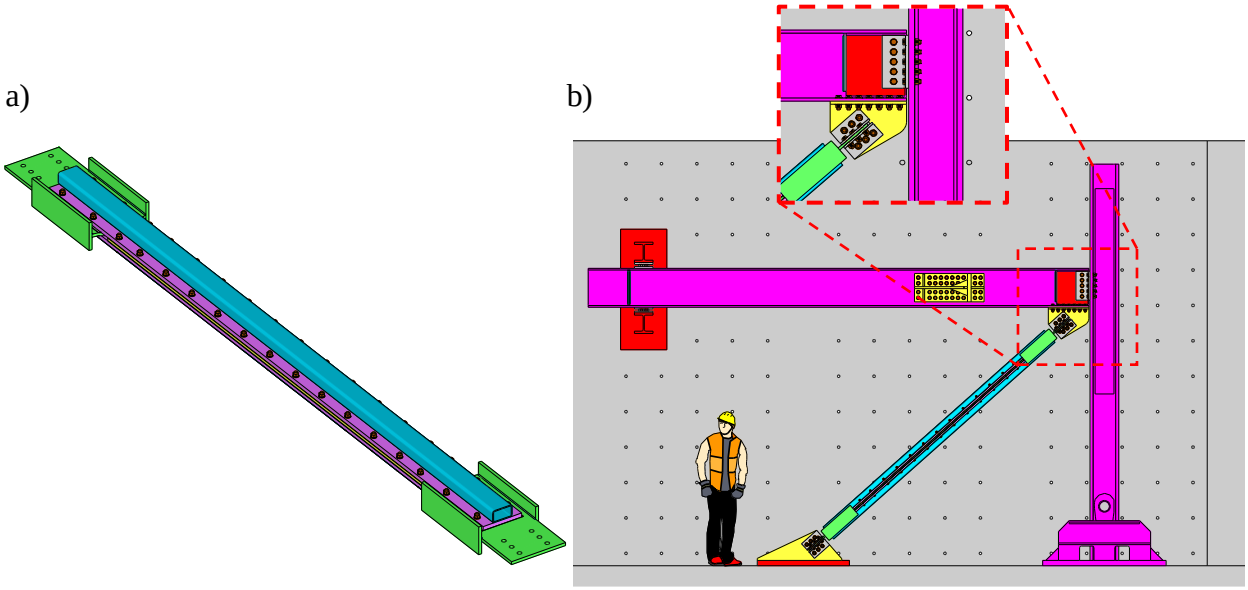

Figure 9.18: a) 3D view of an assembled BRB specimen, b) loading frame with installed BRB specimen.

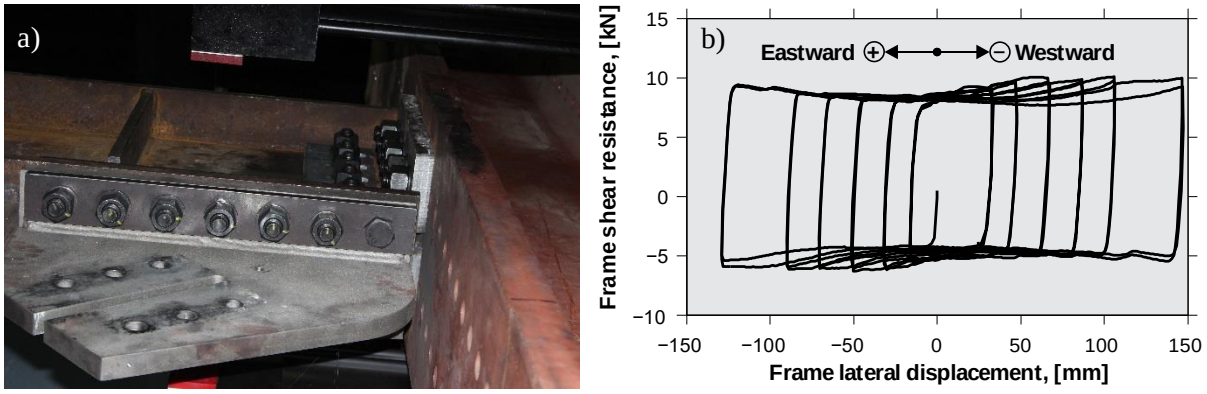

Figure 9.19: a) Close-up view of the loading frame gusset plate, b) lateral response of loading frame without BRB specimen.

Cores of the BRB specimens were fabricated from the G40.21 350WT Category 4 steel grade, same as in the material characterization phase. However, the BRB core steel was supplied by another mill and, although the specifications were the same, considerable differences in tensile properties between the supplied steels from the two manufacturers were found, as shown in Figure 9.20a where load-deformation responses of these two steels are compared. In the figure, Supplier no. 1 is the one who supplied the steel used in the material characterization phase whereas Supplier no. 2 manufactured the steel received for the BRB core plates. Differences in test coupons (plate type coupons with 200 mm gauge length of the cores *vs* short round specimens for material characterization) may have contributed to the ~11% higher yield and tensile resistances of the brace core material. However, as shown in Figure 9.20b, when tensile responses of these two steels are normalized with respect to their respective 0.2% offset yield stresses, nearly the same hardening behaviour can be observed. For this reason, cyclic hardening behaviour in the developed predictive model is expressed in terms of actual yield stress of steel, R_yF_y, rather than the nominal value. The BRB coupon tests were conducted at an extremely slow rate of 1 με/s. Furthermore, BRB cyclic quasi-static tests were performed at constant axial deformation rate of 0.75 mm/s which approximately corresponds to a core strain rate of 0.75/3000 = 250 με/s given the length of the yielding core segment, L_y = 3000 mm, of the BRB specimens. This is 250 times faster than the coupon tests which likely resulted in an extra increase in the yield resistance in the BRB tests. The average yield strength of BRB specimens in the quasi-static cyclic tests was ~1250 kN which implies a core yield stress F_{ysc} = ~440 MPa, i.e. 14% higher than the coupon results. Overall, the measured yield stress of core in the BRB tests was ~26% higher than the nominal 350 MPa value.

In real earthquakes, the rate of deformation in the yielding core segment is expected to be much faster than 0.75 mm/s, suggesting that strain rate effects may impact structural response. For BRBFs exposed to low temperatures, additional brace yield resistance is expected as material testing indicated that the combined effect of cold temperature and earthquake-rate loading rates can lead to 25% increase in yield stress compared to yield measured in quasi-static tests. This may imply that the difference between actual and nominal brace yield strengths may be as high as 40%.

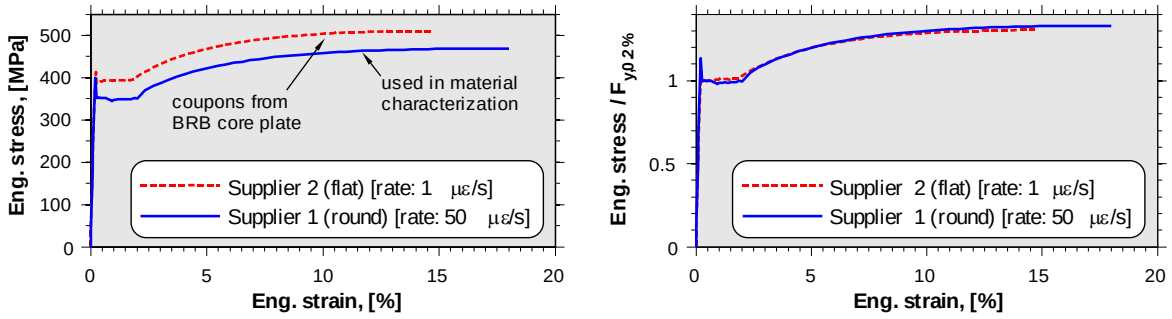

Figure 9.20: Comparison between supplied 350WT steel in two phased of research: a) stress *vs* strain; b) normalized stress *vs* strain.

In total, twelve full-scale heavily-instrumented specimens of the proposed steel-encased BRB system were tested in the vertical loading frame. The BRB members exhibited stable hysteretic response and significant energy dissipation capability was realized. Hysteresis responses and performance indices can be found in Chapter 8 of this dissertation. Very large cumulative inelastic deformations ranging between 320 and 3700 were obtained before brace failure, depending on the specimen characteristics and loading protocol. Response under fast-rate dynamic loading was stable and the testing specimen could resist several intense earthquake loading histories without any strength or stiffness degradation. The proposed BRB also performed well under excitations from long duration megathrust earthquakes. Of the several tested interfacial conditions, the combination of stainless steel and UHMW-PE[9] liner was found to be the most efficient option to manage the frictional actions at the core-restrainer interface. In the past, concerns have been raised on the negative impact of excessively constrained brace end connections (López, *et al.*, 2002;

[9] Ultra-high-molecular-weight polyethylene

Christopulos, 2005; Tsai, *et al.*, 2008). The combination of low-stiffness knife-plate hinges at the brace core-to-gusset plate joints and the single edge gusset plate implemented in this study resulted in an excellent behaviour with no sign of damage or distress under extreme loading conditions. Test results showed that the flexural demand at the knife-plate hinge was predicted with a high accuracy both in terms of bending moment and rotation. Strong-axis buckling of the BRB core was triggered when using partially restrained conditions. This buckling mode resulted in relatively lower frictional forces and the tensile post-yield stiffness was considerably higher compared to the case with weak-axis buckling. This stiffer post-yield response may improve the overall BRBF response, specifically in terms of residual structure lateral displacements. Analysis of test results showed that the frictional forces did not have reflective symmetry with respect to the middle of brace length. This behaviour probably increased the localized demand on the core and reduced the low cycle fatigue life.

CHAPTER 10 SUMMARY AND CONCLUSIONS

10.1 General

The presented doctoral thesis aimed at developing an all-steel buckling-restrained brace (BRB) system that could be used as a reliable source of seismic energy dissipation in various kinds of structures. To this end, a complete design and qualification procedure has been established, and the required data has been acquired, processed, and adopted in the design process. Within the framework of this PhD work, the following original contributions have been made:

- Development of an alternative method for ground motion record selection and scaling that could be used for effective seismic assessment of structures;
- Evaluation of the current Canadian codes' (NBCC and S16) requirements for seismic design and qualification of BRBFs, along with several recommendations to improve the design, analysis, and physical testing of this system;
- Assessment of seismic demand on BRBFs due to inter– and intra–plate earthquake hazard in eastern and western Canada;
- Characterization of mechanical behaviour of CSA G40.21 350WT steel, as a BRB core material, under different loading conditions at room and subfreezing temperatures;
- Development of an analytical approach to estimate the normal thrust due to core inelastic buckling in BRB systems;
- Conceptual development and experimental seismic qualification of a patent-free all-steel BRB.

Results and findings of this PhD work have been published or submitted for publication in scientific journals in the field of civil and structural engineering. In addition to the journal articles, some parts of this research project have been published or accepted for publication in the following conference proceedings:

- Dehghani M, Tremblay R (2012): Development of standard dynamic loading protocol for buckling-restrained braced frames. *Proceeding of the 7th conference on Behaviour of Steel Structures in Seismic Areas*, Santiago, Chile.

- Dehghani M, Tremblay R (2012): Introduction to a Robust Period-independent Ground Motion Selection and Scaling Method. *Proceeding of the 15th World Conference on Earthquake Engineering*, Lisbon, Portugal.
- Dehghani M, Tremblay R (2012): Standard Dynamic Loading Protocols for Seismic Qualification of BRBFs in Eastern and Western Canada. *Proceeding of the 15th World Conference on Earthquake Engineering*, Lisbon, Portugal.
- Dehghani M, Tremblay R (2017): Seismic Induced Floor Accelerations and Diaphragm Forces for Buckling Restrained Braced Frames. *Proceeding of the 16th World Conference on Earthquake Engineering*, Santiago, Chile. (accepted).
- Dehghani M, Tremblay R (2017): Full-Scale Experimental Assessment of Steel-Encased Buckling Restrained Braces. *Proceeding of 16th World Conference on Earthquake Engineering*, Santiago, Chile. (accepted).

In the next section findings from each research stage are summarized. In the last section, limitations of the current study and recommendation for future research are discussed.

10.2 Summary and conclusions

Buckling-restrained braced frame (BRBF) is a standard structural system that has been recently adopted by the major building codes in North America. This system incorporates non-buckling diagonal brace elements that dissipate the earthquake-induced energy through stable inelastic actions. These elements offer symmetric inelastic response in tension and compression which is advantageous to stability and safety of structures during strong earthquakes. Achieving the desired stable energy dissipation in these diagonal elements, requires a careful design of the buckling restraining mechanism that has a complex behaviour. In the recent years, interest has been constantly growing for using BRBFs as a ductile seismic lateral force resisting system in North America and around the world. Currently available buckling-restrained braces (BRBs) in the North American market are proprietary and therefore limited design information is available. Canadian steel fabricators are interested in acquiring the design technology and manufacturing BRBs as an engineering product for applications in Canada or abroad. In Polytechnique Montréal research on this system started in 2002 and has continued in the author's PhD program. To have a complete design and qualification procedure several related subjects have been investigated and addressed

including seismic demand, material behaviour, design methodology, and seismic qualification. Findings of this research can be implemented to design an advanced practical energy dissipating system that could increase the safety of structures in strong earthquakes. These findings are briefly discussed in the following subsections.

10.2.1 Ground motion selection and scaling

In this phase of research an alternative method for selecting and scaling ground motion records was developed. This method could be exploited for compiling sets of ground acceleration time histories for seismic assessment of structures through dynamic analysis. This method takes into account the local site hazard deaggregation and provides a statistical procedure to refine a large set of selected records. In the proposed scaling approach, a special attention is given to the role of frequency content for obtaining scaled spectra with reasonable variance. The developed method is period-independent, and as a result a single suite of records could be complied for analysis of structures with different dynamic properties. A well-established scaling technique that is included in ASCE 7 building code was critically reviewed and several shortcomings that could lead to inconsistent and largely uncertain estimated demand were pointed out. Effectiveness of these methods was validated by the results of exhaustive numerical tools including constant strength and ductility spectra techniques, and nonlinear time history analysis of multi-storey BRBFs. In comparison with conventional methods, the proposed techniques were shown to give more consistent estimation of seismic demand for a wide range of periods. This method was found to be more robust in comparison with one the most advanced available techniques, i.e. Conditional Mean Spectrum (CMS). The selection part of this method requires ground motion intensity data that may not be readily available. A comprehensive dataset of several ground motion intensity measures was generated from records in three major ground motion databases. This dataset is publically available at www.polymtl.ca/structures/en/.

10.2.2 Seismic design and demand on BRBFs

Extensive numerical modeling and analysis was conducted to estimate the seismic demand on multi-storey buildings with BRBF designed according to the recent Canadian national building code (NBCC 2010) and steel design standard (CSA S16-09). Current codes' analysis and design requirements were critically reviewed. The NBCC empirical expression for fundamental period of

steel braced frames was found to underestimate the actual period of BRBFs, especially in the east of Canada. A modified expression was suggested based on analysis of 3- to 15-storeys models in eastern and western Canada. It was found that, when capacity design rules are followed, among several studied configurations "back-to-back Split-X" vertical truss would be the most efficient configuration to obtain optimum steel tonnage of braced bays' beams and columns. Ground motion sets representing different seismicity sources in eastern and western Canada were developed for this study. Results of nonlinear static and dynamic analyses indicated that performance of code-compliant BRBFs is generally satisfactory. Nonetheless, this system is expected to sustain a considerable permanent lateral displacement after being exposed to the design earthquake. Intra–plate earthquakes in the west coast of Canada were found to impose more intense seismic demands on BRBFs in comparison to the west Coast inter–plate and eastern Canadian intra–plate earthquakes. A comparison with a well-known U.S. case study showed that the expected peak and cumulative displacement demand on the Canadian code-complaint BRBF would be considerably lower, especially in the east of Canada. In western Canada, seismic demands on BRBFs designed for soft soil condition is higher than those for the corresponding system on soft rock sites. This non-uniform response suggests that NBCC 2010 foundation factors for soft soil conditions may need to be revisited. NBCC's prescribed force in floor diaphragms was found to be inadequate, especially at the lower levels. It was shown that the floor diaphragms in BRBFs are vulnerable to several intense overloading cycles that may cause failure in the diaphragms and/or their connections to the frame. Such failure could lead to serious may lead to serious disruption or discontinuity in the seismic load path. Analysis of BRBFs' columns showed that the force demand is not likely to exceed the factored design forces prescribed in CSA S16-09. Analysis results showed that simultaneous large axial and bending demands on the BRBF columns is not likely to occur and the combined axial and bending moments currently specified in S16 for the design of BRBF columns was found to be overly conservative. An alternative value for the "additional bending moment" was proposed along with the most probable bending moment profile that should be considered in the design. Earthquake-representative displacement loading histories for qualification testing of BRBs were developed based on response of BRBFs to the different types of design earthquakes anticipated in eastern and western Canada.

10.2.3 Mechanical behaviour of 350WT steel

CSA G40.21-350WT Category 4 represents an excellent choice for BRB core material owing to its ductility and enhanced toughness at low temperatures. Motivated by the lack of reliable data on important mechanical properties of this steel type under seismic loading conditions, a comprehensive material testing program was planned and carried out. This program aimed at characterizing basic mechanical properties, cyclic strain hardening, rate dependency, and low cycle fatigue life of this type of steel under uniaxial loading condition. Response at room (+25 °C) and subfreezing (−40 °C) temperatures were targeted in this testing program and relatively wide range of inelastic strain amplitudes and strain rates were considered. The experimental results indicated that, for the conditions present in the test program, the subfreezing temperature condition does not reduce the fracture ductility and low cycle fatigue life of this type of steel. Yield and tensile resistance of 350WT significantly increased under the combination of fast rate loading and subfreezing temperature. Test results were employed to calibrate parameters of several well-established fatigue damage models. These models were adopted to predict low cycle fatigue failure under simple and complex variable amplitude uniaxial loadings. The predicted failure lives were in excellent agreement with the laboratory observations especially when strain-based damage model was implemented. Based on the test results, prediction models for the essential design inputs of the BRB restraining system were developed and calibrated. It was shown that the lateral stiffness of the loading frame is of great importance for cyclic tests under large inelastic strain. Insufficient stiffness would result in premature failure of specimens due to bending deformation. Consequently, this may lead to a fatigue damage model that underestimates the fracture life under large amplitude inelastic deformations.

10.2.4 Analysis of core normal thrust

The key to obtaining desirable seismic performance from BRBs is the proper design of the buckling-restraining mechanism. Behaviour of this mechanism is controlled by complex interaction between several factors. Central to this behaviour is the generated normal reaction or thrust when inelastic buckling of the core member is laterally constrained. The restrainer must have enough capacity to resist the imposed normal thrust and sufficient stiffness to prevent excessive opening of the restrainer. In this research, a practical analytical approach for estimation of the normal thrust on the restraining system is developed. This method directly accounts for the effects

of core cyclic strain hardening, interfacial friction and its flow path, Poisson's effect, and restrainer flexibility. When validated against the experimental data and the results of finite element analysis, it was shown that this method can reliably predict the normal thrust, buckling mode, and axial resistance of the core member under cyclic loading. A minimum elastic restraining stiffness required for stable inelastic response was also proposed.

10.2.5 Seismic qualification of all-steel BRBs

A patent-free all-steel buckling-restrained brace was conceptually developed, analytically designed, numerically simulated, and experimentally qualified. The developed concept is simple to fabricate and can be easily manufactured by ordinary structural steel fabricators without need for concrete or mortar casting and a curing procedure. This system introduces several innovations:

- An effective new option to reduce friction at the interface of the core and the restrainer;
- A simple hinge connection to limit the frame action-induced bending demand on the BRB member;
- An effective stiffening detail for the non-yielding segment of BRB to prevent localized damage.

In addition to the conventional step-wise symmetrical loading, displacement histories from response of BRBFs to crustal and megathrust subduction earthquakes were considered in the qualification procedure. These are the earthquake types expected in the west coast of Canada. The developed system showed an excellent performance under different severe earthquake loading conditions. In particular, under intensive cyclic loading very large inelastic cumulative ductility was obtained without strength or stiffness degradation. Among the tested interfacial conditions, the combination of stainless steel sheet and UHMW-PE[10] was found to be the most efficient option in managing the frictional forces at the interface between the core and the restrainer. The simple knife-plate hinge implemented at the core-to-gusset plate joint was shown to be effective in controlling the undesirable frame-action induced flexural demand. Very good agreement was found between the experimental measurements and the analytically predicted flexural demand on the knife-plate

[10] Ultra-high-molecular-weight polyethylene

hinge. The developed BRB system can be implemented as a reliable source of seismic energy dissipation in the buildings, bridges, and heavy industrial structures.

10.3 Recommendations

This research work has investigated and addressed a number of issues related to seismic design, analysis and qualification of all-steel buckling-restrained braces with special emphasis on its Canadian applications. This study raised several additional questions and concerns that could be the subjects of further research. For each of the investigated subjects, limitations of the current study and the recommendations for future research will be briefly discussed.

10.3.1 Ground motion selection and scaling

– As discussed in Chapter 4, the south-western part of Canada is exposed to seismic hazard from crustal, deep inslab, and megathrust earthquakes. Currently, there is no established ground motion database for the inslab and megathrust earthquakes. Due to lack of data, in this study, records from inslab earthquakes were not used and in the case of megathrust earthquakes only simulated ground motion records were included in the time history analyses. Historical earthquake data for eastern Canada is also scarce and the available data were limited to the simulated and hybrid ground motion records. Recently, a comprehensive database of ground motion records for eastern North America has been compiled through NGA-East program (Goulet *et al.*, 2014). This database should be considered in future studies.

– In the current study, parameters that define the window size for the Least Moving Average technique were chosen to minimize the scatter of scaling factors. Further studies showed that a better overall fit to the target spectrum can be achieved by changing the average window size. An optimization study could be useful to find the windows size parameters that give the best fitted average spectrum with reasonable variation.

10.3.2 Seismic demand on BRBFs

– In this study, a rather simple BRBF model was used to evaluate the performance of code-conforming building prototypes under a code-prescribed level of seismic hazard. Inelastic behaviour of BRBs were modeled with Bouc-Wen hysteresis law that may not be accurate enough under complex loading histories. Thus, a more refined BRB model may be necessary,

especially if performance beyond 2% in 50 years hazard level is being sought. Ideally, this BRB model should reproduce important inelastic behaviour such as nonlinear kinematic hardening, strain-range memorization, rate dependency, mean stress relaxation, and ratcheting under asymmetric loading cycles. In addition, it is possible that at large interstorey drifts, axial stiffness of restrainer is engaged due to the contact between the restrainer and the non-yielding segment. This can induce larger-than-expected force demand on the framing system which may result in connection fracture or column buckling. In the current study, columns were modeled using elastic beam column elements as column inelastic response was not expected under design earthquake. To have a more reliable response, column modeling should be reconsidered by including material inelasticity, initial imperfections, residual stress, and accurate boundary conditions at the beam-column joints and at the connection to the foundation.

- In the current study, the effect of the gravity system on the lateral response was only partially accounted for. Recent studies have shown that system overstrength may be significantly increased when lateral stiffness and strength of the gravity system is engaged.
- This study showed that large residual drifts in buildings with BRBF should be expected after a design level earthquake. Nevertheless, an advanced inelastic model is required to capture the residual displacement with reliable accuracy. This model may be first calibrated against laboratory results presented in (Fahnestock, *et al.*, 2007a). In addition, recent studies have shown that steel braced frames have an inherent re-centring capability due to continuity of floor diaphragm. In fact, shear-only designed beam-column joints may have significant rotational restraint due to presence of diaphragm slab. This should be accounted for by using more realistic models for beam-column joints of the gravity system.
- This study showed that BRBF floor diaphragms are likely to experience several occasions of intense overloading during the design earthquake. In this study, diaphragms are not modelled explicitly and thus the possible extent of damage could not be known. To have a better insight, diaphragm and its components, i.e. chords, collectors, and connections thereof, should be included in the numerical modeling.
- In the present study, conditional probability of failure was defined according to several performance limits. To have a more reliable decision making tool, complete fragility curves for code-conforming BRBFs should be developed. This requires a refine inelastic model and conducting incremental dynamic analysis for a range of ground motion intensities.

– This research showed that the current NBCC design forces for floor diaphragms may not be adequate, at least for buildings with BRBFs, and the NBCC requirements may need to be reconsidered. Nonlinear time history analysis showed that the diaphragm forces are approximately constant along the building height and are well-correlated with the available lateral strength at the base of building. The possibility of developing a simple method for estimation of diaphragm design loads should be considered.

10.3.3 Characterization of core material behaviour

– Although the test setup devised for this study was very effective in maintaining uniaxial loading conditions, placement of the specimens in the setup was a slow and time consuming process. For future studies, using smaller testing frames equipped with high precision hydraulic collet grips should be considered. This grip type offers a precise alignment and allows quick specimen placement.

– Many cycles with small to moderate inelastic deformation amplitudes are often found in the response of structures to earthquakes. In the current study, focus was given to the strain amplitudes larger than 1% and the low cycle fatigue model obtained from these tests was extrapolated to smaller strains. To have a more inclusive fatigue model, small to moderate inelastic strains, e.g. between 0.3% and 1.0%, should be included in the testing program. This would be especially important for failure prediction under long duration megathrust earthquakes as they contain a large number of small amplitude cycles.

– Complementary heat transfer finite element analysis conducted in this study suggest that, in some experiments, the gauge region temperature can significantly differ from the target value. This was mainly attributed to the thermal conductivity of the test setup. In order to achieve more reliable test data at subfreezing conditions, a stricter thermal insulation of the test setup should be considered in future studies. In particular, the inward heat flux path that allows the heat exchange with the outside should be minimized. This could be achieved by freezing the test fixture outside the cold chamber.

– Analysis of the data from the cyclic tests revealed a strong dependency of isotropic yield size on the largest strain range experienced by the material in preceding loading cycles. This is a known phenomenon and is referred to by *strain-range memorization* effect. This effect would be an important feature of BRB response under seismic loadings with random sequence of

excursions. The BRB member can immediately develop a significant isotropic hardening (cyclic yield strength) following a large excursion. To accurately characterize this effect in structural steels a special loading history should be designed.

– Linear damage accumulation rule (Miner's rule) is widely used for fatigue failure prediction under variable amplitude loading. In the Miner's rule, damage is independent of loading sequence. The results of current study indicate that Miner's rule may not precise enough when amplitudes of the displacement history, e.g. local axial strain in BRB core, has a certain sequence. Use of more advanced damage accumulation rules that account for loading sequence effect is recommended for future studies.

10.3.4 Analysis of normal thrust on restrainer

– Experimental observations and finite element simulations indicate that the core buckling wavelengths and waveforms are not periodic. In this study, the non-periodic nature of wavelengths was considered by accounting for frictional effects However, it was not possible to establish a rule for correctly predicting the waveforms. Observations showed that, under large inelastic deformations, buckling waveforms at the ends and the middle of the core are quite different: at the ends, the core buckles with the single contact point configuration while buckling at the middle often has a line contact form. More in-depth studies are required to understand the conditions that constitute the waveform at different locations along the core.

– The proposed analytical model assumes a total restrainer stiffness for the entire restrainer while the reality is different: the stiffness is in fact distributed along the length of the restrainer and the demand on the restrainer varies along the length of the core depending on the waveforms and wavelengths. Hence, the available stiffness in regions of high demand is likely to be less than assumed in the model. Prediction of normal thrust can probably be improved by including a more realistic model for restraining stiffness. In the analytical model, the restrainer can be assumed as a multi-span continuous beam that is supported at the bolts' positions. Influence lines of this continuous beam could then be used to compute the locally mobilized stiffness against buckling waves that form at given positions along this beam.

– As shown in Chapter 9, results from 2D and 3D finite element models were found to be quite different. This reasons for the observed differences could not be established and further study is needed to fully understand both responses.

- In the current study, Coulomb model was employed to include the effect of friction in both analytical and finite element models. According to the Coulomb model, tangent and normal stresses are linearly correlated by static or kinetic coefficient of friction. In reality, the coefficient of friction is a function of normal pressure and sliding rate. A more refined friction model that could include these effects should be considered in future studies. Calibration of this model would need a comprehensive testing plan.
- In the finite element modeling of the core's inelastic behaviour, characteristics of the steel material such as the upper yield, the yield plateau, strain-range memorization, and degradation of Young's modulus were not considered. It is recommended that these properties be reproduced in future studies.
- In the current study, the fracture of the core under cyclic loading was not incorporated in the analytical and finite element simulation as it was an unlikely failure mode when BRB is designed properly. However, when the friction is severe and the restrainer does not have enough capacity, the core may experience premature fracture under cyclic loading. This possibility should be considered in future studies. The low cycle fatigue damage model that is calibrated in this study could be implemented for this purpose.

10.3.5 Seismic qualification

- In this study, the combination of stainless steel sheet and UHMW-PE liner was found very efficient for minimizing the frictional actions at the core-restrainer interface. Characterizing the frictional behaviour of this interfacial condition should be considered in future studies. Particularly, static and kinetic coefficients of friction under various combinations of normal pressure, sliding rate, and sliding history would be of interest.
- The all-steel BRB developed in this study was qualified under loading conditions which are more intensive than the current S16 requirements. This intensive loading was chosen to investigate the BRB behaviour under ultimate conditions. For real applications, especially for eastern Canada, a lighter restraining system would be sufficient as the displacement demand would be much lower. The findings of this research can be exploited to design all-steel restraining systems for the expected seismic demand in eastern and western Canada. These BRBs are recommended to be tested under loading protocols such as those proposed in (Dehghani, *et al.*, 2012b).

- Due to the long length of the BRB specimens examined in this study, global stability requirement dictated using pretensioned bolts to join the restrainer sections. Due to presence of large bolt preload, the imposed normal thrust on the restrainer could not be directly measured by the instrumented bolts. In the current study, a combination of finite element analysis and bolt readings were exploited to estimate the normal thrust, which required several assumptions. For future tests, considering a shorter length BRB is recommended if precise measurement of normal thrust is sought. The restrainer of this such a BRB can be bolted with small preload without affecting the overall stability of the member.
- A single edge gusset plate was found to be very effective in mitigating the flexural demand on the testing subassembly. With having only one edge of gusset plate connected to the frame, beam and column could rotate rather independently and this prevented the large in-plane stiffness of gusset plate from being activated. However, it was found that transferring the large BRB force to the beam-to-column clip angles resulted in considerable bearing deformation in the bolt holes. Behaviour of this beam-to-column joint should be studied in more details.
- A steel–steel interfacial condition, i.e. without debonding material, represents an economical option for areas with low seismic demand such as eastern Canada. Qualifying this condition was included in the testing program but a poor performance was observed due to an unforeseen jamming problem that can be easily solved by providing a better free sliding condition. It is recommended to design and test an all-BRB with no debonding layer to properly characterize BRB response with this interface condition. To avoid jamming problem, it is recommended to use long slotted holes for the end spacer or to lubricate the counterface of the end spacer and the core using permanent solid lubricants such as molybdenum disulfide. Use of gel grease or oil-based products is not recommended as they may dry and lose their lubricity.
- In the experimental program, most specimens were tested under repeated loading until core fracture took place. Since core fracture typically happened at large tensile forces while the brace was being stretched, no obvious trace of core buckling waves could be obtained when the specimen was opened after the tests. In future studies, it is recommended to stop testing at a large compressive deformation so that buckling waveforms and wavelengths could be easily observed after testing.
- This study indicates that the CSA G40.21-350WT steel can offer a very ductile behaviour at low temperatures. This makes the 350WT a good candidate for the BRB core in special

applications such as exposed structures in cold climates. However, material testing was performed on carefully machined coupons that did not reflect the conditions in actual BRBs. Testing performed in this study should be complemented by full-scale BRB tests to be conducted under low-temperature and seismically induced loading rate conditions.

BIBLIOGRAPHY

Adams, J., & Atkinson, G. M. (2003). Development of seismic hazard maps for the proposed 2005 edition of the National Building Code of Canada. *Canadian Journal of Civil Engineering, 30*(2), 255-271.

AISC. (2005). AISC 341-05, Seismic Provisions for Structural Steel Buildings (Including Supplement No. 1). Chicago, IL: American Institute of Steel Construction, Inc.

AISC. (2010). ANSI/AISC 341-10, Seismic Provisions for Structural Steel Buildings. Chicago, IL: American Institute of Steel Construction, Inc.

Ancheta, T. D., Darragh, R. B., Stewart, J. P., Seyhan, E., Silva, W. J., Chiou, B. S., Wooddell, K. E., Graves, R. W., Kottke, A. R., Boore, D. M., Kishida, T., & Dobahue, J. L. (2013). *PEER NGA-West2 Database*: Pacific Earthquake Engineering Reseach Center.

Antoniou, S., Pinho, R., & Bianchi, F. (2012). SeismoSignal (Version 5.0.0): Seismosoft Ltd.

Ariyaratana, C., & Fahnestock, L. A. (2011). Evaluation of buckling-restrained braced frame seismic performance considering reserve strength. *Engineering Structures, 33*(1), 77-89.

ASCE. (2010). Minimum Design Loads for Buildings and Other Structures (pp. 608). Reston, Virginia: American Society of Civil Engineers.

Asgarian, B., & Shokrgozar, H. R. (2009). BRBF response modification factor. *Journal of Constructional Steel Research, 65*(2), 290-298.

ASTM. (2004). E606 − 04e1 Standard Practice for Strain-Controlled Fatigue Testing. West Conshohocken, PA: ASTM International.

ASTM. (2005). E1049 − 85(2005) Standard Practices for Cycle Counting in Fatigue Analysis. West Conshohocken, PA: ASTM International.

ASTM. (2007). E23 - 07ae1 Standard Test Methods for Notched Bar Impact Testing of Metallic Materials. West Conshohocken, PA: ASTM International.

ASTM. (2009). E8/E8M − 09 Standard Test Methods for Tension Testing of Metallic Materials. West Conshohocken, PA: ASTM International.

ASTM. (2011). A709/A709M – 11 Standard Specification for Structural Steel for Bridges. West Conshohocken, PA: American Society for Testing and Materials,.

ASTM. (2012). E1012 −12 Standard Practice for Verification of Testing Frame and Specimen Alignment Under Tensile and Compressive Axial Force Application: ASTM International.

ATC. (2011). *75% Draft - Seismic Performance Assessment of Buildings* (ATC-58-1). Redwood City, CA: Applied Technology Council.

Atkinson, G. M. (2005). Ground Motions for Earthquakes in Southwestern British Columbia and Northwestern Washington: Crustal, In-Slab, and Offshore Events. *Bulletin of the Seismological Society of America, 95*(3), 1027-1044.

Atkinson, G. M. (2009). Earthquake time histories compatible with the 2005 National building code of Canada uniform hazard spectrum. *Canadian Journal of Civil Engineering, 36*(6), 991-1000.

Atkinson, G. M., & Boore, D. M. (2003). Empirical Ground-Motion Relations for Subduction-Zone Earthquakes and Their Application to Cascadia and Other Regions. *Bulletin of the Seismological Society of America, 93*(4), 1703-1729.

Atkinson, G. M., & Macias, M. (2009). Predicted Ground Motions for Great Interface Earthquakes in the Cascadia Subduction Zone. *Bulletin of the Seismological Society of America, 99*(3), 1552-1578.

Baker, J. W. (2011). Conditional Mean Spectrum: Tool for Ground-Motion Selection. *Journal of*

Structural Engineering, 137(3), 322-331.

Baker, J. W., & Jayaram, N. (2008). Correlation of Spectral Acceleration Values from NGA Ground Motion Models. *Earthquake Spectra, 24*(1), 299-317.

Bazzurro, P., & Cornell, C. A. (1999). Disaggregation of seismic hazard. *Bulletin of the Seismological Society of America, 89*(2), 501-520.

Beaumont, E., & Annan, C.-D. (2016). *Cyclic Response of Structural Stainless Steel Plate Under Large Inelastic Strains*. Paper presented at the Annual Conference of the Canadian Society for Civil Engineering, London, Ontario.

Black, C., Makris, N., & Aiken, I. (2004). Component Testing, Seismic Evaluation and Characterization of Buckling-Restrained Braces. *Journal of Structural Engineering, 130*(6), 880-894.

Black, C. J., Makris, N., & Aiken, I. (2002). *Component Testing, Stability Analysis and Characterization of Buckling-Restrained Unbonded Braces™*. Tokyo: Nippon Steel Corporation.

Black, R. G., Bill, W. W. A., & Popov, E. P. (1980). *Inelastic Buckling of Steel Struts Under Cyclic Load Reversals* (UCB/EERC-80/40). Berkeley, California: Earthquake Engineering Research Center.

Bolduc, P., & Tremblay, R. (2003). *Experimental Study of the Seismic Behaviour of Steel Braces with Concrete Filled Tube and Double Steel Tube Buckling Restrained Mechanisms* (Project EPM/GCS-2003-01). Montreal: Ecole Polytechnique de Montreal.

Bommer, J. J., & Acevedo, A. B. (2004). The Use of Real Earthquake Accelerograms as Input to Dynamic Analysis. *Journal of Earthquake Engineering, 8*(Special Issue 1), 43-91.

Bommer, J. J., & Martínez-Pereira, A. (1999). The Effective Duration of Earthquake Strong Motion. *Journal of Earthquake Engineering, 3*(2), 127-172.

Bondonet, G., & Filiatrault, A. (1997). Frictional Response of PTFE Sliding Bearings at High Frequencies. *Journal of Bridge Engineering, 2*(4), 139-148.

Boore, D. M., & Atkinson, G. M. (2008). Ground-Motion Prediction Equations for the Average Horizontal Component of PGA, PGV, and 5%-Damped PSA at Spectral Periods between 0.01 and 10.0 *Earthquake Spectra, 24*(1), 99-138.

Boore, D. M., & Joyner, W. B. (1997). Site amplifications for generic rock sites. *Bulletin of the Seismological Society of America, 87*(2), 327-341.

Bosco, M., & Marino, E. M. (2013). Design method and behavior factor for steel frames with buckling restrained braces. *Earthquake Engineering & Structural Dynamics, 42*(8), 1243-1263.

Bradley, B. A. (2010). A generalized conditional intensity measure approach and holistic ground-motion selection. *Earthquake Engineering & Structural Dynamics, 39*(12), 1321-1342.

Bradley, B. A. (2012). A ground motion selection algorithm based on the generalized conditional intensity measure approach. *Soil Dynamics and Earthquake Engineering, 40*(2012), 48-61.

Bregoli, G., Genna, F., & Metelli, G. (2016). Analytical estimates for the lateral thrust in bolted steel buckling-restrained braces. *Journal of Mechanics of Materials and Structures, 11*(2), 173-196.

Bridgman, P. (1944). The stress distribution at the neck of a tension specimen. *Transactions of the ASM, 32*, 553-572.

Carr, A. J. (2008). RUAUMOKO-Inelastic dynamic analysis program. Christchurch, New Zealand: University of Canterbury, Department of Civil Engineering.

Cassidy, J., Rogers, G., Lamontagne, M., Halchuk, S., & Adams, J. (2010). Canada's earthquakes: 'The good, the bad, and the ugly'. *Geoscience Canada, 37*(1).

CEN. (1998). EuroCode 8: Design provisions for earthquake resistance – Part 1: General rules, seismic actions and rules for buildings. Bruxelles: European Committee for Standardization.

CEN. (2010). EN 15129:2010 Anti-seismic devices: European Committee for Standardization.

Chaboche, J. L. (1989). Constitutive equations for cyclic plasticity and cyclic viscoplasticity. *International Journal of Plasticity, 5*(3), 247-302.

Chai, H. (1998). The post-buckling response of a bi-laterally constrained column. *Journal of the Mechanics and Physics of Solids, 46*(7), 1155-1181.

Chai, H. (2002). On the post-buckling behavior of bilaterally constrained plates. *International Journal of Solids and Structures, 39*(11), 2911-2926.

Charalampakis, A. E., & Koumousis, V. K. (2008). Identification of Bouc–Wen hysteretic systems by a hybrid evolutionary algorithm. *Journal of Sound and Vibration, 314*(3–5), 571-585.

Charalampakis, A. E., & Koumousis, V. K. (2009). A Bouc–Wen model compatible with plasticity postulates. *Journal of Sound and Vibration, 322*(4–5), 954-968.

Charney, F. A. (2008). Unintended Consequences of Modeling Damping in Structures. *Journal of Structural Engineering, 134*(4), 581-592.

Chen, H., Grondin, G. Y., & Driver, R. G. (2005). *Fatigue Resistance of High Performance Steel* (Structural Engineering Report No. 258). Edmonton: University of Alberta.

Chen, Q., Wang, C.-L., Meng, S., & Zeng, B. (2016). Effect of the unbonding materials on the mechanic behavior of all-steel buckling-restrained braces. *Engineering Structures, 111*, 478-493.

Chopra, A. K. (2011). *Dynamics of structures : theory and applications to earthquake engineering*. Upper Saddle River, NJ: Pearson Prentice Hall.

Chou, C.-C., & Chen, S.-Y. (2010). Subassemblage tests and finite element analyses of sandwiched buckling-restrained braces. *Engineering Structures, 32*(8), 2108-2121.

Christopulos, A. S. (2005). *Improved seismic performance of buckling restrained braced frames.* University of Washington.

Cimellaro, G., Reinhorn, A., D'Ambrisi, A., & De Stefano, M. (2011). Fragility Analysis and Seismic Record Selection. *Journal of Structural Engineering, 137*(3), 379-390.

Clifton, C., Bruneau, M., MacRae, G., Leon, R., & Fussell, A. (2011). Steel structures damage from the Christchurch earthquake series of 2010 and 2011. *Bulletin of the New Zealand Society for Earthquake Engineering, 44*(4), 297-318.

CSA. (2004). G40.20-04/G40.21-04 (R2009) General Requirements for Rolled or Welded Structural Quality Steel/ Structural Quality Steel: Canadian Standards Association.

CSA. (2006). Canadian Highway Bridge Design Code. Mississauga, Ontario, Canada: Canadian Standards Association.

CSA. (2009). CSA S16-09, Limit States Design of Steel Structures. Mississauga, Ontario, Canada: Canadian Standards Association.

CSA. (2014). CSA S16-14, Design of Steel Structures. Mississauga, Ontario, Canada: Canadian Standards Association.

CSI. (2010). Integrated software for structural analysis & design SAP2000 (Version 15.0.1). Berkeley, CA: Computers and Structures, Inc.

D'Aniello, M., Della Corte, G., & Mazzolani, F. (2009). *"All-steel" buckling-restrained braces for seismic upgrading of existing reinforced concrete buildings.* Paper presented at the 6th International Conference on Behaviour of Steel Structures in Seismic Areas - STESSA 2009, Philadelphia, Pennsylvania.

D'Aniello, M., Della Corte, G., & Landolfo, R. (2014). Finite Element Modelling and Analysis of

"All-Steel" Dismountable Buckling Restrained Braces. *Open Construction and Building Technology Journal, 8*(1), 216-226.

Dehghani, M., & Tremblay, R. (2012a). *Development of standard dynamic loading protocol for buckling-restrained braced frames.* Paper presented at the 7th International Conference on Behaviour of Steel Structures in Seismic Areas - STESSA 2012, Santiago, Chile.

Dehghani, M., & Tremblay, R. (2012b). *Standard Dynamic Loading Protocols for Seismic Qualification of BRBFs in Eastern and Western Canada.* Paper presented at the 15th World Conference on Earthquake Engineering, Lisbon, Portugal.

Dehghani, M., & Tremblay, R. (2016a). An Analytical Model for Estimating Restrainer Design Forces in Bolted Buckling-Restrained Braces. *Journal of Constructional Steel Research* (submitted).

Dehghani, M., & Tremblay, R. (2016b). Design and Full-Scale Experimental Evaluation of a Seismically Resilient Steel Buckling Restrained Brace System. *Earthquake Engineering and Structural Dynamics* (submitted).

Dehghani, M., & Tremblay, R. (2016c). Robust Period-Independent Ground Motion Selection and Scaling for Effective Seismic Design and Assessment. *Journal of Earthquake Engineering, 20*(2), 185-218.

Dehghani, M., & Tremblay, R. (2017a). *Seismic Induced Floor Accelerations and Diaphragm Forces for Buckling Restrained Braced Frames*. Paper presented at the 16th World Conference on Earthquake Engineering, Santiago, Chile.

Dehghani, M., & Tremblay, R. (2017b). Seismic Performance of Canadian Code-Conforming Buckling-Restrained Braced Frames. (under preparation).

Dehghani, M., Tremblay, R., & Leclerc, M. (2016d). Fatigue failure of 350WT steel under large-strain seismic loadings at room and subfreezing temperatures. *Construction and Building Materials* (submitted).

Della Corte, G., D'Aniello, M., & Landolfo, R. (2015). Field Testing of All-Steel Buckling-Restrained Braces Applied to a Damaged Reinforced Concrete Building. *Journal of Structural Engineering, 141*(1), 1-11.

Deylami, A., & Mahdavipour, M. A. (2016). Probabilistic seismic demand assessment of residual drift for Buckling-Restrained Braced Frames as a dual system. *Structural Safety, 58*, 31-39.

Dolce, M., Cardone, D., & Croatto, F. (2005). Frictional Behavior of Steel-PTFE Interfaces for Seismic Isolation. *Bulletin of Earthquake Engineering, 3*(1), 75-99.

Domokos, G., Holmes, P., & Royce, B. (1997). Constrained Euler buckling. *Journal of Nonlinear Science, 7*(3), 281-314.

Dowling, N. E. (2009). Mean stress effects in strain–life fatigue. *Fatigue & Fracture of Engineering Materials & Structures, 32*(12), 1004-1019.

Dusicka, P., Itani, A. M., & Buckle, I. G. (2007). Cyclic response of plate steels under large inelastic strains. *Journal of Constructional Steel Research, 63*(2), 156-164.

Dusicka, P., & Tinker, J. (2012). Global Restraint in Ultra-Lightweight Buckling-Restrained Braces. *Journal of Composites for Construction, 17*(1), 139-150.

Dutta, A., & Hamburger, R. O. (2010). Case study of a 40-storey buckling-restrained braced frame building located in Los Angeles. *The Structural Design of Tall and Special Buildings, 19*(1-2), 77-93.

Eatherton, M. R., Fahnestock, L. A., & Miller, D. J. (2014). Computational study of self-centering buckling-restrained braced frame seismic performance. *Earthquake Engineering & Structural Dynamics, 43*(13), 1897-1914.

Elkady, A., & Lignos, D. G. (2015). Effect of gravity framing on the overstrength and collapse

capacity of steel frame buildings with perimeter special moment frames. *Earthquake Engineering & Structural Dynamics, 44*(8), 1289-1307.

Ellyin, F. (2012). *Fatigue damage, crack growth and life prediction*: Springer Science & Business Media.

Ellyin, F., & Kujawski, D. (1984). Plastic Strain Energy in Fatigue Failure. *Journal of Pressure Vessel Technology, 106*(4), 342-347.

Erochko, J., Christopoulos, C., Tremblay, R., & Choi, H. (2011). Residual Drift Response of SMRFs and BRB Frames in Steel Buildings Designed according to ASCE 7-05. *Journal of Structural Engineering, 137*(5), 589-599.

Eryaşar, M. E., & Topkaya, C. (2010). An experimental study on steel-encased buckling-restrained brace hysteretic dampers. *Earthquake Engineering & Structural Dynamics, 39*(5), 561-581.

Fahnestock, L. A. (2006). *Analytical and large-scale experimental studies of earthquake-resistant buckling-restrained braced frame systems.* PhD Dissertation, Lehigh University, Bethlehem, Pennsylvania.

Fahnestock, L. A., Ricles, J. M., & Sause, R. (2007a). Experimental Evaluation of a Large-Scale Buckling-Restrained Braced Frame. *Journal of Structural Engineering, 133*(9), 1205-1214.

Fahnestock, L. A., Sause, R., & Ricles, J. M. (2007b). Seismic Response and Performance of Buckling-Restrained Braced Frames. *Journal of Structural Engineering, 133*(9), 1195-1204.

Fatemi, A., & Yang, L. (1998). Cumulative fatigue damage and life prediction theories: a survey of the state of the art for homogeneous materials. *International Journal of Fatigue, 20*(1), 9-34.

FEMA. (2009). *Quantification of Building Seismic Performance Factors* (FEMA P695). Washington DC: Federal Emergency Management Agency.

Ferguson, W., Nashid, H., Clifton, G., Kral, M., Lopert, S., & MacRae, G. (2013). *The Performance and Remnant Life of Structural Steel in an Earthquake Damaged Building.* Paper presented at the Steel Innovations Conference, Christchurch, New Zealand.

Filippou, F. C., Popov, E. P., & Bertero, V. V. (1983). *Effects of bond deterioration on hysteretic behavior of reinforced concrete joints* (UCB/EERC-83/19). Berkeley, California: Earthquake Engineering Research Center.

Galambos, T. V., & Surovek, A. E. (2008). *Structural stability of steel: concepts and applications for structural engineers*: John Wiley & Sons.

Gatto, K., & Uang, C. (2003). Effects of Loading Protocol on the Cyclic Response of Woodframe Shearwalls. *Journal of Structural Engineering, 129*(10), 1384-1393.

Genna, F., & Bregoli, G. (2014). Small amplitude elastic buckling of a beam under monotonic axial loading, with frictionless contact against movable rigid surfaces. *Journal of Mechanics of Materials and Structures, 9*(4), 441-463.

Genna, F., & Gelfi, P. (2012a). Analysis of the Lateral Thrust in Bolted Steel Buckling-Restrained Braces. I: Experimental and Numerical Results. *Journal of Structural Engineering, 138*(10), 1231-1243.

Genna, F., & Gelfi, P. (2012b). Analysis of the Lateral Thrust in Bolted Steel Buckling-Restrained Braces. II: Engineering Analytical Estimates. *Journal of Structural Engineering, 138*(10), 1244-1254.

Golos, K., & Ellyin, F. (1988). A total strain energy density theory for cumulative fatigue damage. *Journal of pressure vessel technology, 110*(1), 36-41.

Goulet, C. A., Kishida, T., Ancheta, T. D., Cramer, C. H., Darragh, R. B., Silva, W. J., Hashash, Y. M. A., Harmon, J., Stewart, J. P., Wooddell, K. E., & Youngs, R. R. (2014). *PEER NGA-*

East database. Berkeley, California: Pacific Earthquake Engineering Research Center.

Gray, M. G., de Oliveira, J. C., Binder, J. I., & Christopoulos, C. (2014). *Effects of Post-Yield Stiffening and Strengthening on the Collapse Performance of Non-Buckling Braced Frames.* Paper presented at the 10th U.S. National Conference on Earthquake Engineering, Anchorage, Alaska.

Gu, Q., Zona, A., Peng, Y., & Dall'Asta, A. (2014). Effect of buckling-restrained brace model parameters on seismic structural response. *Journal of Constructional Steel Research, 98*, 100-113.

Halchuk, S., & Adams, J. (2003). *Fourth generation seismic hazard maps of Canada: Values for over 650 Canadian localities intended for the 2005 National Building Code of Canada* (Open File 4459). Ottawa, ON: Geological Survey of Canada.

Halchuk, S., Adams, J., & Anglin, F. (2007). *Revised Deaggregation of Seismic Hazard for Selected Canadian Cities.* Paper presented at the Ninth Canadian Conference on Earthquake Engineering, Ottawa, Ontario, Canada.

Hamdoon, M., Zamani, N., & Das, S. (2014). Effect of Combined Cold Temperature and Fatigue Load on Performance of G40. 21 Steel. *Materials Performance and Characterization, 3*(1), 49-64.

Hancock, J., & Bommer, J. J. (2006a). A State-of-Knowledge Review of the Influence of Strong-Motion Duration on Structural Damage. *Earthquake Spectra, 22*(3), 827-845.

Hancock, J., Bommer, J. J., & Stafford, P. J. (2008). Numbers of scaled and matched accelerograms required for inelastic dynamic analyses. *Earthquake Engineering & Structural Dynamics, 37*(14), 1585-1607.

Hancock, J., Watson-Lamprey, J., Abrahamson, N. A., Bommer, J. J., Markatis, A., McCoyh, E., & Mendis, R. (2006b). An Improved Method of Matching Response Spectra of Recorded Earthquake Ground Motion using Wavelets. *Journal of Earthquake Engineering, 10*(sup001), 67-89.

Haselton, C. B. (2009). *PEER 2009/01 - Evaluation of Ground Motion Selection and Modification Methods: Predicting Median Interstory Drift Response of Buildings*: Pacific Earthquake Engineering Research Center.

Heo, Y., Kunnath, S. K., & Abrahamson, N. (2011). Amplitude-Scaled versus Spectrum-Matched Ground Motions for Seismic Performance Assessment. *Journal of Structural Engineering, 137*(3), 278-288.

Higginbotham, A. B., & Hanson, R. D. (1976). Axial hysteretic behavior of steel members. *ASCE Journal of the Structural Division, 102*(7), 1365-1381.

Hoveidae, N., & Rafezy, B. (2013). Global Buckling Prevention Condition of All-Steel Buckling Restrained Braces. *Journal of Theoretical and Applied Mechanics, 51*(4), 891-902.

Hoveidae, N., Tremblay, R., Rafezy, B., & Davaran, A. (2015). Numerical investigation of seismic behavior of short-core all-steel buckling restrained braces. *Journal of Constructional Steel Research, 114*, 89-99.

Iervolino, I., & Cornell, C. A. (2005). Record Selection for Nonlinear Seismic Analysis of Structures. *Earthquake Spectra, 21*(3), 685-713.

Imai, K., Wakiyama, K., Tada, M., Kuwahara, S., & Yoneyama, T. (1991). A study on the stiffening effect of the Double Tube : Part 1 The procedure of the longitudinal loading test. *Summaries of technical papers of Annual Meeting Architectural Institute of Japan. Structures II, 1991*, 1281-1282 (in Japanese).

Imai, K., Yasui, N., & Yasuyoshi, U. (1997). *Development of Tube-in-Tube Type FLD Bracing Member (Force Limiting Device) and It's Impulsive Analysis.* Paper presented at the Annual

Technical Session and Meeting of Structural Stability Research Council, Toronto, Canada.
Imanpour, A., Auger, K., & Tremblay, R. (2016a). Seismic design and performance of multi-tiered steel braced frames including the contribution from gravity columns under in-plane seismic demand. *Advances in Engineering Software, 101*, 106-122.
Imanpour, A., Tremblay, R., Davaran, A., Stoakes, C., & Fahnestock, L. (2016b). Seismic Performance Assessment of Multitiered Steel Concentrically Braced Frames Designed in Accordance with the 2010 AISC Seismic Provisions. *Journal of Structural Engineering*, 1-13.
Isoda, K., Mase, S., Terada, T., & Satake, N. (2001). Development of Unbonded Brace Damper Restrained by Channel Section Steel : (Part 1) Purpose of Development and Outline of Damper. *Summaries of technical papers of Annual Meeting Architectural Institute of Japan. C-1, Structures III, Timber structures steel structures steel reinforced concrete structures, 2001*, 663-664 (in Japanese).
Isoda, K., Satake, N., Mase, S., Terada, T., & Horie, T. (2002). *Development of Unbonded Brace Damper Restrained by Channel Section Steel : (Part 4) Low Cycle Fatigue Tests*. Paper presented at the Academic Conference of Architecture, Structural system (in Japanese).
Jayaram, N., & Baker, J. (2010). *Ground-Motion Selection for PEER Transportation Research Program.* Paper presented at the 7th International Conference on Urban Earthquake Engineering (7CUEE) & 5th International Conference on Earthquake Engineering (5ICEE), Tokyo, Japan.
Jayaram, N., Lin, T., & Baker, J. W. (2011). A Computationally Efficient Ground-Motion Selection Algorithm for Matching a Target Response Spectrum Mean and Variance. *Earthquake Spectra, 27*(3), 797-815.
Jiang, Z., Guo, Y., Zhang, B., & Zhang, X. (2015). Influence of design parameters of buckling-restrained brace on its performance. *Journal of Constructional Steel Research, 105*, 139-150.
Josi, G., & Grondin, G. (2010). *Reliability-based management of fatigue failures* (SER 285). Edmonton, Alberta, Canada: University of Albetra.
Ju, Y. K., Kim, M.-H., Kim, J., & Kim, S.-D. (2009). Component tests of buckling-restrained braces with unconstrained length. *Engineering Structures, 31*(2), 507-516.
Kalkan, E., & Chopra, A. K. (2010). *Practical Guidelines to Select and Scale Earthquake Records for Nonlinear Response History Analysis of Structures* (Open-File Report 2010-1068): U.S. Geological Survey.
Kamaya, M. (2010). Fatigue properties of 316 stainless steel and its failure due to internal cracks in low-cycle and extremely low-cycle fatigue regimes. *International Journal of Fatigue, 32*(7), 1081-1089.
Kaneko, H., Nukui, Y., Tsuchida, T., Aoyagi, T., Kamiyama, H., & Kobayashi, M. (2000). Development of Braces with Tuning-Bolts on Buckling Stiffener and Application to Existing Buildings. *Journal of architecture and building science*(11), 99-104 (in Japanese).
Kanvinde, A. M., & Deierlein, G. G. (2005). *Continuum Based Micro-Models for Ultra Low Cycle Fatigue Crack Initiation in Steel Structures.* Paper presented at the Structures Congress 2005, New York, New York.
Kanvinde, A. M., Marshall, K., Grilli, D., & Bomba, G. (2014). Forensic Analysis of Link Fractures in Eccentrically Braced Frames during the February 2011 Christchurch Earthquake: Testing and Simulation. *Journal of Structural Engineering, 141*(5), 04014146.
Karavasilis, T. L., Kerawala, S., & Hale, E. (2012). Hysteretic model for steel energy dissipation

devices and evaluation of a minimal-damage seismic design approach for steel buildings. *Journal of Constructional Steel Research, 70*, 358-367.

Katsanos, E. I., Sextos, A. G., & Manolis, G. D. (2010). Selection of earthquake ground motion records: A state-of-the-art review from a structural engineering perspective. *Soil Dynamics and Earthquake Engineering, 30*(4), 157-169.

Katz, S., & Givli, S. (2015). The post-buckling behavior of a beam constrained by springy walls. *Journal of the Mechanics and Physics of Solids, 78*, 443-466.

Kawamura, H., Usami, T., Kasai, A., & Fujita, M. (2004). *Performance Tests of Light-weight BRBs.* Paper presented at the 7th Symposium on Ductility Design Method for Bridges, Tokyo (in Japanese).

Kempton, J. J., & Stewart, J. P. (2006). Prediction equations for significant duration of earthquake ground motions considering site and near-source effects. *Earthquake Spectra, 22*(4), 985-1013.

Khatib, I. F., Mahin, S. A., & Pister, K. S. (1988). *Seismic behavior of concentrically braced steel frames* (UCB/EERC-88/01). Berkeley, CA: Earthquake Engineering Research Center, University of California.

Kiggins, S., & Uang, C.-M. (2006). Reducing residual drift of buckling-restrained braced frames as a dual system. *Engineering Structures, 28*(11), 1525-1532.

Kim, J., & Choi, H. (2004a). Behavior and design of structures with buckling-restrained braces. *Engineering Structures, 26*(6), 693-706.

Kim, J., & Seo, Y. (2004b). Seismic design of low-rise steel frames with buckling-restrained braces. *Engineering Structures, 26*(5), 543-551.

Koboevic, S., Rozon, J., & Tremblay, R. (2012). Seismic Performance of Low-to-Moderate Height Eccentrically Braced Steel Frames Designed for North American Seismic Conditions. *Journal of Structural Engineering, 138*(12), 1465-1476.

Korzekwa, A. (2009). *Simulation numérique du comportement inélastique et conception parasismique d'un système de diagonales ductile confinées construit uniquement en acier.* École Polytechnique de Montréal, Montréal. (in French).

Korzekwa, A., & Tremblay, R. (2009, August 16-20). *Numerical simulation of the cyclic inelastic behaviour of BRBs.* Paper presented at the 6th International Conference on Behavior of Steel Structures in Seismic Areas – STESSA 2009, Philadelphia, Pennsylvania.

Kottegoda, N. T., & Rosso, R. (2008). *Applied statistics for civil and environmental engineers*: Wiley-Blackwell.

Kottke, A., & Rathje, E. M. (2008). A Semi-Automated Procedure for Selecting and Scaling Recorded Earthquake Motions for Dynamic Analysis. *Earthquake Spectra, 24*(4), 911-932.

Kramer, S. L. (1996). *Geotechnical earthquake engineering*. Upper Saddle River, N.J.: Prentice Hall.

Krawinkler, H., Gupta, A., Medina, R., & Luco, N. (2000). *Loading Histories for Seismic Performance Testing of SMRF Components and Assemblies - Report SAC/BD-00/10*: SAC Joint Venture (SEAOC, ATC and CUREe).

Krawinkler, H., & Zohrei, M. (1983). Cumulative damage in steel structures subjected to earthquake ground motions. *Computers & Structures, 16*(1–4), 531-541.

Kumar, M., Castro, J. M., Stafford, P. J., & Elghazouli, A. Y. (2011). Influence of the mean period of ground motion on the inelastic dynamic response of single and multi degree of freedom systems. *Earthquake Engineering & Structural Dynamics, 40*(3), 237-256.

Kurama, Y. C., & Farrow, K. T. (2003). Ground motion scaling methods for different site conditions and structure characteristics. *Earthquake Engineering & Structural Dynamics,*

32(15), 2425-2450.

Kuroda, M. (2002). Extremely low cycle fatigue life prediction based on a new cumulative fatigue damage model. *International Journal of Fatigue, 24*(6), 699-703.

Kuwahara, S., Tada, M., Yoneyama, T., & Imai, K. (1993). A Study on Stiffening Capacity of Double-Tube Members. *Journal of structural and construction engineering. Transactions of AIJ*(445), 151-158 (in Japanese).

Lagoda, T. (2001). Energy models for fatigue life estimation under uniaxial random loading. Part I: The model elaboration. *International Journal of Fatigue, 23*(6), 467-480.

Lamontagne, M., Halchuk, S., Cassidy, J. F., & Rogers, G. C. (2008). Significant Canadian Earthquakes of the Period 1600–2006. *Seismological Research Letters, 79*(2), 211-223.

Lemaître, J., & Chaboche, J.-L. (1990). *Mechanics of solid materials*. Cambridge: Cambridge University Press.

Lin, P.-C., Tsai, K.-C., Chang, C.-A., Hsiao, Y.-Y., & Wu, A.-C. (2016). Seismic design and testing of buckling-restrained braces with a thin profile. *Earthquake Engineering & Structural Dynamics, 45*(3), 339-358.

Lin, P.-C., Tsai, K.-C., Wang, K.-J., Yu, Y.-J., Wei, C.-Y., Wu, A.-C., Tsai, C.-Y., Lin, C.-H., Chen, J.-C., Schellenberg, A. H., Mahin, S. A., & Roeder, C. W. (2012). Seismic design and hybrid tests of a full-scale three-story buckling-restrained braced frame using welded end connections and thin profile. *Earthquake Engineering & Structural Dynamics, 41*(5), 1001-1020.

Lin, P.-C., Tsai, K.-C., Wu, A.-C., Chuang, M.-C., Li, C.-H., & Wang, K.-J. (2015). Seismic design and experiment of single and coupled corner gusset connections in a full-scale two-story buckling-restrained braced frame. *Earthquake Engineering & Structural Dynamics, 44*(13), 2177-2198.

Lin, T., Harmsen, S. C., Baker, J. W., & Luco, N. (2013). Conditional Spectrum Computation Incorporating Multiple Causal Earthquakes and Ground-Motion Prediction Models. *Bulletin of the Seismological Society of America, 103*(2A), 1103-1116.

López, W. A., Gwie, D. S., Saunders, C. M., & Lauck, T. W. (2002). *Lessons Learned From Large-Scale Tests of Unbonded Braced Frame Subassemblages.* Paper presented at the 71st annual convention of SEAOC, Sacramento, CA.

López, W. A., & Sabelli, R. (2004). *Steel Tips: Seismic Design of Buckling-Restrained Braced Frames*. Moraga, CA: Structural Steel Educational Council.

Luco, N., & Bazzurro, P. (2007). Does amplitude scaling of ground motion records result in biased nonlinear structural drift responses? *Earthquake Engineering & Structural Dynamics, 36*(13), 1813-1835.

Manabe, N., Shimokawa, H., Kamiya, M., Morino, S., & Kawaguchi, J. (1996). *Elasto-Plastic Behavior of Flat-Bar Brace Stiffened by Square Steel Tube.* Paper presented at the Summaries of technical papers of Annual Meeting Architectural Institute of Japan. C-1, Structures III, Timber structures steel structures steel reinforced concrete structures (in Japanese).

Manson, S. S., & Halford, G. R. (2006). *Fatigue and Durability of Structural Materials*: ASM International.

Mayes, R. L., Goings, C., Naguib, W., Harris, S., Lovejoy, J., Fanucci, J. P., Bystricky, P., & Hayes, J. R. (2004). *Comparative performance of buckling-restrained braces and moment frames.* Paper presented at the 13th World Conference on Earthquake Engineering, Vancouver.

Mazzoni, S., McKenna, F., Scott, M. H., & Fenves, G. L. (2006). *OpenSees command language*

manual: Pacific Earthquake Engineering Research (PEER) Center.

McCormick, J., Aburano, H., & Ikenaga, M. (2008). *Permissible residual deformation levels for building structures considering both safety and human elements.* Paper presented at the 14th World Conference on Earthquake Engineering, Beijing, China.

McGuire, R. K. (1995). Probabilistic seismic hazard analysis and design earthquakes: Closing the loop. *Bulletin of the Seismological Society of America, 85*(5), 1275-1284.

McGuire, R. K., Silva, W. J., & Costantino, C. J. (2002). *Technical basis for revision of regulatory guidance on design ground motions: hazard- and risk-consistent ground motion spectra guidelines* (NUREG/CR-6769). Washington, DC 20555-0001: U.S. Nuclear Regulatory Commission.

McKenna, F., Fenves, G., & Scott, M. (2006). OpenSees: Open system for earthquake engineering simulation: Pacific Earthquake Engineering Center, University of California, Berkeley, CA, http://opensees.berkeley.edu.

Mehdipanah, A., Mirghaderi, S. R., & Razavi Tabatabaei, S. A. (2016). Seismic performance of stiffness-based designed buckling-restrained braced frame and special moment-resisting frame dual systems. *Structure and Infrastructure Engineering, 12*(8), 918-935.

Mergos, P. E., & Beyer, K. (2014). Loading protocols for European regions of low to moderate seismicity. *Bulletin of Earthquake Engineering, 12*(6), 2507-2530.

Merritt, S., Uang, C.-M., & Benzoni, G. (2003). *Subassemblage Testing of Corebrace Buckling-Restrained Braces* (TR-2003/01): Department of Structural Engineering, University of California, San Diego.

Merzouq, S., & Tremblay, R. (2006). *Seismic Design of Dual Concentrically Braced Steel Frames for Stable Seismic Performance for Multi-Story Buildings.* Paper presented at the 8th U.S. National Conference on Earthquake Engineering, San Francisco, California.

Metelli, G., Bregoli, G., & Genna, F. (2016). Experimental study on the lateral thrust generated by core buckling in bolted-BRBs. *Journal of Constructional Steel Research, 122*, 409-420.

Midorikawa, M., Hishida, S., Iwata, M., Okazaki, T., & Asari, T. (2016). Bending Deformation of the Steel Core of Buckling-Restrained Braces *Geotechnical and Structural Engineering Congress 2016* (pp. 613-623): American Society of Civil Engineers.

Midorikawa, M., Iwata, M., Wakayama, T., Iizuka, R., Okazaki, T., & Asari, T. (2014). *Buckling-mode Number and Compressive-to-Tensile Strength Ratio of Buckling-Restrained Braces.* Paper presented at the 10th U.S. National Conference on Earthquake Engineering, Anchorage, Alaska.

Midorikawa, M., Wakayama, T., Iizuka, R., Asari, T., Murai, M., & Iwata, M. (2012). Experimental Study on Buckling-Restrained Braces using Steel Mortar Planks-Evaluation of the buckling mode number, compression-to-tension strength ratio and friction force. *Journal of Structural and Construction Engineering (Transactions of AIJ), 77*(681), 1763-1771 (in Japanese).

Miller, D. J., Fahnestock, L. A., & Eatherton, M. R. (2012). Development and experimental validation of a nickel–titanium shape memory alloy self-centering buckling-restrained brace. *Engineering Structures, 40*, 288-298.

Miner, M. A. (1945). Cumulative damage in fatigue. *Journal of applied mechanics, 12*(3), 159-164.

Moni, M., Moradi, S., & Alam, M. S. (2016). Response modification factors for steel buckling restrained braced frames designed as per the 2010 National Building Code of Canada. *Canadian Journal of Civil Engineering, 43*(8), 702-715.

Morino, S., Kawaguchi, J., Itoh, S., & Shimokawa, H. (1996). *Hysteretic Behavior of Stiffened*

Flat-Bar Braces. Paper presented at the International Conference on Advances in Steel Structures, Hong Kong.

Morrow, J. (1965). Cyclic plastic strain energy and fatigue of metals *Internal friction, damping, and cyclic plasticity*: ASTM International.

Naeim, F., & Lew, M. (1995). On the Use of Design Spectrum Compatible Time Histories. *Earthquake Spectra, 11*(1), 111-127.

Narihara, H., Tsujita, O., & Koetaka, Y. (2000). *The Experimental Study on Buckling Restarined Braces (Part 1: Experiment on Pin Connection Type)*. Paper presented at the Summaries of technical papers of Annual Meeting Architectural Institute of Japan. C-1, Structures III, Timber structures steel structures steel reinforced concrete structures (in Japanese).

Narihara, H., Tsujita, O., & Yasuda, S. (2002). *The Experimental Study on Buckling Restrained Braces (Part 4: Low Cycle Fatigue Test on Aseismic Brace with SN400B, SN490B)*. Paper presented at the Academic Conference of Architecture, Structural system (in Japanese).

NEHRP Consultants Joint Venture. (2012). *Selecting and Scaling Earthquake Ground Motions for Performing Response-History Analysis* (NIST GCR 11-917-15): Engineering Laboratory of the National Institute of Standards and Technology.

Nip, K. H., Gardner, L., Davies, C. M., & Elghazouli, A. Y. (2010). Extremely low cycle fatigue tests on structural carbon steel and stainless steel. *Journal of Constructional Steel Research, 66*(1), 96-110.

NRCC. (2010). National Building Code of Canada, 13th ed. Ottawa, ON.: National Research Council Canada, Institute for Research in Construction.

Ohji, K., Miller, W. R., & Marin, J. (1966). Cumulative Damage and Effect of Mean Strain in Low-Cycle Fatigue of a 2024-T351 Aluminum Alloy. *Journal of Basic Engineering, 88*(4), 801-810.

Palazzo, G., López-Almansa, F., Cahís, X., & Crisafulli, F. (2009). A low-tech dissipative buckling restrained brace. Design, analysis, production and testing. *Engineering Structures, 31*(9), 2152-2161.

PEER. (2005). PEER Strong Ground Motion Database. Retrieved 27/03/2012, from http://peer.berkeley.edu/nga/

Pocheau, A., & Roman, B. (2004). Uniqueness of solutions for constrained Elastica. *Physica D: Nonlinear Phenomena, 192*(3–4), 161-186.

Prakash, V., & Powell, G. H. (1988). DRAIN-2DX: Static and Dynamic Analysis of Inelastic Plane Structures. Berekley, California: University of California, Earthquake Engineering Research Center.

Rathje, E. M., Abrahamson, N. A., & Bray, J. D. (1998). Simplified frequency content estimates of earthquake ground motions. *Journal of Geotechnical and Geoenvironmental Engineering, 124*(2), 150-159.

Rathje, E. M., Faraj, F., Russell, S., & Bray, J. D. (2004). Empirical Relationships for Frequency Content Parameters of Earthquake Ground Motions. *Earthquake Spectra, 20*(1), 119-144.

Razavi Tabatabaei, S. A., Mirghaderi, S. R., & Hosseini, A. (2014). Experimental and numerical developing of reduced length buckling-restrained braces. *Engineering Structures, 77*, 143-160.

Richards, P. W., & Uang, C.-M. (2006). Testing Protocol for Short Links in Eccentrically Braced Frames. *Journal of Structural Engineering, 132*(8), 1183-1191.

Riddell, R. (2007). On Ground Motion Intensity Indices. *Earthquake Spectra, 23*(1), 147-173.

Rizzo, P. C., Shaw, D. E., & Jarecki, S. J. (1975). Development of real/synthetic time histories to match smooth design spectra. *Nuclear Engineering and Design, 32*(1), 148-155.

Rossi, P. P. (2015). Importance of Isotropic Hardening in the Modeling of Buckling Restrained Braces. *Journal of Structural Engineering, 141*(4), 1-11.

Ruiz-García, J., & Miranda, E. (2006). Residual displacement ratios for assessment of existing structures. *Earthquake Engineering & Structural Dynamics, 35*(3), 315-336.

Sabelli, R. (2001). *Research on Improving the Design and Analysis of Earthquake-resistant Steel-braced Frames* (The 2000 NEHRP Professional Fellowship Report). Oakland, California: Earthquake Engineering Research Institute.

Sabelli, R. (2004). Recommended Provisions for Buckling-Restrained Braced Frames. *Engineering Journal - American Institute of Steel Construction, 41*, 155-176.

Sabelli, R., Mahin, S., & Chang, C. (2003). Seismic demands on steel braced frame buildings with buckling-restrained braces. *Engineering Structures, 25*(5), 655-666.

Sahoo, D. R., & Chao, S.-H. (2010). Performance-based plastic design method for buckling-restrained braced frames. *Engineering Structures, 32*(9), 2950-2958.

Samyn, P., De Baets, P., Schoukens, G., & Van Peteghem, A. P. (2006). Large-scale tests on friction and wear of engineering polymers for material selection in highly loaded sliding systems. *Materials & Design, 27*(7), 535-555.

Shimizu, T., Fujisawa, K., Uemura, k., & Inoue, k. (1997). Design Method to Prevent Bucking of Low Yield Strength Steel Tube Brace and Fracturing of Joints : Part 1 Design Method and Test Plan of Braced Braces. *Summaries of technical papers of Annual Meeting Architectural Institute of Japan. C-1, Structures III, Timber structures steel structures steel reinforced concrete structures, 1997*, 781-782.

Shimizu, T., Fujisawa, K., Uemura, K., & Kinoshita, R. (2001). Study on Hysteresis Behavior of Double Tube Steel Bracing : Part 2 Plan of Cyclic Loading Test of Double Tube Steel Bracing. *Summaries of technical papers of Annual Meeting Architectural Institute of Japan. C-1, Structures III, Timber structures steel structures steel reinforced concrete structures, 2001*, 671-672 (in Japanese).

Shome, N., & Cornell, A. C. (1998). *Normalization and Scaling Accelerograms for Nonlinear Structural Analysis.* Paper presented at the 6th U.S. National Conference on Earthquake Engineering, Seattle, Washington.

SIMULIA Inc. (2012). *ABAQUS Analysis User's Manual Version 6.12-1*.

Stephens, R. I., Fatemi, A., Stephens, R. R., & Fuchs, H. O. (2000). *Metal fatigue in engineering*: John Wiley & Sons.

Stephens, R. I., Lee, S. G., & Lee, H. W. (1982). Constant and variable amplitude fatigue behavior and fracture of A572 steel at 25°C(77°F) and −45°C(−50°F). *International Journal of Fracture, 19*(2), 83-98.

Suzuki, N., Kouno, R., Higashibata, Y., Sasaki, T., & Segawa, T. (1994). *Experimental Study on the H-Section Steel Brace Encased in RC or Steel Tube.* Paper presented at the Summaries of technical papers of Annual Meeting Architectural Institute of Japan. C-1, Structures III, Timber structures steel structures steel reinforced concrete structures (in Japanese).

Tada, M., Kuwahara, S., Yoneyama, T., & Imai, K. (1993). Horizontally Loading Test of the Steel Frame Braced With Double-Tube Members. *Journal of Constructional Steel, 1*, 203-208 (in Japanese).

Tadokoro, A., Midorikawa, M., Murai, M., & Iwata, M. (2009). Experimental Study on Buckling-Restrained Braces Using Steel Mortar Planks. *Journal of Structural and Construction Engineering (Transactions of AIJ), 74*(641), 1363-1369 (in Japanese).

Taheri, F., Trask, D., & Pegg, N. (2003). Experimental and analytical investigation of fatigue characteristics of 350WT steel under constant and variable amplitude loadings. *Marine*

Structures, 16(1), 69-91.

Takeuchi, T., Ozaki, H., Matsui, R., & Sutcu, F. (2014). Out-of-plane stability of buckling-restrained braces including moment transfer capacity. *Earthquake Engineering & Structural Dynamics, 43*(6), 851-869.

Tang, X., & Goel, S. C. (1987). *Seismic analysis and design considerations of braced steel structures* (Research Report UMCE 87-4). Ann Arbor, MI: Department of Civil Engineering, University of Michigan.

Tateishi, K., Hanji, T., & Minami, K. (2007). A prediction model for extremely low cycle fatigue strength of structural steel. *International Journal of Fatigue, 29*(5), 887-896.

Tehrani, P., Goda, K., Mitchell, D., Atkinson, G. M., & Chouinard, L. E. (2014). Effects of Different Record Selection Methods on the Transverse Seismic Response of a Bridge in South Western British Columbia. *Journal of Earthquake Engineering, 18*(4), 611-636.

Thorp, J. M. (1986). Tribological Properties of Selected Polymeric Matrix Composites against Steel Surface. In K. Friedrich (Ed.), *Friction and wear of polymer composites* (2 ed., Vol. 1, pp. 89-134): Elsevier.

Tremblay, R. (2003). Achieving a Stable Inelastic Seismic Response for Multi-Story Concentrically Braced Steel Frames. *Engineering Journal - American Institute of Steel Construction, 40*(2003), 111-129.

Tremblay, R. (2005). Fundamental Periods of Vibration of Braced Steel Frames for Seismic Design. *Earthquake Spectra, 21*(3), 833-860.

Tremblay, R., & Atkinson, G. M. (2001). Comparative Study of the Inelastic Seismic Demand of Eastern and Western Canadian Sites. *Earthquake Spectra, 17*(2), 333-358.

Tremblay, R., Bolduc, P., Neville, R., & DeVall, R. (2006). Seismic testing and performance of buckling-restrained bracing systems. *Canadian Journal of Civil Engineering, 33*(2), 183-198.

Tremblay, R., & Bouatay, N. (2002). *Loading Protocols for the Seismic Testing of Ductile Bracing Members in Concentrically Braced Steel Frames.* Paper presented at the 12th European Conference on Earthquake Engineering, London, UK.

Tremblay, R., Degrange, G., & Blouin, J. (1999). *Seismic Rehabilitation of a Four-Storey Building with a Stiffened Bracing System.* Paper presented at the 8th Canadian Conference on Earthquake Engineering, Vancouver, BC, Canada.

Tremblay, R., Dehghani, M., Fahnestock, L. A., Herrera, R., Canales, M., Clifton, C., & Hamid, Z. (2016). Comparison of seismic design provisions for buckling restrained braced frames in Canada, United States, Chile, and New Zealand. *Structures, 8 - Part 2*, 183-196.

Tremblay, R., Filiatrault, A., Bruneau, M., Nakashima, M., Prion, H. G. L., & DeVall, R. (1996). Seismic design of steel buildings: lessons from the 1995 Hyogo-ken Nanbu earthquake. *Canadian Journal of Civil Engineering, 23*(3), 727-756.

Tremblay, R., Filiatrault, A., Timler, P., & Bruneau, M. (1995). Performance of steel structures during the 1994 Northridge earthquake. *Canadian Journal of Civil Engineering, 22*(2), 338-360.

Tremblay, R., Lacerte, M., & Christopoulos, C. (2008). Seismic Response of Multistory Buildings with Self-Centering Energy Dissipative Steel Braces. *Journal of Structural Engineering, 134*(1), 108-120.

Tremblay, R., & Merzouq, S. (2004). *Dual buckling restrained braced steel frames for enhanced seismic response.* Paper presented at the Japan Passive Control Symposium, Yokohama, Japan.

Tremblay, R., & Poncet, L. (2005). Seismic Performance of Concentrically Braced Steel Frames

in Multistory Buildings with Mass Irregularity. *Journal of Structural Engineering, 131*(9), 1363-1375.

Tremblay, R., & Poncet, L. (2007). Improving the Seismic Stability of Concentrically Braced Steel Frames. *Engineering Journal - American Institute of Steel Construction, 2007*(2), 103-116.

Tsai, C. S., Lin, Y. C., Chen, W. S., & Su, H. C. (2009). Mathematical modeling and full-scale shaking table tests for multi-curve buckling restrained braces. *Earthquake Engineering and Engineering Vibration, 8*(3), 359-371.

Tsai, K.-C., Hsiao, P.-C., Wang, K.-J., Weng, Y.-T., Lin, M.-L., Lin, K.-C., Chen, C.-H., Lai, J.-W., & Lin, S.-L. (2008). Pseudo-dynamic tests of a full-scale CFT/BRB frame - Part I: Specimen design, experiment and analysis. *Earthquake Engineering & Structural Dynamics, 37*(7), 1081-1098.

Tsai, K.-C., Lai, J.-W., Hwang, Y.-C., Lin, S.-L., & Weng, C.-H. (2004). *Research and application of Double-Core Buckling Restrained Braces in Taiwan.* Paper presented at the 13th World Conference on Earthqauke Engineering, Vancouver, Canada.

Tsai, K.-C., Wu, A.-C., Wei, C.-Y., Lin, P.-C., Chuang, M.-C., & Yu, Y.-J. (2014). Welded end-slot connection and debonding layers for buckling-restrained braces. *Earthquake Engineering & Structural Dynamics, 43*(12), 1785–1807.

Tzaros, K. A., & Mistakidis, E. S. (2011). The unilateral contact buckling problem of continuous beams in the presence of initial geometric imperfections: An analytical approach based on the theory of elastic stability. *International Journal of Non-Linear Mechanics, 46*(9), 1265-1274.

Uang, C.-M., & Nakashima, M. (2004). Steel Buckling-Restrained Braced Frames. In Y. Bozorgnia & V. V. Bertero (Eds.), *Earthquake Engineering From Engineering Seismology to Performance-Based Engineering*: CRC Press.

Uriz, P. (2005). *Towards earthquake resistant design of concentrically braced steel structures.* PhD Dissertation, University of California, Berkeley, Berkeley, California.

Usami, T., Ge, H., & Kasai, A. (2008). *Overall buckling prevention condition of buckling restrained Braces as a structural control damper.* Paper presented at the 14th World Conference on Earthquake Engineering, Beijing, China.

Usami, T., Ge, H., & Luo, X.-Q. (2009a). *Experimental and analytical study on high-performance Buckling Restrained Brace dampers for bridge engineering.* Paper presented at the 3rd International Conference on Advances in Experimental Structural Engineering (AESE), San Francisco, California, USA.

Usami, T., Lu, Z., & Ge, H. (2005). A seismic upgrading method for steel arch bridges using buckling-restrained braces. *Earthquake Engineering & Structural Dynamics, 34*(4-5), 471-496.

Usami, T., Sato, T., & Kasai, A. (2009b). Developing high-performance buckling-restrained braces. *Kozo Kogaku Ronbunshu. A (Journal of Structural Engineering. A), 55A*, 719-729 (in Japanese).

Wada, A., & Nakashima, M. (2004). *From infancy to maturity of Buckling Restrained Braces research.* Paper presented at the 13th World Conference on Earthquake Engineering, Vancouver, Canada.

Wang, C.-L., Usami, T., & Funayama, J. (2012). Evaluating the influence of stoppers on the low-cycle fatigue properties of high-performance buckling-restrained braces. *Engineering Structures, 41*(2012), 167-176.

Watanabe, A., Hitomi, Y., Saeki, E., Wada, A., & Fujimoto, M. (1988). *Properties of brace encased in buckling-restraining concrete and steel tube.* Paper presented at the 9th World

Conference on Earthquake Engineering, Tokyo-Kyoto, Japan.
Watson-Lamprey, J., & Abrahamson, N. (2006). Selection of ground motion time series and limits on scaling. *Soil Dynamics and Earthquake Engineering, 26*(5), 477-482.
Wen, Y.-K. (1976). Method for random vibration of hysteretic systems. *Journal of the Engineering Mechanics Division, 102*(2), 249-263.
Wu, A.-C., Lin, P.-C., & Tsai, K.-C. (2014). High-mode buckling responses of buckling-restrained brace core plates. *Earthquake Engineering & Structural Dynamics, 43*(3), 375-393.
Wu, B., & Mei, Y. (2015). Buckling mechanism of steel core of buckling-restrained braces. *Journal of Constructional Steel Research, 107*, 61-69.
Wu, J., Liang, R. J., Wang, C. L., & Ge, H. B. (2012). Restrained Buckling Behavior of Core Component in Buckling-Restrained Braces. *Advanced Steel Construction, 8*(3), 212-225.
Xie, Q. (2005). State of the art of buckling-restrained braces in Asia. *Journal of Constructional Steel Research, 61*(6), 727-748.
Yasui, N., Imai, K., Fujisawa, K., Shimizu, T., Nakayama, N., Tabuchi, M., & Kaneko, H. (1996). *Low Cycle Fatigue Test on Low Yield Strength Steel Bracing : Part 2 Double Tube Steel Bracing.* Paper presented at the Summaries of technical papers of Annual Meeting Architectural Institute of Japan. C-1, Structures III, Timber structures steel structures steel reinforced concrete structures (in Japanese).
Ye, L., Ma, Q., Miao, Z., Guan, H., & Zhuge, Y. (2011). Numerical and comparative study of earthquake intensity indices in seismic analysis. *The Structural Design of Tall and Special Buildings, 22*(4), 326-381.
Youngs, R. R., Chiou, S.-J., Silva, W. J., & Humphrey, J. R. (1997). Strong Ground Motion Attenuation Relationships for Subduction Zone Earthquakes. *Seismological Research Letters, 68*(1), 58-73.
Zareian, F., & Krawinkler, H. (2007). Assessment of probability of collapse and design for collapse safety. *Earthquake Engineering & Structural Dynamics, 36*(13), 1901-1914.
Zareian, F., & Medina, R. A. (2010). A practical method for proper modeling of structural damping in inelastic plane structural systems. *Computers & Structures, 88*(1–2), 45-53.
Zayas, V. A., Mahin, S. A., & Popov, E. P. (1980). *Cyclic inelastic behavior of steel offshore structures* (UCB/EERC-80/27). Berkeley, California: Earthquake Engineering Research Center, University of California.
Zhao, J., Lin, F., & Wang, Z. (2016). Effect of non-moment braced frame seismic deformations on buckling-restrained brace end connection behavior: Theoretical analysis and subassemblage tests. *Earthquake Engineering & Structural Dynamics, 45*(3), 359-381.
Zhao, J., Wu, B., & Ou, J. (2010). *Experimental Study on the Seismic Behavior of a Novel Type of All-Steel Buckling-Restrained Braces.* Paper presented at the 9th U.S. National and 10th Canadian Conference on Earthquake Engineering, Toronto, Canada.
Zona, A., & Dall'Asta, A. (2012). Elastoplastic model for steel buckling-restrained braces. *Journal of Constructional Steel Research, 68*(1), 118-125.
Zsarnóczay, Á. (2013). *Experimental and Numerical Investigation of Buckling Restrained Braced Frames for Eurocode Conform Design Procedure Development.* Ph. D. Dissertation, Budapest University of Technology and Economics, Budapest, Hungary.